



Theoretische Physik

# Minimal models for dark matter and neutrino masses

Inaugural-Dissertation  
zur Erlangung des Doktorgrades  
der Naturwissenschaften im Fachbereich Physik  
der Mathematisch-Naturwissenschaftlichen Fakultät  
der Westfälischen Wilhelms-Universität Münster

vorgelegt von  
**Sybrand Wessel Zeinstra**  
aus Stadskanaal

- 2021 -

---

Dekan:	Prof. Dr. Michael Rohlfing
Erster Gutachter:	Prof. Dr. Michael Klasen
Zweiter Gutachter:	Priv.-Doz. Dr. Karol Kovařík
Tag der mündlichen Prüfung:	.....
Tag der Promotion:	.....



# Abstract

The Standard Model is a successful theory that accurately describes elementary particles and their interactions, but even after the discovery of the Higgs boson, which completed the Standard Model, some open questions remain. The discovery of neutrino oscillations implies that neutrinos have a non-zero mass, contrary to the original Standard Model prediction, which does not provide a satisfactory explanation on the origin of neutrino masses. Moreover, the evidence of dark matter on many different length scales strongly favours weakly interactive massive particle (WIMP) dark matter, for which the Standard Model does not contain a suitable candidate.

Thus the answer to these questions should be sought in physics beyond the Standard Model. This work focuses on minimal radiative seesaw models, which have the attractive feature that they address both the issues of the Standard Model that were highlighted above. In order to keep the models simple, we look at minimal extensions of the Standard Model where only a small number of new fields is added to the Standard Model. We start by giving an overview on dark matter and neutrinos. First we discuss the evidence for dark matter, as well as several theories of dark matter that have been proposed, after which we describe the many dark matter detection experiments. Then the basics of neutrino physics are presented, focusing on neutrino oscillations, mechanisms for mass generation, as well as experiments measuring these properties.

Following the introductory chapters comes the main part of the thesis, in which the radiative seesaw models are treated. After presenting a general overview on the classification of these models, we study several models, for which we focus on different dark matter detection aspects. First, the scotogenic model is presented, for which we show the effects of the neutrino mass scale on model parameters related to dark matter. We find a clear relation between the scalar mass splitting, governed by  $\lambda_5$ , and the neutrino mass scale, showing the close relation between neutrino physics and dark matter phenomenology in our models. We also compare our results with the results of the KATRIN experiment, which has set an upper bound on the neutrino mass scale. Next we show how the ICECUBE neutrino telescope can be used to detect neutrino signals from annihilating dark matter in the interior of the Sun. We consider the detection prospects of these neutrinos in the context of the scotogenic and the T1-3-B  $\alpha = 0$  models, that contain different dark matter candidates. For the scotogenic model, we show that dark matter capture in the Sun through inelastic scattering can lead to large event rates that are on the order of  $10^3$  per year at the ICECUBE observatory, making

a dedicated analysis worthwhile. For the T1-3-B  $\alpha = 0$  model we show that indirect detection experiments can play an important role in detecting dark matter with spin dependent scattering interactions.

After this the focus moves to direct detection of dark matter in the XENON1T experiment through dark matter scattering off electrons instead of scattering off heavy nuclei, which is usually considered. We consider the SLIM (Scalar as Light as MeV) model containing a dark matter candidate in the MeV to GeV range, but find that its scattering cross section is too low to detect. Additionally, we calculate an upper limit on the electron recoil cross section for a realistic recoil energy threshold. The  $^{222}\text{Rn}$  isotope is the largest background in the XENON1T experiment, and the next chapter is about the measurement of  $^{220}\text{Rn}$  decays in gaseous xenon. We find that the observed signals match correspond to the  $\alpha$  decays in the  $^{220}\text{Rn}$  decay chain.

The last part of the thesis is sort of an outlook, where extensions of the Standard Model gauge group with a local  $U(1)$  symmetry are considered. For this extension an overview of possible radiative seesaw models is systematically derived and presented. We also discuss how our models differ from similar models in the literature, and how the models we obtain could be embedded in grand unifying theories. Furthermore, new phenomenological aspects related to the  $U(1)_X$  extension, such as a  $Z'$  boson are discussed. Then the detection prospects at the LHC of a heavy singlet scalar in a model with a local  $U(1)_{B-L}$  are presented, for which discovery at the HL-LHC is possible up to a mass of around 1 TeV.

## Kurzfassung

Das Standardmodell ist eine erfolgreiche Theorie die eine präzise Beschreibung von Elementarteilchen und deren Wechselwirkungen bietet. Jedoch gibt es nach der Entdeckung des Higgsbosons, welche das Standardmodell vervollständigte, immer noch offene Fragen. Die Entdeckung der Neutrinooszillationen deutet darauf hin, dass Neutrinos, im Gegensatz zur Vorhersage des ursprünglichen Standardmodells, keine massenlose Teilchen sind. Es gibt im Standardmodell keine befriedigende Erklärung um Neutrinomassen zu erzeugen. Außerdem gibt es auf mehreren verschiedenen Längenskalen Hinweise für dunkle Materie, in der Form eines *weakly interactive massive particle* (WIMPs), wozu es im Standardmodell keinen geeigneten Kandidaten gibt.

Um diese offenen Fragen zu lösen, ist es deshalb notwendig neue Physik jenseits des Standardmodells zu betrachten. In dieser Arbeit liegt der Fokus daher auf minimalen *radiative seesaw* Modellen, die Neutrinophysik und dunkle Materie mit einander verknüpfen, und so eine Lösung zu den offenen Fragen bieten. Das Minimale bezieht sich darauf, dass man versucht die Modelle einfach zu halten in dem man nur wenige neue Felder dem Standardmodell hinzufügt. Wir fangen mit einem Überblick über dunkle Materie an, in dem wir zuerst die Hinweise für dunkle Materie, sowie verschiedene Theorien die zu Erklärung dunklerer Materie vorgeschlagen wurden besprechen. Danach werden die vielen Experimenten um dunkle Materie nachzuweisen diskutiert. Das darauffolgende Kapitel enthält eine Einleitung in die Neutrinophysik, mit einem Fokus auf Neutrinooszillationen und Mechanismen um Neutrinomassen zu erzeugen, inklusive der Experimente zu diesen Phänomenen.

Danach fängt das Hauptteil dieser Arbeit an, das sich auf *radiative seesaw* Modelle bezieht. Nach einer allgemeinen Einführung wo eine generelle Klassifizierung dieser Modelle aufgeführt wird, werden verschiedene Modelle genauer untersucht, wobei der Fokus auf jeweils unterschiedliche Aspekte zur Detektion dunkler Materie liegt. Als Erstes wird das *scotogenic model* betrachtet. Wir zeigen den Einfluss der absoluten Neutrinomassenskala, auf die das KATRIN-Experiment eine obere Grenze gesetzt hat, auf die Parameter für dunkle Materie in diesem Modell. Wir zeigen, dass die Neutrinophysik und die Phänomenologie dunkler Materie in unseren Modellen sehr stark verknüpft sind. Als nächstes wird indirekte Detektion dunkler Materie betrachtet. Wir zeigen wie der ICECUBE Neutrinooteleskop benutzt werden kann um Neutrinosignale erzeugt von annihilierender dunkler Materie aus dem Inneren der Sonne zu detektieren. Dazu werden sowohl das *scotogenic model* als das T1-3-B  $\alpha = 0$  Modell als Ausgangspunkt genommen, da sie verschiedene Arten dunkler Materie enthalten. Für das *scotogenic model* finden wir, dass das Einfangen von dunkler Materie in der Sonne durch

inelastische Streuprozesse zu einer Eventrate in der Größenordnung von  $10^3$  Events pro Jahr in ICECUBE führen kann, was eine spezifische Analyse dazu lohnend macht. Für das T1-3-B  $\alpha = 0$  Modell zeigen wir, dass Experimente zur indirekten Detektion eine wichtige Rolle spielen können um dunkle Materie mit spinunabhängige Streuprozesse zu detektieren.

Das nächste Teil der Arbeit betrifft direkte Detektion mit dem XENON1T-Experiment. Wir betrachten das SLIM-Modell (*Scalar as Light as MeV*), wofür wir den Wirkungsquerschnitt für die Streuung dunkler Materie mit einer Masse im MeV- bis GeV-Bereich an Elektronen, statt wie üblich an schweren Atomkernen, berechnen. Wir finden jedoch, dass die Wirkungsquerschnitt dazu zu niedrig, und somit undetektierbar ist. Auch wird eine obere Schranke auf den Wirkungsquerschnitt für Streuung an Elektronen im Fall einer realistischen unteren Schranke für die Rückstoßenergie hergeleitet. Das Isotop  $^{222}\text{Rn}$  trägt am meisten zu dem Hintergrund des XENON1T-Experiments bei und das nächste Kapitel bezieht sich auf eine Messung von  $^{220}\text{Rn}$  in gasförmigem Xenon. Wir finden klare Hinweise, dass die gemessene Signale mit den  $\alpha$ -Zerfälle aus der Zerfallskette von  $^{220}\text{Rn}$  übereinstimmen.

Das letzte Thema bietet einen Ausblick, in dem die Eichgruppe des Standardmodells um eine lokale  $U(1)$ -Symmetrie erweitert wird. Für diese Erweiterung wird systematisch einen Überblick über die neuen Modelle hergeleitet und gezeigt. Dazu diskutieren wir wie unsere Modelle von ähnlichen Modellen in der Literatur abweichen, und wie sie in eine große vereinheitlichte Theorie eingebettet werden können. Außerdem betrachten wir die neuen phänomenologischen Aspekten der  $U(1)_X$ -Erweiterung, darunter das neue  $Z'$ -Boson. Als letztes werden die Entdeckungsmöglichkeiten eines schweren skalaren Singulets in einem Modell mit einer lokalen  $U(1)_{B-L}$  am LHC gezeigt. Eine Entdeckung am HL-LHC ist bis einer Masse von etwa 1 TeV möglich.

## Publications

- D. Camargo, M. Klasen, SZ. “Discovering heavy  $U(1)$ -gauged Higgs bosons at the HL-LHC”. In: *J.Phys.G* 48 (2020) 2, 025002. arXiv:1903.02572 [hep-ph].
- J. Fiaschi, M. Klasen, M. Vargas, C. Weinheimer, SZ. “MeV neutrino dark matter: Relic density, lepton flavour violation and electron recoil”. In: *JHEP* 11 (2019) 129. arXiv:1908.09882 [hep-ph].
- T. de Boer, M. Klasen, C. Rodenbeck, SZ. “Absolute neutrino mass as the missing link to the dark sector”. In: *Phys.Rev.D* 102 (2020) 5, 051702. arXiv:2007.05338 [hep-ph].
- T. de Boer, R. Busse, A. Kappes, M. Klasen, SZ. “New constraints on radiative seesaw models from IceCube and other neutrino detectors”. In: *Phys.Rev.D* 103 (2021) 12, 123006. arXiv:2103.06881 [hep-ph].
- T. de Boer, R. Busse, A. Kappes, M. Klasen, SZ. “Indirect detection constraints on the scotogenic dark matter model”. In: *JCAP* 08 (2021) 038. arXiv:2105.04899 [hep-ph].
- T. de Boer, M. Klasen, SZ. “Anomaly-free dark matter models with one-loop neutrino masses and a gauged  $U(1)$  symmetry”. *In preparation*.



# Acknowledgements

I would like to thank the people who supported me in my work on this thesis. First, my thanks go out to my supervisor Michael Klasen, whose extensive knowledge of my area of research, as well as related topics was of great help. The discussions we had contributed greatly to my understanding of physics. Furthermore my thanks go out to Thede de Boer, with whom I worked closely together, for the great atmosphere in the office and the very enjoyable collaboration we had.

Next I would like to thank Christian Weinheimer for giving me the opportunity to do a project in his group. I am grateful for his time and the conversations we had. Also I would like to thank Lutz Althüser and Christian Wittweg for the joint lab work, as well as the advice they offered me.

Furthermore I want to thank Juri Fiaschi, Alexander Kappes, Raffaella Busse, Miguel Vargas, Daniel Camargo, and Caroline Rodenbeck for the collaboration on certain projects and their knowledge on amongst other the experiments they are involved in.

Finally my thanks go out to the other members at the institute for the great time I had at the institute. Thank you, Marthijn Sunder, Laura Moreno Valero, Karol Kovařík, Johannes Branahl, Peter Risse, Pia Petrak, Amin Aboubrahim, Daniel Schwartländer, and Saskia Schmiemann.





# Contents

<b>1</b>	<b>Introduction</b>	<b>1</b>
<b>2</b>	<b>The basics of dark matter</b>	<b>3</b>
2.1	Observations of DM . . . . .	3
2.2	Theoretical motivation . . . . .	13
2.3	DM detection . . . . .	20
<b>3</b>	<b>Neutrino physics</b>	<b>43</b>
3.1	Neutrino oscillations . . . . .	44
3.2	Neutrino mass . . . . .	51
<b>4</b>	<b>Radiative seesaw models</b>	<b>59</b>
4.1	Classification . . . . .	59
<b>5</b>	<b>The effects of the absolute neutrino mass on the scotogenic model</b>	<b>65</b>
5.1	Introduction . . . . .	65
5.2	Properties of the model . . . . .	66
5.3	Experimental constraints . . . . .	69
5.4	Numerical scan . . . . .	70
5.5	Summary and outlook . . . . .	78
<b>6</b>	<b>Indirect detection of neutrino signals from scotogenic DM with IceCube</b>	<b>83</b>
6.1	Introduction . . . . .	83
6.2	WIMP capture in the Sun . . . . .	84
6.3	Detection of neutrino signals of elastic and inelastic DM annihilations in the Sun with ICECUBE . . . . .	91
6.4	Numerical scan . . . . .	94
6.5	Conclusion . . . . .	107
<b>7</b>	<b>Indirect detection constraints on the T1-3-B model from IceCube</b>	<b>109</b>
7.1	Introduction . . . . .	109
7.2	Model description . . . . .	109
7.3	Scattering processes . . . . .	112
7.4	Neutrino detection at IceCube . . . . .	117
7.5	Numerical results . . . . .	117
7.6	Conclusion . . . . .	125

<b>8</b>	<b>Electron recoil with MeV neutrino dark matter</b>	<b>127</b>
8.1	Model description . . . . .	128
8.2	Collider, cosmological and neutrino constraints . . . . .	130
8.3	Relic density . . . . .	133
8.4	Lepton flavour violation . . . . .	136
8.5	Electron recoil cross section and experimental sensitivity . . . . .	138
8.6	Experimental sensitivities . . . . .	141
8.7	Conclusion . . . . .	144
<b>9</b>	<b>Measurement of <math>^{220}\text{Rn}</math> decays in gaseous xenon</b>	<b>149</b>
9.1	Setup . . . . .	149
9.2	Gain calibration . . . . .	153
9.3	Measurement setup . . . . .	157
9.4	Results . . . . .	160
9.5	Discussion of the results . . . . .	180
9.6	Outlook . . . . .	181
<b>10</b>	<b>Extending the SM gauge group with a local U(1) symmetry</b>	<b>183</b>
10.1	One-loop classification of models with a local U(1) symmetry . . . . .	184
10.2	Comparison to other U(1) models . . . . .	200
10.3	Z' phenomenology . . . . .	201
10.4	Higgs sector . . . . .	210
10.5	Grand unification . . . . .	212
10.6	Conclusion . . . . .	223
<b>11</b>	<b>The discovery potential of U(1)-gauged heavy Higgs bosons at the LHC</b>	<b>225</b>
11.1	Model description . . . . .	225
11.2	LHC phenomenology . . . . .	233
11.3	Conclusion . . . . .	238
<b>12</b>	<b>Conclusion and outlook</b>	<b>239</b>
<b>A</b>	<b>Gain calibration</b>	<b>241</b>
	<b>Bibliography</b>	<b>245</b>

# 1 Introduction

From many observations over a large mass range, there is overwhelming evidence that the universe contains a large amount of matter that is unknown to us. It has not been directly observed by us, thus rightfully obtaining the name dark matter (DM). The effects of its presence manifest itself through gravity from the cosmologically small scale of our Milky Way, to the large-scale structure of the universe. It is not only present today, but it has left its fingerprint on the Cosmic Microwave Background (CMB) from the very early universe. However, even though the amount of dark matter has been precisely determined, its exact nature remains yet unknown. The sort of particle that would provide a good explanation for the cosmological observations is a Weakly Interactive Massive Particle (WIMP). With a mass in the GeV to TeV range and a coupling strength on the order of the weak interaction, WIMPs can be generated in the right amounts during the early stages of the universe.

This is where particle physics comes into play. The Standard Model (SM) of particle physics describes the properties and interactions of the elementary particles and has been very successful in doing so. The fermions of the SM consist of three generations of quarks, out of which protons, neutrons, or other composite particles such as mesons are made up. Then there are three generations of leptons, consisting of the electrons and its heavier brothers the muon and the tau, as well as three generations of the elusive neutrino, which interact only very little with matter. The SM can also successfully describe the fundamental interactions, which are mediated by the gauge bosons. The gauge bosons originate from the  $SU(3)_C \times SU(2)_L \times U(1)_Y$  gauge symmetry structure that underlies the theory. The  $SU(3)_C$  corresponds to the eight gluons mediating the strong nuclear force, and the  $SU(2)_L \times U(1)_Y$  part corresponds to the unified description of the electromagnetic and weak nuclear forces, called electroweak. It gives rise to the  $W^\pm$ - and  $Z$ -bosons, as well as the photon. Finally, there is the particle that is the keystone to the whole SM, the Higgs boson, which was discovered in 2012 by the Large Hadron Collider (LHC) experiments ATLAS [1] and CMS [2]. The masses of the SM particles are generated through electroweak symmetry breaking (EWSB), in which the Higgs field obtains a non-zero vacuum expectation value (vev). Only three kinds of particles remain massless, the photon and the gluons, for which the respective electromagnetic  $U(1)_Q$  and  $SU(3)_C$  QCD gauge symmetries remain unbroken, and the neutrinos, which are not excused by any symmetry. The neutrinos do not obtain a mass through the Higgs mechanism, as neutrinos in the SM are purely left-handed and no right-handed neutrinos exist within the SM. However, there is a stark contradiction with observations, as the measurement of neutrino oscillations implies that there exist at least two generations of massive neutrinos. The existence of neutrino masses is thus a clear indication of beyond the Standard Model (BSM) physics.

If dark matter consists of particles, then the SM has no suitable candidate fulfilling all necessary criteria. Thus one also needs to extend the SM by introducing new particles, for which many different models have been proposed. One of the well-known theories is Supersymmetry, which pairs the SM fermions to their supersymmetric bosonic partners and vice versa and naturally contains a WIMP-like dark matter candidate. Chapter 2 will give an overview of the evidence for dark matter, as well as different theories that have been proposed. We will also discuss the various experiments that are undertaken to detect dark matter. This is followed by Chapter 3, which goes into further detail about neutrino oscillations, experiments, and mechanisms to generate neutrino masses.

In Chapter 4 we will make the connection between the mystery about the origin of neutrino masses and the nature of dark matter and introduce the class of radiative seesaw models. These are minimal models, which extend the SM only by a small amount of particles, but at the same time can already yield interesting new phenomenology. In these models, neutrino masses are generated at the one-loop level through interactions with the newly added particles. This will be the main focus for the rest of the thesis.

We will consider several radiative seesaw models, and study phenomenological aspects that are inherent to these models. Chapter 5 focusses on the effects of the absolute neutrino mass scale on the scotogenic model. The next chapters will consider indirect detection possibilities of neutrino signals from annihilating dark matter inside the Sun, for the scotogenic model and the T1-3-B  $\alpha = 0$  models in Chapters 6 and 7 respectively. Then we move on with direct detection in Chapter 8, in particular electron recoil in the XENON1T experiment. Chapter 9 is less theoretical in nature and is about the measurement of radon decays in xenon gas, which is the main background in the XENON1T experiment.

After this we will shift gears and move further beyond the SM by extending the SM gauge group with an extra  $U(1)$  symmetry, which introduces a new gauge boson, the  $Z'$ . In Chapter 10 we will present a systematic overview of radiative seesaw models with an additional local  $U(1)$ , and give an overview of new phenomenology in these models. We also briefly touch upon grand unifying theories that describe SM interactions in a unified way. Chapter 11 considers collider searches by the Large Hadron Collider (LHC) for heavy scalars in a model in which the baryon number  $B$  minus the lepton number  $L$  is promoted to a local  $U(1)_{B-L}$  symmetry.

## 2 The basics of dark matter

Before we directly dive into the specific class of radiative seesaw models, it is wise to take a step back and start by discussing several aspects of dark matter in general. In this chapter we will begin by introducing historical development and the well-known (cosmological) evidences for the existence of dark matter. In the next part we will shift to a theorist's perspective and discuss different candidates for dark matter that have been proposed, their properties, as well as their (theoretical) motivation. The production of dark matter is also described. The last part of the chapter will be devoted to the experimental efforts that are undertaken in order to detect dark matter. Here we will discuss different detection methods, the experiments involved, and compare the results of different experiments.

### 2.1 Observations of DM

The start of the 20th century saw great advances in the field of astronomy, and it did not take long for unexpected observations to show up. In 1922, Jacobus Kapteyn observed stellar velocities inside the Milky Way which he could explain through the presence of non-luminous masses, which he dubbed dark matter [3]. Observations on galactic stellar motions by Jan Oort further supported this hypothesis [4]. However, these observations were tentative, and the usual example of the first observation of the effects of dark matter is by the Coma cluster observations of Fritz Zwicky [5]. Based on the virial theorem, which in this case relates the kinetic energy of galaxies in the cluster to the gravitational potential, Zwicky found that the galaxies moved too fast to be bound to the cluster based on the amount of luminous matter meaning there must be an additional source of mass. It must be noted that the concept of dark matter was different in those days compared to the usual current understanding that we will discuss later on in this chapter. To them it was just ordinary matter they could not observe, e.g. due to it being too faint. Next to this initial evidence, the presence of dark matter can be deduced from several other sources at different length scales. We will now give an overview of some of these evidences.

#### 2.1.1 Galactic rotation curves

Instead of observing galaxies in clusters, one can also observe the rotational velocities of stars inside galaxies. For this purpose one can use the relation from Newtonian dynamic for the orbital velocity

$$v = \sqrt{\frac{GM(r)}{r}}, \quad (2.1)$$

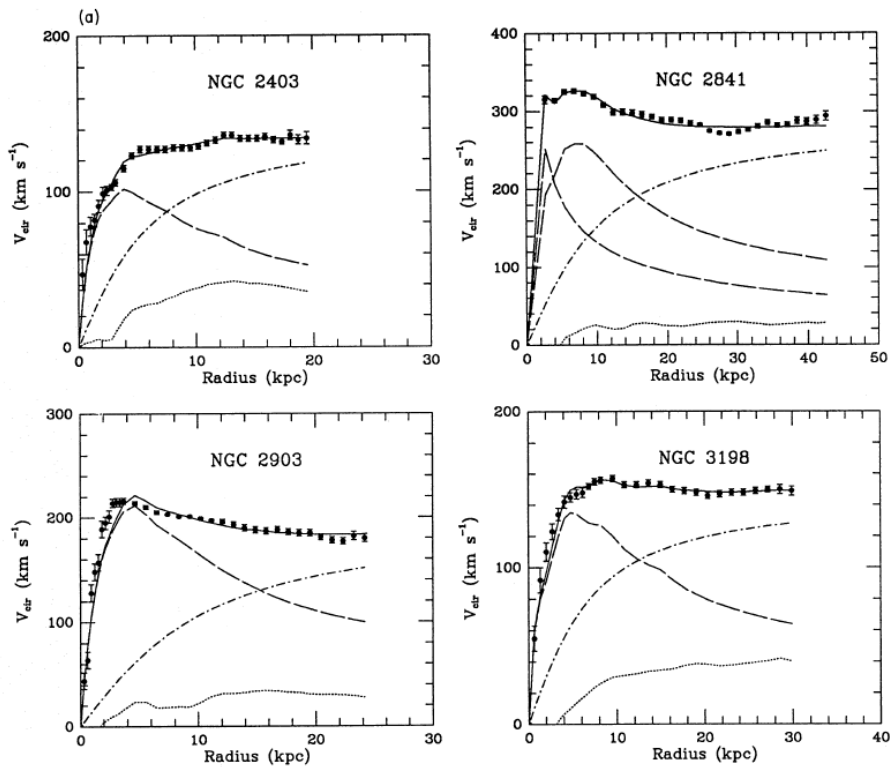


Figure 2.1: Rotation curves of several galaxies, also showing the rotation curves of the individual galactic components. The dashed curves are for visible matter, the dotted curves for gas, and the dashed-dotted lines for the dark halo. Image taken from: [6].

which depends on the mass  $M(r)$  that is enclosed within the radius of orbit  $r$ . As one moves further away from the centers of spiral galaxies, most of the luminous mass of the galaxy will lie within the orbit and  $M(r)$  will be relatively constant from that point on. Moving further outward, the rotational velocity should decrease with

$$v \propto \frac{1}{\sqrt{r}}, \quad (2.2)$$

based on the Newtonian relation. However, Vera Rubin and Kent Ford Jr. measured the rotation curves of several galaxies and found that the rotational increases at first when one moves away from the galactic center, but instead of decreasing when moving further outwards, it stays constant [7]. This is illustrated by Figure 2.1 which shows the rotational velocity of four galaxies as a function of their radii [6]. This discrepancy can be solved if one assumes that there exists a halo of non-luminous massive particles or objects around the galaxy, which is indicated by the dashed-dotted lines. This dark halo does not interact directly with the galaxy, except through its gravitational effects, and should extend further outwards compared to the luminous matter. In such a scenario the contribution of the halo results in a constant rotation velocity in the outer regions of the galaxy.

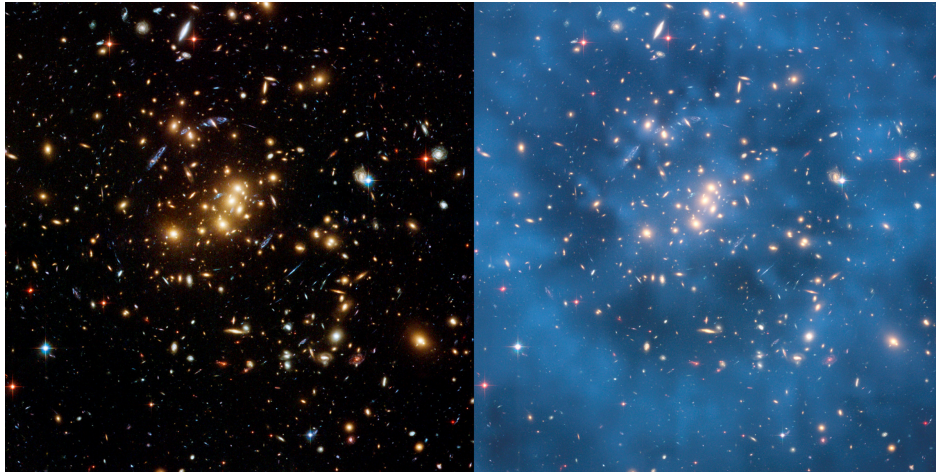


Figure 2.2: Observation of the galaxy cluster Cl 0024+17 by the Hubble Space Telescope [9] showing the gravitational lensing. The images are the same, but on the right the mass distribution in the cluster has been overlaid. Image source: <https://hubblesite.org/contents/news-releases/2007/news-2007-17.html>.

Of course, another explanation for these rotation curves can be that our understanding of gravity is wrong. For this reason the theory of modified Newtonian dynamics (MOND) has been proposed [8]. In MOND, the acceleration of an object is modified, so that Newton's second law reads

$$\mathbf{F} = m\mu(a/a_0)\mathbf{a}, \quad (2.3)$$

depending on a constant  $a_0$  with units of acceleration.  $\mu(x)$  with  $x = a/a_0$  is a function such that in the limit for large accelerations (such as those on Earth)  $\mu(x \gg 1) \approx 1$ , and the laws of Newtonian mechanics are obtained. However, for small acceleration  $\mu(x \ll 1) \approx x$ , which has as a consequence that the rotational velocity becomes independent of the radius. Though MOND can provide an accurate description for the galactic rotation curves, it fails to provide a suitable description for other phenomena that can be explained by DM, hence we will not consider it further.

### 2.1.2 Gravitational lensing

Since dark matter interacts gravitationally, light passing through regions containing dark matter haloes will be deflected following general relativity. This provides astronomers with another tool to probe dark matter, because light travelling from a light source to the Earth can be distorted by galaxies or galaxy clusters containing dark matter in the foreground. The original galaxy can appear slightly more elliptical if the effects are small, but in more extreme cases can be ring-shaped, or even multiple images of the galaxy can appear. This phenomenon is called gravitational lensing.

The effects of gravitational lensing are shown in Figure 2.2 for the galaxy cluster Cl 0024+17 as observed by the Hubble Space Telescope [9]. It is located at a distance of 5 billion light-years, and spans 2.6 million light-years across. This particular cluster is an interesting case,

as a circular distortion of background galaxies can be seen in the left image. On the right the mass distribution of the cluster has been overlaid on the original image. Because the matter density in the cluster fluctuates, the effects of gravitational lensing vary throughout the image. In particular, a ring-like shape is visible on the left, which matches with the higher-density ring in the right image. This peculiar shape was caused by the collision of two previous clusters 1 to 2 billion years ago, creating a ripple of dark matter.

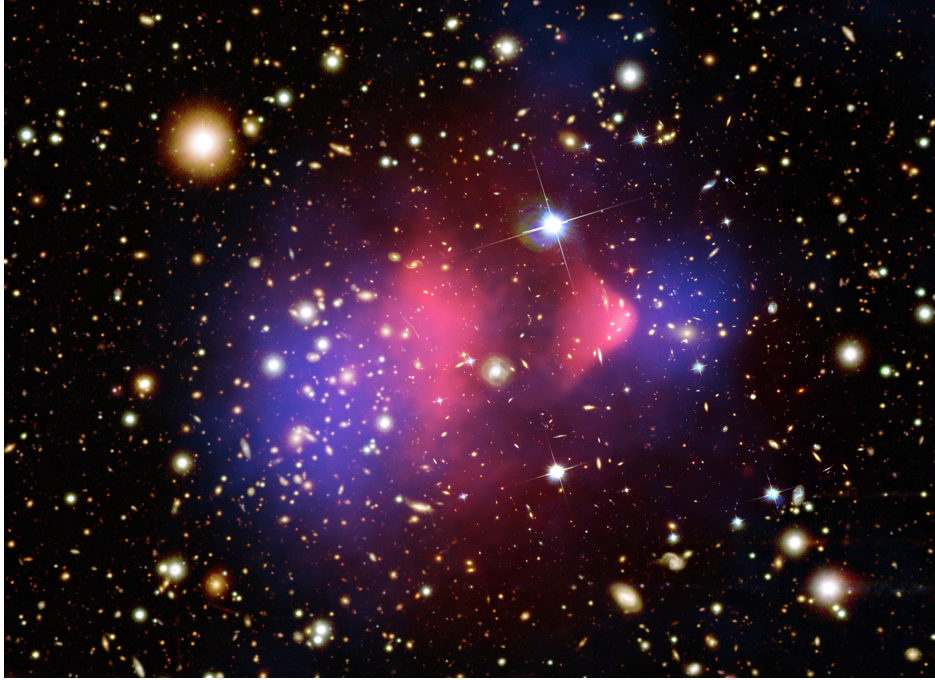


Figure 2.3: Observation of the Bullet Cluster. On top of the optical image that was taken by Magellan and the Hubble Space Telescope, the CHANDRA X-ray observations are shown by the pink cloud. The blue clouds indicate the matter distribution based on gravitational lensing. Image source: <https://chandra.harvard.edu/photo/2006/1e0657/>

More of such remains of cosmic collisions can be found all over the sky. The most famous example is the Bullet Cluster, which is the remnant of two clusters that collided 100 million years ago. In this collision, galaxies of both original clusters passed each other without being greatly affected, as there are generally large distances between them. In contrast, the hot gas that makes up most of the luminous mass interacted during the collision and slowed down. In Figure 2.3 a picture of the Bullet Cluster in the optical spectrum by Magellan and the Hubble Space Telescope is shown. The hot gas emits X-rays, which have been observed by the CHANDRA X-ray satellite, of which the observations are indicated by the pink cloud. Compared to the stars, the gas is clustered more to the center. When the effects of gravitational lensing around the Bullet Cluster were observed, they showed a discrepancy between the visible matter distribution and the distribution deduced from gravitational lensing [10]. The disagreement between the two observations can be resolved if one assumes that both of the clusters involved in the collision were surrounded by dark



matter haloes. During the collision the dark matter haloes of the clusters were not affected, and continued their original courses. They are indicated by the blue layer in Figure 2.3, and as one can see they extend further outwards compared to the hot gas. The observations of gravitational lensing around cluster collisions are therefore solid evidence for the existence of such dark matter haloes.

### 2.1.3 Cosmic microwave background

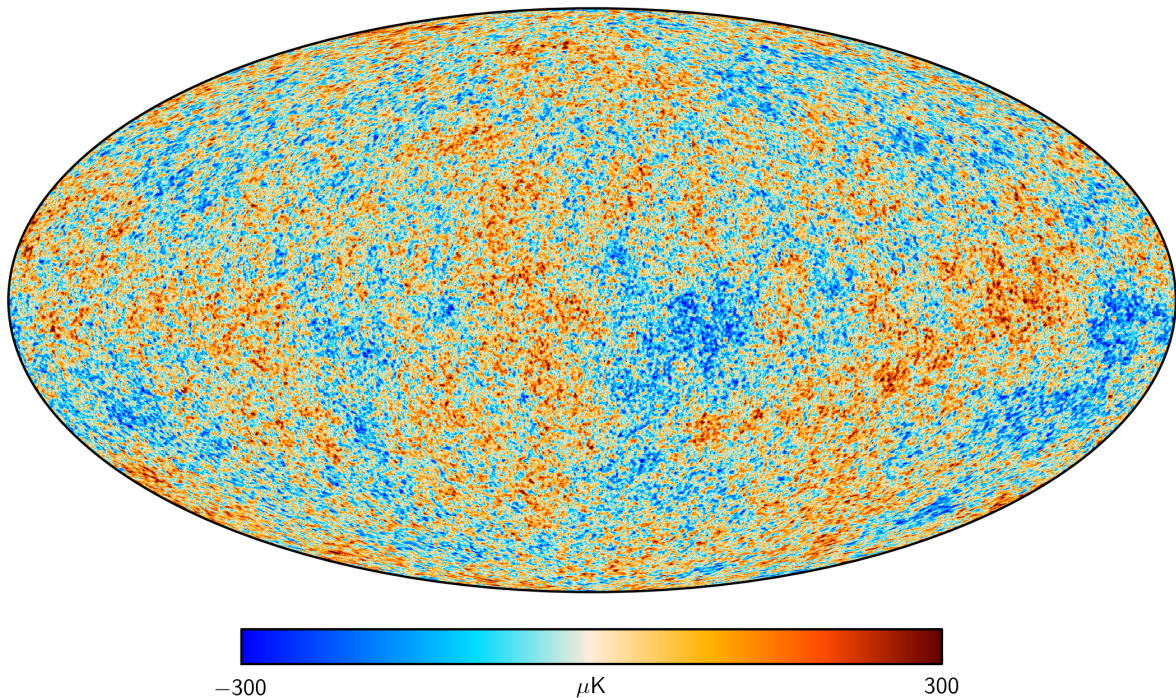


Figure 2.4: A map of the CMB temperature as measured by the Planck satellite [11]. It includes a temperature scale, which shows the detail at which small variations around  $T = 2.73$  have been observed. Image source: ESA and the Planck Collaboration <https://www.cosmos.esa.int/web/planck/picture-gallery>.

In 1964 Arno Penzias and Robert Wilson measured an excess of signals in their radio telescope, which they could not get rid of [12]. It turned out that they had performed the first measurement of the cosmic microwave background (CMB). To understand where the CMB originated we need to travel back to the early universe. At early times, the universe was much hotter than it was today, even too hot for quarks to combine into hadrons. As the universe cooled down further, eventually hadrons (protons) could form, the first step in the formation of atoms. There existed a hot plasma of protons, free electrons, and photons that was opaque to electromagnetic radiation. The next change would come during *recombination*<sup>1</sup>, at which point the electrons had cooled down enough to be able to form hydrogen atoms. At this point, the universe became transparent, and photons could propagate unhindered. This radiation from the *last scattering surface* is what makes up the CMB. Its spectrum is an

<sup>1</sup>The term recombination is a slight misnomer, as it implies that atoms had existed before, which was not the case at that point.

almost perfect black-body spectrum with a temperature of  $T = 2.73\text{K}$  [13, 14], after one has removed the dipole anisotropy. The dipole anisotropy is caused by the doppler effect of the movement of our solar system with respect to the CMB.

After the initial discovery of the CMB, increasingly more accurate measurements have been taken. 1989 saw the launch of the COBE (Cosmic Background Explorer) satellite, which observed that there exists a Gaussian temperature distribution around  $T = 2.73\text{K}$  with a variation of only  $30 \pm 5\mu\text{K}$  [15]. With increased resolution and sensitivity, the WMAP (Wilkinson Microwave Anisotropy Probe) satellite was launched in 2001 [16], which was superseded by the Planck satellite in 2009 [17, 18]. Now the fact that the CMB appears very homogenous puzzled many scientists, as the different regions of the CMB are too far apart to have been in causal contact. This is also referred to as the HORIZON PROBLEM. A widely accepted solution to this problem is the theory of inflation [19, 20]. In its basic form inflation is a phase in the very early universe, in which the energy density of the universe was dominated by its vacuum energy (a de Sitter universe) that caused the universe to expand exponentially, increasing by a factor of around  $e^{60}$  [21, 22]. Regions of the sky that were in causal contact before inflation, were far removed after.

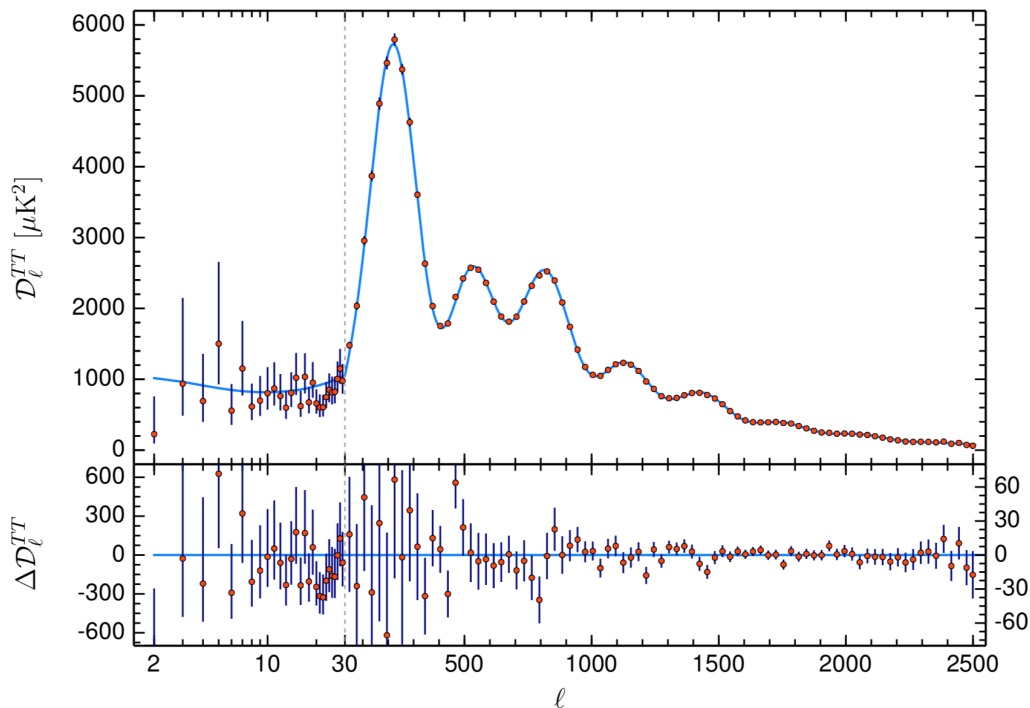


Figure 2.5: The Planck 2018 power spectrum of the CMB as a function of the multipole moment  $\ell$ . The full line included is the fit to the  $\Lambda\text{CDM}$  model. Source: [23].

However, the CMB is not completely isotropic, which is caused by density fluctuations at the time of recombination. The resulting observation of temperature anisotropies by Planck are shown in Figure 2.4. It is common to describe the structure of the anisotropies in terms

of a multipole expansion, in which the temperature fluctuation  $\delta T(\theta, \phi)/\langle T \rangle$  at a point on the sky is described by a series of spherical harmonics

$$\frac{\delta T(\theta, \phi)}{\langle T \rangle} = \sum_{\ell=0}^{\infty} \sum_{m=-\ell}^{m=+\ell} a_{\ell m} Y_{\ell, m}(\theta, \phi), \quad (2.4)$$

where the multipole moment  $\ell$  is roughly inversely proportional to the angular scale on the sky  $\theta$  as  $\theta \sim 180^\circ/\ell$ . Thus one can view the multipole expansion as the analogue of the Fourier transform, but on a spherical basis. The interesting part is to see whether there exist some underlying structures in the fluctuations at certain length scales. For this one can define the two-point autocorrelation function

$$C(\theta) \equiv \left\langle \frac{\delta T(\mathbf{x}_1)}{\langle T \rangle} \frac{\delta T(\mathbf{x}_2)}{\langle T \rangle} \right\rangle, \quad (2.5)$$

where  $\theta$  is the angle between the two points  $\mathbf{x}_1$  and  $\mathbf{x}_2$ . The brackets denote the averaging of this quantity over all (combinations of) directions in the sky. With the temperature fluctuations expanded in terms of the spherical harmonics, one can write the correlation function as [24]

$$C(\theta) = \frac{1}{4\pi} \sum_{\ell=0}^{\infty} (2\ell + 1) C_\ell P_\ell(\cos \theta), \quad (2.6)$$

where the  $P_\ell(\cos \theta)$  are the Legendre polynomials of order  $\ell$ . The factor  $2\ell + 1$  follows from the allowed values of  $m$  for the spherical harmonic  $Y_{\ell, m}(\theta, \phi)$ . The coefficients  $C_\ell$  that show up here follow directly from the multipole expansion given in Equation (2.4), and read

$$C_\ell = \frac{1}{2\ell + 1} \langle |a_{\ell m}|^2 \rangle. \quad (2.7)$$

What is usually plotted are the values

$$\mathcal{D}_\ell^{TT} \equiv \frac{\ell(\ell + 1)}{2\pi} C_\ell \langle T \rangle, \quad (2.8)$$

in units of  $\mu\text{K}^2$ . The resulting power spectrum shows the values of  $\mathcal{D}_\ell^{TT}$  as a function of the multipole moment  $\ell$ . For the Planck 2018 data it is shown in Figure 2.5, including a fit for the  $\Lambda\text{CDM}$  model [23]. It covers the multipoles  $\ell = 2 - 2508$ . For low values of  $\ell$  the errors are relatively large, as a lower multipole means less available modes  $m$  to determine the coefficient in the expansion. The first two multipole moments correspond to the CMB monopole (the average CMB temperature) and the dipole (due to the relative motion of us to the CMB), which have been discussed already. The power spectrum shows clear peaked structures, which can provide us with information about the contents of the universe.

The location of the first peak already gives a lot of information about the universe. Before recombination, the universe consisted of a baryon-photon fluid inside of a gravitational potential due to dark matter. Without the presence of dark matter, density fluctuations in the

baryon-photon fluid would be naturally smoothened over time. However, inhomogeneities in the dark matter attract surrounding baryons, which fall into the gravitational potential, locally increasing the temperature. This leads to the photons inside the fluid to give rise to an increased radiation pressure, which causes oscillations in the fluid that travel outwards called baryon acoustic oscillations. These waves are sound waves, and they travel at a speed of  $v_s = c/\sqrt{3}$ . Now this state was temperature dependent, as it ended at the moment of recombination. At this point the interactions inside the baryon-photon fluid ceased and the sound waves stopped oscillating. The extrema of these waves correspond to the regions with the largest density, and thus temperature anisotropies. As the sound waves move at fixed speed, there exists a largest distance such a wave can have travelled before recombination. This is referred to as the sound horizon, and one would expect to observe this in the CMB. The peak of the power spectrum around  $\ell \sim 200$  corresponds to an angle of  $\sim 1^\circ$  on the sky. The position of the peak in the power spectrum depends on the curvature of the universe. If the universe were curved, then the size of the sound horizon on the sky would change as the light of the CMB follows the curvature of the universe. This is not the case, as it is found that the size of the sound horizon is in agreement with a flat universe [23].

The peaks at higher values of  $\ell$  correspond to higher modes of the sound waves in the baryon-photon fluid, and are thus at shorter length scales. The second peak corresponds to the sound wave that compressed and expanded once. These peaks are modified by the effects of massive baryons falling into potential wells, changing the oscillation amplitudes of the sound waves. An increasing baryon density in the universe enhances the peaks due to compression over the peaks due to expansion. Thus these peaks can provide information on the abundances of dark matter and baryonic matter. At higher multipole moments the power spectrum including the peaks are dampened, which is known as Silk damping [25]. This occurs because the process of recombination is not instantaneous, so instead of the last scattering surface, one should speak of a last scattering shell. This means that as recombination is taking place, small-scale anisotropies can still be washed out before the baryons and photons decouple completely.

Fitting the  $\Lambda$ CDM model to the CMB power spectrum then results in the following densities for the components of the universe [23]:

$$\Omega_\Lambda h^2 = 0.3107 \pm 0.0082 \quad \Omega_c h^2 = 0.1200 \pm 0.0012 \quad \Omega_b h^2 = 0.02237 \pm 0.00015, \quad (2.9)$$

for the dark energy, cold dark matter, and baryon densities respectively.  $h$  is the reduced Hubble constant obtained from the current value of the Hubble constant  $H_0 = 67.27 \pm 0.60$  km s<sup>-1</sup> Mpc<sup>-1</sup> through  $h = H_0 / 100$  km s<sup>-1</sup> Mpc<sup>-1</sup>. It is usual for the densities to be given in terms of the critical density

$$\rho_c = \frac{3H^2}{8\pi G}, \quad (2.10)$$

so that  $\Omega = \frac{\rho}{\rho_c}$ . The critical density is the density for which the universe is spatially flat, and can be derived from the Friedmann equation.

### 2.1.4 Cosmic structure formation

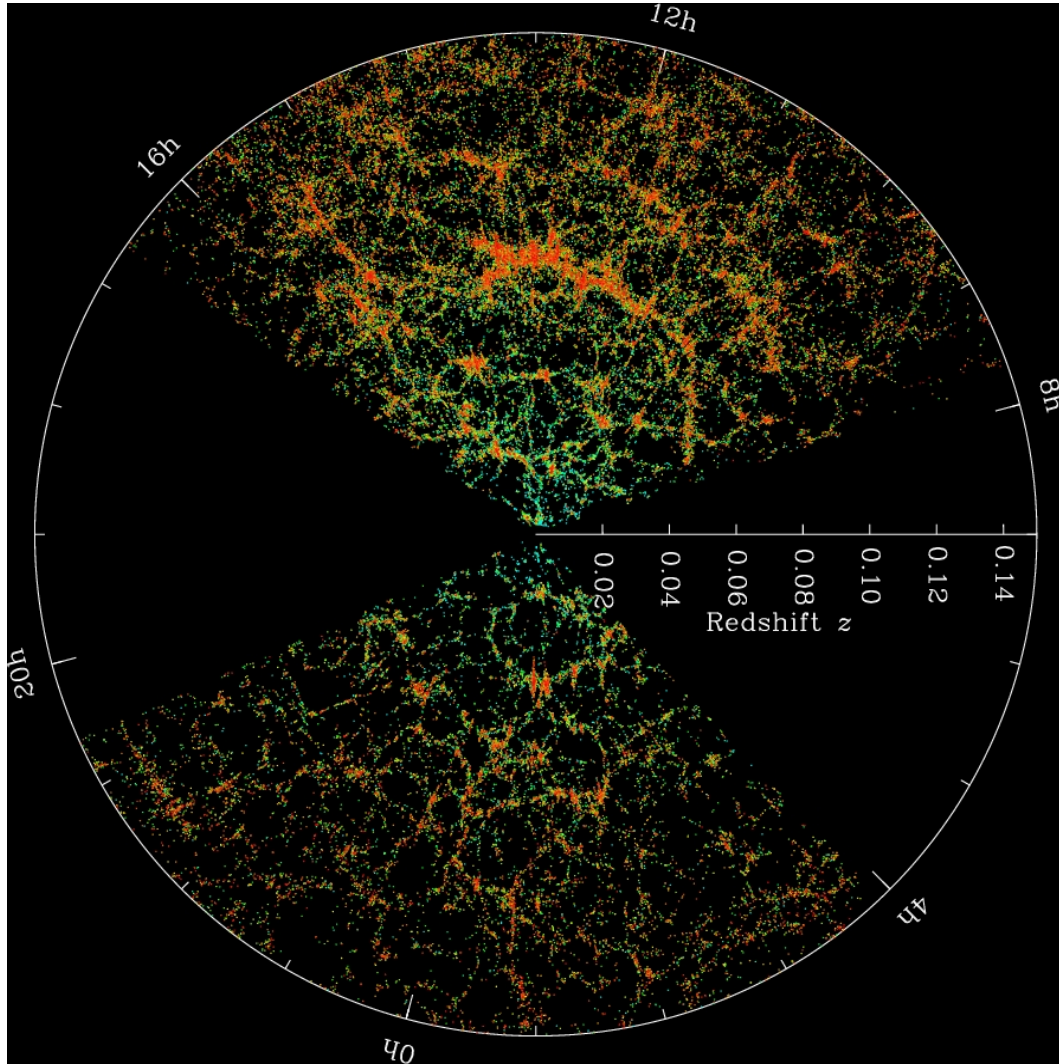


Figure 2.6: A map showing the distribution of galaxies in our vicinity from the Sloan Digital Sky Survey (SDSS) [26]. Each dot represents a galaxy. Image credit: M. Blanton and SDSS <https://www.sdss.org/science/orangepie/>.

We have just extensively discussed the anisotropies in the CMB, but these are only tiny fluctuations in an otherwise isotropic radiation background. Our surroundings in the universe are not definitely not isotropic. There are regions with galaxies, clusters, and even superclusters, but also large voids. The Sloan Digital Sky Survey (SDSS) has observed and mapped many galaxies outside of our Milky Way [26], as well as the 2dF Galaxy Redshift Survey (2dFGRS) [27]. The resulting map is shown in Figure 2.6. Part of the sky was not suitable for observation due to the presence of the Milky Way, these are the two black regions on the side. One can clearly see that there are galaxy clusters, and groups of clusters, which are connected to other clusters via narrow filaments, giving the large scale of the universe the fitting name cosmic web [28]. So how do we get large scale structures from the small fluctuations of the CMB? The usual mechanism is that the initial dark matter clumps that



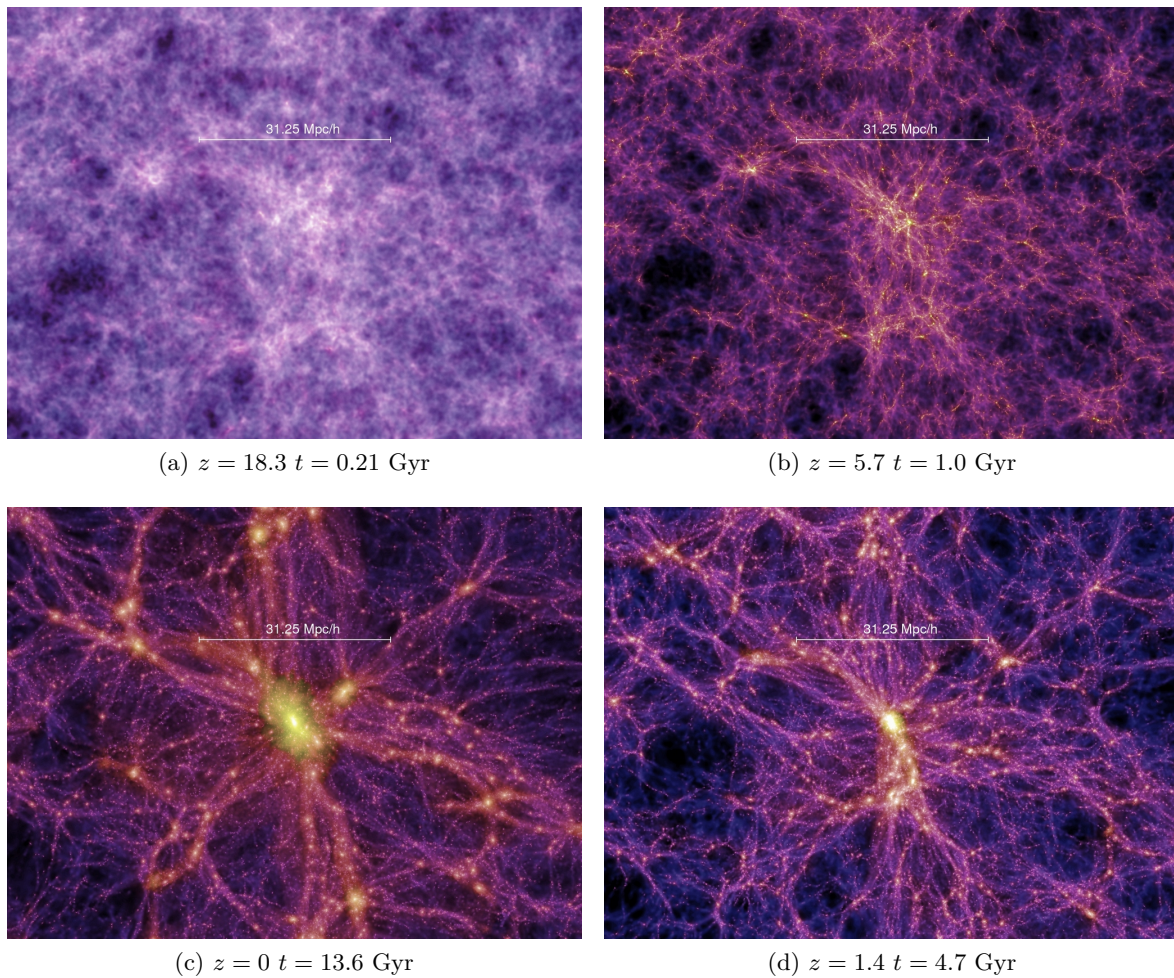


Figure 2.7: Images showing the distribution of galaxies in a region in the Millenium Simulation [29] at different times. The chronological order is clockwise, starting at the top-left image. Image source: <https://wwwmpa.mpa-garching.mpg.de/galform/virgo/millennium/>

were present before recombination attracted each other to form larger perturbations. The baryonic matter that was present followed these processes. Eventually clumps collapsed and larger-scale structures were formed. Thus the process of structure formation is hierarchical, and has been simulated with  $N$ -body simulations. In particular, the Millennium Simulation by the VIRGO collaboration used 10 billion particles in a simulated universe of a cube with side lengths of 2 billion light-years [29]. As an illustration, Figure 2.7 shows the evolution of the dark matter density in a region of the Millenium Simulation at several stages in the universe. The top-left image shows the dark matter distribution at  $z = 18.3$  ( $t = 0.21$  Gyr), with the evolution of this region shown by the other figures in clockwise order. The bottom-left picture would be the present distribution  $z = 0$  ( $t = 13.6$  Gyr). From these images one can clearly see that the distribution of dark matter is more spread out initially, but forms larger structures over time, with narrow filaments connecting the different clumps. In order to obtain such web-like structures, a key requirement for the dark matter is that it is *cold*

[30]. In this context, cold dark matter means that it moves at non-relativistic velocities at decoupling. In this way, the small velocities cause the smaller structures to be formed first, which then grow to larger structures. In the opposite scenario, *hot* dark matter is relativistic when decoupling and forms larger structures first. Structure formation at smaller scales poses a problem for this scenario, as smaller scale structures are washed out by the larger dark matter velocities. Hence cold dark matter is favoured [31, 32]. Even though results of these  $N$ -body simulations agree very well with the observations, there are some discrepancies at the smaller scales. In particular, the  $N$ -body simulations predict many more dwarf galaxies than there are currently in the vicinity of our galaxy, which is called the missing satellite problem [33]. With increasingly sensitive observations and/or dark matter that is not completely collisionless this problem might be resolved in the future [34, 35, 36].

We have only briefly seen several indications for the existence of dark matter and each of these topics warrants its own research field. After giving this overview, we now move on to the next question concerning the nature of dark matter.

## 2.2 Theoretical motivation

So far we have discussed different observations that indicated the existence of some sort of matter, of which we only see the effects through the effects of gravity on its surroundings, dubbed dark matter. Moreover, from observations of the CMB one can even deduce the amount of dark matter in the universe. However, its exact nature is still an open question, although the CMB measurements and cosmic structure formation points in the direction of cold, non-baryonic dark matter candidates: Weakly Interacting Massive Particles (WIMPs). In this section we will discuss some of the most common dark matter candidates, as well as the production mechanism of WIMPs.

### 2.2.1 Baryonic dark matter

A general rule that holds for many situations is that the simplest solution to a problem is the most likely one. It might be possible that there are objects in the universe that we do not see, but constitute a significant part of all the matter in the universe. These type of dark matter candidates are referred to as *massive astrophysical compact halo objects* or MACHOs for short. Several objects that could play such a role are neutron stars, black holes, and brown dwarfs. A brown dwarf is a stellar-like object with a mass below the hydrogen-burning limit at  $0.072M_{\odot}$ , and is too light to sustain nuclear fusion in its core [37]. It can be that the processes of star formation that are considered leave out these lighter objects. During star formation the number density  $n$  at stellar mass  $m$  was taken to follow a simple power law referred to as the initial mass function (IMF)

$$\frac{dn}{d\ln m} \propto m^{-x}, \quad (2.11)$$

with a first value of  $x = 1.35$  that was established by Salpeter in 1955 [38], though nowadays more complex functions are used [37]. Either way, the point is that for the estimate of mass in stars a lower bound on the mass (luminosity) is set around the hydrogen-burning limit. Extending the IMF to lower masses can indicate that dark matter could consist of lower-mass objects that are not considered stars, i.e. brown dwarfs. In order to observe whether dark matter is made up of MACHOs, one can make use of a special form of gravitational lensing, microlensing. Microlensing occurs when the brightness of a background star is enhanced when an object (such as a MACHO) moves in the line of sight to the Earth. The MACHO Project scanned 11.9 million stars in the Large Magellanic Cloud, but found only 13-17 microlensing events, and concluded that MACHOs can contribute at most 20% to the dark halo [39]. Further observations of microlensing by the EROS-2 survey found only a single microlensing event in an observation of 7 million stars, and excluded general MACHOs in the range of  $0.6 \cdot 10^{-7} M_{\odot} < M < 15 M_{\odot}$  [40]. Combined with evidences from the CMB and cosmic structure formation, MACHOs are clearly disfavoured.

### 2.2.2 Non-baryonic dark matter

As it seems that baryonic dark matter does not offer a solution to the range of astronomical observations we discussed in section 2.1, we will now consider the scenario where dark matter consists of (elementary) particles instead of macroscopic objects. This scenario is favoured by the observations of the CMB and cosmic structure formation simulations, which indicate that there exists a large amount of non-baryonic matter in the universe. If dark matter indeed consists of particles then we can, based on the current evidence, list the main properties such a particle must have.

- **Electrically neutral:** The main property of dark matter can easily be guessed from its name. It cannot have electromagnetic interactions, as these interactions can produce photons. Thus dark matter must be electrically neutral.
- **Colourless:** Dark matter cannot interact via standard QCD interactions either, hence we will require dark matter candidates to carry no SU(3) charge.
- **Stability:** Dark matter must be stable (or have a lifetime longer than the age of the universe). Otherwise dark matter created in the early universe would have decayed by now.
- **Cold:** If the dark matter candidate is in thermal equilibrium in the early universe, it must be massive enough to be non-relativistic at decoupling, based on CMB and structure formation data.
- **No influence on BBN:** The addition of a light dark matter candidate can influence Big Bang Nucleosynthesis (BBN). This rules out candidates below a mass of 10 MeV [41].

This leaves us with a massive particle that can only possibly interact through the weak interaction, a Weakly Interacting Massive Particle (WIMP).



### 2.2.3 WIMP production

We will now discuss the production of such a particle in the early universe. At these times, the particle energies were large enough so that annihilation processes of WIMPs  $\chi$  with SM particles  $X_{SM}^{(\prime)}$  and vice versa were kinematically possible,

$$\chi\chi \leftrightarrow X_{SM}X'_{SM}, \quad (2.12)$$

and the WIMPs were in thermal equilibrium with the SM. In thermal equilibrium the number density of a WIMP can be described as

$$n_{\chi}^{\text{eq}} = \frac{g}{(2\pi)^3} \int d^3\mathbf{p} f(\mathbf{p}), \quad (2.13)$$

where  $g$  is the number of internal degrees of freedom (e.g. the spin states of a WIMP), and  $f(\mathbf{p})$  is either the Fermi-Dirac or Bose-Einstein distribution,

$$f(\mathbf{p}) = \frac{1}{e^{(E-\mu)/T} \pm 1}. \quad (2.14)$$

At low temperatures ( $T \ll m_{\chi}$ ), the Fermi-Dirac and the Bose-Einstein distributions reduce to the Maxwell-Boltzmann distribution, resulting in a number density of

$$n_{\chi}^{\text{eq}} = g \left( \frac{m_{\chi} T}{2\pi} \right)^{3/2} e^{-m_{\chi}/T}. \quad (2.15)$$

The annihilation rate of WIMPs can be written as

$$\Gamma = n_{\chi} \langle \sigma v \rangle, \quad (2.16)$$

where  $\langle \sigma v \rangle$  is the total thermally averaged cross section for annihilation into all possible final states. However, as the universe expanded, two factors influenced the interactions of WIMPs with the SM. Firstly, due to the expansion of the universe, the number density of particles dropped, so that both creation as well as annihilation processes appeared less frequently. Secondly, the expansion of the universe cooled down the universe, so that the SM particles did not have enough energy to produce the (generally) heavier WIMPs, breaking thermal equilibrium. From that point on only the annihilation of WIMPs into SM states can take place. It would be terrible for a WIMP to stay in thermal equilibrium with the rest of the universe until the present day, as the number density would be exponentially suppressed. The annihilation rate slows down as the universe expands further, and eventually reaches a point where the interaction rate  $\Gamma$  satisfies

$$\Gamma \lesssim H, \quad (2.17)$$

i.e. when it drops below the Hubble constant  $H$ . It is defined as  $H = \dot{a}/a$ , where  $a$  is the scale factor of the universe, and it quantifies the expansion rate of the universe. At this point

annihilation stops, and the WIMPs decouple completely. Thereafter the comoving number density, the particle density inside a region that scales with the expansion of the universe, remains constant. This is usually called the relic density, as the WIMPs are leftover “relics” of the early universe. The evolution of the number density can be described by the Boltzmann equation

$$\frac{dn_\chi}{dt} + 3Hn_\chi = -\langle\sigma_{\text{eff}}v\rangle(n_\chi - n_\chi^{\text{eq}}). \quad (2.18)$$

The evolution of the number density is determined by the  $3Hn_\chi$  term on the left-hand side, which for a zero right-hand side would yield  $n_\chi \propto a^{-3}$ . The right-hand side of the equation is a source term, which either increases or decreases the number density if it is not equal to the equilibrium value. The rate at which this happens is proportional to the effective thermally averaged cross section  $\langle\sigma_{\text{eff}}v\rangle$ . We will go into more detail about the meaning of the word effective later. There is no analytic solution to the Boltzmann equation, hence one resorts to numerical solutions.

For a single new WIMP one can take as a quick estimate that the relic density depends on the cross section as [42]

$$\Omega_\chi h^2 \simeq \frac{3 \cdot 10^{-27} \text{ cm}^3 \text{ s}^{-1}}{\langle\sigma v\rangle}, \quad (2.19)$$

which for  $\langle\sigma v\rangle \approx 3 \cdot 10^{-26} \text{ cm}^3 \text{ s}^{-1}$  yields a relic density around the observed value. This is the value that is in agreement with a WIMP of a mass around the electroweak scale interacting with the weak force coupling  $G_F$ , which has been called the “WIMP miracle”. More thorough calculations yield slightly different values of  $\langle\sigma v\rangle = 2.2 \cdot 10^{-26} \text{ cm}^3 \text{ s}^{-1}$  for WIMP masses above 10 GeV, which is close to the aforementioned canonical value [43].

## Co-annihilations

We seen from Equation (2.19) that the relic density of a WIMP is closely related to its thermally averaged cross section  $\langle\sigma v\rangle$ . However, new theories often include more than a single new particle, as we will see later. If there exists a particle  $\chi'$  with a mass slightly above the WIMP mass, then processes such as

$$\chi\chi' \leftrightarrow X_{SM}X'_{SM} \quad (2.20)$$

are possible, provided that  $m'_\chi - m_\chi \ll T_f$ , where  $T_f$  is the freezeout temperature. These are called co-annihilations, and they can have a large influence on the relic density even for mass differences at the  $\sim 5 - 10\%$  level. The effective cross section for a system of  $N$  co-annihilating particles  $i$  of mass  $m_i$  is denoted by [45, 46]

$$\sigma_{\text{eff}} = \sum_{i,j=1}^N \sigma_{ij} \frac{g_i g_j}{g_{\text{eff}}^2} (1 + \Delta_i)^{3/2} (1 + \Delta_j)^{3/2} e^{-x(\Delta_i + \Delta_j)}, \quad (2.21)$$

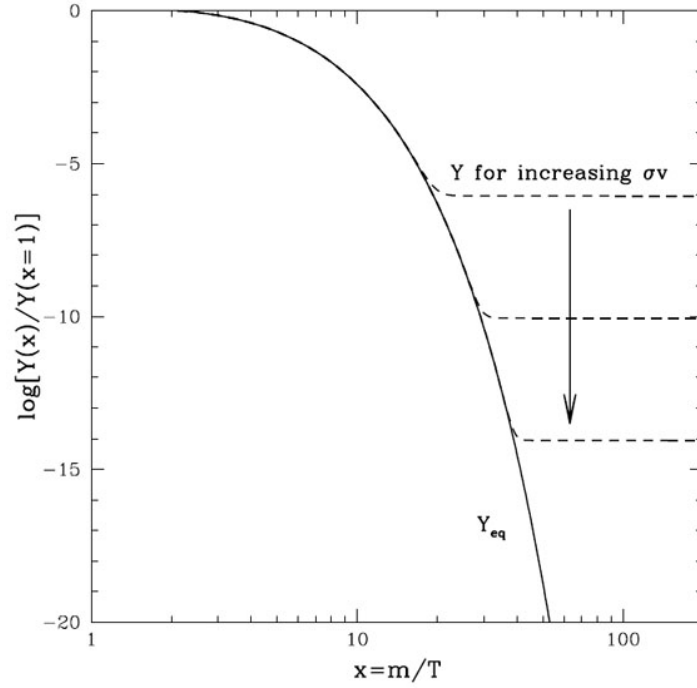


Figure 2.8: The solution of the Boltzmann equation showing the yield as a function of  $x = m_\chi/T$ . The full line shows the equilibrium value  $Y_{\text{eq}}$ , whereas the dashed lines indicate relic densities after freeze-out for different  $\langle\sigma v\rangle$ . Image source: [44].

where  $\Delta_i \equiv m_i - m_\chi/m_{\text{chi}}$  denotes the difference to the WIMP mass.  $g_{\text{eff}}$  is the effective number of degrees of freedom depending on the individual internal degrees of freedom  $g_i$  for particle  $i$ , and is given by

$$g_{\text{eff}} \equiv \sum_{i=1}^N g_i (1 + \Delta_i)^{3/2} e^{-x\Delta_i}. \quad (2.22)$$

We will see the effects of co-annihilation in later chapters.

### Solution

For now, let us return to Equation (2.18), which is usually written in terms of  $Y = n/s$ , the number density in terms of the entropy density, and  $x = m_\chi/T$ . This way, the Boltzmann equation can be brought to the form

$$\frac{dY}{dt} = -\sqrt{\frac{\pi}{45G}} \frac{g_{\text{eff}}^{1/2} m_\chi}{x^2} \langle\sigma_{\text{eff}} v\rangle (Y^2 - Y_{\text{eq}}^2). \quad (2.23)$$

A numerical solution of this equation is shown in Figure 2.8, which shows the WIMP yield as a function of  $x = m_\chi/T$ . The full line shows the thermal equilibrium  $Y_{\text{eq}}$ , whereas the dotted lines show the yield after the WIMP has frozen out for different values of  $\langle\sigma v\rangle$ . It is worth noting that the relic density of a WIMP decreases if its thermally averaged cross section goes up, as could also be deduced from Equation (2.19). The reason for this is simple: a WIMP with a larger  $\langle\sigma v\rangle$  has a higher interaction rate and stays in thermal equilibrium longer. As

the equilibrium value rapidly falls off for larger  $x$ , the resulting relic density after freeze out is also lower. For a WIMP, freeze out generally happens around  $x_f \simeq 20$  [24].

### 2.2.4 WIMP models

There are many different models that provide suitable WIMP candidates. When taking the SM as the starting point the neutrinos seem interesting candidates, as they are neutral, have little interaction with other particles, are stable, and due to neutrino oscillations have a non-zero mass [47]. Moreover, unlike other proposed dark matter candidates, they have the perk of being known to exist. One can calculate that the contribution of relic neutrinos of the early universe contribute to the energy density of the universe as [14]

$$\Omega_\nu h^2 = \frac{\sum m_\nu}{93 \text{ eV}}. \quad (2.24)$$

However, the Planck collaboration has put an upper bound on the sum of the neutrino masses of  $\sum m_\nu < 0.120 \text{ eV}$ , whereas a mass of  $\sim 10 \text{ eV}$  would be necessary to account for the dark matter relic density [23]. They would also be hot instead of cold dark matter, and be disfavoured by cosmic structure formation.

We thus need to move on beyond the Standard Model. A very well known theory that naturally contains WIMPs is supersymmetry. Supersymmetric models relate the SM bosons to fermionic superpartners and vice versa through an extension of the Poincaré space-time symmetries. The Minimal Supersymmetric Standard Model (MSSM) is the model that relates the SM particles to the least amounts of superpartners possible. An attractive feature of supersymmetry is that it provides an elegant solution to the hierarchy problem [48], as the superpartners cancel the quadratic dependence of the Higgs mass on new high-energy physics [49]. Moreover, the MSSM allows for gauge unification of the electroweak and strong interactions at high energies [50, 51]. The natural WIMP candidates of the MSSM are the neutralinos. They arise from the mixing of the Higgsinos, the Bino, and the Wino, the superpartners of the Higgs, and the electroweak  $B$ - and  $W$ -bosons respectively. The MSSM features a  $\mathbb{Z}_2$  symmetry called R-parity, which prevents proton decays, and at the same time prevents the neutralinos from decaying into SM particles. The lightest of the neutralinos is therefore a suitable DM candidate, and is often called the lightest supersymmetric particle (LSP). Still the MSSM contains over 100 free parameters, which is why the phenomenological MSSM (pMSSM) is also often considered, as it contains only 19 new free parameters [52]. Within the framework of the MSSM, many theoretical [53, 54, 55, 56, 57, 58] as well as experimental searches [59, 60, 61, 62, 63] have been performed, yet so far no supersymmetric WIMP has been found.

The lack of discovery in the supersymmetric department has brought other theories into interest. Amongst these are many minimal models, which throw the at some times unwieldy supersymmetric constructions out of the window and focus only, or mainly, on the dark matter phenomenology. An example of these are the inert (Higgs) doublet models, in which

a second Higgs doublet is added to the SM, similar to the Higgs sector of the MSSM. If the second Higgs doublet is odd under a  $\mathbb{Z}_2$  symmetry it can contain a stable WIMP [64, 65, 66, 67]. Next to scalar WIMPs, one can also consider fermionic WIMPs [68, 69, 70, 71].

Other models might employ different symmetries to stabilize dark matter, such as a  $U(1)$  symmetry, which may be global [72] or gauged [73, 74]. Other models consider a combination of several symmetries [75]. Some models even contain no additional symmetries at all [76].

There is no shortage of dark matter models, and studying all of them is an insurmountable task. Hence we will focus on minimal radiative seesaw models in this work. These are minimal models that can contain both fermionic and scalar dark matter candidates, whilst they offer more phenomenology by simultaneously generating neutrino masses. These models will be introduced in Chapter 4.

### 2.2.5 Other candidates

We have discussed several WIMP theories, and we will briefly list some other candidates that are commonly proposed as dark matter candidate before we move on to its detection possibilities..

#### Sterile neutrinos

All fermions in the SM come in two chiral variants: both left- as well as right-handed. Neutrinos are the exception to this rule. It is therefore theoretically attractive to add the right-handed counterparts to the SM neutrinos. As these neutrinos would only interact through mixing with the SM neutrinos, they are often referred to as sterile neutrinos. The addition of such particles also provides for several mechanisms to generate neutrino masses, for more on this see Chapter 3. The general mass range of sterile neutrinos is in the keV range, putting it between cold and hot dark matter, and is therefore called *warm* [77]. Even though sterile neutrinos are lighter, their production mechanism is non-thermal, and the resulting structure formation is similar to that of cold dark matter [78].

After the discovery of an emission line around 3.5 keV, which has been observed in the Milky Way [79], the Andromeda galaxy, as well as other galaxies and clusters [80], a 7 keV sterile neutrino was proposed as a dark matter candidate. However, other observations observed no such line [81, 82]. Unknown instrumental effects due to e.g. solar activity were mentioned as a cause, but observations of the 3.5 keV line by the NuStar satellite ruled out this scenario [83]. Further causes, such as the presence of atomic transitions lines in the 3.5 keV region were proposed, but no evidence was found [84]. The exact nature of the line is still hotly debated, but future X-ray observations aim to probe this signal in ever more detail [85, 86]

## Axions

One further candidate is the axion. It has its origins in the *strong CP problem*, which arises due to the possibility of adding the term

$$\mathcal{L}_\Theta = \frac{g^2}{16\pi^2} \Theta \text{Tr} G^{\mu\nu a} \tilde{G}_{\mu\nu}^a, \quad (2.25)$$

with

$$\tilde{G}_{\mu\nu}^a = \frac{1}{2} \varepsilon_{\mu\nu\rho\sigma} G^{\rho\sigma a} \quad (2.26)$$

to the QCD Lagrangian that violates *CP*. Now the amount of *CP* violation in the strong interaction is small, and bounds on the electric dipole moment of the neutron imply that [47]

$$|\Theta| \lesssim 10^{-10}, \quad (2.27)$$

even though theoretically a value of  $\mathcal{O}(1)$  is also perfectly allowed, and such a small value seems unnatural, unless it is due the breaking of another symmetry per 't Hooft [87]. This can be achieved by implementing the Peccei-Quinn symmetry  $U(1)_{\text{PQ}}$  of which the spontaneous breaking will produce a massive Goldstone boson, the axion [88, 89]. Axions are usually thought to have tiny masses, from the meV level further downwards to the  $\mu\text{eV}$  range or even further. They are sought after by astrophysical constraints and light shining through wall experiments [90]. In these setups a laser beam is shone at wall, and a strong magnetic field is applied. Due to the Primakoff effect, photons interacting with the magnetic field can produce axions, which can pass the wall. The inverse process can take place on the other side of the wall, which could lead to a detectable photon signal. In spite of its low mass, axions can suitably behave as cold dark matter, as they were never in thermal equilibrium in the early universe due to their weak couplings to other matter [91].

## 2.3 DM detection

So far we have discussed the cosmological evidence for dark matter, as well as the properties of a WIMP. Many experimental searches are performed, usually with the idea that a WIMP does not only interact gravitationally, but can also have some interactions via the weak interaction, or via Higgs interactions. All of these interactions (without gravity) can be summarized in the diagram shown in Figure 2.9. In general, one can distinguish three different processes.

- **Direct detection:** In direct detection experiments, a WIMP interacts  $\chi X_{\text{SM}} \rightarrow \chi X_{\text{SM}}$  with a target SM particle  $X_{\text{SM}}$ , often a heavy nucleus.
- **Indirect detection:** As should be clear from its name, in indirect detection experiments WIMPs are not observed directly, but rather the SM particles produced through annihilation processes  $\chi\chi \rightarrow X_{\text{SM}} X_{\text{SM}}$ , such as neutrinos or X-rays.

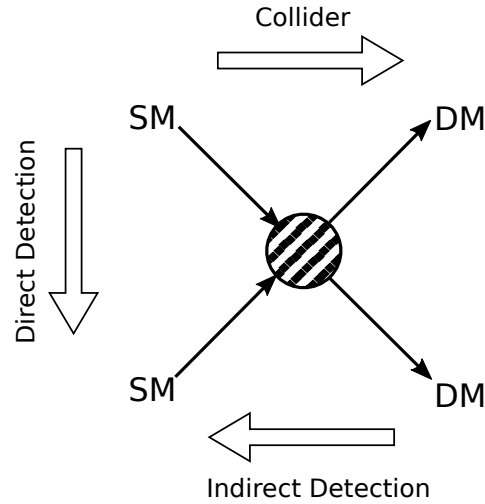


Figure 2.9: Diagram showing the various ways WIMPs interact with the SM as well as the corresponding detection types. Image source: [92]

- **Collider production:** Collider searches aim to observe effects of new particles, for example missing transverse energy  $\cancel{E}_T$  as a result from proton and heavy ion collisions, e.g. lead.

In this section we will discuss the principle of operation for experiments of each of these methods, as well as the obtained results.

### 2.3.1 Direct detection

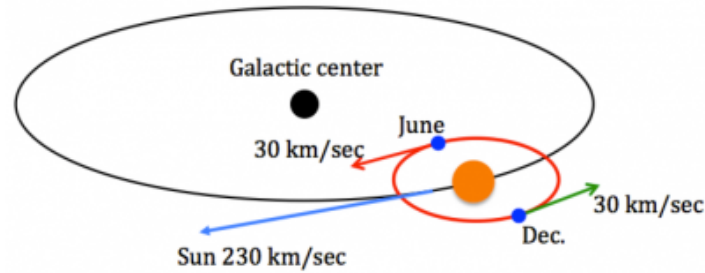


Figure 2.10: An image showing the movement of the Sun and the Earth around the centre of the Milky Way. The relative velocity of the Earth to the galactic dark matter halo depends on the time of the year. Image source: <https://cosine.yale.edu/about-us/annual-modulation-dark-matter>

Direct detection experiments work on the principle measuring signals from WIMP scatterings with the detection medium. As our Solar System orbits the Galactic Centre, it passes through the galaxy's dark matter halo. Thus we experience a WIMP flux on Earth, as is illustrated by the cartoon in Figure 2.10. The relative velocity of the Earth with respect to the DM halo depends on the time of the year, due to the Earth's orbit around the Sun. The dark matter flux through the Earth is then expected to change accordingly, leading to

an annual modulation of the signal. Such an annual modulation has been observed in the DAMA/LIBRA experiment [93]. The observed annual modulation is shown in Figure 2.11 for the two phases of the experiment, including a fit to the data. The data agree with an annual modulation with its maximum in June at the  $9.5\sigma$  level. However, the interpretation of this result as being caused by WIMPs is at tension with other direct detection experiments such as COSINE-100 [94], and XENON1T [95]. Direct detection experiments can be further

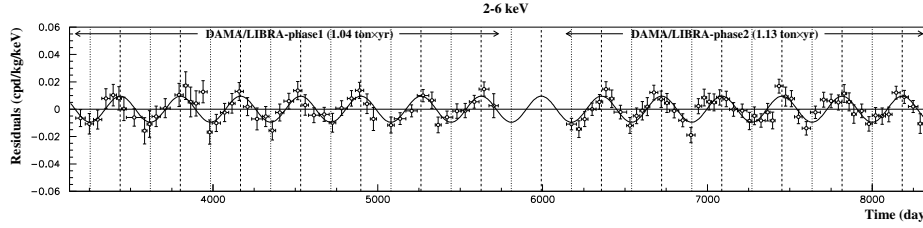


Figure 2.11: Results of the two DAMA/LIBRA phases showing the annual modulation of the observed signal as a function of time including a fit to the data. Image source: [93]

divided, as the type of signal depends on the detection medium used. Irrespective of the type of signal that is emitted, the experiments need to be as sensitive as possible. This can be achieved both through lowering unwanted backgrounds, as well as increasing the size of the detector to maximise exposure. The main three methods used in direct detection experiments are shown in Figure 2.12. Some experiments also use a combination of signals.

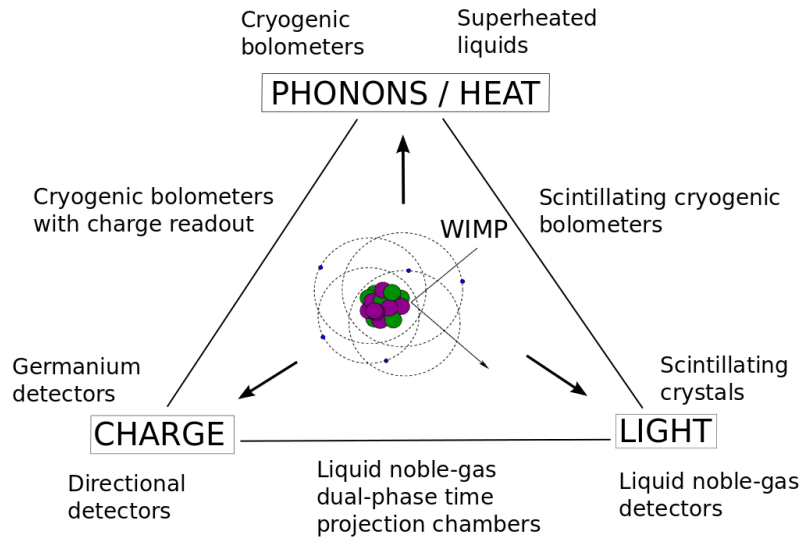


Figure 2.12: Schematic overview of the types of direct detection experiments. Image source: [96].



### Phonons/heat

One of the techniques that makes use of heat deposited in WIMP scatterings is the use of *cryogenic bolometers*. These detectors consist of crystals that rise slightly in temperature when heat is deposited in the system through e.g. WIMP scattering, but also radioactive decays. The temperature increase is measured using thermistors, which are resistances sensitive to temperature changes. In order to measure such signals the materials must be very cold, usually at the mK level, to reduce thermal noise. An example of such an experiment is the CUORE experiment. It was originally built with tellurium dioxide ( $\text{TeO}_2$ ) crystals in order to measure the neutrinoless double beta decay ( $0\nu\beta\beta$ ) of  $^{130}\text{Te}$  (more on this in section 3.2.1), but simultaneously serves as a detector for WIMP interactions [97, 98]. WIMP scatterings and nuclear decays deposit heat into the crystal creating phonons, which can be described as quasi-particle lattice vibrations, that travel through the crystal. The change in heat is measured by the germanium (Ge) sensor which can be seen in Figure 2.13, which shows a cryogenic bolometer as used in the CUORE experiment.

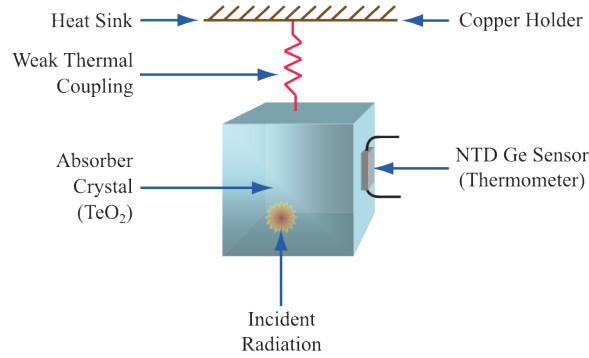


Figure 2.13: Schematic overview of the bolometers used in the CUORE experiment. Image source: <https://cuore.lngs.infn.it/en/about/detectors>.

A different technique based on the deposition of heat in a detector medium is with bubble chambers. These chambers contain a superheated liquid, i.e. a liquid that has been carefully heated to a temperature above its boiling point. As heat from scatterings is deposited in the medium, a phase transition occurs, and bubbles are created inside the medium, which are filmed by cameras. As soon as bubbles are detected, the pressure of the liquid is increased, to prevent the whole medium from boiling. The PICO collaboration used a detector initially filled with  $\text{CF}_3\text{I}$ , but later with  $\text{C}_3\text{F}_8$  in the PICO-60 experiment, which resulted in competitive bounds on the spin-independent scattering cross section, especially for masses around a few GeV [99]. The next generation experiment PICO-40L was finished in 2020 and aims to improve the previous limits by an order of magnitude [100], with plans for further upgrades, PICO-500 already on the table <sup>2</sup>.

<sup>2</sup><https://www.picoexperiment.com/pico-500/>

### Phonons/heat and scintillation

The CRESST experiment uses the same technique as the CUORE experiment. The latest CRESST-III phase uses a 23.6 g calcium tungstate ( $\text{CaWO}_4$ ) detector [101]. The detector is kept at a temperature of 15 mK, which is around the temperature where the tungsten in the detector becomes superconductive. A small increase in temperature thus leads to a large difference in electrical resistance. Most of the energy deposited in scatterings is transferred into phonons, but part of the energy is emitted as scintillation light. Therefore the CRESST bolometers are equipped with an extra calorimeter to measure the scintillation signals. The combination of both signals allows for the elimination of more background events, increasing the sensitivity. Moreover, the different elements in the crystal respond differently to scatterings, yielding further information.

### Ionisation

The energy deposited in a detector by a WIMP can also cause ionisation in a detector medium. This phenomenon has been used in the HDMS [102] and CoGeNT [103] experiments, both of which employed *p*-doped germanium crystals. The crystals are brought to low temperatures to reduce thermal noise. The strength of this approach lies in the low threshold energy of the detector, allowing to probe lower dark matter masses around 10 GeV with good sensitivity. However, the crystal becomes noisier if one scales to larger volumes. Thus experiments usually consider a combination of ionisation and other effects.

### Phonons/heat and ionisation

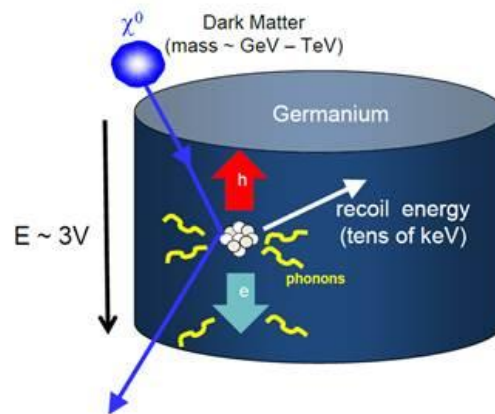


Figure 2.14: Schematic overview processes in the SUPERCDMS experiment. Scattering WIMPs inside the germanium crystal create heat in the form of phonons, as well as charges (electron-hole pairs) that are drifted in an electric field. Image source: <https://supercdms.slac.stanford.edu/overview>.

An experiment that combines both phonons as well as the ionisation charge signals is CDMS and its successor SUPERCDMS [104], using silicon [105] and germanium crystals [106]

that are kept at temperatures of 30 mK to reduce thermal noise. With an ionisation energy of only 3.0 eV for germanium and 3.6 eV for silicon, WIMP scatterings not only produce phonons, but can create electron-hole pairs in the semiconductor as well. The phonons are measured by a transition edge sensor (TES), which is a sensor close to the edge between the normal and superconducting stages, so that small changes in temperature have large effect on the resistance. The combination of the ionisation charge signal with the phonon signal allows for better event discrimination. An illustration of the WIMP interaction inside the germanium crystal for the SUPERCDMS experiment is shown in Figure 2.14, showing the creation of heat in the form of phonons as well as electron-hole pairs. The same technique is used in the EDELWEISS-III experiment using  $\sim 20$  kg of germanium [107]. In a planned joint project by the EDELWEISS and CRESST collaborations the EURECA experiment is planned to scale up the detector to a 1 tonne absorber mass [108].

### Scintillation

We already briefly mentioned scintillation when discussing the CUORE experiments, but there are more experiments that are designed to detect scintillation light from WIMP scattering. In scintillating mediums energy from scatterings is transferred to excite the target atoms. Upon falling back to the ground state, the excited atoms emit scintillation photons, which are detected. Common materials that are used are crystals such as sodium iodine (NaI) or noble gasses xenon (Xe) and argon (Ar). The already discussed DAMA/LIBRA experiment falls in the first class, consisting of 25 highly radio-pure NaI crystal scintillators, with a mass of 9.70 kg each [93]. As was already mentioned the observation of the annual modulation of the WIMP event rate that was observed by DAMA/LIBRA is still hotly debated and has neither been confirmed nor completely ruled out in a model-independent way. The COSINE-100 [94, 109] and ANAIS-112 [110] use similar detectors based on NaI crystals, but found no sign of an annual modulation. The COSINE-100 experiment could not give a final conclusion about the DAMA/LIBRA result because of the relatively high background in the former experiment compared to the latter. Hence the development of the next generation experiment COSINE-200 is underway, specifically aiming at reducing the radioactive contaminations in the detector crystals. In particular, the presence of the isotopes  $^{40}\text{K}$  in naturally present potassium, as well as  $^{210}\text{Pb}$  from  $^{222}\text{Rn}$  contamination are the main sources of background [111].

Another type of scintillating medium that is often used are liquid noble gasses, xenon and argon. There are several advantages to the use of liquid noble gases for dark matter detection experiments. They have low recoil thresholds and can easily produce scintillation signals. Furthermore, pure xenon is radioactively clean, however argon suffers from the presence of  $^{39}\text{Ar}$ , which leads to some unavoidable backgrounds. Of course the presence of impurities can lead to background effects. The scintillation wavelength for liquid xenon is with 178 nm observable in commercially available photocathodes, whereas liquid argon scintillation signals of 128 nm need wavelength shifters to be observed [112]. The large atomic number

of especially xenon enhances the cross section for WIMP scattering due to its scaling of  $A^2$ . This is why xenon is the preferred detector medium in many experiments, more on this in the next paragraph. An exception to this is the MINICLEAN experiment, which also uses liquid neon in addition to liquid argon in order to study the dependence of the signal on the atomic number [113]. An additional attractive feature is that liquid noble gas detectors are self-shielding, i.e. background signals from outside or the edges of the detector do not penetrate deep inside the detector, allowing for a central fiducial volume with lower background. This property makes it attractive to scale up liquid noble gas detectors. In order to further reduce external backgrounds the detectors are shielded further. For example, the XMASS detector containing 800 kg liquid xenon is located 1000 m underground in the Kamioka Observatory in Japan and is also shielded by an 800 tonne water tank [114]. The Cherenkov signals of cosmic rays inside the water tank serve as a useful trigger, so that these external events are quickly identified. A further example of an experiment using liquid argon is the DEAP-3600 experiment, which has a 3600 kg liquid argon target [115].

### Scintillation and ionisation

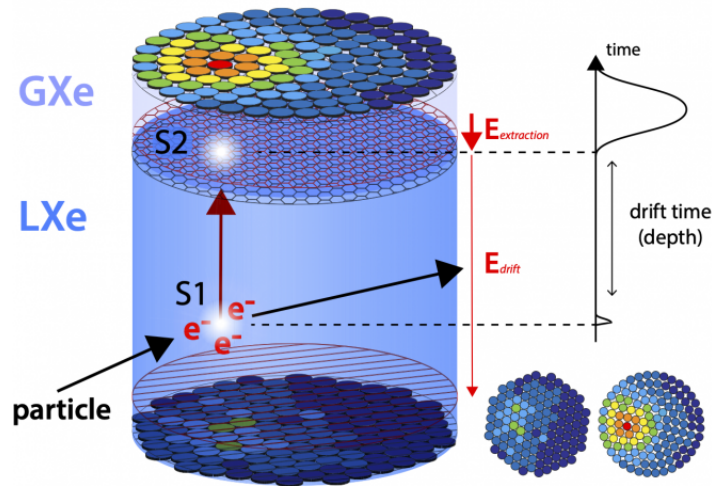


Figure 2.15: Overview of a dual phase xenon TPC. The incoming particle creates a scintillation (S1) signal when scattering with the liquid xenon medium, after which electrons are drifted upwards by an electric field, which creates a light signal (S2) when reaching the gaseous xenon. Image source: XENON collaboration, retrieved from <https://nigroup.ucsd.edu/research-projects/technology/>.

Scatterings inside liquid noble gases can not only cause scintillation, but also ionisation, releasing a charge in the detector medium. These two effects lead to different signals, and can both be used to gain information about the event. For this purpose, many experiments make use of a two-phase time projection chamber (TPC) containing both liquid and gaseous xenon, such as LUX [116], ZEPLIN-III [117], as well as in their planned successor LZ [118]. Further experiments are PANDAX-II [119] and XENON1T, which has set the most stringent bounds

on WIMP-nucleus scattering so far [95]. Some experiments also use two-phase TPCs filled with argon, most notably the DARKSIDE-50 [120] and ARDM [121] experiments.

Irrespective of whether the TPC is filled with xenon or argon, the detection principle stays the same. An overview of such a detector is shown in Figure 2.15. The TPC is mostly filled with liquid noble gas, with a small part at the top of the TPC containing xenon or argon in the gas phase. An incoming WIMP scattering with a nucleus in the liquid target will first produce a direct scintillation signal (S1). The scintillation light is picked up by photomultipliers (PMTs) lined at the top and bottom of the TPC. An electric field is applied across the TPC, so that electrons from atoms that were ionised by the scattering drift upwards to the top of the TPC. Once the electrons reach the surface between the liquid and gas at the top of the TPC they are accelerated and will emit a light signal proportional to the amount of electrons extracted from the liquid (S2), which is also captured by the PMTs. As the electrons take time to drift through the liquid, there is a time delay between the S1 and S2 signals. Combined with the position determination in the  $x, y$  plane by the PMTs, the drift time provides a measurement of the  $z$  position inside the TPC.

Liquid noble gas detectors are being scaled up, the XENON1T detector contains a total of 3.2t of liquid xenon, whereas the upcoming PANDAX-4T will contain 4t in its TPC [122]. The LZ experiment is designed with a 7t detector [118], similar to XENONnT [123]. The follow-up experiment to XENONnT, DARWIN, has been proposed as well, which with its planned 50t liquid xenon would be the biggest detector of its kind by far. For liquid argon detectors, the DARKSIDE-20K experiment will contain a total of 23t detector mass [124], with the ultimate goal of building the ARGO detector containing 300t [125].

On the other side, novel techniques are being applied to the data of current experiments to improve upon existing limits. An example is from the XENON1T experiment, which faces challenges to detect light dark matter with masses below 6 GeV, as it cannot transfer enough energy to give a detectable S1 signal. The S2 signal is detectable from a lower threshold, making an S2-only analysis attractive to probe lower dark matter masses. The downside of this method is that it comes at the cost of an increased background, as one loses the S1-S2 event correlation. Light dark matter cannot only scatter off atomic nuclei, but also off electrons, which can be distinguished through their relative S1 to S2 signal compared to nuclear recoils, and electronic recoils are another interesting probe for light dark matter masses. A first S2-only analysis the XENON1T experiment has already been performed for both nuclear as well as electronic recoils [126].

## Overview

After discussing many experiments, it is useful to see how different experiments compare. WIMP-nucleon scattering is divided into two processes: spin-dependent and spin-independent scatterings, which are mediated by  $Z$  and Higgs bosons respectively. The results for spin-independent scattering are shown in Figure 2.16, showing the exclusion limits of dark matter experiments on the spin-independent nuclear cross section as a function of the dark matter

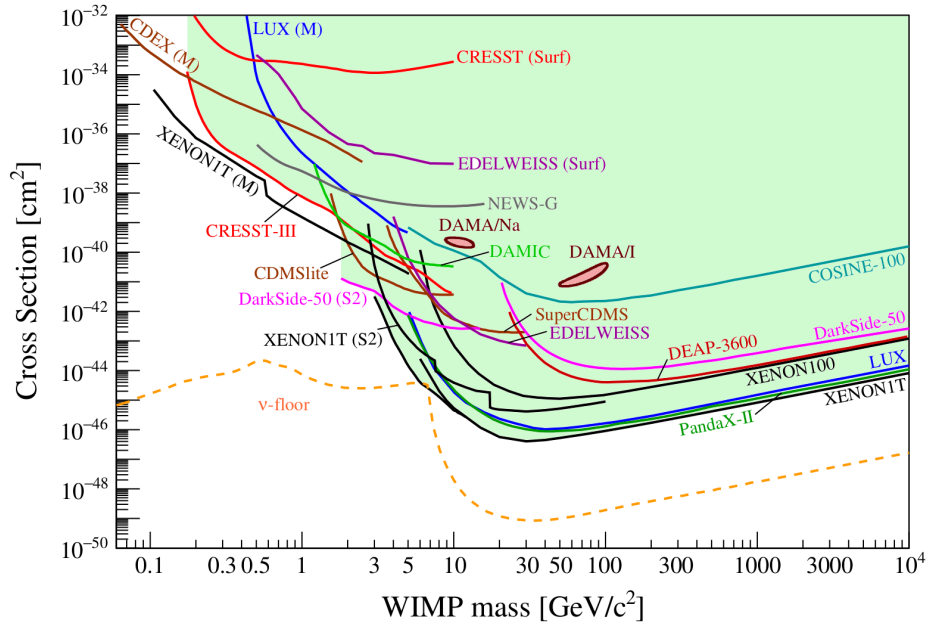


Figure 2.16: Current exclusion limits on the spin-independent WIMP-nucleon cross section as a function of the WIMP mass from a wide range of dark matter direct detection experiments. The DAMA/LIBRA preferred regions have also been included. Source: [127].

mass. The most stringent bounds on the cross section come from the XENON1T experiment over almost the complete mass range, with a minimum of  $\sigma = 4.1 \cdot 10^{-47} \text{ cm}^2$  at a WIMP mass of 30 GeV [95]. Also included are the results from the XENON1T S2-only analysis.

As the direct detection experiments are improved, the expected sensitivity reach moves to smaller cross section. The projected sensitivities of future experiments to the spin-independent cross sections are shown in Figure 2.17. The current experimental limits are indicated by the green-blueish shaded region. The PANDAX-4T will improve on the current results by an order of magnitude already, and LZ and XENONNT aim to probe the cross section by a further margin. DARKSIDE-20K, which is argon-based, can improve the projected sensitivities of the former xenon-based experiments at masses above 70 GeV, but is beaten by LZ and XENONNT below this mass. The planned ARGO and DARWIN experiments are much larger in scale and can probe an additional order of magnitude.

For spin-dependent interactions, the WIMP couples to the nuclear spin of the detector material. Depending on the exact isotope that is used, the coupling to protons and neutrons differs. Figure 2.18 shows the upper limits on the spin-dependent cross sections for WIMP scatterings on neutrons (left) and protons (right) from the XENON1T experiment in comparison with results from other experiments [128]. As can also be seen from the figures, is that the upper limits on the spin-independent cross section are more sensitive by several orders of magnitude. For the WIMP-proton cross section, the upper limit from PICO-60 is the most stringent one, lying at an order of magnitude below the XENON1T result.

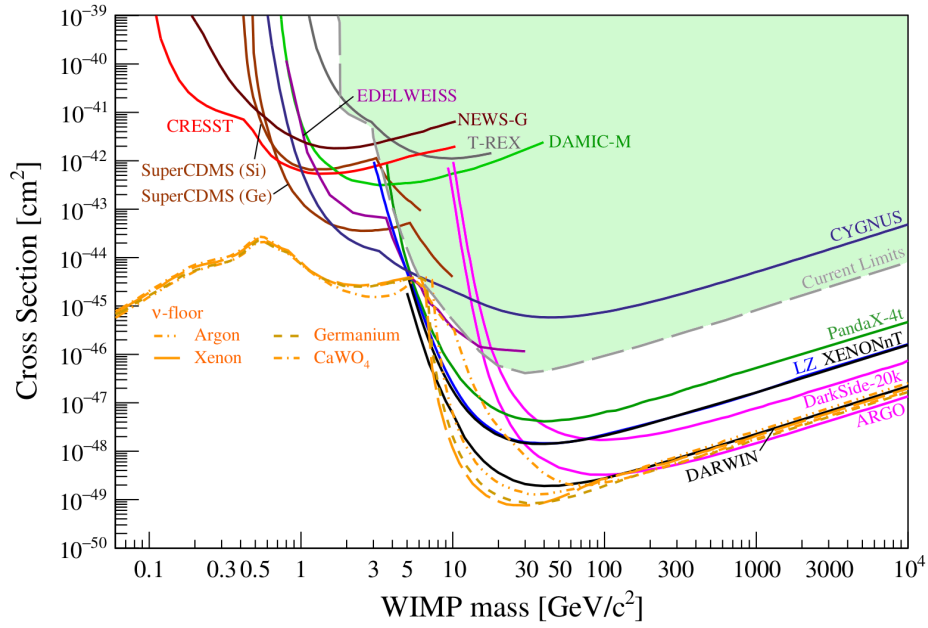


Figure 2.17: Projected sensitivity limits (90% C.L.) on the spin-independent cross section as a function of the WIMP mass from a wide range of dark matter direct detection experiments. Source: [127].

Figure 2.19 shows the resulting upper limits from the XENON1T experiment on dark matter-electron scattering [126]. The cross sections seem relatively large at first, lying around  $10^{-40} \text{ cm}^2$ , however they are a huge improvement in the mass range below a few GeV, compared to Figure 2.16. This shows that electronic recoil signals are a great source of information in the study of low-mass DM.

### A limit to discovery

Sooner or later every type of experiment runs into some kind of technical limit. In the case of direct detection experiments, the increasing sensitivity of the experiments means that they at some point become sensitive to coherent neutrino scattering caused by neutrinos from astrophysical sources. Three main sources for the neutrino background can be identified [129]. The first source are the neutrinos that are produced in nuclear fusion processes inside the Sun. Another source can be found in cosmic rays hitting Earth's atmosphere. In these collisions pions are produced, which decay into muons and neutrinos. The last source is the diffuse supernova neutrino background, which is the flux of neutrinos produced in supernovae. Scattering neutrinos interact in the detectors in almost the same way as WIMPs, making it unclear what particle caused an event. The point at which this happens is often called the “neutrino floor”. It is shown in Figures 2.16 and 2.17, and it depends on the detector material used. The term neutrino floor is slightly misleading, as one does not measure a sudden jump in neutrino events when increasing the sensitivity. Instead, neutrino fog is a more appropriate term. As the sensitivity of a detector increases, it will start measuring higher rates of neutrino

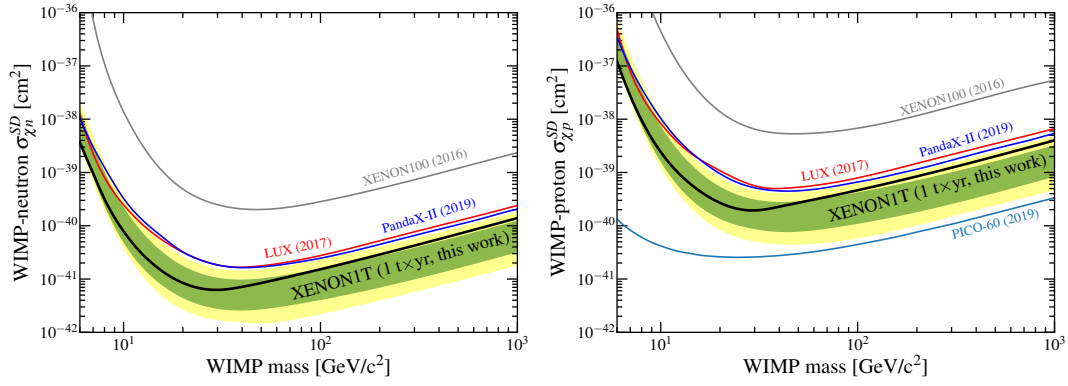


Figure 2.18: XENON1T 90% C.L. upper limit on the spin-dependent WIMP-neutron (left) and WIMP-proton (right) cross sections, with similar results from other experiments also included. The expected sensitivity is indicated by the green ( $1\sigma$ ) and yellow ( $2\sigma$ ) bands. Source: [128]

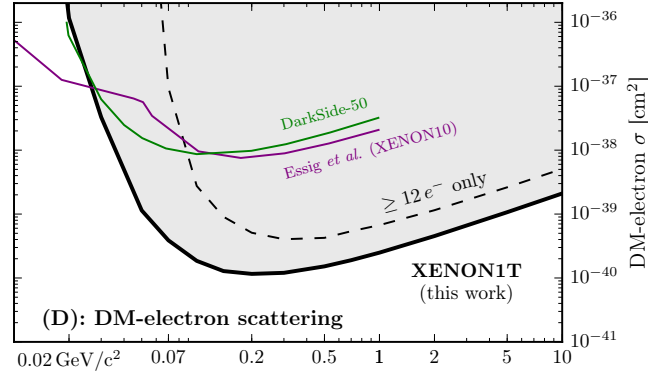


Figure 2.19: XENON1T 90% C.L. upper limit on the WIMP-electron cross section. Source: [126]

events. Eventually this rate is large enough that one is lost in the fog and WIMP events are completely obscured by interacting neutrinos.

### 2.3.2 Indirect detection

A different way of searching for dark matter is not by looking at direct dark matter signatures inside a detector, but to observe photon, neutrino or other cosmic rays signals produced in the annihilation (or decay) of WIMPs. For thermal WIMPs, annihilation processes mainly took place in the early universe before freezeout, and scarcely afterwards. However, in the early universe the dark matter density was homogenous and isotropic, except for some density perturbations that grew over time to form the cosmic structures we see today. The best prospects for the observation of dark matter annihilations are therefore in regions with the universe with a local overdensity of dark matter, such as the Sun or regions with generally higher dark matter density, such as the galactic centre. The relevant quantity for all these processes is the thermally-averaged cross section, which has been introduced previously in



Section 2.2.3. This can give an observable flux from the direction of these astrophysical objects.

The type of experiment is very much dependent on the messenger particle. In order to observe gamma rays that can be produced upon annihilation, one can make use of satellite observatories, as they do not suffer from an atmospheric background from cosmic rays. Charged cosmic rays can also be produced, either directly or e.g. via pion production. In this way charged (anti)leptons can be produced, as well as antiprotons. Because the luminous matter in the universe consists of matter, not antimatter, an excess signal of the latter is a clear signal that something, e.g. annihilating dark matter, is going on. These cosmic rays, as well as  $\gamma$  rays at higher energies can not only be observed in satellites, but also using Cherenkov telescopes that observe the Cherenkov radiation, which is emitted if particles move faster than the local speed of light in a medium, of cosmic ray showers hitting Earth's atmosphere. Neutrinos are notoriously difficult to detect, and would fly unnoticed through a satellite. That is why neutrino telescopes have large dimensions. In this section we will give an overview of the production sites of indirect detection signals, as well as some of the experiments measuring these.

### Signal sources

As ordinary matter feels the gravitational effects of the more abundant dark matter, the formation of astrophysical objects followed the distribution of dark matter during cosmic structure formation. The opposite is also true to a lesser degree. Thus regions with a large amount of ordinary matter, also have an overdensity of dark matter. We will now describe some of the sources that are generally observed in indirect searches.

Upon scattering with nuclei in objects such as stars and planets, WIMPs can be trapped inside the gravitational wells of such objects. A good candidate for this is the Sun, as it is relatively close to the Earth compared to many other astrophysical objects. Our solar system moves through the galactic dark matter halo, giving a flux of WIMPs. The time evolution of WIMPs inside the Sun can be described as

$$\dot{N} = C - 2\Gamma, \quad (2.28)$$

where  $C$  is the capture rate of WIMPs, which is dependent on the WIMP-nucleus cross section, as well as the surrounding dark matter density. Capturing dark matter increases the number of WIMPs, whereas annihilation of two WIMPs decreases it. The decrease of WIMPs is equal to twice the annihilation rate  $2\Gamma = C_A N^2$ , which scales with the number of WIMPs squared. At some point these two processes reach equilibrium, and the annihilation rate becomes directly related to the capture rate as

$$\Gamma = \frac{C}{2}, \quad (2.29)$$

and so the annihilation rate is through this relation dependent on the WIMP-nucleus cross sections that are the same as those probed by direct detection experiments. The annihilation inside the Sun produces SM particles, such as quarks, leptons, and Higgs/gauge bosons, then these decay products will quickly be absorbed through interactions in the interior of the Sun. The exception to this rule are the high-energetic neutrinos that are produced which pass through the Sun unhindered and can reach the Earth. This makes neutrino telescopes well-suited to measure WIMP annihilation signals from the Sun, which is further considered in Chapters 6 and 7. In the case where the capture and annihilation rate have not reached equilibrium yet, the annihilation rate is suppressed as

$$\Gamma = \frac{C}{2} \tanh^2(t/\tau), \quad (2.30)$$

with  $\tau$  being the equilibrium time scale, given as

$$\tau = \frac{1}{\sqrt{CC_A}}, \quad (2.31)$$

which for a typical 100 GeV WIMP with weak cross sections lies around  $\tau \simeq 3 \cdot 10^7$  yr, well below the age of the Sun [130]. Furthermore, WIMPs might “evaporate” when they are upscattered in scatterings with nuclei. Only at light masses of  $\lesssim 10$  GeV WIMPs can undergo evaporation in the Sun, so this mostly poses no large problems [42].

In section 2.1.1 the rotation curves of several galaxies were shown, which all featured a constant rotational velocity in their outer regions. This can be explained through the presence of a galactic dark halo, which can also have denser regions that boost dark matter annihilation. As dark matter and ordinary matter are usually found at the same location, one can expect that a galaxy will have a larger dark matter density near its centre than in its outskirts. Many galaxies, including our own, also have a large amount of mass in the galactic centre due to the presence of a super-massive black hole. The distribution of dark matter is usually described by a so-called density profile. Indirect detection generally depends on the density profile that is assumed. A general form for this density distribution is

$$\rho(r) = \frac{\rho_0}{(r/r_0)^\gamma (1 + (r/r_0)^\alpha)^{(\beta-\gamma)/\alpha}}, \quad (2.32)$$

where the Greek exponents describe the behaviour of different dark matter models. The constants  $\rho_0$  and  $r_0$  are the scale density and radius respectively, which are specific to an individual halo. The isothermal profile corresponds to  $(\alpha, \beta, \gamma) = (2, 2, 0)$ . One of the commonly used profiles is the Navarro-Frenk-White (NFW) profile, which was obtained from N-body simulations, corresponding to  $(\alpha, \beta, \gamma) = (1, 3, 1)$  [131].

However, the galactic halo model has some problems. In section 2.1.4 we already mentioned the missing satellite problem, based on the absence of many dwarf galaxies around our galaxy. For dark matter problems there exists the cuspy halo or cusp-core problem. It has to do with the fact that dark matter profiles from N-body simulations, such as the NFW profile, which

scales as  $\rho \sim (r/r_0)^{-1}$  for  $r \ll r_0$ , whereas observations of galaxies indicate that the density profile in the centre of galaxies is mostly flat. The addition of a small amount of warm dark matter to the universe can resolve this discrepancy, as it would wash out the cusp in the halo [34]. A more fitting phenomenological description of dark haloes is given by the Burkert profile, which with

$$\rho(r) = \frac{\rho_0}{(1 + r/r_0)[1 + (r/r_0)^2]}, \quad (2.33)$$

is similar to the NFW profile at  $r \gg r_0$ , but has a constant central density of  $\rho_0$  [132]. The large dark matter density in the galactic centre makes it an interesting target for indirect detection. However,  $\gamma$  rays from the galactic centre can be absorbed in dust clouds when propagating, obscuring our view. Furthermore, there are many other sources of  $\gamma$  rays, such as the presence of the super-massive black hole in the galactic centre.

In addition to observing the dark matter halo of our own galaxy, one can also observe extragalactic objects. In particular the spheroidal dwarf satellite galaxies of the Milky Way are very suitable for this due to their proximity, their relatively large amount of dark matter, as well as exhibiting no  $\gamma$  rays from non-thermal astrophysical processes [133]. Whereas one can detect  $\gamma$  rays and neutrino signals from these satellite galaxies, it is difficult to detect charged cosmic rays as these are deflected by the galactic magnetic field, and thus information about the direction of origin is lost.

## Cosmic ray searches

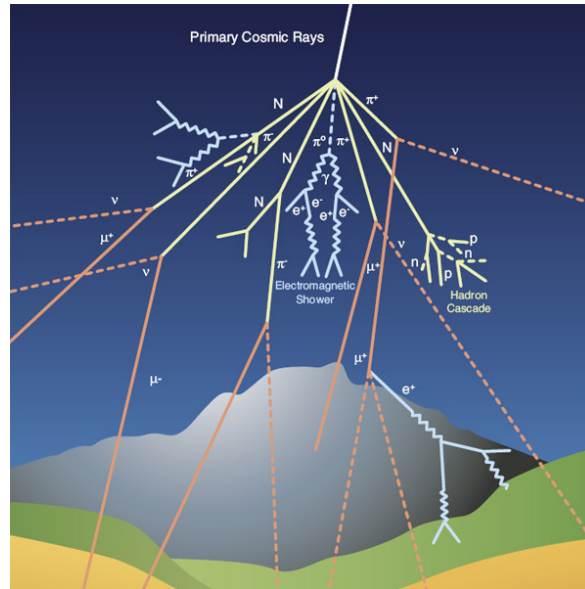


Figure 2.20: Schematic overview of the development of an air shower created by a cosmic ray. Image source: <https://home.cern/science/physics/cosmic-rays-particles-outer-space>

After describing the possible sources of dark matter annihilation signals, we turn to the different kinds of experiments that are used for indirect detection. For cosmic ray searches the types of observation that are used are Cherenkov telescopes and  $\gamma$  ray/cosmic ray satellites.

The principle for Cherenkov telescopes is the Cherenkov radiation that is produced in particle showers in cosmic ray events. A cosmic ray travelling to Earth will collide with nuclei in the atmosphere. In this process a large range of particles can be created, and the general development of an airshower is partly independent of the incoming particle. Figure 2.20 shows the general development of the air shower that is produced by a cosmic ray. The primary interaction starting the shower will usually produce many pions. The neutral pions will mostly decay into photons, which will at later points create electron-positron pairs, which can create more photons through bremsstrahlung, creating an electromagnetic cascade. Charged pions can decay into muons and neutrinos, but they are longer lived, meaning that they can interact with nuclei further down in the atmosphere, creating new particles in the air shower. This is the hadronic component which keeps the air shower going. At some point the created particles have too little energy to create more particles, and the air shower reaches its maximum. If the incoming particle is a  $\gamma$  ray (or an electron or a positron), then the electromagnetic cascade is initiated immediately, with only a small hadronic component. Hence the amount of muons in these showers is low. If the primary particle is a proton or nucleus, then the hadronic component is larger <sup>3</sup>. Furthermore, the cross section is higher, especially for heavier nuclei, meaning that the shower starts at a higher point in the atmosphere [134].

The velocities of the cascading particles are usually greater than the local speed of light in the atmosphere, creating a cone of Cherenkov radiation at specific angle of  $\theta_c \sim 1/n$ , where  $n$  is the refractive index of the medium. Cherenkov telescope operate on the basis of detecting this light in an array of telescopes and in such way reconstruct the energy and direction of the incoming particle, which for dark matter searches is mostly a  $\gamma$  ray, an electron/positron, or an (anti)proton. The Cherenkov light can be detected in two different ways. There are the imaging atmospheric Cherenkov telescopes (IACTs), which directly detect the Cherenkov light from the atmosphere with mirror telescopes. They are mostly sensitive for energies above 100 GeV. Several experiments fall into this category. There is the H.E.S.S. telescope, which has probed the galactic centre [135], as well as the Milky Way's satellite galaxies [136]. Further observations of the latter were made by the MAGIC telescope [137], and VERITAS [138]. The next generation of IACTs will be started by CTA, which will contain more than 100 telescopes in the northern and southern hemispheres, and aims to improve the existing constraints by an order of magnitude [139].

The other method is to observe Cherenkov radiation from air shower remnants in water tanks at the surface. Muons created in air showers can create such signals, as well as electron-positron pairs that are created by  $\gamma$  rays entering the water tank. With an array of these Cherenkov tanks, one can reconstruct the primary particle of the event. These kind of

<sup>3</sup>To see the difference between  $\gamma$  ray and proton-induced air showers, the HAWC collaboration have a small Gamma/Hadron separation game on their website <https://www.hawc-observatory.org/observatory/ghsep.php>

telescopes have a higher threshold than the IACTs. The MILAGRO detector became sensitive at energy ranges on the TeV scale, which was improved in the next-generation experiment HAWC, which is sensitive to energies above 500 GeV [140].

Ground-based Cherenkov detectors are powerful tools, but generally do have a high energy threshold at which they become sensitive. The other option to detect  $\gamma$  rays and cosmic rays is through satellite observations. Satellites can detect these rays directly as they are above Earth's atmosphere. One of these satellites is the FERMI Gamma-ray Space telescope, which contains the Large Area Telescope (LAT). It consists of a tracker built out of silicon detector modules with tungsten layers in between. The tungsten layers are for converting incoming  $\gamma$  rays into electron-positron pairs, which are tracked inside the silicon. These particles then reach the calorimeter, which determines the energy in the event. FERMI-LAT can measure signals in the energy range from 30 MeV up to 300 GeV, which is lower than the ground-based detectors [141, 142].

The PAMELA detector was a spectrometer, and measured charged cosmic rays, mostly electrons, positrons, and (anti)protons. It detected an unexpected amount of positrons [143]. It also measured a flux of antiprotons [144]. A similar, but newer detector is AMS-02, which is mounted on the International Space Station (ISS) [145]. Whereas positron measurements of FERMI-LAT deviated from the PAMELA result, further measurements by AMS-02 agree with PAMELA [146]. However, the question remains whether the observed excess is really due to dark matter or if other causes, such as pulsars, or a lack of understanding about cosmic ray propagation in the galaxy offer a sufficient explanation.

### Comparison of results

Let us now compare the results of the different  $\gamma$  ray and cosmic ray experiments. As an example, we show the resulting upper limits on  $\langle\sigma v\rangle$  from H.E.S.S. observations of dwarf galaxy satellites of the Milky Way in Figure 2.21. The left plot shows the bounds for several possible annihilation channels. From this plot one can see that the strongest bound is found from the  $\gamma\gamma$  channel by far, and is very close to the canonic thermal relic value of  $\langle\sigma v\rangle \approx 3 \cdot 10^{-26} \text{ cm}^3 \text{ s}^{-1}$  for masses below 2 TeV. Of the other channels, the charged lepton channels are the most stringent ones at masses below 5 TeV, especially the  $\tau^+\tau^-$  channel, followed by the  $W^+W^-$  channel. The right plot of figure 2.21 shows the  $W^+W^-$  channel result compared to the results of other Cherenkov telescopes, as well as FERMI-LAT results. This plot illustrates the complementarity of the different types of telescopes nicely, as the FERMI-LAT result is the strongest by a wide margin at low masses, but from 4-5 TeV on gets beaten by the MAGIC limit. Thus the combination of space based  $\gamma$  and cosmic ray satellites, and Earth based Cherenkov telescopes allows for detection over a large mass range.

Figure 2.22 shows the bounds on  $\langle\sigma v\rangle$  from the observation of electron and positron events with FERMI-LAT, as well as the results from the other space-based experiment AMS-02, and the ground-based H.E.S.S. telescope. These bounds are very strong, and can exclude

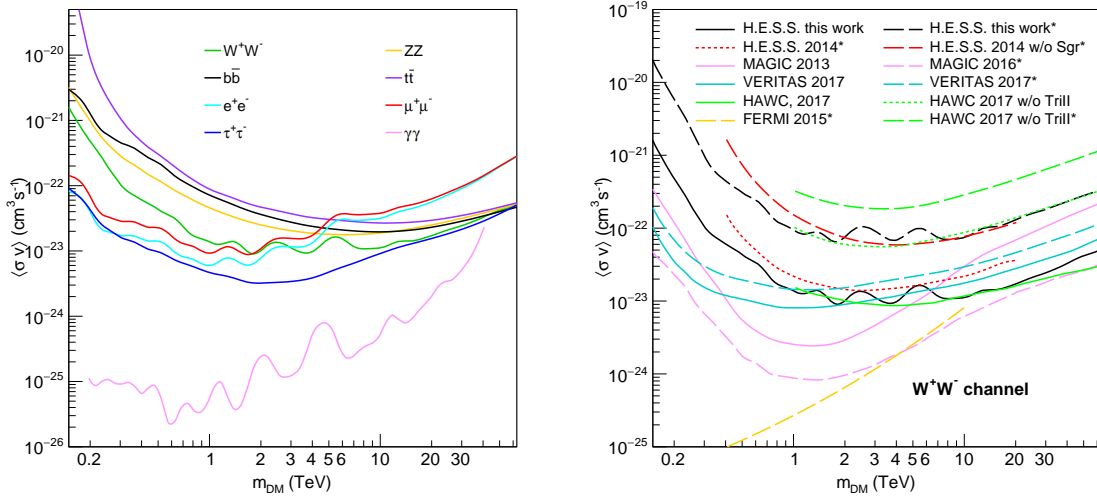


Figure 2.21: H.E.S.S. upper limits on  $\langle\sigma v\rangle$  from the observation of dwarf galaxy satellites of the Milky Way. The left plot shows the H.E.S.S. bounds for different annihilation channels, whereas the right plot compares the H.E.S.S. results for the  $W^+W^-$  channels to bounds obtained in other experiments. Source: [136]

the canonical thermal relic value for  $\langle\sigma v\rangle$  at dark matter masses below 200 GeV. The bounds become much less stringent for increasing mass, and above 1 TeV, the H.E.S.S. bound is the most stringent. These results show that indirect detection of dark matter through  $\gamma$  rays or cosmic rays provides a valuable addition to direct detection.

### Neutrino telescopes

The last type of signal one can expect are the neutrinos. Due to their elusive nature, one needs different types of detectors to be able to detect them. The principle of operation for neutrino telescopes is that neutrinos scattering in charged current interactions produce charged leptons that emit Cherenkov light. This means that the detector medium must be transparent enough for the light to be detected in optical sensor. As the probability of a neutrino interacting is low, a neutrino telescope must have a large volume to obtain a relevant amount of neutrino signals. This is why neutrino telescopes use water or ice as a detection medium.

Current experiments that use water as a detector medium are ANTARES [147, 148], which is located in the Mediterranean Sea, the Baikal Deep Underwater Neutrino Telescope (BDUNT) [149, 150] in Lake Baikal, and Super-Kamiokande [151], located in the Kamioka mine, Japan. The first two make use of natural water bodies, whereas Super-Kamiokande (Super-K, or SK) uses a tank with ultrapure water. Next-generation experiments are at various stages of development, such as KM3NET [152] as a successor to ANTARES, the Hyper-Kamiokande detector [153] as a successor to Super-Kamiokande, and PINGU as a successor to ICECUBE [154]. There is currently one neutrino telescope using ice as a detector

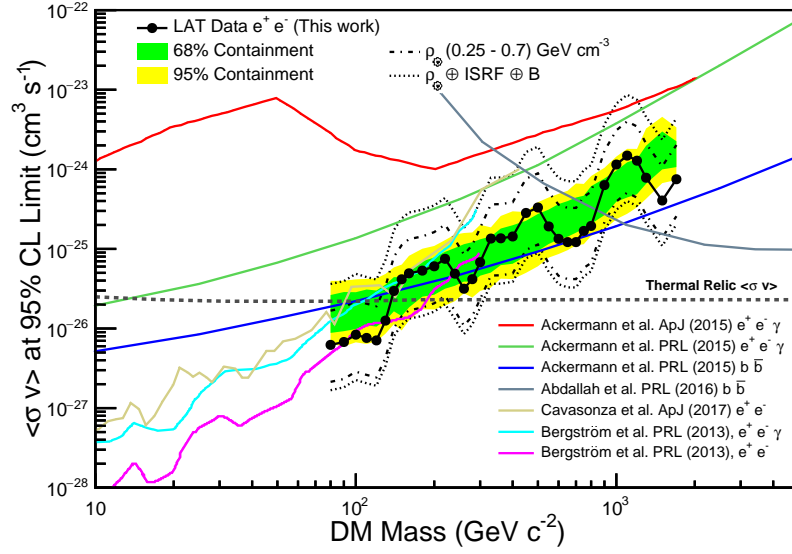


Figure 2.22: FERMI-LAT bounds on  $\langle\sigma v\rangle$  from the observation of electron and positron events. The canonical thermal relic value for  $\langle\sigma v\rangle$  has been marked by the striped line. Other bounds that are included are from FERMI-LAT (Ackermann et al.), H.E.S.S. (Abdallah et al.), and AMS-02 (Cavasonza et al., Bergström et al.). Source: [142]

medium, with bears the fitting name ICECUBE [155, 156, 157, 158]. It is located at the South Pole, and in its current configuration it consists of 86 strings with optical modules that were lowered in the Antarctic ice sheet. An overview of the detector (albeit with an older configuration of 81 strings) is shown in Figure 2.23.

Figure 2.24 shows the upper bounds on the thermally averaged annihilation cross section  $\langle\sigma v\rangle$  from observations of the Galactic Centre for the  $\nu\bar{\nu}$ ,  $b\bar{b}$ ,  $W^+W^-$ , and  $\mu^+\mu^-$  channels by observations by Super-Kamiokande and compared to limits from ANTARES and ICECUBE [151]. All experiments are most sensitive in the  $\nu\bar{\nu}$  channel. This can be explained by the fact that WIMP annihilation into neutrino pairs will give sharp spectral lines at  $E_\nu \simeq m_{\text{DM}}$ . Annihilation into other particle pairs such as  $W^+W^-$  only produce neutrinos in secondary processes, leading to a continuous neutrino energy spectrum. One can also see that the energy threshold of Super-Kamiokande is lower than those of ANTARES and ICECUBE.

The second main source of high-energy neutrinos is our Sun. As was explained at the start of this section, the annihilation rate is directly related to the capture rate of WIMPs in the Sun. This means that observations of high-energy solar neutrinos can be used to constrain the WIMP-nucleus cross section. Because the Sun consists mostly of hydrogen, neutrino telescopes are most sensitive to the spin-dependent cross section on protons. Figure 2.25 shows the projected upper bounds on the spin-dependent WIMP-proton cross section  $\sigma_{\chi p}^{\text{SD}}$  for Hyper-Kamiokande, as well as the comparison with the current ICECUBE and planned PINGU neutrino telescopes. From direct detection experiments, PICO-60 is included, as it is currently the most stringent bound. Also included is its predecessor PICASSO. Current

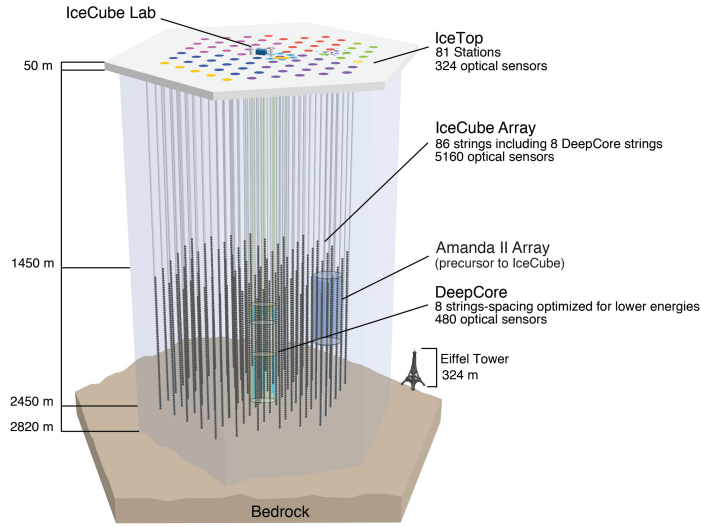


Figure 2.23: Schematic overview of the ICECUBE detector, showing the strings with optical modules that were lowered into the Antarctic ice sheet. Image source: <https://icecube.wisc.edu/gallery/detector/>

bounds from ICECUBE are competitive with direct detection experiments such as PICO-60, in particular at masses above 100 GeV.

### 2.3.3 Collider searches

The third way to study dark matter is through collider experiments. If potential dark matter candidates have a mass within the experimentally reachable energy range, then they can be produced in particle collisions. These dark matter particles will not produce visible signals inside the detector, and thus their presence has to be detected by other means. The quantity that is used for this is the missing transverse energy  $E_T$  perpendicular to the collider beams, which is zero before collision. Currently the Large Hadron Collider (LHC) is the most powerful proton and heavy ion collider where the ATLAS [161] and CMS [162] experiments are searching for BSM physics.

The interactions between SM and DM particles in collider searches can be summarised in the Feynman diagrams shown in Figure 2.26 [160]. When extending the particle content of the SM by just a single new particle, which is a DM candidate, it can be produced through the diagrams (b) and (c), provided that it couples to a mediator, for which one usually assumes a Higgs or  $Z$ -boson. However, one can also assume a new BSM mediator, for which the  $Z'$ -boson, which is a heavier version of the SM  $Z$ -boson, is a popular candidate. If there exists a new mediator, then SM SM  $\rightarrow$  SM SM processes as shown in diagram (d) will occur at different rates compared to the SM prediction. The first diagram (a) describes a further unspecified interaction between the SM and DM particles. If a BSM mediator is at a mass scale beyond the reach of a collider, then the mediator can be integrated out, leaving a direct



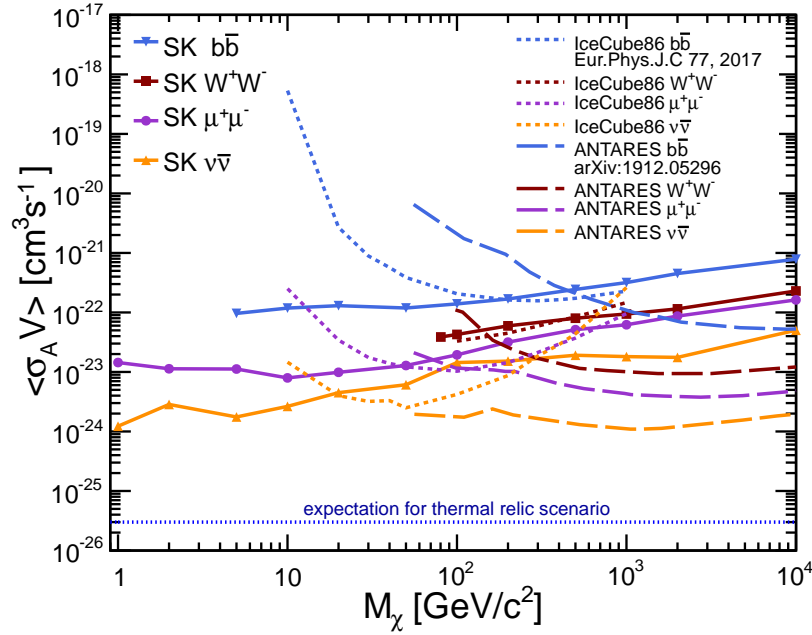


Figure 2.24: Upper bounds at 90% C.L. on the thermally averaged annihilation cross section  $\langle\sigma v\rangle$  from observations of the Galactic Centre for the  $\nu\bar{\nu}$ ,  $b\bar{b}$ ,  $W^+W^-$ , and  $\mu^+\mu^-$  channels. Source: [151]

interaction vertex with an effective coupling that does not depend on the high-energy physics. Such a theory is called an effective field theory (EFT), of which Fermi's description of  $\beta$  decay with coupling constant  $G_F$  is a good example. The EFT description breaks down once the collision energies are on the same scale as the mediator mass.

As an example, if one assumes a Higgs-portal model in which a fermion or scalar dark matter candidate couples to the Higgs, the Higgs boson can decay into dark matter pairs, as in Figure 2.26(b), which would lead to invisible decays. The CMS collaboration has observed an upper bound on the invisible branching ratio of the Higgs of

$$\text{Br}(h \rightarrow \text{invis.}) < 0.19 \quad (2.34)$$

at 95% C.L. [163], which places an upper bound on the DM-Higgs coupling. This, in turn, has consequences for direct detection experiments, as this coupling also determines DM-nucleon scattering. Figure 2.27 shows the 90% C.L. upper bounds on the WIMP-nucleon cross section that can be derived from this measurement. Both the case of fermion (dashed red) as well as scalar (solid orange) dark matter is considered. The results from several direct detection experiments have been included as a comparison. From this one can see that collider searches can provide stringent bounds on scattering cross sections at lower masses  $\lesssim 10$  GeV, where direct detection experiments become less sensitive due to detector thresholds. The downside is that collider searches are generally model dependent if one moves to more complicated models than this simplified Higgs-portal model.

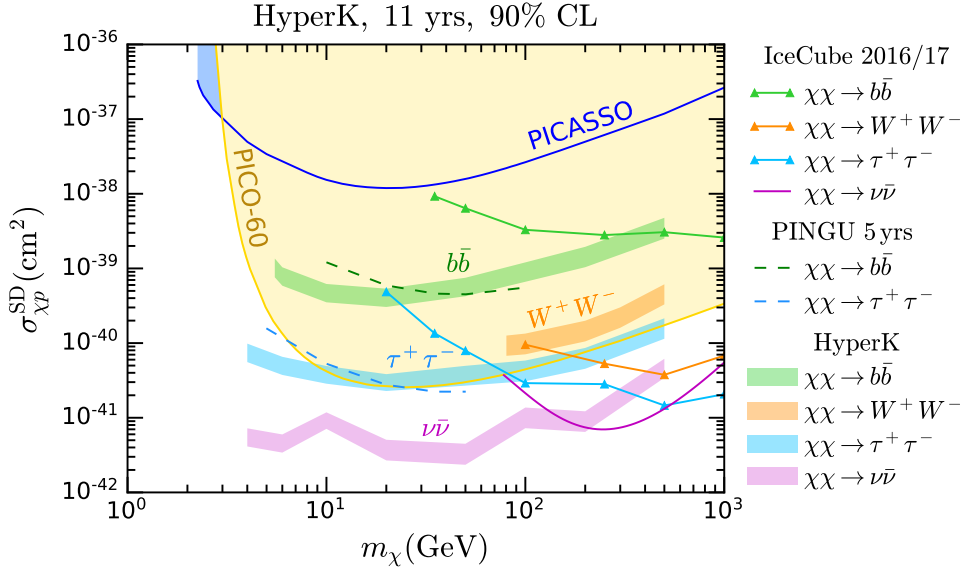


Figure 2.25: Upper bound projections of Hyper-Kamiokande at 90% C.L. on the spin-dependent WIMP-proton cross section  $\sigma_{\chi p}^{SD}$ , with current bounds from ICECUBE, PICO-60, PICASSO, and projections of PINGU. Source: [159]

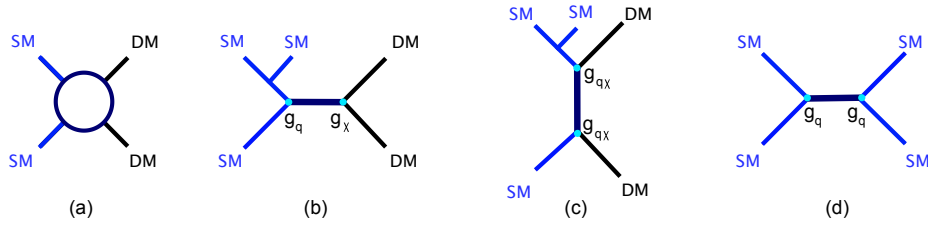


Figure 2.26: Types of interactions probed in collider experiments. (a) Interaction of SM and DM particles via an effective field theory (EFT). (b), (c) Production of DM particles via a mediator with couplings  $g_x$  at the vertices involved. (d) SM particle production via a BSM mediator. Source: [160]

An important quantity in collider searches is the luminosity  $L$ . The number of events per second in a collider experiment is given by

$$\frac{dN}{dt} = L\sigma, \quad (2.35)$$

depending on the cross section  $\sigma$  of the studied process. The luminosity depends on the parameters of the particle beam [164]. A directly related quantity is the integrated luminosity, which is obtained by integrating the luminosity over the detection time

$$\mathcal{L} = \int L(t)dt, \quad (2.36)$$

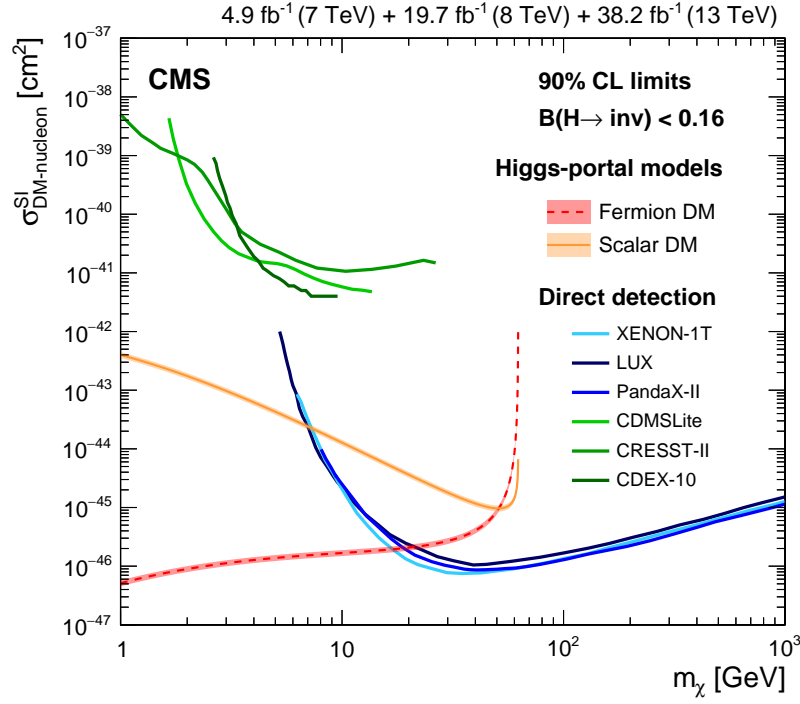


Figure 2.27: 90% C.L. upper limits on the WIMP-nucleon for fermion (dashed red) or scalar (solid orange) DM based on an upper bound on the invisible Higgs decay width. Comparisons with direct detection experiments are also included. Source: [163]

which relates to the number of events through

$$\mathcal{L}\sigma = N. \quad (2.37)$$

Thus when reporting results from collider experiments the integrated luminosity, usually given in units of  $\text{fb}^{-1}$ , is included, like at the top of Figure 2.27.

The combined effort of direct detection, indirect detection, and collider searches is crucial in the search for dark matter. It allows us to probe a wide range of energy ranges in complementary ways, only this way a complete picture of dark matter physics can be obtained.



### 3 Neutrino physics

From observations of the energy spectrum of nuclear beta decays it was found that the resulting energy of the electron followed a continuous distribution, instead of the sharp line that was expected if only an electron would be emitted. In 1930 the solution was proposed by Wolfgang Pauli in the form of the neutrino (which he initially called neutron), which would make beta decay a three-body decay and thus the energy distribution of the electron could be continuous. The first direct observation of the neutrino was in the Cowan-Reines experiment, which used the inverse beta decay reaction

$$\bar{\nu}_e + p \rightarrow n + e^+, \quad (3.1)$$

to observe the 511 keV gamma rays created in electron-positron annihilation. The neutrons that were created in this process were captured by the cadmium in the scintillator, which resulted in a second gamma ray. Neutrinos are produced in many nuclear reactions, and using a nuclear reactor as a source of neutrinos, they were able to confirm the detection of the (electron anti)neutrino [165].

Next to man-made neutrino sources, neutrinos are created by several processes in nature. The Sun is the largest nuclear reactor in our surroundings, and produces neutrinos from the fusion of various isotopes. Observations of the solar neutrino flux lead to a discrepancy where only a third of the expected amount of neutrinos were detected, which was also dubbed the solar neutrino problem. This was a hint that there exist several neutrino types that mix with each other, as we know now. More on this will be discussed in section 3.1.

In the previous chapter, cosmic rays were discussed in section 2.3.2, in which it was mentioned that pions are created in cosmic rays. The neutral pions decay into two photons, but the charged pions decay into

$$\pi^+ \rightarrow \mu^+ + \nu_\mu, \quad (3.2)$$

$$\pi^- \rightarrow \mu^- + \bar{\nu}_\mu, \quad (3.3)$$

of which the muon subsequently decays into

$$\mu^+ \rightarrow e^+ + \nu_e + \bar{\nu}_\mu, \quad (3.4)$$

$$\mu^- \rightarrow e^- + \bar{\nu}_e + \nu_\mu, \quad (3.5)$$

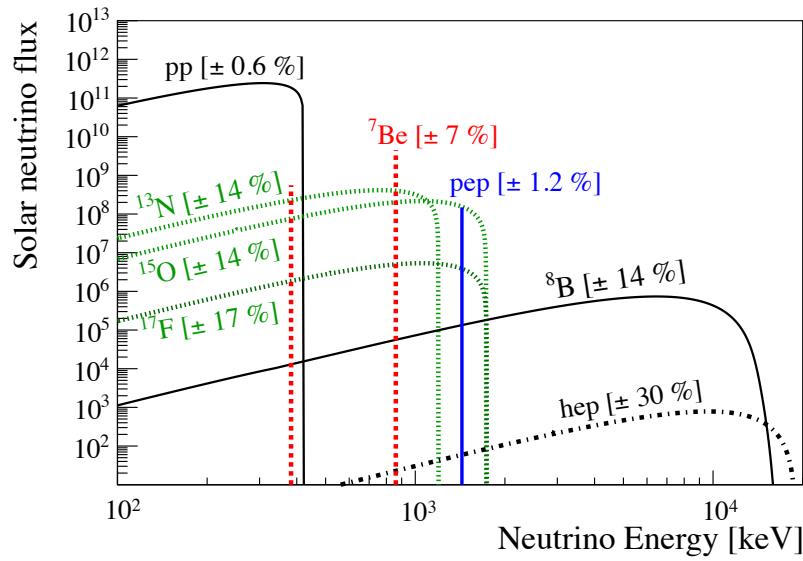


Figure 3.1: The energy spectrum of solar neutrinos. The flux is given in units of  $\text{cm}^{-2} \text{s}^{-1} (10^3 \text{ keV})^{-1}$  for the continuous spectra, and in  $\text{cm}^{-2} \text{s}^{-1}$  for the monochromatic lines. The red-dotted lines correspond to both  ${}^7\text{Be}$  lines. The theoretical uncertainty is shown in brackets. Source: [166].

meaning that one would expect to observe two muon neutrinos for each electron neutrino. Furthermore, neutrinos are produced in supernovae.

## 3.1 Neutrino oscillations

In this section we will go into further detail on the solar neutrino problem, which led to the discovery of neutrino flavour oscillations. We will then describe the mechanism behind the oscillations, and their implications. Then we will discuss some of the experiments involved in measuring neutrino oscillations.

### 3.1.1 Solar neutrino problem

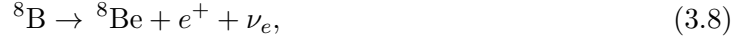
The Homestake experiment aimed to measure the flux of solar neutrinos using the inverse beta decay of  ${}^{37}\text{Cl}$ . Based on the Sun's luminosity, the amount of nuclear reactions and thus the amount of neutrinos produced can be calculated. It was found that the neutrino flux was around one-third of the expected value [167]. The start of the nuclear fusion chain is the  $pp$  chain, which starts with the fusion of two hydrogen nuclei (protons) and ends at  ${}^4\text{He}$  nuclei. At several stages in this process neutrinos are emitted [168]. The first reaction in the chain is the fusion of hydrogen to deuterium

$$p + p \rightarrow {}^2\text{H} + e^+ + \nu_e, \quad (3.6)$$

in which an electron neutrino is emitted. In later stages  ${}^3\text{He}$  nuclei are formed, which fuse to form  ${}^4\text{He}$  and two protons.  ${}^3\text{He}$  can also fuse with a  ${}^4\text{He}$  nucleus to form  ${}^7\text{Be}$ . From this point on there are two possibilities. The first one being that  ${}^7\text{Be}$  interacts with an electron



and emits an electron neutrino. The lithium can fuse with a proton to form two  ${}^4\text{He}$  nuclei. The other process that emits neutrinos is when  ${}^8\text{B}$  formed through  ${}^7\text{Be}$ - $p$  fusion beta decays



after which the beryllium decays via alpha decay into two  ${}^4\text{He}$  nuclei. Further electron neutrinos are emitted from the beta decays in the CNO chain, as well as the rarer  $p + e^- + p \rightarrow {}^2\text{H} + \nu_e$  (pep) and  ${}^3\text{He} + p \rightarrow {}^4\text{He} + e^+ + \nu_e$  (hep) processes. The fluxes for the different processes are shown in Figure 3.1. From this it is clear that most of the solar neutrinos are from  $pp$  fusions. The CNO cycle neutrinos have lower fluxes, but they become the main source of neutrinos above 400 keV, until they fall off between 1 and 2 MeV. Around this energy range one can also observe the  ${}^7\text{Be}$  and the  $pep$  lines. The highest-energy neutrinos that can be produced at decent rates are those from  ${}^8\text{B}$ .

The definitive solution to the solar neutrino problem was provided by Super-Kamiokande [169] and the Sudbury Neutrino Observatory (SNO) [170] from observations of  ${}^8\text{B}$  solar neutrinos. The Homestake experiment measured signals of the inverse beta decay of nuclei, which is a charged current (CC) interaction as it involves  $W^\pm$  exchange. The CC interaction is only sensitive to electron neutrinos, but not to the other two generations. In SNO the neutral current (NC) interaction via  $Z$  exchange was also included, as well as the scattering of neutrinos on electrons (ES), giving the following processes for the scattering of a neutrino  $\nu_x$  ( $x = e, \mu, \tau$ ) with deuterium atoms  $d$  inside the SNO detector

$$\nu_e + d \rightarrow p + p + e^- \quad (\text{CC}), \quad (3.9)$$

$$\nu_x + d \rightarrow p + n + \nu_x \quad (\text{NC}), \quad (3.10)$$

$$\nu_x + e^- \rightarrow e^- + \nu_x \quad (\text{ES}). \quad (3.11)$$

The measurements of SNO and Super-Kamiokande provided the evidence for the flavour oscillation of solar neutrinos. This was in line with other observations from Super-Kamiokande, which had already observed oscillations of atmospheric neutrinos [171].

### 3.1.2 Oscillation mechanism

The reason behind neutrino oscillations is the fact that the gauge eigenstates in which neutrinos partake in weak interactions are not equal to the mass eigenstates with which they propagate. We will show how mass differences between the neutrino eigenstates lead to these

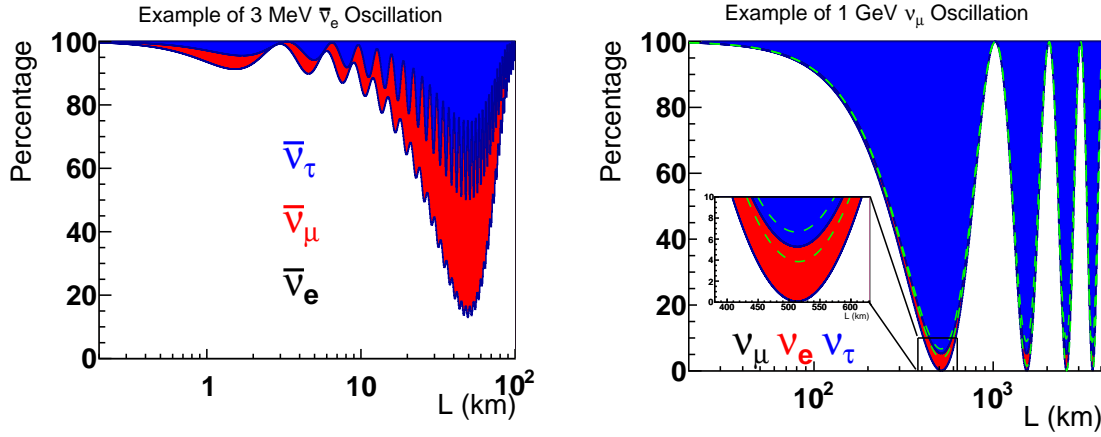


Figure 3.2: Three-flavour neutrino oscillation probabilities as a function of the distance. The left figure shows an example of a 3 MeV  $\bar{\nu}_e$  typical for reactor experiments. The right figure shows the oscillation of a 1 GeV  $\nu_\mu$ , for an atmospheric neutrino or one created in an accelerator beam. Source: [172].

oscillations, following [47]. In a CC interaction a neutrino in the gauge eigenstate  $\nu_\alpha$  can be produced, which is written in terms of a linear combination of mass eigenstates  $\nu_i$

$$|\nu_\alpha(t)\rangle = \sum_{i=1}^3 U_{\alpha i}^* |\nu_i(t)\rangle \quad (3.12)$$

with a mixing matrix  $U$  and explicit time dependence. Making a plane wave ansatz, the time evolution of the neutrino states follows

$$|\nu_i(t)\rangle = e^{-iE_i t} |\nu_i(0)\rangle, \quad (3.13)$$

where  $E_i$  is the relativistic energy belonging to the mass eigenstate  $i$ . As neutrinos have very large energies compared to their masses  $m_i$ , one can approximate  $E_i = \sqrt{p^2 + m_i^2} \simeq p + m_i^2/2E$ , as the momentum for each generation is nearly equal. The probability that the emitted neutrino  $\nu_\alpha$  is encountered in the gauge eigenstate  $\nu_\beta$  in a next interaction, is given by the probability

$$P_{\alpha\beta} = |\langle \nu_\beta | \nu_\alpha(t) \rangle|^2 = \left| \sum_{i=1}^3 \sum_{j=1}^3 U_{\alpha i}^* U_{\beta j} \langle \nu_\beta | \nu_\alpha(t) \rangle \right|^2, \quad (3.14)$$

which can be brought to the form [47]

$$P_{\alpha\beta} = \delta_{\alpha\beta} - 4 \sum_{i < j} \text{Re} [U_{\alpha i} U_{\beta i}^* U_{\alpha j}^* U_{\beta j}] \sin^2(X_{ij}) + 2 \sum_{i < j} \text{Im} [U_{\alpha i} U_{\beta i}^* U_{\alpha j}^* U_{\beta j}] \sin(2X_{ij}), \quad (3.15)$$

where

$$X_{ij} = \frac{(m_i^2 - m_j^2)L}{4E} = 1.267 (\Delta m_{ij}^2 / \text{eV}^2) \frac{(L/\text{km})}{(E/\text{GeV})}, \quad (3.16)$$



after replacing the time dependence by  $t = L$  for neutrinos moving almost at the speed of light, resulting in an oscillation length of

$$L = \frac{4\pi E}{|\Delta m_{ij}^2|}, \quad (3.17)$$

which is energy-dependent, hence a quantity that is often used in oscillation experiments is  $L/E$ . The above expression for the oscillation probability is quite unwieldy, let us therefore consider the case with only two neutrino generations. In this case, the mixing matrix  $U$  can be described in terms of a single angle

$$U = \begin{pmatrix} \cos \theta & \sin \theta \\ -\sin \theta & \cos \theta \end{pmatrix}, \quad (3.18)$$

which gives the probability

$$P_{\alpha\beta} = \sin^2 2\theta \sin^2 \left( \frac{\Delta m_{ij}^2 L}{4E} \right), \quad (3.19)$$

which shows a clearly oscillating behaviour based on the distance. As an example the three-flavour oscillation case is shown for 3 MeV  $\bar{\nu}_e$  (left) and  $\nu_\mu$  (right) in Figure 3.2. The green dotted line in the right plot shows the effect of CP violation on neutrino oscillations. For the SM case of three generations of neutrinos, the mixing matrix is the Pontecorvo–Maki–Nakagawa–Sakata (PMNS) matrix. It is usually parameterized in the following way

$$U_{\text{PMNS}} = \begin{pmatrix} 1 & 0 & 0 \\ 0 & c_{23} & s_{23} \\ 0 & -s_{23} & c_{23} \end{pmatrix} \begin{pmatrix} c_{13} & 0 & s_{13}e^{-i\delta_{CP}} \\ 0 & 1 & 0 \\ -s_{13}e^{i\delta_{CP}} & 0 & c_{13} \end{pmatrix} \begin{pmatrix} c_{12} & s_{12} & 0 \\ -s_{12} & c_{12} & 0 \\ 0 & 0 & 1 \end{pmatrix}, \quad (3.20)$$

where two additional phases  $\alpha_1$  and  $\alpha_2$  are added if neutrinos are Majorana particles. The phase  $\delta_{CP}$  is of much theoretical interest, as it can be a source of CP violation in the electroweak sector. If it is non-zero, then neutrinos and anti-neutrinos oscillate differently. This can be seen in Equation (3.15), where the second term proportional to the imaginary part of a combination of PMNS matrix elements is CP violating, and is present for non-zero  $\delta_{CP}$ . A measure to quantify the amount of CP violation is through the Jarlskog invariant, which for this case matches with the prefactor in front of the sine in the second term of Equation 3.15 [173].

The oscillations thus far only considered propagating neutrinos in a vacuum. If neutrinos propagate through matter, they can undergo NC or CC interactions with the medium. However, whereas all neutrinos can undergo NC interactions, only the electron neutrino can take part in CC interactions. This is called the Mikheev–Smirnov–Wolfenstein (MSW) effect and it changes the way neutrinos oscillate in matter [174, 175].

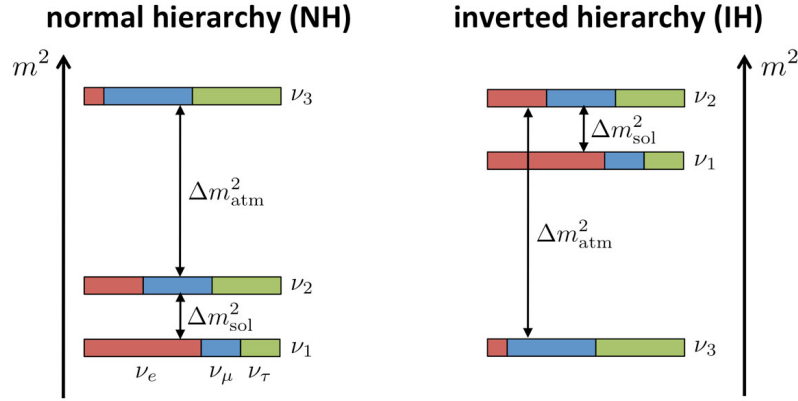


Figure 3.3: The neutrino mass hierarchies illustrated in terms of their gauge eigenstates. Image credit: M. Wurm, JGU Mainz, via <https://www.stereo-experiment.org/scientific.php?>.

Table 3.1: Current values of the squared neutrino mass differences  $\pm 1\sigma$ , the PMNS angles, and the CP phase [176].

Parameter	NH	IH
$\theta_{12}$	$33.44^{+0.77}_{-0.74}$	$33.45^{+0.78}_{-0.75}$
$\theta_{23}$	$49.2^{+0.9}_{-1.2}$	$49.3^{+0.9}_{-1.1}$
$\theta_{13}$	$8.57^{+0.12}_{-0.12}$	$8.60^{+0.12}_{-0.12}$
$\delta_{CP}$	$197^{+27}_{-24}$	$282^{+26}_{-30}$
$\Delta m_{12}^2$ [eV <sup>2</sup> ]	$7.42^{+0.21}_{-0.20} \cdot 10^{-05}$	$7.42^{+0.21}_{-0.20} \cdot 10^{-05}$
$\Delta m_{23}^2$ [eV <sup>2</sup> ]	$+2.517^{+0.026}_{-0.028} \cdot 10^{-03}$	$-2.498^{+0.028}_{-0.028} \cdot 10^{-03}$

As a quick recap we have seen that neutrinos oscillate between their flavour states, which depends on their energy as well as the difference of the squared masses. This means that while the mass differences are known, their ordering is unknown. One of the mass splittings is smaller than the other, leading to the situations where either the lightest two mass eigenstates are close in mass, with the third one clearly heavier, or a single lighter eigenstate with two heavier eigenstates relatively closer. The first scenario is called normal hierarchy or ordering (NH/NO), the second inverted hierarchy or ordering (IH/IO), and an illustration showing the mass eigenstates in terms of the gauge eigenstates is shown in Figure 3.3. The mass splittings  $\Delta_{\text{atm}}^2 = \Delta m_{23}^2$  and  $\Delta_{\text{solar}}^2 = \Delta m_{12}^2$  obtain their names as they are measured through atmospheric and solar neutrinos respectively, more on this in section 3.1.3. Next to the sign of the mass splittings, a second variable that is unknown is the absolute mass scale. However, the existence of neutrino oscillations does mean that at least two neutrinos are massive. The current values of the values of the mass differences, PMNS angles, and the CP phase are listed in Table 3.1, and depend on the assumed mass hierarchy [176].

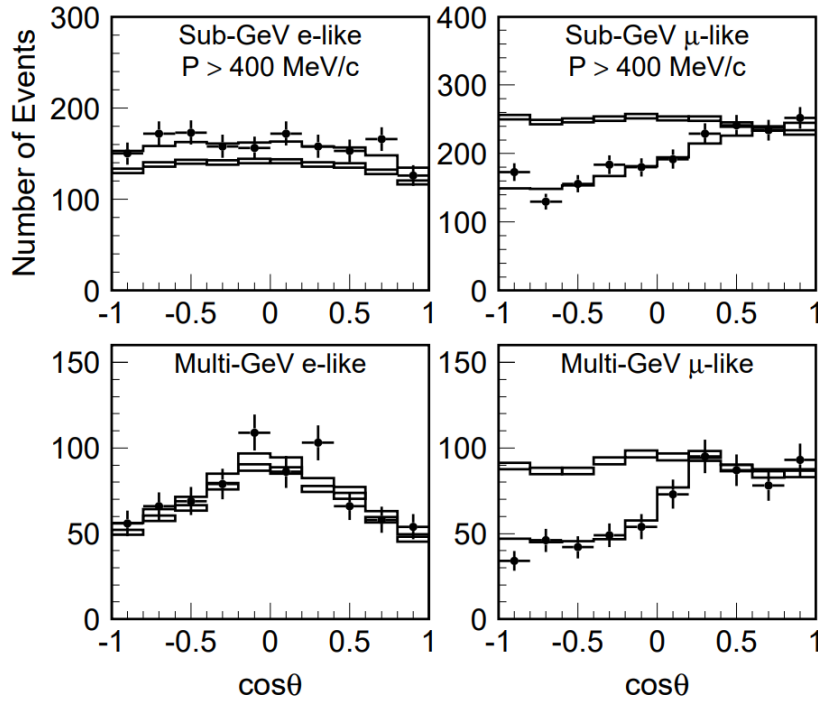


Figure 3.4: Data from the Super-Kamiokande experiment showing the number of events as a function of the cosine of the zenith angle. The fit including  $\nu_\mu \leftrightarrow \nu_\tau$  oscillations is indicated by the black line, the boxes are Monte Carlo events without neutrino oscillations. Source: [177].

### 3.1.3 Experiments

We will now discuss the experiments that are involved in measuring the PMNS mixing angles and neutrino mass differences.

Measurements of  $\theta_{23}$  and  $\Delta m_{23}^2$  are determined from atmospheric neutrinos and accelerator beamline experiments. The Super-Kamiokande experiment, which was already mentioned in section 2.3.2, was originally built to study proton decay, but is also used to study neutrinos from several different sources. One such a source are the atmospheric neutrinos that are produced in cosmic rays, for which we mentioned one would expect a ratio around 2:1 for  $\nu_\mu : \nu_e$ . As neutrinos interact very little with matter, one can not only observe neutrinos produced directly above a detector, but also upward-travelling neutrinos that were produced on the other side of the Earth and propagated through it. If no oscillations are expected, then the observed flux should have no directional dependence. In Super-Kamiokande, the direction of incoming neutrinos can be determined from the direction of the Cherenkov light cone produced through interactions of neutrinos with the detector medium. The results from Super-Kamiokande showed that there is an unexpected dependence on the zenith angle for muon neutrinos, whereas the electron neutrinos do not show an unexpected dependence [177]. Figure 3.4 shows the number of observed neutrino events as a function of the zenith angle for  $\nu_e$  and  $\nu_\mu$ , compared to a Monte Carlo simulation without any oscillation effects indicated by the boxes, with a fit assuming  $\nu_\mu \leftrightarrow \nu_\tau$  oscillations included as a black line. The decrease in

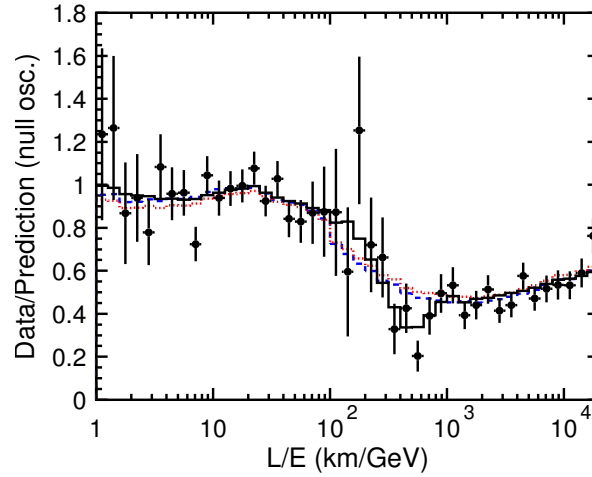


Figure 3.5: Data from the Super-Kamiokande experiment showing the ratio of observed versus expected events in the case of no neutrino oscillation as a function of  $L/E$ , with a fit for  $\nu_\mu \leftrightarrow \nu_\tau$  oscillations (black solid line). Further included are best-fit expectations for neutrino decay (blue dashed line) and neutrino decoherence (red dotted line). Source: [178].

muon neutrino events for angles further away from the zenith can be explained by the fact that these neutrinos travel further from their point of creation, and oscillate more into the unobserved  $\nu_\tau$ .

One further check can be made, by reconstructing the event energies, a determination of the quantity  $L/E$  can be performed. The result from Super-Kamiokande is shown in Figure 3.5 [178]. It shows the ratio of the observed events compared to the prediction of Monte Carlo events without oscillation. Fits that are included are for  $\nu_\mu \leftrightarrow \nu_\tau$  oscillations (black solid line), neutrino decay (blue dashed line), and neutrino decoherence (red dotted line). What is especially noticeable is that the fit of the oscillations shows a dip at around  $L/E = 500$  km/GeV, which corresponds to the first maximum of the oscillation, as illustrated in Figure 3.2 (right). This is a clear feature of neutrino oscillations that does not occur in the other fitted scenarios. Later measurements by the ICECUBE neutrino detector confirmed these observations [179].

Next to neutrino detectors measuring neutrinos from cosmic rays, one can also use beamline experiments to measure the atmospheric neutrino oscillation. One such experiment was the MINOS experiment, which used a muon neutrino beam produced by an accelerator located at Fermilab [180]. It consisted of a near detector close to the accelerator site that characterised the neutrino beam directly after production, and a far detector located at a distance of 734km to measure the neutrino flux and energy spectrum. A similar method is used in the T2K (Tokai to Kamioka) experiment, which uses Super-Kamiokande as a detector [181], as well as in the NOvA experiment, which is a successor to MINOS [182].

Measurements of  $\Delta m_{12}^2$  and  $\theta_{12}$  come from the observation of solar neutrinos, as well as neutrinos from nuclear reactors. As these are lower in energy than the atmospheric neutrinos

$\sim$  few MeV, the muon and tau neutrinos are undetectable with CC interactions, as their energy is too low to create a muon or tau, but can be detected in NC interactions. We already discussed part of the experiments that are used in detecting solar neutrinos when discussing the solar neutrino problem in section 3.1.1, which was resolved by Super-Kamiokande [169] and SNO [170]. The Borexino experiment is a scintillation experiment, which uses an organic scintillator medium in its detector [166]. This has a downside that no information about the incoming neutrino direction is available, but it does offer better light yield at lower energies compared to Cherenkov detectors.

Other experiments use electron antineutrinos emitted by nuclear reactors. The KamLAND experiment measures the  $\bar{\nu}_e$  fluxes from 56 Japanese nuclear power reactors with a scintillator detector [183]. Neutrino oscillation into muon and tau antineutrinos then cause a “disappearance” in the measured  $\bar{\nu}_e$  flux.

The last mixing angle  $\theta_{13}$  is also the smallest one, as can be seen from Table 3.1, and therefore was difficult to measure, and a value of zero for this mixing angle could initially not be excluded. Recently, measurements by the Double Chooz [184], Daya Bay [185], and RENO [186] experiments have confirmed a non-zero value for the last of the PMNS mixing angles. They all make use of multiple detectors filled with gadolinium-doped scintillators to measure the disappearing electron antineutrino flux.

The issue whether the PMNS matrix contains a CP-violating phase is still an open question, as a global fit of combined neutrino oscillation data found that the global best fit point is only  $0.6\sigma$  away from  $\delta_{CP} = 180^\circ$ , which would conserve CP. However, some experiments, such as T2K reported values that are further away from this CP-conserving point, reaching the  $3\sigma$  level in the case of an inverted hierarchy [181]. Further next-generation experiments are coming amongst which long baseline experiments such as DUNE [187] or reactor experiments such as JUNO [188].

## 3.2 Neutrino mass

In the Standard Model all fermions, except the neutrinos, obtain their mass through Yukawa couplings with the Higgs field  $H$ , which can be written in terms of left-handed Weyl spinors as

$$\mathcal{L}_Y = -y^e H^\dagger L e_R^c - y^d H^\dagger Q d_R^c - y^u \tilde{H}^\dagger Q u_R^c + \text{h.c.}, \quad (3.21)$$

with  $\tilde{H} = i\sigma_2 H^* = (H^{0*}, -H^-)^T$  so that the up-type quarks can couple to the Higgs.  $L$ ,  $Q$  denote the left-handed lepton and quark doublets respectively, and  $e_R^c$ ,  $d_R^c$ , and  $u_R^c$  are the right-handed electron, down, and up-type leptons and quarks. The right-handed Weyl spinors are defined in the conjugated representation, such that all spinors are defined in terms

of left-handed ones. The generational indices have been omitted here, but the couplings  $y_f$  are  $3 \times 3$  matrices. Upon electroweak symmetry breaking, the Higgs obtains its vev

$$\langle H \rangle = \frac{1}{\sqrt{2}} \begin{pmatrix} 0 \\ v \end{pmatrix}, \quad (3.22)$$

with  $v^2 = (246 \text{ GeV})^2$  [47] and fermions obtain mass terms in the form of

$$m_f = y_f \frac{v}{\sqrt{2}}. \quad (3.23)$$

Within the SM, there is no Yukawa term possible for neutrinos, as there is no right-handed neutrino. This means that one needs to consider BSM physics to explain neutrino masses. The most obvious choice one can make, is to simply add three right-handed neutrinos  $\nu_R$ , so that all left-handed neutrinos have their counterparts. Then one can construct the two following mass terms

$$\mathcal{L}_\nu = -(y_D)_\nu \tilde{H}^\dagger L \nu_R - \frac{1}{2} M_R \nu_R \nu_R + h.c. \quad (3.24)$$

The first term in the above Lagrangian is a Dirac mass term, similar to the other mass terms in the SM, which leads to a mass of

$$M_D = \frac{y_D v}{\sqrt{2}}. \quad (3.25)$$

If this were the only mass term, then the Yukawa coupling to neutrinos must be very small. Since all fermions from the top quark to the electron are generated through the same mechanism, the Yukawa couplings already span over many orders of magnitude. Adding neutrinos with a mass on the order of 0.1 eV to this results in tiny Yukawa couplings, for which there is no explanation. However, there is a second mass term that can only appear in the case that neutrinos are Majorana particles, which is allowed for fermions that carry no charge. This would mean that Majorana neutrinos are their own antiparticles. One can then rewrite the terms in Equation (3.24) into a mass matrix for the neutrinos

$$\mathcal{L}_\nu = \frac{1}{2} \begin{pmatrix} \nu_L & \nu_R \end{pmatrix} \begin{pmatrix} 0 & M_D^T \\ M_D & M_R \end{pmatrix} \begin{pmatrix} \nu_L \\ \nu_R \end{pmatrix} + h.c. \quad (3.26)$$

in which  $M_D$  and  $M_R$  are  $3 \times 3$  matrices. The entry that is missing is,  $M_L$  which must be zero, as no gauge-invariant Majorana mass term with the lepton  $\text{SU}(2)_L$  doublet is possible. To illustrate the resulting mass eigenvalues we will simplify the calculation by assuming only one generation of neutrinos. In this case one has the eigenvalues

$$\lambda_{\pm} = \frac{1}{2} \left[ M_R \pm \sqrt{M_R^2 + 4M_D^2} \right]. \quad (3.27)$$

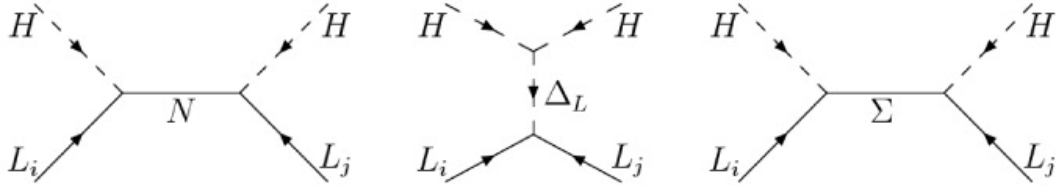


Figure 3.6: Tree-level realisations of the  $d = 5$  Weinberg operator. The diagrams correspond to the Type I (fermionic singlet), Type II (scalar triplet), and Type III (fermionic triplet) respectively. Source: [189].

If the right-handed neutrinos are very heavy then the eigenvalues can be approximated as

$$m_\nu \approx \frac{|M_D|^2}{M_R} \quad M_\nu \approx M_R, \quad (3.28)$$

which means that the mass of the SM neutrinos  $m_\nu$  is suppressed by the mass of the much larger mass of the right-handed neutrinos. For the case of multiple generations, the mass matrices are given by

$$m_\nu \approx -M_D^T M_R^{-1} M_D \quad M_\nu \approx M_R. \quad (3.29)$$

The mechanism of right-handed neutrinos suppressing the mass of the left-handed SM neutrinos is called the seesaw mechanism, more specifically a Type I seesaw, implying that there are more types. Indeed, in general processes generating neutrino masses can be classified using the  $d = 5$  Weinberg operator [190]

$$\mathcal{L} \supset \frac{c_{\alpha\beta}}{\Lambda} (L_\alpha H) (L_\beta H) + \text{h.c.}, \quad (3.30)$$

which violates lepton number by two units. Lepton number is not a fundamental conserved quantity of the Standard Model, it is an accidental symmetry, so there is no reason for new physics to conserve lepton number. One might even want to (slightly) break lepton number, as it is a requirement for leptogenesis [189]. The operator is suppressed by a factor of  $1/\Lambda$ , where  $\Lambda$  is the scale of new physics. This can for example be at the scale of grand unified theories (GUTs), for which a canonical scale is  $\Lambda \sim 10^{15}$  GeV. At tree level there exist three possibilities to realise the Weinberg operator, of which you have just seen Type I, which requires the addition of a fermion singlet. There other processes that generate the operator are through the exchange of a scalar triplet (Type II), or a fermion triplet (Type III), the diagrams of which are shown in Figure 3.6. Other extensions of the Weinberg operator at one-loop will be the focus of Chapter 4. For now we will continue with neutrino mass experiments.

### 3.2.1 Experiments

Due to great experimental efforts, the mechanism of neutrino oscillations has been observed, and the parameters involved are measured with ever increasing precision. As we discussed

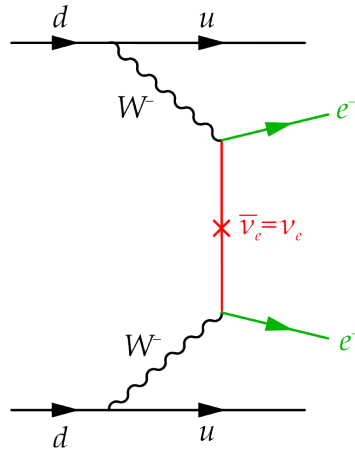


Figure 3.7: Feynman diagram of neutrinoless double beta decay. Source: <https://cuore.lngs.infn.it/en/about/physics>.

in section 3.1 the squared mass differences of the different neutrinos are known, but the sign of the difference is unknown. Moreover, at least two neutrinos must be massive, but the absolute value for the neutrino mass scale is an open question. There is also the additional question whether neutrinos are Dirac or Majorana fermions. The answer to these questions is vital to our understanding of neutrinos, which is why many experiments are undertaken to determine this value. We will now discuss some of the methods that are used.

### Neutrinoless double beta decay

Double beta decay is a process that occurs in which a nucleus undergoes two beta decays simultaneously, described by

$$(A, Z) \rightarrow (A, Z + 2) + 2e^- + 2\bar{\nu}_e, \quad (3.31)$$

in which two electrons and two anti-electron neutrinos are emitted ( $2\nu\beta\beta$ ). It is a relatively rare process, which can occur if the potential daughter nucleus of a single decay is heavier than the original nucleus, as is the case in e.g.  $^{76}\text{Ge}$  [191]. However, there is also a possibility for a nucleus to decay via neutrinoless double beta decay ( $0\nu\beta\beta$ )

$$(A, Z) \rightarrow (A, Z + 2) + 2e^-. \quad (3.32)$$

This process violates lepton number by two units, like Majorana mass terms do. The Feynman diagram of this process is shown in Figure 3.7. As one can see there are no neutrinos in the final states, because this process happens via the exchange of neutrinos, which is only possible if neutrinos are Majorana particles. This also means that  $0\nu\beta\beta$  decays have a sharp energy spectrum,



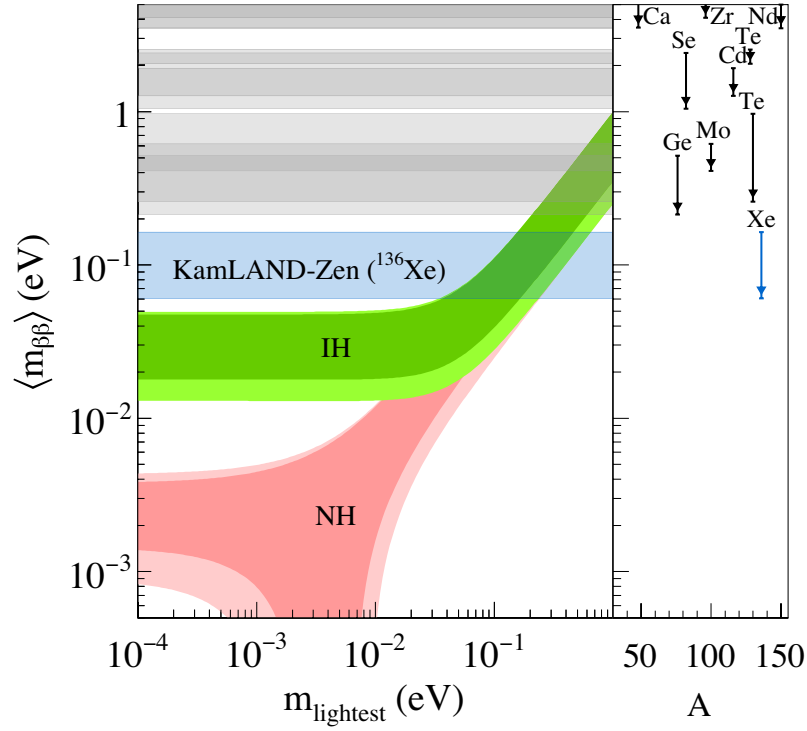


Figure 3.8: The effective electron neutrino mass as a function of the lightest neutrino mass eigenstate, including the KamLAND-Zen result. The shaded regions are the expected regions based on global fits of neutrino oscillation data, for normal hierarchy (NH) as well as inverted hierarchy (IH). The right side of the plot shows the previously obtained bounds with other elements. Source: [192].

The half-life for isotopes decaying through double beta decays is given by

$$(T_{1/2}^{2\nu})^{-1} = G_{2\nu}(Q_{\beta\beta}, Z)|M_{2\nu}|^2, \quad (3.33)$$

where  $G_{2\nu}$  and  $|M_{2\nu}|^2$  are the phase space factor and squared nuclear matrix element of  $2\nu\beta\beta$  respectively, and similar terms are found in the half-life for  $0\nu\beta\beta$  decays

$$(T_{1/2}^{0\nu})^{-1} = G_{0\nu}(Q_{\beta\beta}, Z)|M_{0\nu}|^2\langle m_{ee} \rangle^2, \quad (3.34)$$

with the addition of the effective electron neutrino mass  $\langle m_{ee} \rangle$ <sup>1</sup> [47, 191]. It is given as

$$\langle m_{ee} \rangle = \left| \sum_{k=1}^3 m_k U_{ek}^2 \right| \quad (3.35)$$

in terms of the mass eigenstates  $m_k$  and PMNS matrix elements  $U_{ek}$ . It is sensitive to the CP phase of the PMNS matrix  $\delta_{CP}$ . In this way measuring neutrinoless double beta decay can provide us with information about the neutrino mass scale.

<sup>1</sup>Sometimes also denoted  $\langle m_{\beta\beta} \rangle$

There are many experiments that measure the life-time of isotopes decaying through  $0\nu\beta\beta$ , of which we will briefly mention the main ones. The GERDA experiment uses  $^{76}\text{Ge}$ , and has recently set a new lower bound on the half-life of  $T_{1/2}(^{76}\text{Ge}) > 1.8 \cdot 10^{26}$  yr at 90% C.L., corresponding to  $m_{ee} < 79 - 180$  meV [193]. This is in a similar range as the CUORE experiment, which has already been mentioned in section 2.3 in the context of dark matter searches. From the observation of  $^{130}\text{Te}$  a lower bound on the half-life of  $T_{1/2}(^{130}\text{Te}) > 3.2 \cdot 10^{25}$  yr at 90% C.L., resulting in an upper limit of  $m_{ee} < 75 - 350$  meV [194]. The KamLAND-Zen experiment makes use of  $^{136}\text{Xe}$  and has established a lower bound on the half-life of  $T_{1/2}(^{136}\text{Xe}) > 1.07 \cdot 10^{26}$  yr which translates into  $m_{ee} < 180 - 480$  meV, of which we show the results in Figure 3.8 [192]. It shows the effective electron neutrino mass as a function of the lightest neutrino mass eigenstate for normal hierarchy (NH) and inverted hierarchy (IH). The right part of the plot shows previously obtained bounds with other isotopes <sup>2</sup>. It should be pointed out that for larger masses of the lightest eigenstates, the regions for NH and IH overlap. This is the degenerate region, in which the absolute mass scale dominates over the mass differences. As an upcoming experiment SuperNEMO aims to exclude half-lives up to  $T_{1/2}(^{82}\text{Se}) > 1.2 \cdot 10^{26}$  yr and  $T_{1/2}(^{150}\text{Nd}) > 5.1 \cdot 10^{25}$  yr to be able to probe Majorana masses of  $m_{ee} \approx 70$  meV [195].

### Cosmological observations

Cosmological observations can also serve as an indication for massive neutrinos. From the results of the Planck satellite [23] a bound on the sum of the neutrino masses of

$$\sum m_\nu < 0.12 \text{ eV} \quad (3.36)$$

as a result from the combined  $\Lambda\text{CDM}$  fit to the CMB power spectrum (see section 2.1.3). This is not far removed from the minimum values of  $\sum m_\nu \gtrsim 0.06$  eV (NH) and  $\sum m_\nu \gtrsim 0.10$  eV (IH). Improvements of the upper bound could therefore exclude the IH in the future.

Another source of neutrinos measurements can come from supernovae neutrinos. During the core collapse of a supernova bursts of neutrinos are produced, which can be detected at Earth. At the time of the SN1987a supernova only a few neutrinos were detected, but next-generation experiments such as Hyper-Kamiokande can detect around 200,000 neutrino events from a supernova halfway in our galaxy, which allows for further investigation of neutrino properties [153]. If neutrinos are massive, neutrinos that are emitted in a burst will arrive at a delayed time compared to massless particles. Furthermore, the delay depends on the neutrino energy, and can be written as

$$\Delta t = 2.57 \text{ s} \left( \frac{m_\nu}{\text{eV}} \right) \left( \frac{E}{\text{MeV}} \right)^{-2} \frac{D}{50 \text{ kpc}}. \quad (3.37)$$

---

<sup>2</sup>Some of these results have already been improved upon since the plot was made.

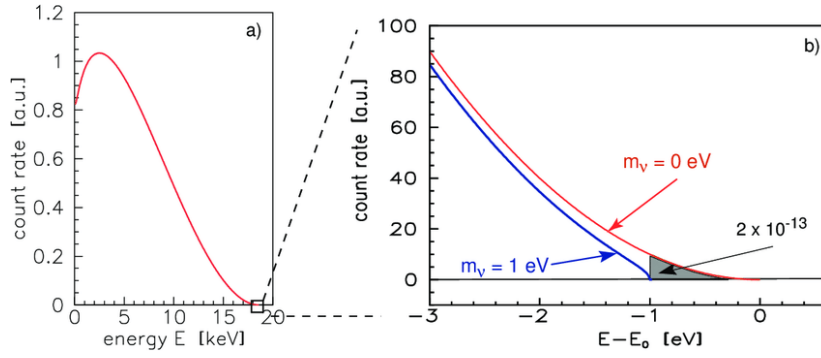


Figure 3.9: The beta energy spectrum of tritium beta decay shown over the complete energy range (a) and a small region around the endpoint  $E_0$  (b) for a neutrino mass of 0 eV and 1 eV. For tritium, the fraction of counts in the grey shaded region is  $2 \cdot 10^{-13}$  of the total counts. Source: [197].

From the SN1987a data an upper bound on the mass of the electron antineutrino of 5.7 eV could be established [196]. This leaves much room for improvement, meanwhile one should patiently wait for the next supernova to occur within an observable distance.

### Kinetic measurements

One further way to measure the absolute neutrino mass scale is through precise measurement of the kinematics in beta decays. In beta decays the created electron and antineutrino share the decay energy, resulting in a continuous energy spectrum. The endpoint of this energy spectrum  $E_0$ , as well as its shape is dependent on the “average” mass of the electron neutrino, which is given by

$$m_{\nu_e}^2 = \sum_k |U_{ek}|^2 m_k^2, \quad (3.38)$$

with PMNS matrix elements  $U_{ek}$ . The energy spectrum for the beta decay of tritium is shown in Figure 3.9 (a) over its full energy range, as well as a small region around the endpoint  $E_0$  (b). The red and blue lines show the spectrum for a neutrino mass of 0 eV and 1 eV respectively. For tritium, the fraction of counts in the grey shaded energy region is  $2 \cdot 10^{-13}$  of the total counts. For the use of tritium over other isotopes as a beta emitter in these experiments there are several good arguments [197]. Firstly the beta decay of tritium



has a half-life of 12.3 yr, which allows for a stronger source compared to more long-lived isotopes. The endpoint energy of the spectrum lies at 18.6 keV, which is the second lowest endpoint of all beta decays. This is desirable, as the fraction of beta energies close to the endpoint of the spectrum decreases for more energetic beta decays. Finally, tritium and  ${}^3\text{He}$  have a simple atomic structure, allowing for easier calculations of nuclear effects.

Currently the KATRIN (Karlsruhe Tritium Neutrino Experiment) is measuring this beta spectrum using a MAC-E-Filter spectrometer, shown in Figure 3.10. The principle of a

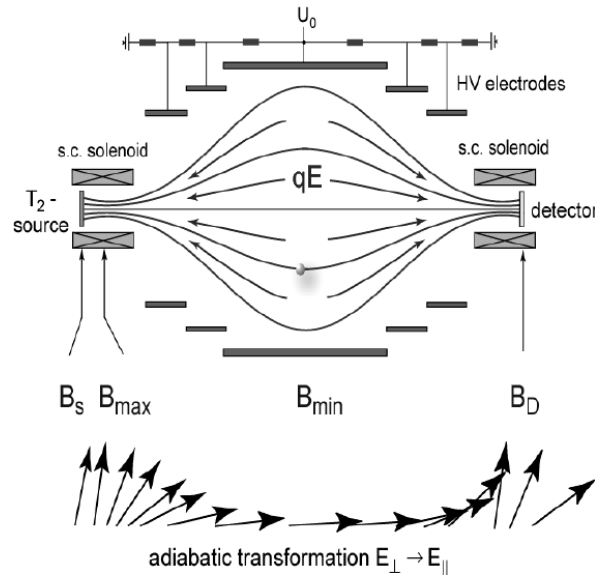


Figure 3.10: Schematic overview of a MAC-E-Filter, showing the retarding electrical potential, as well as the alignment of the momentum of the  $\beta$  decay electrons with the magnetic field. Source: [198].

MAC-E-Filter is as follows [197]: Electrons emitted from tritium beta decays enter the spectrometer at the solenoid on the left-hand side producing a strong magnetic field. Inside the spectrometer they are guided by the magnetic field  $B$ , which is lower by many orders of magnitude in the centre of the spectrometer. In this way the cyclotron energy of the electrons is transformed into a longitudinal motion along the main detector axis. At the same time an electric field is applied as a retardation potential. This electrostatic barrier is adjusted such that only the highest-energy electrons can pass. These electrons are then accelerated again and collimated before leaving the spectrometer at the right-hand side and moving to the detector. This way, an energy resolution of 0.93 eV can be attained [199].

The MAC-E-Filter spectrometer technique was also used in previous neutrino mass searches. The Mainz experiment reported an upper limit on  $m_{\nu_e} < 2.3$  eV at 95% C.L. [200], and the Troitsk experiment determined  $m_{\nu_e} < 2.05$  eV at 95% C.L. [201]. Currently the KATRIN experiment has reported the first sub-eV value of  $m_{\nu_e} < 0.7$  eV at 90% C.L. from the second run,  $m_{\nu_e} < 0.8$  eV at 90% C.L. when combined with the results from the first run [202]. The aim of the KATRIN experiment is to probe neutrino masses down to 0.2 eV [199].

## 4 Radiative seesaw models

In the two previous chapters we have discussed the open questions in the areas of dark matter and neutrino physics. For neutrinos, the observation of neutrino oscillations means that two neutrinos have non-zero masses, which in turn is a strong hint for physics beyond the Standard Model. We have also shown that specific extensions to the SM particle content can generate small neutrino masses via the seesaw mechanism. On the other hand, based on the large amount of cosmological evidence, there exists cold dark matter, the nature of which is unknown. Furthermore, there is no suitable WIMP candidate within the Standard Model, thus an explanation for dark matter has to come from beyond the Standard Model as well.

These two issues are addressed in radiative seesaw models. They are based on one-loop realisations of the  $d = 5$  Weinberg operator, which has several advantages over the tree-level scenarios that were introduced in 3.2. In particular, the neutrino mass generation is suppressed at the one-loop level by the loop integrals, with a further contribution from the suppression of lepton number violation by a factor of  $\epsilon$ . Higher dimensional operators are theoretically also possible and would yield further suppression. Handwavingly, the neutrino mass generated at the  $n$ -loop level through a  $d$  dimensional operator is proportional to [203]

$$m_\nu \propto \frac{\langle H \rangle^2}{\Lambda} \times \left( \frac{1}{16\pi^2} \right)^n \times \epsilon \times \left( \frac{\langle H \rangle^2}{\Lambda} \right)^{d-5}. \quad (4.1)$$

From this form it is easy to see that the tree-level (“0-loop”) purely relies on the seesaw between the Higgs vev and the scale of new physics, whereas generation at loop level causes further suppression by factors of  $1/16\pi^2$ , earning the name radiative seesaw. In this chapter we will show in what ways the topologies of these one-loop realisations can be classified. In doing so, we will mostly follow the work that has been done in [203, 204].

### 4.1 Classification

A systematic classification based on the loop diagram topologies can be made. Starting from the  $d = 5$  Weinberg operator, repeated from Equation (3.30)

$$\mathcal{L} \supset \frac{c_{\alpha\beta}}{\Lambda} (L_\alpha H) (L_\beta H) + \text{h.c.}, \quad (4.2)$$

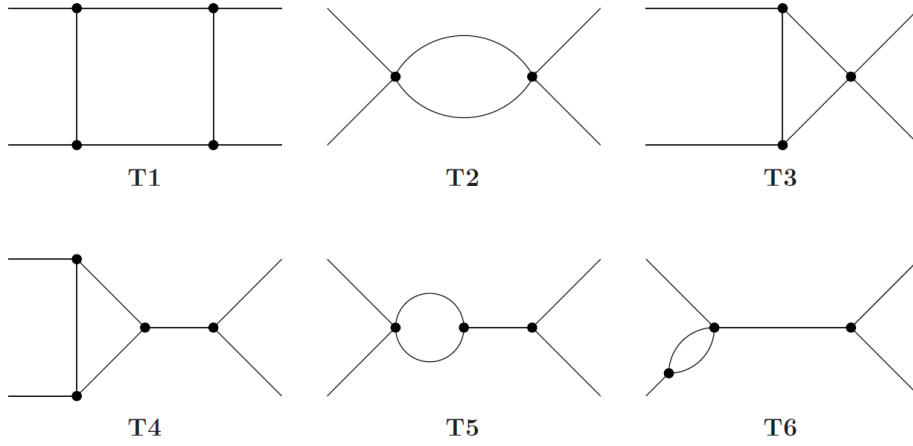


Figure 4.1: One-loop diagram topologies with four external legs. Source: [203].

where  $L_L$  is the left-handed lepton doublet, and  $\tilde{H} = i\sigma_2 H^*$ , 6 different topologies can be distinguished<sup>1</sup>, which are shown in Figure 4.1. However, not all diagrams are suitable to really generate neutrino masses at one loop. For topology T2 it is not possible to construct the vertices in such a way that they are renormalizable due to the  $d = 5$  Weinberg operator requiring that two of the external legs are fermionic. This means that at least one of the vertices will have  $d = 5$ . Diagrams T4 to T6 are not really radiative seesaw topologies. Taking topology T4 as an example, it is possible to see the diagram as an extension of the tree-level diagrams in Figure 3.6, where one of the vertices of the tree-level diagram is an effective coupling that is actually described by the loop. Thus the topologies T4 to T6 can be regarded of extended analogies of the Types I-III seesaw. The remaining T1 and T3 topologies are suitable to generate radiative neutrino masses. However, in order to prevent a larger tree-level contribution, the newly-added fields should be odd under a  $\mathbb{Z}_2$  symmetry, so that each vertex requires an even number of BSM fields. As an additional benefit the new particles cannot decay into SM states. This way, the lightest particle of this new dark sector is a suitable dark matter candidate if it is electrically neutral.

The next step is to specify the possible combinations of particles that can appear inside the diagrams of the T1 and T3 topologies. These are presented in Table 2 and 3 of Ref. [203]. The overview presented there is exhaustive for the case where one assumes at most 4 new fields, as more fields would be redundant for most phenomenological purposes, and one restricts itself to singlet, doublet, and triplet  $SU(2)_L$  representations. The kind of models we consider in this thesis only extend the SM by a few new fields in order to explain different phenomenologies, without considering possible higher-energy physics. These kind of models are thus dubbed minimal models. As a follow-up a study of the compatibility of the different particle contents with neutrino mass and dark matter constraints was performed, which found 35 different viable models [204].

<sup>1</sup>Topologies containing self-energies are discarded.

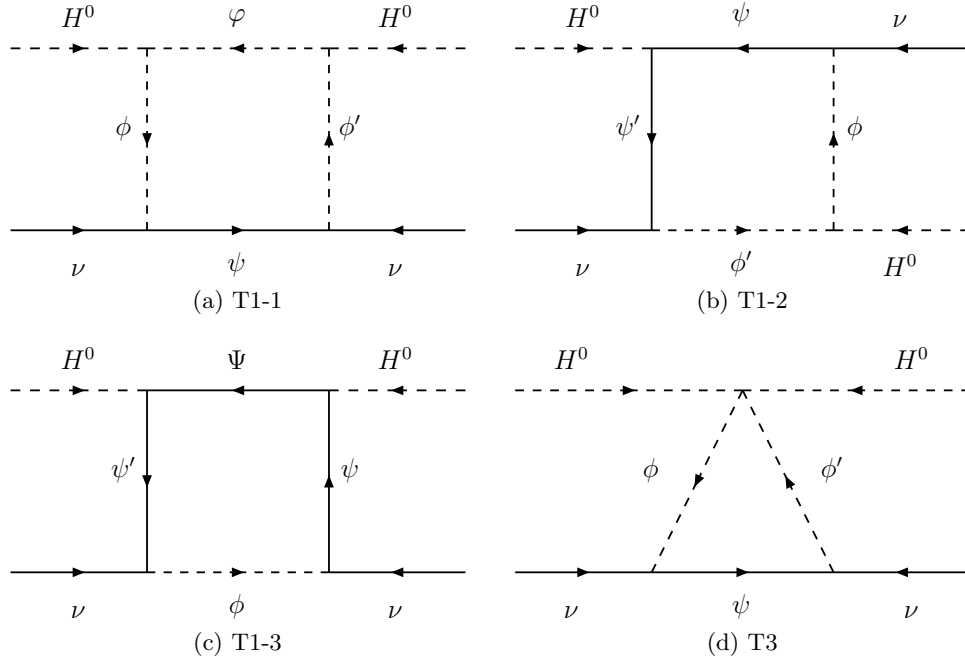


Figure 4.2: Further classification of one-loop diagrams that allow for radiative neutrino masses. Source: [204]

To show how neutrino masses are generated in these models, we will show an explicit calculation. One of the most famous radiative seesaw models is the scotogenic model, proposed by Ernest Ma [205]. In the notation of Ref. [204] it corresponds to the model T3-B with the hypercharge parameter  $\alpha = 1$ . The next chapter goes into further detail about the scotogenic model, but for now it is worth mentioning that the neutrino loop consists of three generations of fermionic singlets  $N_i$  ( $\psi$  in Figure 4.2(d)), and a scalar doublet  $\eta$  ( $\phi^\dagger = \phi'$ ), with the neutral eigenstates  $\eta_R$  and  $\eta_I$ . The contribution from  $\eta_R$  to the neutrino mass corresponds to an integral that can be written as [206]

$$-i(\mathcal{M}_R)_{\alpha\beta} = \sum_i (-1) y_{i\alpha} y_{i\beta} \int \frac{d^4 q}{(2\pi)^4} P_R \frac{\not{p} + \not{q} + m_{N_i}}{(p+q)^2 - m_{N_i}^2 + i\epsilon} \frac{1}{q^2 - m_R^2 + i\epsilon} P_R, \quad (4.3)$$

where  $y$  are the couplings of the neutrinos to the dark sector, and  $P_R = (1 - \gamma^5)/2$  is the right-handed chirality projector since the fermion singlets are purely right-handed. As one should obtain the same result for the mass irrespective of the external momentum, we can set  $p = 0$ . Then the term in the integral proportional to  $\not{q}$  is zero since the numerator is odd. Thus only the term proportional to  $m_{N_i}$  contributes. When evaluating this integral we should be careful as divergences can appear. Thus we make use of dimensional regularization and evaluate the integral in  $D$  instead of 4 dimensions, where we will later take the limit

back to 4 dimensions. In our case the integral corresponds to the Passarino-Veltman integral  $B_0$ , which is given by

$$B_0(p^2, m_0^2, m_1^2) = \frac{(2\pi\mu)^{4-D}}{i\pi^2} \int d^D q \frac{1}{q^2 - m_0^2 + i\epsilon} \frac{1}{(p+q)^2 - m_1^2 + i\epsilon}, \quad (4.4)$$

which for our argument set results in

$$B_0(0, m_R^2, m_{N_i}^2) = \Delta + 1 - \frac{1}{m_{N_i}^2 - m_R^2} \left[ m_{N_i}^2 \ln \left( \frac{m_{N_i}^2}{\mu^2} \right) - m_R^2 \ln \left( \frac{m_R^2}{\mu^2} \right) \right]. \quad (4.5)$$

In this result the first term contains the divergent part as well as some constants

$$\Delta = \frac{1}{\epsilon} - \gamma_E + \ln 4\pi, \quad (4.6)$$

where  $\gamma_E$  is the Euler-Mascheroni constant, and  $\epsilon = (4 - D)/2$  is the deviation from 4 dimensions. Upon taking the limit back to 4 dimensions  $\epsilon \rightarrow 0$  and the  $1/\epsilon$  term diverges. From this result the contribution of the scalar  $\eta_R$  is

$$-i(\mathcal{M}_R)_{\alpha\beta} = i \sum_i \frac{y_{i\alpha} y_{i\beta}}{32\pi^2} m_{N_i} B_0(0, m_R^2, m_{N_i}^2). \quad (4.7)$$

For the other scalar  $\eta_I$  the calculation is completely analogous, with the exception of an overall minus sign. In this way the divergent terms of the loop integral cancel exactly, and the neutrino masses are determined by the convergent terms

$$(M_\nu)_{\alpha\beta} = (\mathcal{M}_R)_{\alpha\beta} - (\mathcal{M}_I)_{\alpha\beta} = \sum_i \frac{y_{i\alpha} y_{i\beta}}{32\pi^2} m_{N_i} \left[ \frac{m_R^2}{m_R^2 - m_{N_i}^2} \ln \frac{m_R^2}{m_{N_i}^2} - \frac{m_I^2}{m_I^2 - m_{N_i}^2} \ln \frac{m_I^2}{m_{N_i}^2} \right], \quad (4.8)$$

which requires a mass splitting between the scalars  $\eta_R$  and  $\eta_I$  as can be seen from the last term. In the next chapter we go into further detail on the relation between this mass splitting and the effect on the neutrino masses.

## Lepton flavour violation

In the quark sector of the SM weak interactions the existence of the CKM matrix allows for weak decays to couple between generations. This is why SM processes conserve baryon number, but there is no conservation of baryon flavour, i.e the number of baryons of a certain generation can change in weak interactions. Even so, the conservation of baryon and lepton number is not an imposed, but an accidental symmetry of the SM. Unlike the quark sector of the SM, the leptons were thought to conserve flavour as observed in e.g. muon decays

$$\mu^- \rightarrow e^- + \nu_\mu + \bar{\nu}_e. \quad (4.9)$$



However the discovery of neutrino oscillations, means that leptons can violate flavour too. The non-zero mass of neutrinos can in principle result in lepton flavour violation (LFV) for the charged leptons in a way analogous to the CKM matrix. Still, the rate of LFV processes such as  $\mu^- \rightarrow e^- + \gamma$  is heavily suppressed by the small neutrino masses [207]. The addition of new fields beyond the Standard Model can change this situation. This makes lepton flavour violation a probe for BSM physics. For example, the addition of a second Higgs doublet in 2 Higgs doublet models (2HDM) can induce flavour changing neutral currents (FCNC) [208]. For the case of radiative seesaw models, the realisations of the  $d = 5$  Weinberg operator will also cause LFV violation, as the SM neutrinos are in the same  $SU(2)_L$  doublets as the charged leptons, and can thus also couple to the new fields. This topic will be discussed in more detail in Chapter 8.



## 5 The effects of the absolute neutrino mass on the scotogenic model

### 5.1 Introduction

The general concept of radiative seesaw models was introduced in the previous chapter. In this chapter we will go into detail for a specific model, the scotogenic model. Originally proposed by Ma [205], it is one of the best known models in its class. Its attractiveness stems from the fact that it is a relative minor extension to the SM, whilst still being able to generate radiative neutrino masses through interactions with a dark sector containing two kinds of DM candidates.

In the scotogenic model, the dark sector consists of a scalar doublet and three singlet fermions, all of which are odd under a  $\mathbb{Z}_2$  symmetry. Both the neutral component of the scalar doublet, as well as the singlet fermions are viable DM candidates, provided that the particle in question is the lightest particle in the dark sector. Through the interactions between the SM neutrinos and this dark sector, the neutrinos obtain their mass.

As was previously mentioned in Chapter 3, the KATRIN experiment aims to establish the absolute mass scale of the neutrinos. At the time of writing, the most current KATRIN result put an upper limit on the absolute mass of 1.1 eV [209], with the expected sensitivity limit aiming to probe down to an absolute mass scale of 0.2 eV [199]. However, more recently an improvement on this limit down to 0.8 eV has been achieved [202]. Due to the close connection between the neutrino masses and the dark sector in radiative seesaw models, neutrino experiments such as KATRIN can indirectly put constraints on these models. Our aim is to study the effect of the absolute neutrino mass scale on the scotogenic model. This chapter is based on the work published in Ref. [210].

We will first give an overview of the particle content and properties of the scotogenic model. In the next sections we will show results of a general scan in its parameter space, with emphasis on the relation between the neutrino and DM physics. Due to the elegance of the scotogenic model, this chapter is simultaneously used to introduce several concepts that will return in later chapters, such as the tools that are used in performing the numerical scan of the parameter space.

Table 5.1: The new particles that are added to the SM particle content in the scotogenic model including their SM gauge group and  $\mathbb{Z}_2$  properties.

Field	Type	Generations	$SU(3)_C$	$SU(2)_L$	$U(1)_Y$	$\mathbb{Z}_2$
$N$	Majorana spinor	3	1	1	0	-1
$\eta$	Scalar doublet	1	1	2	+1	-1

## 5.2 Properties of the model

In this section we describe the particle content, the Lagrangian, as well as the mass eigenstates. We will then consider the form of the equation for the radiative neutrino masses.

### 5.2.1 Particle content

As was mentioned, the particle content of the SM is extended by adding a scalar doublet  $\eta$  and three fermion singlets  $N_i$ . These are listed with their gauge group properties in Table 5.1. Furthermore, both fields are odd under a  $\mathbb{Z}_2$  symmetry. This introduces the following terms in the Lagrangian of the model

$$\mathcal{L}_N = -\frac{m_{N_i}}{2} N_i N_i + y_{i\alpha} \left( \eta^\dagger L_\alpha \right) N_i + h.c. - V, \quad (5.1)$$

where  $L_\alpha$  denotes the left-handed SM lepton doublets with a generational index  $\alpha = 1, 2, 3$ . From Equation (5.1) the link between the neutrino and DM sector becomes very clear already, since the Yukawa coupling  $y_{i\alpha}$  directly connects the SM neutrinos to the dark sector.

$V$  is the scalar potential. The scalar sector consists of the following two doublets

$$H = \begin{pmatrix} H^+ \\ H^0 \end{pmatrix} \quad \eta = \begin{pmatrix} \eta^+ \\ \eta^0 \end{pmatrix},$$

where the doublet  $H$  corresponds to the SM Higgs doublet. The scalar sector is similar to that of the two Higgs doublet model (2HDM), with  $\langle \eta^0 \rangle = v_2 = 0$ , because the  $\mathbb{Z}_2$  symmetry does not allow  $\eta$  to obtain a vev.  $H$  then has the SM vev of  $\langle H \rangle = 246 \text{ GeV}/\sqrt{2}$ . The scalar potential is as follows

$$V = m_H^2 H^\dagger H + m_\eta^2 \eta^\dagger \eta + \frac{\lambda_1}{2} \left( H^\dagger H \right)^2 + \frac{\lambda_2}{2} \left( \eta^\dagger \eta \right)^2 + \lambda_3 \left( H^\dagger H \right) \left( \eta^\dagger \eta \right) + \lambda_4 \left( H^\dagger \eta \right) \left( \eta^\dagger H \right) + \frac{\lambda_5}{2} \left[ \left( H^\dagger \eta \right)^2 + \left( \eta^\dagger H \right)^2 \right], \quad (5.2)$$

where  $m_H$  and  $\lambda_1$  are fixed by the SM vev  $\langle H \rangle$  and the measured Higgs boson mass of 125 GeV [211]. Rewriting  $\eta^0 = \frac{1}{\sqrt{2}}(\eta_R + i\eta_I)$  gives then the following masses in the scalar sector

$$\begin{aligned} m_{\eta^+}^2 &= m_\eta^2 + \lambda_3 \langle H \rangle, \\ m_{\eta_R}^2 &\equiv m_R^2 = m_\eta^2 + (\lambda_3 + \lambda_4 + \lambda_5) \langle H \rangle, \\ m_{\eta_I}^2 &\equiv m_I^2 = m_\eta^2 + (\lambda_3 + \lambda_4 - \lambda_5) \langle H \rangle. \end{aligned} \quad (5.3)$$

The parameter  $\lambda_5$  induces a mass splitting between the real scalar components, which, as was shown in the previous chapter, is of great importance to the neutrino masses. If  $\lambda_5$  were exactly zero, lepton number would be conserved, and no neutrino masses would be generated. Hence  $\lambda_5$  is allowed to be small. After electroweak symmetry breaking (EWSB) we end up with the six physical particles in total:

$$\eta^+, \eta^{0R}, \eta^{0I} \text{ and } N_1, N_2, N_3.$$

The  $\eta^{0R}$  and  $\eta^{0I}$  both stem from the neutral component of the scalar doublet. Either one of these, or the lightest fermion of the  $N_i$  plays the role of DM, and it is stabilized by the  $\mathbb{Z}_2$  symmetry. Throughout this chapter we will consider the latter case. The masses of the  $N_i$  follow directly from the matrix  $m_{N_i}$ , which we choose diagonal since it does not influence the phenomenology of the model. We define  $N_1$  to be the lightest fermion.

Vacuum stability requires that the scalar couplings obey the following relations [212]:

$$\begin{aligned} \lambda_1 &> 0, \quad \lambda_2 > 0, \\ \lambda_3 &> -\sqrt{\lambda_1 \lambda_2}, \\ \lambda_3 + \lambda_4 - |\lambda_5| &> -\sqrt{\lambda_1 \lambda_2}, \end{aligned} \quad (5.4)$$

with perturbativity imposing  $|\lambda| < 4\pi$ .

### 5.2.2 Neutrino masses

The  $\mathbb{Z}_2$  symmetry forbids a seesaw mechanism in this model. However, as can be seen from Equation (5.1) the neutrinos couple to the dark sector. This allows the neutrinos to obtain their masses at one loop level. The relevant diagram is shown in Figure 5.1. The resulting neutrino mass matrix, repeated here from Equation (4.8), is given as

$$(M_\nu)_{\alpha\beta} = \sum_i \frac{y_{i\alpha} y_{i\beta}}{32\pi^2} m_{N_i} \left[ \frac{m_R^2}{m_R^2 - m_{N_i}^2} \ln \frac{m_R^2}{m_{N_i}^2} - \frac{m_I^2}{m_I^2 - m_{N_i}^2} \ln \frac{m_I^2}{m_{N_i}^2} \right]. \quad (5.5)$$

From this we can see that the small mass difference between  $\eta_R$  and  $\eta_I$ , caused by a non-zero value of  $\lambda_5$ , results in non-zero neutrino masses. This clearly illustrates the direct relation

between neutrino masses and the dark sector. If  $|\lambda_5| \ll 1$ , the mass difference  $m_R^2 - m_I^2 = \lambda_5 v^2$  is small as well. With  $m_0^2 = (m_R^2 + m_I^2)/2$ , Equation (5.5) can be simplified to

$$(M_\nu)_{\alpha\beta} \approx \frac{\lambda_5 v^2}{32\pi^2} \sum_{i=1}^3 \frac{y_{i\alpha} y_{i\beta} m_{N_i}}{(m_{R,I}^2 - m_{N_i}^2)} \times \left[ 1 + \frac{m_{N_i}^2}{m_{R,I}^2 - m_{N_i}^2} \ln \left( \frac{m_{N_i}^2}{m_{R,I}^2} \right) \right] \quad (5.6)$$

which shows the relation between the neutrino masses and  $\lambda_5$  explicitly.

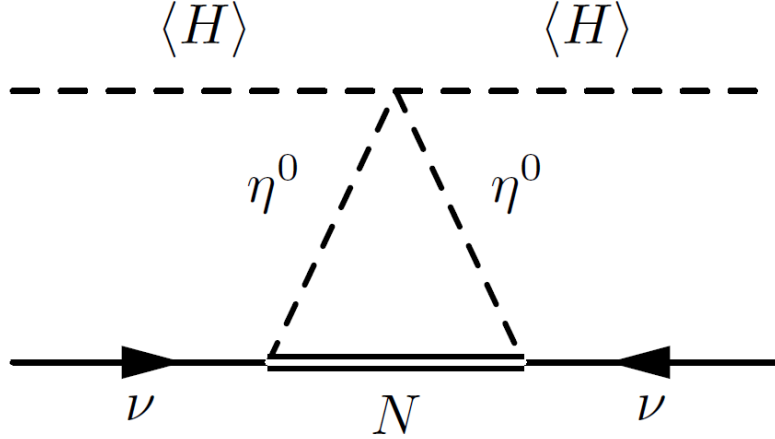


Figure 5.1: Diagram of the neutrino mass generation in the scotogenic model.

### 5.2.3 PMNS matrix

The Pontecorvo–Maki–Nakagawa–Sakata (PMNS) matrix is a mixing matrix that describes the mixing between the mass and gauge interaction eigenstates of the neutrinos:

$$\begin{pmatrix} \nu_e \\ \nu_\mu \\ \nu_\tau \end{pmatrix}_L = U_{\text{PMNS}} \begin{pmatrix} \nu_1 \\ \nu_2 \\ \nu_3 \end{pmatrix}_L = \begin{pmatrix} U_{e1} & U_{e2} & U_{e3} \\ U_{\mu 1} & U_{\mu 2} & U_{\mu 3} \\ U_{\tau 1} & U_{\tau 2} & U_{\tau 3} \end{pmatrix} \begin{pmatrix} \nu_1 \\ \nu_2 \\ \nu_3 \end{pmatrix}_L, \quad (5.7)$$

where in the above equation the indices  $e$ ,  $\mu$ , and  $\tau$  denote the eigenstates in which the neutrinos partake in weak interactions, and the indices 1, 2, and 3 denote the mass eigenstates. The matrix is commonly written in terms of three mixing angles between the generations  $\theta_{12}$ ,  $\theta_{13}$ , and  $\theta_{23}$ , and a CP-violating phase  $\delta_{CP}$ , in terms of the sine  $s_{ij}$  and cosine  $c_{ij}$  of mixing angle  $\theta_{ij}$

$$U_{\text{PMNS}} = \begin{pmatrix} 1 & 0 & 0 \\ 0 & c_{23} & s_{23} \\ 0 & -s_{23} & c_{23} \end{pmatrix} \begin{pmatrix} c_{13} & 0 & s_{13}e^{-i\delta_{CP}} \\ 0 & 1 & 0 \\ -s_{13}e^{i\delta_{CP}} & 0 & c_{13} \end{pmatrix} \begin{pmatrix} c_{12} & s_{12} & 0 \\ -s_{12} & c_{12} & 0 \\ 0 & 0 & 1 \end{pmatrix}. \quad (5.8)$$

## 5.3 Experimental constraints

### 5.3.1 Relic density

Another important experimental constraint for any DM model is the relic density. The current value for the relic density, as measured by the Planck satellite, is  $\Omega h^2 = 0.120 \pm 0.001$  [23]. Here we allow for a theoretical uncertainty of 0.02.

Next to the relic density constraints, we put several other experimental constraints on the parameter space. These constraints concern neutrino-related constraints, such as the neutrino mass splittings, as well as upper bounds on lepton flavour violating processes.

### 5.3.2 Neutrino constraints

With the relation between the SM neutrino mass matrix and the BSM masses and couplings established through Equation (5.5), we can invert the relation and use the measured neutrino mass differences and mixing angles of the PMNS matrix to constrain the Yukawa couplings  $y_{i\alpha}$ .

We apply the measured neutrino masses and mixing angles at  $3\sigma$  [213]. In order to guarantee that the model automatically satisfies these neutrino constraints, we apply the Casas-Ibarra parametrisation [214]. The neutrino mass matrix can be compactly written as

$$(M_\nu)_{\alpha\beta} = (y^T \Lambda y)_{\alpha\beta}, \quad (5.9)$$

where  $\Lambda$  is a diagonal matrix with eigenvalues

$$\Lambda_i \frac{m_{N_i}}{32\pi^2} \left[ \frac{m_R^2}{m_R^2 - m_{N_i}^2} \ln \frac{m_R^2}{m_{N_i}^2} - \frac{m_I^2}{m_I^2 - m_{N_i}^2} \ln \frac{m_I^2}{m_{N_i}^2} \right]. \quad (5.10)$$

It is diagonalised by the PMNS matrix  $U_\nu$ ,

$$\hat{m}_\nu = U_\nu^\dagger M_\nu U_\nu \equiv \text{diag}(m_{\nu 1}, m_{\nu 2}, m_{\nu 3}). \quad (5.11)$$

This implies

$$\hat{m}_\nu = U_\nu^\dagger y^T \Lambda y U_\nu, \quad (5.12)$$

and upon multiplying the above equation by  $\hat{m}_\nu^{-1/2}$  from the left and right we obtain

$$\text{diag}(1, 1, 1) = \hat{m}_\nu^{-1/2} U_\nu^\dagger y^T \Lambda y U_\nu \hat{m}_\nu^{-1/2} \equiv R^T R. \quad (5.13)$$

Solving this expression for  $y$ , leads to the following expression for the Yukawa couplings

$$y = \Lambda^{-1/2} R \hat{m}_\nu^{-1/2} U_\nu^\dagger, \quad (5.14)$$

meaning that they can be constrained up to an orthogonal matrix  $R$  with three arbitrary angles  $\theta_i \in [0, 2\pi]$ .

### 5.3.3 Lepton flavour violation

In the SM the lepton flavour number is a conserved quantity, the exception being neutrino oscillations. From Equation (5.1) it can be seen that not only the neutrinos, but also the charged leptons couple to the dark sector. Off-diagonal elements of  $y_{i\alpha}$  allow for lepton flavour violating (LFV) processes at one-loop order. This allows processes such as  $\mu \rightarrow e\gamma$  that are forbidden in the SM. The current and future bounds on the branching ratio of the most important LFV processes are listed in Table 5.2.

Table 5.2: Current and future bounds on the lepton flavour violating processes that were imposed in the parameter scan.

Process	Current bound	Future bound
$\text{BR}(\mu \rightarrow e\gamma)$	$4.2 \times 10^{-13}$ [215]	$2 \times 10^{-15}$ [216]
$\text{BR}(\mu \rightarrow 3e)$	$1.0 \times 10^{-12}$ [217]	$10^{-16}$ [218]
$\text{CR}(\mu - e, \text{Ti})$	$4.3 \times 10^{-12}$ [219]	$10^{-18}$ [220]

## 5.4 Numerical scan

### 5.4.1 Tool chain

In order to perform a numerical scan of the scotogenic model, we make use of several programs that calculate different features of the model. For this purpose, we built a tool chain that takes as an input a specific model and parameter values, and returns the quantities that we are interested in by connecting the different programs. Many of these tools were originally made to analyze supersymmetric models, but can nowadays also be used for non-supersymmetric models. A schematic overview of the programmes involved is shown in Figure 5.2. The complete tool chain can be divided into two parts: model generation & setup, and the numerical evaluation. We will go through the overview step by step.

The first step is to implement the scotogenic model so that it can be handled by the programs further down the tool chain. This task can be performed by SARAH [222, 223]. The input files for SARAH can be made by hand, but for radiative seesaw models, the program MINIMAL-LAGRANGIANS has been developed by Simon May [224]. After specifying the particle content of a radiative seesaw model, it generates the most general Lagrangian allowed by the gauge symmetries, as well as a global  $\mathbb{Z}_2$  symmetry, and moreover produces the required input files for SARAH.

Based on a specific particle content and the accompanying Lagrangian, SARAH returns analytic expressions for vertices, particle mass eigenstates up to the one-loop level and mixing matrices, as well as the renormalization group equations up to two-loop. These results are



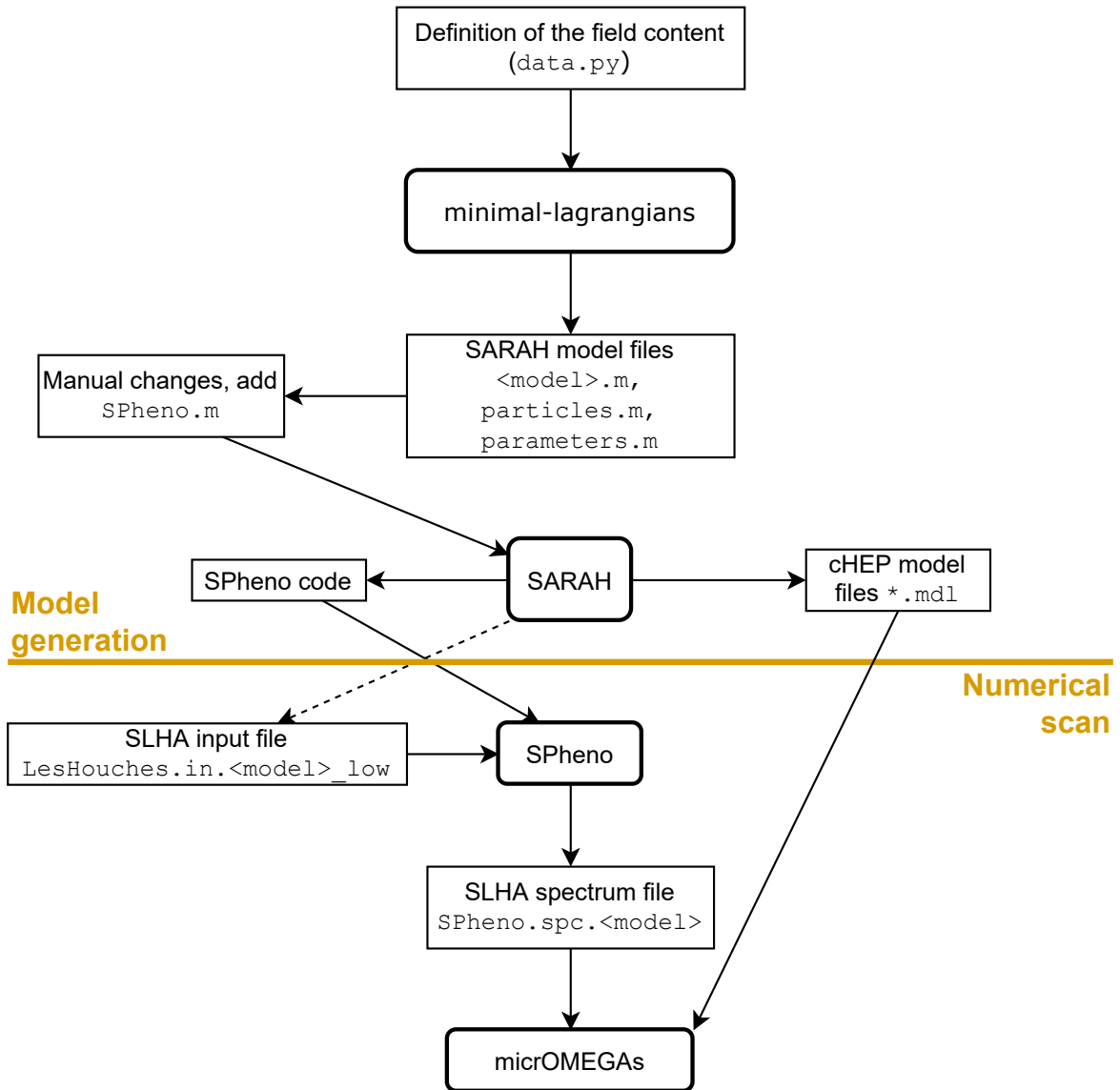


Figure 5.2: Schematic overview of the toolchain involved in the numerical evaluation of this model. Based on Figure 6.1 in [221].

then used to automatically create input files for SPHENO and MICRAMEGAS, the next programs in the tool chain.

The previous steps up to SARAH only have to be performed once. Once the model files for the other programs are created, the role of SARAH has been completed. The next step in the tool chain is handled by SPHENO, which stands for Supersymmetric Phenomenology, but also works with non-SUSY models[225, 226]. With the model files created by SARAH, SPHENO takes an input file containing the model parameters, and calculates the mass spectrum, particle decay modes, mixing matrices, as well as contributions of BSM physics to the  $\rho$ -parameter,  $(g - 2)_\mu$ , and LFV processes.

From there the output is passed to MICRAMEGAS [227], which calculates properties related to dark matter phenomenology, using the model files that have been generated by

SARAH. Amongst the values that can be calculated by this package are e.g. the relic density including the contributing annihilation channels, as well as WIMP-nucleus cross sections that are relevant for direct detection.

A single parameter point in the numerical scan is written into the input file of SPHENO, which is passed on to MICROMEGAS. After enough parameter points have been scanned, the data is analyzed further.

### 5.4.2 Parameter ranges

With experimental constraints in the neutrino sector and the lepton flavour violation bounds, we perform our numerical scan. We vary the masses of the scalar doublet  $\eta$ , as well as those of the fermion singlets  $N_i$  in the range  $0.1 - 10$  TeV. The lower limit of this range is motivated by the LEP bound on charged particles [228]. For the scalar couplings there is the perturbativity constraint  $|\lambda_{2,3,4,5}| < 4\pi$ . However, since  $\lambda_2$  only induces self interactions of  $\eta$ , its value is not relevant to the phenomenology, so we set  $\lambda_2 = 0.5$  without loss of generality. We allow  $\lambda_5$  to be very small, and following previous work [229] we sample  $10^{-12} < |\lambda_5| < 10^{-8}$ . For normal (inverted) hierarchy,  $m_{\nu_1}$  ( $m_{\nu_3}$ ) is sampled between  $4 \times 10^{-3} - 2$  eV, the upper range just above the KATRIN limit of  $m_{\nu_e}^{\text{eff}} < 1.1$  eV. For the moment we are not interested in studying the CP phenomenology, hence we set  $\delta_{CP} = 0$ . The three angles from the Casas-Ibarra parameterisation are unconstrained, as was mentioned in section 5.3.2, and therefore we sample  $0 < \theta_i < 2\pi$ . As an overview, the parameters and their respective sampling ranges are shown in Table 5.3.

Since the Yukawa couplings  $y_{i\alpha}$  are not sampled directly, but determined through the Casas-Ibarra parameterisation, they are not listed in Table 5.3. However, we also impose the perturbativity constraint  $|y_{i\alpha}| < 4\pi$  like was done for the scalar couplings.

Table 5.3: Overview of parameters that were used in the numerical scan.

Parameter	Range
$m_\eta$	$0.1 - 10$ TeV
$m_{N_i}$	$0.1 - 10$ TeV
$\lambda_2$	0.5
$\lambda_3$	$-4\pi - 4\pi$
$\lambda_4$	$-4\pi - 4\pi$
$ \lambda_5 $	$10^{-12} - 10^{-8}$
$m_{\nu_1}$ (NH) / $m_{\nu_3}$ (IH)	$4 \times 10^{-3} - 2$ eV
$\delta_{CP}$	0
$\theta_i$	$0 - 2\pi$

### 5.4.3 Coannihilations

In our scan, we are mainly interested in the case where the lightest fermion singlet is the DM candidate. The fermion singlet can annihilate either as  $N_1 N_1 \rightarrow \nu\nu$  or  $N_1 N_1 \rightarrow l^+ l^-$ , where respectively the neutral or the charged component of the new scalar doublet acts as a mediator. In principle, coannihilation processes such as  $N_1 \eta^0 \rightarrow W^+ l^-$  can occur if the masses of the initial particles are mass-degenerate. We are not interested in these processes, since they require a degree of fine-tuning. Hence we will only consider the points for which these coannihilation processes contribute less than 1% to the relic density.

### 5.4.4 Results for fermionic DM

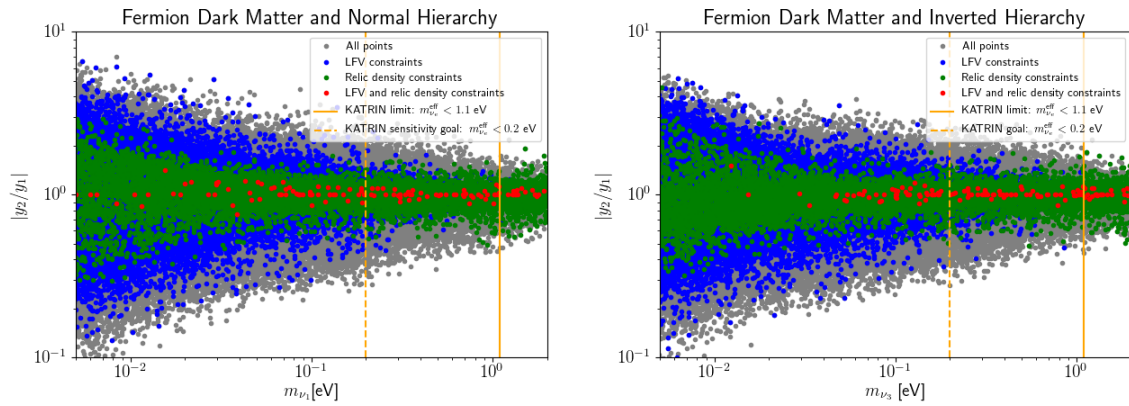


Figure 5.3: Ratio of Yukawa couplings as a function of the lightest neutrino mass, with all points that satisfy the perturbativity (grey), LFV constraints (blue), relic density (green), and all constraints (red).

As was mentioned in section 5.3.2, the Yukawa couplings  $y_{i\alpha}$  in our scan were calculated through the Casas-Ibarra parameterisation, with its eigenvalues  $y_\alpha$  ( $\alpha = 1, 2, 3$ ). The result of this parameterisation is shown in Figure 5.3. It shows the ratio of  $|y_2/y_1|$  versus the lightest neutrino mass that was obtained in our scan, with different constraints imposed on the sampled points, both for NH (left) and IH (right). The grey points include all sampled points, with only the perturbativity constraint included. The blue points are those that satisfy the current LFV bounds for the processes as listed in Table 5.2. The green points satisfy the relic density constraint we demanded, and the red points fulfil both constraints. From these plots, it can be seen that for low neutrino masses, the ratio  $|y_2/y_1|$  varies over almost the full range as shown in the plots, but this spread is reduced for larger neutrino masses. In the region where the electron neutrino mass lies between the current and expected KATRIN sensitivity of 1.1 eV and 0.2 eV respectively, the neutrino mass differences and the PMNS matrix play a subdominant role. Furthermore, the imposed LFV and relic density constraints reduce the overall spread of the points, but the trend of reduced spread for larger neutrino masses is still there. However, imposing both constraints simultaneously leaves only the points that lie on or close to  $|y_2/y_1| \sim 1$ . This behaviour is independent of the neutrino

hierarchy, and holds for the ratios  $|y_3/y_1|$  and  $|y_3/y_2|$  as well. This is explicitly illustrated in Figure 5.4, which shows all three eigenvalues plotted against each other (the third eigenvalue being the temperature scale).

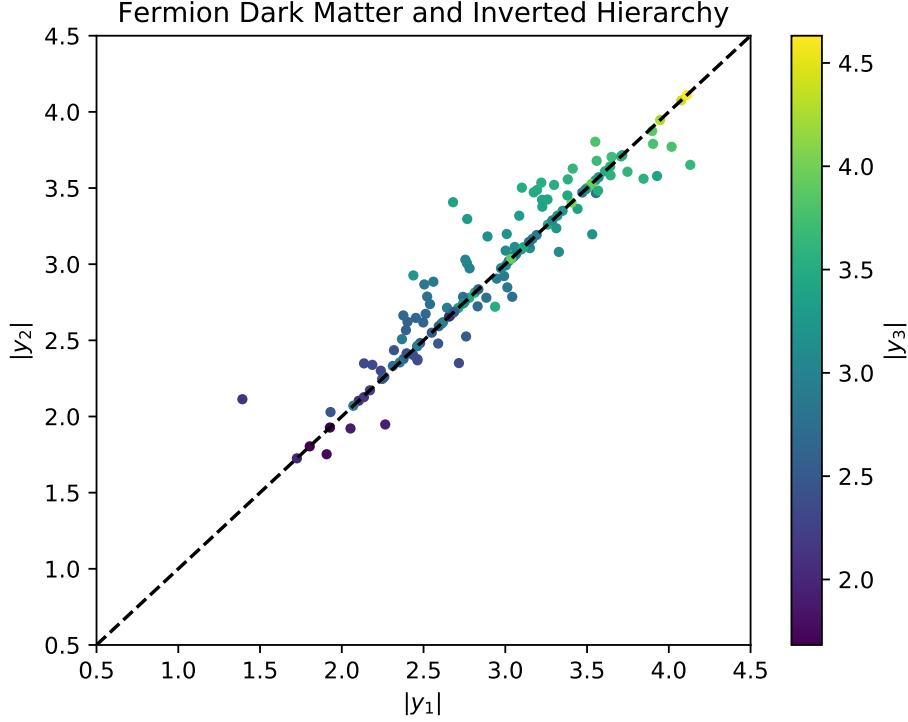


Figure 5.4: The absolute eigenvalues of the Yukawa couplings  $|y_1|$  and  $|y_2|$  with the value of the third eigenvalue  $|y_3|$  denoted by the color gradient (right). The points in these plots are those that satisfy all constraints (red points from Figure 5.3).

Next we turn to the relation between the neutrino mass scale and the scalar mass splitting, parameterised by  $\lambda_5$ . Figure 5.5 shows the dependence of  $|\lambda_5|$  on the mass of the lightest neutrino  $m_{\nu_1}$ . A clear relation between the two quantities only arises after imposing the LFV (blue), relic density (green), and all (red) constraints. This dependence is linear, for masses above  $\sim 0.052$  eV for the lightest neutrino. Below this mass, the mass of the lightest neutrino is smaller than the neutrino mass differences. Therefore the heaviest neutrino mass dominates, and  $\lambda_5$  becomes independent of  $m_{\nu_1}$  ( $m_{\nu_3}$ ) for NH (IH). At 90% C.L., the points that satisfy all constraints (red points) can be fitted by a line with a slope of

$$\lambda_5 = \begin{cases} (3.08 \pm 0.05) \times 10^{-5} m_{\nu_1} \text{ eV (NH)} \\ (3.11 \pm 0.06) \times 10^{-5} m_{\nu_3} \text{ eV (IH)}, \end{cases} \quad (5.15)$$

and the constant region can be fitted with

$$\lambda_5 = \begin{cases} (1.6 \pm 0.7) \times 10^{-10} \text{ (NH)} \\ (1.7 \pm 1.5) \times 10^{-10} \text{ (IH)}. \end{cases} \quad (5.16)$$

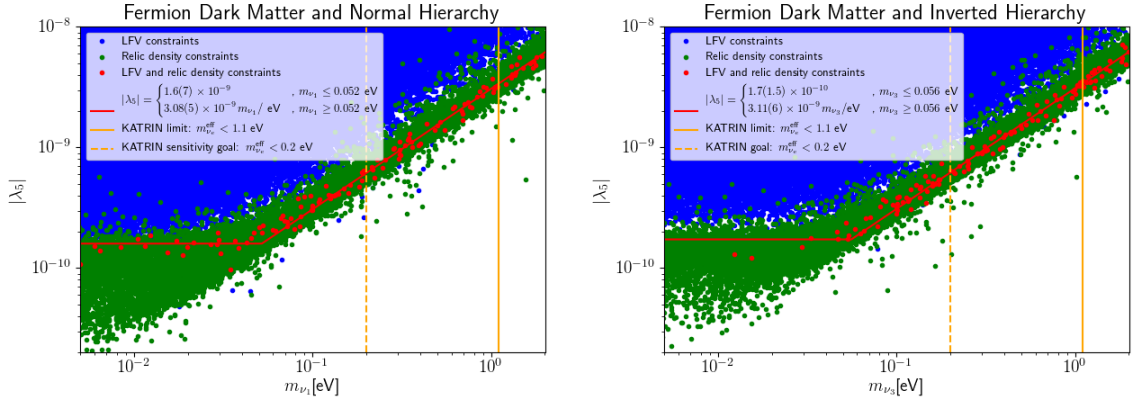


Figure 5.5: The dark sector-Higgs boson coupling  $|\lambda_5|$  versus the lightest neutrino mass.

From this we see that bounds on the absolute neutrino mass scale result in clear bounds on  $\lambda_5$ . Once the absolute neutrino mass scale is known, the dark sector-Higgs coupling  $\lambda_5$  will be fixed. For the region where  $\lambda_5$  is constant, the fit error is relatively large for IH. This can be attributed to the low statistics in this region, as can be seen in Figure 5.5.

With our findings for  $\lambda_5$  in mind, we turn to the Yukawa couplings. With the ratio  $m_{\nu_1}/|\lambda_5|$  fixed, one can expect from Equation (5.6) that there exists some relation between the DM mass and the Yukawa couplings as well. From Figure 5.6 it becomes clear that there is a relation between the masses of the DM fermion and the scalar doublet when considering the points that satisfy the relic density and LFV constraints. In particular, the ratio of masses lies around  $m_{R,I}/m_{N_1} \sim 1.5$ . The leading term in Equation (5.6) is then proportional to  $|y_1|^2/m_{N_1}$ .

Figure 5.7 shows the Yukawa coupling of the lightest neutrino as a function of the DM mass. Furthermore, the red line indicates a square root that was fitted, with the 90% C.L. marked in grey. We find the following dependence

$$|y_1| = \begin{cases} (0.078 \pm 0.021) \sqrt{m_{N_1}/\text{GeV}} & (\text{NH}) \\ (0.081 \pm 0.012) \sqrt{m_{N_1}/\text{GeV}} & (\text{IH}). \end{cases} \quad (5.17)$$

One can rephrase the result in the following way: once the DM mass is known, its Yukawa coupling to the SM leptons is fixed. Since the off-diagonal elements of  $y_{i\alpha}$  cause LFV violating processes, we will also show how future LFV measurements affect the model.

The selection of points by the branching ratios of LFV processes was done with the current experimental bounds as presented in Table 5.2. The table also lists expected future sensitivities. Figure 5.8 again shows the same set of points as in Figures 5.6 and 5.7, namely those that passed the relic density and current LFV constraints. In this figure both the current as well as the future bounds of the  $\mu \rightarrow e\gamma$  and  $\mu \rightarrow 3e$  processes are indicated. From this one can see that the future LFV bounds, combined with the KATRIN sensitivity goal probe deep into the parameter space of the model. As an illustration, we provide a benchmark

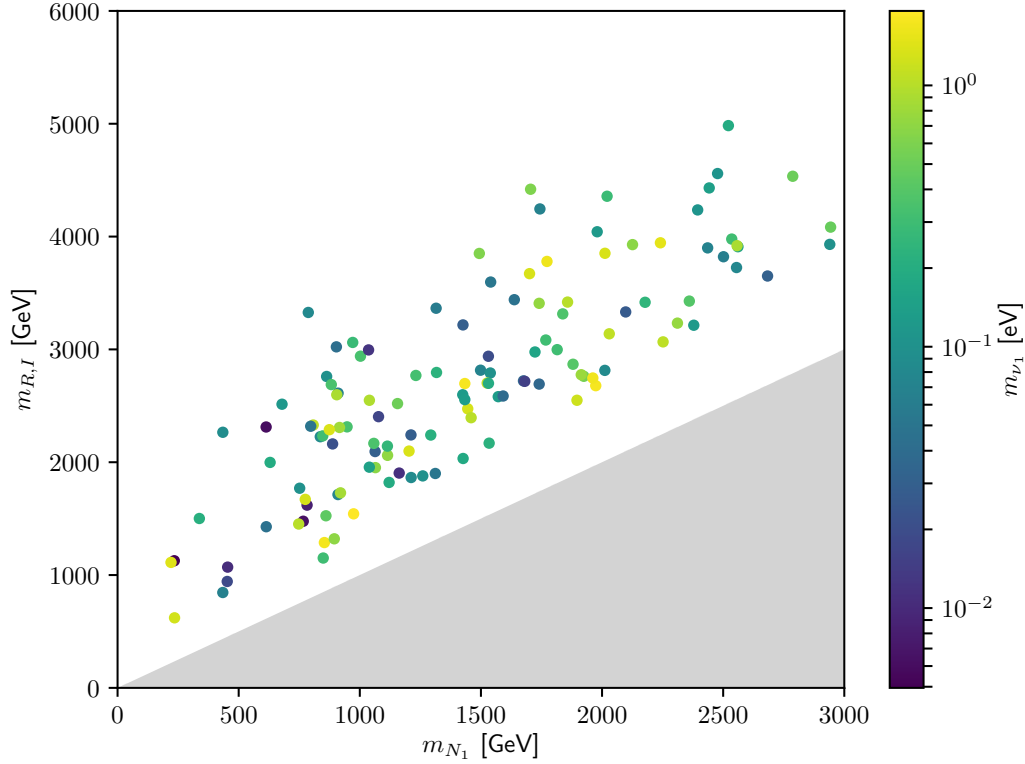


Figure 5.6: The masses for the scalars vs the lightest fermion mass for fermionic DM and NH. The points in this plot are those that satisfy all constraints (red points from Figures 5.3 and 5.5).

point at the KATRIN sensitivity limit. The input parameters are shown in Table 5.4, and the neutrino masses and mixing angles are listed with the resulting relic density and LFV branching ratios in Table 5.5.

### The effect of coannihilations

We explicitly stated in Section 5.4.3 that all points with more than a 1% contribution of coannihilations to the relic density are disregarded. It turns out, that due to coannihilations between the fermion and the scalar doublet, the effect of the Yukawa couplings  $y_{i\alpha}$  (which are determined by the Casas-Ibarra parameterization) on the relic density decreases. This

Table 5.4: Input parameters for a typical benchmark point at the KATRIN sensitivity limit (all masses in GeV).

$m_{N_1}$	$m_{N_2}$	$m_{N_3}$	$m_\eta$	$\lambda_1$	$\lambda_2$	$\lambda_3$	$\lambda_4$	$\lambda_5$
1926	3773	3607	3371	0.26	0.5	7.576	6.060	$6.2 \cdot 10^{-10}$
$y_{11}$	$y_{12}$	$y_{13}$	$y_{21}$	$y_{22}$	$y_{23}$	$y_{31}$	$y_{32}$	$y_{33}$
-3.055	-2.471	0.183	1.748	-2.003	2.038	-1.180	1.690	2.673

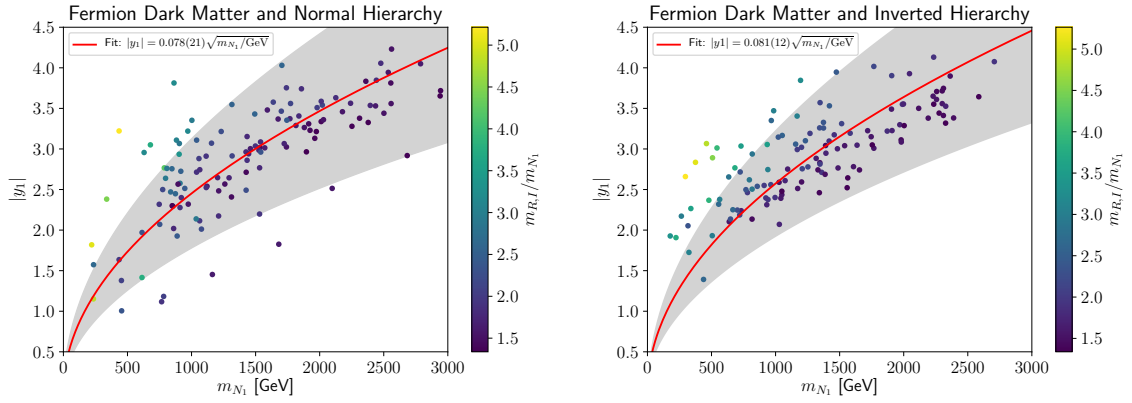


Figure 5.7: Yukawa coupling of the lightest neutrino vs the DM mass. The temperature scale is the ratio of the scalar mass over the DM mass.

Table 5.5: Neutrino masses and mixings, relic density and branching ratios/conversion rate for our NH benchmark point (all masses in eV, angles in  $^\circ$ ).

$m_{\nu_1}$	$\Delta m_{21}^2$	$\Delta m_{31}^2$	$\theta_{12}$	$\theta_{23}$	$\theta_{13}$	$\Omega h^2$
0.2	$7.231 \cdot 10^{-5}$	$2.444 \cdot 10^{-3}$	32.03	44.28	8.50	0.120
		$\text{BR}(\mu \rightarrow e\gamma)$	$\text{BR}(\mu \rightarrow 3e)$	$\text{CR}(\mu - e, \text{Ti})$		
		$2.990 \cdot 10^{-13}$	$8.321 \cdot 10^{-13}$	$3.180 \cdot 10^{-13}$		

greatly decreases the influence of  $\lambda_5$ , and no correlation between the absolute neutrino mass scale and  $|\lambda_5|$  is observed if scenarios with coannihilations are considered.

#### 5.4.5 Results for scalar DM

The case where one of the real scalars of the neutral component  $\eta_R$  or  $\eta_I$  is the lightest particle can also be considered. Figure 5.9 shows the quantities as Figure 5.5, but now for scalar DM. There is no linear dependency of  $|\lambda_5|$  on  $m_{\nu_1}$  anymore. Instead there is a cloud of points which satisfy all constraints starting from  $|\lambda_5| = 3 \cdot 10^{-10}$ , which is larger than the lowest values in the fermion case ( $|\lambda_5| = 1.6 \cdot 10^{-10}$ ), but can in principle extend upwards to values near the perturbativity limit of  $4\pi$ .

The main difference with the fermion case is that the scalar DM candidates stem from an  $SU(2)$  doublet, whereas the fermions are singlets. Hence scalar dark matter couples to the electroweak gauge bosons. Furthermore, there is a direct coupling to the Higgs boson through the  $\lambda_3$ ,  $\lambda_4$ , and  $\lambda_5$  terms. The Yukawa coupling  $y_{i\alpha}$  now only plays a marginal role as the main interaction channel with ordinary matter is through the 4-point interaction of  $\eta_{R,I}$  to  $W^+W^-$  pairs.

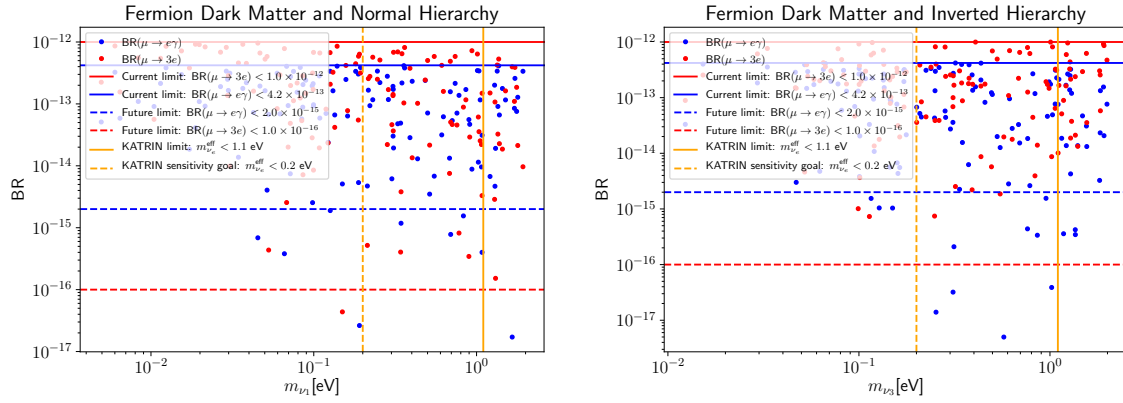


Figure 5.8: Branching ratios for the LFV processes  $\mu \rightarrow e\gamma$  and  $\mu \rightarrow 3e$  vs the lightest neutrino mass. The solid(dashed) lines indicate current(expected) limits.

## 5.5 Summary and outlook

We studied the effects of the absolute neutrino mass scale on the parameter space of the scotogenic model, with the lightest fermionic singlet being the DM candidate. In our parameter scan we took the measured neutrino mass differences and mixings in order to calculate the Yukawa couplings through the Casas-Ibarra parameterisation. We have shown that the parameter space can be probed in two orthogonal ways: via LFV, as well as through a KATRIN measurement of the electron neutrino mass.

We have shown a linear relation between the parameter  $\lambda_5$  that governs the mass splitting between the neutral components of the scalar doublet and the absolute neutrino mass scale, after applying perturbativity, LFV, as well as relic density constraints. This linear relation is valid for a lightest neutrino mass of 0.052 eV and 0.056 eV for NH and IH respectively, below this threshold  $\lambda_5$  remains constant. Around this scale, the mass of the lightest neutrino becomes comparable to the mass difference with the heaviest neutrino. Thus one moves away from the regime with an approximately massless neutrino, to a regime with three massive, and for larger absolute mass scales degenerate, neutrinos. Having shown this linear relation, a KATRIN measurement would result in a clear prediction for the dark sector-Higgs coupling  $\lambda_5$ .

Based on the relation between  $m_{\nu_1}$  and  $\lambda_5$ , together with the observation that the ratio of the scalar masses to the DM mass  $m_{R,I}/m_{N_1} \sim 1.5$ , we established that the first eigenvalue of the Yukawa matrix  $|y_1|$  is proportional to the square root of the DM mass. This means that a measurement of the DM mass combined with a KATRIN measurement allows us to predict the values of these crucial parameters in the scotogenic model. Even when considering the improved KATRIN results, our conclusions remain the same.

Furthermore, these findings generalise to models with triplet fermions [230] and/or singlet-doublet scalars [231], since the neutrino mass matrices are similar to the one presented here.



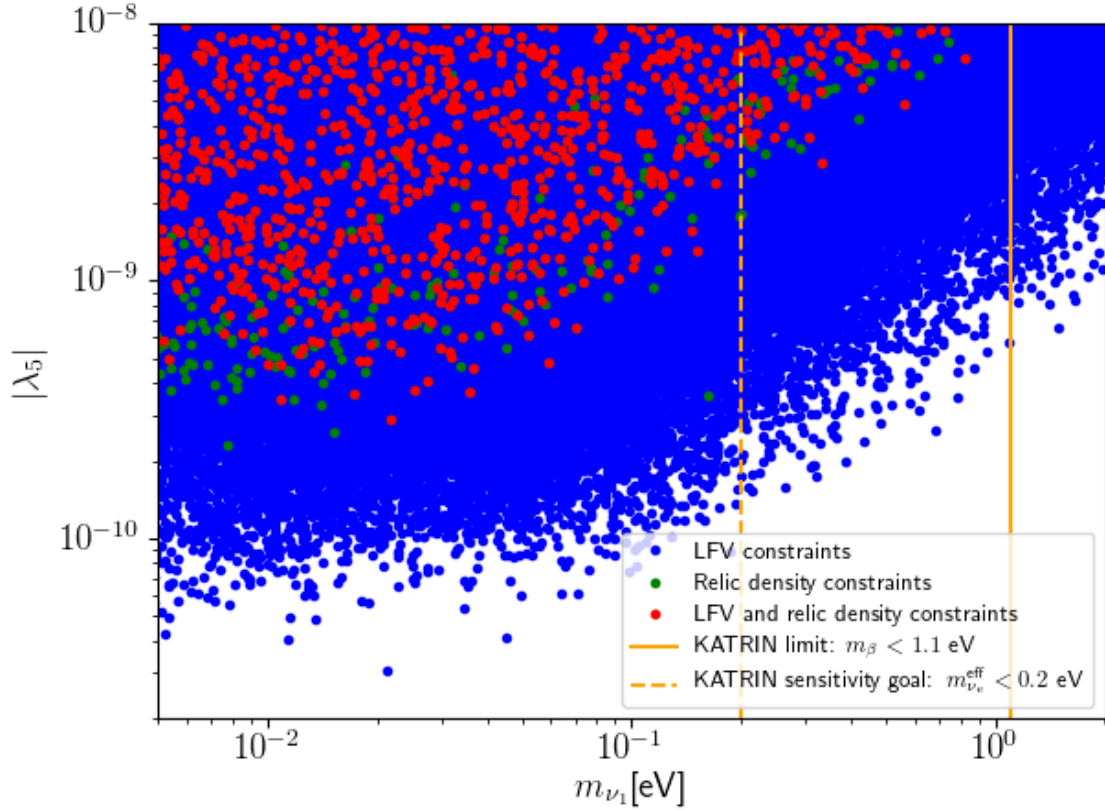


Figure 5.9: The dark sector-Higgs boson coupling  $|\lambda_5|$  versus the lightest neutrino mass, now for the case of scalar dark matter.

For the case of scalar dark matter, no relation between the absolute neutrino mass scale and the dark sector-Higgs coupling was found. This can be attributed to the fact that scalar dark matter does not solely communicate through the newly introduced couplings, unlike fermionic dark matter whose sole interaction with SM particles is via the newly introduced Yukawa coupling. In particular, scalar dark matter mainly interacts with the electroweak gauge bosons. The next chapter will consider the scalar DM candidates of the scotogenic model instead, albeit from a different perspective. The coupling to the electroweak gauge bosons makes it an interesting candidate for observation through indirect detection, compared to the fermionic singlet that out of all SM particles only couples to the leptons.

## Outlook

The effect of the CP phase in the PMNS matrix was not considered, and  $\delta_{CP}$  was set to zero. As an outlook for further studies we show in Figure 5.10 the influence of the CP phase on the relic density, which shows a clear, albeit minor, effect on  $\Omega h^2$ . The parameter values used in the plot are listed in Table 5.6. Further effects on LFV process as a function of the CP phase is also an open question that could warrant further research. As shown in Figure 5.11 the CP phase seems to have an effect on the branching ratio, though it is generally small compared

to the effect of the absolute neutrino mass and only becomes clear when one fixes nearly all model parameters. For completeness, the used input parameters for Figure 5.11 are listed in Table 5.7. One can see that the branching ratio increases for larger absolute neutrino mass, since the Yukawa couplings grow in size, with the exact value depending on the value of the CP phase. What is interesting to see is the extent in which the CP phase affects the couplings to different generations. As can be seen in Figure 5.11 (right), depending on the CP phase one of the branching ratios  $\text{Br}(\mu \rightarrow e\gamma)$  and  $\text{Br}(\tau \rightarrow e\gamma)$  can be dominant over the other. In this way one could use the experimental constraints on LFV processes to constrain the CP phase, but this is left for future work.

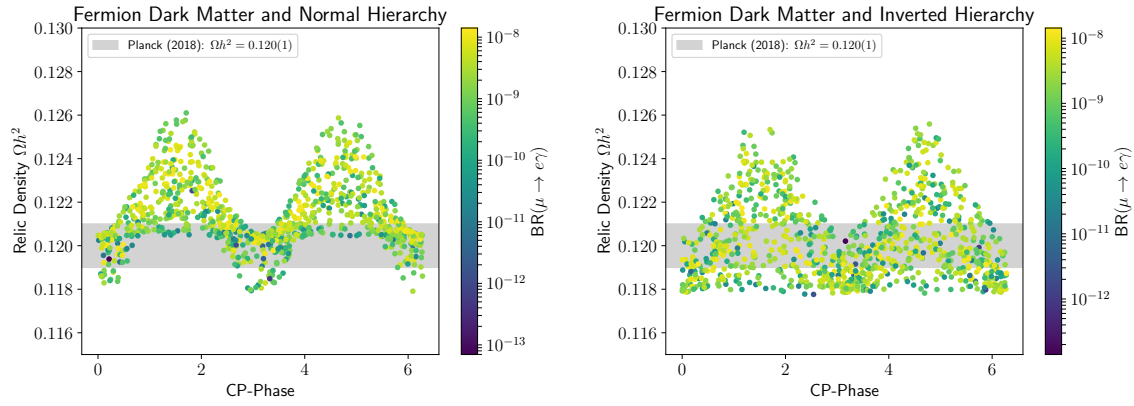


Figure 5.10: The relic density  $\Omega h^2$  plotted versus the CP-phase  $\delta_{CP}$  of the PMNS matrix.

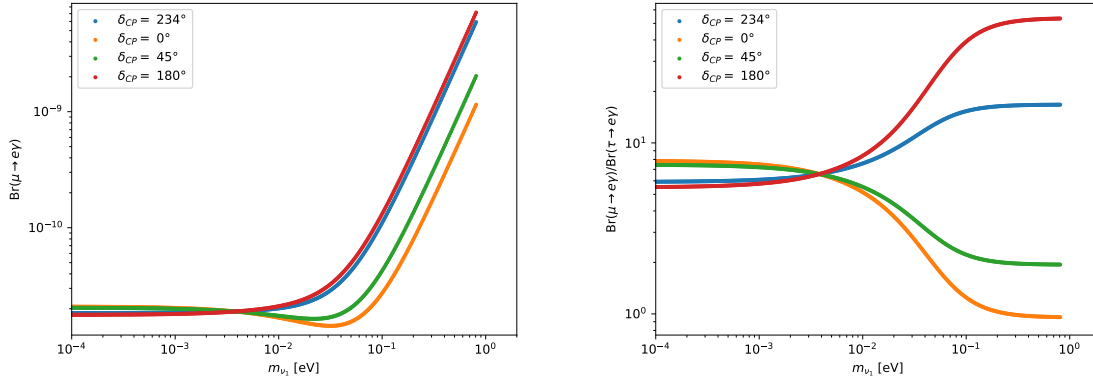


Figure 5.11: The branching ratio of  $\mu \rightarrow e\gamma$  (left) and the ratio  $\text{Br}(\mu \rightarrow e\gamma)/\text{Br}(\tau \rightarrow e\gamma)$  as a function of the lightest neutrino mass  $m_{\nu_1}$  for different values of  $\delta_{CP}$ , assuming normal hierarchy.

Table 5.6: Input parameters that were used in making Figure 5.10. All masses are in GeV, except the few mass parameters explicitly denoted otherwise. Neutrino mass differences and mixing angles were applied at  $3\sigma$  [213].

Parameter	Value
$m_{N_1}$	1000
$m_{N_2}$	4000
$m_{N_3}$	4000
$m_\eta$	2000
$\lambda_1$	0.26
$\lambda_2$	0.5
$\lambda_3$	2
$\lambda_4$	1
$\lambda_5$	$1.0 \cdot 10^{-9}$
$m_{\nu_{1/3}}$ [eV]	0.315

Table 5.7: Input parameters that were used in making Figure 5.11. All masses are in GeV, except the few mass parameters explicitly denoted otherwise.

Parameter	Value
$m_{N_1}$	1000
$m_{N_2}$	4000
$m_{N_3}$	8000
$m_\eta$	2000
$\lambda_1$	0.26
$\lambda_2$	0.5
$\lambda_3$	0.5
$\lambda_4$	-0.5
$\lambda_5$	$1.0 \cdot 10^{-9}$
$m_{\nu_1}$ [eV]	$[10^{-4} - 8.1 \cdot 10^{-1}]$
$\Delta_{12}^2$ [eV <sup>2</sup> ]	$7.53 \cdot 10^{-5}$
$\Delta_{23}^2$ [eV <sup>2</sup> ]	$2.44 \cdot 10^{-3}$
$\delta_{CP}$	$\{0^\circ, 45^\circ, 180^\circ, 234^\circ\}$
$\theta_{PMNS}$ {12,23,13}	$\{33.62^\circ, 47.2^\circ, 8.54^\circ\}$
$\theta_i$	$\{0.2\pi, 0.5\pi, 0.7\pi\}$



## 6 Indirect detection of neutrino signals from scotogenic DM with IceCube

### 6.1 Introduction

As has been discussed in previous chapters, radiative seesaw models connect neutrinos directly to the dark sector. A method for observing DM signals in the context of these models is therefore by looking at products produced in annihilation processes of DM, for which an overview was given in Chapter 2. If such processes are abundant enough, the created high energy neutrinos that are eventually created can be observed with neutrino telescopes on Earth. The shape of the neutrino spectrum depends on the annihilation processes that occur. Direct annihilation of WIMPs into neutrinos creates a sharp line at  $E_\nu \simeq m_{\text{DM}}$ . The spectrum from neutrinos that are created in secondary processes, e.g. from DM annihilating into  $W^+W^-$  pairs, does not show such a feature. Instead the resulting spectrum is continuous. Previous works mainly focused on direct annihilation into neutrinos, see [232, 233, 234, 235]. In this chapter we will consider the general case, i.e. both direct annihilation into neutrinos, as well as neutrinos from secondary processes.

Our galaxy is surrounded by a halo of dark matter in which dark matter can annihilate. This annihilation rate can be enhanced through boosts in the local relic density. As our Sun moves through the galactic halo, dark matter can scatter with a nucleus inside the Sun, and subsequently be captured in its gravitational potential. This leads to an accumulation of WIMPs in the core of the Sun, leading to a local overdensity. Other astrophysical objects that have been considered in the literature are e.g. the Earth [236, 237], the Galactic Center [238, 147, 239], or super massive black holes [234].

In this scenario, WIMP-nucleon scattering plays an important role. Direct detection experiments, amongst which XENON1T and PICO-60, have put stringent constraints on the WIMP-nucleon scattering cross section [47, 130, 95, 128, 126]. In this chapter, we consider neutrino signals that can be produced from DM in the scotogenic model. The IceCube Observatory [155] is the largest neutrino telescope worldwide, and is at the forefront of the search for neutrino signals from WIMP annihilations. The goal of this chapter is to find out whether the scotogenic model allows for neutrino fluxes from WIMP annihilations that are large enough to be detectable in IceCube. In this way, results from the IceCube Observatory can be used to constrain the parameter spaces of these models.

Contrary to the previous chapter where we studied fermionic dark matter, we will now consider the scenario in which the scalar DM candidate is the lightest  $\mathbb{Z}_2$  odd particle. Since the model has been introduced in the previous chapter, we will here start by discussing the processes that lead to the capture of DM in the Sun. We go beyond the scope of standard elastic DM-nucleon scattering by also considering the inelastic case in which a WIMP can scatter to a slightly heavier state. We follow up on this by discussing the subsequent annihilations and their signals in the ICECUBE Observatory configuration with 86 strings (IC86). This chapter is based on the work that was published in Ref. [240].

The concepts that are worked out in this section are also relevant for the next chapter, which discusses DM annihilation signals from the Sun for the model T1-3-B  $\alpha = 0$ .

## 6.2 WIMP capture in the Sun

If WIMPs from the galactic DM halo lose sufficient energy when scattering off nuclei in the Sun they are trapped by its gravitational potential, accumulating in the Sun's core. This capture of DM is in large part determined by the scattering processes that can occur in the Sun, as well as the corresponding cross section. In this section we go into further detail about the mechanisms behind DM capture, for which we consider the scotogenic model. Remember that the scotogenic model has two classes of DM candidates, a fermionic ( $N_i$ ), or a scalar ( $\eta^{0R}$  and  $\eta^{0I}$ ) one, both with their own phenomenology.

First, we consider singlet fermionic DM, as was done in the previous chapter. For this scenario we can be brief. It does not scatter off nucleons at tree level, and can hence pass through the Sun unhindered. It does not accumulate in the Sun, and is thus undetectable in neutrino telescopes on Earth. Moreover, these fermions can only annihilate into two SM charged leptons or neutrinos, of which the cross section is suppressed by the required heavy mediator mass and the small Yukawa couplings involved. This also rules out detection from the Galactic Centre, where DM can accumulate gravitationally without the need for energy loss through scattering.

The case for scalar doublet DM is completely different. It has two different scattering processes through which it can scatter off nuclei (quarks), which is why we will consider this scenario for the rest of the chapter. These scattering processes are shown in Fig. 6.1. These processes differ in two ways. Not only is the mediated particle different (Higgs vs  $Z$ -boson), but for the  $Z$ -mediated process the outgoing scalar particle is not the same as the incoming one, as is usually the case. The process in which both incoming and outgoing particles are the same is referred to as the elastic scattering, whereas for inelastic scattering the outgoing particle is a slightly heavier state. The possibility of such an upscattering was proposed in Ref. [241], under the condition that the mass splitting between the states  $\delta = |m_{\eta^{0R}} - m_{\eta^{0I}}|$  is smaller than

$$\delta < \frac{\mu v^2}{2}, \quad (6.1)$$

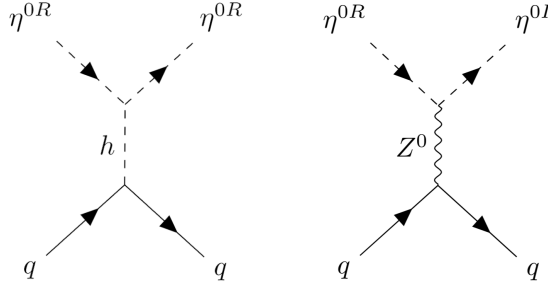


Figure 6.1: Feynman diagrams of the elastic (left) and inelastic (right) scalar DM-nucleon scattering processes in the scotogenic model. If  $\eta^{0I}$  is the DM candidate,  $\eta^{0R}$  and  $\eta^{0I}$  change their roles. For mass splittings larger than a few hundred keV, the right diagram is kinematically forbidden.

where  $\mu$  is the WIMP nucleus reduced mass and  $v$  is the relative velocity. In the framework of the scotogenic model, this mass splitting is realised through  $\lambda_5$ . As was shown in Chapter 5, this parameter can take small values, also for scalar DM, though there exists no relation to the neutrino mass in this case. In this way, a small mass splitting between the neutral scalar states becomes possible, which can be written

$$\delta \approx \frac{\lambda_5 \langle \phi^0 \rangle^2}{m_{\eta^{0R,I}}}. \quad (6.2)$$

For each of the processes we will calculate the WIMP-nucleus scattering cross sections from the WIMP-quark scattering diagrams assuming  $\eta^{0R}$  is the lighter of the two neutral scalars. This result is general, as the results for the case where  $\eta^{0I}$  is lighter are similar, but with  $\eta^{0R}$  and  $\eta^{0I}$  swapped.

### 6.2.1 Elastic scattering

We start by calculating the elastic cross section, shown in the left of Fig. 6.1. Even though elastic scattering cross section routines are already present in MICROMEGAS, it is beneficial to manually calculate the elastic cross section for comparison. This process is mediated by the Higgs boson, for which the relevant interaction terms in the Lagrangian can be written as [242]

$$\mathcal{L} = -\frac{1}{2} g_{\eta^{0R}\eta^{0R}h} (\eta^{0R})^2 h - g_{\bar{q}qh} \bar{q}qh, \quad (6.3)$$

The coupling  $g_{\eta^{0R,I}\eta^{0R,I}h} = (\lambda_3 + \lambda_4 \pm \lambda_5) \langle \phi^0 \rangle \sqrt{2}$  can be extracted from the high-energy Lagrangian that was given in Chapter 5, and the couplings  $g_{\bar{q}qh} = y_q / \sqrt{2}$  are the SM Higgs-quark Yukawa couplings, which can be written in terms of their masses as  $y_q = m_q / \langle \phi^0 \rangle$ . These can also be obtained through SARAH [223].

For scattering energies much smaller than the Higgs mass of 125 GeV, which is the case for such non-relativistic scattering processes, one can describe the process through an effective

Table 6.1: Values of the scalar quark form factors in nucleons that were used [227].

	proton	neutron
$f_d^{(N)}$	0.0191	0.0273
$f_u^{(N)}$	0.0153	0.011
$f_s^{(N)}$	0.0447	0.0447

operator in the Lagrangian by integrating out the mediator. For the elastic case, this results in [242, 42]

$$\mathcal{L}_{\text{eff}} = \frac{1}{2} a_q 2m_{\eta^{0R}} (\eta^{0R})^2 \bar{q}q. \quad (6.4)$$

A factor  $2m_{\eta^{0R}}$  has been taken out of the prefactor and included in the operator, so that it has the same mass dimension if the scattering particle were a fermion [243]. We thus define the coupling of this effective operator as

$$a_q = g_{\eta^{0R}, I} g_{\eta^{0R}, I h} g_{\bar{q}q h} / (2m_{\eta^{0R}, I} m_h^2), \quad (6.5)$$

with mass dimension -2. We now make the next step from scattering off quarks to nuclei, which is the scattering amplitude on a nucleon  $N$ , which can either be a proton  $p$  or a neutron  $n$ . It is written as

$$\mathcal{M} = 4m_{\eta^{0R}} m_N \sum_q a_q \langle N | \bar{q}q | N \rangle, \quad (6.6)$$

for a nucleon mass  $m_N$ , with  $|N\rangle$  begin the nucleon state in the non-relativistic normalisation. For the light quarks ( $q = u, d, s$ ) the matrix element can be evaluated as [242, 42]

$$m_q \langle N | \bar{q}q | N \rangle = m_N f_q^{(N)}, \quad (6.7)$$

with quark masses  $m_q$ . The  $f_q^{(N)}$  denote the scalar quark form factor of a quark  $q$  in nucleons, which can be extracted experimentally. We use the values shown in Table 6.1 [227]. The heavy quarks ( $Q = c, b, t$ ) deserve a different treatment. These induce triangle diagrams that indirectly couple the Higgs boson to gluons, as was pointed out in Ref. [244]. For these quarks the matrix element can be written as

$$m_Q \langle N | \bar{Q}Q | N \rangle = \frac{2}{27} m_N \left[ 1 - \sum_{q=u,d,s} f_q^{(N)} \right]. \quad (6.8)$$

The resulting effective coupling to protons (neutrons) is then

$$\frac{f_{p(n)}}{m_{p(n)}} = \sum_{q=u,d,s} f_q^{p(n)} \frac{a_q}{m_q} + \frac{2}{27} \left[ 1 - \sum_{q=u,d,s} f_q^{p(n)} \right] \sum_{Q=c,b,t} \frac{a_Q}{m_Q}. \quad (6.9)$$



Now we can make the final step from nucleon to nucleus, by considering a nucleus of mass number  $A$  with mass  $m_A$ . Spin independent interactions couple coherently to the  $Z$  protons and  $A - Z$  neutrons that make up the nucleus. In the limit of zero momentum transfer  $|\mathbf{q}|$  the scattering cross section can be written as [242, 42]

$$\sigma_A^0 = \frac{\mu^2}{\pi} [Zf_p + (A - Z)f_n]^2. \quad (6.10)$$

At higher momentum transfer one needs to take into account loss of coherence, and the differential cross section is given as

$$\frac{d\sigma_A}{d|\mathbf{q}|^2} = \frac{\sigma_A^0}{4\mu^2 v^2} F^2(Q), \quad (6.11)$$

which is dependend on the nuclear form factor  $F^2(Q)$ .  $Q$  is the energy transfer, sometimes also denoted recoil energy  $E_R$ , and is  $|\mathbf{q}|^2/(2m_A)$ . It ranges from a minimum  $Q_{\min} = 0$  to the maximum at  $Q_{\max} = 4\mu^2 v^2/(2m_A)$ . In our analysis, we use a Gaussian form factor [245]

$$F^2(Q) = \exp(-Q/Q_0) \quad (6.12)$$

with  $Q_0 = 3/(2m_A R^2)$  and

$$R = \left[ 0.91 \left( \frac{m_A}{\text{GeV}} \right)^{\frac{1}{3}} + 0.3 \right] \times 10^{-13} \text{ cm}. \quad (6.13)$$

This allows us to evaluate the integral of the scattering cross section analytically, which speeds up our further numerical evaluation and scans through the parameter space.

### 6.2.2 Inelastic scattering

The inelastic scattering scattering process is mediated by the  $Z$  boson, as shown in Figure 6.1 (right). It is worth noting that the inelasticity does not play a large role in the scattering amplitude, but enters through the kinematics later on. Generally, a  $\bar{q}qZ$  vertex contains a vector and an axial vector part ( $V - A$  interaction). However, in the non relativistic limit, the axial vector contribution vanishes. The vector part describing the coupling of the  $Z$  boson is given by [242]

$$\mathcal{L} = g_{\eta^0 R \eta^0 I Z^0} (\eta^{0R} \partial^\mu \eta^{0I} - \partial^\mu \eta^{0R} \eta^{0I}) Z_\mu^0 + g_{\bar{q}q Z^0} \bar{q} \gamma^\mu q Z_\mu^0. \quad (6.14)$$

The vector interaction contributes to the spin independent cross section. In the context of the scotogenic model, the couplings are determined by the  $\text{SU}(2)_L \times \text{U}(1)_Y$  gauge group of

the electroweak sector, with gauge couplings  $g$  and  $g'$  respectively. The couplings can be obtained from SARAH and read

$$\begin{aligned} g_{\eta^{0R}\eta^{0I}Z^0} &= ig/(2c_W) \\ g_{\bar{q}qZ^0} &= g(I_q - 2Q_q s_W^2)/(2c_W), \end{aligned} \quad (6.15)$$

with  $s_W$  and  $c_W$  being the sine and cosine respectively of the Weinberg angle  $\tan \theta_W = s_W/c_W = g'/g$ . Further relevant quantum numbers are the weak isospin for the up- and down-type quarks of  $I_q = \pm 1/2$  and their electric charges  $Q_{u,d} = (2/3, -1/3)$ . Once again one can integrate out the mediator to obtain the following effective Lagrangian [242]

$$\mathcal{L}_{\text{eff}} = -b_q(\eta^{0R}\partial_\mu\eta^{0I} - \partial_\mu\eta^{0R}\eta^{0I})\bar{q}\gamma^\mu q, \quad (6.16)$$

with the effective coupling to a quark  $q$

$$b_q = g_{\eta^{0R}\eta^{0I}Z^0}g_{\bar{q}qZ^0}/m_Z^2. \quad (6.17)$$

The resulting scattering amplitude is

$$\mathcal{M} = 4m_{\eta^{0R}}m_N \sum_q b_q \delta_\mu^0 \langle N | \bar{q}\gamma^\mu q | N \rangle, \quad (6.18)$$

as the scalar four-momenta, which entered through the derivative term in the effective Lagrangian, add up to  $p_\mu^{\eta^{0R}} + p_\mu^{\eta^{0I}} \approx 2m_{\eta^{0R,I}}\delta_\mu^0$ . As the vector current is conserved, only the valence quarks contribute to the sum in the scattering amplitude. In the non relativistic normalization for the nucleon states the contribution of a quark inside a nucleon with  $n_q$  quarks to the matrix element is [242]

$$2m_N \langle N | \bar{q}\gamma^\mu q | N \rangle = n_q \bar{u}_N \gamma^\mu u_N \approx n_q 2m_N \delta_0^\mu. \quad (6.19)$$

This means that for the inelastic process there will be a difference between scattering off protons compared to neutrons, which was not present in the elastic case. Since only the valence quarks contribute, one obtains

$$\begin{aligned} b_p &= 2b_u + b_d, \\ b_n &= b_u + 2b_d. \end{aligned} \quad (6.20)$$

Now scaling up a step, one can obtain the cross section on a nucleus by means of a coherent sum over the nucleons. This is analogous to the scalar interaction in the inelastic process, for a nucleus with  $A$  nucleons and  $Z$  protons the cross section is

$$\sigma_A^0 = \frac{\mu^2}{\pi} [Zb_p + (A - Z)b_n]^2. \quad (6.21)$$

As we will show later, the cross section for the inelastic case is much larger than for the elastic case, which stems from the fact that the gauge couplings with which the  $Z$  couples in the former process are larger than the Higgs couplings that appear in the latter. As was mentioned before, the kinematics of the inelastic process do not play a large role for the differential cross section

$$\frac{d\sigma_A}{d|\mathbf{q}|^2} = \frac{\sigma_A^0}{4\mu^2 v^2} F^2(Q). \quad (6.22)$$

It does however change the integration boundaries, as part of the energy lost by the incoming particle must be spent on the upscattering to the heavier state. These are modified to the following forms [246, 247, 248]

$$Q_{\min} = \frac{1}{2} m_{\eta^{0R,I}} v^2 \left( 1 - \frac{\mu^2}{m_A^2} \left( 1 + \frac{m_A}{m_{\eta^{0R,I}}} \sqrt{1 - \frac{\delta}{\mu v^2/2}} \right)^2 \right) - \delta, \quad (6.23)$$

$$Q_{\max} = \frac{1}{2} m_{\eta^{0R,I}} v^2 \left( 1 - \frac{\mu^2}{m_A^2} \left( 1 - \frac{m_A}{m_{\eta^{0R,I}}} \sqrt{1 - \frac{\delta}{\mu v^2/2}} \right)^2 \right) - \delta. \quad (6.24)$$

### 6.2.3 Capture rate

With expressions derived in the previous sections, we have established the scattering cross sections for both processes. In this section we will again move to larger scales, by determining the capture rate of DM inside the Sun. The capture rate per unit shell volume in a celestial object, including the Sun, is given by [245, 246, 247, 248]

$$\frac{dC}{dV} = \int_0^\infty du \frac{f(u)}{u} w \Omega_v^-(w), \quad (6.25)$$

with  $f(u)$  being the velocity distribution of DM in region the galactic halo where the Sun's gravitational pull has no effect. We assume it follows a Maxwell-Boltzmann distribution. As DM falls into the gravitational potential of the Sun, it accelerates to a velocity

$$w = \sqrt{u^2 + v(r)^2}, \quad (6.26)$$

with  $v(r)$  being the escape velocity in a shell at radius  $r$ . The scattering rate  $\Omega_v^-$  which is the rate at which a DM particle with velocity  $w$  scatters off a nucleus  $A$  so that the final velocity lies below the escape velocity  $v(r)$  is

$$\Omega_v^- = \frac{n_A \sigma_A^0 w}{4\mu^2 v^2 / (2m_A)} \int_{Q'_{\min}}^{Q_{\max}} dQ F^2(Q). \quad (6.27)$$

This expression consists of two parts. The first part contains the total scattering rate  $n_A \sigma_A^0 w$  on a nucleus  $A$  with solar number density  $n_A$ . The second part is an integral over the possible energy transfer range  $Q$ . For inelastic scattering, the kinematics of the process constrain  $Q$  to

lie between the values given in Equations (6.23) and (6.24), for  $v = w$ . For inelastic scattering there is an additional capture condition that must be satisfied, which reads

$$Q_{\text{cap}} = \frac{1}{2} m_{\eta^{0R,I}} (w^2 - v(r)^2) - \delta, \quad (6.28)$$

so that the lower bound of the integral in Equation (6.27) has the following condition:  $Q'_{\text{min}} = \max(Q_{\text{cap}}, Q_{\text{min}})$ . The case of elastic scattering is recovered in the limit  $\delta \rightarrow 0$  [245]. As we will discuss later, the capture rate is almost constant below a mass splitting of  $\mathcal{O}(100 \text{ keV})$ . For larger mass splittings the capture rate drops off slowly at first, before eventually dropping off quickly as the process becomes kinematically forbidden.<sup>1</sup>

As a quick recap from Chapter 2.3.2, remember that the time evolution of the number of WIMPs inside the Sun is controlled by the capture and annihilation rates as

$$\dot{N} = C - 2\Gamma. \quad (6.29)$$

The capture rate  $C$  is dependent on the cross sections of the scattering processes involved, as well as the nuclear abundances inside the Sun as was discussed in the last section.  $\Gamma$  is the annihilation rate and depends on the available channels. In principle, evaporation of DM from the Sun can also take place if the DM is very light, but it has been neglected in this work. Under the condition that the WIMP-nucleus scattering cross section is large enough, the two rates will reach equilibrium at a time that is well below the current lifetime of our Sun [249]. In this case the annihilation rate is completely dependent on the capture rate

$$\Gamma = C/2, \quad (6.30)$$

which in turn depends on the elastic and inelastic scattering cross sections. For the case of inelastic scattering this assumption is not a trivial one. A scenario in which purely inelastic scattering processes take place has been discussed in Ref. [249]. There it was found that equilibrium is not reached for DM masses above 100 GeV and  $\delta > 200 \text{ GeV}$ , with the assumption of an inelastic cross section of  $\sigma_p \approx 10^{-6} \text{ pb}$ . As we will discuss later, we obtain an inelastic cross section on protons of  $\sigma_p \approx 10^{-4} \text{ pb}$  for our scenario, meaning that equilibrium is reached at an earlier time. Moreover, the scotogenic model also contains an elastic scattering process. This means that WIMPs can be captured through an inelastic scattering process, and subsequently thermalize in the Sun through elastic scattering processes. This scenario has been discussed in Ref. [247], which concluded that equilibrium can be reached for elastic scattering cross sections on the order of  $10^{-12} \text{ pb}$ . It should be stressed that even though for most models these requirements for equilibrium are easily fulfilled, there exist regions of the parameter space, in particular those with large mass splittings and small elastic cross sections, where this is not the case. As a consequence equilibrium has not settled in yet,

---

<sup>1</sup>We have reproduced the numerical results for the capture rate in Figure 3 of Ref. [247] up to a missing factor of two in  $E_{\text{max}}^{\text{elastic}}$  as well as those in Figures 1 and 2 of Ref. [248]. Note that Ref. [246] uses  $Q'_{\text{min}} = Q_{\text{cap}}$ , which ignores the case where  $Q_{\text{min}} > Q_{\text{cap}}$  and thus gives too large capture rates for large mass splittings.

which causes a suppression in the DM annihilation rate, and as a consequence the ICECUBE event rate decreases.

### 6.3 Detection of neutrino signals of elastic and inelastic DM annihilations in the Sun with IceCube

Our aim is to perform a numerical scan of the scotogenic model to see whether ICECUBE can detect neutrino signals from annihilating DM in the Sun. As we have assumed equilibrium between DM capture and annihilation in the Sun, we can describe the differential flux of neutrinos on Earth by

$$\frac{d\phi_\nu}{dE_\nu} = \frac{1}{4\pi d_\odot^2} \Gamma \sum_f Br_{f\bar{f}} \frac{dN_f}{dE_\nu}. \quad (6.31)$$

The equation has several different terms, with  $d_\odot$  the distance Earth-Sun and the annihilation rate  $\Gamma = C/2$  related to the capture rate. The last term is a sum over all possible final states  $f\bar{f}$  with corresponding branching ratios  $Br_{f\bar{f}}$  and the neutrino or antineutrino energy spectra  $dN_f/dE_\nu$ . These are computed by MICROMEGAS based on tables and feature neutrino propagation and oscillation effects inside the Sun and in the vacuum. The function `neutrinoFlux` automatically calculates the elastic capture rate and subsequently determines the annihilation branching ratios and energy spectra of the channels, and then provides the total neutrino flux at the Earth. However, for the inelastic process there was no such implementation in MICROMEGAS. Hence we made use of CALCHEP 3.7 [250], which is already included in MICROMEGAS to compute the DM-quark scattering matrix elements and cross sections with the formulae of the previous section. In order to calculate the capture rate inside the Sun, we used the DARKSUSY 6.2.3 package [251], which contains the routine `dssenu_capsunnum` which was modified to calculate the inelastic capture rate. This output could then be used in MICROMEGAS similar to the elastic case. A schematic overview can be seen in Figure 6.2, which is the extended version of 5.2 that was shown in the previous chapter. From the neutrino flux arriving at the Earth given by (6.31), one can deduce the amount of signal events in the ICECUBE detector, by convoluting it with the effective detector area of IC86. This means that we do not consider effects stemming from neutrino propagation through the Earth's interior, such as absorption and tau-regeneration. Though these effects are expected to have only minor effects on the result, they should be considered in future analyses.

The differential number is given by [252]

$$\frac{dN_s}{dE} = t_e \left( \frac{d\phi_{\nu_\mu}}{dE} A_{\nu_\mu}(E) + \frac{d\phi_{\bar{\nu}_\mu}}{dE} A_{\bar{\nu}_\mu}(E) \right), \quad (6.32)$$

for an exposure time  $t_e$  and the effective area of the detector for muon (anti)neutrinos, which is energy dependent. The routine `IC22nuAr` for the effective area of the obsolete IC22 configuration with 22 data-taking strings was already present in MICROMEGAS. It has been

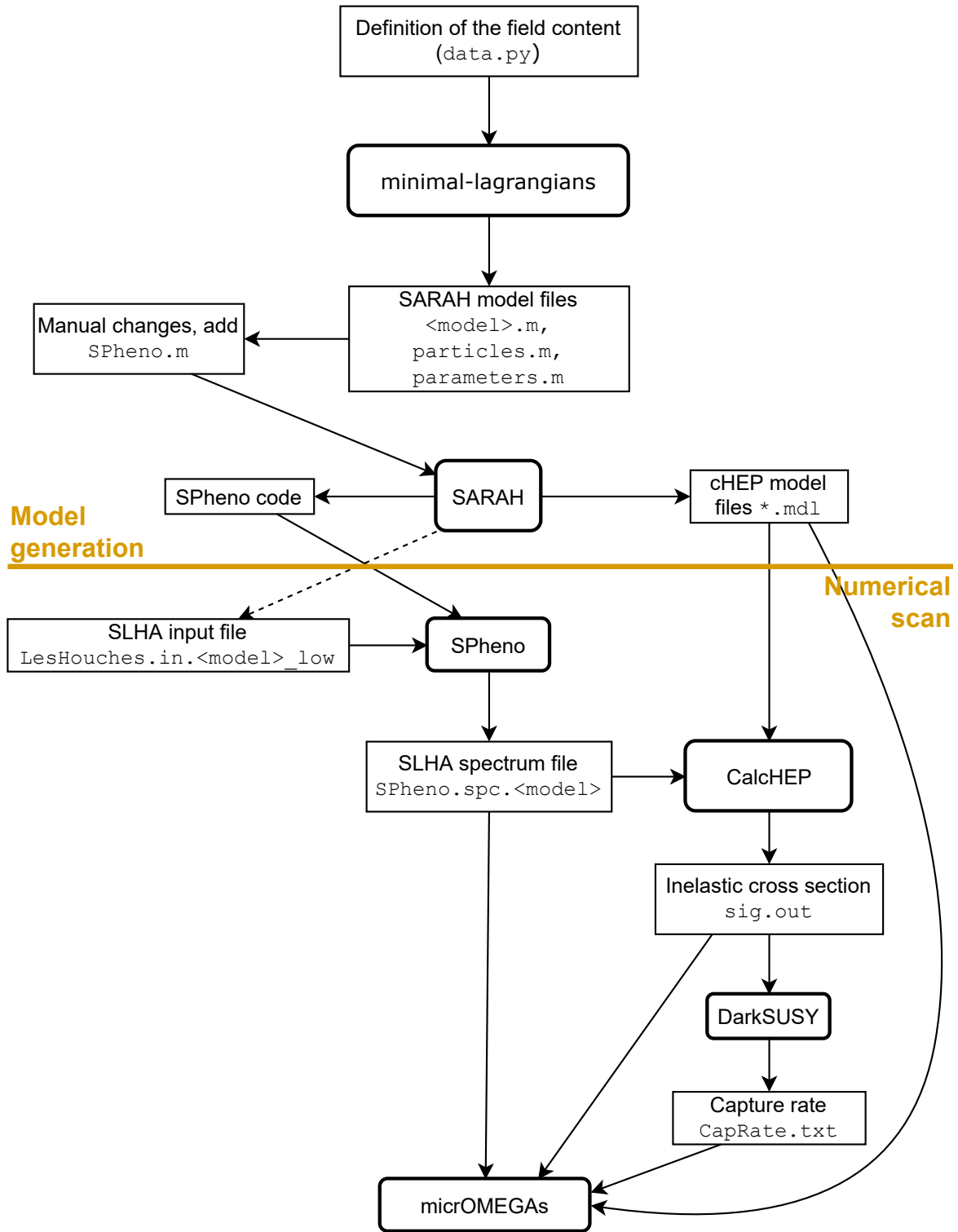


Figure 6.2: Schematic overview of the toolchain involved in the numerical evaluation of this model. Based on Figure 6.1 in [221].

updated for the effective area of the current IC86 configuration, using the data from Ref. [157]. This configuration also includes eight DeepCore strings that can lower the energy threshold of the detector from above 30 GeV down to 10 GeV. Figure 6.3 shows the effective area as a

function of the neutrino and antineutrino energy. Above 2.5 TeV the effective area has been extrapolated linearly to fit with our scan range. As was already mentioned, the corresponding data points have been taken from Ref. [157]. In the region where both selections overlap, we use the ICECUBE effective area, as it is larger than the one from DEEPCORE [253]. ICECUBE

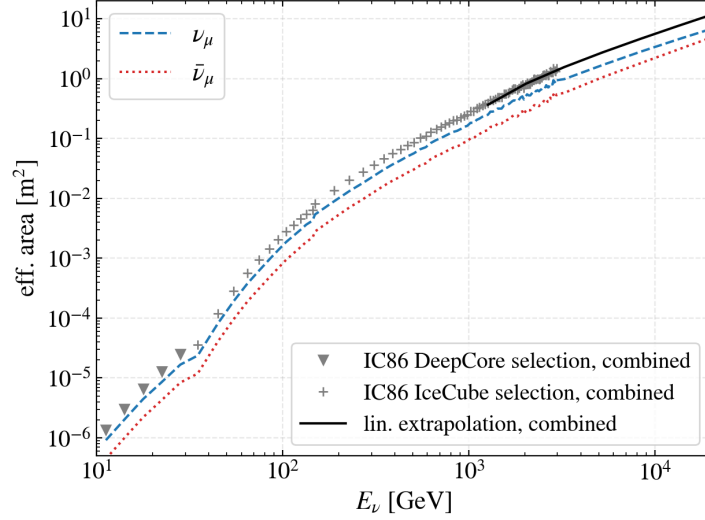


Figure 6.3: The  $\nu_\mu$  and  $\bar{\nu}_\mu$  effective areas of the DEEPCORE detector and the ICECUBE detector configuration IC86 as a function of the neutrino energy. The data for the combined effective area is taken from Ref. [157] (triangles and crosses) and linearly extrapolated (solid black line). The individual effective areas for neutrinos (dashed blue line) and antineutrinos (dotted red line) are calculated with the deep inelastic scattering cross sections taken from Ref. [254]. Both the ICECUBE and DEEPCORE selections of the effective area are used in our work.

is sensitive to muon neutrinos as well as antineutrinos. However, the corresponding energy dependent deep-inelastic scattering cross sections with nucleons in the detector are slightly different. In Ref. [157] only the combined effective area  $\nu_\mu + \bar{\nu}_\mu$  was given, hence we take the different cross sections  $\sigma_{\nu_\mu(\bar{\nu}_\mu)}$  from Ref. [254] into account and calculate both effective areas separately through the relation

$$A_{\nu_\mu(\bar{\nu}_\mu)} = \frac{A_{\text{combined}}}{1 + \frac{\sigma_{\bar{\nu}_\mu(\nu_\mu)}}{\sigma_{\nu_\mu(\bar{\nu}_\mu)}}}. \quad (6.33)$$

With these relations in place, we can now show the expected neutrino fluxes that arrive at ICECUBE, as well as how they relate to the signal event rate. We do this by means of a benchmark point BPA, for which the values are listed in Table 6.2. The benchmark point has been obtained through random sampling and therefore is a good representation of a general point in the parameter space. For BPA we have a scalar DM candidate  $\eta^{0I}$  with a mass of 1007.38 GeV. The main annihilation channels are  $W^+W^-$  (58.36%),  $Z^0Z^0$  (23.51%),  $hh$  (12.30%) and  $W^+W^-\gamma$  (4.99%). As one could have expected, the dominant annihilation channel with a branching fraction of over 63% is due to  $W^+W^-$  pair production (with or

Table 6.2: Parameters of the scotogenic model for our benchmark point BPA. Shown are the coupling parameters  $\lambda_i$ , the squared mass  $m_\eta^2$  of the new scalar doublet, the (diagonal) mass matrix  $m_N$  for the three new fermion singlets, and the real and imaginary parts of the Yukawa matrix,  $y^R$  and  $y^I$ .

$\lambda_1$	$\lambda_2$	$\lambda_3$	$\lambda_4$	$\lambda_5$	$m_\eta^2$ [GeV <sup>2</sup> ]	$m_{N_1}$ [GeV]	$m_{N_2}$ [GeV]	$m_{N_3}$ [GeV]
0.26	0.50	0.56	-0.14	$2.00 \cdot 10^{-7}$	$1.00 \cdot 10^6$	$1.32 \cdot 10^3$	$3.13 \cdot 10^3$	$3.44 \cdot 10^3$
$y^R/10^{-2}$					$y^I/10^{-3}$			
$\begin{pmatrix} -17.20 & 2.07 & -6.91 \\ -4.94 & 9.41 & 15.17 \\ 5.22 & 15.98 & -8.20 \end{pmatrix}$					$\begin{pmatrix} 2.58 & 4.46 & 5.10 \\ -6.88 & 2.02 & 2.30 \\ -2.08 & -1.23 & -1.40 \end{pmatrix}$			

without a photon). As we will show later, this is generally the case for DM masses with  $m_{\eta^{0R,I}} > m_W$ . Processes into fermion pairs are generally suppressed by the mass of the mediating Higgs boson, whereas the 4-vertex into  $W^+W^-$  pairs receives no such suppression. Direct annihilation into neutrinos is in principle allowed, but is suppressed by the small Yukawa couplings  $y_{i\alpha}$  and the heavy mass of the propagator  $m_{N_i}$ . Figure 6.4 (top) shows the differential neutrino and antineutrino fluxes in full and dashed lines respectively for the elastic (blue) and inelastic case (red). The vertical line at 1007.38 GeV corresponds to the DM mass and marks the end of the spectrum. As we have no direct annihilation into neutrinos, we do not have a peak in the spectrum at the DM mass. The differences between the neutrino and antineutrino fluxes, which become substantial at higher energies are due to absorption, oscillation and regeneration effects that take place inside the Sun [255]. The bottom plot of Figure 6.4 shows the differential number of events in the IC86 detector. It is obtained by convoluting the neutrino spectra with the effective detector area. We see that at low energies the amount of events starts out very low in spite of the high fluxes at these energies, which can be explained by the low effective detector area. Integrating over the neutrino area yields a total event rate for BPA of only 0.07 expected events per year for the elastic case. On the contrary, the inelastic case yields a much larger amount of  $8.65 \cdot 10^4$  expected events.

## 6.4 Numerical scan

In the previous section we have presented our numerical routines, schematically shown in Figure 6.4, as well as the results for a specific benchmark points. For further evaluation of the model, the scalar couplings are varied within the following ranges

$$\lambda_3 \in \left[ -\sqrt{\lambda_1 \lambda_2}, 4\pi \right] , \quad \lambda_4 \in \left[ \max\{ -\sqrt{\lambda_1 \lambda_2} - \lambda_3 + |\lambda_5|, -4\pi \}, 0 \right] , \quad |\lambda_5| \in [10^{-10}, 10^{-3}] . \quad (6.34)$$

For these ranges vacuum stability and perturbativity constraints are satisfied, as well as the requirement that the lightest scalar is electrically neutral.  $\lambda_5$  is restricted to small values,



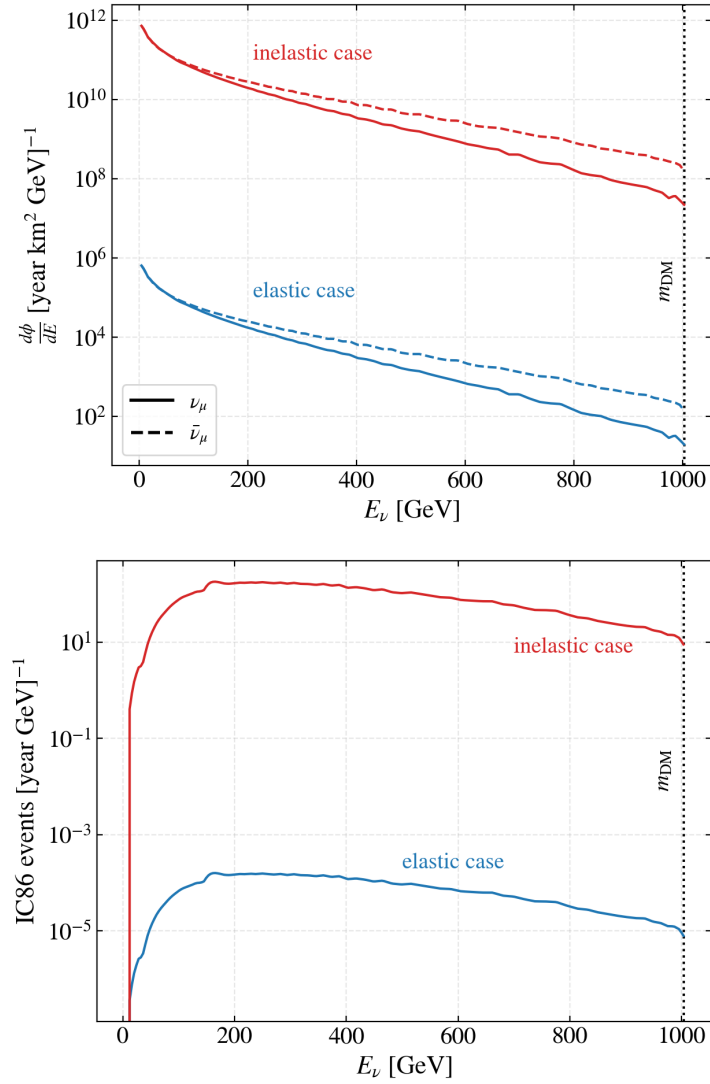


Figure 6.4: Top: Elastic (blue) and inelastic (red) muon neutrino (full) and antineutrino (dashed) fluxes at Earth as a function of the neutrino energy, calculated with the modified function `neutrinoFlux` in `MICROMEGAS` at the parameter point BPA. The mass of the DM particle  $\eta^{0I}$  is 1007.38 GeV. Bottom: Expected number of signal events in IC86 per year as a function of the neutrino energy.

as has been extensively discussed in Chapter 5. The mass parameter of the scalar doublet is varied over the wide range

$$m_\eta \in [1 \text{ GeV}, 10 \text{ TeV}]. \quad (6.35)$$

Since we only consider scalar DM as the fermions do not accumulate in the Sun, their masses must be larger than the lightest scalar. We performed two different scans. In the first scan the masses of the fermions are sampled randomly in the range of the scalar mass up to 10 GeV, so that they are always heavier. However, in the second scan we choose a particular scenario in which the fermions have a mass that lies only 0.1 GeV above the scalar mass to demonstrate the effects of coannihilation processes on the model [256]. The SM neutrino

oscillation parameters are taken from Ref. [213] within the  $3\sigma$  range for normal ordering. The CP violating phase  $\delta_{CP}$  is allowed to take any general value 0 and  $2\pi$ . The mass of the lightest neutrino is varied in the range  $[10^{-4}, 1.1]$  eV, which corresponds with the upper limit of the KATRIN experiment as was reported in Ref. [209]. As was explained in Chapter 5, the Yukawa couplings are calculated through the Casas-Ibarra parametrization, and must satisfy the perturbative limit of  $|y_{i\alpha}|^2 < 4\pi$ .

### Relic density

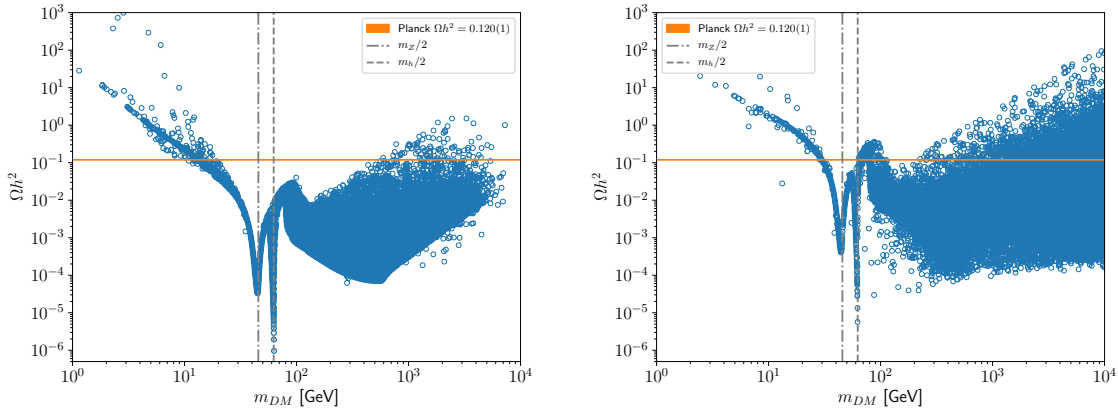


Figure 6.5: Relic density of scalar dark matter in the scotogenic model, for the normal (left) and coannihilation (right) scan. As an indication, the observed relic density by PLANCK [23] has been included, as well as lines at  $m_Z/2$  and  $m_h/2$ .

With these input parameters, the relic density of the model points can be calculated. Without imposing any constraints, the relic density as a function of the DM mass is shown in Figure 6.5, for the normal (left) and coannihilation (right) scan. The observed relic density by PLANCK [23] is indicated by the narrow orange band. For the normal scan without coannihilations, there is a region between 10-20 GeV in which the relic density is within the PLANCK limits, but it decreases for higher masses. Only above 400 GeV can the model points yield the correct relic density again. There are certain mass regions where the expected relic density changes rapidly. These usually occur near thresholds. As an illustration, lines have been drawn at half the  $Z$  and Higgs boson ( $h$ ) mass. At these masses the processes  $\eta\eta \rightarrow Z/h \rightarrow \text{SM SM}$  have a resonance. This enhances the annihilation cross section, resulting in a lower relic density. Further thresholds can be seen around the  $W$ ,  $Z$ , and  $h$  masses, at which point the channels  $\eta\eta \rightarrow W^+W^-/ZZ/hh$  become available. In the case where coannihilations are included, the relic density is boosted, which was also concluded in [256]. The overall shape of the parameter region does not change. This has as a consequence that the low-mass region with the correct relic density is shifted to around 30 GeV, and that there now is a region from  $m_h/2$  to slightly above 100 GeV with a correct relic density. At higher masses, the correct relic density is obtained for masses from around 200 GeV and upwards. There is thus a larger viable mass range for the coannihilation case.

## Experimental constraints

In order to evaluate the rest of the scan results, we impose further experimental constraints, similar to those of Chapter 5, which we repeat here. We constrain the relic density of PLANCK [23], to which we add a relatively large margin of  $\Omega h^2 = 0.12 \pm 0.02$  to account for theoretical uncertainties [257]. The following LFV branching ratios (BR) and conversion rates (CR) are imposed

$$\begin{aligned} \text{BR}(\mu \rightarrow e + \gamma) &< 4.2 \cdot 10^{-13}, \\ \text{BR}(\mu \rightarrow 3e) &< 1.0 \cdot 10^{-12}, \\ \text{CR}(\mu - e, \text{Ti}) &< 4.3 \cdot 10^{-12}, \end{aligned} \tag{6.36}$$

published by the MEG [215], SINDRUM [217] and SINDRUM II [219] collaborations. Furthermore, there are LEP limits on the invisible decay width of the  $Z^0$  boson due to new physics [258]

$$\text{BR}(Z^0 \rightarrow \text{new}) < 0.008, \tag{6.37}$$

which are so tight that it effectively excludes  $m_{\text{DM}} < m_Z/2$  [259, 260], as well as constraints on the invisible Higgs decay width from ATLAS (CMS) at the LHC [261, 163]

$$\text{BR}(h \rightarrow \text{inv.}) < 0.11 \text{ (0.19)}. \tag{6.38}$$

From direct detection experiments there are constraints on the elastic and inelastic cross sections by XENON1T [95], XENON100 [262, 263] and PANDA-II [264]. The possible annual modulation of the DAMA/LIBRA [93, 265], its ongoing verification [266, 267, 268] as well as further indirect detection limits from DM annihilation into neutrinos in the Sun [269, 157, 270] or the Galactic Centre [147, 158, 239, 151] are discussed in the following sections. These constraints are viewed in light of the expected event rates from the Sun for the current IC86 configuration.

### 6.4.1 Elastic cross section limits

The scattering cross sections play an important role in the capture of DM, which is why we will discuss these extensively. Our results for the spin independent cross section are shown in Figure 6.6. These results are in agreement with Figure 9 in Ref. [256], when taking into account the difference in scan ranges, as well as the updated imposed constraints on the Higgs mass, relic density, neutrino masses, and LFV. We find that the parts in the parameter space with low DM mass generally contain sufficiently heavy charged scalars to satisfy the LEP2 bound ( $> 97$  GeV) [228]. However, these are excluded by the LEP limit on the invisible  $Z^0$  decay width [259, 260]. There are no further models in the mass range  $m_Z/2 < m_{\text{DM}} < m_h/2$  that can be constrained by the less stringent invisible Higgs decay bounds [261, 163]. Apart from these models that lie in the low mass range, all viable models lie above a mass of 500 GeV (top), which gets significantly lowered to 200 GeV when including coannihilations

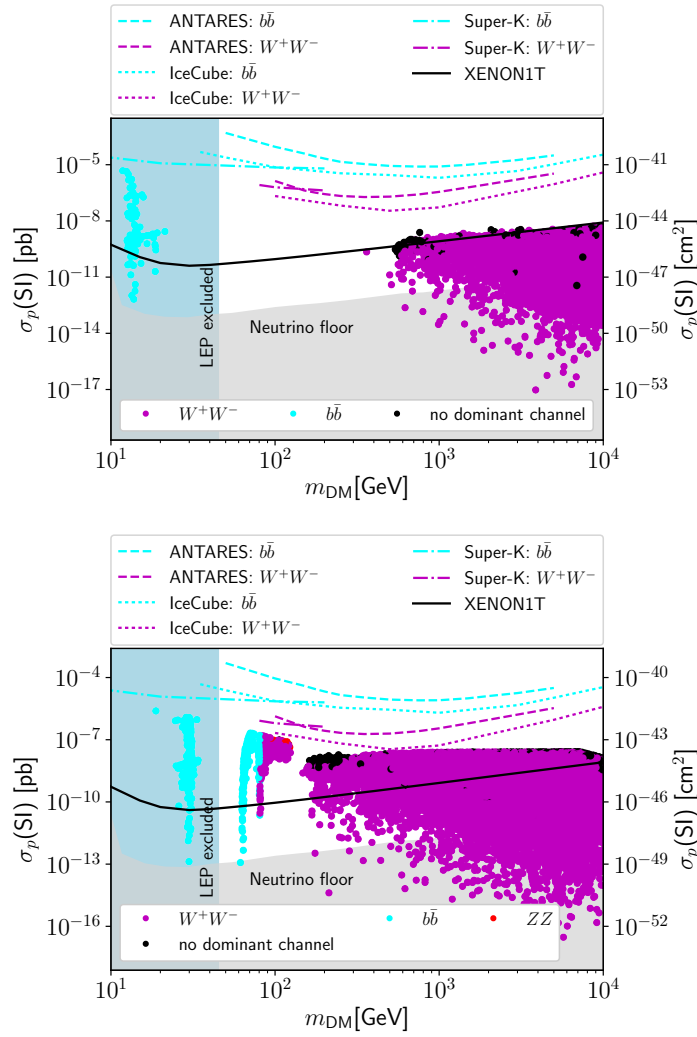


Figure 6.6: The spin independent (SI) elastic cross section with ANTARES [269], IceCUBE [157], SUPER-KAMIOKANDE [270] and XENON1T [95] exclusion limits as a function of the DM mass. All points and lines are color coded according to the main annihilation channel, provided there is one with a branching ratio of over 50%. Also shown are the LEP exclusion from the invisible  $Z^0$  boson width [259, 260] and the neutrino floor [129]. In the lower plot, coannihilation processes are enhanced by the small scalar-fermion mass difference.

(bottom) [256]. The models are colour coded according to the dominant annihilation channel, which is the case if a single branching ratio reaches 50%. If no branching ratio reaches 50%, a point is marked as having no dominant annihilation channel. For most models at higher masses the main annihilation channel is into  $W$  boson pairs, as was also the case for BPA. If the DM mass is too low to produce a  $W$  boson pair, the dominant channel is  $b\bar{b}$  instead. In Figure 6.6 we have included several direct and indirect detection constraints. The channel-dependent indirect constraints come from ANTARES [269], IceCUBE [157] and SUPER-KAMIOKANDE [270], which are a few orders of magnitude weaker than the direct detection bound of XENON1T [95]. Of the indirect bounds, only the IceCUBE constraint

on the  $W^+W^-$  channel comes close to reaching the viable parameter space for the model with coannihilations, whereas the XENON1T bound cuts into the parameter space. The elastic cross section can take very small values, and even dip into the neutrino floor [129], where direct DM detection might be difficult.

#### 6.4.2 Inelastic cross section limits

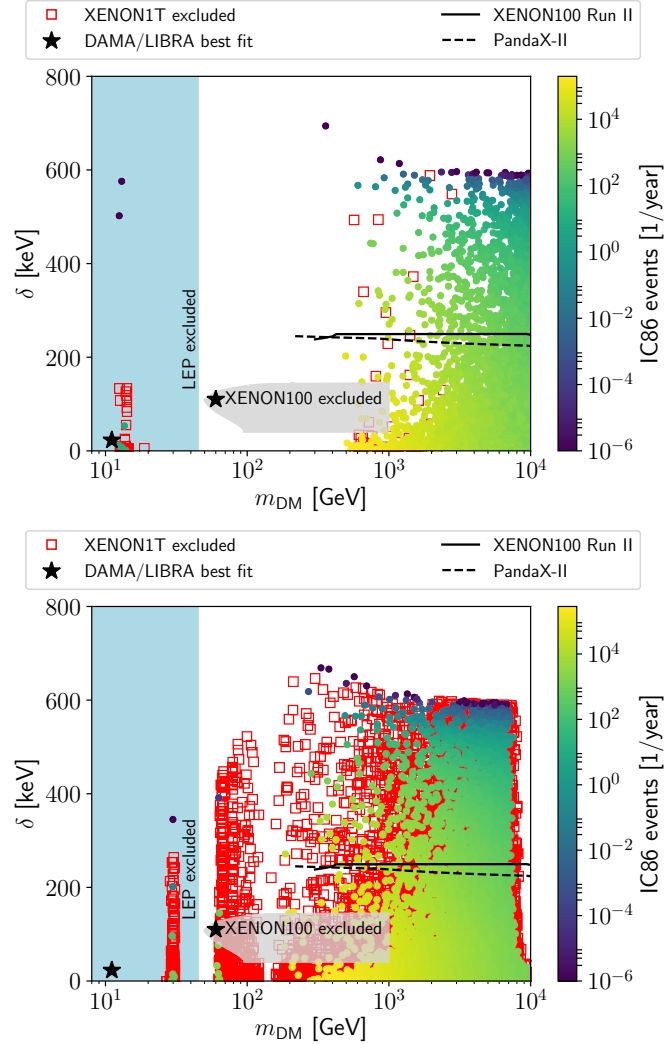


Figure 6.7: Scotogenic models in the plane DM mass vs. neutral scalar mass splitting, color coded for expected IC86 events (temperature scale) and elastic scattering exclusion by XENON1T (red boxes) [95]. Also shown are the exclusion of the low-(sodium) [271] and high-mass (iodine) DAMA/LIBRA preferred regions [93, 265] by LEP and XENON100 [262] and the upper limits on the mass splitting from the XENON100 Run II data [263] and by the PANDAX-II experiment with smaller recoil energy window and larger background [264]. In the lower plot, coannihilation processes are enhanced by the small scalar-fermion mass difference.

The DAMA/LIBRA experiment observed an annual modulation signal [93, 265], which has been interpreted as DM with a mass of around 10 and 50 GeV [272, 273]. Still there

remains tension with other direct detection experiments, which led to the hypothesis that DM undergoes inelastic scattering off nuclei in DAMA/LIBRA, to which other direct detection experiments are insensitive [241]. In fitting the DAMA/LIBRA observation, the inelastic scattering cross section that was generally assumed is  $10^{-4}$  pb [246, 247, 248], which is very close to the value of the inelastic WIMP-proton cross section  $1.7 \cdot 10^{-4}$  that we found from our analysis. The mediator is not a Higgs boson but a  $Z^0$  boson, as was shown in Figure 6.1. This scattering process violates isospin by a factor

$$b_n/b_p = 1/(4 \sin^2 \theta_W - 1) \simeq -6.6, \quad (6.39)$$

resulting in a WIMP-neutron cross section of  $1/(2\pi)G_F^2 m_N^2 = 74.3 \cdot 10^{-4}$  pb that is much larger [274, 275]. It is in line with the typical cross sections obtained in the inert doublet model, which is the only model with just a single scalar DM multiplet that can exhibit naturally small mass splittings in the neutral components at a renormalizable level.

Figure 6.7 shows the viable models, i.e. the points that survive the experimental constraints listed in Section 6.4, in a plane of the mass splitting versus the DM mass. The models that pass all further experimental constraints are color coded by means of a temperature gradient according to the IC86 event rate. As a teaser for the next section, we would like to point out the dependence of the event rate on  $\delta$  to the reader. If the model is ruled out by XENON1T [95] it is marked by a red box. Based on the DAMA/LIBRA observations [93, 265] other experiments have specifically looked for inelastic DM. From a XENON100 run with 100.9 live days with a fiducial volume of 48 kg of liquid xenon the grey shaded area in Figure 6.7 containing one of the preferred DAMA/LIBRA (iodine) regions was excluded [262]. The run II data with 224.6 live days with a fiducial volume of 34 kg liquid xenon was reanalyzed in the light of effective field theory descriptions of dark matter. For the inelastic process in the scotogenic model this amounts to the following correspondence

$$\sigma_N^0 = (C_1^N)^2 \frac{\mu_N^2}{\pi}, \quad (6.40)$$

where  $\mu_N$  is the DM-nucleon reduced mass, and  $C_1^N$  is the coefficient, which for our spin-independent process stems from the operator  $\mathcal{O}_1$  [263]. This analysis was done using isospin conservation. Since we just showed that the inelastic scattering process in the scotogenic model does not conserve isospin, we translate the limits on the coefficient  $C_1^N$  in Ref. [263] to the WIMP-proton cross section as [276]

$$\sigma_p^0 = \sigma_N^0 \left[ \frac{Z}{A} + \left( 1 - \frac{Z}{A} \right) \frac{b_n}{b_p} \right]^{-2}. \quad (6.41)$$

In principle one should sum over the different xenon isotopes weighted by their abundance, however we assumed for simplicity  $A = 132$  as it is the most abundant xenon isotope. This has little effect on the results. As a consequence, DM masses above 300 GeV with mass splittings smaller than 250 keV are excluded, indicated by the full black line in Figure 6.7. Further

limits come from PANDAX-II, with 79.6 live days with a 329 kg liquid xenon fiducial volume. Their results were only given for DM masses of 1 and 10 TeV, which has been interpolated and marked by the dotted black line. The limits are slightly weaker than XENON100 in spite of the much larger fiducial volume because of higher background and a smaller recoil energy region. The exclusion of inelastic scattering in direct detection experiments is limited by the maximum recoil energy, so further exclusion would need much larger cross sections than obtained here [277]. The other DAMA/LIBRA fit point around 10 GeV (sodium) is still possible, but would require a larger cross section of  $10^{-2}$  pb with different isospin violation  $b_n/b_p \simeq -0.7$  [278, 273]. Together with the higher (albeit already excluded) point, the results are closely investigated by the DM-ICE17 [266], COSINE-100 [267, 279], SABRE [280], and ANAIS-112 [268] experiments, with the expectation of a  $3\sigma$  C.L. test of the DAMA/LIBRA results by autumn 2022.

### 6.4.3 Expected event rates in IC86 from (in)elastic scattering in the Sun

After an extensive discussion about the scattering cross sections and the relevant constraints on these, we can now turn to the final goal of this paper: To study the possible event rate in ICECUBE. The expected number of events was shown on a temperature scale in Figure 6.7 as a function of the DM mass and  $\delta$ . The event rate as a function of the DM mass is shown in Figure 6.8. The event rates are spread over many orders of magnitude, from below  $10^{-6}$  events per year up to  $10^5$ . The careful reader might by now already have spotted that the points can be divided into two categories: those due to inelastic and elastic scattering, with the former yielding much more events than the latter. For each model there are two points in the plot, for both inelastic and elastic scattering. A blue line at the level of one event per year has been included to guide the eye. For the elastic case, the event rate stays below one event per year in all mass ranges. The event rate can be boosted if one includes coannihilations. In this case event rates are enhanced to above 10 per year. However, all model points that would yield such elastic event rates are generally excluded by direct detection experiments. This means that purely elastic scattering in this model cannot yield detectable event rates.

Figure 6.9 shows the event rate as a function of the mass splitting  $\delta$ . From the plot it is quite clear that the inelastic scattering process is very sensitive to the value of  $\delta$ , whereas the elastic process is unaffected, as expected. At least 10 events per year can be expected for mass splittings of  $\delta \leq (500 \pm 20)$  keV. On the lower end of the scale, points below 250 keV have already been excluded by XENON100 [263], as was shown in Figure 6.7, which still leaves plenty of room in the parameter space to be probed by ICECUBE. Since the mass splitting is directly related to the value of  $\lambda_5$ , applying Equation (6.2) would give a lower bound of

$$\lambda_5 \gtrsim 1.6 \cdot 10^{-5} \cdot m_{\text{DM}}/\text{TeV}. \quad (6.42)$$

if no neutrino signals due to DM annihilation in the Sun are observed. In Figures 6.8 and 6.9 we have color coded the point depending on whether they pass experimental constraints or not. We implemented the results from XENON1T [95] (red boxes), XENON100 [262,

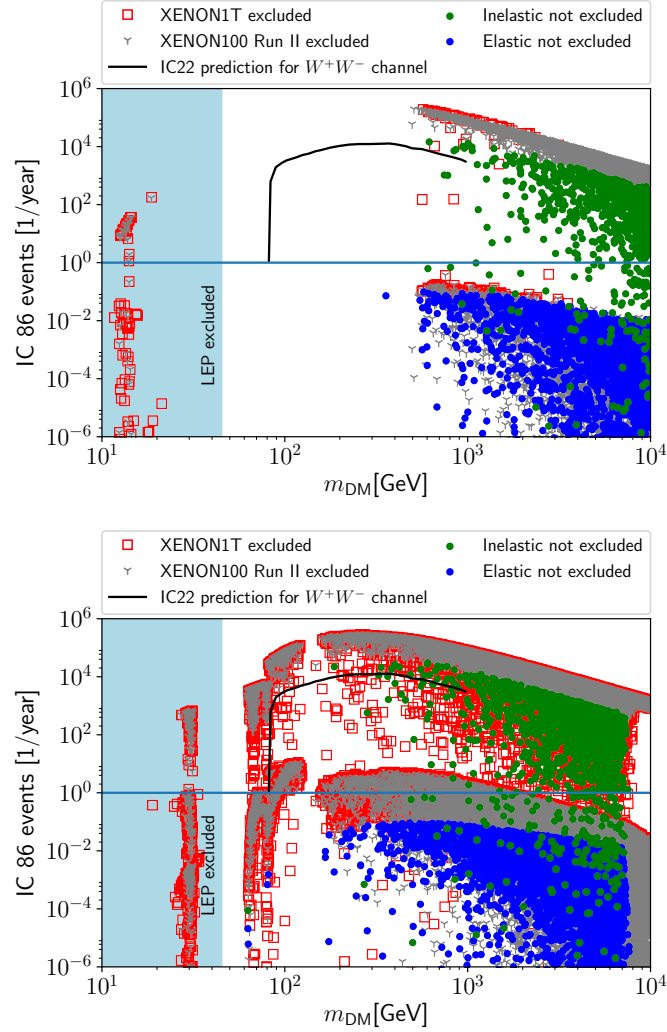


Figure 6.8: The expected number of events per year in the current ICECUBE configuration with 86 strings (IC86) as a function of the DM mass from inelastic and elastic DM scattering in the Sun. The black line marks the number of expected events in the  $W^+W^-$  channel for an IC22 study [248]. The blue line marks one event per year for orientation. Also shown are the points excluded by XENON1T [95], XENON100 [262, 263] and LEP from the invisible  $Z^0$  boson width [259, 260]. In the lower plot, coannihilation processes are enhanced by the small scalar-fermion mass difference.



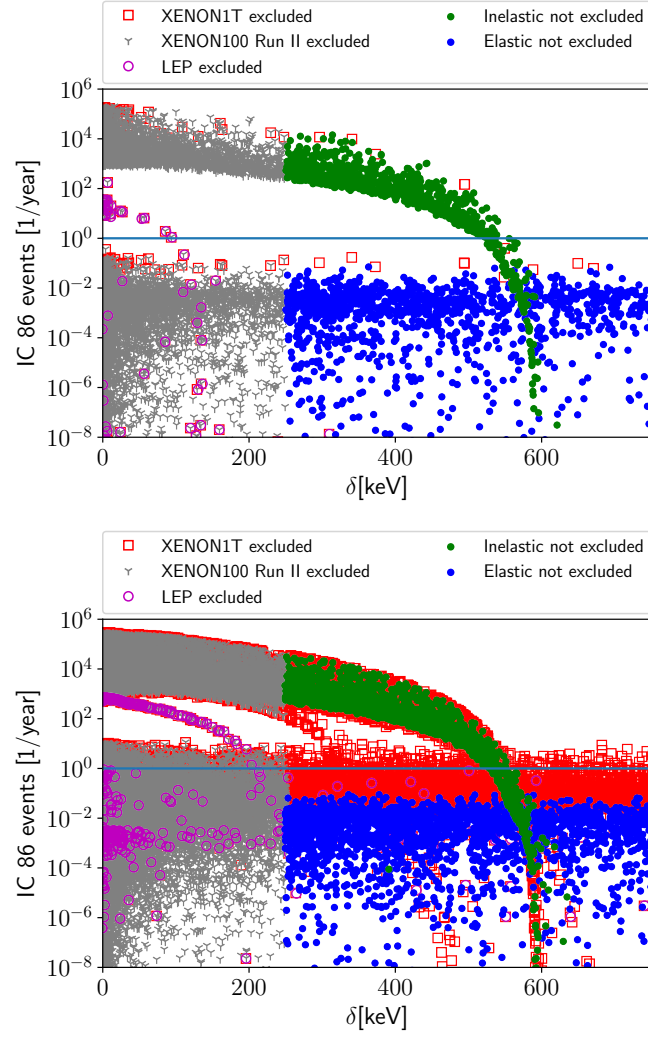


Figure 6.9: Same as Fig. 6.8 as a function of the neutral scalar coupling splitting  $\delta$ .

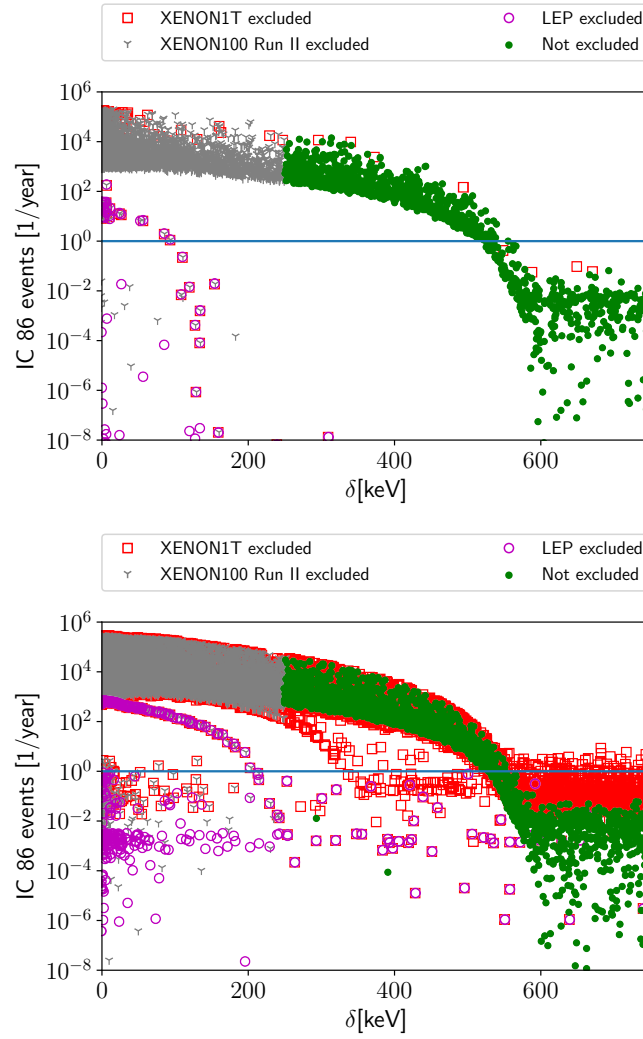


Figure 6.10: Same as Fig. 6.9, where the inelastic and elastic event rates have been summed.

263] (grey markers), as well as the invisible  $Z^0$  decay constraints from LEP [259, 260] (blue shaded area in Figure 6.8 and purple circles in Figure 6.9). Points that pass these constraints are marked green or blue for inelastic or elastic scattering respectively. We have also included the full black line in Figure 6.8, which is an estimate of the number of inelastic events for annihilation into  $W^+W^-$  pairs for the older IC22 configuration [248]. As could be seen from Figure 6.6, this is also the main dominant channel for  $m_{\text{DM}} > m_W$  in our setup. The trend for the expected events is similar, though the number of expected events is of course larger in our IC86 prediction.

Taking a closer look at Figure 6.9 we see the quick dropoff for larger values of  $\delta$ . This rapid decline can be related to the DM mass and the value of  $\lambda_5$  through Equation (6.2). In the previous Chapter, one can see in Figure 5.9 that the lower bound for  $\lambda_5$  is constrained by the neutrino mass scale. For small absolute neutrino mass there exist viable points for a value above  $|\lambda_5|$  a few times  $10^{-10}$ , whereas this lower bound increases by more than an order of magnitude at the KATRIN limit at 1.1 eV. For the coannihilation scenario, one

generally needs values of  $|\lambda_5| \geq 10^{-8}$  due to relic density constraints. As inelastic scattering for  $\delta < 250$  keV has already been excluded (see Figure 6.7), a lower bound on  $\lambda_5$  can be obtained through equation (6.2). For the lowest viable DM masses of 500 (200) GeV in the normal (coannihilation) scenario, a lower bound of  $\lambda_5 \gtrsim 4.1$  ( $1.7$ )  $\cdot 10^{-6}$  is obtained. For IC86, the event rate due to inelastic scattering remains detectable up until mass splittings of around 500 keV, which for the highest sampled masses at 10 TeV would mean a value of  $|\lambda_5| \sim 1.6 \cdot 10^{-4}$  could be probed. Dark matter can be captured by means of inelastic or elastic scattering, but the resulting neutrino signals that are produced upon DM annihilation cannot be distinguished by the IC86 detector. Figure 6.10 illustrates this by summing the inelastic and elastic event rates shown in Figure 6.9. From this it is clear that below the kinematic edge the inelastic scattering process dominates by many orders of magnitude over the elastic process, so that the former in practice is wholly responsible for DM capture in the Sun that is directly related to the IC86 event rate. The points that lie below the main bulk are those with a DM mass below the  $W$  mass, which have distinctly lower inelastic event rates due to the  $\bar{b}b$  channel now being dominant, as can be seen from Figures 6.6 and 6.8.

#### 6.4.4 Galactic Center constraints

Another region of interest for indirect detection with neutrino telescopes is the Galactic Center of our Milky Way, as it too features a higher density of DM. Signals from this region can therefore also be used to constrain the self annihilation rate of WIMPs. We compare predictions of the thermally averaged cross section  $\langle\sigma v\rangle$  with bounds from a combined analysis of ANTARES and ICECUBE [239], as well as results from SUPER-KAMIOKANDE [270], assuming a NFW DM halo distribution [131]. Figure 6.11 shows the thermally averaged cross section  $\langle\sigma v\rangle$  as a function of the DM mass for the normal (top) and coannihilation (bottom) scans. The color coding is the same as in Figures 6.6 and 6.8. The dotted line is the prediction for a generic thermal WIMP with a mass above 10 GeV [43]. For the normal scan this agrees relatively well, but for the coannihilation scan there are many points that lie far above this line. This can be attributed to the coannihilation processes increasing the relic density [256], requiring larger values for  $\langle\sigma v\rangle$  to obtain the correct relic density. As the local relic density in the Galactic Center depends on the NFW profile, and is not dependent on the WIMP-nucleon scattering cross section as in the Sun, the close relation to bounds from direct detection experiments loosens. In this case, the XENON1T [95] and XENON100 [262, 263] experiments exclude mainly points with lower  $\langle\sigma v\rangle$ , as well as those in the lower mass ranges. These low-mass points are furthermore excluded by the LEP constraints on the invisible decays of the  $Z^0$  boson [259, 260]. The SUPER-KAMIOKANDE limits on the  $\bar{b}b$  channel are weaker by multiple orders of magnitude. At higher masses, the bounds of the joint ANTARES and ICECUBE analysis on the  $W^+W^-$  channel are tighter than those of SUPER-KAMIOKANDE. The former bounds do come almost within an order of magnitude for the coannihilation scan. Further improvements to their analysis, as well as extending the

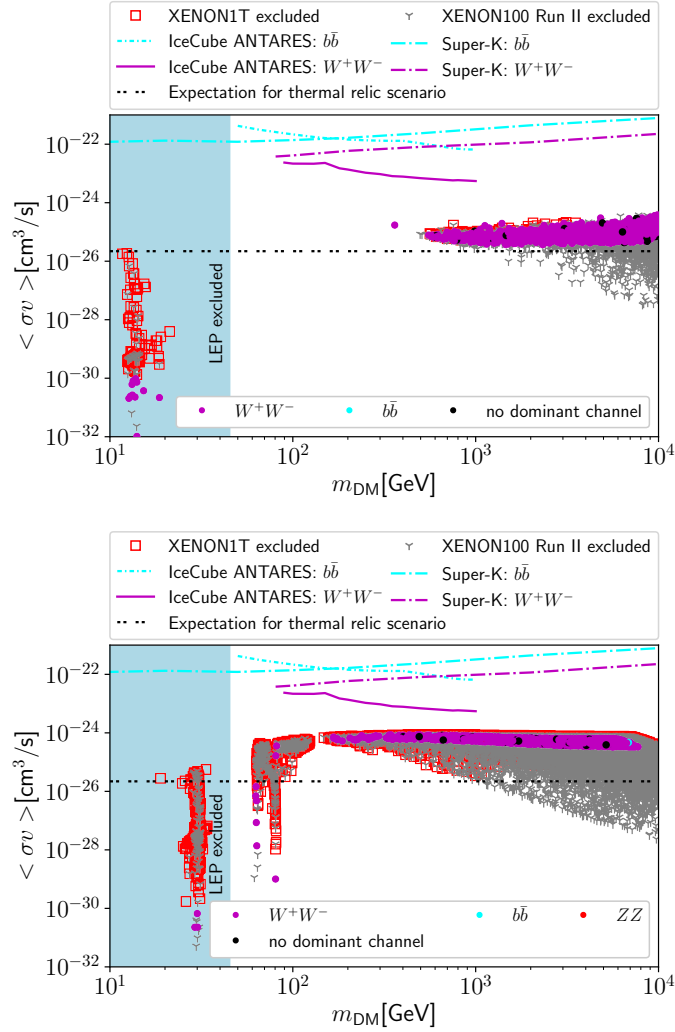


Figure 6.11: Thermally averaged cross section  $\langle\sigma v\rangle$  with combined ICECUBE ANTARES [239] and SUPER-KAMIOKANDE [151] exclusion limits as a function of the DM mass. All points are colored according to the main annihilation channel, provided there is one with a branching ratio of over 50%. Also shown are the points excluded by XENON1T [95], XENON100 [262, 263] and LEP from the invisible  $Z^0$  boson width [259, 260] as well as the expected cross section for a thermal relic [43]. In the lower plot, coannihilation processes are enhanced by the small scalar-fermion mass difference.

mass range of the bounds would likely be able to dip into the parameter space of our scan results.

## 6.5 Conclusion

In this chapter we have investigated the possibilities for indirect detection of scalar DM in the scotogenic model with the IC86 setup. We mainly focused on the scenario where DM is captured by scattering processes with nuclei inside the Sun. The resulting local overdensity boosts the DM annihilation rate. We introduced the relevant scattering processes that are involved in DM capture, which we could divide in an inelastic through Higgs exchange and an elastic process through  $Z$  exchange. For each of these processes we derived the scattering cross section and related this via the capture rate to the event rate in IC86. To this end we constructed a toolchain of different programmes, to which we implemented routines for inelastic scattering in DARKSUSY 6.2.3. We modified existing indirect detection routines inside MICROMEGAS 5.0.8 to account for the newer effective detector area of IC86.

With these tools in place we performed two parameter scan of the scotogenic model, one normal scan which was sampled completely random, and a second coannihilation scan in which we forced a small mass splitting between the scalar DM candidate and the fermion singlets. Under the influence of the coannihilation processes, the relic density is increased [256], and the mass range in which the DM candidate can satisfy the relic density constraint is lowered to 200 GeV down from 500 GeV in the normal scan. The results of the scan were subjected to further constraints from neutrino physics, LFV, collider bounds from LEP(2) and the LHC concerning the presence of charged scalars and hidden decays of the Higgs and  $Z$  boson, as well as bounds from direct and indirect detection experiments.

We found that the spin-independent cross section is on the one side constrained by direct detection experiments, ruling out larger cross sections, especially in the coannihilation scan. On the other hand there were many model points with cross sections below the neutrino floor, which would make these difficult to probe by direct detection experiments. For inelastic scattering direct detection experiments rule out the part of the parameter space with mass splittings of  $\delta < 250$  keV. However, a substantial amount of IC86 events are predicted even for much larger values, up to around 500 keV. In this region one could expect an event rate on the order of  $10^3$  per year, making a dedicated analysis in IC86 worthwhile. For larger mass splittings the event rate drops steeply. Since the scalar mass splitting is directly related to  $\lambda_5$ , constraints on  $\delta$  can be translated into bounds on  $\lambda_5$ . In the case where no neutrino events are observed, a lower bound of  $|\lambda_5| \gtrsim 1.6 \cdot 10^{-5} \cdot m_{\text{DM}}/\text{TeV}$  can be placed. We also found that the models with purely elastic scattering cannot yield enough predicted events to be detectable. In particular, direct detection constraints on the elastic cross section restrict the event rate for purely elastic scattering to 0.1 event per year.

Next to neutrino signals from annihilating DM inside the Sun, we also compared the results of our scan with constraints of DM annihilation in the Galactic Centre, assuming

a NFW DM halo profile. For this region we found that the points with lower thermally averaged cross sections  $\langle\sigma v\rangle$  were mostly excluded by direct detection experiments. Apart from the low-mass points that mainly annihilate into  $\bar{b}b$ , which were excluded by LEP and detection experiments, nearly all high-mass points have annihilation into  $W^+W^-$  pairs as the dominant channel. Whereas the bound from a joint ANTARES and ICECUBE analysis for this channel clearly lies above our scan results for the normal scan, the gap is much smaller for the coannihilation scenario, coming within one order of magnitude. Further improvement of this limit is particularly interesting, as it can bring the parameter space of our model within detection reach of IC86.

Furthermore, our findings can be extended to other dark matter models that feature a scalar sector with small mass splittings allowing for inelastic scattering. A candidate for further studies is the AMEND model, which contains a small singlet-triplet scalar mass splitting due to additional symmetries of the Lagrangian [75]. Even though inelastic scattering processes can lead to large event rates in IC86, not every model has a suitable particle content to allow this. Thus far we have only considered spin-independent processes, as there are no spin-dependent scattering processes in the scotogenic model. Hence a study of a model which features both spin-dependent as well as spin-independent scattering would also be an interesting scenario to study. As the elastic spin-independent cross section was tightly constrained by direct detection, and does therefore not lead to a detectable event rate, the addition of a spin dependent process might increase the event rate. This idea is studied further in the next chapter in the context of the model T1-3-B with  $\alpha = 0$  [281, 221].

## 7 Indirect detection constraints on the T1-3-B model from IceCube

### 7.1 Introduction

We have seen how the scotogenic model only exhibits spin-independent scattering processes, but does allow for inelastic scattering processes, which greatly increased the event rate. We now turn to the model T1-3-B with  $\alpha = 0$  [281, 221], which can either contain a scalar or a fermionic DM candidate. In contrast to the scotogenic model, it is now the fermionic sector that is our main interest, since those DM candidates are of singlet-doublet nature and can scatter via spin-dependent scattering.

In many ways this chapter will be a continuation of Chapter 6, and many topics that appear in the current chapter will already have been introduced there. We will give an overview of the model, and then discuss the WIMP-nucleon scattering processes that are present in this model. Contrary to the scotogenic model, there is no inelastic scattering, but instead there exists a spin-dependent process for the singlet-doublet fermion DM. The scalar triplet DM candidate only scatters through spin-independent scattering. We will present the results of a numerical scan of the parameter space, where we focus on the expected event rates from WIMP annihilations in the Sun in IC86. Furthermore we discuss the resulting SI and SD cross sections, as well as the thermally averaged cross section  $\langle\sigma v\rangle$  in the Galactic Center and compare these results to limits from the direct detection experiments XENON1T and PICO-60. We also consider limits from neutrino observations in the Sun and Galactic Center from ANTARES, ICECUBE and SUPER-KAMIOKANDE. This chapter is based on the work presented in Ref. [253]

### 7.2 Model description

The model considered in this chapter belongs to the T1-3 topology, which is shown in Figure 7.1. The specific particle content that is added to the SM for the model T1-3-B with  $\alpha = 0$  is listed in Table 7.1. In order to see which components of the new fields are electrically neutral and hence suitable as DM candidates, we write the fields componentwise as

$$\Psi = \Psi^0, \quad \psi = \begin{pmatrix} \psi^0 \\ \psi^- \end{pmatrix}, \quad \psi' = \begin{pmatrix} \psi'^+ \\ \psi'^0 \end{pmatrix}, \quad \phi_i = \begin{pmatrix} \frac{1}{\sqrt{2}}\phi_i^0 & \phi_i^+ \\ \phi_i^- & -\frac{1}{\sqrt{2}}\phi_i^0 \end{pmatrix}, \quad (7.1)$$

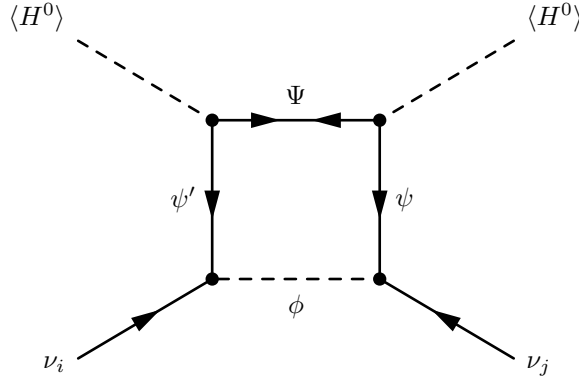


Figure 7.1: Topology of neutrino mass generation in the T1-3 class of radiative seesaw models [204, 281, 221].

Table 7.1: New fields in the model T1-3-B with  $\alpha = 0$ .

Field	Type	Generations	$SU(3)_C$	$SU(2)_L$	$U(1)_Y$	$\mathbb{Z}_2$
$\Psi$	Majorana spinor	1	1	1	0	-1
$\psi$	Weyl spinor	1	1	2	-1	-1
$\psi'$	Weyl spinor	1	1	2	1	-1
$\phi$	Real scalar	2	1	3	0	-1

where the subscript  $i$  for the scalar triplet denotes the generation. In this chapter we restrict ourselves to the case where there are only two scalar triplet generations ( $n_s = 2$ ), as it is the minimum requirement to generate two non-zero neutrino masses. In further studies one could consider the case  $n_s = 3$ , which generally results in three massive neutrinos. Looking at the above field components, one can see that both the scalar and the fermion sector contain neutral components. The Weyl spinors of the fermion doublets form a vector-like doublet containing the Dirac spinors:

$$\psi_D^0 = \begin{pmatrix} \psi^0 \\ i\sigma_2(\psi'^0)^* \end{pmatrix}, \quad \psi_D^- = \begin{pmatrix} \psi^- \\ i\sigma_2(\psi'^+)^* \end{pmatrix}. \quad (7.2)$$

We follow Refs. [281, 221] in their notation, meaning that the Lagrangian of the model can be written as

$$\begin{aligned} \mathcal{L} = & \mathcal{L}_{\text{SM}} + \mathcal{L}_{\text{kin}} - \frac{1}{2}(M_\phi^2)^{ij}\text{Tr}(\phi_i\phi_j) - \left(\frac{1}{2}M_\Psi\Psi\Psi + \text{H. c.}\right) - (M_{\psi\psi'}\psi\psi' + \text{H. c.}) \\ & - (\lambda_1)^{ij}(H^\dagger H)\text{Tr}(\phi_i\phi_j) - (\lambda_3)^{ijkm}\text{Tr}(\phi_i\phi_j\phi_k\phi_m) \\ & - \left(\lambda_4(H^\dagger\psi')\Psi + \text{H. c.}\right) - (\lambda_5(H\psi)\Psi + \text{H. c.}) - ((\lambda_6)^{ij}L_i\phi_j\psi' + \text{H. c.}). \end{aligned} \quad (7.3)$$

The dark sector couples to the Higgs boson through the interaction term  $\lambda_1$  for the scalar triplet, and through the  $\lambda_4$  and  $\lambda_5$  Yukawa couplings for the fermionic sector.  $\lambda_6$  couples the SM leptons  $L_\alpha$  to the dark sector, completing the neutrino loop shown in Figure 7.1. The



$\lambda_3$  term only induces self interactions for the scalar triplet, and is of little importance to the phenomenology of the model. Therefore  $\lambda_3$  is set to zero. Furthermore we choose  $M_\phi^2$  and  $\lambda_1$  to be diagonal, i.e. we neglect the mixing between the scalar generations as this does not change the phenomenology. Due to the coupling of the fermionic sector to the Higgs, the Higgs vev  $v$  contributes to the fermionic mass matrix. After EWSB the mass matrix of the neutral fermions is given by

$$M_f = \begin{pmatrix} M_\Psi & \frac{\lambda_5 v}{\sqrt{2}} & \frac{\lambda_4 v}{\sqrt{2}} \\ \frac{\lambda_5 v}{\sqrt{2}} & 0 & M_{\psi\psi'} \\ \frac{\lambda_4 v}{\sqrt{2}} & M_{\psi\psi'} & 0 \end{pmatrix}, \quad (7.4)$$

which is diagonalized by the unitary mixing matrix  $U_\chi$ . The resulting three Majorana mass eigenstates  $\chi_i$  with masses  $m_{\chi_i^0}$ , are

$$\begin{pmatrix} \chi_1^0 \\ \chi_2^0 \\ \chi_3^0 \end{pmatrix} = U_\chi \begin{pmatrix} \Psi^0 \\ \psi^0 \\ \psi'^0 \end{pmatrix}. \quad (7.5)$$

This shows that the fermion sector contains a mixed singlet-doublet DM candidate, induced by  $\lambda_4$  and  $\lambda_5$ . In the scalar sector the triplets also pick up a contribution from the Higgs vev, resulting in the mass eigenstates

$$M_{\phi^0}^2 = M_{\phi^\pm}^2 = M_\phi^2 + \lambda_1 v^2. \quad (7.6)$$

Diagonalizing the mass matrix by a matrix  $O_\eta$  yields the squared masses of the scalar components  $m_{\eta_i^{0,\pm}}^2$ . The mass eigenstates are denoted by

$$\begin{pmatrix} \eta_1^{0,\pm} \\ \eta_2^{0,\pm} \end{pmatrix} = O_\eta \begin{pmatrix} \phi_1^{0,\pm} \\ \phi_2^{0,\pm} \end{pmatrix}. \quad (7.7)$$

This is the most general treatment, but as was mentioned before, we do not consider mixing between the triplet generations. At tree level, all triplet components have the same masses, but loop corrections induce a mass splitting between the neutral and charged components. In particular, the charged component is 166 MeV heavier at one-loop level [282].

From the neutrino loop in Fig. 7.1 one can derive the analytical expression for the neutrino mass matrix

$$\begin{aligned} (M_\nu)_{ij} &= \frac{1}{32\pi^2} \sum_{l=1}^{n_s} \lambda_6^{im} \lambda_6^{jn} (O_\eta)_{ln} (O_\eta)_{lm} \sum_{k=1}^{n_f} (U_\chi)_{k3}^* \frac{m_{\chi_k^0}^3}{m_{\eta_l^0}^2 - m_{\chi_k^0}^2} \frac{m_{\chi_k^0}^2}{m_{\eta_l^0}^2} \\ &=: \frac{1}{32\pi^2} \sum_{l=1}^{n_s} \lambda_6^{im} \lambda_6^{jn} (O_\eta)_{ln} (O_\eta)_{lm} A_l, \end{aligned} \quad (7.8)$$

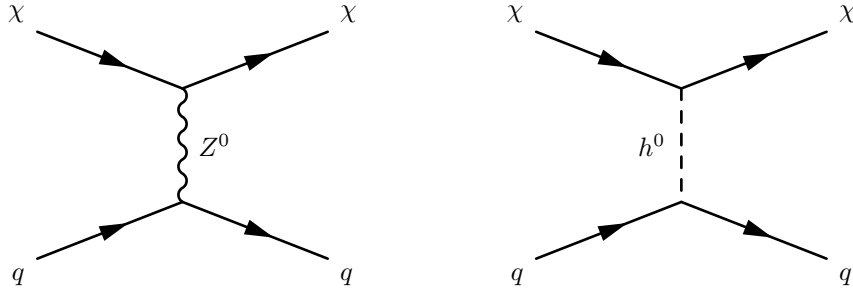


Figure 7.2: Feynman diagrams for DM scattering on quarks (nucleons) through  $Z^0$  (left) and Higgs boson exchange (right).

where  $n_s = 2$  as explained before, and  $n_f = 3$  the number of neutral fermions. For the above expression, we apply the Casas-Ibarra parameterisation [214], which returns the entries of  $\lambda_6$ :

$$\lambda_6^{im} = U_{\text{PMNS}}^{ij} \sqrt{m_{\nu_j}} R^{jl} \sqrt{A_l}^{-1} O_\eta^{lm}. \quad (7.9)$$

The mixing matrix for the scalar mass matrix are explicitly present, as well as the PMNS matrix  $U_{\text{PMNS}}$  [47]. The mixing matrix for the fermion masses also plays a role, but its entries have been absorbed in  $A_l$ .  $m_{\nu_j}$  are the eigenvalues of the neutrino mass matrix  $M_\nu$ . The matrix  $R$  was also present when discussing the Casas-Ibarra parameterisation in Chapter 5 for the case with three non-zero neutrino masses. In the current case of two non-zero neutrino masses,  $R$  is a  $3 \times 2$  matrix fulfilling the condition

$$RR^T = \begin{pmatrix} 0 & 0 & 0 \\ 0 & 1 & 0 \\ 0 & 0 & 1 \end{pmatrix}, \quad (7.10)$$

meaning that  $R$  can be parameterized as

$$R = \begin{pmatrix} 0 & 0 \\ \cos(\theta) & -\sin(\theta) \\ \sin(\theta) & \cos(\theta) \end{pmatrix} \quad (7.11)$$

by a single  $\theta$ , which is allowed to take any value between 0 and  $2\pi$ , unlike the previous case where 3 angles were needed.

### 7.3 Scattering processes

Having introduced the model, its particles, as well as the generation of neutrino masses, we now turn to the scattering processes of WIMPs inside the Sun. Both the spin dependent and the spin independent cross sections determine the scattering rate of WIMPs on nucleons, and thus the capture rate. Dark matter in this model is either fermionic or scalar in nature,

resulting in different scattering phenomenology. Contrary to the scotogenic model, the T1-3-B  $\alpha = 0$  model does allow for SD scattering processes, but there are no inelastic scattering processes. In the scalar triplet DM scenario, the only scattering process possible is the SI scattering through Higgs exchange. Scattering through  $Z$  boson exchange is not possible, as the triplet carries no hypercharge, making its neutral component a real scalar. The absence of a SD scattering contribution results in a lower cross section, which we will later show to have a clear effect on the event rate in ICECUBE.

In the singlet-doublet fermionic DM scenario there is exactly one tree level scattering diagram possible for SD scattering through a  $t$ -channel diagram with  $Z$  exchange, as well as a similar diagram but with a Higgs exchange for SI scattering [42]. The scattering diagrams are shown in Figure 7.2. An  $s$ -channel diagram is not possible, since none of the particles in the dark sector couple to quarks.

In this particular model the SI and SD cross sections are correlated for fermionic DM, due to their common dependence on the mixing between the fermion singlet and doublet that is induced by  $\lambda_4$  and  $\lambda_5$ . In the case of scalar DM, there is no SD scattering, and the SI scattering via the Higgs solely depends on  $\lambda_1$ . As can be seen in Fig. 7.2, the scattering cross sections depend on the coupling between the mediator (either the Higgs or the  $Z$ -boson) with quarks and WIMPs. For a neutral fermion  $\chi_g$  of generation  $g$ , the vertex rules as calculated by SARAH are given by [223]:

$$\begin{aligned}
 \begin{array}{c} \chi_g \\ \diagdown \\ \text{---} h_0 \text{---} \\ \diagup \\ \chi_{g'} \end{array} &= -\frac{1}{\sqrt{2}} i \left\{ (U_\chi)_{g1}^* [\lambda_4 (U_\chi)_{g'3}^* + \lambda_5 (U_\chi)_{g'2}^*] + \lambda_4 (U_\chi)_{g3}^* (U_\chi)_{g'1}^* + \lambda_5 (U_\chi)_{g2}^* (U_\chi)_{g'1}^* \right\} P_L \\
 &\quad - \frac{1}{\sqrt{2}} i \left\{ (U_\chi)_{g1} [\lambda_4 (U_\chi)_{g'3} + \lambda_5 (U_\chi)_{g'2}] + \lambda_4 (U_\chi)_{g3} (U_\chi)_{g'1} + \lambda_5 (U_\chi)_{g2} (U_\chi)_{g'1} \right\} P_R,
 \end{aligned} \tag{7.12}$$

$$\begin{aligned}
 \begin{array}{c} \chi_g \\ \diagdown \\ \text{---} Z_0^\mu \text{---} \\ \diagup \\ \chi_{g'} \end{array} &= -\frac{1}{2} i [g_1 \sin(\theta_W) + g_2 \cos(\theta_W)] [(U_\chi)_{g2} (U_\chi)_{g'2}^* - (U_\chi)_{g3} (U_\chi)_{g'3}^*] \gamma^\mu P_L \\
 &\quad + \frac{1}{2} i [g_1 \sin(\theta_W) + g_2 \cos(\theta_W)] [(U_\chi)_{g'2} (U_\chi)_{g2}^* - (U_\chi)_{g'3} (U_\chi)_{g3}^*] \gamma^\mu P_R.
 \end{aligned} \tag{7.13}$$

Because the neutral fermions are generally not close in mass, the only relevant case is the elastic process with  $g = g'$ . Both vertices depend on  $\lambda_4$  and  $\lambda_5$  in different levels of explicitness. Only the coupling with the Higgs contains explicit entries of  $\lambda_4$  and  $\lambda_5$ , but these parameters contribute implicitly through the mixing matrix  $U_\chi$  because of the off-diagonal entries in the fermion mass matrix in Equation (7.4). Analytically diagonalizing the fermion

mass matrix is non-trivial and yields quite unwieldy expressions. Hence we choose to use perturbation theory and expand the fermion mass matrix for small  $\lambda_4$

$$M_f = M_0 + \lambda_4 M_\lambda = \begin{pmatrix} M_\Psi & 0 & 0 \\ 0 & 0 & M_{\psi\psi'} \\ 0 & M_{\psi\psi'} & 0 \end{pmatrix} + \lambda_4 \begin{pmatrix} 0 & \frac{\tilde{\lambda}v}{\sqrt{2}} & \frac{v}{\sqrt{2}} \\ \frac{\tilde{\lambda}v}{\sqrt{2}} & 0 & 0 \\ \frac{v}{\sqrt{2}} & 0 & 0 \end{pmatrix}, \quad (7.14)$$

with the ratio  $\tilde{\lambda} = \lambda_5/\lambda_4$  fixed. We then approximately diagonalise the above matrix, resulting in

$$\begin{pmatrix} M_\Psi + \frac{v^2(\lambda_5^2 M_\Psi + 2\lambda_4 \lambda_5 M_{\psi\psi'} + \lambda_4^2 M_\Psi)}{2(M_\Psi - M_{\psi\psi'})(M_\Psi + M_{\psi\psi'})} & 0 & 0 \\ 0 & -M_{\psi\psi'} - \frac{(\lambda_4 - \lambda_5)^2 v^2}{2(M_\Psi + M_{\psi\psi'})} & 0 \\ 0 & 0 & M_{\psi\psi'} - \frac{(\lambda_4 + \lambda_5)^2 v^2}{2(M_\Psi - M_{\psi\psi'})} \end{pmatrix}, \quad (7.15)$$

up to second order in  $\lambda_4$ . The associated mixing matrix can be written as

$$U_\chi = \begin{pmatrix} 1 & 0 & 0 \\ 0 & -\frac{1}{\sqrt{2}} & \frac{1}{\sqrt{2}} \\ 0 & \frac{1}{\sqrt{2}} & \frac{1}{\sqrt{2}} \end{pmatrix} + \begin{pmatrix} v^2 \frac{(\lambda_5^2 + \lambda_4^2)(M_\Psi^2 + M_{\psi\psi'}^2) + 4\lambda_4 \lambda_5 M_\Psi M_{\psi\psi'}}{4(M_\Psi - M_{\psi\psi'})^2 (M_\Psi + M_{\psi\psi'})^2} & -\frac{(\lambda_4 - \lambda_5)v}{2(M_\Psi + M_{\psi\psi'})} & -\frac{(\lambda_4 + \lambda_5)v}{2(M_\Psi - M_{\psi\psi'})} \\ \frac{(\lambda_4 M_{\psi\psi'} + \lambda_5 M_\Psi)v}{\sqrt{2}(M_\Psi - M_{\psi\psi'})(M_\Psi + M_{\psi\psi'})} & v^2 \frac{(\lambda_4^2 - \lambda_5^2)M_\Psi + 2\lambda_4 M_{\psi\psi'}(\lambda_4 - \lambda_5)}{8\sqrt{2}M_{\psi\psi'}(M_\Psi + M_{\psi\psi'})^2} & v^2 \frac{(\lambda_4^2 - \lambda_5^2)M_\Psi - 2\lambda_4 M_{\psi\psi'}(\lambda_4 + \lambda_5)}{8\sqrt{2}M_{\psi\psi'}(-M_\Psi + M_{\psi\psi'})^2} \\ \frac{(\lambda_4 M_\Psi + \lambda_5 M_{\psi\psi'})v}{\sqrt{2}(M_\Psi - M_{\psi\psi'})(M_\Psi + M_{\psi\psi'})} & v^2 \frac{(\lambda_4^2 - \lambda_5^2)M_\Psi + 2\lambda_5 M_{\psi\psi'}(\lambda_4 - \lambda_5)}{8\sqrt{2}M_{\psi\psi'}(M_\Psi + M_{\psi\psi'})^2} & v^2 \frac{(\lambda_5^2 - \lambda_4^2)M_\Psi - 2\lambda_5 M_{\psi\psi'}(\lambda_5 + \lambda_4)}{8\sqrt{2}M_{\psi\psi'}(-M_\Psi + M_{\psi\psi'})^2} \end{pmatrix}. \quad (7.16)$$

There are two cases to be distinguished:  $M_\Psi < M_{\psi\psi'}$  (assuming  $\lambda_{4,5}^2 v^2 < M_{\psi\psi'}^2 - M_\Psi^2$ )<sup>1</sup>, for which  $\chi_1$  is the lightest eigenstate, and  $M_\Psi > M_{\psi\psi'}$  in which  $\chi_3$  takes this role. Since the quantity  $(\lambda_4 - \lambda_5)^2$  is always positive,  $\chi_2$  is never the lightest fermion.

We now return to the expressions for the DM-mediator vertices from Equations (7.12) and (7.13), in which the approximated entries for the mixing matrix  $U_\chi$  can be substituted, which depend on the parameters  $\lambda_4$  and  $\lambda_5$ , but also on the mass terms  $M_\Psi$  and  $M_{\psi\psi'}$ . Including only the terms which are at most second order in  $\lambda_4$  and  $\lambda_5$  or a combination thereof, results in the following couplings:

<sup>1</sup>Otherwise a more careful analysis is required. E.g. if  $\lambda_4 \lambda_5 > 0$  or  $\lambda_{4,5} < \lambda_{5,4} \frac{M_\Psi}{M_{\psi\psi'}}$ , the statement above is also true.

$$\chi_1\chi_1 h^0 : -\frac{iv(M_\Psi\lambda_5^2 + 2M_{\psi\psi'}\lambda_5\lambda_4 + M_\Psi\lambda_4^2)}{M_\Psi^2 - M_{\psi\psi'}^2} + \mathcal{O}(\lambda_{4,5}^3), \quad (7.17)$$

$$\chi_2\chi_2 h^0 : \frac{iv(\lambda_4 - \lambda_5)^2}{2(M_\Psi + M_{\psi\psi'})} + \mathcal{O}(\lambda_{4,5}^3), \quad (7.18)$$

$$\chi_3\chi_3 h^0 : \frac{iv(\lambda_4 + \lambda_5)^2}{2(M_\Psi - M_{\psi\psi'})} + \mathcal{O}(\lambda_{4,5}^3), \quad (7.19)$$

$$\chi_1\chi_1 Z_0^\mu : \frac{g_2}{\cos(\theta_W)} \frac{iv^2}{4(M_\Psi^2 - M_{\psi\psi'}^2)} (\lambda_4^2 - \lambda_5^2) \gamma^5 \gamma^\mu + \mathcal{O}(\lambda_{4,5}^3), \quad (7.20)$$

$$\chi_2\chi_2 Z_0^\mu : \frac{g_2}{\cos(\theta_W)} \frac{-iv^2}{8M_{\psi\psi'}(M_\Psi + M_{\psi\psi'})} (\lambda_4^2 - \lambda_5^2) \gamma^5 \gamma^\mu + \mathcal{O}(\lambda_{4,5}^3), \quad (7.21)$$

$$\chi_3\chi_3 Z_0^\mu : \frac{g_2}{\cos(\theta_W)} \frac{iv^2}{8M_{\psi\psi'}(M_\Psi - M_{\psi\psi'})} (\lambda_4^2 - \lambda_5^2) \gamma^5 \gamma^\mu + \mathcal{O}(\lambda_{4,5}^3). \quad (7.22)$$

The vertices for  $\chi_2$  have been included for completeness, despite the fact that it is never the lightest fermion. All cross sections depend on  $\lambda_4$  and  $\lambda_5$  directly, however the way in which they do differs. Independent of the DM candidate, the coupling to the  $Z$  boson vanishes in the case  $|\lambda_4| = |\lambda_5|$ , resulting in a zero spin dependent cross section. For the spin independent case, the situation depends on the DM candidate involved. If  $\chi_3$  is the lightest fermion, it is trivial to see that the vertex disappears for  $\lambda_4 = -\lambda_5$ . For  $\chi_1$  this is the case if the following relation is satisfied:

$$\lambda_4 = \lambda_5 \left( \pm \sqrt{\left( \frac{M_{\psi\psi'}}{M_\Psi} \right)} - 1 - \frac{M_{\psi\psi'}}{M_\Psi} \right). \quad (7.23)$$

Because the cross sections ultimately depend on the squared DM-mediator couplings, we can compare our results with the output of SPHENO 4.0.3 [225, 226] and micrOMEGAs 5.0.8 [227] to see if this approach is valid.

The comparison between the two methods is shown in Figure 7.3 for the  $\chi_1$  (left) as well as the  $\chi_3$  case (right). Especially for the latter case, the results are in agreement. For  $\chi_1$  DM, the results do agree up to a certain extent, but there is a deviation that increases for larger values of  $|\lambda_4|$ . This can be expected from the perturbative calculation under the assumption  $\lambda_{4,5} \ll 1$ . Moreover, one can see that the dips in the cross sections for some values of  $\lambda_4$  correspond well to the values for which the vertices of Eqs. (7.17)-(7.22) vanish. Based on this we can conclude that due to their common dependence on the Yukawa couplings  $\lambda_4$  and  $\lambda_5$ , the spin dependent and spin independent cross sections are correlated. As an illustration, Figure 7.4 shows as a preview the  $\sigma_p(\text{SD})$  versus  $\sigma_p(\text{SI})$  results from the numerical scan, which clearly illustrates the correlation. The correlation is only lifted for fine-tuned scenarios that are not exemplary for the general parameter space.

This relation explains how the limits on the spin independent cross section set by XENON1T also indirectly restrict the spin dependent cross section.

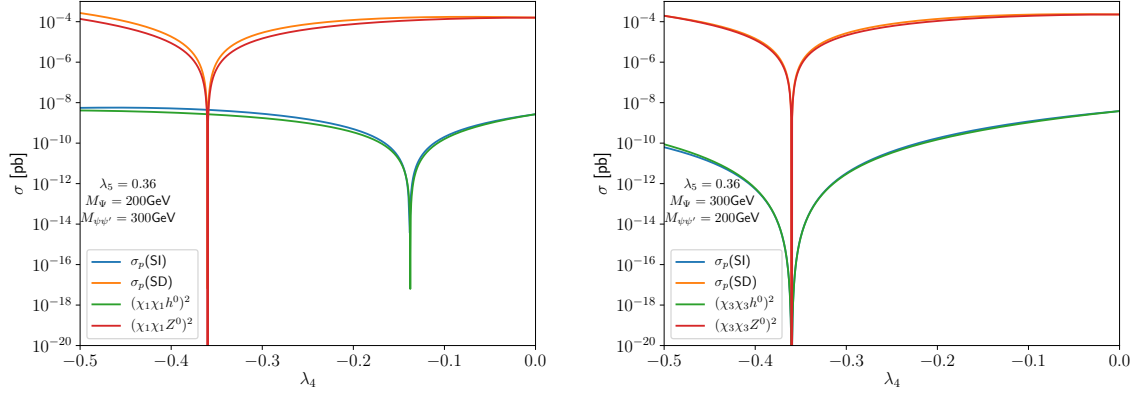


Figure 7.3: Spin dependent (orange) and independent (blue) cross sections calculated numerically and the vertex factors squared (red and blue) for both  $\chi_1$  (left) and  $\chi_3$  (right) as DM. The vertex factors have been rescaled so they agree with the cross sections at  $\lambda_4 = 0$ . The scalar singlet has been decoupled by setting  $m_\phi = 10$  TeV and  $\lambda_1$  has been set to zero (cf. Ref. [221], Fig. 7.1).

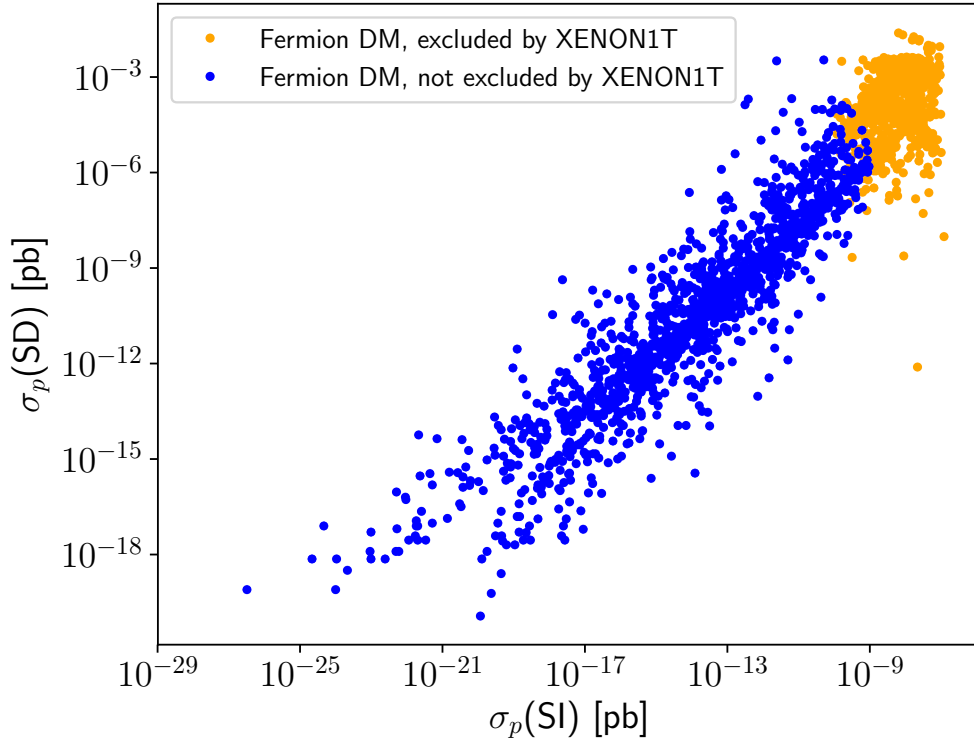


Figure 7.4: Dependence of the spin dependent cross section on the spin independent cross section.

Table 7.2: Parameters used for our benchmark point (masses in GeV). The matrix elements not mentioned (e.g.  $\lambda_1^{12}$ ) are set to zero.

$M_\Psi$	$M_{\psi\psi'}$	$(M_\phi^2)_{11}$	$(M_\phi^2)_{22}$	$\lambda_4$	$\lambda_5$	$\lambda_1^{11}$	$\lambda_1^{22}$
362	614	$2.4 \cdot 10^6$	$4.3 \cdot 10^7$	-0.17	-0.65	0.011	0.012

$\lambda_6^{11}$	$\lambda_6^{12}$	$\lambda_6^{21}$	$\lambda_6^{22}$	$\lambda_6^{31}$	$\lambda_6^{32}$
$-1.74 \cdot 10^{-5}$	$-5.28 \cdot 10^{-5}$	$0.90 \cdot 10^{-5}$	$-18.67 \cdot 10^{-5}$	$5.36 \cdot 10^{-5}$	$11.91 \cdot 10^{-5}$

## 7.4 Neutrino detection at IceCube

Having discussed the scattering processes, the next step is to determine the event rates in ICECUBE. The most important concepts concerning the neutrino flux, effective area and numerical routines have already been introduced in Chapter 6, and these have not changed for this chapter. Instead, we will present a benchmark point and highlight its most important features. In Tab. 7.2 we show the parameters for a typical point in the parameter space, which has an expected event rate in ICECUBE of 16 events per year. The DM candidate in this benchmark point is fermionic.

Figure 7.5 (left) shows the differential (anti-)neutrino fluxes from the Sun. The difference in spectral shape is due to absorption, oscillation, and regeneration effects in the Sun [255]. The corresponding event rate per energy is shown on the right. Similar to the benchmark point that was shown in Figure 6.4 for the scotogenic model, the high flux at low neutrino energies results in few events at ICECUBE due to the small effective area at these energies. Also in this case there is no increase in flux at  $E_\nu = m_{\text{DM}}$ , meaning there is little contribution from direct annihilation of fermion DM into neutrinos. These processes are generally suppressed by the Yukawa couplings  $\lambda_6$  that are small due to the neutrino masses and LFV constraints [281]. We do however see a continuous spectrum. The SI cross section of the benchmark point is  $\sigma_p(\text{SI}) = 1.75 \cdot 10^{-8}$  pb, meaning that it lies above the XENON1T limits. However, this statement does not generalize.

## 7.5 Numerical results

Unlike the scotogenic model, we do not have inelastic scattering processes in this model. Therefore we do not use the complete toolchain with all the routines as was shown in Figure 6.2, but instead the shorter toolchain of Figure 5.2 suffices. We of course do use the modified MICROMEGAS routines that were updated to include the IC86 effective detector area.

In our scan we choose the following ranges for the parameters. The mass parameters  $M_{\Psi, \psi\psi', \phi}$  are scanned between 100 GeV and 10 TeV, with the non-diagonal entries of  $M_\phi$  set to zero. The couplings  $|\lambda_{1,4,5}|$  are varied between  $1 \cdot 10^{-3}$  and 10, where  $\lambda_1$  taken to be diagonal so that there is no mixing between the scalar triplet generations as was mentioned before. We allow the sign for these parameters to be positive or negative. We need not

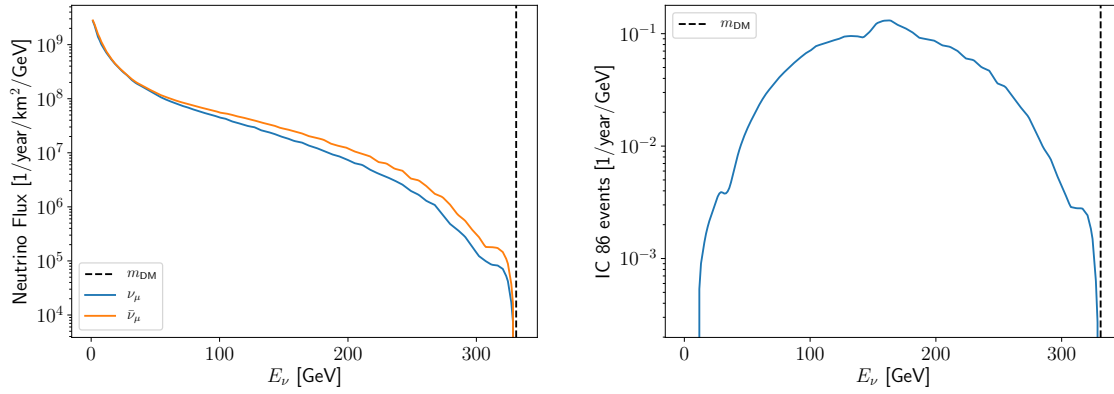


Figure 7.5: (Anti-)neutrino flux from the Sun (left) and expected event rate at ICECUBE (right) for the benchmark point given in Tab. 7.2. The dashed lines indicate the value of the DM mass.

sample values for  $\lambda_6$ , as these are determined through the Casas-Ibarra parameterisation of Equation (7.9). As input values for the Casas-Ibarra parameterisation we vary the neutrino mass difference and the PMNS mixing angles in the  $3\sigma$  range [213], assuming normal ordering. The matrix  $R$  in (7.9) contains an angle  $\theta$  which we allow to vary over its full range from 0 up to  $2\pi$ . The relic density of  $\Omega h^2 = 0.12$  [23] is allowed to vary by  $\pm 0.02$ . Furthermore we impose LFV constraints for the most stringent processes. For this model these are the current limits on  $\text{BR}(\mu \rightarrow e\gamma) < 4.2 \cdot 10^{-13}$  [215] and  $\text{BR}(\mu \rightarrow 3e) < 1.0 \cdot 10^{-12}$  [217].

### 7.5.1 Relic density

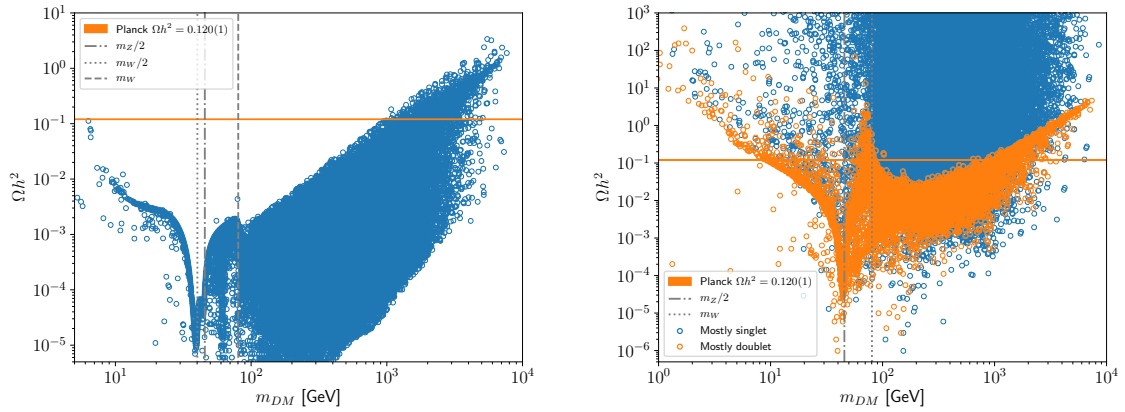


Figure 7.6: Relic density of scalar (left) and fermionic (right) dark matter in the T1-3-B model with  $\alpha = 0$ . As an indication, the observed relic density by PLANCK [23] has been included, as well as lines at  $m_Z/2$  and  $m_h/2$ .

For each of the dark matter candidates, one can look in which region of the parameter space the correct relic density is obtained, before considering further constraints. Figure 7.6 shows the relic density as a function of the dark matter mass for scalar (left) and fermionic



(right) dark matter. In the case of scalar dark matter, the relic density at low masses shows features from annihilation processes through electroweak gauge bosons. Possible processes are in this case caused by coannihilations of the form  $\phi^0\phi^+ \rightarrow W^+ \rightarrow \text{SM SM}$  and a resonance around  $m_W/2$  appears. These coannihilations become dominant, since processes of the form  $\phi^0\phi^0 \rightarrow Z \rightarrow \text{SM SM}$  are not possible for a real scalar triplet, unlike the case of the scalar doublet of the scotogenic model in Figure 6.5. This coannihilation is inherent to this model, since the charged triplet component is 166 MeV heavier. At the  $W$  mass direct annihilation into  $W^\pm$  pairs becomes possible. Without any further constraints, the viable mass range is around 1 to 3 TeV. For lower masses, the relic density is generally too low.

The case of fermion dark matter is slightly more complex. Fermionic dark matter consists of a singlet and a doublet component that can mix. For pedagogical purposes, the plot in Figure 7.6 distinguishes between these two types. For mostly singlet dark matter, the case is relatively easy, as there are no couplings to the SM gauge bosons, except for a slight contribution from the mixing with the doublet. This can result in a small annihilation cross section, and hence a (much too) large relic density. In a mass range from several tens of GeV up to around 2 TeV it is possible to obtain a correct relic density for mostly singlet dark matter. For mostly doublet dark matter there exist couplings to the electroweak gauge bosons and the Higgs boson, as can be seen at the resonance around  $m_Z/2$ . The relic density increases from there until reaching a maximum just before the  $W$  mass. Thus a correct amount of mostly doublet dark matter can be generated around 10 GeV, in the mass region of the electroweak gauge bosons, and in a region just above 1 TeV. Please note that this discussion of mostly singlet and mostly doublet is not completely black and white, as there must always exist some amount of singlet-doublet mixing to have couplings to the  $Z$  and Higgs bosons, following section 7.3.

### 7.5.2 Spin independent scattering

The results for spin independent scattering of the numerical scan, taking into account all experimental constraints, are shown in Figure 7.7, where the spin independent cross section is plotted versus the dark matter mass. Accounting for the slightly different parameter ranges, the results agree with Figures 7 and 10 of [281]. The figure contains both scalar and fermionic DM candidates, which can be distinguished based on their mass. Scalar DM corresponds to the cluster of points around 2 TeV, whereas the points with masses from just over 1 TeV and below are fermionic in nature. The color coding of the points shows the dominant annihilation branching ratio. For this purpose we defined that a branching ratio is dominant if it reaches at least 50 %. In case no single branching ratio reaches this threshold a point is marked as having no dominant channel.

Scalar dark matter forms a cluster of points around  $\sim 2$  TeV. The dominant channel is annihilation into  $W^+W^-$  pairs through a direct 4-point vertex. In the case of fermion dark matter, the main annihilation channel depends strongly on the mass. At masses up until the  $W$  mass the main annihilation channel is into  $b\bar{b}$  states through an  $s$ -channel Higgs boson.

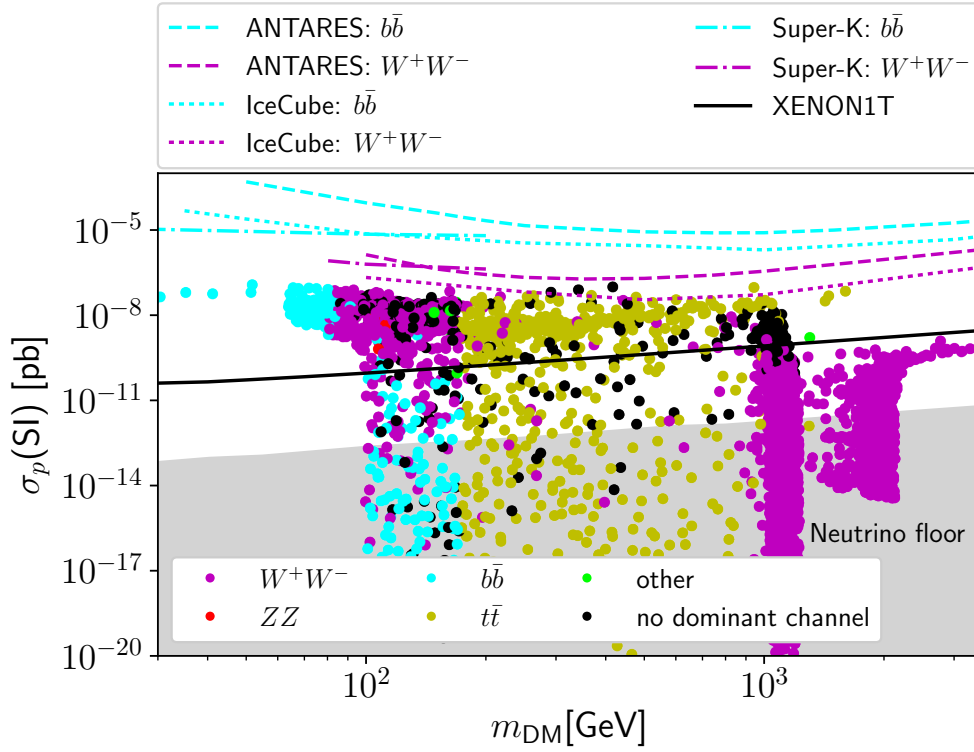


Figure 7.7: The spin independent (SI) cross section in pb with ANTARES [269], ICECUBE [157], SUPER-KAMIOKANDE [270] and XENON1T [95] exclusion limits as a function of the DM mass for both fermion (below about 1 TeV) and scalar DM (above). All points and lines are color coded according to the main annihilation channel, provided there is one with a branching ratio of over 50%. Also shown is the neutrino floor [129].

Above the  $W$  mass, but below the top mass  $W^+W^-$  is the dominant channel. Above the top mass the  $t\bar{t}$  channel becomes kinematically allowed and quickly becomes the main channel. Like the  $b\bar{b}$  channel,  $t\bar{t}$  production also takes place through  $s$ -channel Higgs exchange, with the former process becoming irrelevant due to the large Higgs-top Yukawa coupling. At masses slightly above 1 TeV there exists a small transition region without any dominant process, but for the rest  $W$  production becomes the main channel again. These results can be explained by the singlet-doublet nature of the fermionic DM candidates. The points with masses around 1 TeV are those which are mainly  $SU(2)$  doublet in nature, meaning their coupling to the electroweak gauge bosons is relatively stronger. The opposite holds for the points at masses below 1 TeV, which have a large singlet component (except around the  $W$  and  $Z$  masses). Thus their coupling to the gauge bosons completely has to come from the singlet-doublet mixing, and the coupling to top quarks through the Higgs is more prominent.

The charged components of the vector-like doublet are usually close in mass to the neutral components, which means that one must be careful and consider bounds on charged fermions as established by the LEP experiments [228]. Because fermionic DM is mostly singlet at low masses, the mass of the charged component of the doublet lies above the LEP limit of

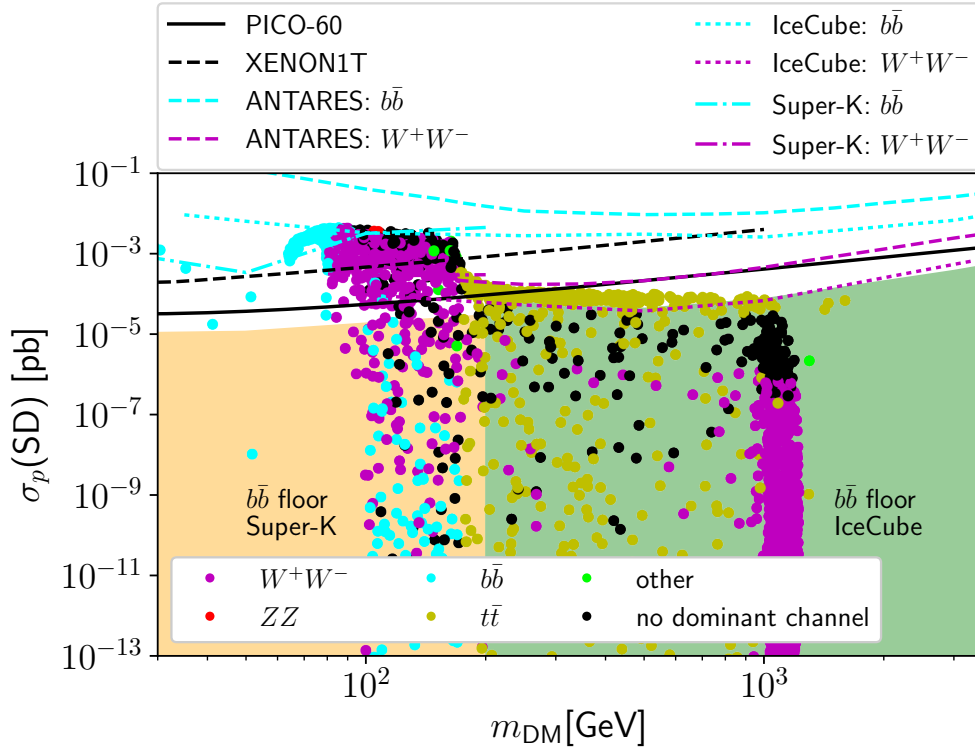


Figure 7.8: The spin dependent (SD) cross section in pb with PICO-60 [99], XENON1T [128], ANTARES [269], ICECUBE [157] and SUPER-KAMIOKANDE [270] exclusion limits as a function of the DM mass for singlet-doublet fermion DM. All points and lines are color coded according to the main annihilation channel, provided there is one with a branching ratio of over 50%. Also shown is the neutrino floor for  $b\bar{b}$  final states [283].

102 GeV. An exception to this is the region around the electroweak gauge boson mass, as shown in 7.6 (right). We sample the mass parameters from 100 GeV up to 10 TeV, and whereas the neutral doublet components mix under the influence of  $\lambda_4$  and  $\lambda_5$ , resulting in dark matter masses below 100 GeV, the charged component has no such mixing and thus stays close in mass to  $M_{\psi\psi'}$ . In this way the LEP limit is satisfied. Previous limits on the spin independent cross section set by the ANTARES [269], ICECUBE [157] and SUPER-KAMIOKANDE [270] collaborations from DM annihilations in the Sun are a few orders of magnitude weaker compared to the bound from direct detection as established by the XENON1T experiment [95]. The ICECUBE  $W^+W^-$  bound is the most stringent one, almost cutting into the region with sampled points, with the  $b\bar{b}$  bounds being several orders of magnitude weaker. The grey shaded region represents the neutrino “floor” stemming from the atmospheric and diffuse supernova neutrino background, making DM direct detection difficult [129].

### 7.5.3 Spin dependent scattering

Next to a spin independent scattering process, there exists a spin dependent scattering process for fermionic DM, but not for scalar DM. Figure 7.8 shows the spin dependent cross section and the main annihilation channel, with the same color coding as Figure 7.7. Again the  $W^+W^-$  channel imposes the strongest constraints, with the bounds from ANTARES [269] and ICECUBE [157] being more stringent than the XENON1T [128] bound. The full PICO-60 data set [99] has a sensitivity comparable with the indirect detection experiments. Following Ref. [284], ICECUBE and PICO-60 have removed the Standard Halo Model assumption and released velocity independent limits, which have the disadvantage of being weaker [285]. The yellow and green shaded area in the plot is the neutrino floor for  $b\bar{b}$  states, which is due to high-energy neutrinos produced in cosmic ray interactions in the solar atmosphere. This makes indirect detection difficult [283], especially in the low mass region, where only a small band between the PICO-60 bound and the  $b\bar{b}$  channel neutrino floor as established by SUPER-KAMIOKANDE.

### 7.5.4 Limits from the Galactic Center

Figure 7.9 shows the thermally averaged cross section  $\langle\sigma v\rangle$  for both fermion and scalar dark matter points that were shown in Figure 7.7. The same color coding as in the previous plots that were shown is used here as well. In the calculation of this quantity, a NFW profile for the galactic DM halo was assumed [131]. The expectation for the standard thermal relic scenario is plotted using the dashed line [43]. It is an upper limit in the case of fermionic DM, whereas it is a lower limit for scalar DM. All points lie well below the bounds established by ICECUBE [158], ANTARES [147] and their combination [239] as well as by SUPER-KAMIOKANDE [151], hence these measurements do not further constrain the model. The region that could most easily be probed by future ICECUBE ANTARES analyses would be for heavy scalar DM above 1 TeV.

### 7.5.5 Expected event rates in IceCube

After discussing the scattering cross sections and  $\langle\sigma v\rangle$  in detail, the next step is to make the connection to the expected event rate in ICECUBE. Fig. 7.10 shows the calculated event rate in the ICECUBE observatory, where we have drawn a line at one event per year as orientation. The green points show the triplet scalar DM, which have extremely low event rates due to the absence of a SD cross section, and SI cross sections below the current XENON1T limit, leading to little accumulation in the Sun. This makes the scalar DM in this model unfeasible for detection in ICECUBE.

The case of singlet-fermionic DM (the other points) is more interesting. For some parts of the parameter space, an event rate of up to 1000 events per year can be reached. However, we need to take the previously shown direct and indirect detection constraints into account, which are represented by the different markers in Fig. 7.10. A constraint that was not

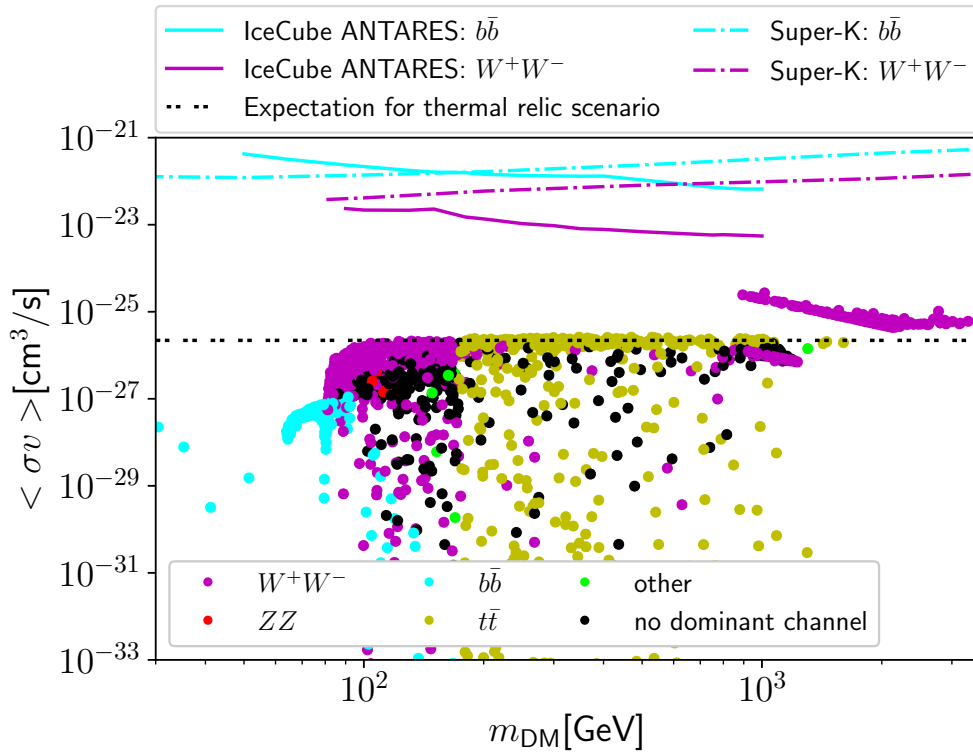


Figure 7.9: Thermally averaged cross section  $\langle\sigma v\rangle$  with combined ICECUBE ANTARES [239] and SUPER-KAMIOKANDE [151] exclusion limits as a function of the DM mass for both fermion (below about 1 TeV) and scalar DM (above). All points are colored according to the main annihilation channel, provided there is one with a branching ratio of over 50%. Also shown is the expected cross section for a thermal relic [43].

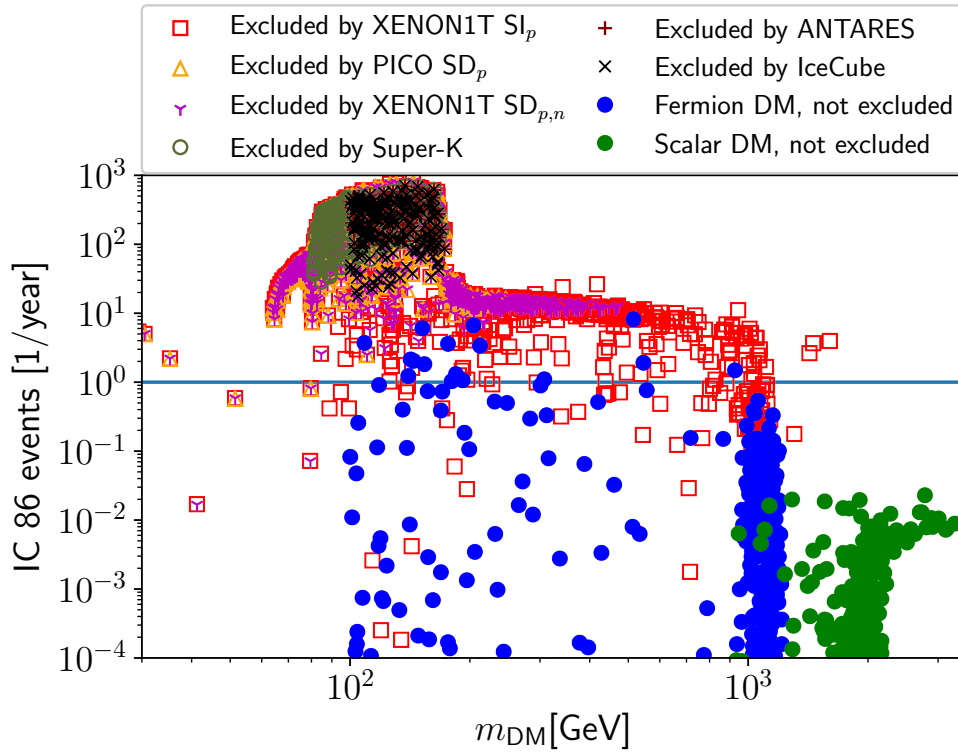


Figure 7.10: The expected number of events per year in the current ICECUBE configuration with 86 strings (IC86) as a function of the DM mass for singlet-doublet fermion (blue) and triplet scalar (green) DM. Allowed points are shown together with points excluded by direct and indirect detection (other colors and symbols). The blue line marks one event per year for orientation.

previously shown, but is included in this plot is the XENON1T bound on spin dependent scattering on neutrons that is not very prominent in the Sun. The viable models that pass all constraints (blue) do not reach up to 1000 events, as they have already been excluded by ICECUBE (black crosses). The viable points can reach up to 10 events per year in IC86, which makes it competitive compared to limits from direct detection on the SD cross section by PICO-60 (orange triangles) in particular. Since the spin dependent and spin independent cross sections are correlated in this model, the stringent limits from XENON1T on the spin independent cross section also constrain the spin dependent cross section. In some regions of the parameter space this correlation is lifted, but this requires fine-tuned scenarios which we do not consider here.

## 7.6 Conclusion

In this chapter we focused on neutrino signals from DM annihilation inside the Sun for the T1-3-B model with  $\alpha = 0$ , which contains either triplet scalar or singlet-doublet fermion DM. We found that for both DM candidates direct annihilation into neutrinos is in principle possible. However, due to constraints on the involved Yukawa couplings from LFV and neutrino physics constraints these are small and no monochromatic neutrino lines at  $E_\nu = m_{\text{DM}}$  are observed.

Instead the resulting spectra are continuous, with the main annihilation channels being either to the electroweak gauge bosons  $W$  and  $Z$ , or the heavy  $b$  and  $t$  quarks. Annihilations into leptons such as  $\mu$  or  $\tau$  are in principle allowed, these are however subdominant. DM accumulation in the Sun can boost the local relic density by a large enough amount to make indirect detection of DM annihilations in neutrino telescopes feasible. From our analysis of the expected amount of events in ICECUBE we conclude that the scalar triplet DM scenario cannot be detected at present. In this scenario there exists no spin dependent scattering cross section, making the capture rate inside the Sun too small to provide for detectable neutrino fluxes. The resulting event rate lies clearly below one event per year.

In the case of singlet-doublet DM the case is very different. This DM candidate does allow for a spin dependent scattering process next to the spin independent one, which results in rates of 1000 events per year. We also showed that these two processes are correlated through the singlet-doublet mixing terms  $\lambda_4$  and  $\lambda_5$ . This result became apparent in the numerical scan, where we used the more stringent XENON1T spin independent limits to constrain the spin dependent cross section through this correlation. A considerable part of the parameter space that has large event rates could thus be excluded. We also applied previously obtained constraints from ANTARES, ICECUBE, and SUPER-KAMIOKANDE from the Sun and Galactic Center to our results, but these were found to be much weaker. Further bounds from PICO-60, and results from ICECUBE and ANTARES on the spin dependent cross section restricted the event rate in viable models to up to 10 per year. This means that

indirect detection with the ICECUBE neutrino telescope is competitive with direct detection experiments.

As an outlook, we would like to point out that our findings can provide motivation for a dedicated ICECUBE analysis on this topic. Furthermore, these conclusions can be extended to models with real scalar triplet DM and/or singlet-doublet mixed fermion DM, that feature similar WIMP-nucleon scattering processes. But for now, we will leave the South Pole and in the next chapter focus on direct detection of DM.



## 8 Electron recoil with MeV neutrino dark matter

In the last two chapters, the main focus was on indirect detection of neutrinos by the ICECUBE observatory. We now shift gears and focus on direct detection instead. As we have seen in the scotogenic and T1-3-B  $\alpha = 0$  models, WIMPs in radiative seesaw models usually have masses from several tens of GeV up to a few TeV, in line with the usual models of cold dark matter (CDM) [29]. In this chapter we instead focus on an entirely different and little explored mass range; the SLIM (Scalar as Light as MeV) model, which as its name suggests can accomodate a DM candidate at the MeV scale [72, 231]. The original motivation for this model was that it can explain the 511 keV line from the Galactic Centre [286]. The lower mass range is of further interest as warm DM, e.g. in the form of keV sterile neutrinos, has often been proposed as a solution to several cosmological open questions relating to the density profile and distribution of DM haloes in the Universe [287]. Whereas this model has been studied before [72, 231], there are several open ends that warrant further investigation. This chapter is based on the work published in Ref. [288].

So far the precise value of the relic density from PLANCK measurements had not been considered in the literature yet [23], and neither were the effects of the neutrino mass differences and mixing angles, that both constrain the parameter space of the model. Moreover, we study the best-known lepton flavor violating channels, which constrain key couplings of the model [289]. The DM we consider in our studies will have a mass in the MeV to GeV range. As it plays a role in generating the neutrino masses, it couples to leptons, but does not couple to quarks at tree level. At higher masses, one-loop scattering processes may be possible, but for the MeV to GeV range no nuclear scattering signal is expected from this WIMP [290]. However, at lower masses WIMP-electron scattering becomes a possible scattering process, compared to the usual detection experiments that measure recoils of heavy nuclei. There has been a recent interest for this process [291, 292], that do not explicitly consider a new light vector boson, but other mediators (scalars) as well.

In this chapter we will address these topics. We start by introducing the particle content of the model, the couplings, and the mass eigenstates. The next step is to discuss several experimental constraints on the relic density, as well as further cosmological and collider constraints. We then perform a numerical scan of the parameter space of the model. As was also done for the scotogenic and T1-3-B  $\alpha = 0$  models, the neutrino masses and mixing angles enter through the Casas-Ibarra parametrization, fixing the couplings to the SM leptons.

This is relevant for the LFV processes  $\mu \rightarrow e\gamma$ ,  $\mu \rightarrow 3e$ , and  $\mu^- \text{Ti} \rightarrow e^- \text{Ti}$ , of which we compare the results from our scan to the current and projected experimental sensitivities. After studying these constraints, we move to the topic of electron recoil for MeV DM. Here our approach is twofold: we compute the electron recoil cross sections for this model, which we then compare to new, realistic estimates of XENON1T and further future experiments.

## 8.1 Model description

### 8.1.1 Particle content

The SLIM model is in many aspects similar to the by now extensively discussed scotogenic model [205]. Its scalar sector consists not only of the SM Higgs doublet  $H$  with a mass term  $m_1$ , the self-coupling  $\lambda_1$ , such that its vev satisfies  $v^2 = -2m_1^2/\lambda_1 = (246 \text{ GeV})^2$  which results in the SM Higgs boson mass  $m_h^2 = \lambda_1 v^2 = (125 \text{ GeV})^2$ . At low energy the scalar sector can be extended by either a real or a complex scalar singlet. In our studies we make the choice for a complex scalar

$$\rho = \frac{1}{\sqrt{2}}(\rho_R + i\rho_I), \quad (8.1)$$

for which we will later discuss the phenomenological implications. Moreover, the scalar sector is extended further by adding an additional scalar doublet [231]

$$\eta = \begin{pmatrix} \eta^+ \\ \frac{1}{\sqrt{2}}(\eta_R + i\eta_I) \end{pmatrix}. \quad (8.2)$$

Next to these scalars, two SM singlet right-handed neutrinos  $N_i$  are added. With the addition of these particles, radiative neutrino mass generation at the one-loop level becomes possible [72]. The choice for two right-handed neutrinos results in two non-zero neutrino masses. A third generation could be included, which would yield three massive neutrinos, but this does not significantly change the phenomenology. Furthermore we add a global  $U(1)$  symmetry under which all new particles have the same charge of  $+1$ , stabilizing the lightest neutral dark particle as DM candidate. The global  $U(1)$  symmetry is softly broken to a  $\mathbb{Z}_2$  symmetry, the phenomenology of this will be discussed later.

The model bears many similarities with the scotogenic model [205], because of the addition of a second doublet and right-handed neutrinos. However, the addition of the complex scalar singlet and the soft breaking of the  $U(1)$  symmetry opens up new phenomenology not present in the scotogenic model. In particular, the model allows for MeV neutrino DM and two similarly light neutral scalars can provide a solution to the missing satellite and too-big-to-fail problems [293]. As a reference, the scotogenic and the SLIM models correspond to models T3-B and T1-1-A with hypercharge parameters  $\alpha = -1$  and  $0$ , respectively following the notation of Ref. [204].

### 8.1.2 Lagrangian

In order to simplify the notation, we choose to work in the mass basis of the right-handed neutrinos  $N_i$  ( $i = 1, 2$ ), so that its mass matrix is diagonal with entries  $m_{N_i}$ . This choice does not affect the phenomenology. When including the SM leptons  $L_j$  ( $j = 1, 2, 3$ ), the additional terms can be written as

$$\begin{aligned} \mathcal{L} = & -m_1^2 H^\dagger H - m_2^2 \eta^\dagger \eta - m_3^2 \rho^* \rho - \frac{1}{2} m_4^2 (\rho^2 + (\rho^*)^2) - \mu(\eta^\dagger H \rho + h.c.) - \frac{1}{2} m_{N_i} N_i N_i \\ & - \frac{1}{2} \lambda_1 (H^\dagger H)^2 - \frac{1}{2} \lambda_2 (\eta^\dagger \eta)^2 - \frac{1}{2} \lambda_3 (\rho^* \rho)^2 - \lambda_4 (\eta^\dagger \eta)(H^\dagger H) - \lambda_5 (\eta^\dagger H)(H^\dagger \eta) \\ & - \lambda_6 (\rho^* \rho)(H^\dagger H) - \lambda_7 (\rho^* \rho)(\eta^\dagger \eta) - (\lambda_8)_{ij} N_i \eta^\dagger L_j + h.c.). \end{aligned} \quad (8.3)$$

As can be seen from the Yukawa coupling  $|\lambda_8|$ , the DM candidates in this model have a direct connection with the SM leptons. The global  $U(1)$  is softly broken to a  $\mathbb{Z}_2$  symmetry through the presence of the  $m_4^2$  term, which means that this term can be naturally small. The same goes for the Majorana mass term for the fermionic singlets. It remains renormalizable in spite of the global  $U(1)$  to  $\mathbb{Z}_2$  breaking, meaning that  $m_4$  should have a small value.

### 8.1.3 Physical mass eigenstates after EWSB

In the scotogenic model, no mixing in the scalar sector is possible. However, in this model there exists a mixing between the neutral component of the scalar doublet and the complex singlet. The charged component of the scalar doublet does not mix and after EWSB obtains the mass

$$m_{\eta^\pm}^2 = m_2^2 + \frac{1}{2} \lambda_4 v^2. \quad (8.4)$$

Because of the contribution of the Higgs vev  $v$  in the  $\mu$  term of the Lagrangian, a mixing between the neutral scalar components is induced. The mass matrix is written as

$$M_{R,I}^2 = \begin{pmatrix} m_2^2 + (\lambda_4 + \lambda_5) \frac{v^2}{2} & \mu \frac{v}{\sqrt{2}} \\ \mu \frac{v}{\sqrt{2}} & m_3^2 + \lambda_6 \frac{v^2}{2} \pm m_4^2 \end{pmatrix} =: \begin{pmatrix} A & B \\ B & C_{R,I} \end{pmatrix}, \quad (8.5)$$

where for the real and imaginary components there is respectively a plus or minus sign in front of the  $m_4^2$ . This term in Equation (8.3) causes a small mass splitting in the components of the complex scalar. For the neutral scalars we define the following mixing matrix

$$\begin{pmatrix} \zeta_{1R,I} \\ \zeta_{2R,I} \end{pmatrix} = \begin{pmatrix} \cos \theta_{R,I} & -\sin \theta_{R,I} \\ \sin \theta_{R,I} & \cos \theta_{R,I} \end{pmatrix} \begin{pmatrix} \eta_{R,I} \\ \rho_{R,I} \end{pmatrix}, \quad (8.6)$$

with mixing angles  $\theta_{R,I}$ . The resulting eigenvalues of the mass matrix are

$$m_{R,I}^2 = \frac{1}{2} \left( A + C_{R,I} \pm \sqrt{(A - C_{R,I})^2 + 4B^2} \right). \quad (8.7)$$

Table 8.1: Overview of model parameters with their values or scan ranges and phenomenological impact, respectively.

Parameter	Value	Range	Phenomenological impact
$m_1^2$	$-(89 \text{ GeV})^2$	—	Fixed by $v$ and $m_h$
$m_2$	83 GeV	—	Fixed by $v$ , $\lambda_4$ and $\lambda_5$
$m_3$	264 GeV	—	Fixed by $v$ and $\lambda_6$
$m_4$	—	10 keV ... 10 MeV	Induces soft $U(1)$ breaking
$\mu$	—	251 GeV ... 252 GeV	Fixed by $v$ and $\epsilon$
$\epsilon$	—	$(10^{-5} \dots 6.1 \cdot 10^1) \text{ GeV}^2$	Induces MeV masses
$m_{N_1}$	—	$(0.1 \dots 0.98) \cdot m_{\zeta_2}$	$\mathcal{O}(\text{MeV})$ DM candidate
$m_{N_2}$	—	10 GeV ... 200 GeV	$\mathcal{O}(\text{GeV})$ sterile neutrino
$\lambda_1$	0.26	—	Fixed by $v$ and $m_h$
$\lambda_2$	0.12	—	Induces only scalar conversions
$\lambda_3$	0.13	—	Induces only scalar conversions
$\lambda_4$	0.097	—	Fixed by $v$ , $m_{\eta^\pm} = 99 \text{ GeV}$ , $R_{\gamma\gamma}$
$\lambda_5$	0.13	—	Fixed by $v$ , $m_{\eta^\pm} = 99 \text{ GeV}$ , $R_{\gamma\gamma}$
$\lambda_6$	2.3	—	Induces MeV masses
$\lambda_7$	0.17	—	Induces only scalar conversions
$\lambda_8$	—	$10^{-6} \dots 10^2$	Fixed by Casas-Ibarra parametr.

In the region of the parameter space where  $B^2$  is close to  $AC_{R,I}$ , with a difference  $\epsilon$

$$AC_{R,I} - B^2 =: \epsilon(A + C_{R,I}) \quad (8.8)$$

yields to two neutral scalar eigenstates  $m_{\zeta_{2R,I}}$  that can lie at the MeV scale. The other two eigenstates  $m_{\zeta_{1R,I}}$  have masses that are on the higher mass scale around  $m_{\eta^\pm}$ . In this chapter, we assume that the lightest particle of the dark sector is  $N_1$ , i.e. we consider fermionic dark matter.

## 8.2 Collider, cosmological and neutrino constraints

Having introduced the model, we now turn to experimental constraints from different fields. Even though the SLIM model has a wide parameter space, restrictions from experiment and theory could in principle exclude large parts of it. Table 8.1 shows allowed values and ranges of the parameters that are used throughout this chapter. A small phenomenological explanation is included for each of the parameters.

The parameters  $m_1$  and  $\lambda_1$ , often denoted  $\mu$  and  $\lambda$  in SM contexts, have been discussed in section 8.1.1. There are theoretical constraints on the parameter space, considering unitarity, which requires several combinations of the other  $\lambda_i$  couplings to lie below  $8\pi$ . Furthermore there are bounded from below conditions, so that no particles with negative squared masses are present. However, these constraints are automatically fulfilled once experimental constraints from cosmology, neutrino observation and collider measurements are imposed.

### 8.2.1 Collider constraints

Postulating new particles in the usual SM mass range instead of at the TeV scale has several implications. One of the issues is that of an allowed invisible Higgs decay, in which the Higgs decays into two particles of the dark sector. In this model, the decay channel  $h \rightarrow \zeta_{2R,I} \zeta_{2R,I} \rightarrow N_1 N_1 \nu \nu$  is generally allowed due to the low masses around the MeV scale. The channel  $h \rightarrow \zeta_{1R,I} \zeta_{1R,I}$  can in principle also be available, but it can be closed by ensuring that the relation  $m_{\zeta_{1R,I}} > m_h/2$  is satisfied at all times. The current experimental limits on the branching ratio of invisible Higgs decays lie at 26% from ATLAS, and 19% from CMS [294, 163]. The Higgs doublet  $H$  couples to the scalar sector in the following way

$$\begin{pmatrix} \eta \\ \rho \end{pmatrix}^\dagger \begin{pmatrix} (\lambda_4 + \lambda_5)v & \frac{\mu}{\sqrt{2}} \\ \frac{\mu}{\sqrt{2}} & \lambda_6 v \end{pmatrix} H \begin{pmatrix} \eta \\ \rho \end{pmatrix}. \quad (8.9)$$

Comparing the above matrix to the scalar mass matrix given in Equation (8.5), one can see that they become proportional to each other when making the identifications [293]

$$m_2^2 = (\lambda_4 + \lambda_5) \frac{v^2}{2} \quad \text{and} \quad m_3^2 = \lambda_6 \frac{v^2}{2}, \quad (8.10)$$

under the assumption of small  $m_4^2$ . With the coupling to the Higgs proportional to the mass of the light MeV scalars, large invisible branching ratios can be avoided. Due to the above identifications,  $m_2$  and  $m_3$  are now dependent on  $\lambda_{4,5,6}$ .

Further collider constraints come from the model-independent LEP result, which excludes charged scalars below a mass of 98.5 GeV [228]. This means that the combination  $\lambda_4 + \lambda_5$  that shows up in the expression for the charged scalar  $\eta^\pm$  must be restricted to satisfy this constraint. The Higgs branching ratio into two photons, on which the CMS measured a ratio of  $R_{\gamma\gamma} = 1.20^{+0.18}_{-0.14}$  [295]. Our choice  $\lambda_4 = 0.097$ ,  $\lambda_5 = 0.13$  satisfies both constraints, in accordance with Figure 3 in Ref. [293]. This results in a mass  $m_{\eta^\pm} = 99$  GeV. Since this charged scalar acts as a mediator in electron recoil, which will be discussed later, a larger value for  $\lambda_4$  would only increase its mass and result in smaller electron recoil cross sections. Furthermore, larger  $\lambda_4$  and  $\lambda_5$  lead to larger lepton flavour violation branching rates.

### 8.2.2 Cosmological constraints

The initial motivation for the SLIM model was to explain the 511 keV line that had been observed from the galactic centre [286], which prompted studies on scalar MeV DM [72, 231]. Only later it was noticed that considering MeV neutrino DM, if it can scatter off the active neutrinos in the early Universe through the exchange of a slightly heavier scalar ( $\zeta_{2R,I}$ ) [293], can solve the problems of missing satellite galaxies, the cusp core of inner DM density profiles and the fact that the unobserved satellites are too big to not have visible stars [287]. For the slightly heavier scalar  $\zeta_{2R,I}$  to have a mass in the MeV region the relation introduced in Equation (8.8) must be satisfied. The scalar couplings  $\lambda_{2,3,7}$  only induce interaction within

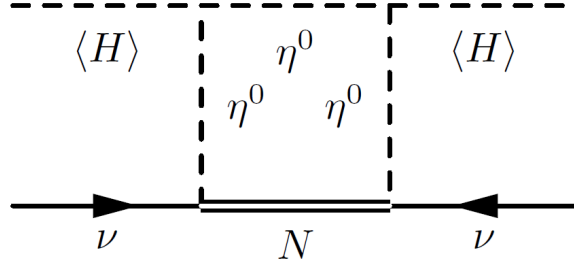


Figure 8.1: One-loop diagram leading to the active neutrino mass matrix in the SLIM model.

the scalar sector itself, they have little influence on the phenomenology and we thus set them to the values  $\lambda_2 = 0.12$ ,  $\lambda_3 = 0.13$ , and  $\lambda_7 = 0.17$ . The mass parameter of the singlet  $m_3$  should not dominate over  $v$ , restricting the value of  $\lambda_6 \leq 3$ , in accordance with Figure 2 of Ref. [293]. There,  $\lambda_6$  was varied, with the value of  $\epsilon$  from Equation (8.8) fixed to  $10^{-4} \text{ GeV}^2$ . In contrast, we fix  $\lambda_6 = 2.3$  and vary  $\epsilon$  over the following range

$$\epsilon = (10^{-5} \dots 6.1 \cdot 10^1) \text{ GeV}^2. \quad (8.11)$$

This way we can more easily control the mass of the two light scalars via the mixing parameter  $\mu$ . In Refs. [296, 297] it was shown that weak-strength DM interactions can erase primordial fluctuations of DM provided that the DM candidate has a mass in the MeV range and couples to neutrinos and/or photons. For this scenario the elastic cross sections must be temperature-independent which requires, next to the previously mentioned characteristics, a small mass splitting between the MeV neutrino and the light scalar(s). This is reflected in the scan ranges of  $\epsilon$ ,  $m_4$ , and  $\lambda_6$  (related to  $m_3$ , the mass term of the scalar singlet).

In order to satisfy the requirement for a small mass splitting between the lightest Majorana neutrino and the lightest scalar, we constrain the ratio of their masses  $m_{N_1}/m_{\zeta_{2R,I}}$  to lie in the region  $0.1 \dots 0.98$ . As for the heavier Majorana neutrino, it has a mass in the 10 to 200 GeV range, and due to its rapid decay  $N_2 \rightarrow \eta\nu \rightarrow N_1\nu\nu$  does not contribute to any relevant phenomenology.

### 8.2.3 Neutrino constraints

The SLIM model also belongs to the class of radiative seesaw models, and hence the SM neutrinos obtain their masses at one-loop level, through the diagram shown in Figure 8.1. This results in a neutrino mass matrix that is given by [293]

$$(M_\nu)_{ij} = \sum_k \frac{(\lambda_8)_{ik}(\lambda_8)_{jk}}{16\pi^2} m_{N_k} \left[ \frac{\cos^2 \theta_R m_{1R}^2}{m_{1R}^2 - m_{N_k}^2} \ln \frac{m_{1R}^2}{m_{N_k}^2} + \frac{\sin^2 \theta_R m_{2R}^2}{m_{2R}^2 - m_{N_k}^2} \ln \frac{m_{2R}^2}{m_{N_k}^2} - \frac{\cos^2 \theta_I m_{1I}^2}{m_{1I}^2 - m_{N_k}^2} \ln \frac{m_{1I}^2}{m_{N_k}^2} - \frac{\sin^2 \theta_I m_{2I}^2}{m_{2I}^2 - m_{N_k}^2} \ln \frac{m_{2I}^2}{m_{N_k}^2} \right], \quad (8.12)$$

with the angles  $\theta_{R,I}$  coming from the scalar mixing matrix given in Equation (8.6). The form of the expression for the neutrino mass matrix is very similar to that of the scotogenic model, however this time the mass splitting is realised through the soft breaking of the global  $U(1)$  to  $\mathbb{Z}_2$  through the non-zero  $m_4^2$ . Furthermore, the SLIM model has 4 physical neutral scalars compared to the 2 of the scotogenic model, due to the addition of the complex scalar singlet. In Ref. [293] the value of  $m_4^2$  was fixed to 3 MeV, but we allow it to vary over the range 10 keV ... 10 MeV, because as we will soon show, the scalar mass splitting directly affects the couplings to the SM leptons  $\lambda_8$ .

In order to constrain the parameter space in such a way that it satisfies the neutrino mass difference and mixing constraints, we use the Casas-Ibarra parameterization [214]. Similar to the procedure we already performed for the scotogenic and T1-3-B  $\alpha = 0$  models, we write the diagonalized neutrino mass matrix using the PMNS matrix  $U$

$$D_\nu = U_\nu^\dagger M_\nu U_\nu = \text{diag}(0, m_{\nu 2}, m_{\nu 3}), \quad (8.13)$$

with two massive neutrinos due to our choice of adding two Majorana neutrinos. In this case one can separate the couplings  $\lambda_8$  from the sum in Equation (8.12) and write

$$M_\nu = \lambda_8^T M \lambda_8, \quad (8.14)$$

with  $M$  being the diagonal  $3 \times 3$  matrix with entries that depend on the loop particle masses and mass differences. Eventually this results in an expression for the lepton-dark sector coupling

$$\lambda_8 = M^{-1/2} R D_\nu^{1/2} U_\nu^\dagger. \quad (8.15)$$

In this case the matrix  $R$  is written as

$$R = \begin{pmatrix} 0 & \cos \theta & \sin \theta \\ 0 & -\sin \theta & \cos \theta \end{pmatrix}, \quad (8.16)$$

with an arbitrary angle  $\theta$  ranging from 0 to  $2\pi$ . The parameter  $\lambda_8$ , which couples the neutrinos to the dark sector, has direct influence many important properties of the model. It determines the relic density, the electron recoil cross section, as well as the branching ratio of lepton flavour violating processes. As we have shown, it can be constrained based on particle masses and neutrino data.

### 8.3 Relic density

After discussing the different constraints that are relevant to this model, we now turn to the discussion of the results of the numerical scan. The general tool chain has already been discussed, as shown in Figure 5.2, but we would like to mention the specific versions that were used. We generated the Feynman rules and model properties with SARAH 4.12.2 [223], the

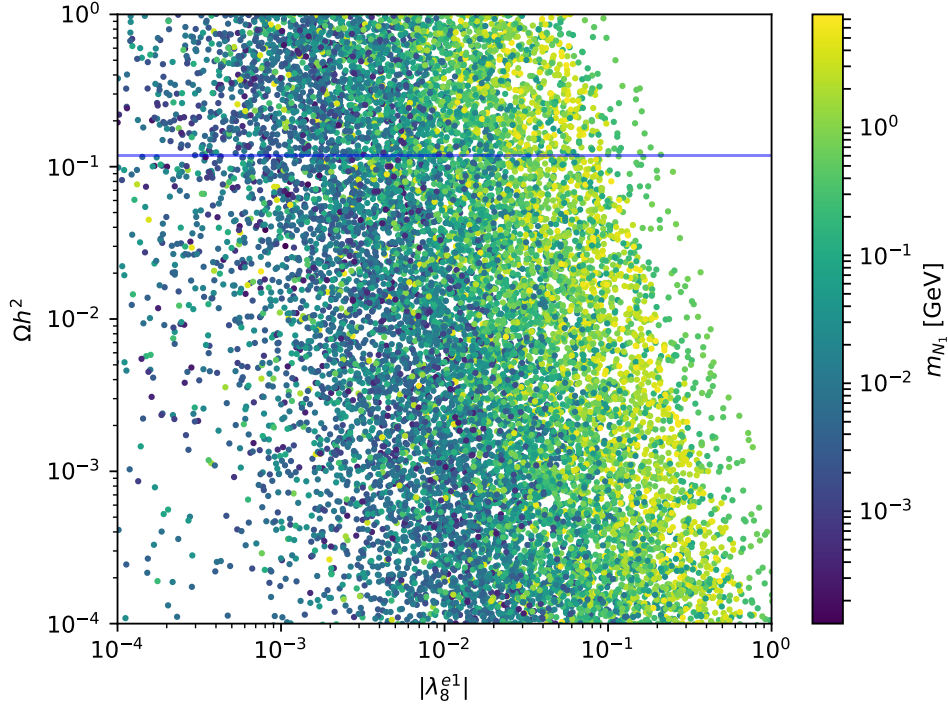


Figure 8.2: The relic density  $\Omega h^2$  obtained in the SLIM model with right-handed neutrino DM versus the absolute value of its coupling to electrons and electron neutrinos  $\lambda_8^{e1}$ . The relic density measured by Planck [23] is shown as a blue horizontal band, and the lightest Majorana neutrino mass  $m_{N_1}$  is given on a colour scale.

output of which was implemented in SPHENO 4.0.3 [226]. The output of SPHENO was then passed on to MICROMEGAS 4.3.5 [298].

In this process, the constraints presented in the last section were included, but also further relevant outputs from SPHENO 4.0.3 such as the  $\rho$  parameter, as well as the branching ratio of the  $b \rightarrow s\gamma$  process. The viable sampled parameter points, i.e. those satisfying all mentioned constraints, are then passed to MICROMEGAS 4.3.5, which calculates the relic density.

The relic density  $\Omega h^2$  of all viable parameter points is shown in Figure 8.2 as a function of  $|\lambda_8^{e1}|$ , the absolute value of the coupling between the electron and the lightest right-handed neutrino, with the points color coded according to the DM mass  $m_{N_1}$ . This coupling is important, as it plays a role in annihilation processes in the early universe. The relic density depends on both these parameters, and the relic density  $\Omega h^2 = 0.120 \pm 0.001$  as measured by PLANCK [23] is indicated by the blue band. The relic density drops off quickly for increasing  $\lambda_8^{e1}$ . The opposite is true for the dark matter mass, thus one can keep the relic density constant and increase the coupling to the SM  $\lambda_8^{e1}$  by simultaneously increasing  $m_{N_1}$  from the MeV to the GeV scale. This means that we can obtain couplings of almost  $\mathcal{O}(1)$  if the DM mass is increased to the GeV scale. To show this relation further, in Figure 8.3 we show the size of the coupling  $|\lambda_8^{e1}|$  versus the DM mass for the points from Figure 8.2 that satisfy the



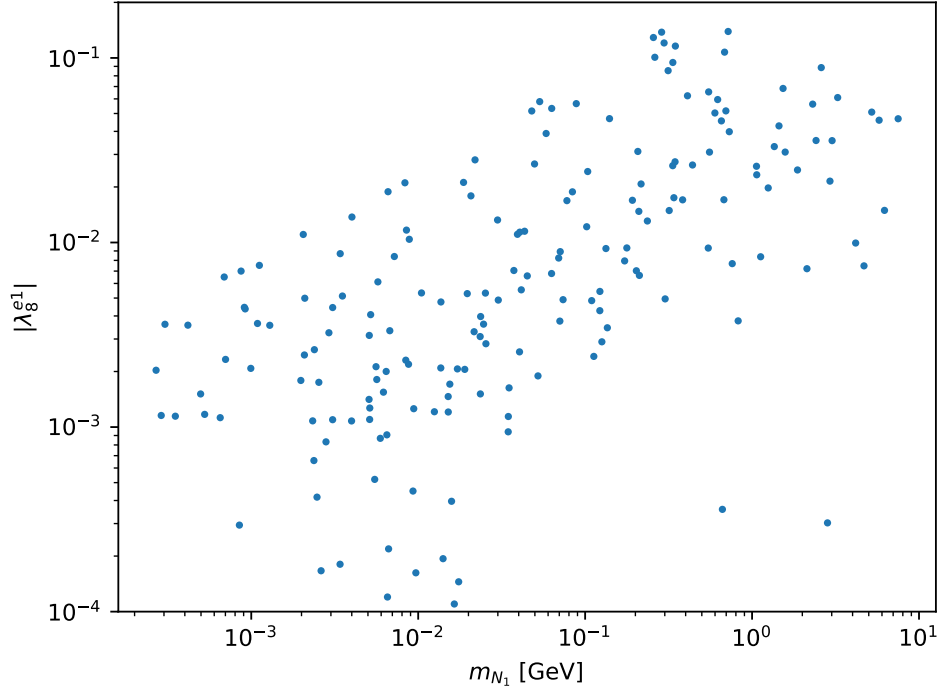


Figure 8.3: DM-electron coupling  $\lambda_g^{e1}$  versus DM mass  $m_{N_1}$  for models which satisfy not only collider, cosmological and neutrino mass constraints, but also lead to the correct relic density.

PLANCK relic density constraint. This can be attributed to heavier DM requiring larger couplings to the SM, enhancing annihilation processes that lower the relic density to the observed level.

In order to show the effect of the Casas-Ibarra parameterization has on our parameter space, we show the relation between the relic density and  $m_4$  in Figure 8.4. As we vary  $m_4$  over its mass range from 10 keV to 10 MeV, the relic density changes by many more orders of magnitude. The reason that this parameter has such a large effect is because  $m_4$  breaks the global  $U(1)$  symmetry to  $\mathbb{Z}_2$ , and induces the mass splitting shown in Equation (8.7). These masses are in turn important for the generation of neutrino masses, given by Equation (8.12), which depends on the difference of scalar masses. In the limit of  $m_4 \rightarrow 0$  neutrinos become massless. This is similar to the scotogenic model in Chapter 5, where the scalar mass splitting  $\lambda_5$  played a similar crucial role. A similar argument on the relation of the parameters in the neutrino mass formula can be made here. For decreasing values of  $m_4$ , the term in square brackets in Equation (8.12) becomes smaller. In order to generate the same neutrino masses, either the fermion masses  $M_{N_k}$  or the couplings  $\lambda_8$  have to increase. However, as shown in figure 8.3, increasing values of  $\lambda_8$  lead to larger annihilation cross sections, which in turn results in a lower relic density.

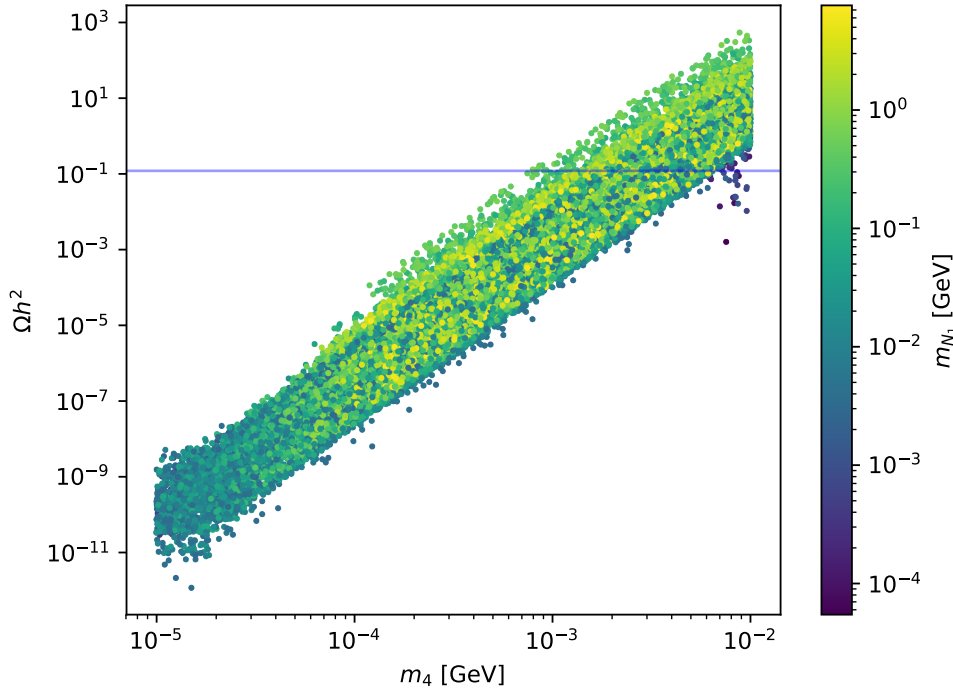


Figure 8.4: The relic density as a function of the mass splitting parameter  $m_4$ . The dark matter mass is included as a colour scale, and the relic density measured by Planck [23] is shown as a blue horizontal band.

## 8.4 Lepton flavour violation

Similar to the previously discussed scotogenic and T1-3-B  $\alpha = 0$  models, also in this model charged SM leptons can interact with the dark sector through couplings that are generally not diagonal in flavour space. The most stringent bound comes again from the  $\mu \rightarrow e\gamma$  process, of which the possible diagrams are shown in Figure 8.5.

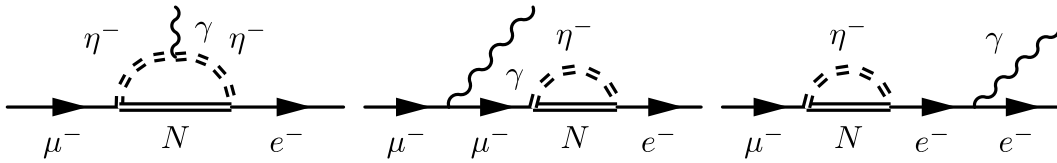


Figure 8.5: Feynman diagrams contributing to the lepton flavour violating process  $\mu \rightarrow e\gamma$  at one loop through the exchange of  $Z_2$ -odd right-handed neutrinos ( $N$ ) and charged scalars ( $\eta^-$ ).

Since the charged leptons and charged scalar are in a doublet with the neutrinos and neutral scalars respectively, these processes depend on the same parameter  $\lambda_8$  that in our scan is constrained through the Casas-Ibarra parameterization. In particular, the process depends on the couplings  $\lambda_8^{ei}$  and  $\lambda_8^{\mu i}$ . Since  $N_1$  is the lightest fermion, loops involving the much heavier  $N_2$  do not contribute much. Figure 8.6 shows the branching ratio of the

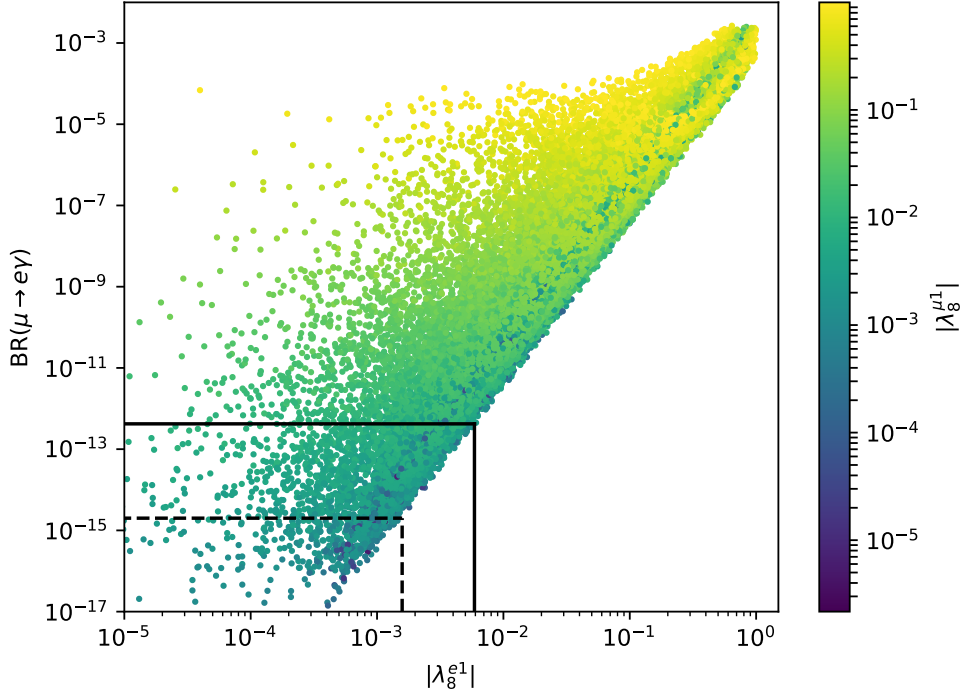


Figure 8.6: Branching ratio of the lepton flavour violating process  $\mu \rightarrow e\gamma$  versus the DM-electron coupling  $|\lambda_8^{e1}|$ . The DM-muon coupling  $|\lambda_8^{\mu1}|$  is shown on a colour scale. Also shown are the current (solid black line) [215] and expected future (dashed black line) [216] limits on the branching ratio by the MEG experiment.

process  $\mu \rightarrow e\gamma$  as a function of the absolute value of the DM-electron coupling  $|\lambda_8^{e1}|$ . The other important coupling, the DM-muon coupling,  $|\lambda_8^{\mu1}|$  is implemented as a colour scale. The plot clearly shows that the branching ratio is strongly dependent on the mentioned  $\lambda_8$  elements. In particular, there is a clear lower bound on the branching ratio for a specific  $|\lambda_8^{e1}|$ . An overall lower bound on the branching ratio can also be seen in the plot, which is due to the neutrino masses and mixing which we take as input in the Casas-Ibarra parameterization. The black solid line shows the current upper limit on the branching ratio as determined by the MEG experiment, at a value of  $4.2 \times 10^{-13}$  [215], which already excludes a large part of the parameter space. Due to the clear lower bound on the branching ratio, this results in the bounds  $|\lambda_8^{e1}| \leq 6 \times 10^{-3}$  and  $|\lambda_8^{\mu1}| \leq 10^{-2}$ . This is in agreement with the literature where similar values were obtained in approximate calculations [231]. Further planned upgrades of the MEG experiment will improve its sensitivity, lowering the bound on the branching ratio to around  $2 \times 10^{-15}$ , further restricting the parameter space [216]. This is shown by the dotted line, from which one can also see that the values of  $|\lambda_8^{e1}|$  and  $|\lambda_8^{\mu1}|$  must be smaller.

A further LFV process that has been relatively tightly constrained is  $\mu \rightarrow 3e$ . The current upper bound for the branching ratio of this process has been established at  $10^{-12}$  by the SINDRUM experiment [217], close to the bound on  $\mu \rightarrow e\gamma$ . Furthermore, the SINDRUM

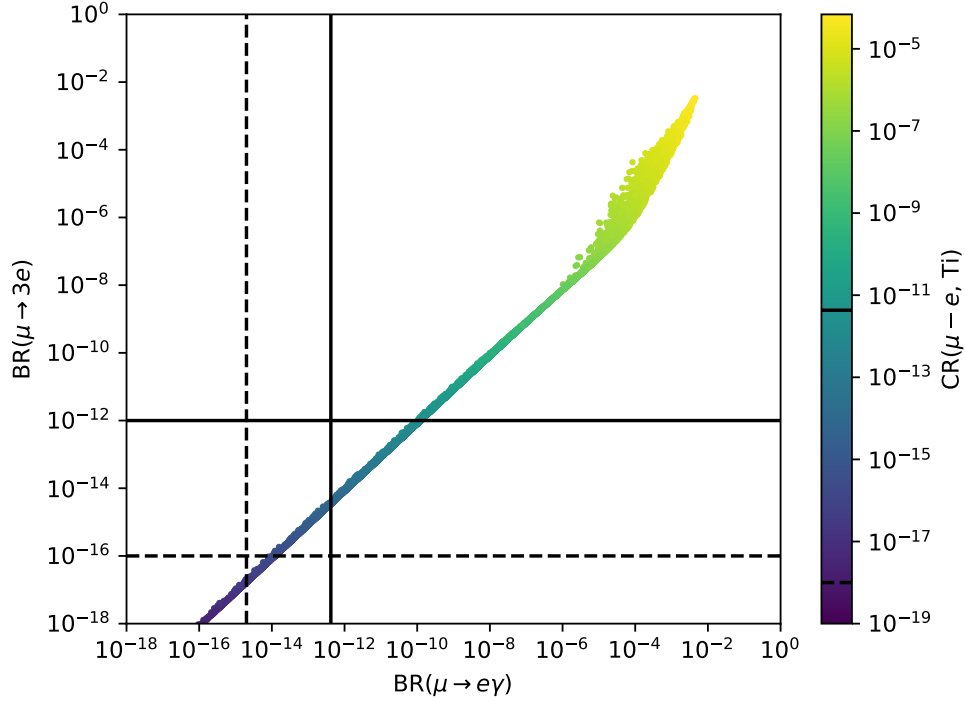


Figure 8.7: Branching ratio of the lepton flavour violating process  $\mu \rightarrow 3e$  versus the one of the (usually most constraining) process  $\mu \rightarrow e\gamma$ . The rate of muon conversion in the field of titanium atoms  $\mu^- \text{Ti} \rightarrow e^- \text{Ti}$  is shown on a colour scale. Also shown are the current (solid black lines) [215, 217, 219] and expected future (dashed black lines) [216, 218, 299] experimental limits on the branching ratios and conversion rate.

II experiment determined a limit of  $4.3 \times 10^{-12}$  on the conversion rate of muons to electrons in titanium [219]. Future experiments are set to improve upon these limits, with projected sensitivities of  $10^{-16}$  [218] and  $10^{-18}$  [299] respectively. Figure 8.7 shows  $\text{BR}(\mu \rightarrow 3e)$  versus  $\text{BR}(\mu \rightarrow e\gamma)$ , with  $\text{CR}(\mu - e, \text{Ti})$  as a colour scale to compare the strength of the different bounds. The current and future bounds are again indicated using full and dashed lines respectively. It can be seen that there is a clear correlation between the different LFV processes, as all points lie on a small line, with only a small spread at higher branching ratios. Furthermore, the current bound on  $\mu \rightarrow e\gamma$  is the strongest one, but in the future, the  $\mu \rightarrow 3e$  bound can become slightly stronger. Note that the constraints from these LFV processes on the parameter space as shown in Figures 8.6 and 8.7 are valid irrespective of the relic density, as this constraint was not applied in the scan for these plots.

## 8.5 Electron recoil cross section and experimental sensitivity

We now turn to direct detection of MeV DM in the SLIM model. The usual way of WIMP direct detection uses scintillation signals released by WIMP-nucleon scatterings. This way, the

XENON1T experiment has reached the current most stringent limit on the spin-independent cross section in a mass range from 6 GeV up to 1 TeV [95]. Further experiments such as XENON100 have been able to reach lower mass ranges down to 3.7 GeV by an ionisation (S2) signal only analysis [300], or in the case of CRESST-III with the use of cryogenic  $\text{CaWO}_4$  crystals down to 160 MeV [101]. In the case of the SLIM model, the DM is leptophilic and does not couple to nuclei at tree level. However, there exists a coupling to the SM leptons, which can induce electron recoil signals which might be observable, provided that the involved couplings are large enough. There is also much interest both from an experimental, as well as from a theoretical perspective in sub-GeV DM. Current detectors should not only be sensitive to electron recoil through the exchange of vector bosons ( $Z'$  or dark photons), but to other mediators as well [291, 292]. The goal of this section is to derive theoretical and experimental predictions for the electron recoil cross section of a general MeV DM candidate, as well as the exclusion limit using new XENON1T sensitivities which are then compared to other experiments. The obtained results are also applied to the SLIM model.

For a general DM particle  $\chi$  with a mass  $m_\chi$  the differential ionisation rate with respect to the electron recoil (er) energy  $E_{\text{er}}$  is given as

$$\frac{dR_{\text{ion}}}{d \ln E_{\text{er}}} = N_T \frac{\rho_\chi}{m_\chi} \sum_{n\ell} \frac{d\langle \sigma_{\text{ion}}^{n\ell} v \rangle}{d \ln E_{\text{er}}}, \quad (8.17)$$

which mainly depends on  $N_T$ , the number of target nuclei per unit mass, the local density in the galactic DM halo  $\rho_\chi = 0.4 \text{ GeV}/\text{cm}^3$  [301], as well as the thermally averaged annihilation cross section  $\langle \sigma_{\text{ion}}^{n\ell} v \rangle$ . The differential thermally averaged cross section is calculated from

$$\frac{d\langle \sigma_{\text{ion}}^{n\ell} v \rangle}{d \ln E_{\text{er}}} = \frac{\bar{\sigma}_{\chi e}}{8\mu_{\chi e}^2} \int |f_{\text{ion}}^{n\ell}(k', q)|^2 F(k', Z_{\text{eff}}) |F_{\text{DM}}(q)|^2 \eta(v_{\text{min}}, t) q dq, \quad (8.18)$$

which is summed over all allowed electron states  $(n, \ell)$ . It chiefly depends on the DM-electron scattering cross section, which will be primarily discussed in section 8.5.1. Other dependencies are on the reduced DM-electron mass  $\mu_{\chi e}$ , as well as the form factor  $f_{\text{ion}}^{n\ell}(k', q)$  that depends on the outgoing electron momentum  $k' = \sqrt{2m_e E_{\text{er}}}$  and the momentum transfer  $q$ . Under the plane wave assumption for the scattered electrons and a spherically symmetric atom with full electron shells, the form factor can be expressed as

$$|f_{\text{ion}}^{n\ell}(k', q)|^2 = \frac{(2\ell + 1)k'^2}{4\pi^3 q} \int |\chi_{n\ell}(k)|^2 k dk, \quad (8.19)$$

with  $\chi_{n\ell}(k)$  being the radial part of the bound electron wave function in momentum space [290]. The wave function of the ionised electron is distorted due to the influence of the nearby atom. Hence the thermally averaged cross section has to be corrected by the Fermi function

$$F(k', Z_{\text{eff}}) = \frac{2\pi\nu}{1 - e^{-2\pi\nu}} \quad \text{with} \quad \nu = Z_{\text{eff}} \frac{\alpha m_e}{k'}. \quad (8.20)$$

The effective charge felt by the ionised electron  $Z_{\text{eff}}$  is generally larger than unity, as the nucleus is not wholly screened by the (remaining) bound electrons. However, the approximation  $Z_{\text{eff}} = 1$  holds for outer shell electrons [291, 292]. We treat the electrons in the target atom as single-particle states of an isolated atom, and use the tabulated numerical Roothaan-Hartree-Fock (RHF) wave functions [302]. The last term in Equation (8.18) is where the astrophysics comes into play with the mean inverse velocity [292]

$$\eta(v_{\text{min}}, t) = \int_{v_{\text{min}}}^{\infty} \frac{d^3v}{v} f(\mathbf{v}, t), \quad (8.21)$$

which depends on the DM velocity distribution in the Earth's frame  $f(\mathbf{v}, t)$ . The time dependence of this distribution is caused by the Earth's orbit around the Sun. Asymptotically far from the Sun's gravitational potential, we take the velocity distribution  $f_{\infty}(\mathbf{v})$  as the Standard Halo Model in the Galactic frame

$$f_{\infty}(\mathbf{v}) = 1/N_{\text{esc}} (\pi v_0^2)^{-3/2} e^{-\mathbf{v}^2/v_0^2}, \quad \text{if } |\mathbf{v}| \leq v_{\text{esc}}, \quad (8.22)$$

where  $N_{\text{esc}}$  serves as a normalisation factor. The orbital velocity around the Galactic centre is  $v_0 = 220\text{km/s}$ , and the Galactic escape velocity is taken as  $v_{\text{esc}} = 544\text{km/s}$  [303]. The minimal DM velocity required to scatter off a bound electron is

$$v_{\text{min}} = \frac{E_{\text{B}}^{n\ell} + E_{\text{er}}}{q} + \frac{q}{2m_{\chi}}. \quad (8.23)$$

It depends on the sum of the electron binding energy  $E_{\text{B}}^{n\ell}$  and the recoil energy  $E_{\text{er}}$ .

### 8.5.1 Theoretical expectations

In Equation (8.18) the DM-electron scattering cross section  $\bar{\sigma}_{\chi e}$  plays a large role. The scattering of a majorana WIMP off an electron can take place via the exchange of a  $\mathbb{Z}_2$ -odd charged scalar  $\eta^-$  via the  $s$ - and  $u$ -channel, which are shown in Figure 8.8. A  $t$ -channel diagram is not possible due to the presence of the  $\mathbb{Z}_2$  symmetry. The cross section is usually factorised in the following non-relativistic way

$$\bar{\sigma}_{\chi e} = \frac{\mu_{\chi e}^2}{16\pi m_{\chi}^2 m_e^2} |\overline{\mathcal{M}_{e\chi}(q)}|^2 \Big|_{q^2=\alpha^2 m_e^2}, \quad (8.24)$$

with fixed momentum transfer  $q = \alpha m_e$ , with the electromagnetic fine structure constant  $\alpha$ . The matrix element can be derived from the diagrams in Figure 8.8. The form factor

$$|F_{\text{DM}}(q)|^2 = |\overline{\mathcal{M}_{e\chi}(q)}|^2 / |\overline{\mathcal{M}_{e\chi}(\alpha m_e)}|^2, \quad (8.25)$$

relates the matrix element at different values of transferred momentum  $q$ . In the case where the mediator is light  $F_{\text{DM}}(q) = \alpha^2 m_e^2 / q^2$ , but for heavy mediators the form factor is constant  $F_{\text{DM}}(q) = 1$ . The case we consider here is the scenario in which the DM candidate  $\chi$  has

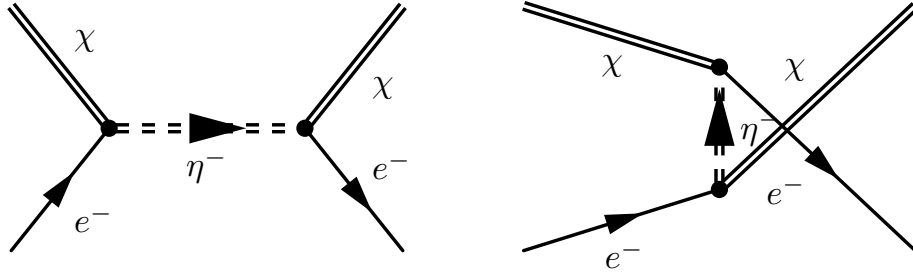


Figure 8.8: Feynman diagrams contributing to the scattering of right-handed neutrino DM ( $\chi = N_1$ ) off electrons ( $e^-$ ) through  $s$ - and  $u$ -channel exchanges of the charged  $Z_2$ -odd scalars ( $\eta^-$ ).

a mass of  $\mathcal{O}(\text{GeV})$ . As was already mentioned in section 8.2.1, charged scalars with masses below 98.5 GeV have been excluded by the LEP results [228]. Due to the large mass of the mediator  $\eta^-$  it can be integrated out, resulting in a form factor  $F_{\text{DM}}(q) = 1$ . Together with the DM-mediator coupling  $\lambda_8^{e1}$  this results in a reference cross section of

$$\bar{\sigma}_{\chi e} = \frac{\mu_{\chi e}^2 (\lambda_8^{e1})^4}{\pi m_{\eta^\pm}^4}. \quad (8.26)$$

For the points in the parameter space satisfying the experimental constraints mentioned in section 8.2, as well as the relic density constraint shown in figure 8.2 in section 8.3, the electron recoil cross section was calculated. Figure 8.9 shows the cross section for the models satisfying all constraints as a function of the DM mass. The absolute value of the DM-electron coupling,  $|\lambda_8^{e1}|$ , is shown as a color scale. Even for the largest possible values  $|\lambda_8^{e1}| \geq 0.1$  the cross sections do not exceed  $10^{-46} \text{ cm}^2$  by much. The LFV constraints that were shown in Figures 8.6 and 8.7 put tight bounds on the value of the coupling, meaning that the cross section only reaches  $10^{-52} \text{ cm}^2$  at most. Even though the couplings are not extremely small, the reason for the suppression is due to the mass of the heavy mediator, which is constrained by the previously mentioned LEP limit of 98.5 GeV. Since this mass enters the denominator to the fourth power, one obtains these small values. Most of the viable models have masses above several MeV, meaning that they are in agreement with experimental bounds on big-bang nucleosynthesis [41].

## 8.6 Experimental sensitivities

With the theoretical expectations in mind, we now turn to the (expected) experimental sensitivities. Liquid xenon (LXe) experiments canonically rely on the recoil of nuclei due to WIMP scatterings. However, for DM in the sub-GeV regime without any interaction with nuclei the only possible ionisation signals can come from the recoil of electrons. For an LXe experiment with an exposure of 1 kg-year, under the assumption of a constant form factor, as well as no recoil energy threshold in the detector, with only the irreducible neutrino

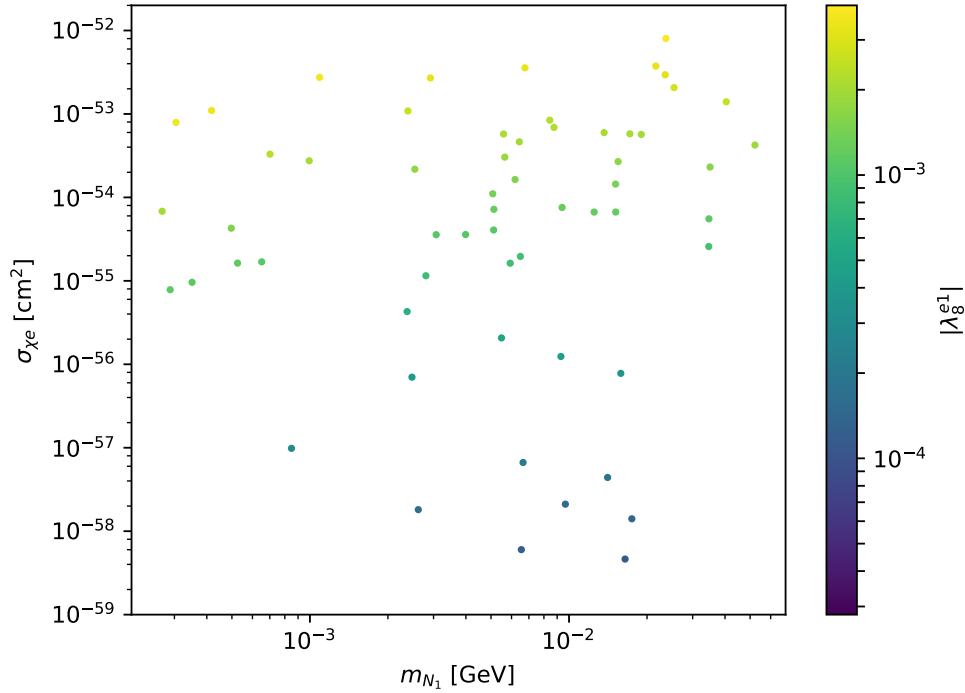


Figure 8.9: Scattering cross section of right-handed neutrino DM off electrons versus the DM mass. The DM-electron coupling  $\lambda_8^{e1}$  is shown on a colour scale.

background, the sensitivity was estimated on the order of a few times  $10^{-41} \text{ cm}^2$  for sub-GeV masses in the few tens of MeV range [291]. We will argue that a larger exposure of 60 kg-year is realistically within reach for current experiments. The red dotted line in Figure 8.10 shows the expected sensitivity for 1 kg-year, scaled down by a factor of 60 to account for the increased exposure. It reaches a value of just above  $10^{-42} \text{ cm}^2$  for masses of several tens of MeV. This is however still ten orders of magnitude above the largest cross sections shown in Figure 8.9.

This estimate is a best-case scenario, as in reality detector energy thresholds and the neutrino background will play a role in a LXe experiment. We will investigate the effects of these assumptions in the case of XENON1T, as it is the largest LXe detector. With an electron recoil background of  $82_{-3}^{+5} \text{ events}/(\text{ton}\cdot\text{year}\cdot\text{keV})$  at low energies, it has the lowest background level for a DM direct detection experiment worldwide. This low background level is reached by ensuring low radioactive materials in the detector setup, as well as a self-shielding LXe volume. An event in the XENON1T time projection chamber (TPC) is reconstructed by the direct scintillation light from ionisation (S1) as well as the time-delayed charge signal from the drifted electrons (S2). The requirement of the presence of an S1 signal means that there exists a threshold for the electron recoil energy of 2.5 (2.3) keV for XENON10 (XENON100) [308], down to 1.3 keV for XENON1T [95]. These energies are much larger than the binding energy of an electron, which lies around several tens of eV.



We first make an estimate of the sensitivity of the XENON1T experiment for a 1 ton-year exposure that was collected for the spin-independent WIMP nuclear recoil analysis [95]. In this estimation we make use of realistic recoil backgrounds and energy thresholds, as well as the standard mode of fiducialisation that considers both the S1 and the S2 signals. The electron recoil background in XENON1T is expected to be flat in the region of interest (ROI). It is dominated by the  $\beta$ -decays of the  $^{214}\text{Pb}$  originating from  $^{222}\text{Rn}$  that is naturally present in the detector material. There is the further sub-dominant background from  $\beta$ -decays of  $^{85}\text{Kr}$ , whose concentration is reduced by means of cryogenic distillation, leaving only a sub-ppt presence [309]. The energy threshold of an event is set at a corrected scintillation (cS1) signal between 3 and 70 photoelectrons (PEs) and an S2 signal of 200 PEs [95].

Analogously to the methods that were deployed in Ref. [310], we derive a conversion between the S1 signal in terms of PEs and the energy recoil in keV by means of the Noble Element Simulation Technique (NEST) [311]. NEST contains a global analysis of LXe measurements from all available historical data for the mean photon and charge yield, including XENON1T, as is further discussed in Ref. [312]. This conversion is reliable down to a recoil energy of 1 keV, at which point the XENON1T detection drops below 10%. We apply the NEST conversion function to a conservative scenario with a threshold of 2 keV, for which a full triggered efficiency is still a possibility, as well as 1 keV, where the detection efficiency is limited, as already mentioned. With the use of Poisson statistics, following Table XXII of Ref. [313]), one can obtain an average upper limit on the event rate for each desired DM mass. This corresponds to an experimental sensitivity on the reference cross section  $\bar{\sigma}_{\chi e}$ , as illustrated by the green and blue lines in figure 8.10.

The sensitivity can be enhanced by using the expected annual modulation due to the annually modulated velocity of the Earth relative to the DM galactic halo due to its orbit around the Sun. This way, the XENON100 experiment became sensitive to DM masses down to 600 MeV with an energy threshold of 2.3 keV. The best sensitivity is for a DM mass of 2 GeV with a cross section of  $6 \cdot 10^{-35} \text{ cm}^2$  for an axial vector coupling [304], illustrated by the black line in figure 8.10.

So far, all the sensitivity limits were still far removed from the ideal red dashed curve. In order to get closer to this line, a lower energy threshold is a necessity. This can be done by disregarding the S1 signal and only looking at the S2 signal, for which the energy threshold lies lower. The downside is that one loses information about the event, since no correlations between S1 and S2 signal events can be established. This can also increase the background, as the event depth  $z$  cannot be estimated without the S1 signal. A reliable background model becomes more difficult, since there are additional single-electron backgrounds arising from impurities in the LXe and metal components inside the TPC [314]. Currently, DM nuclear recoil searches by XENON10 with a 1 keV threshold and a 15 kg-days exposure [315] and XENON100 with a 0.7 keV threshold and a 30 kg-years exposure [300] have been performed,

with the conservative assumption that all counts in the search window are potential signal counts. These were reinterpreted in Ref. [291] as coming from DM-electron scattering, reaching exclusion limits of  $3 \cdot 10^{-38} \text{ cm}^2$  or slightly below  $10^{-38} \text{ cm}^2$  at 100 MeV.

Newer XENON1T results of an S2-only analysis have just been released [126], driving the energy threshold down further to 0.4 keV. With strict cuts on the data the background could be reduced drastically to 1 event/(ton·day·keV), with a remaining effective exposure of 22 ton-days or 60 kg-years. The electron recoil background spectrum that was considered was flat and originated mainly from  $\beta$ -decays of  $^{214}\text{Pb}$ , coherent elastic neutrino-nucleon scatterings, and cathode events due to low energy  $\beta$ -electrons from the cathode wire grid inside the TPC. Thus the sensitivity could be extended to lower masses of 100 to 20 MeV, indicated by the grey lines in figure 8.24.

In spite of these experimental advancements, the experimental upper limits and sensitivities shown in figure 8.10 are still ten orders of magnitude larger than the largest value we found in the SLIM model of  $10^{-52} \text{ cm}^2$ . This small value can be attributed to the suppression by the large mediator mass to the fourth power, despite the large DM-electron couplings. We also observe that the XENON1T experiment with its unprecedented low background is mostly limited by its detection threshold. The S2-only analysis managed to push this threshold down to 0.4, making great improvements upon previous results. However, there are still some orders of magnitude with the theoretical best exclusion limit, leaving room for further improvements. Cryogenic bolometers such as CRESST-III [101] have even lower energy thresholds, but suffer from smaller detector masses, resulting in less exposure. New detection principles as employed in the charge-coupled-device (CCD) experiments SENSEI [316] and DAMIC [317] with 0.1 kg to 1 kg target masses respectively, as well as a low-threshold Generation-2 SuperCDMS detector [318] and a superconducting aluminium cube [319] are currently being explored with the goal of improving upon the current LXe experiments [306]. The LXe experiment LBECA seeks to improve the sensitivity by through a significant background reduction for single or few electron signals [307], as indicated by the dashed purple line in figure 8.10. It can be observed that the projected sensitivity lies quite close to the ideal red dashed line. In the same plot the projected sensitivity of the SENSEI experiment is shown as a blue dashed line. The current limits from the first shallow underground run are still eight orders of magnitude weaker than the projected sensitivity [316].

## 8.7 Conclusion

The absence of a DM candidate in the SM, as well as the presence of non-zero neutrino masses is the main motivation for considering radiative seesaw models. With usual WIMP candidates having masses from several GeV to beyond the electroweak scale, we instead put our focus on right-handed neutrinos with a mass in the MeV to GeV range. These can provide an explanation for the observation of DM as well as generate neutrino masses at one-loop level when also extending the SM by a  $\mathbb{Z}_2$  odd scalar doublet that mixes with an additional scalar

singlet. If the mass of the lightest scalar is in the same MeV to GeV mass range, this model can additionally solve the cosmological missing satellite, cusp-core, and the too-big-to-fail problems.

We then performed a scan through the full parameter space of the SLIM model with MeV to GeV right-handed neutrinos to identify models that are in agreement with current relic density observations. The production of the correct neutrino mass differences and mixings was guaranteed by applying the Casas-Ibarra parameterization. We have shown the effects of the scalar mass splitting  $m_4$ , which has been shown to affect the relic density through the DM-electron couplings  $\lambda_8$  that are fixed through the Casas-Ibarra parameterization. These couplings varied between  $10^{-4}$  and the already sizable value of  $10^{-1}$ . Moreover, these models had masses mostly over a few MeV, making them in agreement with bounds from big-bang nucleosynthesis.

Due to the multitude of interactions between the SM leptons and the new particles in the dark sector, lepton flavour violating processes are common in these models, as was also shown when discussing e.g. the scotogenic model. These processes had not been analysed in this model yet. We showed that the usually most sensitive branching ratio, that of the  $\mu \rightarrow e\gamma$  process, leads to tight restrictions on the parameter space. In particular, this process puts strict upper bounds on the size of the DM-electron coupling  $\lambda_8^{e1}$ . The non-zero neutrino masses indirectly put a lower bound on the branching ratio through the Casas-Ibarra parameterization, so that the planned MEG upgrade is able to verify or exclude this model. Furthermore, we also included the  $\mu \rightarrow 3e$  as well as muon to electron conversion in titanium processes in a direct comparison. These processes are currently less restrictive than  $\mu \rightarrow e\gamma$ , but future experiments can reach similar or even slightly better sensitivities.

Since the DM particles do not couple to nuclei at tree level, no signal from nuclear recoil is expected in LXe detectors. The DM particles are leptophilic, hence we considered signals from electron recoils, which had already been suggested as a method to detect DM at the MeV to GeV scale. Even with the sizable couplings of up to  $\lambda_8^{e1} = 10^{-1}$  the cross section does not exceed  $10^{-46} \text{ cm}^2$  when low-energy, collider, cosmological and neutrino mass differences and mixing constraints were imposed. This can be attributed to the large mediator mass, which must be at least 98.5 GeV to be consistent with LEP result. The electron scattering cross section is suppressed by the mass to the fourth power. Upper bounds on the DM-electron coupling set by lepton flavour violation constraints reduced the cross section to an upper value of  $10^{-52} \text{ cm}^2$ .

The experimental expectations for the sensitivity to electron recoil of the XENON and other direct detection experiments were then studied. We compared exclusion limits for a 1 ton-year exposure with realistic background and energy threshold values to a theoretical estimate without backgrounds or detector thresholds. An experimental value for the cross section of  $10^{-36} \text{ cm}^2$  is more realistic than a few times  $10^{-41} \text{ cm}^2$  in the ideal case. Furthermore, the bounds are tighter for DM masses of a few 100 MeV rather than a few tens of MeV, due to energy threshold limitations. The recently published S2-only analysis from the XENON1T

experiment features a much lower energy threshold of 0.4 keV, and includes a simplified yet realistic background model. The obtained values of  $10^{-39} \text{ cm}^2$  for the electron recoil cross sections at masses of a few tens of MeV showed great improvement upon previous limits, and even approaches the theoretical sensitivity limit. This can be improved by exploring the S2-only analysis further, as well as increasing the exposure. In the future, XENONnT will be challenged by experiments employing different detection principles in the MeV mass range such as SENSEI, DAMIC-1K, SuperCDMS-G2+, or superconducting aluminium cubes. These values have to be taken with a grain of salt, as the first run of the SENSEI experiment is eight orders of magnitude above its projected sensitivity.

Some of the results presented in this chapter are model independent and can thus be generalised to models that feature a DM candidate similar to the right-handed neutrino in the MeV to GeV mass range that was considered here. It should not depend on the softly broken  $U(1)$  symmetry that was introduced here to stabilise the DM, as well as on the presence of the light scalar, as the main feature was the coupling of the DM candidate to the SM leptons via the charged component of the scalar doublet. As an outlook, the global  $U(1)$  could be promoted to a local symmetry, offering a rich, new phenomenology. A future direction of research could consider the effects spontaneous breaking of this symmetry in cosmological and collider searches [320]. Chapter 10 will focus on radiative seesaw models with a local  $U(1)$  symmetry.

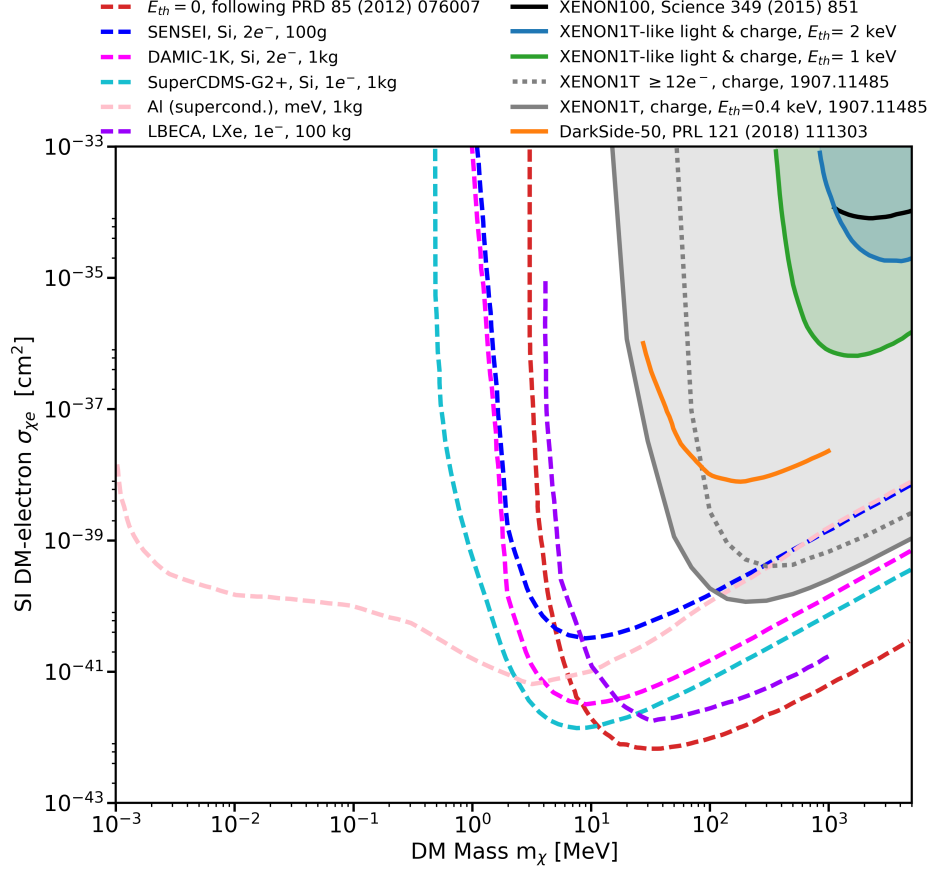


Figure 8.10: Experimental upper limits and estimated sensitivities for the DM-electron scattering cross section  $\bar{\sigma}_{\chi_e}$  in LXe, LAr and other detectors. Shown are the previously estimated sensitivity for a 60 kg-year exposure assuming only irreducible neutrino backgrounds and no detection thresholds (red dotted) [291] together with our sensitivity estimates for an assumed electron energy detection threshold of 2 keV (blue) and 1 keV (green), respectively, for a 1 ton-year exposure of XENON1T with realistic assumptions at 95 % confidence level (C.L.) [95]. Also shown are published limits from XENON100 (black) [304] and a charge-only analysis of XENON1T [126] (gray full line), both at 90 % C.L. The gray dotted line is a more conservative version of the latter limit considering that electron recoils below 186 eV (12 produced electrons) are undetectable, as the LXe charge yield  $Q_y$  has never been measured below these energies [126]. For comparison, we also show the ionisation-only limit in Argon from DarkSide-50 (orange full line) [305] and sensitivity projections (dashed lines) for SENSEI (blue), DAMIC-1K (magenta), Al (supercond.) (pink), SuperCDMS (cyan) [306] and LBECA (purple) [307].



## 9 Measurement of $^{220}\text{Rn}$ decays in gaseous xenon

In Chapter 2 we also discussed different detection methods that are used to directly detect dark matter. Experiments using dual-phase noble gas TPCs, such as XENON1T [95], LUX [116], and PANDAX-II [119] have put stringent bounds on the WIMP-nucleus spin-independent scattering cross section. In order to improve the sensitivity of such experiments, the background in the detector needs to be as low as possible. For the XENON1T experiment the biggest challenge is to purify the detector medium from contaminations. In particular, the  $^{222}\text{Rn}$  isotope is the largest source of background [321]. It is part of the  $^{238}\text{U}$  decay chain, and thus its parent nucleus  $^{226}\text{Ra}$  is present in the detector material. From there  $^{222}\text{Rn}$  can diffuse itself inside the xenon volume of the detector with its half-life of 3.8 days, where the beta decays of the daughter isotope  $^{214}\text{Pb}$  mimicks electronic recoil events [322]. Next to selecting detector materials that emanate relatively little radon, methods that are used to extract the radon from the xenon are by means of adsorption (e.g. with active charcoal [323]) or cryogenic distillation [324]. The XENON1T experiment uses the latter method, and a new pumping system for the upcoming XENONnT experiment has been developed [325].

The goal of this chapter is to present the measurement results to detect the presence of  $^{220}\text{Rn}$  through the  $\alpha$  decays in its decay chain. The choice of  $^{220}\text{Rn}$  over  $^{222}\text{Rn}$  is a pragmatic one, as the longest half-life in the decay chain of the former is only 10.64 hours. We will first describe the measurement setup that was used, after which the calibration of the photomultiplier tubes (PMTs) is discussed. Then the data from two different measurements are analysed and presented.

### 9.1 Setup

We made use of the Münster gas system, which is filled with gaseous xenon. A schematic overview of the setup is shown in Figure 9.3. For these measurements not all of the detectors and features of the system were used. We will only discuss the parts that were used in these measurements.

#### PMTs

For our measurements we used three R8520-406 SEL HAMAMATSU PMTs, which capture photons caused by  $\alpha$  decays. One of the PMTs was placed in a T-shaped frame, hence the

name T-detector. In this detector the PMT is located perpendicular to the gas flow. The other PMTs were placed opposite from each other in an X-shaped frame, which is accordingly named cross- or X-detector. These are the two leftmost detectors at the top of the gas system overview as shown in figure 9.3. Figure 9.1 shows a photo the T- and X-detectors. The gas flows through the vertical pipe from the bottom to the top of the picture, first passing the X-, then the T-detector.

Figure 9.2 shows two of the PMTs in their mounts that were used to place (and keep) them in place inside the detectors. The PMTs are connected to the base of the mounts with two wires, one is used to power the PMT, the other to carry the signal.

The main advantage of the cross detector over the T-detector is that the former contains two PMTs, and therefore one can require that only events where a coincidence between both PMTs is present are taken into account. This reduces the noise levels due to events caused by dark counts or other (electronic) noise sources. Throughout this chapter Channel 0 corresponds to the PMT in the T-detector, and Channels 1 and 2 to the PMTs in the cross detector.

### Qdrive

A crucial component in this system is the Qdrive, which is shown in figure 9.3 directly above Flow Control 2 (FC2). It pumps the xenon through the system. The flow control (FC) modules are used to monitor the gas flow through the system. Similarly, the P modules measure the pressure in the pipes. This becomes very relevant if the gas is led through some of the modules such as the getter or the thorium source, as they add resistance to the gas flow, locally increasing the pressure.

### $^{228}\text{Th}$ Thorium source

For our experiments we made use of the thorium source, which emanates the  $^{220}\text{Rn}$ . The source is separated from the rest of the gas system by the pneumatic valves (PV) PV10 and 12, as well as two manual valves directly next to the source. PTFE filters inside the source prevent the  $^{228}\text{Th}$  and  $^{224}\text{Ra}$ , so that only  $^{220}\text{Rn}$  and its decay products leave the source and enter the gas system.

### Getter

The getter contains material with which isotopes can be filtered out of the system. Atoms that interact with the getter material are absorbed. Being a noble gas, xenon is unaffected by this, and hence the getter can be used to filter impurities out of the xenon gas. One of the goals of our measurements is to determine whether the decay products of  $^{220}\text{Rn}$  are filtered out.



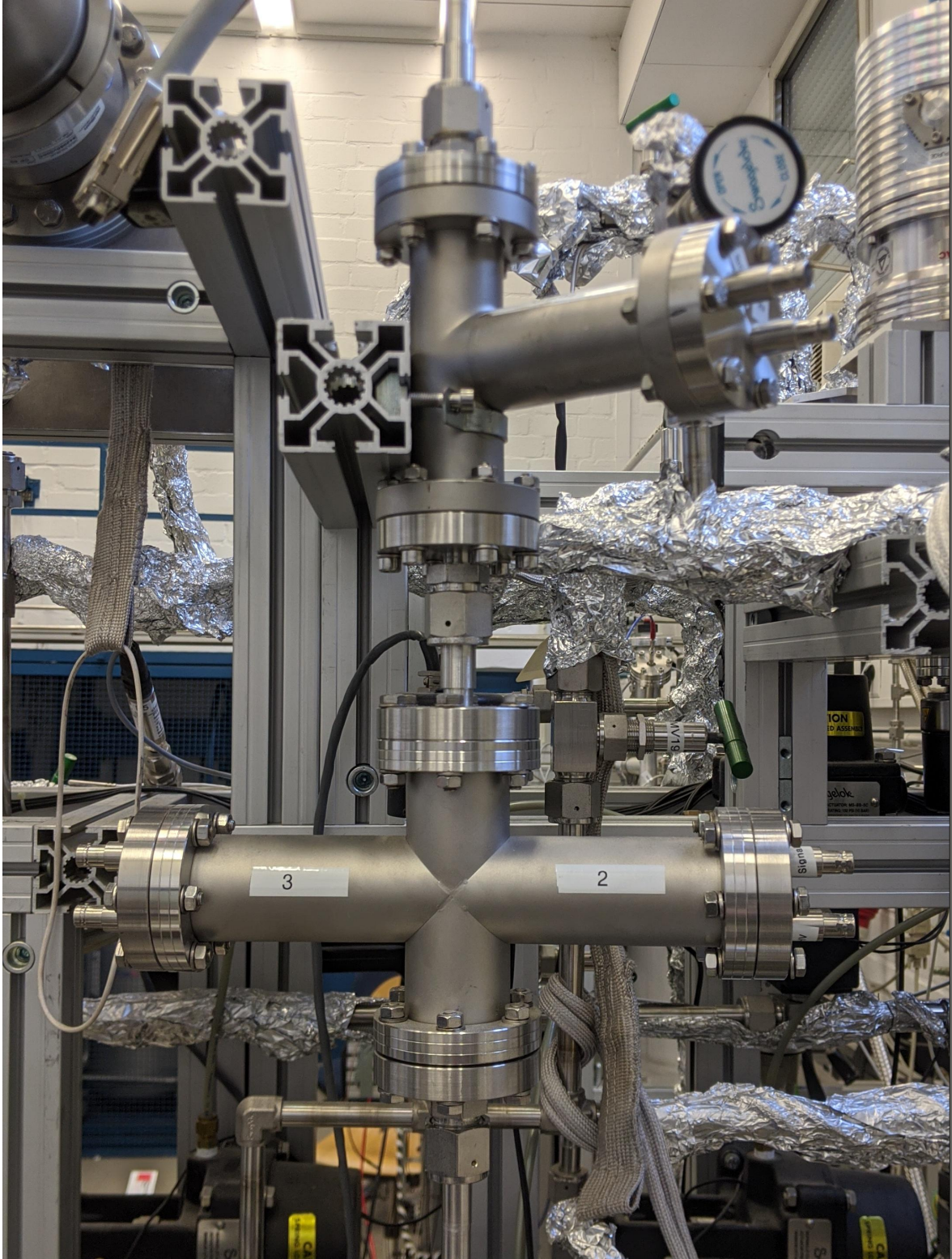


Figure 9.1: The T- and X- detectors in the Münster gas system. The T-detector can be seen at the top of the picture, the X-detector is directly below it. Not shown in this picture are the power- and signal-cables.

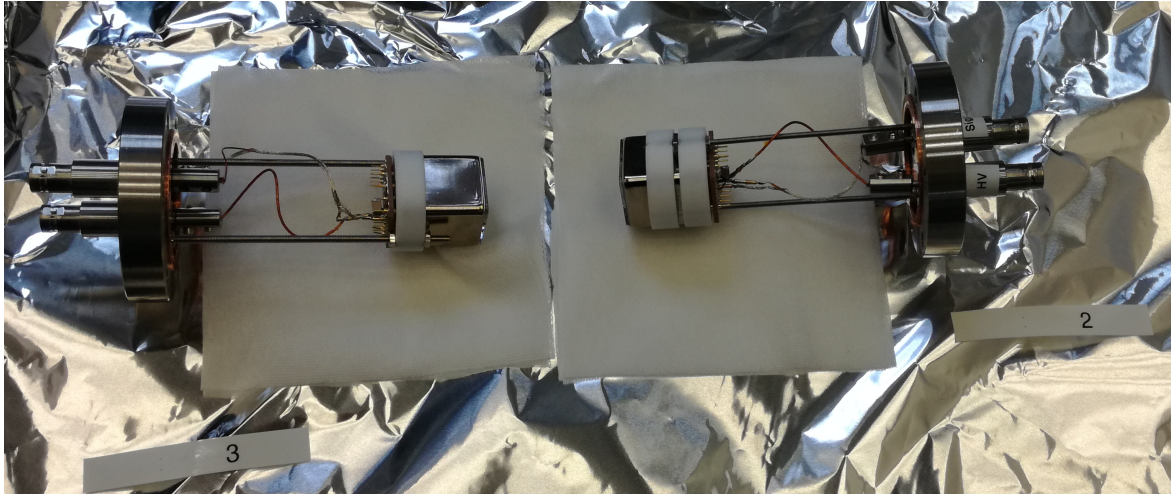


Figure 9.2: Two of the PMTs that were used in the measurements, both of which are placed in their mounts.

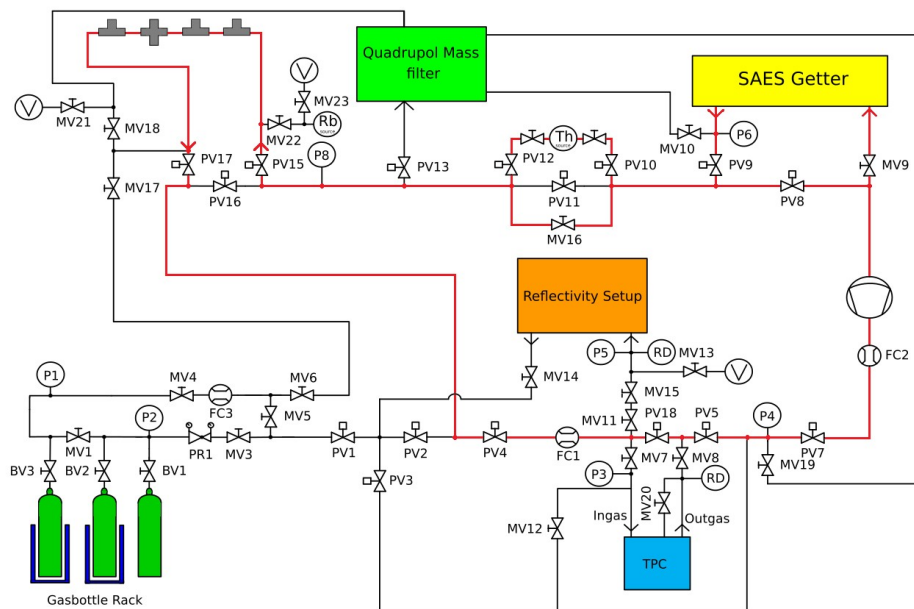


Figure 9.3: Schematic setup of the Münster gas system. The flow paths used in these measurements have been marked red.



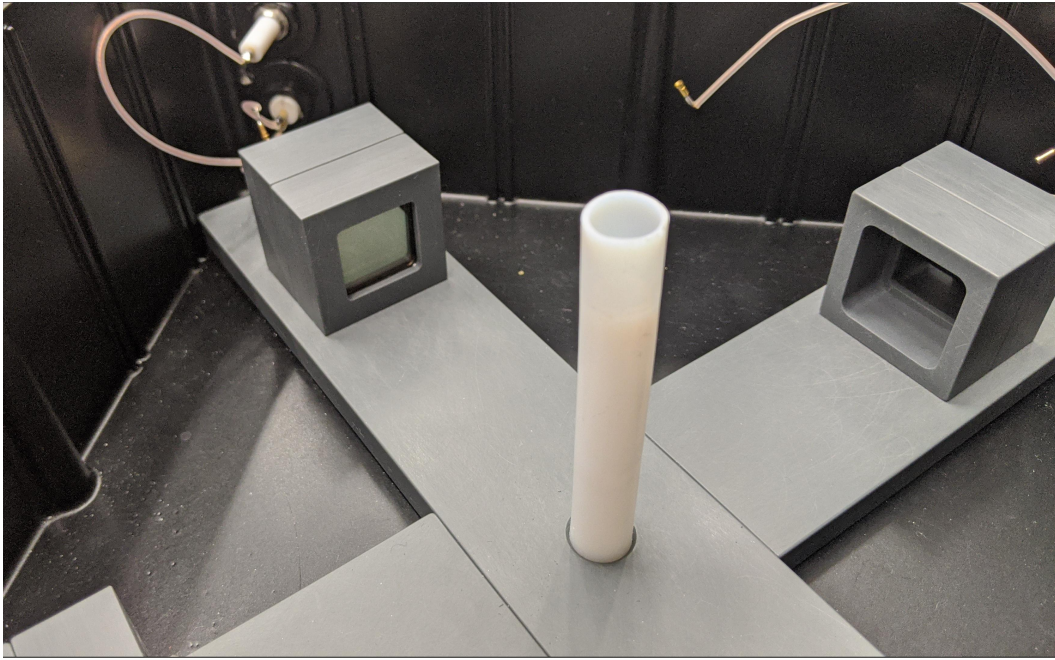


Figure 9.4: A PMT built into one of the mounts in the dark box. The PTFE diffuser is in the centre.

## 9.2 Gain calibration

In order to establish a relation between the number of analog to digital converter (ADC) counts given as signal by the PMTs and the energy which was deposited in the xenon through the decays that is independent of the detector geometry, one needs to know the gain of the different PMTs. The ADC used is the CAEN V1724, which has a 14 bit output in a 2.55 V peak-to-peak input range. For this purpose a gain calibration was performed using the dark box. This is a box whose interior is completely dark when shut. The PMTs that are to be calibrated are placed inside mounts in the corners of the dark box. As an example, figure 9.4 shows a single PMT mounted in one of the corners of the dark box. The light source is located in the centre of the dark box. It consists of an LED inside of a PTFE diffuser. In this calibration a UV LED was used.

The LED is triggered by a signal with a frequency of 100 kHz, whilst the ADC receives a trigger signal with a frequency of 1 kHz. The PMT output signals were first led to the 10x amplifier, before reaching the ADC. We take measurements of 512 samples, with a sample size of 10 ns. One series of measurements was taken at a PMT voltage of 800V, with the LED voltage ranging from 3.500V up to 3.700V in steps of 50 mV. A second series of measurements was taken for an LED voltage of 3.550 V, and a PMT voltage in a range from 700 to 850 V in steps of 50 V. For each of the PMT voltages, a measurement without LED was also taken in order to determine the noise distribution.

In order to determine the gain, a conversion between ADC counts and photoelectrons is made first. The relation used is:

$$N_{\text{pe}} = 0.137 * 10^{-3} \frac{t_s}{10 * R_{\text{ADC}} * Q_e}, \quad (9.1)$$

where  $t_s = 10$  ns is the sample time. The resistance of the ADC is  $R_{\text{ADC}} = 50\Omega$ .  $Q_e = -1e$  is the electron charge. The factor 10 in the denominator corresponds to the factor 10 from the amplifier. The factor  $0.137 * 10^{-3}$  comes from the peak-to-peak voltage of the ADC (2.55 V), divided by its 14 bit range of  $2^{14}$ . Only the part of the event that contains the LED signal is of interest, hence the five samples after the middle of the event are selected. These contain the peak from the LED signal, since the settings of the ADC were selected such that the event window is centred around the trigger. The samples are then summed to obtain the total amount of photoelectrons. This yields the gain.

### 9.2.1 Noise distribution

In order to differentiate photoelectron signals from noise, it is very important to have information about the noise coming from the system. In this section we will go into detail about the noise spectrum. Ideally, the PMTs in the dark box would measure no signals, and hence one would expect these events to form a sharp peak at 0 gain. An ideal, noiseless, measurement set-up only exists in a gedankenexperiment, therefore in practice this utopian peak at 0 gain will have a certain width and shape, to which we refer as the pedestal. This is due to the noise affecting the baseline of the PMTs. This can cause quasi-events, where one sees a non-zero signal due to a noise effect causing the signal to slightly deviate from the baseline level.

There can be several causes for this. A possible cause of this can be a fluctuating baseline of the PMTs. Moreover, since the PMTs are at room temperature, thermal electrons are emitted as well. These can be detected by the PMTs, leading to dark counts. Noise is not only created inside the PMTs, but can be introduced at a later stage as well. For example, if the signal cables are not isolated well, and are in contact with other objects, some of the charge might leak away to the ground or to other signal cables. Before the signal is processed in the ADC it first passes an amplifier. Both of these can be sources as noise as well. Under the assumption that the noise is symmetrically distributed around 0, one could describe the pedestal by a Gaussian distribution centered at 0.

In a perfect measurement where the LED is pulsed, one expects peaks in the gain spectrum for single, double photoelectron events (and so on). These peaks are at regular intervals, i.e. the position of the double photoelectron peak is at twice the gain of the single photonelectron peak. As was mentioned in the discussion about the noise, this is not obtained in practice and noise in the system affects the photoelectron events in the same way. Even so, the region around 0 gain is dominated by background signals, and the data in this region should look similar, regardless whether the LED is pulsed or not.

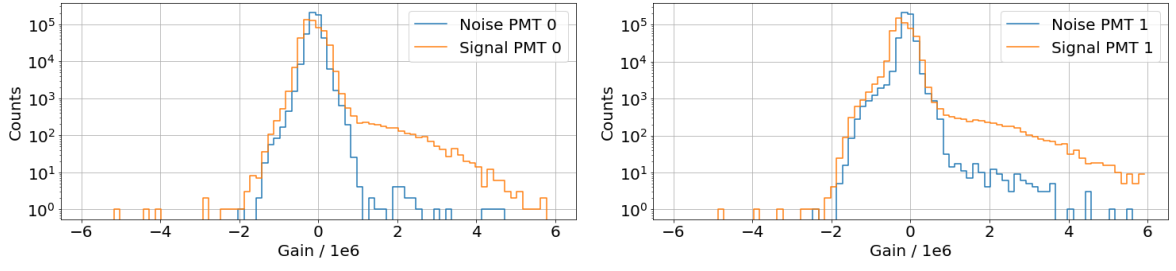


Figure 9.5: Gain histogram for a measurement at a PMT voltage of 800V and an LED voltage of 3.55 V. Shown are the background and data for PMTs 0 and 1.

Figure 9.5 shows the noise spectrum for PMTs 0 and 1, as well as the data for the measurement with an LED voltage of 3.55 V. In this measurement, the PMTs were operated at 800 V. It can be seen that the background for each of the PMTs is different. The background has a sharp peak around 0, but there is a “shoulder” on the left side of the peak which is more prominent for PMT1 compared to PMT0. This makes the background broader and non-Gaussian. From around a gain of  $0.5 \times 10^6$  upwards, the number of events in the signal where the LED was pulsed is much larger than off. This is where the (smeared out) photoelectron peaks are expected. At a first glance, the two data sets seem to overlap in the region around 0 gain, but upon further inspection it turns out that the shapes are slightly different. There are two things to notice. Firstly, the pedestal is broader for the data with LED than for the background data on both sides. But not only is it broader, it is also shifted. The top of the peak is slightly shifted towards negative gain. This is in contrast with the similar measurements found in the literature [326], which applied the same principles, and found a high but narrow pedestal.

A possible explanation for this can be that when the LED is switched on the signal oscillates around two symmetric offsets, but with an uneven probability. This can explain both the breadth of the peak as well as the shift of the top, when one considers a larger peak slightly shifted left, and a smaller peak shifted to the right, resulting in an asymmetric pedestal. The reason for this behaviour is not known.

Based on the previous discussion, the following function consisting of Gaussians can be an ansatz to fit to the data:

$$f(\mu) = g(x, a_{\text{bg}}, 0, \sigma_{\text{bg}}) + g(x, a_1, \mu, \sigma) + g(x, a_2, 2\mu, \sqrt{2}\sigma) + g(x, a_3, 3\mu, \sqrt{3}\sigma), \quad (9.2)$$

with the amplitudes of the Gaussians of the single, double and triple photoelectron peaks  $a_1$ ,  $a_2$ , and  $a_3$  following a Poisson distribution, which is given by

$$P(k; \lambda) = \frac{\lambda^k e^{-\lambda}}{k!}. \quad (9.3)$$

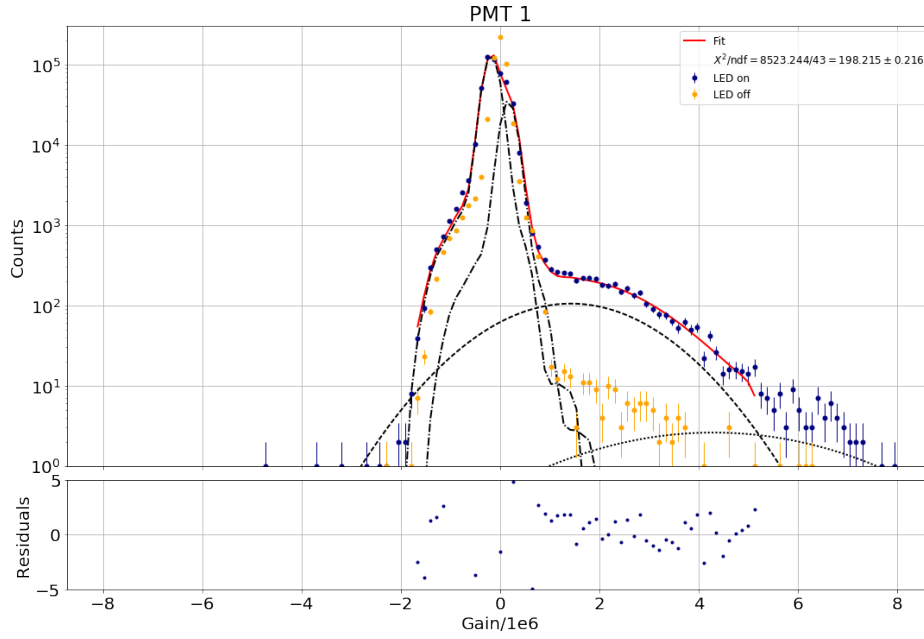


Figure 9.6: Gain fit for PMT 1, at a PMT voltage of 800V, with an LED voltage of 3.55 V.

The amplitudes can be varied with a relative factor  $d_*$ . The Gaussians themselves are defined as

$$g(x, a, \mu, \sigma) = \frac{a}{\sqrt{2\pi}\sigma} e^{-\frac{(x-\mu)^2}{2\sigma^2}}. \quad (9.4)$$

As was mentioned before, and as one can see from figure 9.5, the noise data looks clearly non-Gaussian. In order to describe the data in light of an oscillation between two symmetric offsets (but with different probabilities) we therefore do not fit single Gaussian peaks. In an attempt to describe this behaviour, we allow that each of the Gaussians in our fit shifted into the positive and negative direction on the x-axis, with an offset  $p_0$ . Due to the uneven probabilities the Gaussians that have been shifted by  $\pm p_0$  need not have the same amplitude. This asymmetry is captured by the parameter  $\tilde{a}$ , with the shifted Gaussians having amplitudes of  $(1 \pm \tilde{a}) * a$ . Furthermore, the Gaussians are convoluted with the noise data, which serves as a template for the noise signals. The idea behind this is that the way the noise “distorts” the noise signals in the same fashion as the signals when the LED is switched on.

Figure 9.6 shows the same data as the right plot in Figure 9.5, but includes a fit to the LED on data with the residuals shown below. To have sufficient statistics to apply a Poissonian error, only the bins that contained at least 10 counts have been used in the fitting. Some of the individual parts of the fit have been shown. One can see two peaks in the noise region around 0 gain. They have the same shape, but are shifted by the aforementioned factor  $\pm \text{pos0}$ . Furthermore, single and double photoelectron peaks have been shown. For the sake of clarity, only an unshifted Gaussian is shown for these peaks, but both are shifted analogously to the double peaks in the noise region.

Table 9.1: Fit parameter values from Equation (9.2) that were used in the fit shown in Figure 9.6.

	Name	Value	Para Error	Error+	Error-	Limit+	Limit-	FIXED
1	$a_{\text{bg}}$	3.109e+04	4.576e+01			1.000e+04	1.000e+09	
2	$\sigma_{\text{bg}}$	8.417e-02	4.790e-04			1.000e-02	3.000e+00	
3	$a_1$	5.331e+03	1.163e+03			5.000e+03	1.000e+07	
4	$\mu_1$	1.436e+00	5.992e-02			5.000e-01	1.800e+00	
5	$\sigma_1$	1.373e+00	4.847e-02			5.000e-02	2.000e+00	
6	$\lambda$	2.848e-01	4.116e-02			1.000e-03	3.000e-01	
7	rel $d_1$	3.186e-01	7.787e-02			1.000e-02	1.000e+00	
8	rel $d_2$	1.000e-02	1.142e-01			1.000e-02	1.000e+00	
9	rel $d_3$	9.999e-01	7.438e-01			0.000e+00	1.000e+00	
10	$p_0$	1.719e-01	2.780e-04			0.000e+00	7.000e-01	
11	$\tilde{a}$	-5.810e-01	1.761e-03			-1.000e+00	1.000e+00	

However, with a reduced  $\chi^2$  of around 198, this fit is far from good. The residual plot shows in which region of the fit the deviations are largest. This is especially the case in the region around 0 gain, where the fit is more than 5 standard deviations away from many of the data points, on one occasion even 49 standard deviations. There are two reasons why the errors are especially large in this region. The first being the different shape of the noise, as has been mentioned before, which becomes quite pronounced when the noise spectrum is convoluted with the fitted Gaussians. The second being that the relative error in each bin scales as  $\sim 1/\sqrt{n}$ , which only exacerbates the first issue, as most of the counts are in the noise region. Due to these factors, the fit function is not a suitable fit to the data. These issues to not only show up in figure 9.6, they are present in each of the three PMTs, as well as at different LED and/or PMT voltages. Therefore new gain calibration measurements are advisable.

## 9.3 Measurement setup

### 9.3.1 $^{220}\text{Rn}$ decay chain

$^{220}\text{Rn}$  is the isotope of radon that occurs in the decay chain of  $^{232}\text{Th}$ , the most common thorium isotope.  $^{232}\text{Th}$  decays via an  $\alpha$ -decay into  $^{228}\text{Ra}$  and two  $\beta^-$ -decays into  $^{228}\text{Ac}$ , and subsequently into  $^{228}\text{Th}$ , which is the isotope in the radioactive source that was used in these measurements.

Figure 9.7 shows the decay chain of  $^{228}\text{Th}$ . It decays to  $^{224}\text{Ra}$  with a lifetime of 1.9 years. The  $^{224}\text{Ra}$  decays to  $^{220}\text{Rn}$  with a lifetime of 3.6 days. We do not observe these  $\alpha$ -decays since the isotopes cannot leave the source due to the PTFE filters that prevents these nuclei from exiting the source. The  $^{220}\text{Rn}$  which is released into the system decays through two successive  $\alpha$ -decays into  $^{216}\text{Po}$  with a lifetime of 55.6 s, which then decays into  $^{212}\text{Pb}$  with a comparatively short lifetime of 0.16 s. With a lifetime of 10.64 hours,  $^{212}\text{Pb}$  has the longest

lifetime of all radioactive daughter nuclei in this decay chain [327]. It decays via a  $\beta^-$ -decay into  $^{212}\text{Bi}$ .

$^{212}\text{Bi}$  has a lifetime of 61 minutes and decays through two different decay channels. In 35.94% of the cases it decays via an  $\alpha$ -decay into  $^{208}\text{Tl}$ . With a half-life of 3.1 minutes the  $^{208}\text{Tl}$  decays via a  $\beta^-$  decay to the stable  $^{208}\text{Pb}$ . In 64.06% of the cases  $^{212}\text{Bi}$  decays into  $^{212}\text{Po}$  via  $\beta^-$  decay. The  $^{212}\text{Po}$  is very short lived, with a half-life of  $3 \times 10^{-7}$  seconds, whereupon it quickly decays into the stable  $^{208}\text{Pb}$  via an  $\alpha$ -decay.

Hence we can distinguish two parts in the decay chain: the decays before  $^{212}\text{Pb}$ , as well as the decays that happen after the  $^{212}\text{Pb}$  decay. Our aim is to detect  $^{220}\text{Rn}$  through its  $\alpha$ -decays, as more energy is released in these decays compared to  $\beta$ -decays. The energies that are released during the  $\alpha$ -decays are shown in Table 9.2.

Table 9.2: Table showing the  $\alpha$ -decay energies of the isotopes in the  $^{220}\text{Rn}$  decay chain [327]. The isotopes are listed in the order they occur.

Isotope	$\alpha$ -decay energy [MeV]
$^{220}\text{Rn}$	6.288
$^{216}\text{Po}$	6.778
$^{212}\text{Bi}$	6.051
$^{212}\text{Po}$	8.784

### 9.3.2 Measurement procedure

As a test, a measurement using a  $^{83}\text{Rm}$  source releasing  $^{83m}\text{Kr}$ . No increase in the event rate was seen after opening the source. This is likely due to the low activity of the source, as well as the fact that the energies involved in the decay of  $^{83m}\text{Kr}$  to  $^{83}\text{Kr}$  are 32.1 and 9.4 keV. These energies are very small compared to  $\alpha$ -decays that have energies the MeV scale.

On 26-02-2020 a measurement was started during which the  $^{228}\text{Th}$  source was opened. The initial flow path is the one shown in Figure 9.3, with MV9 and PV 9 closed in order to bypass the getter, and PV10 and PV12 closed to bypass the thorium source. Therefore we refer to this measurement as the getter bypass measurement. Gas circulation was started by switching on the Qdrive. This was left for about 120 minutes in order to have some data whilst the source has not been opened yet. The thorium source was opened by opening PV 10 and 12, as well as the two manual valves next to it. Then MV16 was closed to force the gas flow through the thorium source. Due to the resistance the thorium source adds to the gas flow, the Qdrive voltage was increased to keep the flow at a similar level. After 180 minutes, the source was closed by first opening MV16, and subsequently closing PV10, 12, and the manual valves next to the thorium source. Since the Qdrive did not have to pump against the resistance of the thorium source anymore, the voltage was lowered back to the original level. In order to measure the drop off in rate of the daughter nuclei of  $^{220}\text{Rn}$  the measurement was continued for around four more days.

On 03-03-2020 a measurement was started during which the  $^{228}\text{Th}$  source was opened, it was performed in the same fashion as the one from 26-02-2020, however this time the getter



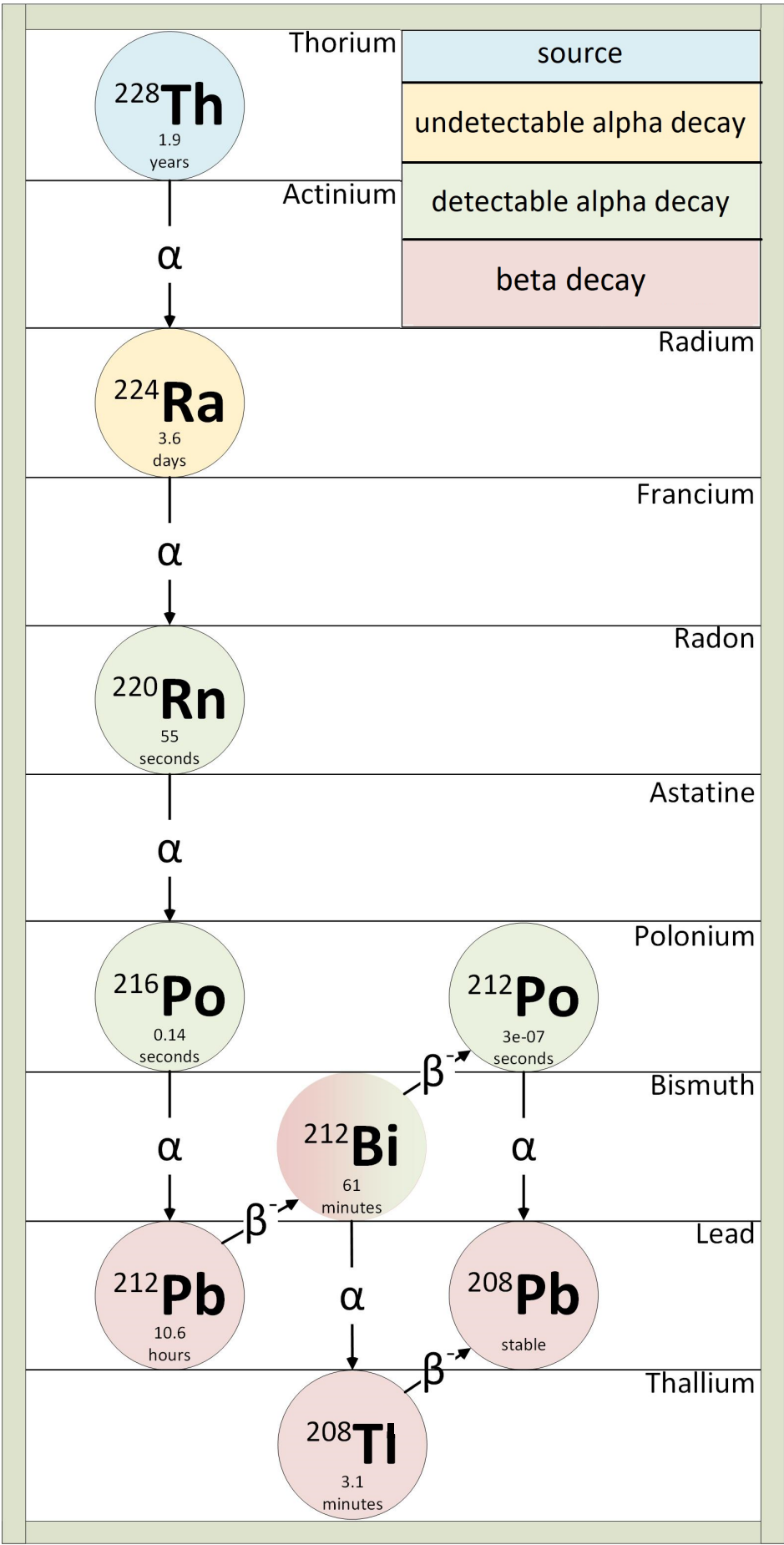


Figure 9.7: Decay chain of  $^{228}\text{Th}$ , including the lifetimes and decay mode(s) of each isotope. Source (with slight correction): [328]

was not bypassed. Thus this is referred to as the getter measurement. In this measurement PV8 was closed, whereas MV9 and PV9 were opened in order to lead the gas through the getter. This is also indicated in Figure 9.3.

## 9.4 Results

### 9.4.1 Getter bypass measurement results

Figure 9.8 shows the event rate that was measured over five days of measurements. In this plot one can clearly see the large increase in rate at the moment the source is opened, as well as the quick drop-off in rate the moment the source is closed. After the source is closed, one can see that over the next few days the rate drops back to the background level before the source was opened. In order to look at some details, Figure 9.9 shows the first 1000 minutes of this measurement. One thing to notice here is that there is a spike in the rate the moment the source was opened before the rate remains (relatively) constant. This feature can be attributed due to the fact that the source builds up amounts of  $^{220}\text{Rn}$  and its daughter nuclei whilst the source is closed. Upon opening the source, this build-up of nuclei is released into the system. After this, the radon gas from the source enters the system at a constant rate.

When the source is closed again,  $^{220}\text{Rn}$  decays quickly due to its short lifetime. Hence, one sees a quick drop-off in the measured rate. Due to the presence of daughter nuclei the rate does not drop back to the background level. Through two  $\alpha$ -decays  $^{220}\text{Rn}$  decays via  $^{216}\text{Po}$  into  $^{212}\text{Pb}$ . This last nucleus is with its half-life of 10.64 hours relatively long-lived compared to the other daughter nuclei. Hence, upon closing the source, there has not been enough time yet for an equilibrium to settle between the abundance of  $^{212}\text{Pb}$  and  $^{212}\text{Bi}$ . Because of this the abundance of  $^{212}\text{Bi}$  will increase at first. As we are not sensitive to  $\beta$ -decays, we do not observe the decay of  $^{212}\text{Pb}$  to  $^{212}\text{Bi}$ . Hence we need to observe the decays of  $^{212}\text{Bi}$  and its daughter nuclei. Therefore the rate increases slightly at first as the amount of  $^{212}\text{Bi}$  increases due to the  $^{212}\text{Pb}$  decays. Since the amount of  $^{212}\text{Bi}$  depends directly on the amount of  $^{212}\text{Pb}$ , we expect that the observed rate after the source has been closed should decrease proportionally to the amount of  $^{212}\text{Pb}$  i.e. with a life-time of 10.64 hours ( $= 638.4$  m).

Figure 9.10 shows the decrease of the rate from  $t = 1000$  m to  $t = 7000$  m. The data were fitted with a function of the form

$$\dot{N} = A * 2^{-t/t_{1/2}} + c, \quad (9.5)$$

where  $t$  and  $t_{1/2}$  are in minutes. Assuming a Poissonian error distribution, we obtained a least squares fit with the following values:

name	value	$\sigma$
$A$	30.6	0.17
$t_{1/2}$	645.2	2.1
$c$	1.924	0.005

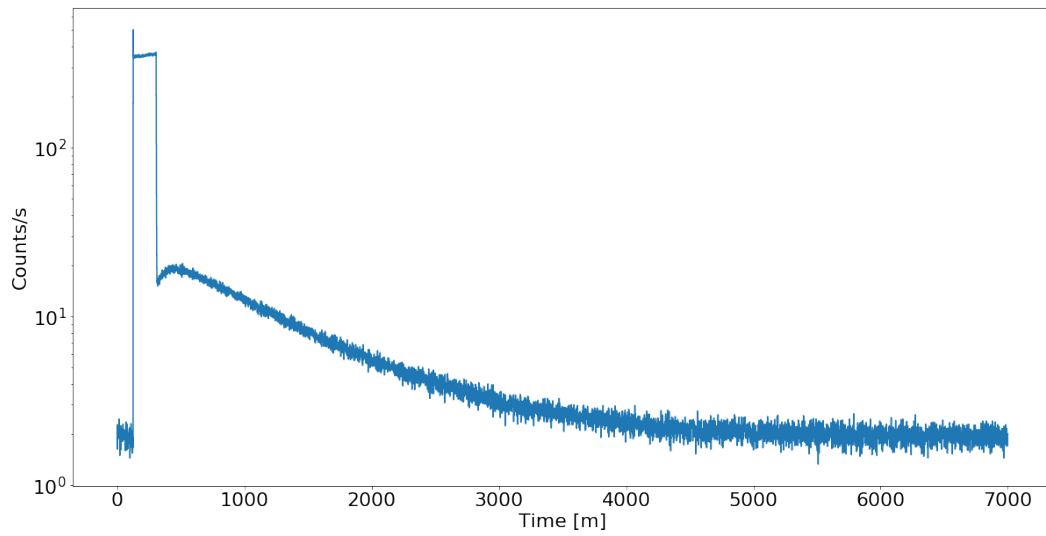


Figure 9.8: Count rate for the measurement started on 26-02-20.

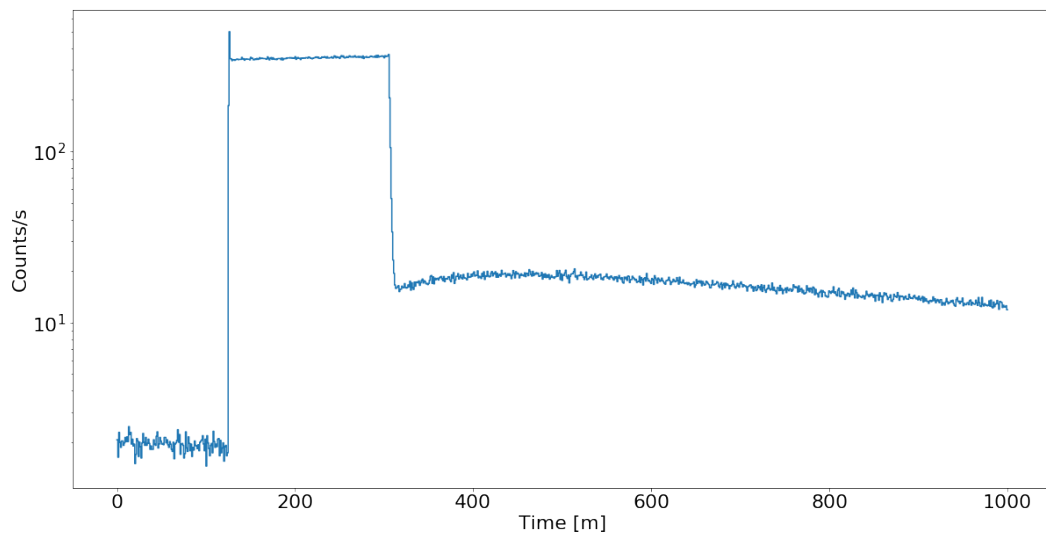


Figure 9.9: Count rate for the measurement started on 26-02-20, zoom-in on the first 1000 minutes.

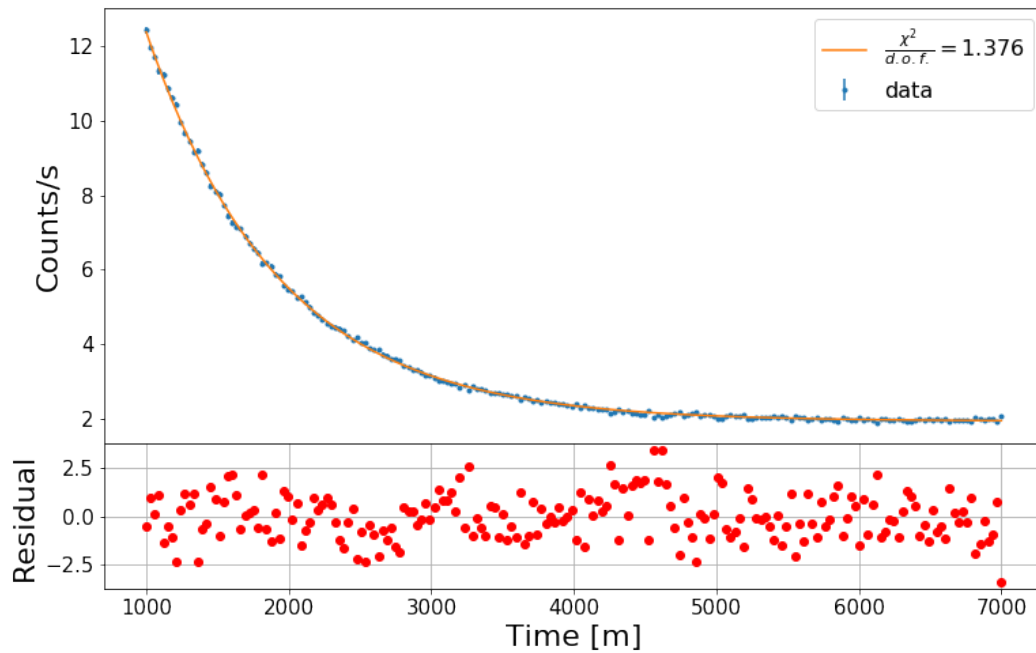


Figure 9.10: Count rate for the measurement started on 26-02-20 from  $t = 1000$  m, including fit and residuals.

The rate seems to drop off at a slightly slower rate compared to the half-life of  $^{212}\text{Pb}$ .

Figure 9.11 shows a histogram of the peak area for each of the three PMTs. In this plot, the different gains of the PMTs have not been taken into account, therefore the spectra are shifted relative to each other. Nonetheless one can see at a first glance that the spectra of channels 1 and 2 are very similar, as was expected for the two PMTs in the cross detector. Note that this histogram represents the absolute number of counts, not the rate on the y-axis.

#### 9.4.2 Time cuts

As a next step, let us consider the event rate at different times in the experiment. For this purpose we will only regard the events from the T-detector, i.e. channel 0. There are four main phases to be considered, namely the time pre source, with an open source, post source, and the time where the event rate has fallen back to the background level again, which we denote as “post source background”. This is illustrated in Figure 9.12 where the count rate is shown at each peak area during each of the four phases of the experiment. The first thing that is worth pointing out is that the rates of the time pre source and of the background long after closing the source match closely. However, there are some slight differences, since the pre source line falls off quickly compared to the post source background line. This is partly due to the statistics, as the total amount of events in the pre source timeframe is lower, but also small traces of radioactive isotopes cause tiny rates at higher peak area in the post source background.

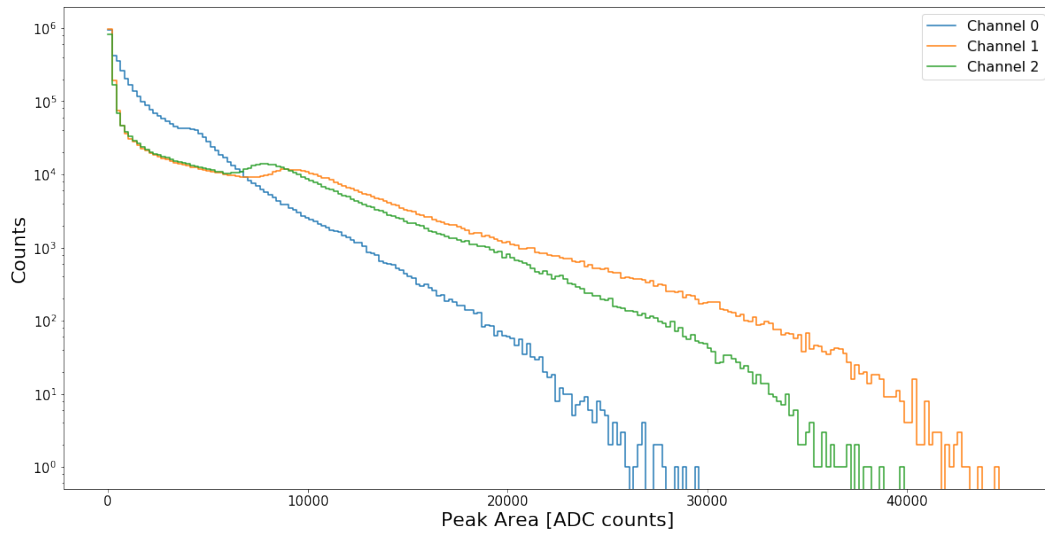


Figure 9.11: Histogram of the peak area for each of the detectors for the measurement started on 26-02-20.

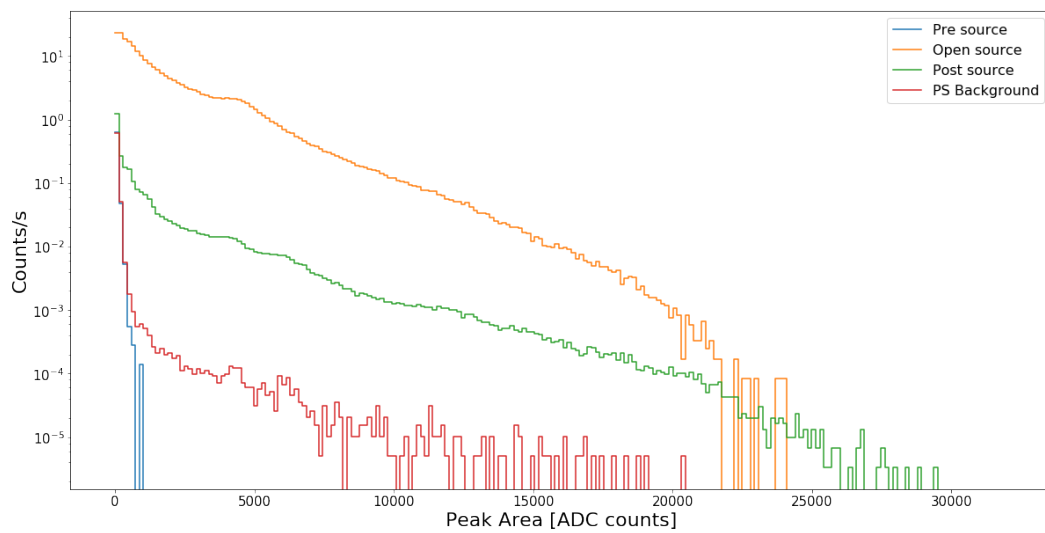


Figure 9.12: Histogram of the peak area count rate for Channel 0 (T-detector) for the different phases in the measurement from 26-02-20.

For each of the phases the count rate decreases with increasing peak area. Looking at the timeframe where the source was open, the event rate is greater across all peak areas. An interesting feature that is clearly visible is the bump slightly below 5000 ADC counts. This feature was already visible in Figure 9.11, but we can now clearly see that it originates from this phase. In section 9.4.2 we will discuss this feature further.

For the time-frame post source, we see that the rate is close to the background rates at low peak area. Furthermore, one can slightly discern two distinct peaks around 5000 ADC counts, very close in peak area to the bump visible for the line for the open source. This feature could not be seen in Figure 9.11, since it is obscured by the larger amount of events from the period with the source opened. Less profound, but still somewhat visible are two peaks around 1000 ADC counts. These are not visible in the data with open source.

### Alpha peaks

As mentioned in section 9.4.2, we will take a closer look at the peaks that are visible in the data in Figure 9.12. Let us repeat Table 9.2 showing the energies of the  $\alpha$ -decays. However, it

Table 9.3: Table showing the  $\alpha$ -decay energies of the isotopes in the  $^{220}\text{Rn}$  decay chain [327].

The isotopes are listed in the order they occur.

Isotope	$\alpha$ -decay energy [MeV]
$^{220}\text{Rn}$	6.288
$^{216}\text{Po}$	6.778
$^{212}\text{Bi}$	6.051
$^{212}\text{Po}$	8.784

is unlikely that all the energy released in these decays is detected in the PMTs. Therefore we make the ansatz that these decay events show up as Gaussians in a peak area histogram. The data set of the open source data should contain primarily  $^{220}\text{Rn}$  and  $^{216}\text{Po}$  decays. Because these decays are close in energy, this would result in a wide, single Gaussian which would agree with the observations of section 9.4.2. On the contrary, the decays of  $^{212}\text{Bi}$  and  $^{212}\text{Po}$  have energies that are clearly apart from each other, resulting in two separate Gaussians in the post source data. For both phases we fit the histogram data with a function containing an exponential background, two Gaussians corresponding to the two  $\alpha$ -decays in each phase, as well as an offset. The functions then look as follows:

$$\begin{aligned} N_1 &= A_1 * e^{-\lambda_1 x} + g(x, ga_1, \mu, \sigma_1, E_{\text{Rn-220}}) + g(x, ga_1, \mu, \sigma_1, E_{\text{Po-216}}) + c_1 \\ N_2 &= A_2 * e^{-\lambda_2 x} + g(x, ga_2, \mu, \sigma_2, E_{\text{Bi-212}}) + g(x, ga_3, \mu, \sigma_2, E_{\text{Po-212}}) + c_2, \end{aligned} \quad (9.6)$$

where the Gaussians are defined in the following way:

$$g(x, ga, \mu, \sigma, E_{X-123}) = \frac{ga}{\sqrt{2\pi}\sigma} e^{-\frac{(x-E_{X-123}\mu)^2}{2\sigma^2}}. \quad (9.7)$$

In this way the mean value of each Gaussian is located at a peak area that is proportional to the energy of the decay, with a proportionality factor  $\mu$ . Additionally, we assume that for

$N_1$  the amplitudes of both Gaussians were equal. This is based on the large difference in lifetime between  $^{220}\text{Rn}$  and  $^{216}\text{Po}$ . Based on the discussion in section 9.3.1, we expect that the  $^{216}\text{Po}$  formed through the  $^{220}\text{Rn}$  rapidly decays into  $^{212}\text{Pb}$ , and hence that the amount of events for both decays is equal. The functions  $N_1$  and  $N_2$  are fitted to the open source and post source data respectively in a combined fit. The resulting fit of this function to the data is shown in Figure 9.13, with the following parameters:

Name	Value	Para Error
$A_1$	1.532e+04	2.121e+02
$A_2$	1.246e+03	4.806e+01
$\lambda_1$	3.581e-04	8.734e-06
$\lambda_2$	3.144e-04	2.651e-05
$ga_1$	6.291e+05	2.046e+04
$ga_2$	6.827e+04	8.837e+03
$ga_3$	2.926e+04	6.005e+03
$\mu$	6.875e+02	9.733e-01
$\sigma_1$	4.784e+02	1.155e+01
$\sigma_2$	3.346e+02	3.222e+01
$c_1$	-5.226e+02	6.326e+01
$c_2$	-2.063e+01	2.131e+01

The two Gaussians in the open source data correspond to the  $^{220}\text{Rn}$  and  $^{216}\text{Po}$  decay signals. Since their decay energies are close to each other, this results in a wide, single peak. For the post source data, the two different peaks can clearly be distinguished. The ansatz that the means of the Gaussians are proportional to the decay energies of the respective isotopes seems to put the Gaussians at the same location as the peaks in the data. As a critical side remark, one can notice the values of  $c_1$  and  $c_2$ , which are both negative. One might wonder why these are negative, as the number of counts tends to  $c_1$  and  $c_2$  for large peak area, but a number counts smaller than 0 is unphysical. For this we point back to Figures 9.11 and 9.12. In these figures the number of counts or count rates respectively decrease exponentially, but there is a noticeable sharper decline at larger peak area. The takeaway from this discussion is that the fit function that was used is only applicable to this region around the  $\alpha$ -peaks, but should not be used to describe regions with different peak areas. But since we are interested in the  $\alpha$ -decay signals, this does not affect our results.

### Cross-detector

Thus far, for most of the analysis only the T-detector has been considered. However, the cross detector can offer a much better picture, since one has the ability to only select events which were seen in both PMTs. This reduces the background rate, since noise signals in a single PMT are excluded. The T- and cross detector should be independent from each other, since they are at different locations inside the gas system. If the T- and cross detector consistently trigger simultaneously, it would point towards a mistake in the setup or electronics.

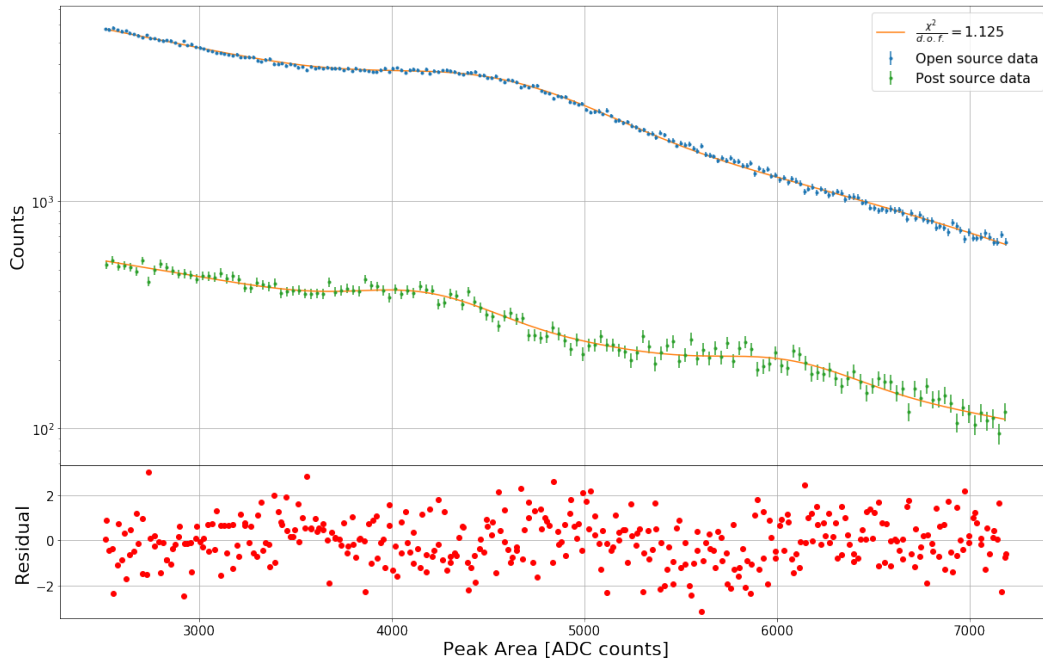


Figure 9.13: Histogram of the peak area for Channel 0 (T-detector) for the open- and post source data in the region of the alpha peaks. The fit to the data is included as well. 26-02-20

As an illustration, Figure 9.11 has been remade, this time only the events in which both PMTs in the cross detector measured a signal were selected, as can be seen in Figure 9.14. The graphs of Channels 1 and 2 still look very similar (though shifted because of the differing gain in the PMTs), but the amount of events from the T-detector has been reduced to a tiny amount at small peak areas. Moreover, there are less counts in the region below 1000 ADC counts. This indicates that many of these events were just noise (possibly pile-up). Figure 9.15 is likewise a remake of Figure 9.12, though the differences between these two figures are not as stark, since we only consider the events of a single PMT and not of both cross detector PMTs simultaneously.

As previously mentioned, the graphs of Channels 1 and 2 look similar, but are slightly shifted due to different gain of the PMTs. Because a meaningful gain calibration could not be performed, a manual change was made to the peak area in order to be able to compare the data of the two PMTs. In particular, scaling the peak area of Channel 2 by a factor of 1.155 seems to make the spectra of both detectors overlap. This is a shaky and ad hoc solution. The normal procedure would be to scale the spectra relative to the PMT gains. Figure 9.16 shows again the count rates per adjusted peak area for each of the phases in the measurement. This time the peak areas of both PMTs within a single event were summed. The formulation adjusted peak area is chosen because of the manual change to the peak area of the events of Channel 2.

There are several differences when comparing Figures 9.15 and 9.16. First of all, the count rate drops off less for higher peak area for the combined data than for the single



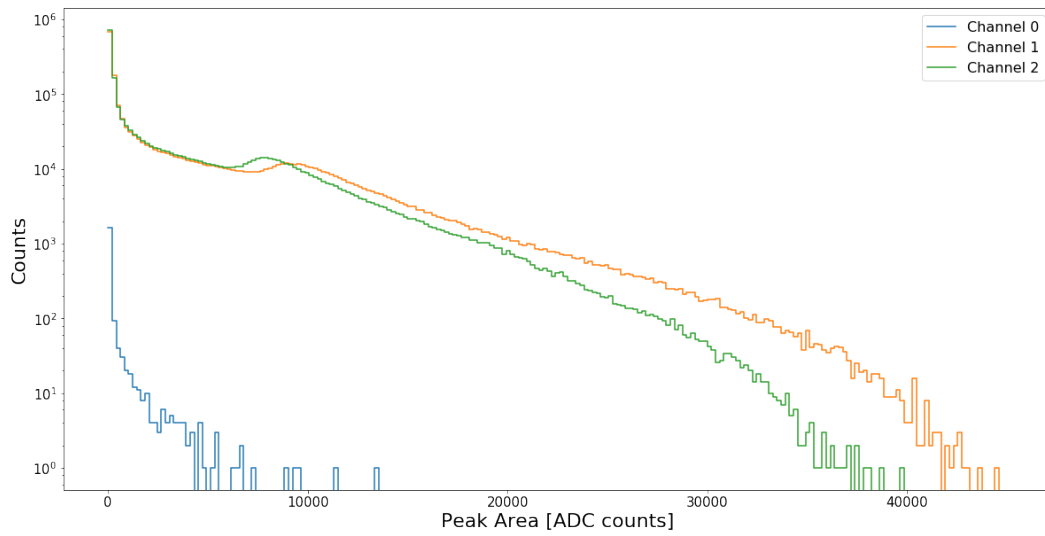


Figure 9.14: Histogram of the peak area for each of the detectors for the measurement started on 26-02-20. Only the events in which both Channel 1 and Channel 2 (cross detector) were triggered were taken.

PMT. Furthermore, the peaks that are visible in the data for a single PMT are clearer when combining the events of both cross detector PMTs. This is to be expected since the part of the signals of one decay might not all end up in a single PMT, but might reach the opposite PMT instead. However, the peaks also seem to be broader, especially the peak around an adjusted peak area of 32000 ADC counts in the post source data in Figure 9.16.

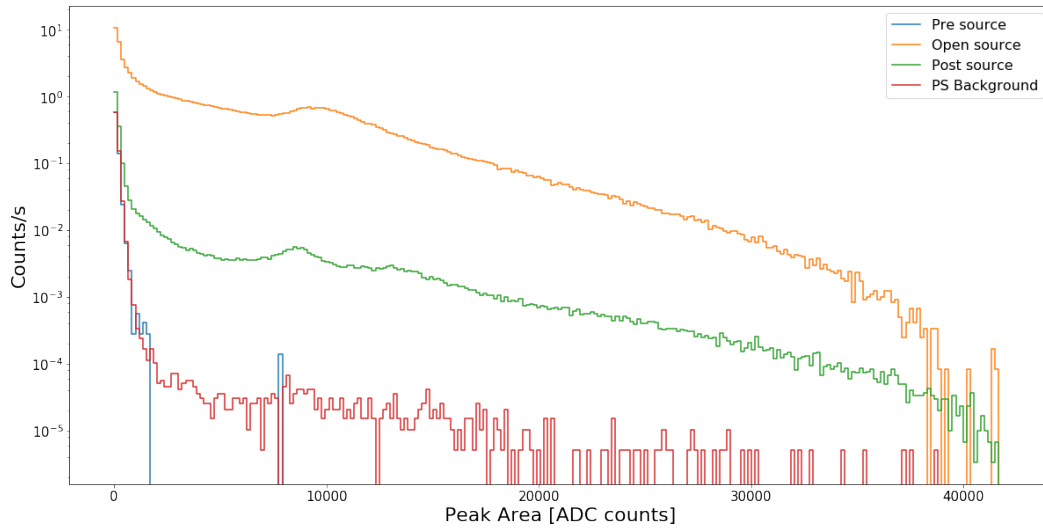


Figure 9.15: Histogram of the peak area count rate for Channel 1 (in the cross detector) for the different phases in the measurement from 26-02-20.

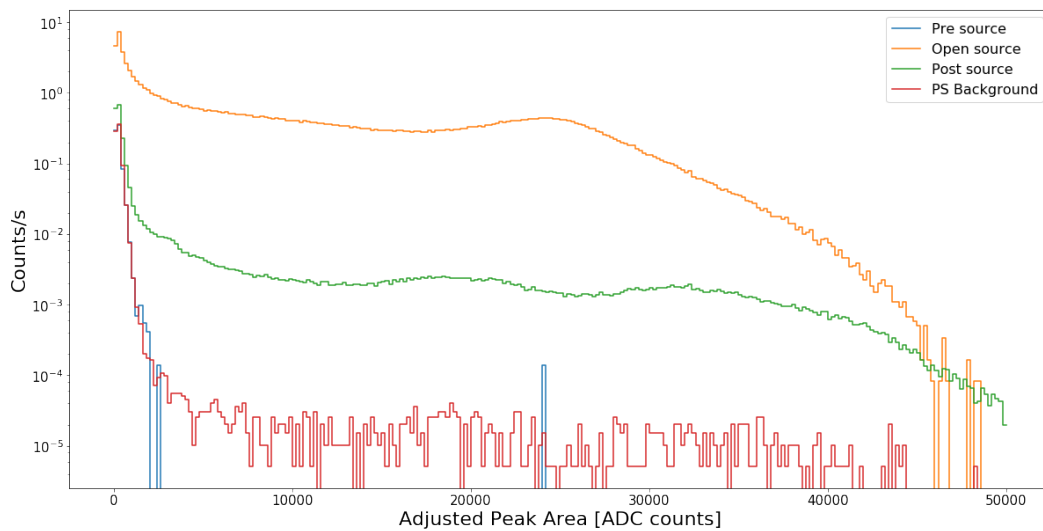


Figure 9.16: Histogram of the adjusted peak area count rate for Channel 1 and 2 combined for the different phases in the measurement from 26-02-20.

### Alpha peaks

Similar to the discussion of the alpha peaks in the discussion of the T-detector data, equation (9.6) was fitted to the data in the region of the alpha peaks again. The result can be seen in Figure 9.17. The fit is not good, the clearest deviation can be seen in the open source data. The two alpha peaks in the post-source data can be distinguished, but only one of the two fitted peaks fits the data. In order to investigate this behaviour more closely, one can just take the open-source data, and only fit  $N_1$  of equation (9.6). This was done for the combined data of PMTs 1 and 2, as well as just the data of PMT 1. The results are shown in Figures 9.18 and 9.19 respectively. In both cases the shape of the fit does not seem to match with the shape of the peak, whereas for the T-detector data the peaks could be described by Gaussians, see Figure 9.13.

Turning to the post-source data, things change. As can be seen in Figure 9.20, the position of the fitted peaks is indeed off, similar to Figure 9.17. The same fits are shown for the data of the single PMTs in Figures 9.21 and 9.22 for PMT 1 and 2 respectively. These fits look slightly better, however it is now the right peak which is a bit off, though less than the left peak in the combined PMT data was.

### Summary

Using the Münster gas system, we let gaseous xenon flow through a  $^{228}\text{Th}$  source emanating  $^{220}\text{Rn}$ . The gas was then led to our measurement setup consisting of 3 PMTs, one single PMT in the cross detector, whereas the other two were placed oppositely from each other in the cross detector. We observed a clear increase in event rate after opening the source, which quickly dropped off to a lower level after closing the source. Thereafter the event rate decreased slower than was expected from the half-life of  $^{212}\text{Pb}$ . Separation of the data based on the phase of the measurement uncovered peaks that were not visible in the complete data set. Using a fit with Gaussians located proportional to the decay energies of the  $\alpha$ -decays we were able to describe the peaks in the T-detector data. However, this approach did not work for the X-detector data, neither for the individual PMTs nor for the combined signals.

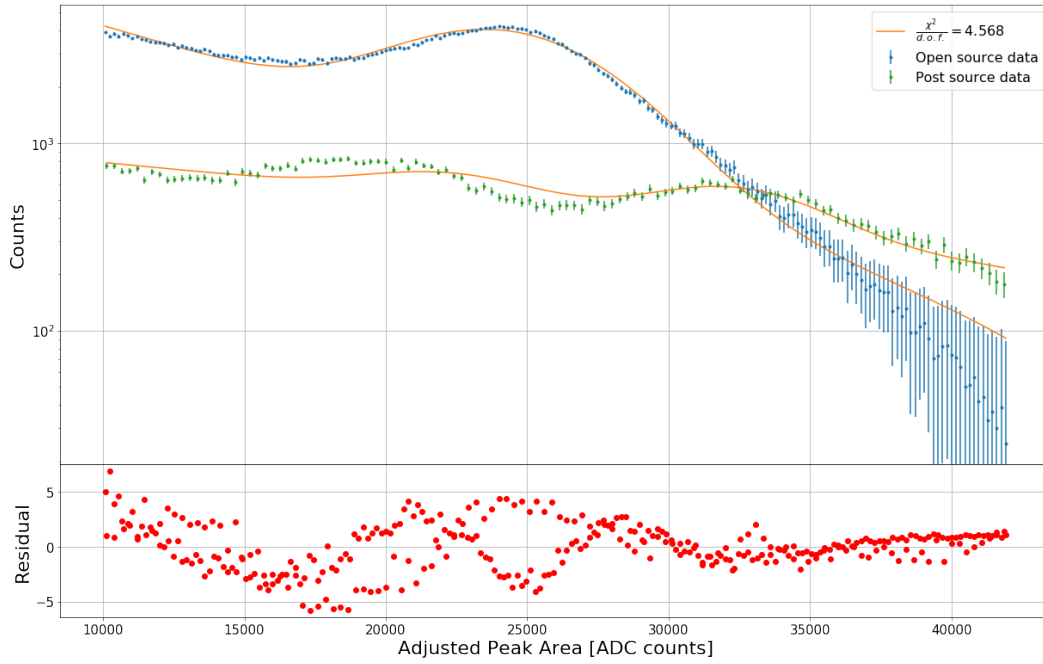


Figure 9.17: Histogram of the peak area for Channels 1 and 2 (X-detector) for the open- and post source data in the region of the alpha peaks. The fit to the data is included as well. 26-02-20

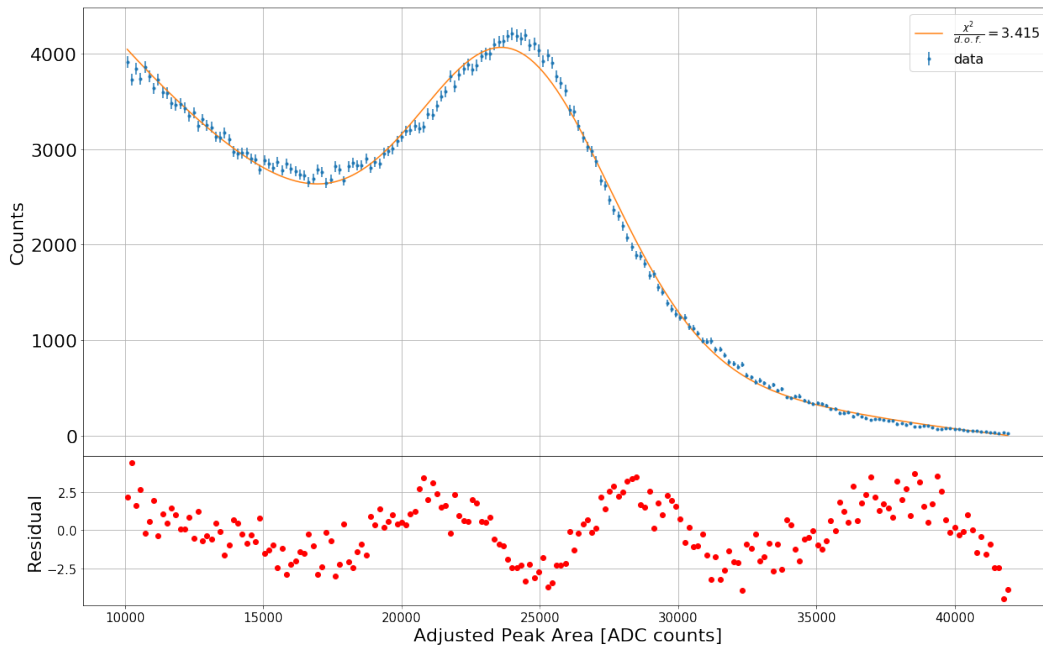


Figure 9.18: Histogram of the peak area for Channels 1 and 2 (X-detector) for the open source data in the region of the alpha peaks. The fit to the data is included as well. 26-02-20

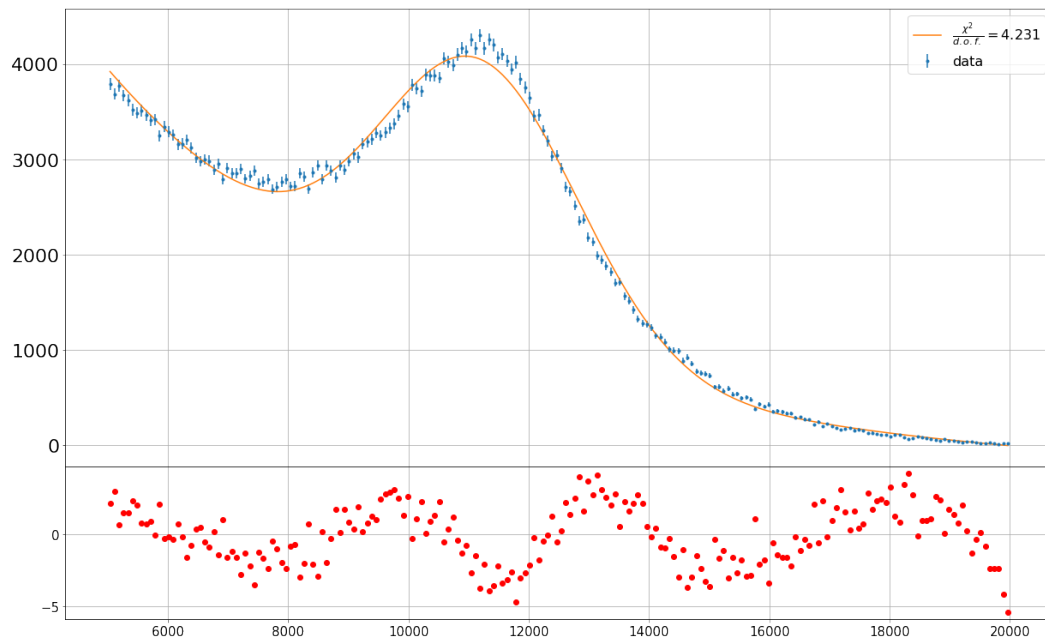


Figure 9.19: Histogram of the peak area for Channel 1 (X-detector) for the open source data in the region of the alpha peaks. The fit to the data is included as well. 26-02-20

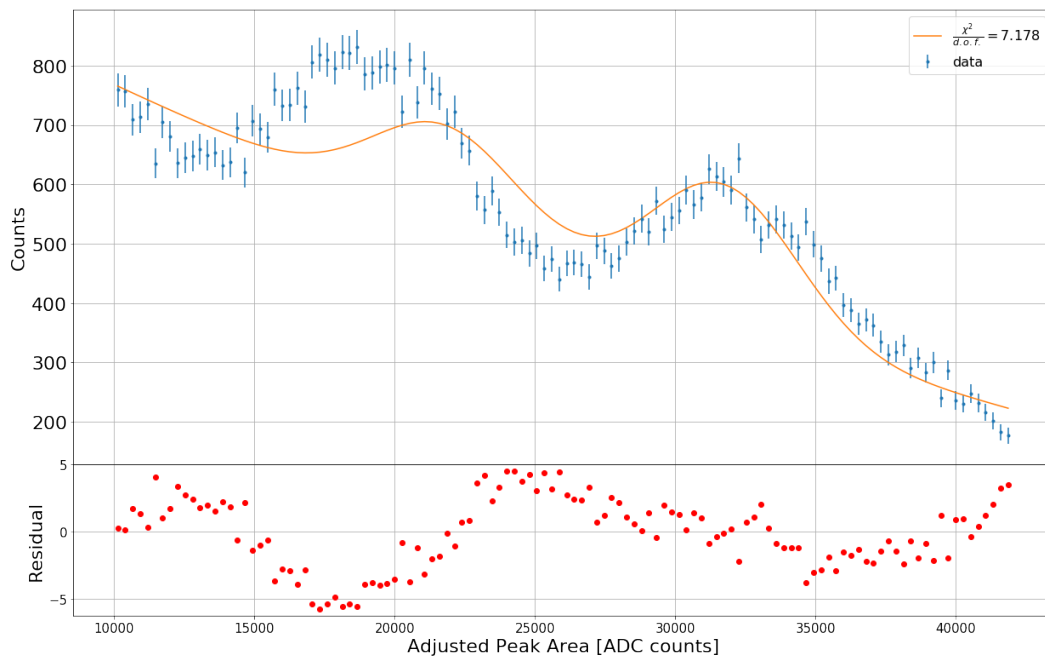


Figure 9.20: Histogram of the peak area for Channels 1 and 2 (X-detector) for the post-source data in the region of the alpha peaks. The fit to the data is included as well. 26-02-20

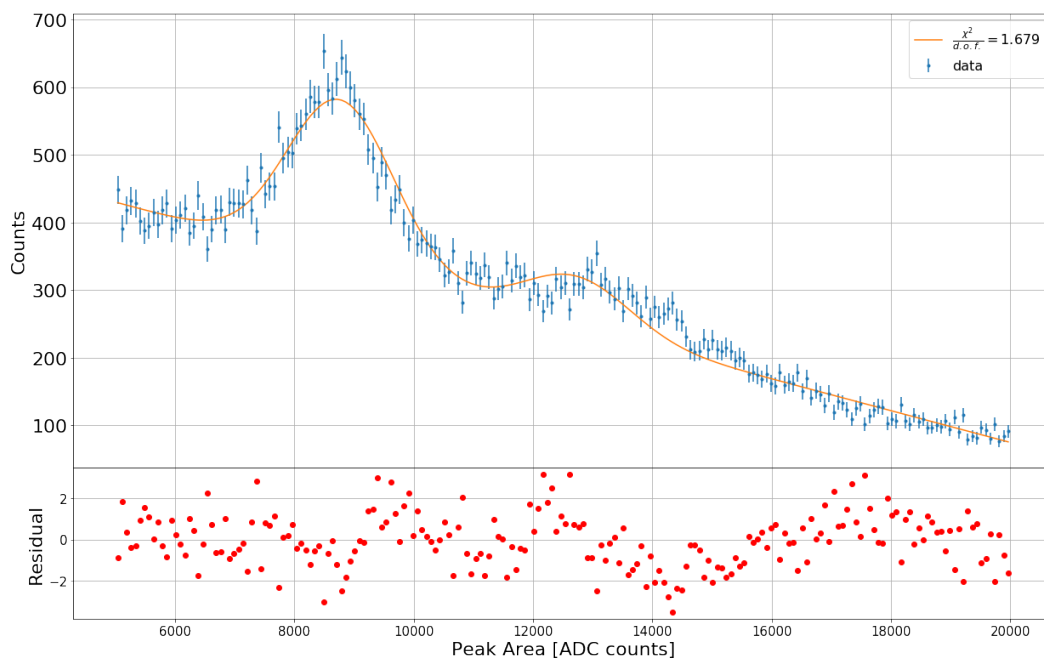


Figure 9.21: Histogram of the peak area for Channel 1 (X-detector) for the post-source data in the region of the alpha peaks. The fit to the data is included as well. 26-02-20

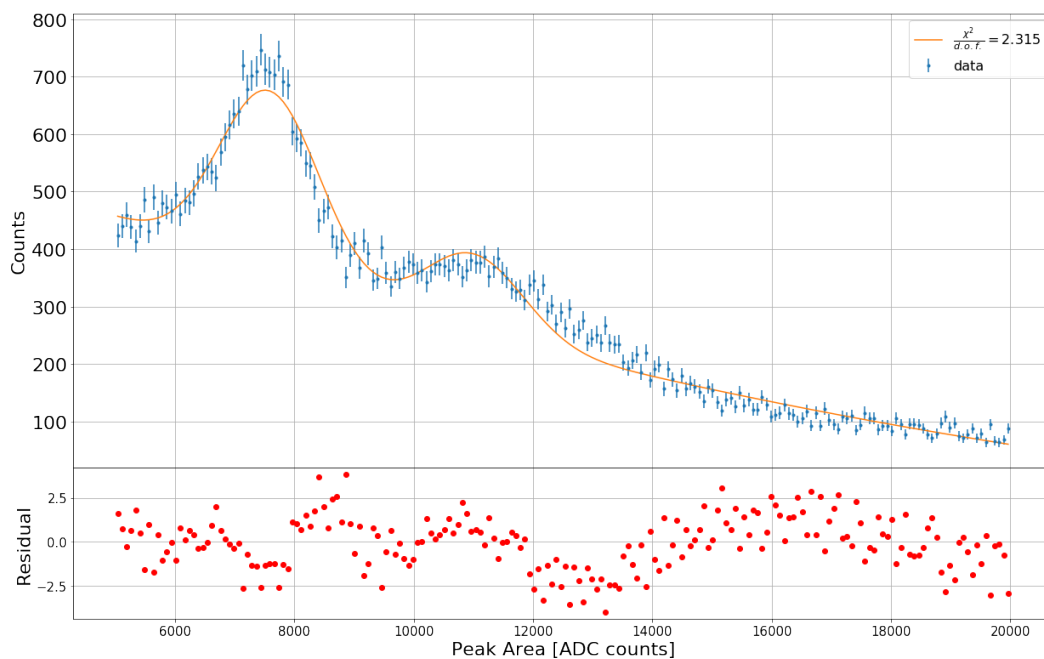


Figure 9.22: Histogram of the peak area for Channel 2 (X-detector) for the post-source data in the region of the alpha peaks. The fit to the data is included as well. 26-02-20

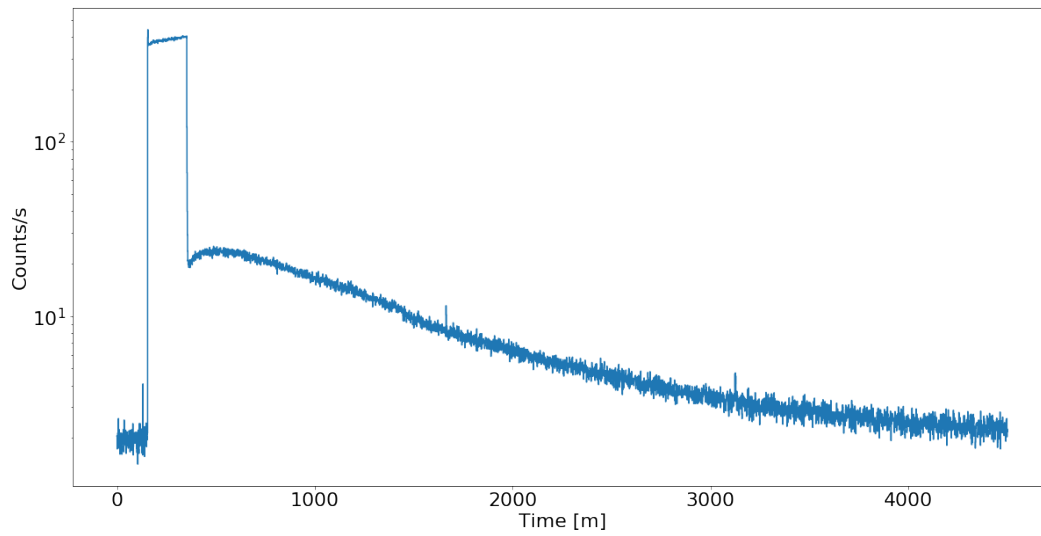


Figure 9.23: Count rate for the measurement started on 03-03-20.

### 9.4.3 Getter measurement results

The measurement was done with the getter included. The getter should function as filter for the daughter nuclei of  $^{220}\text{Rn}$ . If this is the case, then the event rate should fall off quicker than the rate that was measured in the measurement without the getter as radioactive nuclei are filtered out of the system. In particular, the  $^{212}\text{Pb}$ , which is relatively long-lived, can be filtered by the getter as it is present in the system for a long time. In such a scenario, the signals of the  $^{212}\text{Bi}$  and  $^{212}\text{Po}$  decays will become much weaker. The  $^{220}\text{Rn}$  and  $^{216}\text{Po}$  decays are expected not to be influenced by the getter, since the gas that has passed the source will pass the PMTs first, before reaching the getter. If we look at Figures 9.23 and 9.24, we see that they qualitatively look similar to Figures 9.8 and 9.9. However, there is a slight bend in the event rate around  $t = 1400$  m. At this point the flow in the system dropped, and as a consequence the count rate decreased slightly. It should also be noted that the measurement time is shorter compared to the 26-02-2020 measurement. This means that there is less data on the period where the event rate has fallen back to background levels, resulting in slightly worse statistics.

Focusing on the decrease of the event rate after the source has been closed, this drop becomes clearly visible. Both in the graph of the data with the fit itself and in the plotted residual there is quite some variation just before  $t = 1500$  m. For the fitted function as in (9.5), we obtain the following values:

name	value	$\sigma$
$A$	46.61	0.20
$t_{1/2}$	579.7	1.8
$c$	2.105	0.009

The half-life is now clearly lower than the  $645.2 \pm 2.1$  m that was obtained from the 26-02 measurement without the getter, but this result cannot be considered valid given the large

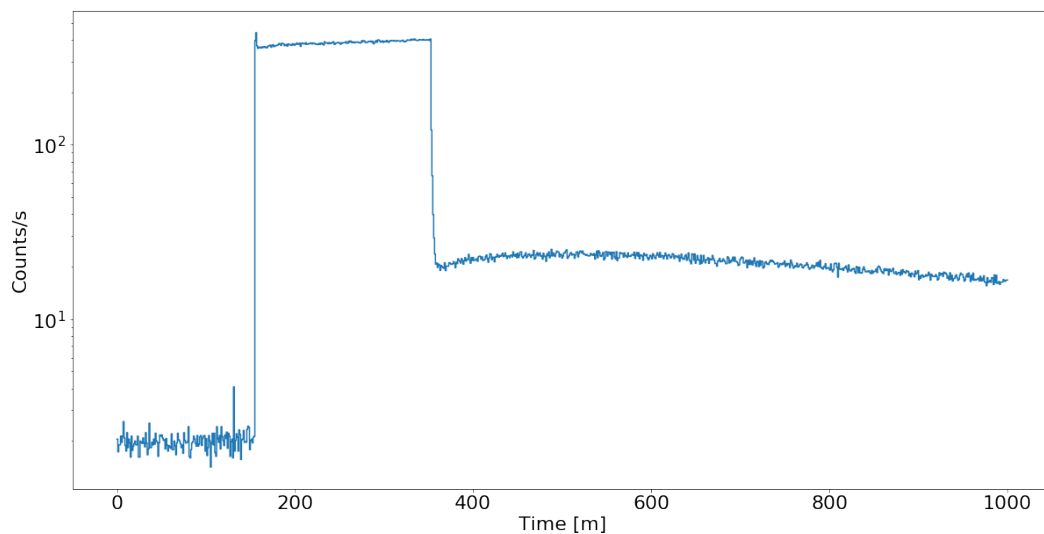


Figure 9.24: Count rate for the measurement started on 03-03-20, zoom-in on the first 1000 minutes.

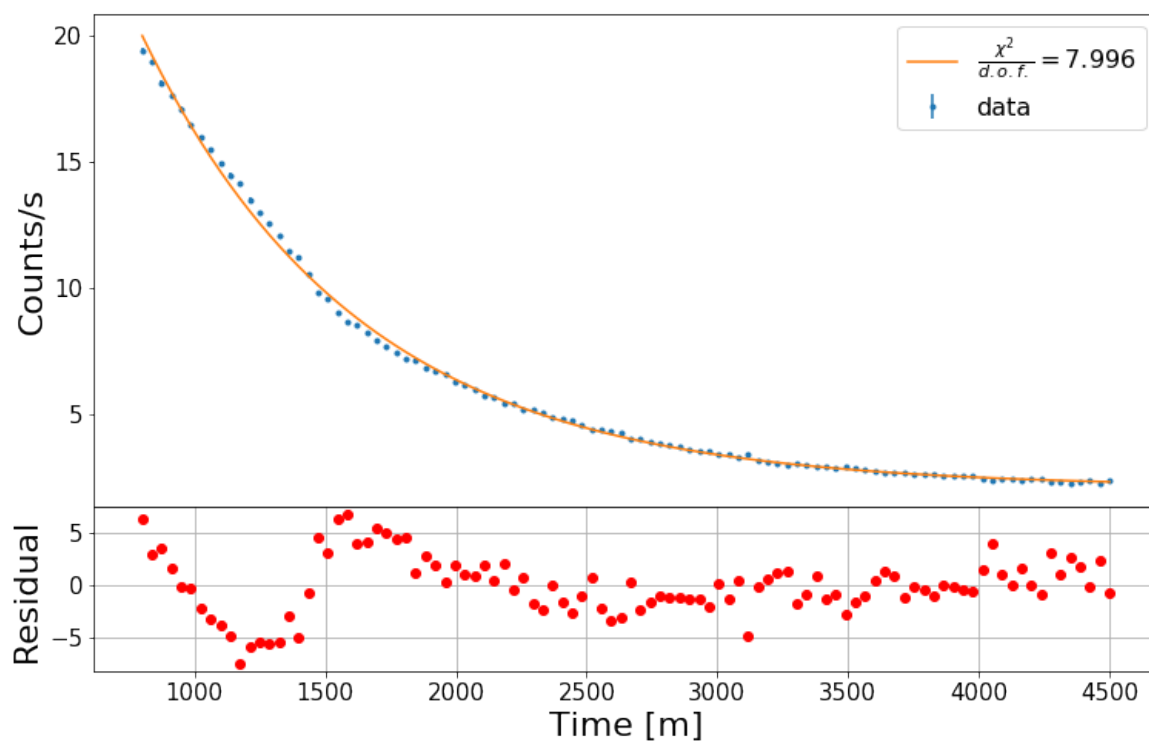


Figure 9.25: Count rate for the measurement started on 03-03-20 from  $t = 800$  m, including fit and residuals.



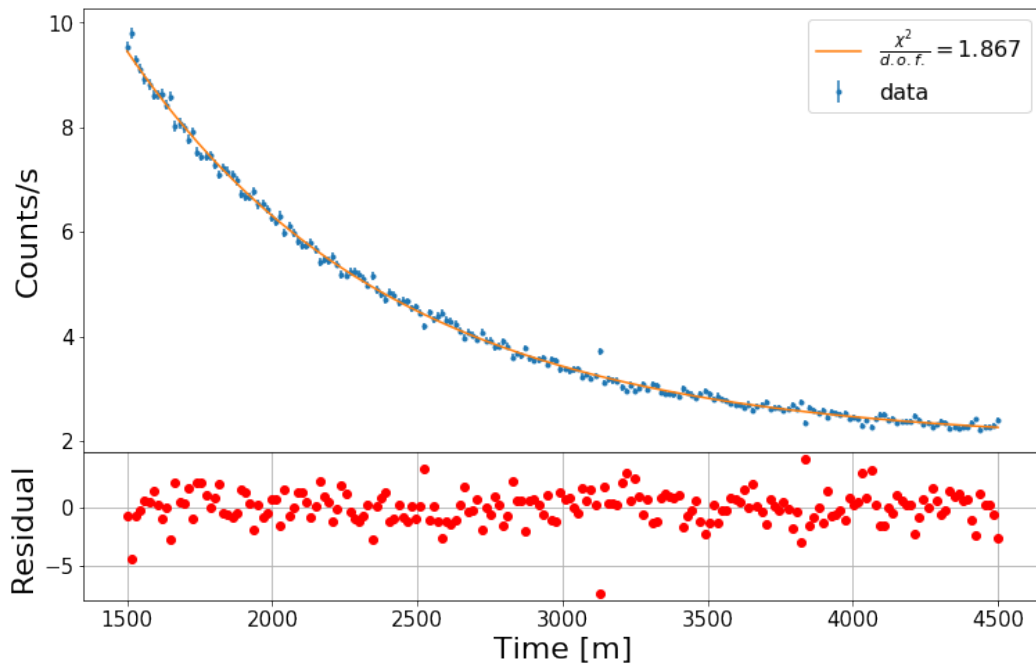


Figure 9.26: Count rate for the measurement started on 03-03-20 from  $t = 1500$  m, including fit and residuals.

deviations of the fit to the data. Therefore the same function was fitted again, but this time only the data points from  $t=1500$  m were taken into the fit. This gave the following results:

name	value	$\sigma$
$A$	38.52	0.53
$t_{1/2}$	633.7	4.8
$c$	1.989	0.014

The lifetime that is obtained from this fit is much more in line with the one from the 26-02 measurement. It seems that even though the gas was led through the getter, the event rate still decreases at roughly the same rate as the amount of  $^{212}\text{Pb}$ . If the getter filters out the lead, the rate should drop more quickly. The absence of this decrease cannot be attributed to the nuclei depositing themselves on the wall in the system. In that case, the event rate visibly drops at the same time the gas flow dropped. If a large fraction of the nuclei had been deposited on the wall, changes in the flow rate should not have mattered. Based on the event rate alone, the influence of the getter cannot be determined.

### Alpha peaks

To find out whether the getter did filter out the daughter nuclei of the radon, we made a histogram of the peak area of the events, shown in Figure 9.27. The result is similar between both measurements, and one can distinguish peaks at the same places in the spectrum as in Figure 9.11.

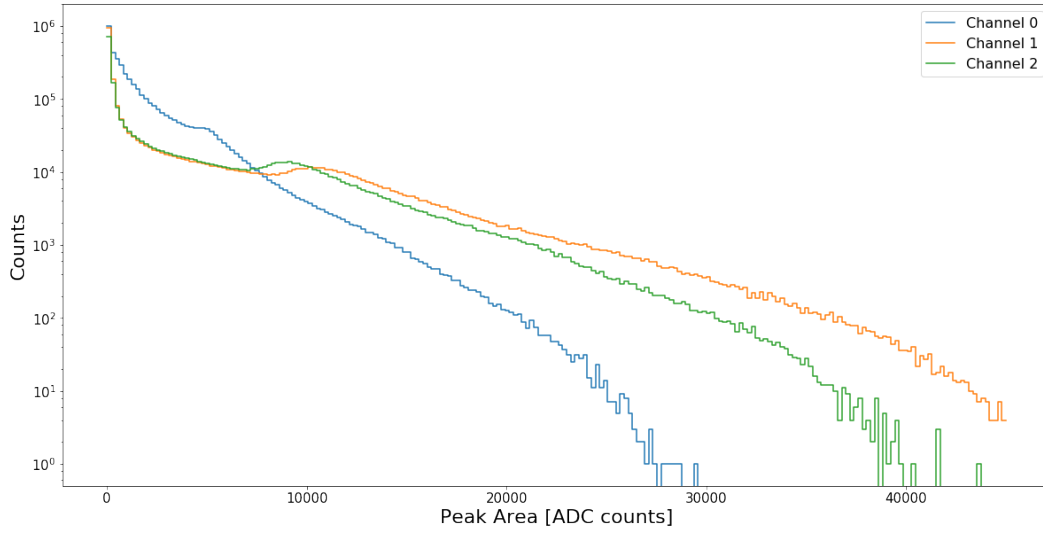


Figure 9.27: Histogram of the peak area for each of the detectors for the measurement started on 03-03-20.

We will again go into more detail by selecting the events measured by the T-detector, because it detected the most events, and divide the data based on the phase of the experiment. Like in Figure 9.12, the data is divided into four parts: pre source, open source, post source, and the background after the source has been closed for a long time. This is shown in Figure 9.28 for the 03-03 measurement. The peak in the open source data around 5000 ADC counts is still clearly visible, and also the two peaks in the post source background can be distinguished 9.12. Furthermore, there are also weak features visible at 1000 ADC counts.

In order to describe the region containing the alpha peaks, equation (9.6) was fitted to the data again. The result is shown in Figure 9.29. The following parameter values were obtained:

Name	Value	Para Error
$a_1$	1.650e+04	2.928e+02
$a_2$	1.403e+03	1.213e+02
$\lambda_1$	3.436e-04	6.805e-06
$\lambda_2$	3.067e-04	4.114e-05
$ga_1$	8.250e+05	2.623e+04
$ga_2$	1.035e+05	2.542e+04
$ga_3$	6.063e+04	1.615e+04
$\mu$	7.854e+02	1.409e+00
$\sigma_1$	5.987e+02	1.414e+01
$\sigma_2$	4.952e+02	6.277e+01
$c_1$	-3.127e+02	4.185e+01
$c_2$	-5.641e+00	2.767e+01

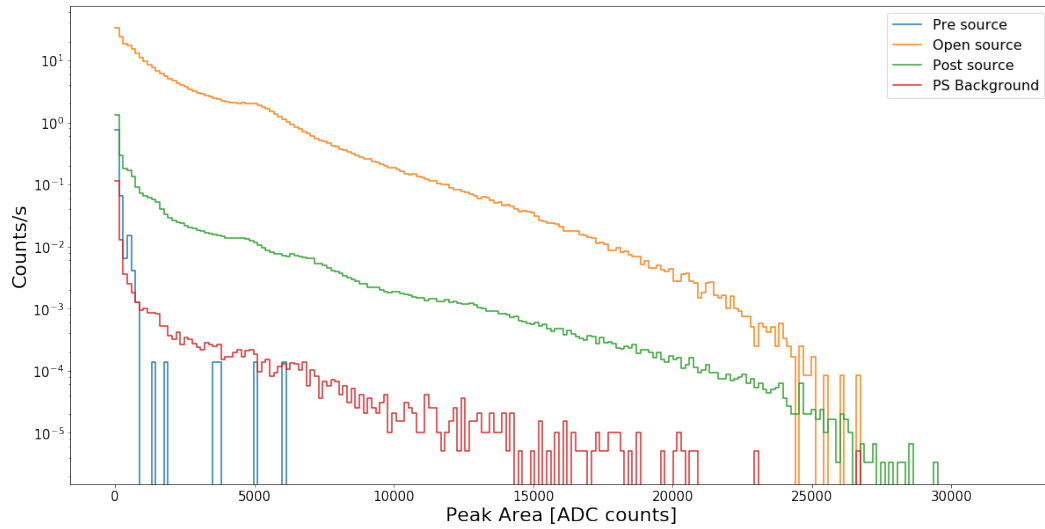


Figure 9.28: Histogram of the peak area count rate for Channel 0 (T-detector) for the different phases in the measurement from 03-03-20.

The errors in  $ga_2$  and  $ga_3$  are relatively large, around a quarter of the parameter value. This can be attributed due to the peaks in the post source data being not as large compared to the rest of the data. For the peaks in the open source data this difference is much larger. But even so, there is again a clear correspondence between the position of the peaks and the energy released in the alpha decays of the  $^{220}\text{Rn}$  chain.

### Cross-detector

We select only the events that were measured in both PMTs of the cross detector. The result in Figure 9.30 is very similar to 9.14. Again, events that were picked up simultaneously in the T-detector are at low peak area and few in number. There are some differences when looking at the count rates for different phases in the experiment. Figure 9.31 (left) shows a histogram of the count rate versus the peak area for Channel 1. The result looks globally similar to the measurement without the getter, as shown in Figure 9.15, but the second peak in the post source data now looks weaker when compared to the other measurement. However, combining the events in Channel 1 and 2 a second peak in the post source data is visible, see Figure 9.31 (right). As was noticed in section 9.4.2 these peaks are broader than those for a single PMT.

When trying to fit equation (9.6) the same problems as in the other measurement show up. As can be seen in Figures 9.32 and 9.33 the peaks of the fit neither match the shape of the peaks in the data, nor are they located at the correct positions.

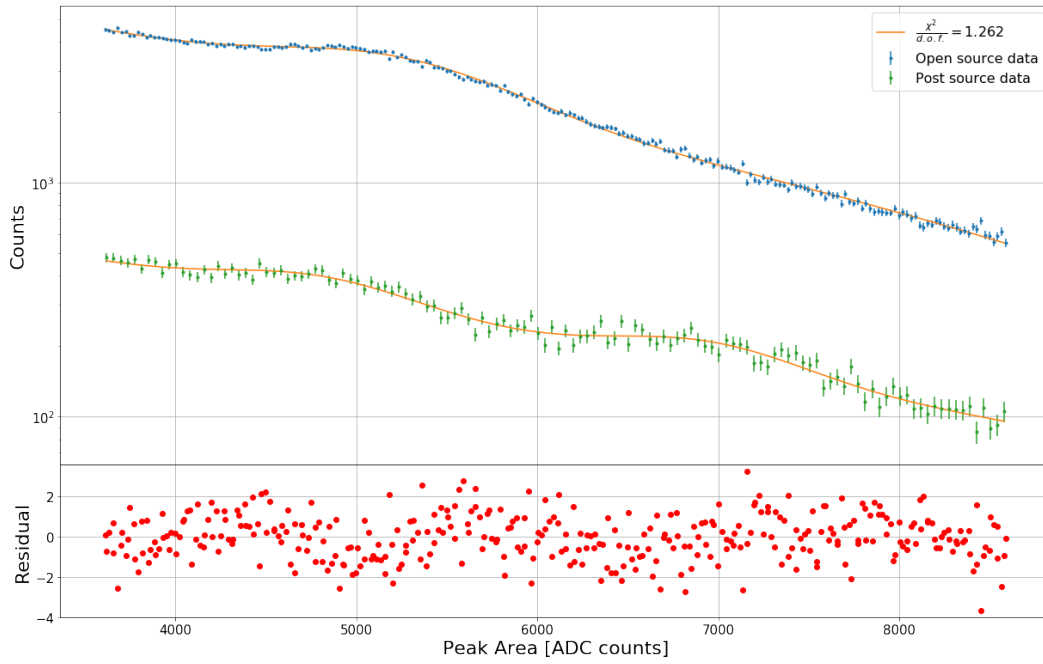


Figure 9.29: Histogram of the peak area for Channel 0 (T-detector) for the open- and post source data in the region of the alpha peaks. The fit to the data is included as well. 03-03-20

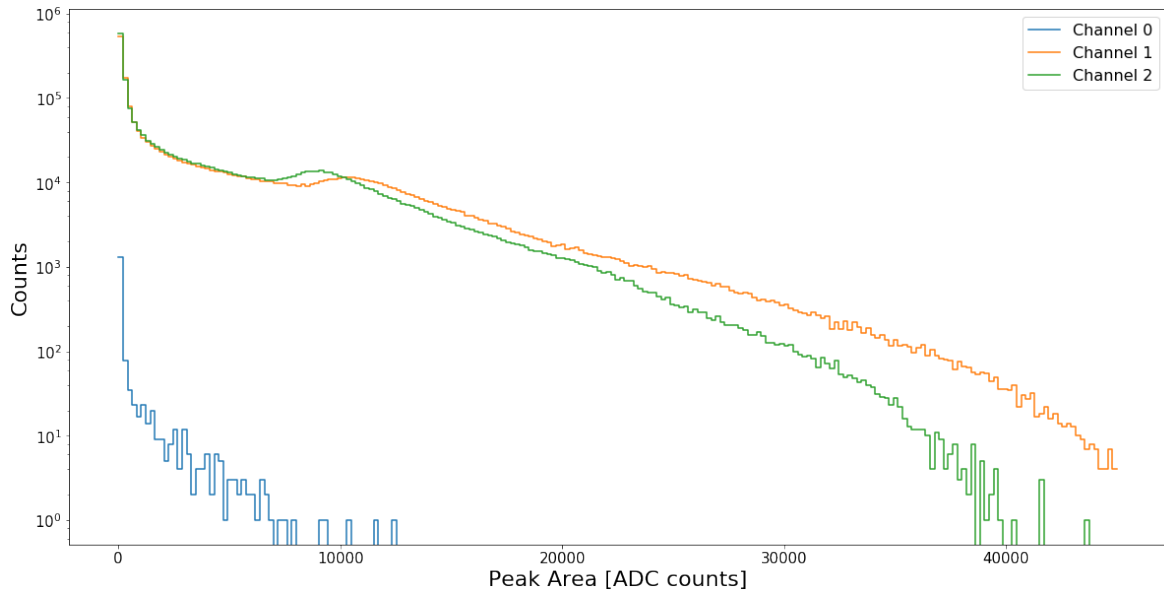


Figure 9.30: Histogram of the peak area for each of the detectors for the measurement started on 03-03-20. Only the events in which both Channel 1 and Channel 2 (cross detector) were triggered were taken.

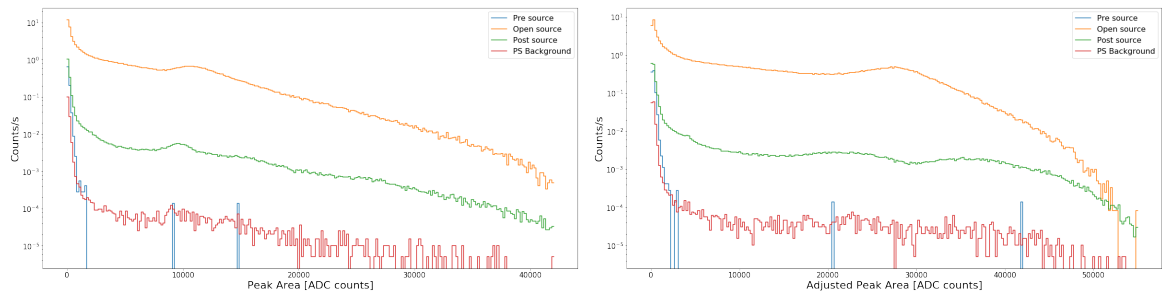


Figure 9.31: Histogram of the peak area count rate for Channel 1(left) and the adjusted peak area count rate for Channel 1 and 2 combined (right) for the different phases in the measurement from 03-03-20

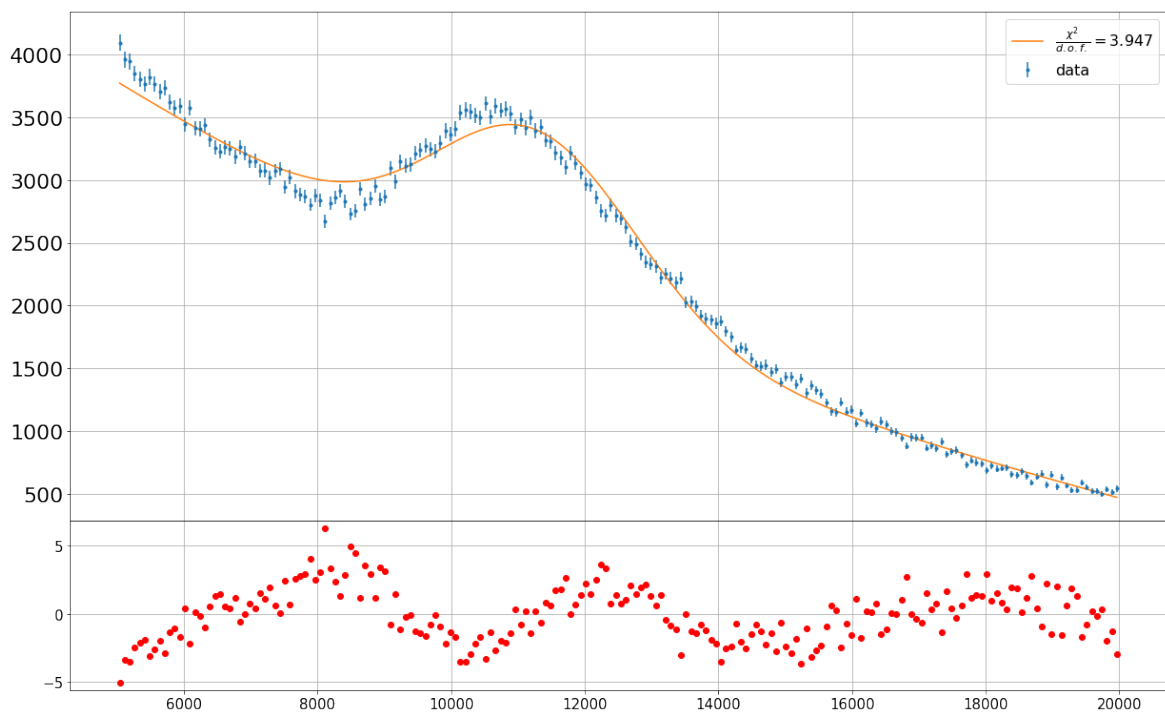


Figure 9.32: Histogram of the peak area for Channel 1 (X-detector) for the open source data in the region of the alpha peaks. The fit to the data is included as well. 03-03-20

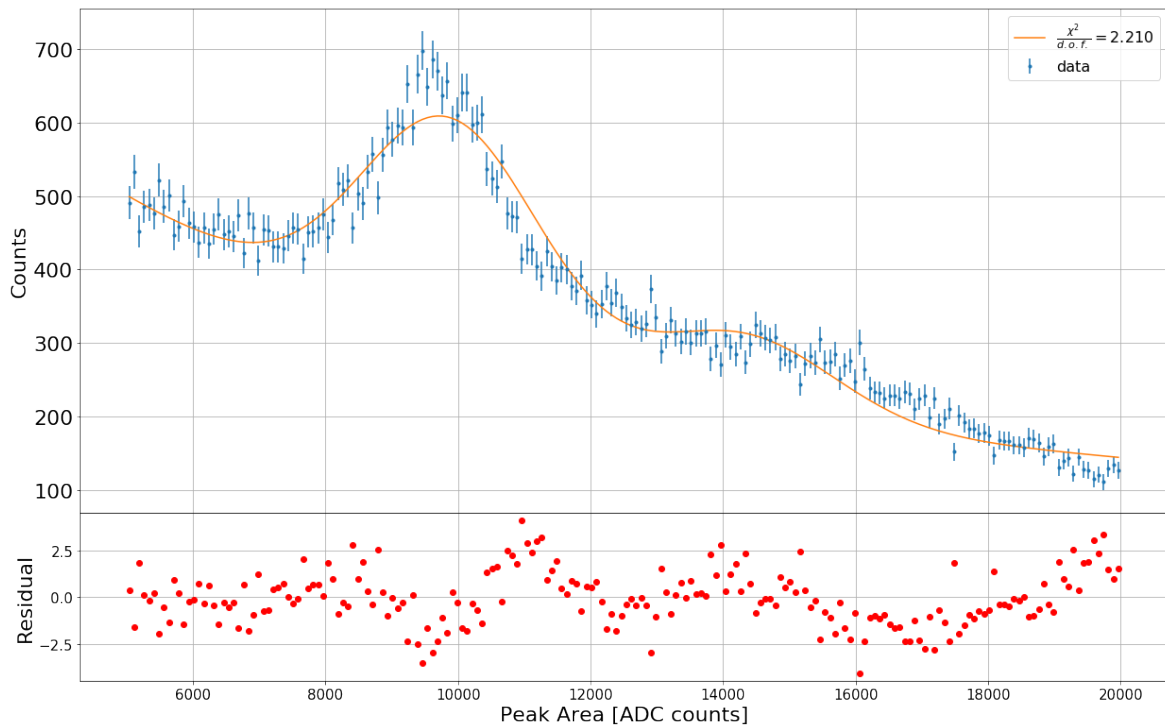


Figure 9.33: Histogram of the peak area for Channel 1 (X-detector) for the post-source data in the region of the alpha peaks. The fit to the data is included as well. 03-03-20

## 9.5 Discussion of the results

The aim of this measurement was to detect the presence of  $^{220}\text{Rn}$  and its daughter isotopes in xenon gas, as well as to see whether the getter is able to remove some of these isotopes from the xenon gas inside the Münster gas system. For this purpose we used three PMTs, one of which was placed in the T-detector, the other two opposite from each other in the X-detector. Two measurements were taken, one where the gas was led through the getter, and one where the gas bypassed it.

In both measurements a large increase in count rate was observed quickly after the thorium source was opened. The count rate dropped off rapidly after the source was closed, since  $^{220}\text{Rn}$  has a lifetime of 56 seconds, and its daughter nucleus  $^{216}\text{Po}$  only 0.16 s, meaning an amount of  $^{212}\text{Pb}$  with a relatively long half-life of 10.64h ( $\approx 638\text{m}$ ) was built up. The subsequent decrease of the count rate was steady. The count rate halved every  $645.2 \pm 2.1\text{m}$  (getter bypass) and  $633.7 \pm 4.8\text{m}$  (with getter), and both values are in agreement with the half-life of  $^{212}\text{Pb}$ .

For the T-detector data, a histogram of the counts by peak area was made in both measurements. In doing this, the data of the different phases was taken into account separately as well. This was done in order to prevent the large amount of measured  $^{220}\text{Rn}$  and  $^{216}\text{Po}$  decays overshadowing those of  $^{212}\text{Bi}$  and  $^{212}\text{Po}$ . With the data separated in this way, Gaussians were fitted to the  $\alpha$ -decay peaks, where the means of the each of the Gaussians was proportional

to the  $\alpha$ -decay energy of one of isotopes that is present in the  $^{220}\text{Rn}$  decay chain. In the case where the getter was bypassed, this fit described the data well. This shows that we have indeed observed the  $\alpha$ -decays of  $^{220}\text{Rn}$  and its daughter isotopes. The same was done for the measurement in which the getter was used. Also in this case the fit described the data well. The getter did not seem to have any effect on the presence of the daughter nuclei of  $^{220}\text{Rn}$  in the xenon gas. The results of the T-detector are strong evidence of the presence of  $^{220}\text{Rn}$  and its daughter nuclei.

The X-detector data showed clear similarities in the observed signals between both PMTs, these recorded events were independent of the ones measured in the T-detector. The same fit that had been used for the T-detector, was used  $\alpha$ -peaks in the X-detector data as well. The fit did not describe the data well, as one of the Gaussians ends up shifted away from one of the peaks in the data. It is difficult to pinpoint the exact cause of the difference between the T- and X-detector data sets. A possible explanation can be that the X-detector captures a substantial larger amount of scintillation signals. Indeed, the peak areas of events in the X-detector are larger than those in the T-detector. The PMTs might capture too much signals to handle, distorting the data. To test this scenario, one could decrease the volume at which the PMTs were operated.

Looking at the data of just a single PMT in the X-detector, the fitted Gaussian peaks in the data with open source deviate from the data in shape. Furthermore, for the data post-source the position one of the fitted Gaussian peaks is clearly off compared to the measurement. Thus the deviation between the fit and data is not an artefact of combining the data of both PMTs, but is already present in the data of a single PMT. Hence this issue is neither caused nor can it be resolved by a thorough gain calibration.

The gain calibration of the PMTs was not successful, as the data was of a too poor quality. This is mainly because the noise spectra that were taken had a non-Gaussian shape. On top of this there were differences in the shape of the data in the noise region between the noise spectra and the data with pulsed LED. The noise region contained most of the counts, also with a pulsed LED. With Poissonian errors, the relative error is smallest for these bins. These factors made it difficult to apply a good fit to the data, hence new measurements should be taken.

## 9.6 Outlook

We have detected the decays of  $^{220}\text{Rn}$  and its daughter nuclei in xenon gas. The next step is to test whether the radon can be separated from the xenon by charging it and drifting it through an electric field. Xenon gas entering a chamber can be led into an electric field. On one side, there is a gold surface that is illuminated by a UV LED. This causes electrons in the gold surface to escape and drift in an electric field towards the anode through the gas present in the system. During this time, the electrons encounter xenon and radon nuclei, as well as any daughter nuclei. If there is a difference in the rate in which these elements absorb

these extra electrons, one can separate them using the electric field. The second part of the chamber is divided into two parts by a piece of steel in the middle. A single PMT is mounted on each side. The idea is that if the radon is indeed drifted to one side by the electric field, the PMT in one of the parts will measure a larger rate than the other one. If successful, this principle could be used to remove radon on a larger scale.



## 10 Extending the SM gauge group with a local U(1) symmetry

Most of the radiative seesaw models that have been considered thus far have a  $\mathbb{Z}_2$  symmetry as a common feature, with the exception of the SLIM model of Chapter 8 that featured a global U(1) symmetry that was broken to  $\mathbb{Z}_2$  however. The reasons for this feature were discussed in Chapter 4, and are repeated here. In particular, the  $\mathbb{Z}_2$  symmetry has the following effects:

- It ensures that neutrino masses are generated through radiative corrections at the one-loop level, by preventing any tree-level seesaw contribution.
- It stabilises the particles in the dark sector by preventing decays into SM particles. This makes the neutral particles in the dark sector suitable dark matter candidates.
- It prevents flavour changing neutral currents (FCNCs) at tree-level induced by the otherwise allowed Yukawa couplings between SM quarks and leptons and BSM scalars.

Whereas there are many valid phenomenological arguments in favour of this symmetry, its inclusion in radiative seesaw models is ad hoc and does not come with a direct motivation from a theoretical perspective. A similar role can be fulfilled by other symmetries, which makes it attractive to study new symmetries that can have the above mentioned effects. These can be divided into two separate categories.

The first class of symmetries used in the literature are the global symmetries, which can be divided further into discrete and continuous symmetries. The extensively discussed  $\mathbb{Z}_2$  symmetry falls into the former category, as well as the related  $\mathbb{Z}_3$  [329, 330] or higher  $\mathbb{Z}_n$  [331] symmetries. An example of a  $\mathbb{Z}_2$  symmetry that more underlying theoretical motivation is  $R$ -parity in supersymmetric theories. Other symmetries that are sometimes included in the literature are so-called family symmetries, e.g.  $A_4$  [332, 333]. For a continuous symmetries a global U(1) symmetry is used [293, 288, 334], which can then broken to a  $\mathbb{Z}_n$  symmetry [335].

The other class of symmetries are local (gauge) symmetries. In this chapter, we will focus on the extension of the SM  $SU(3)_c \times SU(2)_L \times U(1)_Y$  gauge group by an extra  $U(1)$  group. This scenario has already been considered in the literature, such as a U(1) gauged version of the scotogenic model [336], but no systematic overview exists. The addition of an extra U(1) results in the appearance of a new  $Z'$  gauge boson. If the symmetry is (spontaneously) broken by a new Higgs field, then the new gauge boson is massive. Popular choices for assigning charges under the new gauge groups are those that are based on accidental symmetries of the

Standard Model. In the SM baryon ( $B$ ) and lepton ( $L$ ) numbers are conserved separately, as well as the quantity  $B - L$ . Hence some models consider extensions based on gauged lepton number  $U(1)_L$  [337, 338] or  $B - L$   $U(1)_{B-L}$  symmetries [339]. Another option is to have a “dark”  $U(1)$  symmetry, under which the SM is completely uncharged, and only the new fields are charged [336, 340, 341]. Furthermore, there exist models with a gauged  $U(1)$  symmetry in which Dirac instead of Majorana masses are generated [342, 343, 344, 345, 346]

As was explained in Chapter 4, a classification of radiative seesaw models with a  $\mathbb{Z}_2$  symmetry was presented in Refs. [203, 204], where models with  $\leq 4$  new multiplets were considered. The aim of this chapter is to present a systematic overview of the the same models for the case where a gauged  $U(1)$  symmetry takes the role as a stabilising symmetry, and to discuss the different criteria that need to be considered. We will then discuss some of the phenomenology related to the  $Z'$  boson and the extended scalar sector. We then turn to grand unifying theories (GUTs) and discuss the prospects of embedding our models into an  $SO(10)$  GUT. This chapter is based on joint work with Thede de Boer and Michael Klasen, a publication is in preparation at the time of writing.

## 10.1 One-loop classification of models with a local U(1) symmetry

In radiative seesaw models, the neutrino masses are generated by one-loop realisations of the  $d = 5$  Weinberg operator [190] that was first introduced in Equation (3.30) in Chapter 3 as

$$\mathcal{L} \supset \frac{c_{\alpha\beta}}{\Lambda} (L_\alpha H) (L_\beta H) + \text{h.c.}, \quad (10.1)$$

which generates a Majorana mass term for the neutrinos after electroweak symmetry breaking. For the case where the number of new multiplets is  $\leq 4$ , and all multiplets are either singlets, doublets, or triplets of  $SU(2)_L$ , an exhaustive overview of possible models has been found in Ref. [203], of which a part can accomodate a dark matter candidate [204]. This was already discussed in Chapter 4. These models all use a  $\mathbb{Z}_2$  symmetry. The different topologies of models that can generate viable neutrino masses are shown in Figure 4.2.

The goal of this section is to replace the  $\mathbb{Z}_2$  symmetry of these radiative seesaw models by a gauged  $U(1)_X$  symmetry, following the same assumptions as was done in Refs. [203, 204]. The only difference is that an extra complex scalar  $\zeta$ , which must be uncharged under all SM symmetries, is added in order to break the  $U(1)_X$  symmetry. This scalar is allowed to develop a vev  $v_\zeta$ . The scalar can couple to the neutrino loop, so that the  $d = 5$  Weinberg operator is modified to

$$\mathcal{L} \supset \frac{c_{\alpha\beta}}{\Lambda^{1+2n}} (L_\alpha H) (L_\beta H) |\zeta|^{2n} + \text{h.c.}, \quad (10.2)$$

in which an even number of  $\zeta$  is included. Then two cases can be distinguished. If  $v_\zeta$  is small with respect to the scale of new physics  $v_\zeta \ll \Lambda$ , then it does not affect the  $d = 5$  Weinberg operator from Equation (10.1), as all contributions of operators with  $n \neq 0$  are

suppressed by one or multiple factors of  $v_\zeta^2/\Lambda^2$ . If the vev is on the order of the new physics scale  $v_\zeta \approx \Lambda$ , then the operator receives no suppression for  $n \neq 0$ . In this case, the operator will be similar to the ordinary  $d = 5$  Weinberg operator after  $\zeta$  has obtained a vev. Either way, the operator after the breaking of  $U(1)_X$  is not modified, and thus the complete model overviews presented in Refs. [203, 204] are applicable here. However, the addition of  $\zeta$  with a vev can induce new mixings between fields.

### 10.1.1 Theoretical conditions

The first step is to consider the general theoretical conditions that need to be fulfilled when embedding radiative seesaw models into an extra  $U(1)_X$  gauge symmetry. In doing so, one has to assign how each field is charged under the new symmetry. Not all distributions of the charges under the new symmetry are possible. The first of these aspects are the gauge anomalies, which for a consistent theory must vanish. Furthermore, the  $d = 5$  Weinberg operator should not be explicitly forbidden by the theory, and neither should the couplings that are involved in the neutrino mass diagrams. Also the SM Yukawa couplings, responsible for the SM fermion masses, should be preserved. The former leads to the condition

$$X_L + X_H = 0. \quad (10.3)$$

Finally, the  $U(1)_X$  symmetry must be imposed in such a way that eventual dark matter candidates are prevented from decaying into SM final states. As a final note, this discussion is done under the assumption that different generations are equally charged under the new symmetry.

### General solutions

In this section we derive general constraints that are only dependent on the SM particle content, and thus are applicable to any radiative seesaw model with an extra  $U(1)$  symmetry. Remind yourself that the Yukawa terms of the Standard Model are written as (omitting generational indices), repeated from Equation (3.21)

$$\mathcal{L}_Y = -y^e H^\dagger L e_R^c - y^d H^\dagger Q d_R^c - y^u \tilde{H}^\dagger Q u_R^c + \text{h.c.}, \quad (10.4)$$

which must be preserved as such. Likewise, the  $d = 5$  Weinberg operator from Equation (10.1) must also be allowed. One can then see that the charge assignments  $X_\psi$  for a field  $\psi$  must satisfy the following relations

$$X_Q - X_H + X_{d_R^c} = 0 \quad (10.5)$$

$$X_Q + X_H + X_{u_R^c} = 0 \quad (10.6)$$

$$X_L - X_H + X_{e_R^c} = 0, \quad (10.7)$$

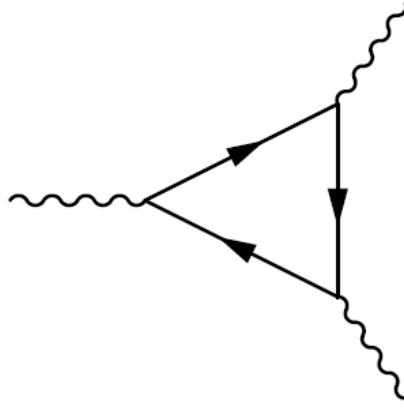


Figure 10.1: Triangle diagram contributing to gauge anomalies.

which upon inserting Equation (10.3) can be reduced to

$$X_{d_R^c} = -X_Q - X_L \quad (10.8)$$

$$X_{u_R^c} = -X_Q + X_L \quad (10.9)$$

$$X_{e_R^c} = -2X_L. \quad (10.10)$$

### Gauge anomalies

Further constraints come from gauge anomaly cancellations. Anomalous symmetries arise from field theories where the Lagrangian of the classical theory obeys this symmetry, but the quantum theory based on the same Lagrangian does not. This has no consequences if the symmetry in question is a global symmetry, but for anomalous local symmetries problems arise. If a local symmetry is anomalous, then the Ward identity will be violated and the corresponding massless gauge boson picks up an unphysical longitudinal polarisation [347]. The anomaly can be described in terms of triangle diagrams, such as those in Figure 10.1. Gauge bosons couple to the triangle, in which the chiral fermions of a theory run. In order to be anomaly free, all contributions of the diagrams must cancel. Whether this can be achieved, depends on the generators  $T$  of the gauge group, which is written in terms of

$$A(R)d^{abc} \equiv 2A(R)\text{Tr} \left[ T^a \{T^b, T^c\} \right], \quad (10.11)$$

in which the generators are in the fundamental representation, and  $A(R)$  is the anomaly coefficient, which depends on the representation of the fermion running in the triangle [347]. For the fundamental representation this coefficient is always 1. An anomaly free theory is satisfied if  $d^{abc} = 0$ , or the sum over the anomaly coefficients of all fermions cancels. All of the conditions are given in Table 10.1. These depend on the complete (SM+BSM) particle content. A fixed contribution to the gauge anomalies comes from the Standard Model fields

Table 10.1: Conditions for gauge anomaly cancellation for the gauge group  $SU(3)_C \times SU(2)_L \times U(1)_Y \times U(1)_X$ . The sums run over all components of fermion fields  $\psi$ . For this table, we assume that all multiplets are either  $SU(3)_C$  triplets  $3_3$  or singlets  $1_3$ , and that all multiplets are  $SU(2)_L$  triplets  $3_2$ , doublets  $2_2$ , or singlets  $1_2$ .

Anomaly	Constraint
$U(1)_Y^3$	$\sum_{\psi} Y_{\psi}^3 = 0$
$U(1)_X^3$	$\sum_{\psi} X_{\psi}^3 = 0$
$U(1)_Y^2 \times U(1)_X$	$\sum_{\psi} Y_{\psi}^2 X_{\psi} = 0$
$U(1)_X^2 \times U(1)_Y$	$\sum_{\psi} X_{\psi}^2 Y_{\psi} = 0$
$SU(3)_C^2 \times U(1)_Y$	$\sum_{\psi \in 3_3} Y_{\psi} = 0$
$SU(3)_C^2 \times U(1)_X$	$\sum_{\psi \in 3_3} X_{\psi} = 0$
$SU(2)_L^2 \times U(1)_Y$	$\sum_{\psi \in 2_2} Y_{\psi} + 4 \sum_{\psi \in 3_2} Y_{\psi} = 0$
$SU(2)_L^2 \times U(1)_X$	$\sum_{\psi \in 2_2} X_{\psi} + 4 \sum_{\psi \in 3_2} X_{\psi} = 0$
$\text{grav}^2 \times U(1)_Y$	$\sum_{\psi} Y_{\psi} = 0$
$\text{grav}^2 \times U(1)_X$	$\sum_{\psi} X_{\psi} = 0$

themselves. With the constraints from Equations (10.8-10.10), the following contributions are obtained

$$SU(3)_C^2 \times U(1)_X : 0 \quad (10.12)$$

$$SU(2)_L^2 \times U(1)_X : 3[6X_Q + 2X_L] \quad (10.13)$$

$$\text{grav}^2 \times U(1)_X : 0 \quad (10.14)$$

$$U(1)_Y^2 \times U(1)_X : \frac{3}{2}[-3X_Q - X_L] \quad (10.15)$$

$$U(1)_Y \times U(1)_X^2 : 3X_L[6X_Q + 2X_L] \quad (10.16)$$

$$U(1)_X^3 : 3X_L^2[-6X_Q - 2X_L] \quad (10.17)$$

for the new  $U(1)_X$  group. All gauge contributions involving only SM gauge groups vanish for the SM particle content. One further anomaly that must be taken into account is the Witten anomaly [348]. It states that an  $SU(2)$  gauge theory with an odd number of left-handed fermion doublets is inconsistent. Whatever extension of the SM particle content we will make, the contribution of the SM particle content to the gauge anomalies must always be cancelled by the contribution from the BSM fields.

### 10.1.2 Fermion charge considerations

The general constraints that were just presented impose further restrictions on the charge assignment of new fermions if one also takes into account that a tree-level seesaw must be avoided, and that the topology of the neutrino loop must be conserved. Based on this one can make several observations about the characteristics of fermions for the minimal radiative seesaw models we consider here, which contain at least one, and at most three fermion multiplets. To illustrate our train of thought, we first make some observations about the

fermions inside the neutrino loop, to which we give an argument. With these observations, we derive constraints on the BSM fermions for the specific topologies.

**Observation 1.** *All contributions to the gauge anomalies from vector-like fermions vanish due to opposite contributions from the other vector-like component. Thus only fermions that are not vector-like contribute to the anomaly cancellation conditions.*

**Observation 2.** *If there is a single new fermion  $\psi$  that is not a priori part of a vector-like fermion,  $\psi$  must be made vector-like.*

*Argument:* From the Witten anomaly it is clear that  $\psi$  must be made vector-like if it is a doublet, which is satisfied if a second doublet is added, and the components are combined into a vector-like fermions. If  $\psi$  is a singlet or a triplet, the anomalies associated with hypercharge must cancel. Because the SM and other new vector-like fermions do not contribute to the hypercharge anomalies,  $\psi$  must either be vector-like or have zero hypercharge. However, in the latter case, if a singlet or triplet has zero hypercharge, it must have a non zero  $U(1)_X$  charge in order to prevent contributions from seesaw types I or III.<sup>1</sup> In this case the contribution of the fermion to the  $\text{grav}^2 \times U(1)_X$  anomaly must cancel, since it has no contributions from the SM (see Equation (10.14)). This is only possible if  $\psi$  is made vector-like.

**Observation 3.** *If there are two or more new fermions that are relevant in the neutrino loop, at least one of these fermions must be a doublet and at least one fermion must be a singlet or triplet.*

*Argument:* In any minimal model with more than one fermion, i.e. of the topology T1-2 or T1-3 in our case (see Chapter 4), there always exists a direct coupling of two fermions  $F_1$  and  $F_2$  to the SM Higgs doublet. This is only possible if one of the new fermions is a doublet. The second fermion coupling to this vertex must be a triplet or singlet to complete the vertex in an  $SU(2)_L$  invariant way.

**Observation 4.** *If there are two fermion fields that both are either singlets or triplets under  $SU(2)_L$ , then they must be vector-like or identified with each other in order to form a vector-like field.*

*Argument:* In order to cancel the hypercharge anomalies, both fields must be vector-like, identified with each other or have zero hypercharge. Only in these cases there is no BSM contribution to the  $U(1)_Y \times U(1)_X^2$ . From this condition, it can then be seen that the SM must be uncharged under  $U(1)_X$ , or that the  $U(1)_X$  charges are a copy of the hypercharge. It follows that all BSM contributions to the  $U(1)_X$  anomalies must cancel amongst themselves. As the singlets and triplets with zero hypercharge must have a  $U(1)_X$  charge in order to avoid seesaw type I and III, one finds that both must be vector-like or identified with each other.

With these general considerations for the fermionic sector in mind, the consequences for the various topologies of radiative seesaw models, which include different numbers of fermions in more detail.

---

<sup>1</sup>Note that this argument works even if the SM neutrino is charged under  $U(1)_X$  as  $X_L = -X_H$ .

**Models with one new fermion (T1-1, T3)** From Observation 2 it follows that the fermion must be vector-like in all cases.

**Models with two new fermions (T1-2)** From Observation 3 it is clear that one of these fermions must be a doublet and the other one is either a singlet or a triplet. As the doublet must be vector-like in order to cancel the Witten anomaly, from Observation 2 it follows that the second fermion is also vector-like.

**Models with three new fermions (T1-3)** The discussion for three fermion fields is a bit more involved. From Observation 3 at least one of the fermions is a doublet. We start with the case with only one fermion doublet, which must be vector-like following Observation 2. Then it follows from Observation 4 that the two remaining fermions must be vector-like or identified with each other.

The other possibility for the other fermions is the case of two doublets and one singlet/triplet. From the anomaly cancellation conditions for hypercharges, one finds that for the case of two doublets, the doublets must have opposite hypercharge or they must form a vector-like doublet. If both doublets are vector-like, the argument is reduced to the one given for one fermion for the remaining singlet/triplet. Thus the singlet/triplet must be vector-like following Observation 2. Finally if the doublets are not vector-like (i.e. they have different  $U(1)_X$  charges), one needs to specifically calculate the anomaly cancellation conditions. Doing so, the only solution is that the singlet/triplet is vector-like and carries a  $U(1)_X$  charge, to avoid a tree-level seesaw contribution. Furthermore both doublets must have opposite  $U(1)_X$  charge in order to have no tree level seesaw mechanism.

One can see that with these considerations all new fermions must either be made vector-like, or they must be combined with another fermion to form a vector-like fermion.

### The SM is uncharged

Because any BSM fermion that is added must be vector-like, the conditions for gauge anomaly cancellation are simplified. For the BSM fermions, the contribution to the gauge anomalies is a trivial one, as all contributions from vector-like fermions vanish separately for each vector-like fermion. Therefore the cancellation conditions from Table 10.1 have no BSM contribution, and only the SM has to be considered. In order to assign  $U(1)_X$  charges to the SM fields, one can make use of the results of Chapter 30.4 in Ref. [347] for the case of an extra  $U(1)$  group on top of the SM hypercharge. For the charge assignment of the new  $U(1)_X$  charges there is either the trivial possibility of a charge proportional to the hypercharge, or the  $B - L$  charges

$$X_L = -X_{e_R^c} = -X_{\nu_R^c} = -1, \quad X_Q = -X_{u_R^c} = -X_{d_R^c} = \frac{1}{3}, \quad (10.18)$$

which require a charge  $X_{\nu_R^c}$  from the addition of a right-handed neutrino. In our work, we do not introduce right-handed neutrinos, as they would induce non-radiative neutrino mass terms, and could allow for Dirac neutrino masses. Moreover, the  $B - L$  symmetry is violated by the Weinberg operator by two units.

For the BSM fields inside the neutrino loop, one is free to choose any  $U(1)_X$  charge configuration that does not alter the loop topology, since there will be no contribution to the gauge anomalies. One can start by giving each of the fields inside the neutrino loop a charge  $X_{\text{in}}$ , provided that the vertices in the neutrino loop are conserved. In principle one can then give all SM fields a  $U(1)_X$  charge that is proportional to their hypercharge. As the loop topologies conserve hypercharge, the fields inside the loop can be shifted in a similar fashion, which can be described as

$$X_{\text{out}} = X_{\text{in}} + \lambda Y_\psi, \quad (10.19)$$

where one is free to assign an additional charge for the particles inside the loop  $X_{\text{in}}$ . In the case of two abelian groups, such as two  $U(1)$  groups, one is free to make a change of basis. By defining a new basis in which all  $U(1)_X$  charges are shifted by  $-\lambda Y_\psi$  for every field, one can arrive at the case where the SM is uncharged under  $U(1)_X$ , and only the new fields have the original charge of  $X_{\text{in}}$ .

### Dark matter stability

A further requirement is that at least one of the potential dark matter candidates in our models is stable. The stability of dark matter requires that none of the new particles has zero charge under the new symmetry as in that case, there is no symmetry restricting DM interactions with the SM, meaning that any otherwise viable DM candidate would decay into SM states. Thus all new particles must have non zero  $U(1)_X$  charge. In models in which one of the fields in the neutrino loop has the same  $U(1)_X$  charge as  $\zeta$ , there can be no stable dark matter candidate. In this case there must always exist a scalar field with an equal or opposite charge to  $\zeta$ , which can mix. This allows the scalar field to decay into two Higgs bosons  $U(1)_X$  breaking. Therefore charge assignments in which new fields have the same charges as  $\zeta$  under  $U(1)_X$  should also be avoided.

### Unbroken symmetry

Since we previously argued that the SM particles can be made uncharged under the  $U(1)_X$  symmetry, it follows that all the particles inside the neutrino loop have the same  $U(1)_X$  charge. This is possible if this symmetry is unbroken, or if the vev of  $\zeta$  is far below the scale of new physics  $\Lambda$ , such that neutrino masses are generated through Equation (10.2) with  $n = 0$ .



### Broken symmetry and mass mixing

For the case where  $v_\zeta \approx \Lambda$ , the contributions of the operators in Equation (10.2) with  $n \neq 0$  contribute, and  $\zeta$  couples to the particles in the neutrino loop. However, the fact that  $\zeta$  can couple to the new fields, causes mass mixing when  $\zeta$  obtains its vev. Furthermore, the coupling to  $\zeta$  can lead to  $U(1)_X$  violation after symmetry breaking, allowing for more charge assignments. There are two places where these effects show up.

First, the mass dimension three vertices with the Higgs, which show up in the T1-1 and T1-2 topologies, can violate  $U(1)_X$ . These can violate  $U(1)_X$  by one unit of  $X_\zeta$ . These are realized through vertices of the form

$$\lambda H \phi \phi' \zeta, \quad (10.20)$$

which after  $U(1)_X$  breaking turn in to the three scalar vertices that are present in the  $\mathbb{Z}_2$  versions of the models

$$\mu H \phi \phi', \quad (10.21)$$

where  $\mu = \lambda v_\zeta / \sqrt{2}$ .

The second place where  $U(1)_X$  charges can be violated is in the propagators. This happens through vertices of the form  $\psi \psi' \zeta$ ,  $\phi \phi' \zeta$ , and  $\phi \phi' \zeta \zeta$  by one or two (for the last vertex) units of  $X_\zeta$ . These terms are only allowed if  $\psi/\phi$  and  $\psi'/\phi'$  are in conjugate  $SU(3)_C \times SU(2)_L \times U(1)_Y$  representations. If the fields involved have no hypercharge, the identifications  $\psi = \psi'$  and  $\phi = \phi'$  can be made. In this case, one must have  $X_{\psi/\phi} = -\frac{X_\zeta}{2}$ , no mixing is induced, instead it contributes to the mass of the particles.

Not all mixing terms are allowed. As mentioned above, we require that the dark matter candidate is stable, and that the new fields cannot have the same charge as  $\zeta$ . For scalars, this excludes mixing terms of the form  $H \phi \zeta$  and  $H \phi \zeta H$  for doublets and singlets/triplets respectively, as well as the  $\phi \phi \zeta \zeta$  vertex. In the case of a fermion with the same charge as  $\zeta$  there must exist a scalar with the same charge, after which the argument for scalars applies.

#### 10.1.3 Complete overview of charge assignments

Keeping the DM stability and mass mixing effects in mind, we can now present the different possibilities in distributing charges for each of the topologies. The effects of mass mixing differ per topology, hence we will discuss each of the topologies separately. As explained above, for each of the topologies it is always possible to assign all new fields the same  $U(1)_X$  charge. The other possibilities can then be obtained by considering  $U(1)_X$  violation in propagators via mixing and vertices as explained in the previous section. For each topology, this results in a list of non-equivalent charge distributions. In this section we set  $X_\zeta = 2$  without loss of generality, since  $U(1)$  charges can be freely rescaled. The hypercharge assignment of the models is given by the parameter  $\alpha$ , following Refs. [203, 204]. We introduce  $\beta$  as the parameter for the  $U(1)_X$  charges.

**T1-1**

For this topology both vertices that couple to the Higgs are completely scalar vertices, which can violate  $U(1)_X$ . Thus for any  $\alpha$  one can have the distributions

$$X_\psi = X_{\phi'} = X_\varphi = X_\phi = \beta \quad (10.22)$$

$$X_\psi = X_{\phi'} = X_\varphi \pm X_\zeta = X_\phi = \beta, \quad (10.23)$$

where the second charge assignment includes the effect of the  $U(1)_X$  violating dimension three vertex. For some values of  $\alpha$ , some of the fields have zero hypercharge, possibly allowing for more different charge assignments.

$\alpha = 1$  In the case of  $\alpha = 1$ , the scalar  $\phi'$  has zero hypercharge. All new possible charge assignments can be found from the above ones by redefining  $\phi' \rightarrow (\phi')^\dagger$ .

$\alpha = -1$  The scalar  $\phi$  has zero hypercharge. The new possibilities for charge assignments are equivalent to the ones already found if one redefines  $\phi \rightarrow (\phi)^\dagger$ .

$\alpha = 0$  Both  $\psi$  and  $\varphi$  have zero hypercharge. In this case is one more non equivalent charge assignment given by

$$X_\psi = -X_{\phi'} = X_\varphi = X_\phi = \pm \frac{X_\zeta}{2}. \quad (10.24)$$

Further charge distributions can be obtained if  $\phi$  and  $\phi'$  are in the same representation of  $SU(2)_L$ , in which case mixing between  $\phi$  and  $(\phi')^\dagger$  is introduced by the breaking of  $U(1)_X$ . This allows for the following new non equivalent charge assignments for this model

$$X_\varphi = X_{\phi'} \pm 2X_\zeta = X_\psi = X_\phi = \pm \frac{X_\zeta}{2}, \quad (10.25)$$

$$X_\varphi = X_{\phi'} \mp X_\zeta = X_\psi = X_\phi = \pm \frac{X_\zeta}{2}, \quad (10.26)$$

$$X_\varphi \mp X_\zeta = X_{\phi'} \mp X_\zeta = X_\psi = X_\phi = \pm \frac{X_\zeta}{2}. \quad (10.27)$$

If  $\phi$  and  $\phi'$  are in the same  $SU(2)_L$  representation, and have opposite  $U(1)_X$  charge, we can identify them with each other by defining  $\phi' = \phi^\dagger$ . However in order to have at least two massive neutrinos, there must be two generations of either  $\psi$  or  $\phi$ . The latter case is equivalent to the case where the fields are not identified with each other.

Equivalent models can be found by redefining  $\varphi \rightarrow \varphi^\dagger$  and/or  $\psi \rightarrow \psi^c$  and if possible  $\phi' \rightarrow \phi^\dagger$ . As an example, we show the case of Equation (10.25), where we again set  $X_\zeta = 2$ . If we assume that  $\phi$  and  $\phi'$  are in the same  $SU(2)_L$  representation, mixing can occur. Then  $X_\psi = X_\phi = 1$ , but  $X_\varphi = -1$  and  $X_{\phi'} = 3$ . The corresponding neutrino loop is shown in Figure 10.2. At a vertex, the propagator of a scalar field  $\chi$  that runs inside the neutrino

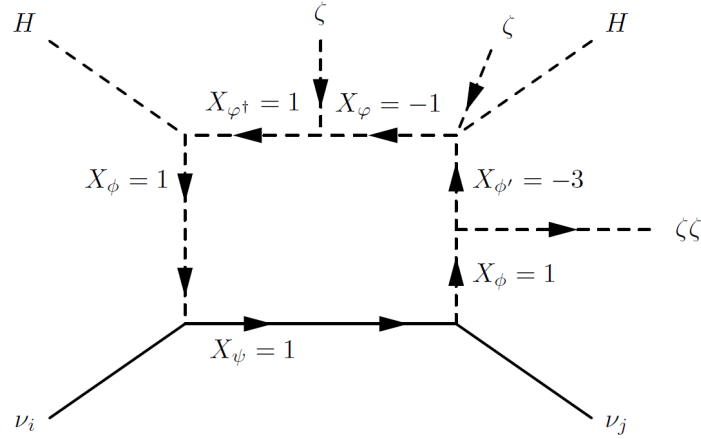


Figure 10.2: Neutrino loop in T1-1 models with the addition of some  $U(1)_X$  violating vertices. The arrows indicate the flow of the  $U(1)_X$  charge at the vertices.

loop contributes  $\chi$  to the vertex term in the Lagrangian if the arrow is pointing inwards to the vertex, and  $\chi^\dagger$  if it points outwards. Thus, starting from the fermion in the loop and going counter clockwise, one can see that a vertex of the form  $\phi\phi'^\dagger\zeta^\dagger\zeta^\dagger$  induces a violation of the  $U(1)_X$  charge by two units of  $X_\zeta$  after breaking. Next there is a vertex  $H\phi'\phi^\dagger\zeta$ , which violates the  $U(1)_X$  charge by a single unit of  $\zeta$ . The last  $U(1)_X$  violating term is  $\varphi\varphi\zeta$ , after which the ordinary  $H\varphi^\dagger\phi^\dagger$  closes off the loop. This is illustrated in Figure 10.2 by the arrows, which denote the flow of the  $U(1)_X$  charge. The internal propagators are labelled with the charge of the corresponding field. Note that this charge assignment is different to Equation (10.25) by the sign of  $X_\varphi$ . The case presented as an example is equivalent. Because  $\varphi$  has no hypercharge, one can define the same model with  $\varphi \rightarrow \varphi^\dagger$ .

**List of models T1-1** The resulting list of all non-equivalent models is shown in Table 10.2, where  $X_\zeta$  has been set to 2. Models with different charges of  $\zeta$  are equivalent and can be obtained by rescaling the  $U(1)_X$  gauge coupling. The parameter  $\beta$  cannot take the values 0 and  $\pm 2$ , as this would make the DM candidate unstable. Note that if a scalar doublet has the charge  $X = \pm 4$  there may be mixing of a new scalar doublet and the SM Higgs doublet through the vertex  $H\phi\zeta\zeta$  making the dark matter candidate unstable. In Table 10.2, as well as the following ones, the notation is similar to Ref. [204], with the field content denoted as  $X_Y^\mathcal{L}$ , where  $X$  is the type of  $SU(2)$  multiplet (1 for singlet, 2 for doublet, 3 for triplet),  $\mathcal{L}$  denotes whether the field is a scalar ( $S$ ) or a fermion ( $F$ ), and  $Y \equiv 2(Q - I_3)$  is the hypercharge. The hypercharge of the particles itself is described in terms of the parameter  $\alpha$ .

Table 10.2: Non-equivalent models of topology T1-1.  $X_\zeta$  is normalized to 2.

Model	$\alpha$	$\varphi$	$\phi'$	$\psi$	$\phi$	$X_\varphi$	$X_{\phi'}$	$X_\psi$	$X_\phi$
T1-1-A	0	$1_0^S$	$2_{-1}^S$	$1_0^F$	$2_1^S$	$\beta$	$\beta$	$\beta$	$\beta$
T1-1-A	0	$1_0^S$	$2_{-1}^S$	$1_0^F$	$2_1^S$	$\beta \pm 2$	$\beta$	$\beta$	$\beta$
T1-1-A	0	$1_0^S$	$2_{-1}^S$	$1_0^F$	$2_1^S$	1	-1	1	1
T1-1-A	0	$1_0^S$		$1_0^F$	$2_1^S$	1		1	1
T1-1-A	0	$1_0^S$	$2_{-1}^S$	$1_0^F$	$2_1^S$	1	$\pm 3$	1	1
T1-1-A	0	$1_0^S$	$2_{-1}^S$	$1_0^F$	$2_1^S$	3	3	1	1
T1-1-A	$\pm 2$	$1_{\pm 2}^S$	$2_{1,-3}^S$	$1_{\pm 2}^F$	$2_{3,-1}^S$	$\beta$	$\beta$	$\beta$	$\beta$
T1-1-A	$\pm 2$	$1_{\pm 2}^S$	$2_{1,-3}^S$	$1_{\pm 2}^F$	$2_{3,-1}^S$	$\beta \pm 2$	$\beta$	$\beta$	$\beta$
T1-1-B	0	$1_0^S$	$2_{-1}^S$	$3_0^F$	$2_1^S$	$\beta$	$\beta$	$\beta$	$\beta$
T1-1-B	0	$1_0^S$	$2_{-1}^S$	$3_0^F$	$2_1^S$	$\beta \pm 2$	$\beta$	$\beta$	$\beta$
T1-1-B	0	$1_0^S$	$2_{-1}^S$	$3_0^F$	$2_1^S$	1	-1	1	1
T1-1-B	0	$1_0^S$		$3_0^F$	$2_1^S$	1		1	1
T1-1-B	0	$1_0^S$	$2_{-1}^S$	$3_0^F$	$2_1^S$	1	$\pm 3$	1	1
T1-1-B	0	$1_0^S$	$2_{-1}^S$	$3_0^F$	$2_1^S$	3	3	1	1
T1-1-B	$\pm 2$	$1_{\pm 2}^S$	$2_{1,-3}^S$	$3_{\pm 2}^F$	$2_{3,-1}^S$	$\beta$	$\beta$	$\beta$	$\beta$
T1-1-B	$\pm 2$	$1_{\pm 2}^S$	$2_{1,-3}^S$	$3_{\pm 2}^F$	$2_{3,-1}^S$	$\beta \pm 2$	$\beta$	$\beta$	$\beta$
T1-1-C	$\pm 1$	$2_{\pm 1}^S$	$1_{0,-2}^S$	$2_{\pm 1}^F$	$1_{2,0}^S$	$\beta$	$\beta$	$\beta$	$\beta$
T1-1-C	$\pm 1$	$2_{\pm 1}^S$	$1_{0,-2}^S$	$2_{\pm 1}^F$	$1_{2,0}^S$	$\beta \pm 2$	$\beta$	$\beta$	$\beta$
T1-1-D	1	$2_1^S$	$1_0^S$	$2_1^F$	$3_2^S$	$\beta$	$\beta$	$\beta$	$\beta$
T1-1-D	1	$2_1^S$	$1_0^S$	$2_1^F$	$3_2^S$	$\beta \pm 2$	$\beta$	$\beta$	$\beta$
T1-1-D	-1	$2_{-1}^S$	$1_{-2}^S$	$2_{-1}^F$	$3_0^S$	$\beta$	$\beta$	$\beta$	$\beta$
T1-1-D	-1	$2_{-1}^S$	$1_{-2}^S$	$2_{-1}^F$	$3_0^S$	$\beta \pm 2$	$\beta$	$\beta$	$\beta$
T1-1-F	$\pm 1$	$2_{\pm 1}^S$	$3_{0,-2}^S$	$2_{\pm 1}^F$	$3_{2,0}^S$	$\beta$	$\beta$	$\beta$	$\beta$
T1-1-F	$\pm 1$	$2_{\pm 1}^S$	$3_{0,-2}^S$	$2_{\pm 1}^F$	$3_{2,0}^S$	$\beta \pm 2$	$\beta$	$\beta$	$\beta$
T1-1-G	0	$3_0^S$	$2_{-1}^S$	$1_0^F$	$2_1^S$	$\beta$	$\beta$	$\beta$	$\beta$
T1-1-G	0	$3_0^S$	$2_{-1}^S$	$1_0^F$	$2_1^S$	$\beta \pm 2$	$\beta$	$\beta$	$\beta$
T1-1-G	0	$3_0^S$	$2_{-1}^S$	$1_0^F$	$2_1^S$	1	-1	1	1
T1-1-G	0	$3_0^S$		$1_0^F$	$2_1^S$	1		1	1
T1-1-G	0	$3_0^S$	$2_{-1}^S$	$1_0^F$	$2_1^S$	1	$\pm 3$	1	1
T1-1-G	0	$3_0^S$	$2_{-1}^S$	$1_0^F$	$2_1^S$	3	3	1	1
T1-1-G	$\pm 2$	$3_{\pm 2}^S$	$2_{1,-3}^S$	$1_{\pm 2}^F$	$2_{3,-1}^S$	$\beta$	$\beta$	$\beta$	$\beta$
T1-1-G	$\pm 2$	$3_{\pm 2}^S$	$2_{1,-3}^S$	$1_{\pm 2}^F$	$2_{3,-1}^S$	$\beta \pm 2$	$\beta$	$\beta$	$\beta$
T1-1-H	0	$3_0^S$	$2_{-1}^S$	$3_0^F$	$2_1^S$	$\beta$	$\beta$	$\beta$	$\beta$
T1-1-H	0	$3_0^S$	$2_{-1}^S$	$3_0^F$	$2_1^S$	$\beta \pm 2$	$\beta$	$\beta$	$\beta$
T1-1-H	0	$3_0^S$	$2_{-1}^S$	$3_0^F$	$2_1^S$	1	-1	1	1
T1-1-H	0	$3_0^S$		$3_0^F$	$2_1^S$	1		1	1
T1-1-H	0	$3_0^S$	$2_{-1}^S$	$3_0^F$	$2_1^S$	1	$\pm 3$	1	1
T1-1-H	0	$3_0^S$	$2_{-1}^S$	$3_0^F$	$2_1^S$	3	3	1	1
T1-1-H	$\pm 2$	$3_{\pm 2}^S$	$2_{1,-3}^S$	$3_{\pm 2}^F$	$2_{3,-1}^S$	$\beta$	$\beta$	$\beta$	$\beta$
T1-1-H	$\pm 2$	$3_{\pm 2}^S$	$2_{1,-3}^S$	$3_{\pm 2}^F$	$2_{3,-1}^S$	$\beta \pm 2$	$\beta$	$\beta$	$\beta$

**T1-2**

For this topology, the three scalar vertex can violate  $U(1)_X$ , whereas the Yukawa coupling of  $\psi$  and  $\psi'$  to the SM Higgs cannot. This means that the only distribution that is allowed for all  $\alpha$  is

$$X_\psi = X_{\psi'} = X_\phi = X_{\phi'} = \beta. \quad (10.28)$$

For specific values of  $\alpha$  there are the possibilities:

$\alpha = -1$  Both  $\psi'$  and  $\phi$  have zero hypercharge. This allows for the new non equivalent charge assignment of

$$X_\psi = X_\phi = -X_{\phi'} = X_{\psi'} = \pm \frac{X_\zeta}{2}. \quad (10.29)$$

$\alpha = 0$  Now both  $\psi$  and  $\phi'$  have zero hypercharge. We find the new non equivalent charge assignment

$$X_\psi = -X_\phi = X_{\phi'} = X_{\psi'} = \pm \frac{X_\zeta}{2}. \quad (10.30)$$

**List of models T1-2** The resulting list of all non-equivalent models is shown in Table 10.3. Similar to Table 10.2,  $X_\zeta$  has been normalized to 2. Again, the parameter  $\beta \neq 0, \pm 2$  and the assignment  $\beta = \pm 4$  may yield problems with dark matter stability if the SM Higgs mixes with a new scalar doublet.

Table 10.3: Non-equivalent models of topology T1-2.  $X_\zeta$  is normalized to 2.

Model	$\alpha$	$\psi$	$\phi$	$\phi'$	$\psi'$	$X_\psi$	$X_\phi$	$X_{\phi'}$	$X_{\psi'}$
T1-2-A	0	$1_0^F$	$2_1^S$	$1_0^S$	$2_1^F$	$\beta$	$\beta$	$\beta$	$\beta$
T1-2-A	0	$1_0^F$	$2_1^S$	$1_0^S$	$2_1^F$	1	-1	1	1
T1-2-A	-2	$1_{-2}^F$	$2_{-1}^S$	$1_{-2}^S$	$2_{-1}^F$	$\beta$	$\beta$	$\beta$	$\beta$
T1-2-B	0	$1_0^F$	$2_1^S$	$3_0^S$	$2_1^F$	$\beta$	$\beta$	$\beta$	$\beta$
T1-2-B	0	$1_0^F$	$2_1^S$	$3_0^S$	$2_1^F$	1	-1	1	1
T1-2-B	-2	$1_{-2}^F$	$2_{-1}^S$	$3_{-2}^S$	$2_{-1}^F$	$\beta$	$\beta$	$\beta$	$\beta$
T1-2-D	1	$2_1^F$	$1_2^S$	$2_1^S$	$3_2^F$	$\beta$	$\beta$	$\beta$	$\beta$
T1-2-D	-1	$2_{-1}^F$	$1_0^S$	$2_{-1}^S$	$3_0^F$	$\beta$	$\beta$	$\beta$	$\beta$
T1-2-D	-1	$2_{-1}^F$	$1_0^S$	$2_{-1}^S$	$3_0^F$	1	1	-1	1
T1-2-F	1	$2_1^F$	$3_2^S$	$2_1^S$	$3_2^F$	$\beta$	$\beta$	$\beta$	$\beta$
T1-2-F	-1	$2_{-1}^F$	$3_0^S$	$2_{-1}^S$	$3_0^F$	$\beta$	$\beta$	$\beta$	$\beta$
T1-2-F	-1	$2_{-1}^F$	$3_0^S$	$2_{-1}^S$	$3_0^F$	1	1	-1	1

**T1-3**

As three out of the four multiplets inside the loop are fermionic, none of the vertices can violate  $U(1)_X$ . For any  $\alpha$  the distribution

$$X_\Psi = X_{\psi'} = X_\phi = X_\psi = \beta. \quad (10.31)$$

is possible.

$\alpha = \mathbf{0}$  Both  $\Psi$  and  $\phi$  have zero hypercharge. There is one more non equivalent charge assignment

$$X_\Psi = -X_{\psi'} = X_\psi = X_\phi = \pm \frac{X_\zeta}{2} \quad (10.32)$$

If  $\psi$  and  $\psi'$  are in the same representation of  $SU(2)_L$ , mixing between  $\psi$  and  $(\psi')^c$  can be introduced by the breaking of  $U(1)_X$ . No new non-equivalent charge assignments are found. If  $\psi$  and  $\psi'$  are in the same  $SU(2)_L$  representation, and have opposite  $U(1)_X$  charge, we can combine them to form a vector-like doublet instead of making both fields vector-like separately. However in order to have at least two massive neutrinos, there must be two generations of either  $\phi$  or  $\psi$ . The latter case is equivalent to the case where the fields are not identified with each other.

**List of models T1-3** The resulting list of all non-equivalent models is shown in Table 10.4. Similar for the previous topologies,  $X_\zeta$  is set to 2 and the parameter  $\beta$  must be  $\neq 0, \pm 2$  and in case of a scalar doublet  $\neq \pm 4$ .

Table 10.4: Non-equivalent models of topology T1-3.  $X_\zeta$  is normalized to 2.

Model	$\alpha$	$\Psi$	$\psi'$	$\phi$	$\psi$	$X_\Psi$	$X_{\psi'}$	$X_\phi$	$X_\psi$
T1-3-A	0	$1_0^F$	$2_1^F$	$1_0^S$	$2_{-1}^F$	$\beta$	$\beta$	$\beta$	$\beta$
T1-3-A	0	$1_0^F$	$2_1^F$	$1_0^S$	$2_{-1}^F$	1	-1	1	1
T1-3-A	0	$1_0^F$	$2_1^F$	$1_0^S$		1	-1	1	
T1-3-A	0	$1_0^F$	$2_1^F$	$1_0^S$	$2_{-1}^F$	-1	1	1	1
T1-3-B	0	$1_0^F$	$2_1^F$	$3_0^S$	$2_{-1}^F$	$\beta$	$\beta$	$\beta$	$\beta$
T1-3-B	0	$1_0^F$	$2_1^F$	$3_0^S$	$2_{-1}^F$	1	-1	1	1
T1-3-B	0	$1_0^F$	$2_1^F$	$3_0^S$		1	-1	1	
T1-3-B	0	$1_0^F$	$2_1^F$	$3_0^S$	$2_{-1}^F$	-1	1	1	1
T1-3-C	$\pm 1$	$2_{\pm 1}^F$	$1_{2,0}^F$	$2_{\pm 1}^S$	$1_{0,-2}^F$	$\beta$	$\beta$	$\beta$	$\beta$
T1-3-D	1	$2_1^F$	$1_2^F$	$2_1^S$	$3_0^F$	$\beta$	$\beta$	$\beta$	$\beta$
T1-3-D	-1	$2_{-1}^F$	$1_0^F$	$2_{-1}^S$	$3_{-2}^F$	$\beta$	$\beta$	$\beta$	$\beta$
T1-3-F	$\pm 1$	$2_{\pm 1}^F$	$3_{2,0}^F$	$2_{\pm 1}^S$	$3_{0,-2}^F$	$\beta$	$\beta$	$\beta$	$\beta$
T1-3-G	0	$3_0^F$	$2_1^F$	$1_0^S$	$2_{-1}^F$	$\beta$	$\beta$	$\beta$	$\beta$
T1-3-G	0	$3_0^F$	$2_1^F$	$1_0^S$	$2_{-1}^F$	1	-1	1	1
T1-3-G	0	$3_0^F$	$2_1^F$	$1_0^S$		1	-1	1	
T1-3-G	0	$3_0^F$	$2_1^F$	$1_0^S$	$2_{-1}^F$	-1	1	1	1
T1-3-H	0	$3_0^F$	$2_1^F$	$3_0^S$	$2_{-1}^F$	$\beta$	$\beta$	$\beta$	$\beta$
T1-3-H	0	$3_0^F$	$2_1^F$	$3_0^S$	$2_{-1}^F$	1	-1	1	1
T1-3-H	0	$3_0^F$	$2_1^F$	$3_0^S$		1	-1	1	
T1-3-H	0	$3_0^F$	$2_1^F$	$3_0^S$	$2_{-1}^F$	-1	1	1	1

**T3**

This topology has fewer vertices, none of which can violate  $U(1)_X$ . For any value of  $\alpha$  the distribution

$$X_\phi = X_{\phi'} = X_\psi = \beta \quad (10.33)$$

is possible. There are no values for  $\alpha$  for which more assignments are possible.

If  $\phi$  and  $\phi'$  are in the same representation of  $SU(2)_L$ , mixing between  $\phi$  and  $(\phi')^\dagger$  can be introduced by the breaking of  $U(1)_X$ . This is the case for  $\alpha = 0$  in which  $\psi$  has no hypercharge, and  $\phi$  and  $\phi'$  have opposite hypercharge. However, this results in no additional possibilities for the charge assignments.

**List of models T3** The resulting list of all non-equivalent models is shown in Table 10.5. Same as for the previous topologies  $X_\zeta = 2$ , the parameter  $a$  is again constrained by  $\beta \neq 0, \pm 2$  and if  $\beta = \pm 4$  a new scalar doublet may mix with the SM Higgs boson which makes the DM candidate unstable.

Table 10.5: Non-equivalent models of topology T3.  $X_\zeta$  is normalized to 2.

Model	$\alpha$	$\phi'$	$\phi$	$\psi$	$X_{\phi'}$	$X_\phi$	$X_\psi$
T3-A	0	$1_0^S$	$3_2^S$	$2_1^F$	$\beta$	$\beta$	$\beta$
T3-A	-2	$1_{-2}^S$	$3_0^S$	$2_{-1}^F$	$\beta$	$\beta$	$\beta$
T3-B	1, -3	$2_{1,-3}^S$	$2_{3,-1}^S$	$1_{2,-2}^F$	$\beta$	$\beta$	$\beta$
T3-B	-1	$2_{-1}^S$	$2_1^S$	$1_0^F$	$\beta$	$\beta$	$\beta$
T3-C	1, -3	$2_{1,-3}^S$	$2_{3,-1}^S$	$3_{2,-2}^F$	$\beta$	$\beta$	$\beta$
T3-C	-1	$2_{-1}^S$	$2_1^S$	$3_0^F$	$\beta$	$\beta$	$\beta$
T3-E	0, -2	$3_{0,-2}^S$	$3_{2,0}^S$	$2_{1,-1}^F$	$\beta$	$\beta$	$\beta$



### 10.1.4 Residual global symmetry

After breaking the  $U(1)_X$  gauge symmetry, a smaller symmetry can remain as a residual global symmetry. This would be advantageous, as this guarantees that DM remains stable and prohibits a tree-level seesaw contribution. Before  $U(1)_X$  breaking, the gauge transformation

$$\{\phi, \psi, \zeta\} \rightarrow e^{i\alpha(x)X_{\{\phi, \psi, \zeta\}}} \{\phi, \psi, \zeta\}, \quad (10.34)$$

leaves the Lagrangian invariant. If one fixes the value of  $\alpha = 2\pi/X_\zeta$ , then  $\zeta$  automatically transforms trivially. This means that after  $U(1)_X$  symmetry breaking the Lagrangian is invariant if all fields are transformed under

$$\{\phi, \psi\} \rightarrow e^{i2\pi \frac{X_{\{\phi, \psi\}}}{X_\zeta}} \{\phi, \psi\}. \quad (10.35)$$

As we have seen in the previous section, the charges of the fields are either all equal, or they differ in units of  $X_\zeta$ . Thus the charge of a field  $\phi$  can be described in terms of the ratio of  $X_\phi$  and  $X_\zeta$  as

$$\frac{X_\phi}{X_\zeta} = r + n(\phi) \quad (10.36)$$

where we assume that all fields have an integer charge, then  $r \in \mathbb{Q}$  and  $n \in \mathbb{Z}$ . In this case  $r$  is dependent on the model, but not on the fields, and  $n$  does depend on  $\phi$ . Inserting the above expression into Equation (10.35), one can see that the term containing  $n$  does not affect the invariance of the Lagrangian. Therefore the important quality that determines the remaining global symmetry after  $U(1)_X$  breaking is the quantity  $r$ . For the ratios  $r = \frac{1}{2}, \frac{1}{3}, \frac{1}{4}$  a remnant global  $\mathbb{Z}_{2,3,4}$  symmetry is left. Some of the models can exhibit an even larger symmetry, specifically a global  $U(1)$  symmetry, which of course contains the  $\mathbb{Z}_n$  as subgroups. The models with a  $\mathbb{Z}_2$  symmetry are just as in Ref. [204], though the particle content of the particular models differs slightly because of the vector-like fermions and the complex scalars.

### 10.1.5 Neutrino masses

In order to give a valid phenomenological description of neutrino masses, each of the models should be able to generate at least two generations of massive neutrinos. This has already been stated in a few locations in Section 10.1.3, but here we will go into further detail. In Ref. [203] the formulae for the neutrino masses for each of the topologies are given. Under the assumption that all new fields only have a single generation, a simple pattern emerges in the neutrino mass formulae. Denoting the Yukawa couplings of the SM neutrinos to the dark sector with  $y, y'$ , the resulting mass matrix can be written as being proportional to

$$(M_\nu)_{\alpha\beta} \propto y_\alpha y'_\beta + y'_\alpha y_\beta =: A_{\alpha\beta} + A_{\alpha\beta}^T, \quad (10.37)$$

where the exact proportionality depends on the masses and couplings of the new fields. One can verify that in this case the matrix  $A$  has rank 1. The rank of  $M_\nu$  and thus the number of massive neutrinos can be estimated to be  $\leq 2$ . As the entries of the Yukawa couplings are not fixed a priori, the neutrino matrix will actually have rank two unless two particles in the loop are identified with each other, which yields  $y = y'$ . Some models allow for the case where two fields are identified with each other. In this case, only a single massive neutrino would be generated, unless multiple generations of one of the new fields are added.

## 10.2 Comparison to other U(1) models

After presenting the overview of all possible models we will now give some concrete examples of models found in our overview that have already been studied in the literature. Of course it is also possible to construct U(1) gauged models that rely on other symmetries, such as  $U(1)_{B-L}$  or  $U(1)_L$  gauge symmetries. We will also compare these models to our results.

### 10.2.1 Concrete examples of our models

As a first example of a radiative seesaw model, there exists a U(1) gauged version of the scotogenic model [336, 340]. It corresponds to the model T3-B with  $\alpha = -1$  and  $a = 1$  of our overview, see Tab. 10.5. It contains two scalar doublets with an opposite U(1) charge of  $\pm 1$  and three generations of fermion singlets with charge 1. In the case where the complex scalar that breaks the U(1) symmetry has a charge of 2, a  $\mathbb{Z}_2$  symmetry is obtained, whereas a global U(1) is obtained if the complex scalar has a charge of 3. The lightest fermion singlet is then a suitable DM candidate. The extra scalar, as well as the new gauge boson are then argued to provide an explanation for the cosmic ray positron excess observed by PAMELA [143]. A light force carrier could increase the annihilation cross section by the Sommerfeld enhancement, which could explain AMS-02 results in the same way [349]. Further focus is on the self interacting DM, which can solve problems in cosmic structure formation for a new gauge boson or scalar mass on the MeV scale.

### 10.2.2 Comparison to B-L gauged models

A popular scenario is to promote the accidental B-L symmetry of the SM to a gauge symmetry, which often shows up in GUTs. An overview of models with a gauged  $U(1)_{B-L}$  symmetry generating Majorana neutrino masses was derived in Ref. [339] for the one-loop case with remnant  $\mathbb{Z}_2$  symmetry, the two-loop case with a remnant  $\mathbb{Z}_3$  symmetry, and a three-loop case with a remnant  $\mathbb{Z}_4$  symmetry. For the one-loop case, the starting point is the particle content of the scotogenic model [205], to which two complex scalar singlets  $\sigma$  and  $\chi$  are added, the former of which develops a vev that breaks the  $U(1)_{B-L}$  symmetry. In order to avoid a tree-level seesaw contribution, the right-handed fermionic singlets  $N_R$  have charges  $Q_{B-L} \neq -1$ . In order to satisfy gauge anomaly cancellation constraints additional exotic Dirac and Majorana fermions are added to the models, which are not directly related to the

generation of neutrino masses. For realizations with at a higher loop level, extra fermions need to be added as well. This is in contrast to this work, where we only consider fields that are involved in the neutrino mass loop, and an additional scalar to break the  $U(1)_X$  symmetry.

### 10.2.3 Comparison to L gauged models

Scenarios, where the lepton number symmetry was promoted to a local gauge symmetry have also been considered [337, 338]. Whereas Majorana masses can be generated with a global  $U(1)_L$ , only scenarios with Dirac neutrinos are considered if the symmetry is made local. In Ref. [337] one-loop Dirac neutrino masses with a remnant  $\mathbb{Z}_3$  symmetry is obtained if 3, 9, 3 copies of right-handed fermion singlets with  $U(1)_L$  charges  $-2, 3, -4$  respectively are added to satisfy gauge anomaly conditions. Two scalar singlets with charges 3 and 6 are also included to obtain non-zero fermion masses.

### 10.2.4 Comparison to Dirac neutrinos

As was already mentioned in comparisons with some of the previous models, it is also possible to consider models in which Dirac neutrino masses are generated instead of Majorana ones. This requires the addition of right-handed fermions, and neutrino masses are not generated by the  $d = 5$  Weinberg operator anymore. In Ref. [342] an overview of these models is presented, for the case where varying numbers of right-handed singlet fermions that are charged under a new  $U(1)$  gauge symmetry are added, for which the gauge anomaly conditions are solved. vector-like fermions are explicitly excluded. The Dirac masses are generated through  $d = 5$  and  $d = 6$  operators, which also require additional scalars. The smallest number of singlets one can add is 6, which is anomaly free for the  $U(1)$  charges  $(-1, -1, -1, -4, -4, 5)$  and  $(-1, 2, 3, -5, -5, 6)$ , when the SM remains uncharged [343].

Further models that generate Dirac masses often employ B-L symmetry again. In order to satisfy the  $B - L$  gauge anomalies, three right-handed neutrinos, with  $L = -1$  suffice, though it leads to a tree-level seesaw contribution. Another solution is to give the right-handed neutrinos the  $B - L$  charges  $-4, -4, 5$ . Further fermions can then be added, as long as the contributions to the gauge anomalies vanish separately among all additional fermions. In order to generate neutrino masses, scalars need to be added as well. This way, a number of different models can be constructed, see e.g. [344, 345, 346].

## 10.3 Z' phenomenology

In the previous sections we have derived an overview for  $U(1)_X$  gauged models, and compared the results to models in the literature. We now focus on the phenomenology of  $U(1)_X$  gauged models, in which we focus on phenomenological aspects that are in general present, and depend as little as possible on the specific particle content of the model. One of the common

features of models with an extra gauged U(1) symmetry is the appearance of a new gauge boson, the  $Z'$ . For an extensive overview of  $Z'$  physics, see Ref. [350]. In this section we will discuss several aspects related to the new  $Z'$  gauge boson.

### 10.3.1 Gauge kinetic mixing

The gauge sector looks fundamentally different in theories with two (or more) U(1) groups [351]. For theories with two Abelian gauge groups, the kinetic Lagrangian terms for the gauge fields can be written in general as

$$\mathcal{L}_{\text{kin}} = -\frac{1}{4}\tilde{F}_{1\mu\nu}\tilde{F}_1^{\mu\nu} - \frac{1}{4}\tilde{F}_{2\mu\nu}\tilde{F}_2^{\mu\nu} - \frac{\tilde{\epsilon}}{2}\tilde{F}_{1\mu\nu}\tilde{F}_2^{\mu\nu}, \quad (10.38)$$

where the final term is allowed for Abelian gauge groups, as the field tensors are gauge invariant. This term induces gauge kinetic mixing, and can be generated from radiative corrections, even if it is absent at tree level [350]. The form of the covariant derivatives, taking only the U(1) groups into account, is most generally given by

$$D_\mu\phi = \left( \partial_\mu - i \sum_{i,j} Q_\phi^i g_{ij} \tilde{A}_j^\mu \right) \phi \quad (10.39)$$

Here,  $Q_\phi^i = X_\phi, Y_\chi$  is the U(1) charge of the particle  $\phi$  under the gauge group  $U(1)_i$ , ( $i = X, Y$ ). The coupling  $g_{ij}$  thus couples a field with charge  $Q_\phi^i$  to a gauge field  $A_j^\mu$  and is in its most general form not diagonal. The interactions of the gauge fields can then be written as

$$\mathcal{L} \supset \begin{pmatrix} \tilde{A}_{1\mu} & \tilde{A}_{2\mu} \end{pmatrix} \begin{pmatrix} g_{11} & g_{12} \\ g_{21} & g_{22} \end{pmatrix} \begin{pmatrix} j_Y^\mu \\ j_X^\mu \end{pmatrix} \quad (10.40)$$

with the currents  $j_Y^\mu$  and  $j_X^\mu$  defined in terms of the charges

$$\begin{aligned} j_Y^\mu = & \sum_\phi iY_\phi \left( \partial^\mu \phi^\dagger \phi - \phi^\dagger \partial^\mu \phi \right) + Y_\phi \left( \sum_{i,j} Q_\phi^i g_{ij} \tilde{A}_j^\mu \right) |\phi|^2 \\ & + \sum_\psi Y_\psi \bar{\psi}_{\dot{a}} (\bar{\sigma}^\mu)^{\dot{a}b} \psi_b, \end{aligned} \quad (10.41)$$

$$\begin{aligned} j_X^\mu = & \sum_\phi iX_\phi \left( \partial^\mu \phi^\dagger \phi - \phi^\dagger \partial^\mu \phi \right) + X_\phi \left( \sum_{i,j} Q_\phi^i g_{ij} \tilde{A}_j^\mu \right) |\phi|^2 \\ & + \sum_\psi X_\psi \bar{\psi}_{\dot{a}} (\bar{\sigma}^\mu)^{\dot{a}b} \psi_b. \end{aligned} \quad (10.42)$$

The spinor sum is taken over Weyl spinors. The basis of the gauge fields can be freely chosen, whereas it is inconvenient to redefine the currents as the charges are defined beforehand. In

order to make the connection with literature, we first transform the coupling matrix into a diagonal form. This is done by decomposing the matrix as follows

$$\begin{pmatrix} g_{11} & g_{12} \\ g_{21} & g_{22} \end{pmatrix} = \begin{pmatrix} \frac{g_{11}}{g_Y} & \frac{g_{12}}{g_X} \\ \frac{g_{21}}{g_Y} & \frac{g_{22}}{g_X} \end{pmatrix} \begin{pmatrix} g_Y & 0 \\ 0 & g_X \end{pmatrix} \quad (10.43)$$

We now redefine the gauge fields (using a non unitary transformation) by

$$\begin{pmatrix} A_Y^\mu \\ A_X^\mu \end{pmatrix} = \begin{pmatrix} \frac{g_{11}}{g_Y} & \frac{g_{12}}{g_X} \\ \frac{g_{21}}{g_Y} & \frac{g_{22}}{g_X} \end{pmatrix} \begin{pmatrix} \tilde{A}_1^\mu \\ \tilde{A}_2^\mu \end{pmatrix}. \quad (10.44)$$

$g_X$  and  $g_Y$  need to be chosen in such a way, that the kinetic Lagrangian takes the canonical form as in Eq. (10.38).<sup>2</sup> Such a field redefinition also gives new contributions to the kinetic mixing term. With the redefinition of  $\tilde{\epsilon} \rightarrow \epsilon$ , the Lagrangian takes the following form, which is often found in the literature as starting point [352, 353]

$$\mathcal{L} \supset -\frac{1}{4}F_Y^{\mu\nu}F_{Y\mu\nu} - \frac{\epsilon}{2}F_Y^{\mu\nu}F_{X\mu\nu} - \frac{1}{4}F_X^{\mu\nu}F_{X\mu\nu} + \begin{pmatrix} A_{Y\mu} & A_{X\mu} \end{pmatrix} \begin{pmatrix} g_Y & 0 \\ 0 & g_X \end{pmatrix} \begin{pmatrix} j_Y^\mu \\ j_X^\mu \end{pmatrix}. \quad (10.45)$$

This form with a diagonal coupling matrix is often found in the literature as starting point. In order to bring the kinetic terms to the canonical form without kinetic mixing, they can be diagonalized by transforming the fields with the non-orthogonal transformation

$$\begin{pmatrix} A_Y^\mu \\ A_X^\mu \end{pmatrix} = \frac{1}{\sqrt{2}} \begin{pmatrix} \frac{1}{\sqrt{1+\epsilon}} & \frac{1}{\sqrt{1-\epsilon}} \\ \frac{1}{\sqrt{1+\epsilon}} & \frac{-1}{\sqrt{1-\epsilon}} \end{pmatrix} \begin{pmatrix} A_1^\mu \\ A_2^\mu \end{pmatrix}, \quad (10.46)$$

after which the Lagrangian is given by

$$\mathcal{L} \supset -\frac{1}{4}F_1^{\mu\nu}F_{1\mu\nu} - \frac{1}{4}F_2^{\mu\nu}F_{2\mu\nu} + \frac{1}{\sqrt{2}} \begin{pmatrix} A_{1\mu} & A_{2\mu} \end{pmatrix} \begin{pmatrix} \frac{g_Y}{\sqrt{1+\epsilon}} & \frac{g_X}{\sqrt{1+\epsilon}} \\ \frac{g_Y}{\sqrt{1-\epsilon}} & \frac{-g_X}{\sqrt{1-\epsilon}} \end{pmatrix} \begin{pmatrix} j_Y^\mu \\ j_X^\mu \end{pmatrix}. \quad (10.47)$$

The matrix coupling the gauge bosons to the currents can in general not be diagonalized. However using the QR decomposition it can be transformed to a lower triangular matrix in the following way:

$$\frac{1}{\sqrt{2}} \begin{pmatrix} \frac{g_Y}{\sqrt{1+\epsilon}} & \frac{g_X}{\sqrt{1+\epsilon}} \\ \frac{g_Y}{\sqrt{1-\epsilon}} & \frac{-g_X}{\sqrt{1-\epsilon}} \end{pmatrix} = \frac{1}{\sqrt{2}} \begin{pmatrix} \sqrt{1+\epsilon} & \sqrt{1-\epsilon} \\ \sqrt{1-\epsilon} & -\sqrt{1+\epsilon} \end{pmatrix} \begin{pmatrix} g_Y & 0 \\ \frac{-g_Y\epsilon}{\sqrt{1-\epsilon^2}} & \frac{g_X}{\sqrt{1-\epsilon^2}} \end{pmatrix} =: QR \quad (10.48)$$

We can now rotate the fields with the redefinition

$$\begin{pmatrix} A^\mu \\ A'^\mu \end{pmatrix} := \frac{1}{\sqrt{2}} \begin{pmatrix} \sqrt{1+\epsilon} & \sqrt{1-\epsilon} \\ \sqrt{1-\epsilon} & -\sqrt{1+\epsilon} \end{pmatrix} \begin{pmatrix} A_1^\mu \\ A_2^\mu \end{pmatrix}. \quad (10.49)$$

---

<sup>2</sup>The analytic expressions are quite unwieldy and are thus not given here.

which leaves us with the following Lagrangian

$$\mathcal{L} \supset -\frac{1}{4}F^{\mu\nu}F_{\mu\nu} - \frac{1}{4}F'^{\mu\nu}F'_{\mu\nu} + \begin{pmatrix} A_\mu & A'_\mu \end{pmatrix} \begin{pmatrix} g_Y & 0 \\ \frac{-g_Y\epsilon}{\sqrt{1-\epsilon^2}} & \frac{g_X}{\sqrt{1-\epsilon^2}} \end{pmatrix} \begin{pmatrix} j_Y^\mu \\ j_X^\mu \end{pmatrix}. \quad (10.50)$$

This result agrees with case b) in Ref. [354]. If we would have chosen  $R$  to be an upper diagonal matrix, we would have ended up with case a) in Ref. [354]. Thus it is, starting from the most general case, always possible to transform into a basis such that the SM gauge boson  $A_\mu$  couples to the charges  $Y$  only. On the other hand, the gauge boson  $A'_\mu$  picks up a small coupling to the current  $j_Y^\mu$  as well, but still chiefly couples to  $j_X^\mu$ .

### 10.3.2 Gauge mass mixing

The previous section concerned itself with basis transformations inside the gauge kinetic terms. The next step is to consider the breaking of the  $U(1)_X$  symmetry as well as electroweak symmetry breaking. In this process, the gauge bosons obtain their masses. The scalar sector will be discussed in section 10.4. The covariant derivative for  $SU(2)_L \times U(1)_Y \times U(1)_X$  in the basis as in equation (10.50) is given by

$$D_\mu = \partial_\mu - i \left( g_Y A_\mu + \frac{-\epsilon g_Y}{\sqrt{1-\epsilon^2}} A'_\mu \right) Y - i \frac{g_X}{\sqrt{1-\epsilon^2}} A'_\mu X - i g \tau^a W_\mu^a \quad (10.51)$$

where  $X, Y$  and  $\tau^a$  are the generators of  $U(1)_X$ ,  $U(1)_Y$  and  $SU(2)_L$  respectively. The part of the Lagrangian relevant for the mass of the gauge bosons is given by

$$\mathcal{L} \supset |D_\mu H|^2 + |D_\mu \zeta|^2. \quad (10.52)$$

Expanded around the minimum this expression yields for the neutral gauge bosons

$$\mathcal{L} \supset \frac{v_H^2}{8} \left( g_Y A_\mu + \frac{-\epsilon g_Y}{\sqrt{1-\epsilon^2}} A'_\mu - g W_\mu^3 \right)^2 + \frac{v_\zeta^2}{2} \left( \frac{g_X}{\sqrt{1-\epsilon^2}} A'_\mu X_\zeta \right)^2 \quad (10.53)$$

$$= \begin{pmatrix} A_\mu & W_\mu^3 & A'_\mu \end{pmatrix} \begin{pmatrix} \frac{g_Y^2 v_H^2}{8} & -\frac{gg_Y v_H^2}{8} & -\frac{\epsilon g_Y^2 v_H^2}{8\sqrt{1-\epsilon^2}} \\ -\frac{gg_Y v_H^2}{8} & \frac{g^2 v_H^2}{8} & \frac{\epsilon gg_Y v_H^2}{8\sqrt{1-\epsilon^2}} \\ -\frac{\epsilon g_Y^2 v_H^2}{8\sqrt{1-\epsilon^2}} & \frac{\epsilon gg_Y v_H^2}{8\sqrt{1-\epsilon^2}} & \frac{\epsilon^2 g_Y^2 v_H^2}{8(1-\epsilon^2)} + \frac{g_X^2 v_\zeta^2 X_\zeta^2}{2(1-\epsilon^2)} \end{pmatrix} \begin{pmatrix} A^\mu \\ W^{3\mu} \\ A'^\mu \end{pmatrix}. \quad (10.54)$$

Through the Weinberg angle,  $A_\mu$  and  $W_\mu^3$  mix to form the photon and the  $Z$  boson. This results in the following mass matrix

$$\begin{pmatrix} \gamma & \tilde{Z} & A'_\mu \end{pmatrix} \frac{1}{2} \begin{pmatrix} 0 & 0 & 0 \\ 0 & M_Z^2 & \Delta \\ 0 & \Delta & \frac{M_X^2}{(1-\epsilon^2)} \left( 1 + \epsilon^2 \sin^2 \theta_w \frac{M_Z^2}{M_X^2} \right) \end{pmatrix} \begin{pmatrix} \gamma \\ \tilde{Z} \\ A'^\mu \end{pmatrix}, \quad (10.55)$$

with

$$M_Z^2 = \frac{(g^2 + g_Y^2)v_H^2}{4} = \frac{g^2 v_H^2}{4 \cos^2 \theta_w} \quad (10.56)$$

being the SM  $Z$  mass in absence of kinetic mixing. The mixing terms are given by

$$\Delta = \epsilon \frac{g_Y \sqrt{g^2 + g_Y^2} v_H^2}{4 \sqrt{1 - \epsilon^2}} = \frac{\epsilon \sin \theta_w}{\sqrt{1 - \epsilon^2}} M_Z^2, \quad (10.57)$$

and completely depend on the kinetic mixing parameter. The term in the lower right corner has been rewritten in terms of the mass

$$M_X^2 = g_X^2 X_\zeta^2 v_\zeta^2 \quad (10.58)$$

of the new gauge boson in the absence of kinetic mixing. This means the complete term can be written as

$$M_{A'}^2 = \frac{M_X^2}{(1 - \epsilon^2)} \left( 1 + \epsilon^2 \sin^2 \theta_w \frac{M_Z^2}{M_X^2} \right) \quad (10.59)$$

The remaining non-diagonal part can be diagonalized by a second mixing angle  $\theta'$ , of which the value is given by

$$\tan 2\theta' = \frac{2\Delta}{M_Z^2 - M_{A'}^2}. \quad (10.60)$$

Up to second order in  $\epsilon$ , the squared masses of  $\gamma$ ,  $Z$  and  $Z'$  are then given by

$$\begin{pmatrix} 0 & & \\ M_Z^2 \left( 1 - \epsilon^2 \sin^2 \theta_w \frac{M_Z^2}{M_X^2 - M_Z^2} \right) & & \\ M_X^2 \left( 1 + \epsilon^2 \left( 1 + \sin^2 \theta_w \frac{M_Z^2}{M_X^2 - M_Z^2} \right) \right) & & \end{pmatrix}. \quad (10.61)$$

The  $Z^0$  boson mass has been experimentally measured by e.g. the LEP experiment and matches the SM prediction. As the shift in the  $Z^0$  mass that depends on the kinetic mixing and the  $Z'$  mass, this can be used to constrain the viable parameter space. We compute the  $Z^0$  mass numerically and show the area in the  $m_{Z'} - \epsilon$  plane, where  $m_Z$  deviates more than  $3\sigma$  from the experimental value of  $m_Z = 91.1876$  GeV. The results are presented in Fig. 10.3. We also show the limits set by BABAR [356] and NA64 [357] as well the the favored region to explain the anomalous magnetic moment of the muon, which will be discussed in section 10.3.3.

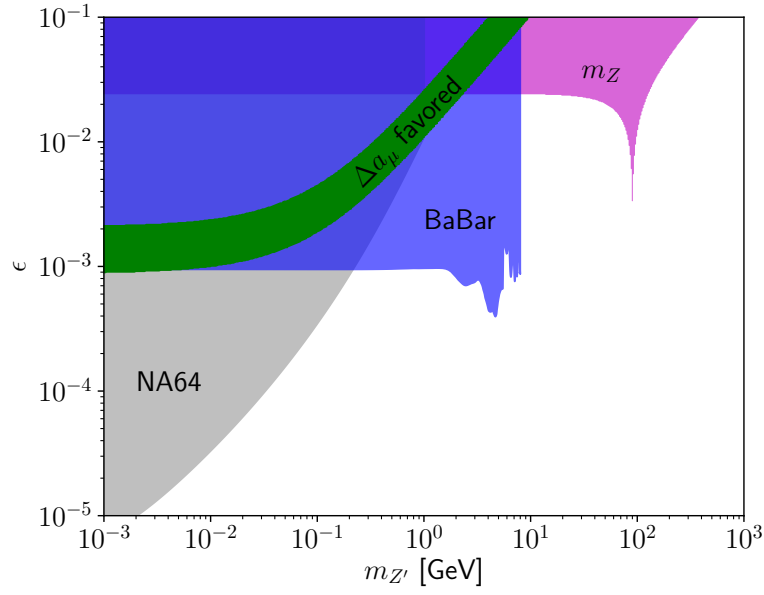


Figure 10.3: Excluded regions in the  $m_{Z'} - \epsilon$  plane from various experimental constraints. The parameters are  $g_X = 0.1$ ,  $X_\zeta = 3$ , while  $\epsilon$  and  $v_\zeta$  are varied. Also included is the  $(g - 2)_\mu$  favoured region [355].

### Gauge couplings

As a consequence of the mixing into mass eigenstates, the interaction term in the Lagrangian can be expressed as

$$\mathcal{L} \supset (\gamma_\mu \quad Z_\mu \quad Z'_\mu) \begin{pmatrix} c & s & 0 \\ -sc' & cc' & s' \\ ss' & -cs' & c' \end{pmatrix} \begin{pmatrix} g_Y & 0 & 0 \\ 0 & g & 0 \\ \frac{-g_Y \epsilon}{\sqrt{1-\epsilon^2}} & 0 & \frac{g_X}{\sqrt{1-\epsilon^2}} \end{pmatrix} \begin{pmatrix} j_Y^\mu \\ j_{\tau^3}^\mu \\ j_X^\mu \end{pmatrix} \quad (10.62)$$

where  $j_{\tau^3}^\mu$  is the current belonging to the generator  $\tau^3$  of  $SU(2)_L$ . We see that the photon does not couple the  $U(1)_X$  charge, but the  $Z$  and  $Z'$  boson couple to both isospin as well as the  $U(1)_X$  charge.

### 10.3.3 Anomalous magnetic moment

In the  $\mathbb{Z}_2$  case a contribution to the anomalous magnetic moment from the models' particle content comes from loops similar to the ones relevant for LFV or the neutrino masses. These usually give only small contributions to the anomalous magnetic moment as they are suppressed by the masses of the fields running in the loop [75, 358].



If the mass of the  $Z'$  is not too large it can contribute to the anomalous magnetic moment through a similar loop as the photon does. Through kinetic mixing the  $Z'$  boson obtains a coupling to the SM leptons. The couplings can be extracted from equation (10.62). With

$$g_V = \frac{1}{2}(g_R + g_L) \quad (10.63)$$

$$g_A = \frac{1}{2}(g_R - g_L) \quad (10.64)$$

the contribution of a neutral vector boson to  $a_\mu \equiv (g - 2)_\mu/2$  is given by [359]

$$\Delta a_\mu = \frac{m_l^2}{8\pi^2} \int_0^1 dx \frac{g_V^2 2x^2(1-x) + g_A^2 \left[ 2x(1-x)(x-4) - 4 \frac{m_l^2}{m_{Z'}^2} x^3 \right]}{(1-x)(m_{Z'}^2 - m_l^2 x) + m_l^2 x}. \quad (10.65)$$

We calculate the contribution of the  $Z'$  boson numerically and mark the area where solely the contribution of the new gauge boson can explain the discrepancy between SM and the latest Fermilab result in the  $3\sigma$  range [355] in Fig. 10.3. The entire area is already excluded by other experiments such as BABAR.

### 10.3.4 Direct detection

If the hidden sector is stabilized by a  $\mathbb{Z}_2$  symmetry, dark matter can scatter on nuclei via Higgs and  $Z^0$  exchange. Whether the WIMPs couple to these bosons is dictated by their SM gauge group representation as well as their Lorentz representation. The coupling to the Higgs boson is given by a new parameter of the model whereas the coupling to the  $Z^0$  boson is given by the SM gauge couplings. If the latter case is not suppressed for example by singlet doublet mixing (see Ref. [253]), the dark matter candidate is usually ruled out by direct detection experiments.

In the case where the  $\mathbb{Z}_2$  symmetry is replaced by the  $U(1)_X$  symmetry, we have an additional possibility for dark matter to scatter off nuclei. As the WIMPs are charged under  $U(1)_X$ , the coupling of  $Z'$  is given by  $g_X X_{\text{DM}}$  at leading order in  $\epsilon$ . Kinetic mixing introduces some corrections so that the  $Z'$  boson also couples to hypercharge and weak isospin. Similarly there is always a contribution from the SM Z-boson. If the charge of the dark matter field  $X_{\text{DM}} = \pm \frac{X_\zeta}{2}$ , the vev of  $\zeta$  can introduce a mass splitting between the oppositely charged components of the dark matter field. In this case elastic scattering via the  $Z'$  boson is not possible. As an example for a case where this scattering process is relevant, we consider the case of Dirac dark matter. For simplicity we assume that the Dark matter is a singlet under the SM gauge group. The couplings of the  $Z$  and  $Z'$  boson to dark matter and to quarks can be extracted from Equation (10.62). The scattering cross section for protons is given by (see e.g. Ref. [242])

$$\sigma_p = \frac{\mu^2}{\pi} |2b_u + b_d|^2 \quad (10.66)$$

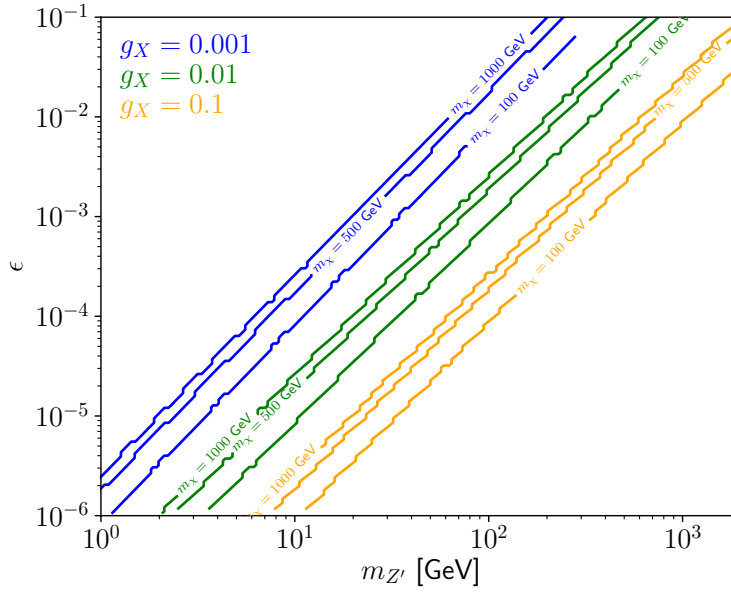


Figure 10.4: XENON1T limits [95] for Dirac dark matter in the  $m_{Z'} - \epsilon$  plane for different values of  $m_{\text{DM}}$  and  $g_X$ . The area above the lines is excluded by direct detection. The parameters are  $X_{\text{DM}} = 1, X_\zeta = 3$  while  $\epsilon$ ,  $v_\zeta$ , and the DM mass are varied.

where  $\mu$  is the WIMP-nucleon reduced mass which depends on the terms

$$b_q = \frac{g_{\bar{\chi}\chi Z',V} g_{\bar{q}q Z',V}}{m_{Z'}^2} + \frac{g_{\bar{\chi}\chi Z^0,V} g_{\bar{q}q Z^0,V}}{m_{Z^0}^2}, \quad (10.67)$$

that describe the interaction of the gauge bosons with the quarks through the quark-gauge boson couplings  $g_{\dots,V}$ .

To illustrate the sensitivity of direct detection experiments to  $Z'$  scattering, we calculate the cross section for different dark matter masses and different values of  $g_X$ , in which we vary the kinetic mixing parameter and  $v_\zeta$ . We then calculate what parts of the parameter space are excluded by XENON1T [95]. We show the results in Figure 10.4. One can see that large parts of the parameter space are excluded by XENON1T, especially at lower  $Z'$  masses. A comparison to Figure 10.3 shows that for most values of  $g_X$ , direct detection proves to be the most stringent limit. It is important to note that this finding holds true for Dirac dark matter as well as for complex scalar dark matter, whereas for Majorana and real scalar fields there is no elastic scattering via  $Z'$  exchange.

### Inelastic scattering

If the charge of the dark matter is  $X_{\text{DM}} = \pm \frac{X_\zeta}{2}$ , a mass splitting between the oppositely charged components of the dark matter field is induced. The mass matrix is then generally generated by terms in the Lagrangian as

$$\mathcal{L} \supset -m_\psi \psi \psi' - \lambda_\psi \psi \psi \zeta - \lambda_{\psi'} \psi' \psi' \zeta + \text{h.c.}, \quad (10.68)$$

which after  $U(1)_X$  breaking this turns into

$$\mathcal{L} \supset -\frac{1}{2} \begin{pmatrix} \psi & \psi' \end{pmatrix} \begin{pmatrix} \sqrt{2}v_\zeta \lambda_\psi & m_\psi \\ m_\psi & \sqrt{2}v_\zeta \lambda_{\psi'} \end{pmatrix} \begin{pmatrix} \psi \\ \psi' \end{pmatrix}. \quad (10.69)$$

For small  $v_\zeta$ , the mass splitting between the two components will be small. The two mass eigenstates then have a mass splitting of

$$\delta = \sqrt{2}v_\zeta(\lambda_\psi + \lambda_{\psi'}), \quad (10.70)$$

for which the inelastic scattering is possible if  $v_\zeta$  lies at  $\mathcal{O}(100 \text{ keV})$ .

### 10.3.5 Astrophysical effects

The standard scenario for cold dark matter assumes that DM is collisionless in structure formation. However, this has led to discrepancies between results from simulations and observations. There is the core-vs-cusp problem, where simulations expect galactic DM haloes to have a density cusp at the center, whereas observations from dwarf galaxies seem to indicate a flat core. A second problem is the missing satellites problem, where the amount of satellite DM haloes of the Milky Way predicted by simulations is larger than observed. Related to this is the too-big-to-fail problem, which comes from the issue that the simulated satellite DM haloes are so large, that they must host galaxies and have star formation. These are absent in observations. These problems can be ameliorated if DM is allowed to have a self-interaction with a cross section of  $\sigma \sim 10^{-24} \text{ cm}^2$ , flattening DM halo cores. It needs to work on longer distance scales, which can be fulfilled by a light force carrier with a mass  $\sim 10 \text{ MeV}$  [360, 361].

In the case where the  $U(1)_X$  remains unbroken, a massless gauge boson exists. In this case, the range of the force is long-range ('dark electromagnetism') and couples only to gauge fields. The primary limit on the coupling comes from the demand that the dark matter be effectively collisionless in galactic dynamics, which implies  $\alpha' < 10^{-4}$  for TeV-scale DM [362]. These values are easily compatible with constraints from structure formation and primordial nucleosynthesis.

### 10.3.6 Lepton Flavour Violation

LFV processes are generally present in radiative seesaw models. Mostly these processes occur through diagrams of similar topology as the neutrino mass loop, but then with charged leptons and charged components of the BSM field multiplets. There are no gauge bosons involved in these processes (except for radiated photons in e.g.  $\mu \rightarrow e\gamma$ ). The addition of a  $Z'$  boson that couples to leptons is in the most general case not diagonal in generation space. This can induce LFV processes both at tree level as well as the one-loop level, e.g. through box diagrams [363]. However, in our setup, the  $Z'$  couplings to leptons are generated through

kinetic mixing, and are thus equal to the SM  $Z$  couplings up to a factor from kinetic mixing. This also ensures that lepton flavour universality is maintained.

## 10.4 Higgs sector

The addition of the new complex scalar singlet  $\zeta$  introduces new phenomenology in the Higgs sector. In this section we will work out some of the new features of the extended scalar sector, as well as some related phenomena. For more extensive discussions, see Refs. [364, 208].

### 10.4.1 Higgs sector

We will now work out the features of a Higgs sector involving the most general potential containing the SM Higgs doublet  $H$  and the new scalar singlet  $\zeta$ , with charges 0 and  $X_\zeta$  under the new  $U(1)_X$  group respectively. The scalar potential is given by

$$V = -m_H^2(H^\dagger H) - m_\zeta^2(\zeta^\dagger \zeta) + \frac{\lambda}{2}(H^\dagger H)^2 + \frac{\lambda_\zeta}{2}(\zeta^\dagger \zeta)^2 + \lambda_{H\zeta}(H^\dagger H)(\zeta^\dagger \zeta). \quad (10.71)$$

In many ways this is similar to a type I 2HDM Higgs sector<sup>3</sup>, with the difference that  $\zeta$  is a singlet instead of a doublet. Therefore terms like  $(H^\dagger \zeta)(\zeta^\dagger H)$  and  $(H^\dagger \zeta)^2 + \text{h.c.}$  that do appear in 2HDMs do not appear here. We denote the vevs of the scalars by

$$\langle H \rangle = \begin{pmatrix} 0 \\ \frac{v_H + h}{\sqrt{2}} \end{pmatrix} \quad \langle \zeta \rangle = \frac{v_\zeta + \sigma}{\sqrt{2}}. \quad (10.72)$$

With these vevs one can derive the two minimum equations of the potential, which we solve for the mass terms. This results in

$$\begin{aligned} m_H^2 &= \frac{\lambda v_H^2}{2} + \frac{\lambda_{H\zeta} v_\zeta^2}{2} \\ m_\zeta^2 &= \frac{\lambda_\zeta v_\zeta^2}{2} + \frac{\lambda_{H\zeta} v_H^2}{2}. \end{aligned} \quad (10.73)$$

With the above minimum equations this results in the mass matrix

$$M = \begin{pmatrix} \lambda v_H^2 & \lambda_{H\zeta} v_H v_\zeta \\ \lambda_{H\zeta} v_H v_\zeta & \lambda_\zeta v_\zeta^2 \end{pmatrix} \quad (10.74)$$

with eigenvalues

$$m_{h_1}^2 = \frac{1}{2} \left( \lambda v_H^2 + \lambda_\zeta v_\zeta^2 - \sqrt{(\lambda v_H^2 - \lambda_\zeta v_\zeta^2)^2 + 4\lambda_{H\zeta}^2 v_H^2 v_\zeta^2} \right) \quad (10.75)$$

$$m_{h_2}^2 = \frac{1}{2} \left( \lambda v_H^2 + \lambda_\zeta v_\zeta^2 + \sqrt{(\lambda v_H^2 - \lambda_\zeta v_\zeta^2)^2 + 4\lambda_{H\zeta}^2 v_H^2 v_\zeta^2} \right), \quad (10.76)$$

<sup>3</sup>In these models the second Higgs doublet  $\phi_2$  is odd under a  $Z_2$  symmetry, as are the right-handed fermions. Thus only  $\phi_2$  couples to the SM fermions.

that are obtained by diagonalizing  $M$  through an orthogonal matrix, with a mixing angle given by

$$\tan 2\alpha = \frac{2\lambda_{H\zeta}v_Hv_\zeta}{\lambda v_H^2 - \lambda_\zeta v_\zeta^2}. \quad (10.77)$$

### Higgs couplings

The mixing in the scalar sector has an effect on the Yukawa couplings through which the SM fermions obtain their masses. The SM fermions do not couple to  $\zeta$  in the unbroken phase, and receive no contribution from  $v_\zeta$ . In the SM, the couplings of a fermion  $f$  can be brought to the form

$$\frac{m_f}{v_H}, \quad (10.78)$$

with which they couple to  $h$ . Because of the mixing between  $h$  and  $\sigma$  to  $h_1$  and  $h_2$ , these couplings get modified as the  $h$  state can be written as

$$h = \cos \alpha h_1 - \sin \alpha h_2. \quad (10.79)$$

We identify  $h_1$  with the SM-like Higgs boson. The couplings of  $h_1$  and  $h_2$  to the SM fermion are then

$$\frac{m_f \cos \alpha}{v_H} \quad \frac{m_f \sin \alpha}{v_H} \quad (10.80)$$

respectively. Through mixing, the SM fermions obtain a coupling to  $h_2$ . Both couplings are similar to the SM Higgs couplings, up to a rescaling factor depending on the mixing angle. The couplings to the electroweak gauge bosons are modified in the same way. The couplings can be probed in collider experiments. This singlet extension scenario was considered in an ATLAS analysis, which placed an upper limit on the mixing angle of  $\sin^2 \alpha = 0.12$  [365]. Further global fits to the LHC 7 and 8 TeV data constrained the mixing angle  $\cos \alpha \gtrsim 0.86$  [366]. Precision measurements of the  $W$  mass can place upper bounds of  $|\sin \alpha| < 0.19$  [367]. The High Luminosity (HL) LHC could reach  $\sin^2 \alpha \sim 4 - 8 \times 10^{-2}$  [368]. From Equation (10.77) one can see that the mixing angle is suppressed by a factor  $v_H/v_\zeta$  if the latter vev is larger or by the inverse ratio if  $v_\zeta$  smaller. Thus, the bounds on the mixing angle can generally be satisfied if  $v_\zeta$  is not close to the SM Higgs vev  $v_H$ .

### Direct detection

Irrespective of the  $U(1)_X$  charge, there can exist a coupling between the dark matter candidate and  $\zeta$  in the form of  $(H^\dagger H)(\zeta^\dagger \zeta)$ . Through Higgs mixing this allows for dark matter scattering on nuclei via scalar exchange. Such a scattering is model dependent, as the coupling of dark matter to  $\sigma$  is a free parameter. If a DM candidate is scalar, a direct coupling to the SM Higgs is generally possible through a  $(H^\dagger H)(\chi^\dagger \chi)$  term. For fermion DM a direct coupling to the SM Higgs is only possible if there exists a singlet-doublet or triplet-doublet coupling to the Higgs. If no such particle content is available, the only contribution is through Higgs mixing. In this case, the scattering takes place through the exchange of  $h_2$ . Compared to the

exchange of the SM-like Higgs  $h_1$ , its coupling to the quarks is then suppressed by the factor  $\sin \alpha$ , see Equations (10.77) and (10.80). If  $h_2$  is heavier than  $h_1$ , it receives an additional suppression as the scattering cross section scales with  $m_{h_2}^{-4}$ . Thus, such a contribution is generally subdominant.

## 10.5 Grand unification

The question whether all fundamental interactions can be expressed in terms of a unified description is a fundamental question in theoretical physics. The theories that offer such a description for the SM interactions are called *Grand Unified Theories* (GUTs). The work by Glashow, Weinberg, and Salam resulted in a succesful theory that unified the weak and electromagnetic interactions, and together with QCD the gauge symmetries of the SM are given by the  $SU(3)_c \times SU(2)_L \times U(1)_Y$  gauge group. However, in the GWS electroweak theory there are still two separate gauge couplings  $(g, g')$ . A first attempt to unify the SM interactions into a single gauge group with a single couplings strength was put forward by Georgi and Glashow, and was based on the  $SU(5)$  gauge group [369]. The SM gauge group has rank<sup>4</sup> 4, and a unifying group must have at least the same rank, which  $SU(5)$  fulfils<sup>5</sup>. Another well known class consists of GUTs based on the rank 5  $SO(10)$  group, which was proposed by Fritzsch and Minkowski [370]. However, even larger unification groups are considered, an example is the exceptional group  $E_6$  of rank 6 [371].

There are also examples of GUTs that are not based on a simple lie group, but on a product of several groups. The Pati-Salam model is based on the  $SU(4)_C \times SU(2)_L \times SU(2)_R$  group. It has several interesting aspects: first, the  $SU(4)$  group correspond to the quark colour charges, to which lepton number is added as a fourth colour [372]. Furthermore, the model contains a left-right symmetry through the inclusion of an  $SU(2)_R$  group. Smaller left-right symmetric models can also be realised through an  $SU(2)_L \times SU(2)_R \times U(1)_{B-L}$  gauge group [373]. These are often accompanied by a parity symmetry, so that at higher energies the gauge couplings are equal  $g_L = g_R$ . They are theoretically attractive as in this way the parity violation of the (left-handed) weak interaction is restored, and right-handed counterparts of the  $W$  and  $Z$  bosons appear ( $W_R$  and  $Z_R$ ). Another interesting type of GUTs are *trinification* models that have a  $SU(3)_C \times SU(3)_L \times SU(3)_R$  gauge group, which can have a single gauge coupling if a  $\mathbb{Z}_3$  symmetry is added.

It should be noted that many of these models can be embedded into larger models. For example,  $SO(10)$  GUTs can contain

$$\begin{aligned} SO(10) &\supset SU(5) \times U(1), \\ SO(10) &\supset SU(3)_C \times SU(2)_L \times SU(2)_R \times U(1)_{B-L}, \end{aligned} \tag{10.81}$$

<sup>4</sup>The rank of a lie group is the number of diagonal generators.

<sup>5</sup>For the  $SU(N)$  groups, the rank is equal to  $N - 1$ . The rank of  $U(1)$  is 1.

which in turn can be embedded in an  $E_6$  model. For a single GUT group there can exist different paths to break the symmetry down to that of the SM. We will now highlight some aspects of SU(5) and SO(10) unification.

### 10.5.1 SU(5) unification

As was mentioned in the introduction, the first attempt to unify the SM in a single gauge group was based on SU(5) [369]. The group contains 24 generators  $\lambda_i$ , which is 12 more than the total number of generators in the SM ( $8 + 3 + 1$ ). To see how the SM can be described in terms of SU(5) multiplets, we need to consider its representations. Starting from the fundamental  $\underline{5}$  representation, higher-dimensional representations can be constructed. For the purpose of unification, we can restrict ourselves to the following representations, whose decomposition into  $SU(3) \times SU(2) \times U(1)$  is given by

$$\begin{aligned}\bar{\underline{5}} &\rightarrow (\bar{3}, 1, \frac{1}{3}) + (1, 2, -\frac{1}{2}) \\ \underline{10} &\rightarrow (3, 2, \frac{1}{6}) + (\bar{3}, 1, -\frac{2}{3}) + (1, 1, 1)\end{aligned}\quad (10.82)$$

The reducible  $\bar{\underline{5}} + \underline{10}$  representation suffices to accomodate all SM fermions. The decomposition can be understood as follows: the  $\bar{\underline{5}}$  contains the SU(3) right-handed down-type quark triplet, as well as the SU(2) lepton doublet containing the electron and the neutrino. The other fermions are contained in the  $\underline{10}$ . These multiplets can be written as [374]

$$\begin{aligned}\chi &= \begin{pmatrix} d_R^{c1} & d_R^{c2} & d_R^{c3} & e_L & -\nu_{eL} \end{pmatrix} \\ \psi &= \frac{1}{\sqrt{2}} \left( \begin{array}{ccc|cc} 0 & u_R^{c3} & -u_R^{c2} & -u_{L1} & -d_{L1} \\ -u_R^{c3} & 0 & u_R^{c1} & -u_{L2} & -d_{L2} \\ u_R^{c2} & -u_R^{c1} & 0 & -u_{L3} & -d_{L3} \\ \hline u_{L1} & u_{L2} & u_{L3} & 0 & -e_R^c \\ d_{L1} & d_{L2} & d_{L3} & e_R^c & 0 \end{array} \right).\end{aligned}\quad (10.83)$$

Note that these multiplets do not contain the right handed neutrino. It is however possible to add the right-handed neutrino as an SU(5) singlet. The SU(5) group contains 24 gauge bosons that correspond to the 24 generators of the group. These live in the adjoint representation<sup>6</sup>  $\underline{24}$  [375]. It can be decomposed in terms of the SM gauge group as

$$\underline{24} \rightarrow (8, 1, 0) + (1, 3, 0) + (1, 1, 0) + (3, 2, -\frac{5}{6}) + (\bar{3}, 2, \frac{5}{6}), \quad (10.84)$$

one can read the individual decomposed terms to see that this representation contains the 8 SM gluons, the  $W^\pm$  and  $W^3$  SU(2) gauge fields, and the  $B$  field that mixes with  $W^3$  to form the photon. There are two new terms, that contain the 12 new gauge bosons, which

---

<sup>6</sup>In the adjoint representation, the structure constants  $f_c^{ab}$  obtained from  $[\lambda^a, \lambda^b] = f_c^{ab} \lambda^c$  are used as generators.

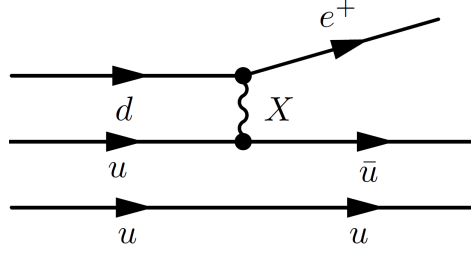


Figure 10.5: Proton decay in an SU(5) GUT mediated by the new X boson.

transform non-trivially under both SU(3) and SU(2), these are the  $X$  and  $Y$  bosons. We will discuss their effects later.

In order to unify the fundamental interactions, the gauge couplings of the SM gauge group must become equal at a single energy scale, i.e.

$$g_1 = g_2 = g_3 = g_5, \quad (10.85)$$

where the U(1) coupling  $g_1$  is related to the hypercharge coupling  $g'$  with the normalisation factor  $g_1 \equiv \sqrt{5/3} g'$ , and  $g_5$  is the single SU(5) gauge coupling. This leads to the prediction that the value of the Weinberg angle is

$$\sin^2 \theta_W = \frac{3}{8}, \quad (10.86)$$

which is far removed from the current value of  $\sin^2 \theta_W = 0.22337 \pm 0.00010$  [47].

### Proton decay

The embedding of quarks and leptons in the same SU(5) multiplets allows for proton decay mediated by the  $X$  and  $Y$  gauge bosons. These *leptoquarks* are charged under both SU(3) and SU(2), and couple the leptons directly to quarks, . An example of proton decay through  $p \rightarrow e^+ \pi^0$  with the exchange of an  $X$  boson is shown in Figure 10.5. The proton becomes unstable, with a mean lifetime of [374]

$$\tau_p \approx \frac{M_X^4}{g^4 m_p^5}. \quad (10.87)$$

The latest experimental bounds on the proton lifetime from Super-Kamiokande have placed a lower bound of  $2.4 \times 10^{34}$  years on this channel [376], meaning that the leptoquarks must be very heavy to suppress proton decay. For the SU(5) model, the unification scale of  $10^{15}$  GeV is on the low end, and would imply a too short proton lifetime [374]. In general, proton decay is a feature of GUTs, and proton lifetime bounds provide stringent constraints on these theories.



### Higgs sector

In order to break the gauge symmetry two Higgs multiplets are introduced. One multiplet in the  $\underline{24}$  adjoint representation  $\Phi$ , and a quintuplet  $H$  [374]

$$\Phi = \sum_{i=1}^{24} \frac{\lambda^i}{\sqrt{2}} \Phi^i \quad H = \begin{pmatrix} \mathcal{H}_3 \\ H^+ \\ H^0 \end{pmatrix}, \quad (10.88)$$

the first of which breaks SU(5) down to the SM symmetry at the GUT scale of  $\approx 10^{15}$  GeV. The quintuplet contains a coloured triplet  $\mathcal{H}_3$ , as well as the  $H^+$  and  $H^0$  that form the SM Higgs doublet, which induces electroweak symmetry breaking. However, the Higgs sector in this theory (and generally in other GUTs) faces is unsatisfactory from a theoretician's perspective. This has to do with the large mass scales that are present in the theory. First there is the *gauge hierarchy* problem, which is the question why there are very large mass ratios of 13 orders of magnitude in a single theory. The second problem is the *doublet-triplet splitting* problem, which is related to the quintuplet. It contains the SM-like Higgs doublet that causes electroweak symmetry breaking at the weak scale, and the coloured triplet  $\mathcal{H}_3$  that must be heavy, as it can contribute to proton decay, leading to a large mass difference between the quintuplet components. Of course one could then fine-tune the parameters of the theory up to a precision of  $10^{-13}$  to ensure these mass ratios, but this adjustment is not guaranteed if one then includes radiative corrections. For more extensive discussions on this topic, see Refs. [377, 378].

#### 10.5.2 SO(10) unification

The SO(10) group has a rank of 5, which is larger compared to SU(5) (rank 4), and can contain the latter as a subgroup [370]. Its main attractiveness stems from the fact that all SM fermions can be included in its  $\underline{16}$  representation. One can decompose this representation in terms of SU(5)  $\times$  U(1) as

$$\underline{16} \rightarrow (10, -1) + (\bar{5}, 3) + (1, -5), \quad (10.89)$$

which next to the SU(5)  $\underline{10}$  and  $\bar{5}$  representations that contained the SM fermions, naturally includes an SU(5) singlet to accomodate a right-handed neutrino. The larger rank allows for several different breaking patterns to the SM gauge groups. The two main routes are either via the SU(5) path or the Pati-Salam SU(4)<sub>C</sub>  $\times$  SU(2)<sub>L</sub>  $\times$  SU(2)<sub>R</sub> and left-right symmetric model paths. SO(10) GUTs can be broken down to the SM gauge group with an additional U(1) group.

Table 10.6: One loop coefficients for complex scalars. For other particle types this is multiplied by the corresponding factor from Equation (10.93). The values are taken from [379].

$(\text{SU}(3)_C, \text{SU}(2)_L, \text{U}(1)_Y)$	$b_k^{\text{CS}}$
$(1, 1, y)$	$(0, 0, \frac{1}{5}y^2)$
$(1, 2, y)$	$(0, \frac{1}{6}, \frac{2}{5}y^2)$
$(1, 3, y)$	$(0, \frac{2}{3}, \frac{3}{5}y^2)$

### 10.5.3 Running of coupling constants

The gauge coupling constants have different values depending on the energy. The evolution, or *running*, of a coupling constant  $g_k$  is described by the *renormalization group equation* (RGE) [374]

$$\frac{dg_k}{d \ln(\mu)} \equiv \beta(g^2) = b_k \frac{g_k^3}{(4\pi)^2}, \quad (10.90)$$

at one-loop order at an energy scale  $\mu$ . The  $\beta$  function  $\beta(g^2)$  is here given at one order, but from more advanced loop calculations loop contributions at two-loop or even higher orders can be determined. At one-loop it only depends on the coefficient  $b_k$ , which in turn depends on the particle content of a specific theory. Generally the contribution of each particle can be considered separately, so that the contributions to  $b_k$  can be written as [379]

$$b_k = b_k^{\text{SM}} + \sum_i^N n_i b_k^i, \quad (10.91)$$

in which  $i$  sums over the BSM field content, which can have  $n_i$  generations of each field. The contribution of the Standard Model is

$$b_k^{\text{SM}} = \begin{pmatrix} \frac{41}{10} \\ -\frac{19}{6} \\ -7 \end{pmatrix}. \quad (10.92)$$

Each of the new fields adds a contribution to  $b_k$  depending on the type of particle, as well as its representation under the gauge group(s). They can be expressed in terms of a complex scalar field in a certain representation  $b_k^{\text{CS}}$  with an additional factor of

$$b_k^i = b_k^{\text{CS}} \begin{cases} 1 & \text{complex scalar} \\ \frac{1}{2} & \text{real scalar} \\ 2 & \text{Weyl fermion} \\ 4 & \text{Dirac fermion} \end{cases}. \quad (10.93)$$

As we are interested in radiative seesaw models, we only consider new fields that are  $SU(3)_C$  singlets, and at most triplets under  $SU(2)_L$ . For these fields the contribution to the  $\beta$  functions are listed in Table 10.6. At one loop the RGEs can be solved analytically

$$\alpha_k^{-1}(\mu) = \alpha_k^{-1}(\mu_0) - \frac{b_k}{2\pi} \ln \frac{\mu}{\mu_0}, \quad (10.94)$$

for which it is common to express the couplings in terms of  $\alpha_k \equiv g_k^2/4\pi$ .

## Two U(1) groups

The discussion has so far only considered the running of gauge groups that do not mix. In a gauge theory with two (or more) abelian groups one must take mixing between these groups into account. These can be calculated in the basis where only one off-diagonal coupling is non-zero, and are given by [380]

$$\frac{d}{d \ln(\mu)} g' = \frac{1}{(4\pi)^2} (A^{XX} g'^3 + 2A^{XY} g'^2 g_{XY} + A^{YY} g' g_{XY}^2), \quad (10.95)$$

$$\frac{d}{d \ln(\mu)} g_Y = \frac{1}{(4\pi)^2} A^{YY} g_Y^3, \quad (10.96)$$

$$\frac{d}{d \ln(\mu)} g_{XY} = \frac{1}{(4\pi)^2} (A^{YY} g_{XY} (g_{XY}^2 + 2g_Y^2) + 2A^{XY} g' (g_{XY}^2 + g_Y^2) + A^{XX} g'^2 g_{XY}), \quad (10.97)$$

which depend on the coefficients  $A^{ij}$ , that are analogous to the  $b_k^i$  coefficients in Equation (10.90). They are

$$A^{ij} = \frac{1}{3} Y^i Y^j \quad (10.98)$$

for a complex scalar. To reconcile this notation with our previous expressions, we relate the above couplings to those of Equation (10.50). The following terms correspond to each other

$$\begin{aligned} g' &= \frac{g_X}{\sqrt{1-\epsilon^2}}, \\ g_{XY} &= \frac{-g_Y \epsilon}{\sqrt{1-\epsilon^2}}, \\ g_Y &= g_Y. \end{aligned} \quad (10.99)$$

For the normalization of the U(1) groups we choose the values of

$$\begin{aligned} g_1 &= \sqrt{5/3} g_Y, \\ \tilde{g} &= \sqrt{5/3} g_{XY}, \\ g_4 &= \sqrt{3/2} g'. \end{aligned} \quad (10.100)$$

Table 10.7: One loop coefficients for complex scalars for two U(1) groups.

$(\text{SU}(3)_C, \text{SU}(2)_L, \text{U}(1)_Y, \text{U}(1)_X)$	$b_k^{\text{CS}} \triangleq (b_3, b_2, b_1, b_4, \tilde{b})$
$(1, 1, y, x)$	$(0, 0, \frac{1}{5}y^2, \frac{2}{9}x^2, \sqrt{\frac{2}{45}}xy)$
$(1, 2, y, x)$	$(0, \frac{1}{6}, \frac{2}{5}y^2, \frac{4}{9}x^2, 2\sqrt{\frac{2}{45}}xy)$
$(1, 3, y, x)$	$(0, \frac{2}{3}, \frac{3}{5}y^2, \frac{6}{9}x^2, 3\sqrt{\frac{2}{45}}xy)$

With these definitions, the RGEs can be written as

$$\frac{d}{d\ln(\mu)}g_4 = \frac{1}{(4\pi)^2} \left( b_4 g_4^3 + 2\tilde{b} g_4^2 \tilde{g} + b_1 g_4 \tilde{g}^2 \right), \quad (10.101)$$

$$\frac{d}{d\ln(\mu)}g_1 = \frac{1}{(4\pi)^2} b_1 g_1^3, \quad (10.102)$$

$$\frac{d}{d\ln(\mu)}\tilde{g} = \frac{1}{(4\pi)^2} \left( b_1 \tilde{g}(\tilde{g}^2 + 2g_1^2) + 2\tilde{b} g_4(\tilde{g}^2 + g_1^2) + b_4 g_4^2 \tilde{g} \right). \quad (10.103)$$

At the one-loop level the running of the SM hypercharge coupling  $g_1$  can receive contributions from particles that are charged under  $\text{U}(1)_Y$ , but it does not depend on  $\text{U}(1)_X$  charges or the new gauge couplings  $g_4$  and  $\tilde{g}$ . This means that the different charge assignments of the models we found does not affect the unification of the SM gauge couplings. However, the running of  $g_4$  and  $\tilde{g}$  are sensitive to different charge distributions. The contributions of new fields to the RGEs at one-loop for the case of two U(1) groups are listed in Table 10.7.

#### 10.5.4 Gauge unification in radiative seesaw models

We now apply this formalism to the radiative seesaw models we found in section 10.1.3. A similar studies of unification in radiative seesaw models with a  $\mathbb{Z}_2$  symmetry has been performed in Ref. [379]. In order to compare our results, we will use the same procedure in evaluating the RGEs numerically. We set the scale of new physics  $\Lambda_{\text{NP}} = 1$  TeV, up to which we run the gauge couplings with purely the SM contribution  $b_i^{\text{SM}}$ . Above  $\Lambda_{\text{NP}}$ , Equation (10.91) is used to calculate the contributions of the BSM fields for each of the models. The start of the RGE running is at the  $Z$  mass  $m_Z = 91.1876$  GeV, for which we take the same initial values as in Ref. [379]:

$$\alpha_1(m_Z) = 0.01704, \quad \alpha_2(m_Z) = 0.03399, \quad \alpha_3(m_Z) = 0.1185. \quad (10.104)$$

Of course the values of  $g_4$  and  $\tilde{g}$  are unknown at  $\Lambda_{\text{NP}}$ , but these are found after running the SM RGEs. In order to numerically quantify the degree to which the couplings unify, the intersection points of the gauge couplings in the  $(\mu, \alpha^{-1})$  plane are determined. Based on

these points, the unification scale  $\Lambda$  is determined from the average of the energy scale of the three intersections in log space. The error in  $\Lambda$  is determined through

$$\frac{\Delta \log_{10}(\Lambda)}{\log_{10}(\Lambda)}, \quad (10.105)$$

in which  $\Delta \log_{10}(\Lambda)$  is the distance between the intersection points that are furthest apart. The value of the coupling at unification  $\alpha^{-1}(\Lambda)$  and its error are calculated completely analogously. With the unification point determined, the unified gauge coupling can be used as an initial condition for  $g_4$ , which is then run down to  $\Lambda_{\text{NP}}$ . At the unification scale there exists no mixing between the U(1) groups, and  $\tilde{g} = 0$ , which can then also be calculated down to  $\Lambda_{\text{NP}}$ .

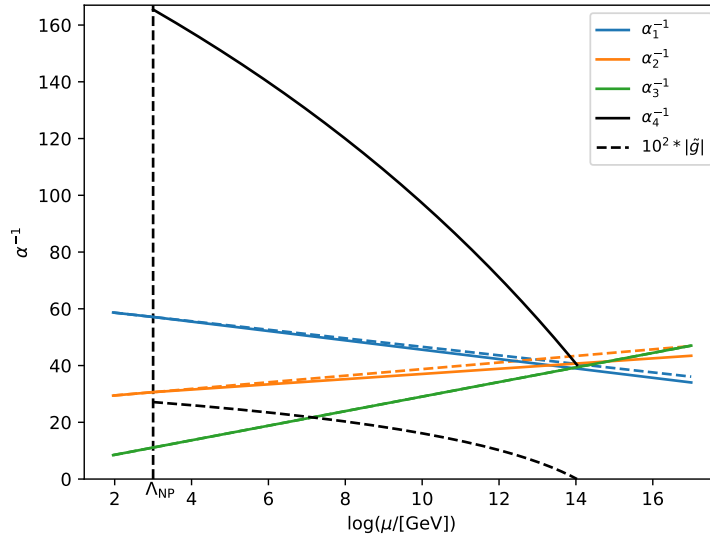


Figure 10.6: Running of the gauge coupling constants in the T1-3-A model with  $\alpha = 0$  for the case of two scalar singlets at one-loop. The running of the new gauge coupling  $\alpha_4^{-1}$  is included, as well as the mixing coupling  $\tilde{g}$ , which has been increased by a factor 100 for clearer visibility. For comparison, the running of the gauge couplings in the SM at one-loop are also included.

As an example, the running of the coupling constants in the T1-3-A model with  $\alpha = 0$  at the one-loop level is shown in Figure 10.6. In this case  $\psi$  and  $\psi'$  are identified with each other to form a vector-like doublet. Hence the charge assignment is  $X_\Psi = -X_\psi = X_\phi = 1$ , following Table 10.4, with  $X_\zeta = 2$ . The running of the new gauge coupling  $\alpha_4^{-1}$  is included, as well as the mixing coupling  $\tilde{g}$ , which has been increased by a factor 100 for clearer visibility. To illustrate how the running of the coupling constant changes by the addition of new fields, the coloured dashed lines indicate the SM running at one-loop. Since none of the new particles are charged under SU(3), the running of the corresponding coupling constant is equal to that of the SM.

The complete overview for all models is listed in Tables 10.8 to 10.11. No general statement can be made, as the possibility of unification for a model should be considered on a case by case basis. Some of the models unify relatively well, with an error in the unification scale of at most a few percent. However, some of the models show large deviations, and are thus unlikely to unify. It should be noted that we considered the one-loop case here. The study in Ref. [379] considered the two-loop RGEs, which add a slight correction to our results. We find that models with a good chance to unify generally do so in the  $\mathcal{O}(10^{12} \text{ GeV}) - \mathcal{O}(10^{14} \text{ GeV})$  range, which is in line with the literature. Compared to the “benchmark” SU(5) scenario with a unification scale of  $10^{15} \text{ GeV}$ , we find that for our models the scale is even lower. This can be explained by Figure 10.6, where it can be seen that the running of  $\alpha_1^{-1}$  and  $\alpha_2^{-1}$  tends to smaller values if new fields are added. As was explained just before, the running of  $\alpha_3^{-1}$  is unchanged. Therefore the unification scale is pushed to lower values, which inevitably leads to issues with proton decay, as was discussed in the overview of SU(5) unification of section 10.5.1. A possible solution to increase the unification scale is to introduce heavier coloured states between the TeV scale of radiative seesaw models and the GUT scale, which would push  $\alpha_3^{-1}$  to lower values.

Table 10.8: Models with Topology T1-1. Models marked with \* have two generations of  $\psi$  when  $\phi' = \phi^\dagger$ .

Model	$m$	$\Lambda \text{ [GeV]}$	$\frac{\Delta \log_{10}(\Lambda)}{\log_{10}(\Lambda)} \text{ [%]}$	$\alpha^{-1}(\Lambda)$	$\frac{\Delta \alpha}{\alpha} \text{ [%]}$
T1-1-A	2	1.43e+13	35.66	39.54	20.75
T1-1-A	0	2.21e+14	18.47	41.55	10.32
T1-1-A*	0	3.34e+14	22.55	42.27	12.78
T1-1-B	2	3.23e+11	12.12	31.77	6.03
T1-1-B	0	4.99e+14	57.09	34.11	24.94
T1-1-B*	0	3.55e+21	153.25	21.04	201.32
T1-1-C	1	5.37e+13	9.31	39.36	5.04
T1-1-D	1	1.86e+13	4.08	37.10	2.11
T1-1-D	-1	4.01e+13	8.77	37.53	4.47
T1-1-F	1	1.89e+13	20.96	35.43	10.24
T1-1-G	2	3.59e+12	21.33	37.20	11.86
T1-1-G	0	1.27e+14	1.13	39.50	0.59
T1-1-G*	0	1.70e+14	2.45	40.11	1.30
T1-1-H	2	2.04e+11	21.32	30.22	11.76
T1-1-H	0	2.59e+15	77.36	32.03	38.94
T1-1-H*	0	3.94e+28	192.07	9.68	780.08

Table 10.9: Models with Topology T1-2.

Model	$m$	$\Lambda$ [GeV]	$\frac{\Delta \log_{10}(\Lambda)}{\log_{10}(\Lambda)}$ [%]	$\alpha^{-1}(\Lambda)$	$\frac{\Delta \alpha}{\alpha}$ [%]
T1-2-A	0	7.74e+13	7.10	39.60	3.82
T1-2-A	-2	1.46e+13	17.48	38.49	9.65
T1-2-B	0	6.07e+13	11.24	37.76	5.69
T1-2-B	-2	4.92e+12	4.39	36.33	2.32
T1-2-D	1	7.56e+11	27.49	30.96	14.37
T1-2-D	-1	4.76e+14	65.96	32.39	31.85
T1-2-F	1	5.47e+11	36.60	29.32	22.36
T1-2-F	-1	3.33e+15	86.49	30.11	51.83

Table 10.10: Models with Topology T1-3. Models marked with \* have two generations of  $\phi$  as  $\psi'$  is combined with  $\psi$  into a vector-like doublet.

Model	$m$	$\Lambda$ [GeV]	$\frac{\Delta \log_{10}(\Lambda)}{\log_{10}(\Lambda)}$ [%]	$\alpha^{-1}(\Lambda)$	$\frac{\Delta \alpha}{\alpha}$ [%]
T1-3-A	0	3.41e+13	3.16	37.86	1.64
T1-3-A*	0	1.07e+14	10.75	40.23	5.86
T1-3-B	0	3.42e+13	20.59	36.14	10.08
T1-3-B*	0	8.64e+13	26.03	36.58	12.54
T1-3-C	1	1.98e+13	15.53	38.70	8.54
T1-3-D	1	3.57e+13	51.69	31.90	25.70
T1-3-D	-1	1.06e+12	29.78	31.05	15.50
T1-3-F	1	6.17e+13	92.44	23.21	100.62
T1-3-G	0	5.13e+14	74.63	30.64	42.35
T1-3-G*	0	4.77e+14	63.03	32.97	28.84
T1-3-H	0	4.95e+15	95.56	28.10	68.46
T1-3-H*	0	5.78e+16	106.39	27.89	77.93

Table 10.11: Models with Topology T3.

Model	$m$	$\Lambda$ [GeV]	$\frac{\Delta \log_{10}(\Lambda)}{\log_{10}(\Lambda)}$ [%]	$\alpha^{-1}(\Lambda)$	$\frac{\Delta \alpha}{\alpha}$ [%]
T3-A	0	2.35e+13	0.88	37.64	0.46
T3-A	-2	5.04e+13	5.52	38.08	2.85
T3-B	1	1.84e+13	33.96	39.73	19.69
T3-B	-1	2.21e+14	18.47	41.55	10.32
T3-C	1	1.00e+13	34.83	32.98	16.27
T3-C	-1	7.45e+13	46.67	33.59	21.05
T3-E	0	2.23e+13	18.02	35.94	8.89

### 10.5.5 Embedding scotogenic models in a GUT

Even if some of the models seem to allow for unification, and we ignore proton decay, there is still the issue of finding a unification group with suitable representations. Let us as an example consider SO(10) and see whether it is possible to embed the SM fields in such a way that the SM is uncharged under the extra U(1) group contained in SO(10). For this we decompose SO(10) representations into  $SU(3)_c \times SU(2)_L \times U(1) \times U(1)$  via  $SU(5) \times U(1)$ , using LieART [381]. Up to the 144 representation of SO(10), the decompositions are

$$\underline{10} \rightarrow (3, 1, 2, 2)_{VL} + (1, 2, -3, 2)_{VL}, \quad (10.106)$$

$$\underline{16} \rightarrow (3, 2, -1, -1) + (\bar{3}, 1, 4, -1) + (1, 1, -6, -1) + (\bar{3}, 1, -2, 3) + (1, 2, 3, 3) + (1, 1, 0, -5), \quad (10.107)$$

$$\underline{\bar{16}} \rightarrow (\bar{3}, 2, 1, 1) + (3, 1, -4, 1) + (1, 1, 6, 1) + (3, 1, 2, -3) + (1, 2, -3, -3) + (1, 1, 0, 5), \quad (10.108)$$

$$\underline{45} \rightarrow (8, 1, 0, 0) + (3, 2, 5, 0)_{VL} + (1, 3, 0, 0) + (1, 1, 0, 0) + (3, 2, -1, 4)_{VL} + (\bar{3}, 1, 4, 4)_{VL} + (1, 1, -6, 4)_{VL} + (1, 1, 0, 0), \quad (10.109)$$

$$\underline{54} \rightarrow (8, 1, 0, 0) + (3, 2, 5, 0)_{VL} + (1, 3, 0, 0) + (1, 1, 0, 0) + (6, 1, 4, 4)_{VL} + (3, 2, -1, 4)_{VL} + (1, 3, -6, 4)_{VL}, \quad (10.110)$$

$$\underline{120} \rightarrow (8, 2, -3, 2)_{VL} + (\bar{6}, 1, 2, 2)_{VL} + (3, 3, 2, 2)_{VL} + (\bar{3}, 2, 7, 2)_{VL} + (\bar{3}, 1, -8, 2)_{VL} + (3, 1, 2, 2)_{VL} + (1, 2, -3, 2)_{VL} + (3, 2, -1, -6)_{VL} + (\bar{3}, 1, 4, -6)_{VL} + (1, 1, -6, -6)_{VL} + (3, 1, 2, 2)_{VL} + (1, 2, -3, 2)_{VL}, \quad (10.111)$$

$$\underline{126} \rightarrow (8, 2, -3, 2)_{VL} + (\bar{6}, 3, 2, 2) + (6, 1, -8, 2) + (\bar{3}, 2, 7, 2)_{VL} + (3, 1, 2, 2)_{VL} + (1, 1, 12, 2) + (6, 1, -2, -2) + (\bar{3}, 3, -2, -2) + (3, 1, 8, -2) + (1, 2, 3, -2)_{VL} + (6, 1, 4, -6) + (3, 2, -1, -6)_{VL} + (1, 3, -6, -6) + (3, 1, -4, 6) + (1, 1, 6, 6) + (3, 1, 2, 2) + (1, 1, 0, 10), \quad (10.112)$$

$$\underline{144} \rightarrow (8, 2, 3, 3) + (6, 1, -2, 3) + (\bar{3}, 3, -2, 3) + (3, 2, -7, 3) + (3, 1, 8, 3) + (\bar{3}, 1, -2, 3) + (1, 2, 3, 3) + (8, 1, -6, -1) + (\bar{6}, 2, -1, -1) + (\bar{3}, 3, 4, -1) + (3, 2, -1, -1) + (\bar{3}, 1, 4, -1) + (1, 2, 9, -1) + (8, 1, 0, -5) + (3, 2, 5, -5) + (\bar{3}, 2, -5, -5) + (1, 3, 0, -5) + (1, 1, 0, -5) + (6, 1, 4, -1) + (3, 2, -1, -1) + (1, 3, -6, -1) + (3, 2, -1, -1) + (\bar{3}, 1, 4, -1) + (1, 1, -6, -1) + (\bar{3}, 1, -2, 3) + (1, 2, 3, 3) + (3, 1, 2, 7) + (1, 2, -3, 7), \quad (10.113)$$

in which the representations with VL indicate that there exists a second, but conjugated irreducible representation. As was discussed in section 10.5.2, the SM is usually embedded into the 16 representation, which also includes a right-handed neutrino. This would imply that all SM fields are charged under the second U(1). Even though one has the liberty to make a basis transformation, it is not possible to make the SM uncharged. Since we add new particles in our radiative seesaw models, it is possible that the SM + the new fields are



accommodated by a higher-dimensional representation. However, none of the representations contain the required representations in which the SM is uncharged<sup>7</sup> and thus it is not possible to embed our models into SO(10). This issue could be resolved by considering unifying groups of higher rank such as  $E_6$ , which contain extra U(1) groups, but this is beyond the scope of this work. Furthermore, the  $\underline{16}$  representation of SO(10) in particular, but GUTs in general can accommodate a right-handed neutrino in the same representation as other SM fields, making tree-level seesaw contributions unavoidable.

## 10.6 Conclusion

We have studied the extension of the SM gauge group by an extra U(1) gauge group in the context of minimal radiative seesaw model. Through arguments based on gauge anomaly cancellation, the neutrino loop topology, as well as the Weinberg operator structure, we found that the fermions in the dark sector must be vector-like, with the SM remaining uncharged under the new symmetry. Moreover, we have considered mixing between mass states that occurs after the breaking of U(1), which allows for additional charge assignment possibilities. One can for each of the previously classified radiative seesaw models with  $\mathbb{Z}_2$  symmetry find a model that includes a U(1) gauge group in such a way that the SM is uncharged, but the fields of the dark sector do carry a charge. We made a classification of the possible charge assignments. Upon breaking of the new gauge symmetry, it is possible to obtain a remaining  $\mathbb{Z}_2$ ,  $\mathbb{Z}_n$  or even a global U(1) symmetry, similar to the original versions of these models. The difference is that now this stabilizing symmetry is not added ad hoc, but results from the added gauge group. We compared our models to other U(1) gauged models, and found that gauged radiative seesaw models in which the SM is uncharged have hardly been explored.

The addition of a new U(1) gauge group brings with it new phenomenology, most prominently in the form of a new gauge boson, which through kinetic mixing mixes with the  $Z$ . We showed the effects of kinetic mixing on the gauge couplings, as well as the induced mass mixing between the  $Z$  and  $Z'$  bosons, and discussed related experimental constraints. We then discuss some other phenomenological aspects of a  $Z'$  prime boson from astrophysics and direct detection, which are model dependent. The presence of an extra Higgs boson also induces mixing in the scalar sector.

We then discuss several aspects of GUTs, before we study the prospects for grand unification in radiative seesaw models, for which we find that some of the models can unify. However, the unification scales are lower than the usual scale of  $10^{15}$  GeV in SU(5) GUTs, and thus have already been excluded by constraints on proton decay. For the next step we considered whether our models can be embedded into an SO(10) GUT group. For this purpose we considered decompositions of SO(10) representations into  $SU(3)_c \times SU(2)_L \times U(1) \times U(1)$  via the SU(5) path. It is not possible to embed the SM into an SO(10) representation, such that

---

<sup>7</sup>Compare this to the SU(5) decompositions in Equation (10.82) which are the required representations for the SM, in this case with an extra 0 charge under the second U(1).

it is uncharged under the second  $U(1)$  group. Further studies might consider  $E_6$  as a GUT group.

We have presented a general overview of radiative seesaw models with an extra local  $U(1)$  symmetry. For future studies, the rich phenomenology of these models can be studied for specific models in further detail.

# 11 The discovery potential of U(1)-gauged heavy Higgs bosons at the LHC

In the previous chapter we extensively discussed radiative seesaw and made the case that a U(1) extension of the SM gauge group offers attractive features. We have also mentioned models where the accidental global baryon and lepton are promoted to a local  $B-L$  symmetry in section 10.2.

In order to probe the new gauge and dark matter sectors in such models at the TeV scale, collider experiments, such as at the LHC are well suited. Recently, lower bounds on the masses of new gauge bosons have been imposed [382, 383]. It has also been shown that collider constraints leave some of the parameter space of U(1) $_{B-L}$  models open [384]. We therefore explore a model with an extended U(1) $_{B-L}$  gauge symmetry. In particular we want to determine the discovery potential of the LHC at a center-of-mass energy of 13 TeV for a heavy scalar resonance in the dilepton channel. For the upcoming high-luminosity (HL) phase at the LHC, integrated luminosities of  $\sim 1000 \text{ fb}^{-1}$  or more will be reached [385].

Even though the model is different from the U(1) extended radiative seesaw models of the previous chapter, the results of this particular study are applicable to them as well. This has to do with the fact that the scalar singlet considered in this chapter has similar properties to the singlet  $\zeta$  introduced before. A large difference is that neutrino masses are generated through the tree-level seesaw mechanism, which is different from the radiative seesaw models considered before. However, the focus of this study is on the scalar sector, in which the neutrino mass mechanism plays no role.

## 11.1 Model description

The particle content of the SM is extended by several new fields. In the fermionic sector  $n$  generations of right-handed neutrinos  $N$  are added, whereas the scalar sector is more extensive. A second Higgs doublet is added, so that the scalar sector mimics a two Higgs doublet model (2HDM) with doublets  $\Phi_1$  and  $\Phi_2$ , which is further extended by a scalar singlet field  $\Phi_s$ . Moreover, these fields, as well as the SM fields, are charged under a U(1) $_{B-L}$  gauge symmetry, listed in Tab. 11.1. This is done in such a way that the model allows for neutrino masses, but at the same time only one of the doublets couples to the SM fermions, thereby preventing FCNCs in a way similar to type-I 2HDMs. In type-I 2HDMs the SM fermions

Table 11.1: U(1)<sub>B-L</sub> charges for all fermions and scalars of our model. In particular, this assignment of charges is able to explain neutrino masses and the absence of flavor-changing currents in the type-I 2HDM.

Fields	$u_R^c$	$d_R^c$	$Q$	$L$	$e_R^c$	$N_R^c$	$\Phi_2$	$\Phi_1$	$\Phi_s$
Charges	$-u$	$-d$	$\frac{(u+d)}{2}$	$\frac{-3(u+d)}{2}$	$2u+d$	$u+2d$	$\frac{(u-d)}{2}$	$\frac{5u}{2} + \frac{7d}{2}$	$2u+4d$
U(1) <sub>B-L</sub>	$-1/3$	$-1/3$	$1/3$	$-1$	$1$	$1$	$0$	$2$	$2$

only couple to  $\Phi_2$ , by imposing a  $\mathbb{Z}_2$  symmetry under which  $\Phi_1 \rightarrow -\Phi_1$  [208]. The Yukawa Lagrangian is given by

$$\begin{aligned} \mathcal{L}_{Y_{2\text{HDM}}} = & y_2^d \Phi_2^\dagger Q d_R^c + y_2^u \tilde{\Phi}_2^\dagger Q u_R^c + y_2^e \Phi_2^\dagger L e_R^c \\ & + y^D \tilde{\Phi}_2^\dagger L N_R^c + Y^M N_R \Phi_s N_R + \text{h.c.} \end{aligned} \quad (11.1)$$

From this one can see that the right-handed neutrinos obtain both a Dirac and a Majorana mass through the coupling to  $\Phi_2$  and  $\Phi_s$  respectively. Componentwise, the scalar fields are written as follows

$$\Phi_i = \begin{pmatrix} \phi_i^+ \\ (v_i + \rho_i + i\eta_i)/\sqrt{2} \end{pmatrix} \quad \text{and} \quad \Phi_s = (v_s + \rho_s + i\eta_s)/\sqrt{2}. \quad (11.2)$$

The vevs of the doublets are constrained by the relation  $v^2 = v_1^2 + v_2^2 = (246 \text{ GeV})^2$ . A very important parameter in for such scalar sectors is the ratio between the two vevs, which is written as

$$\tan \beta = \frac{v_2}{v_1}. \quad (11.3)$$

The scalar potential of 2HDMs is already quite extensive, even without including the scalar singlet, which adds yet more terms. However, the U(1)<sub>B-L</sub> symmetry greatly reduces the number of allowed terms in the scalar potential. In this specific model this is the case due to  $\Phi_1$  and  $\Phi_2$  transforming differently under U(1)<sub>B-L</sub> in order to avoid FCNCs. At lower energies, this symmetry has the same effect as a, by now familiar,  $\mathbb{Z}_2$  symmetry. The complete scalar potential is given as

$$\begin{aligned} V(\Phi_1, \Phi_2) = & m_{11}^2 \Phi_1^\dagger \Phi_1 + m_{22}^2 \Phi_2^\dagger \Phi_2 \\ & + \frac{\lambda_1}{2} (\Phi_1^\dagger \Phi_1)^2 + \frac{\lambda_2}{2} (\Phi_2^\dagger \Phi_2)^2 \\ & + \lambda_3 (\Phi_1^\dagger \Phi_1) (\Phi_2^\dagger \Phi_2) + \lambda_4 (\Phi_1^\dagger \Phi_2) (\Phi_2^\dagger \Phi_1), \end{aligned} \quad (11.4)$$

$$\begin{aligned} V_s = & m_s^2 \Phi_s^\dagger \Phi_s + \frac{\lambda_s}{2} (\Phi_s^\dagger \Phi_s)^2 + \mu_1 \Phi_1^\dagger \Phi_1 \Phi_s^\dagger \Phi_s \\ & + \mu_2 \Phi_2^\dagger \Phi_2 \Phi_s^\dagger \Phi_s + (\mu_S \Phi_1^\dagger \Phi_2 \Phi_s + \text{h.c.}). \end{aligned} \quad (11.5)$$

Compared to the canonical type-1 2HDM with a  $\mathbb{Z}_2$  symmetry, the  $\lambda_5$  term containing  $(\Phi_1^\dagger \Phi_2)^2$  terms is absent in the above potential due to the different U(1)<sub>B-L</sub> charges of the scalar

doublets. Usually this term is responsible for giving mass to the new pseudoscalar. For this model, interactions with the scalar singlet now take this role. This gives us the requirement that the couplings  $\mu_i$  must be non-zero in order to avoid massless states.

### 11.1.1 Scalar masses

We will now discuss the masses in the scalar sector that arise from the spontaneous symmetry breaking of the scalars. Whilst the doublet vevs are constrained by the sum of their squared values being equal to the SM Higgs vev, there is no such constraint for the scalar singlet. As we are interested in a resonance due to a singlet Higgs-like scalar, we choose a setup in which  $(v_1, v_2) \ll v_s$ , such that we obtain a weakly-coupled heavy scalar. The  $CP$ -even eigenstates  $\rho_i$  and  $\rho_s$  mix after the breaking of  $U(1)_{B-L}$  and EWSB. This results in three mass eigenstates, whose mixing can be written as

$$\begin{pmatrix} h \\ H \\ S \end{pmatrix} = \begin{pmatrix} c_{\alpha_2} & 0 & -s_{\alpha_2} \\ 0 & 1 & 0 \\ s_{\alpha_2} & 0 & c_{\alpha_2} \end{pmatrix} \begin{pmatrix} 1 & 0 & 0 \\ 0 & c_{\alpha_1} & -s_{\alpha_1} \\ 0 & s_{\alpha_1} & c_{\alpha_1} \end{pmatrix} \times \begin{pmatrix} c_\alpha & s_\alpha & 0 \\ -s_\alpha & c_\alpha & 0 \\ 0 & 0 & 1 \end{pmatrix} \begin{pmatrix} \rho_1 \\ \rho_2 \\ \rho_s \end{pmatrix}. \quad (11.6)$$

Where  $h$  is identified with the SM-like Higgs boson,  $H$  is the lighter scalar, and  $S$  is a heavy scalar that couples weakly to the SM. From Eqs. (11.4) and (11.5) it can be seen that the mixing between the two doublets themselves is governed by the  $\lambda_3$  and  $\lambda_4$  terms. The  $\mu_1$  and  $\mu_2$  mix the singlet with  $\Phi_1$  and  $\Phi_2$  respectively, whilst the  $\mu_s$  terms mixes all three scalars. The mixing angles  $\alpha_i$  and  $\alpha_s$  depend on these parameters, as well as on the vevs.

In the limit where  $\mu_i \ll 1$ , the singlet-doublet mixing angles  $\alpha_1$  and  $\alpha_2$  are small. The scalar sector can thus be divided in the heavy singlet and a 2HDM-like Higgs sector. This makes the phenomenology of the heavy scalar similar to the case that was considered in section 10.4, if  $\zeta$  mixes weakly with the SM-like Higgs. The mixing angle  $\alpha$  then corresponds to the usual scalar mixing in 2HDM setups, which is given by [386, 208]

$$\begin{pmatrix} H \\ h \end{pmatrix} \sim \begin{pmatrix} \cos \alpha & \sin \alpha \\ -\sin \alpha & \cos \alpha \end{pmatrix} \begin{pmatrix} \phi_1 \\ \phi_2 \end{pmatrix} \quad (11.7)$$

where the mixing angle is given as

$$\tan 2\alpha \sim \frac{2(\lambda_3 + \lambda_4)v_1v_2}{\lambda_1v_1^2 - \lambda_2v_2^2}. \quad (11.8)$$

For small  $\alpha_{1,2} \ll 1$  the CP-even scalar masses are approximatively given by

$$\begin{aligned} m_s^2 &\sim \lambda_s v_s^2, \\ m_H^2 &\sim \frac{1}{2} \left( \lambda_1 v_1^2 + \lambda_2 v_2^2 - \sqrt{(\lambda_1 v_1^2 - \lambda_2 v_2^2)^2 + 4(\lambda_3 + \lambda_4)^2 v_1^2 v_2^2} \right), \\ m_h^2 &\sim \frac{1}{2} \left( \lambda_1 v_1^2 + \lambda_2 v_2^2 + \sqrt{(\lambda_1 v_1^2 - \lambda_2 v_2^2)^2 + 4(\lambda_3 + \lambda_4)^2 v_1^2 v_2^2} \right). \end{aligned} \quad (11.9)$$

From this it can be seen that the lighter scalars  $H$  and  $h$  stemming from the doublet only contain contributions of  $v_1^2$  and  $v_2^2$ . On the contrary, the scalar singlet only depends on its vev  $v_s^2$  and its self-coupling  $\lambda_s$ . As is common in 2HDM setups, the addition of a second Higgs doublets results in two additional massive eigenstates. First the charged scalar  $H^+$ , which has a mass of

$$m_{H^+}^2 = \frac{(\sqrt{2}\mu_s v_s - \lambda_4 v_1 v_2) v^2}{2v_1 v_2}, \quad (11.10)$$

and a new pseudoscalar  $A$ , with a mass

$$m_A^2 = \frac{\mu_s (v_1^2 v_2^2 + v^2 v_s^2)}{\sqrt{2} v_1 v_2 v_s}, \quad (11.11)$$

which is proportional to the cubic  $\mu_s$  coupling, which contains  $\Phi_1$ ,  $\Phi_2$ , and  $\Phi_s$ .

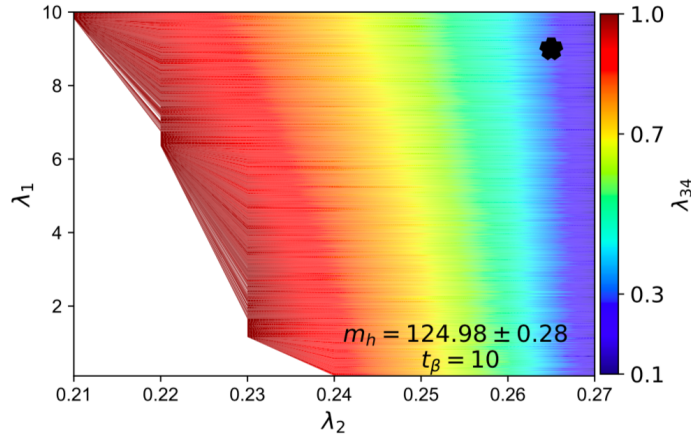


Figure 11.1: Parameter space in the  $\lambda_{1,2,3,4}$  plane compatible with current measurements of the SM Higgs boson mass  $m_h$  for a ratio of Higgs doublet VEVs  $t_\beta = \tan \beta = v_2/v_1 = 10$ . Our benchmark point is shown in black.

From Eqs. (11.9) one can see that the mass of the SM-like Higgs boson  $h$  depends on the couplings  $\lambda_1$ ,  $\lambda_2$ , as well as the combination  $\lambda_{34} = \lambda_3 + \lambda_4$ . Its mass is coupled with that of the lighter Higgs boson  $H$ , and is sensitive to the mass splitting  $\lambda_{34}$ . Fig. 11.1 shows the part of the parameter space of  $\lambda_{1,2,3,4}$  for which the mass of the SM-like Higgs boson falls in the range  $m_h = 124.98 \pm 0.28$  GeV, with  $\tan \beta = 10$ . A benchmark point that will be used further in this analysis is indicated by the black dot. From this figure one can see that the allowed range for  $\lambda_2$  of  $[0.21 - 0.27]$  is very narrow, compared to the much broader

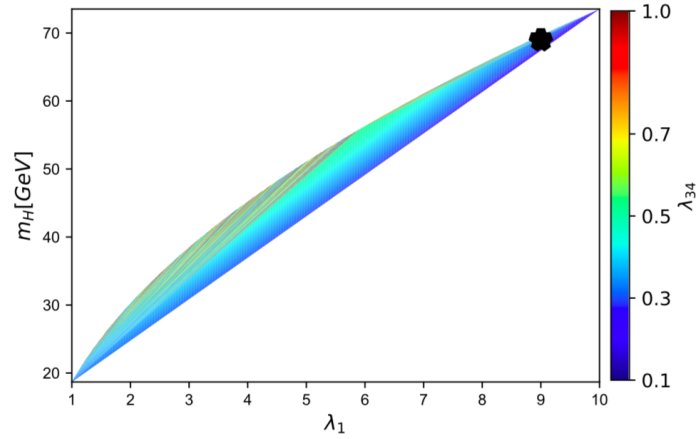


Figure 11.2: Dependence of the mass of the lighter Higgs  $H$  on the self-couplings  $\lambda_1$  and  $\lambda_{34}$ . Our benchmark point is shown in black.

Table 11.2: Scalar coupling constants of the SM fermions.

Vertex	Coupling constant
$H t\bar{t}, H b\bar{b}, H \tau\bar{\tau}$	$\frac{\sin \alpha \cos \alpha_2 - \cos \alpha \sin \alpha_1 \sin \alpha_2}{\sin \beta}$
$h t\bar{t}, h b\bar{b}, h \tau\bar{\tau}$	$\frac{\cos \alpha \cos \alpha_2 - \sin \alpha \sin \alpha_1 \sin \alpha_2}{\sin \beta}$
$S t\bar{t}, S b\bar{b}, S \tau\bar{\tau}$	$\frac{\cos \alpha_1 \sin \alpha_2}{\sin \beta}$

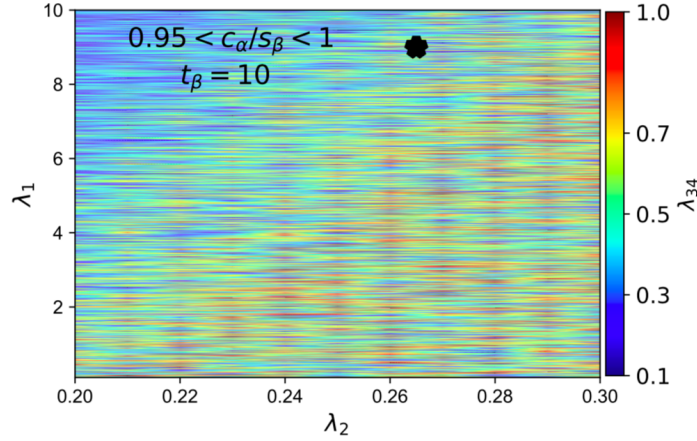
compatible values of  $0.01 < \lambda_1 < 10$  and  $0.1 < \lambda_{34} < 1$ . This can be attributed to the value of  $\tan \beta = 10$ , making  $v_2 > v_1$ , hence  $m_h$  is more sensitive to changes in  $\lambda_2$ . For all points that fall in these parameter ranges, stability and perturbativity requirements of the potential are satisfied [387, 388].

Since the masses of  $h$  and  $H$  are coupled, the allowed parameter ranges for the SM-like Higgs  $h$  result in a mass range for  $H$ . Fig. 11.2 shows this mass range as a function of  $\lambda_1$ , with the value of  $\lambda_{34}$  as a colour scale. It can be seen that under these circumstances there exists a linear relation between  $m_H$  and  $\lambda_1$ , with the breadth of the region being determined by the value of  $\lambda_{34}$ . The benchmark point is included in this figure as well. It has been chosen such as to comply with low-energy constraints from the  $STU$  parameters, which provide stringent bounds on the mass differences between the scalars. This has been accomplished by selecting a mass for the pseudoscalar  $A$  that is close to  $H$ . For the benchmark point we have the following values:  $\tan \beta = 10$ ,  $v_s = 1 \times 10^6$  GeV, and  $\mu_s = 1 \times 10^{-2}$  GeV. From Eqn. (11.11) one can verify that this leads to  $m_A = 72$  GeV, which is almost degenerate with  $m_H$  and thus satisfies the  $STU$  constraints.

Furthermore, the mixing between the neutral  $CP$ -even scalars changes the couplings to the SM fermions. The complete resulting couplings are shown in Tab. 11.2. For the weakly coupled scalar that is considered here, the couplings reduce to those shown in Tab. 11.3. Since we have identified the scalar  $h$  as the SM-like Higgs boson, we also constrain its couplings to be SM-like by requiring that  $0.95 < \cos \alpha / \sin \beta < 1$ . Fig. 11.3 shows the compatibility

Table 11.3: Same as Tab. 11.2 in the limit  $\alpha_1, \alpha_2 \ll 1$ .

Vertex	Coupling constant
$H t\bar{t}, H b\bar{b}, H \tau\bar{\tau}$	$\frac{\sin \alpha}{\sin \beta}$
$h t\bar{t}, h b\bar{b}, h \tau\bar{\tau}$	$\frac{\cos \alpha}{\sin \beta}$
$S t\bar{t}, S b\bar{b}, S \tau\bar{\tau}$	$\frac{\sin \alpha_2}{\sin \beta}$

Figure 11.3: Compatibility of the 2HDM with an additional scalar singlet with SM-like fermionic branching ratios of the Higgs boson  $h$  for  $t_\beta = 10$ . Our benchmark point is shown in black.

of the couplings of  $h$  with the SM in same region of the parameter space shown in Fig. 11.1 (except for a slightly larger range for  $\lambda_2$ ). This is the case for the complete region that is shown, including the benchmark point that is also marked in the plot by the black dot.

Of course the lighter scalar  $H$  can also couple to SM fermions, making it in principle observable in the LHC. For our benchmark point we find that  $H$  has a main decay channel with  $BR(H \rightarrow b\bar{b}) = 97\%$ . This leads to large QCD backgrounds, which obscure its presence, and make its discovery difficult. For the charged scalar  $H^\pm$  the main decay channels are into  $c\bar{b}$ , and  $\tau^+ \nu_\tau$ , both of which involve QCD processes at some stage.

### 11.1.2 Gauge sector

The extension of the SM gauge group by an extra U(1) symmetry introduces a new gauge boson with corresponding gauge coupling constant to the phenomenology, an overview of which was given in section 10.3. This changes the branching ratios of the scalars into gauge bosons. Whereas  $H$  is too light to decay into  $W$  or  $Z$  boson pairs, the heavy scalar  $S$  is kinematically allowed to do so, even though it is an SM singlet. This can be attributed to the interaction that is possible between different U(1) gauge groups. Even though many expressions have been worked out in section 10.3, we will repeat them here, as the expressions are slightly different due to the 2HDM-like setup. In our case, the gauge kinetic terms in



the Lagrangian of the  $U(1)_Y$  group with field strength tensor  $B_{\mu\nu}$  and  $U(1)_{B-L}$  with field strength tensor  $X_{\mu\nu}$  can be written as

$$\mathcal{L}_{\text{gauge}} = -\frac{1}{4}B_{\mu\nu}B^{\mu\nu} + \frac{\epsilon}{2\cos\theta_W}X_{\mu\nu}B^{\mu\nu} - \frac{1}{4}X_{\mu\nu}X^{\mu\nu}. \quad (11.12)$$

For the case where the kinetic mixing parameter  $\epsilon$  is small, the covariant derivative can be brought to the following form

$$D_\mu = \partial_\mu + igT^a W_\mu^a + ig'\frac{Q_Y}{2}B_\mu + \frac{i}{2}\left(g'\frac{\epsilon Q_Y}{\cos\theta_W} + g_X Q_X\right)X_\mu, \quad (11.13)$$

from which it can be seen that particles that carry no  $Q_X$  can still couple to the new gauge field  $X_\mu$  due to the kinetic mixing term. This can be cast into a matrix form in the following way

$$D_\mu = \partial_\mu + \frac{i}{2}\begin{pmatrix} gW_\mu^3 + g'Q_Y B_\mu + G_X X_\mu & g\sqrt{2}W_\mu^+ \\ g\sqrt{2}W_\mu^- & -gW_\mu^3 + g'Q_Y B_\mu + G_X X_\mu \end{pmatrix}, \quad (11.14)$$

in which the coupling to the  $X_\mu$  boson has been abbreviated as

$$G_{Xi} = \frac{g'\epsilon Q_{Y_i}}{\cos\theta_W} + g_X Q_{X_i}. \quad (11.15)$$

The hypercharge  $Q_{Y_i}$  is +1 for both doublets, whereas  $Q_{X_i}$  is the charge of doublet  $i$  under  $U(1)_X$ , which is +2 for  $\Phi_1$ , but 0 for  $\Phi_2$ . From this covariant derivative one can derive the mass terms the gauge bosons obtain from the vevs of the scalar doublets and singlet. One obtains the following terms in the Lagrangian

$$\mathcal{L}_{\text{mass}} = m_W^2 W_\mu^- W^{+\mu} + \frac{1}{2}m_Z^2 Z_\mu Z^\mu - \Delta^2 Z_\mu X^\mu + \frac{1}{2}m_X^2 X_\mu X^\mu. \quad (11.16)$$

The first two mass terms are as in the SM, with

$$m_W^2 = \frac{1}{4}g^2(v_1^2 + v_2^2) = \frac{1}{4}g^2v^2 \quad m_Z^2 = \frac{1}{4}\frac{g^2}{\cos^2\theta_W}(v_1^2 + v_2^2) = \frac{1}{4}g_Z^2v^2. \quad (11.17)$$

There is a mass term belonging to the new gauge boson  $X_\mu$ , which also receives contributions from the scalar singlet vev  $v_s$ . It is given by

$$m_X^2 = \frac{1}{4}(v_1^2 G_{X1}^2 + v_2^2 G_{X2}^2 + v_s^2 g_X^2 q_X^2). \quad (11.18)$$

Next to these mass terms, there appears a mixing term between the  $Z_\mu$  and  $X_\mu$  gauge fields. This is due to the Higgs doublets coupling to both the  $Z_\mu$  and the  $X_\mu$  fields. It is given by

$$\Delta^2 = \frac{1}{4}g_Z(G_{X1}v_1^2 + G_{X2}v_2^2), \quad (11.19)$$

leading to the neutral gauge boson mass matrix

$$m_{ZX}^2 = \frac{1}{2} \begin{pmatrix} m_Z^2 & \Delta^2 \\ \Delta^2 & m_X^2 \end{pmatrix} = \frac{1}{8} \begin{pmatrix} g_Z^2 v^2 & -g_Z (G_{X1} v_1^2 + G_{X2} v_2^2) \\ -g_Z (G_{X1} v_1^2 + G_{X2} v_2^2) & v_1^2 G_{X1}^2 + v_2^2 G_{X2}^2 + v_S^2 g_X^2 q_X^2 \end{pmatrix}. \quad (11.20)$$

For a  $2 \times 2$  matrix, its eigenvalues can readily be determined and read

$$m_Z^2 = \frac{1}{2} \left[ m_Z^2 + m_X^2 - \sqrt{(m_Z^2 - m_X^2)^2 + 4(\Delta^2)^2} \right], \quad (11.21)$$

$$m_{Z'}^2 = \frac{1}{2} \left[ m_Z^2 + m_X^2 + \sqrt{(m_Z^2 - m_X^2)^2 + 4(\Delta^2)^2} \right]. \quad (11.22)$$

In more detail, the matrix in Eqn. 11.20 can be diagonalized by the orthogonal matrix  $O(\xi)$

$$\begin{pmatrix} Z \\ Z' \end{pmatrix} = \begin{pmatrix} \cos \xi & -\sin \xi \\ \sin \xi & \cos \xi \end{pmatrix} \begin{pmatrix} Z \\ X \end{pmatrix}, \quad (11.23)$$

where the mixing angle is parameterized by

$$\tan \xi = \frac{\Delta^2}{m_Z^2 - m_X^2}. \quad (11.24)$$

Since we work in the framework where  $v_s \gg v_{1,2}$ , the resulting masses of the  $Z'$  boson lies far above the SM  $Z$  mass. In this limit, the mixing angle  $\xi$  can be approximated by

$$\sin \xi \simeq \frac{G_{X1} v_1^2 + G_{X2} v_2^2}{m_{Z'}^2}, \quad (11.25)$$

or to make the relation more explicit, this can be rewritten into

$$\sin \xi \simeq \frac{m_Z^2}{m_{Z'}^2} \left( \frac{g_X}{g_Z} (Q_{X1} \cos^2 \beta + Q_{X2} \sin^2 \beta) + \epsilon \tan \theta_W \right). \quad (11.26)$$

This mixing angle will later play a role in the partial widths of the heavy scalar decays into gauge bosons. In the rest of this chapter we will take the kinetic mixing parameter  $\epsilon = 10^{-4}$  to agree with experimental bounds [389, 352]. Because the heavy scalar  $S$  has a dominant  $\Phi_s$  component, which is a singlet under the SM, this means that the decays of  $S$  into SM gauge bosons is suppressed.

Fig. 11.4 shows the mass of the new gauge boson  $Z'$  as a function of the singlet vev  $v_s$ . It can be seen that for a small coupling of  $g_{B-L} = 0.01$ , the mass of the  $Z'$  is constant at small  $v_s$ , since the main contribution comes from the doublets (remember that  $\Phi_1$  is charged under  $U(1)_{B-L}$ ). For larger couplings, or at higher  $v_s$ , the singlet vev dominates and the  $Z'$  mass becomes proportional to it. Also included is the benchmark point, for which we take  $g_{B-L} = 0.01$  in agreement with the latest LHC limits [390].

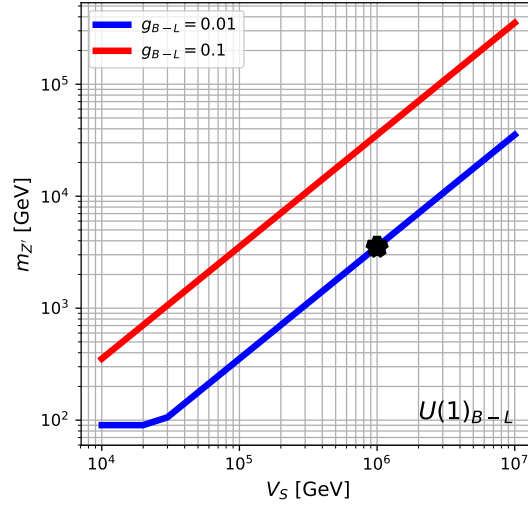


Figure 11.4: Mass of the extra gauge boson  $m_{Z'}$  as a function of the singlet vev  $v_s$  for two values of  $g_{B-L} = 0.1$  and  $g_{B-L} = 0.01$ . Our benchmark point is shown in black.

## 11.2 LHC phenomenology

Having discussed the particle content and parameter space of the model, we now turn to the main goal of this chapter: to study the production and decay of the new heavy scalar at the LHC. As can be seen from Tabs. 11.2 and 11.3, the coupling constant of the scalar  $S$  depends on the (small) value of  $\alpha_2$ . In general, the decays of the scalar are strongly dependent on the model parameters, especially if the available phase space is increased. Depending on the mass of the  $Z'$  boson, which is influenced by  $v_s$  and  $g_{B-L}$ , decays into  $Z'Z'$  and/or  $Z'Z$  can be kinematically allowed. While these decays are interesting, as they can probe the new gauge coupling, they are not the focus of this chapter. Instead, the processes that are of interest are the decays of the scalar into SM particles, and hence we work in a scenario in which decays into  $Z'$  bosons are kinematically forbidden.

The partial decay width of  $S$  of the most relevant channels for our studies, being  $\mu\bar{\mu}$ ,  $b\bar{b}$ ,  $hH$ ,  $hh$ , and  $ZZ$ , are given here. Even though the channels are closed in this particular scenario, the partial widths into  $Z'Z'$  and  $Z'Z$  are listed for completeness.

$$\Gamma_{S\mu\bar{\mu}} = \frac{s_{\alpha_2}^2 (m_S^2 - 4m_{\mu}^2)^{3/2}}{8\pi m_S^2 s_{\beta}^2} \quad (11.27)$$

$$\Gamma_{Sb\bar{b}} = \frac{3s_{\alpha_2}^2 (m_S^2 - 4m_b^2)^{3/2}}{8\pi m_S^2 s_{\beta}^2} \quad (11.28)$$

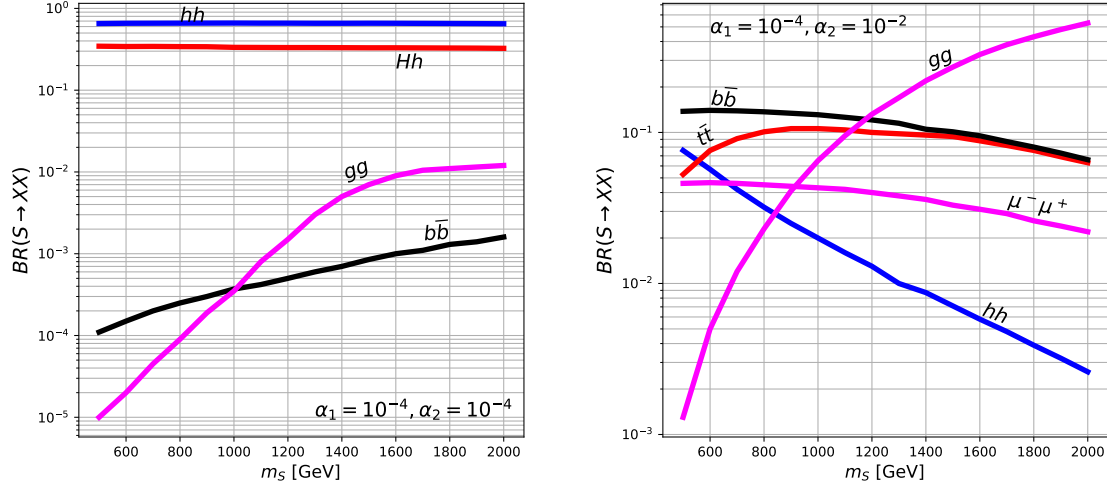


Figure 11.5: Dominant branching ratios of the heavy scalar  $S$  as a function of its mass for mixing angles  $\alpha_1 = \alpha_2 = 10^{-4}$  (left) and  $\alpha_1 = 10^{-4}, \alpha_2 = 10^{-2}$ .

$$\Gamma_{ShH} = \frac{\sqrt{-2m_h^2 m_H^2 - 2m_h^2 m_S^2 + m_h^4 - 2m_H^2 m_S^2 + m_H^4 + m_S^4}}{64\pi m_S^3} \times (-s_\alpha \mu_2 v_s - s_\alpha \mu_1 v_s + c_\alpha^2 \mu_s + s_\alpha^2 \mu_s)^2 \quad (11.29)$$

$$\Gamma_{Shh} = \frac{\sqrt{m_S^2 - 4m_h^2}}{32\pi m_S^2} (s_\alpha^2 \mu_2 v_S + c_\alpha^2 \mu_1 v_s + s_\alpha^2 \mu_1 v_s - c_\alpha s_\alpha \mu_s)^2 \quad (11.30)$$

$$\Gamma_{SZZ} = g_{B-L}^4 \frac{\sqrt{m_S^2 - 4m_Z^2} (m_S^4 - 4m_S^2 m_Z^2 + 12m_Z^4) q_S^4 s_\xi^4 v_s^2}{128\pi m_Z^4 m_S^2} \quad (11.31)$$

$$\Gamma_{SZ'Z'} = g_{B-L}^4 \frac{\sqrt{m_S^2 - 4m_Z'^2} (m_S^4 - 4m_S^2 m_Z'^2 + 12m_Z'^4) q_S^4 c_\xi^4 v_s^2}{128m_Z'^4 \pi m_S^2} \quad (11.32)$$

$$\Gamma_{SZ'Z} = g_{B-L}^4 \frac{\sqrt{m_S^4 - 2m_S^2 m_Z'^2 + m_Z'^4 - 2m_S^2 m_Z'^2 - 2m_Z'^2 m_Z'^2 + m_Z'^4}}{256m_Z'^2 m_Z'^2 \pi m_S^3} \times (m_S^4 - 2m_S^2 m_Z'^2 + m_Z'^4 - 2m_S^2 m_Z'^2 + 10m_Z'^2 m_Z'^2 + m_Z'^4) q_S^4 s_\xi^2 c_\xi^2 v_s^2 \quad (11.33)$$

For brevity, we have written  $s_\xi = \sin \xi$ ,  $c_\xi = \cos \xi$  from Eq. (11.24), as well as  $s_\beta = \sin \beta$  and  $s_\alpha = \sin \alpha$ . We will now examine the branching ratios of the scalar decays for two different scenarios. In both cases  $\alpha_1$  is set to the small value of  $\alpha_1 = 10^{-4}$ , whereas in the first scenario  $\alpha_2 = 10^{-4}$ , and in the second scenario  $\alpha_2 = 10^{-2}$ . The most prominent branching ratios for these scenarios are shown in Fig. 11.5.

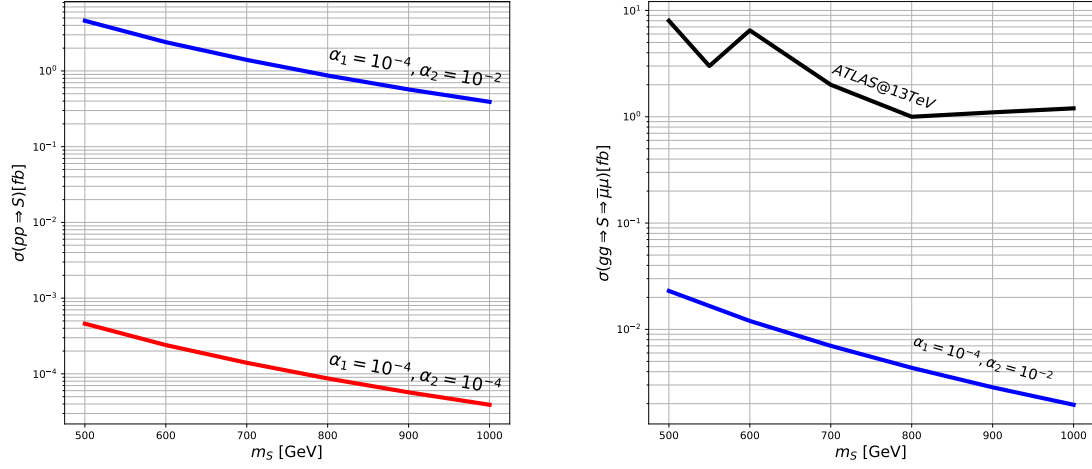


Figure 11.6: Left: Total production cross sections of heavy scalars  $S$  for scenarios with  $\alpha_1 = \alpha_2 = 10^{-4}$  and  $\alpha_1 = 10^{-4}, \alpha_2 = 10^{-2}$ . Right: Upper limit on the gluon-gluon fusion production of scalars decaying into dimuons imposed by the ATLAS collaboration (black) and our model prediction assuming  $\alpha_1 = 10^{-4}$  and  $\alpha_2 = 10^{-2}$  (blue).

In the first scenario the coupling of the heavy scalar  $S$  to both doublets is small, with  $\mu_i \sim 10^{-6}$ , and it primarily decays into  $hh$  and  $Hh$ , see Fig. 11.5 (left). Despite this small coupling, these are the dominant channels. The reasons for this are twofold. On the one hand the branching ratio of these channels are enhanced by their proportionality to the large value of  $v_s$ , counteracting the small values of  $\mu_i$ . On the other hand the branching ratios into the SM fermions are suppressed by the small value of  $\alpha_2 = 10^{-4}$ . The second scenario, with  $\alpha_2 = 10^{-2}$ , is shown in Fig. 11.5 (right). In this scenario decays into SM fermions play a larger role.

Let us now focus on the production and detection prospects at the HL-LHC with a center-of-mass energy of 13 TeV. The production process takes place through the gluon fusion process in  $pp$  collisions. For the first scenario the main decay channels are into  $hh$  and  $Hh$ , which include little QED background. However, as can be seen in Fig. 11.6 (left), the production cross section of the heavy scalar is too low in this scenario to be explored at the upcoming HL-LHC. For the second scenario the production cross section is much larger, hence we focus on this case. As can be seen from Fig. 11.5 (right), there is a large lepton di-jet signal. However, due to the large branching ratios into the 3rd generation quarks, as well as gluons, there also exists a huge QCD background. For the dimuon channel the main background contribution is  $Z$  boson production, hence we explore the discovery possibilities through the following process

$$pp \rightarrow S \rightarrow l^- l^+, \quad (11.34)$$

where we consider final-state  $l^\pm$  representing electrons or muons.

Table 11.4: Cut-flow chart for  $m_S = 500$  GeV and an integrated luminosity of  $220 \text{ fb}^{-1}$  at the LHC with 13 TeV and without systematic errors ( $x = 0$ ).

Cuts	Signal	Background	Significance
Initial (no cut)	1130	983000	1.1
$p_{T1,2} > 20 \text{ GeV}$	1050	732200	1.2
$ \eta_\ell  < 2.5$	1045	511800	1.4
$m_{2\ell} > 250 \text{ GeV}$	945	114000	2.7
Hard cut on $m_{\ell\ell}$	181	1109	5.0

The model is implemented using FeynRules [391], after which the partonic events are simulated using MadGraph5 [392]. Further hadronization and detector effects were handled with the Pythia8 [393] and Delphes3 [394] MadGraph5 interfaces respectively, using the kT-MLM jet matching scheme [395].  $S$  production at one-loop has been implemented following Ref. [396]. The relevant background contributions, which were simulated in the same way, are the  $Z$ ,  $h$ ,  $\gamma$ ,  $b\bar{b}Z$ ,  $WZ$  and  $b\bar{b}Z$  production processes. The following cuts were applied to the data to reduce the backgrounds and select the relevant signal events

$$p_{T1,2} > 20 \text{ GeV}, \quad |\eta_\ell| < 2.5 \quad (11.35)$$

$$\cancel{E}_T < 40 \text{ GeV}, \quad m_{2\ell} > 250 \text{ GeV}, \quad (11.36)$$

with  $p_{Tn}$  being the  $n$ -th hardest lepton within an event. Events with missing transverse energy above 40 GeV are rejected to filter out  $W$ ,  $Z$ , and  $t\bar{t}$  events. Bottom jets fall out after applying lepton isolation criteria. As a last step, a hard cut on the di-lepton invariant mass  $m_S - 40 \text{ GeV} < m_{\ell\ell} < m_S + 40 \text{ GeV}$  can identify leptons produced by a heavy resonance decay.

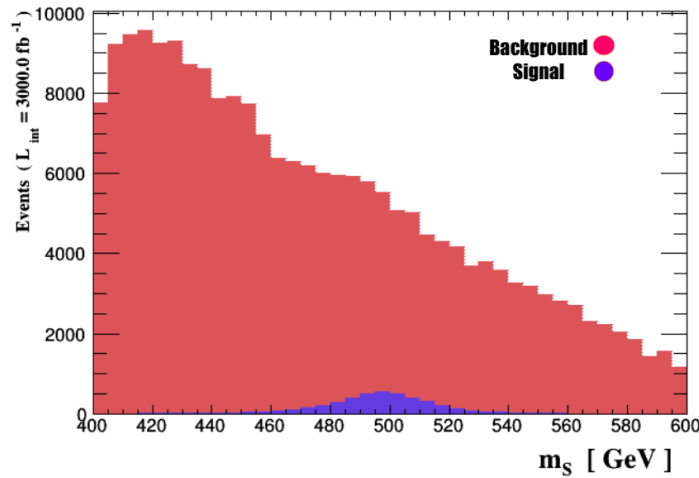


Figure 11.7: Dilepton invariant mass distribution for a singlet-like scalar boson of mass  $m_s = 500$  GeV (blue) and its SM background (red) before cuts and for an integrated luminosity of  $3000 \text{ fb}^{-1}$ .

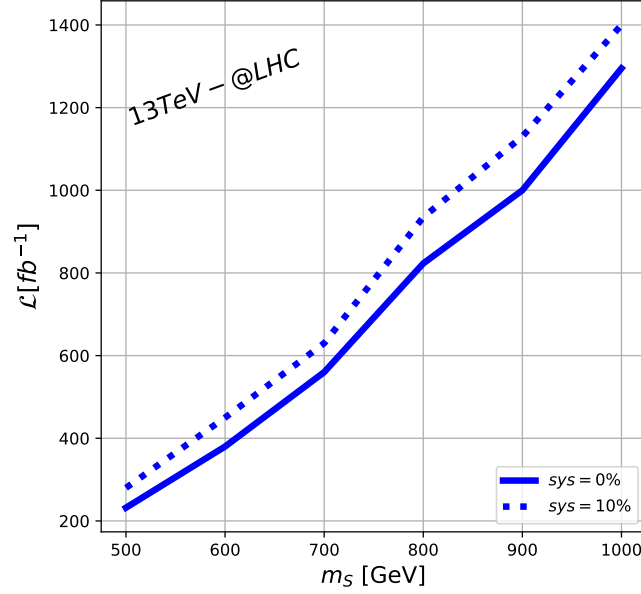


Figure 11.8: Required luminosity of the HL-LHC at 13 TeV center-of-mass energy to discover a singlet-like Higgs boson  $S$  with  $5\sigma$  as a function of its mass for an assumed systematic error of 10% (dotted line) and 0% (continuous line).

Fig. 11.7 then shows the signal of a resonance due to a heavy scalar with a mass of 500 GeV against the background due to the previously mentioned processes before any cuts are applied. The signal can be made visible at the  $5\sigma$  level after applying these cuts. As an illustration, Tab. 11.4 shows the cut-flow chart for  $m_S = 500$  GeV and an integrated luminosity of 220 fb $^{-1}$ , without taking systematic errors into account. In each step the number of signal and background events are indicated, as well as the significance. The significance for a number of signal ( $N_S$ ) and background ( $N_B$ ) events is calculated as

$$\frac{N_S}{\sqrt{N_S + N_B + (xN_B)^2}}, \quad (11.37)$$

with the last factor taking systematic errors into account. Fig. 11.8 shows the required luminosity for a  $5\sigma$  signal at the HL-LHC as a function of the scalar mass for an assumed systematic error of 10% (dotted line) and 0% (full line). From this one can see that the current LHC luminosity of 100 fb $^{-1}$  is not sufficient to discover a singlet scalar as studied here. However, the planned HL-LHC upgrade can reach integrated luminosities of  $\sim 1400$  fb $^{-1}$ , which is enough to detect singlet scalars up to the TeV scale, even with a systematic error included.

### 11.3 Conclusion

We have explored the phenomenology of a  $U(1)_{B-L}$  gauged model with a 2HDM + singlet scalar sector. In our setup we focused on the weakly coupled scalar singlet. We have shown how the model can accommodate an SM-like Higgs boson with the correct mass and couplings, which however does come at a cost in the form of restrictions on the parameter space. Then we studied the discovery prospects of the weakly-coupled scalar singlet through its dilepton decay, for which we found that the current LHC luminosity is not sufficient to detect such a scalar, but the planned HL-LHC can have sufficient luminosity to discover a scalar singlet up to masses of around 1 TeV.

These results can be extended to other  $U(1)$  gauged models containing a weakly-coupled scalar singlet, such as the models that were introduced in Chapter 10.



## 12 Conclusion and outlook

Even though the Standard Model is a successful theory, it has its shortcomings when describing neutrino masses and dark matter. In this thesis, we have shown how radiative seesaw models can provide answers to both of these open questions. We have presented many aspects of these models, with our focus on minimal realizations of radiative seesaw models. After introducing the current status of dark matter and neutrino physics in Chapters 2 and 3 respectively, we introduced these models in Chapter 4.

In Chapter 5 we investigated the role of the absolute neutrino mass in the scotogenic model. We found that if the dark matter candidate is fermionic, the absolute neutrino mass, and the absolute value of the dark sector-Higgs coupling  $\lambda_5$  become linearly proportional. This parameter is important because it generates a mass splitting between the neutral scalar states, which is crucial for the generation of neutrino masses. We then related our results to the KATRIN experiment, which has established an upper bound on the absolute neutrino mass scale. Our results imply that a KATRIN measurement will fix the  $\lambda_5$  parameter.

Chapters 6 and 7 considered the same topic: the detection of neutrino signals from dark matter annihilations in the Sun with ICECUBE, for the scotogenic model and the T1-3-B  $\alpha = 0$  models respectively. For the scotogenic model, we considered the case where dark matter is captured in the Sun through an inelastic scattering process. We found that this can lead to large event rates in ICECUBE of around  $10^3$  events per year. Inelastic scattering is very sensitive to the mass splitting between the scalar states, and thus in the case where no events are observed this leads to a lower bound on  $\lambda_5$ . For a scenario in which coannihilations are included, bounds on the thermally averaged cross section from the Galactic Centre set by ANTARES and ICECUBE are within one order of magnitude, making it in reach of further indirect detection experiments. For the T1-3-B  $\alpha = 0$  no inelastic scattering is possible, but it contains two dark matter candidates, a singlet-doublet fermion or a triplet scalar. The singlet-doublet fermion can also scatter via a spin dependent process, for which the direct detection constraints are relatively weaker. Thus indirect detection, which is more sensitive to this, can play an important role. The resulting event rate is high enough to warrant a dedicated ICECUBE analysis. For triplet scalar dark matter, there is no spin dependent scattering, and the resulting event rate is too low to be detectable.

In Chapter 8 we put the focus on direct detection instead, and we considered the SLIM model, which contains MeV to GeV right-handed,  $\mathbb{Z}_2$ -odd, neutrinos. We then made a random numerical scan from the parameter space, which showed the effects of different model parameters on the relic density. Furthermore, we showed that LFV processes such as  $\mu \rightarrow e\gamma$

and the dark matter-electron coupling  $\lambda_g^{e1}$  are related, and the former impose an upper bound on the size of the latter. This is important, since we then calculate the dark matter-electron recoil cross section, and find that it is too low to be detectable experimentally, due to the necessary large mass of the mediator. We then present a derivation of the electron recoil cross section sensitivity of XENON1T when taking into account realistic detector background and threshold effects. Of all background sources in the XENON1T experiment,  $^{222}\text{Rn}$  is the main contributor. In Chapter 9 we presented a measurement of a different, but similar isotope,  $^{220}\text{Rn}$ . This isotope was mixed with gaseous xenon, and the resulting signals corresponded well to the  $\alpha$  decays that are present in the  $^{220}\text{Rn}$  decay chain.

In the last part of the thesis, models with an extension to the Standard Model gauge symmetry were considered. Chapter 10 considered radiative seesaw models with an additional local  $U(1)$  group. With arguments based on the gauge anomaly cancellation and the topology of the neutrino mass loops, we presented a systematic overview of minimal radiative seesaw models with a  $U(1)_X$  symmetry. For the charge assignments of the new symmetry we also took mixing effects into account. We compared our models to existing models with an extra  $U(1)$  symmetry, and found that our particular setup has received little attention in the literature thus far, which gives plenty of opportunities to study specific models in more detail. We consider the case where the new gauge symmetry is broken by a scalar singlet  $\zeta$ , resulting in a  $\mathbb{Z}_n$  or global  $U(1)$  remnant symmetry. We then show the general  $Z'$  phenomenology inherent to all models, as well as the more extensive scalar sector. As a last step, we investigated the possibility of embedding our minimal models in a GUT setup, but we found that embedding our models in an  $SO(10)$  GUT is incompatible with our requirement that the Standard Model is uncharged under the new symmetry. Finally, in Chapter 11 we considered a model with a  $U(1)_{B-L}$  gauge symmetry, and investigated the discovery potential of a heavy, weakly coupled, scalar singlet at the LHC. We found that such a heavy state can be detected at the HL-LHC with a mass of up to around 1 TeV.

## A Gain calibration

For pedagogical purposes, we apply the same gain calibration methods and fitting to the data that was used by Henning Schulze Eißing to determine the gain of the PMTs in the Münster TPC [397]. Figure A.1 shows the result for PMT 11. The difference with Figure 9.6 is clear: With a  $\chi^2$  value of 1.697 this fit is much better. This has to do with the fact that the pedestal is narrower and more Gaussian. We find a gain of  $(2.100 \pm 0.097) \times 10^6$ , which is slightly lower than the value of  $(2.305 \pm 0.075) \times 10^6$  that was found previously [397]. However, this difference could be explained by the fact that we excluded all bins with  $< 10$  counts to have sufficient statistics, whereas previously every bin was taken into account. The fit parameters are:

	Name	Value	Para Error	Error+	Error-	Limit+	Limit-	FIXED
1	$a_{bg}$	2.043e+04	3.110e+02			1.000e+04	1.000e+09	
2	$\sigma_{bg}$	2.962e-02	6.025e-04			1.000e-02	3.000e+00	
3	$a_1$	5.671e+04	1.891e+03			5.000e+02	1.000e+07	
4	$\mu_1$	2.100e+00	9.717e-02			5.000e-01	3.500e+00	
5	$\sigma_1$	1.580e+00	1.224e-01			5.000e-02	4.000e+00	
6	$\lambda$	1.277e-03	4.199e-05			1.000e-03	1.000e-01	
7	rel $d_1$	8.216e-01	8.717e-03			1.000e-02	1.000e+00	
8	rel $d_2$	1.000e+00	1.455e-02			1.000e-02	1.000e+00	
9	rel $d_3$	0.000e+00	1.000e-03			0.000e+00	1.000e+00	FIXED
10	$p_0$	9.684e-02	2.466e-04			-5.000e-01	7.000e-01	
11	$\tilde{a}$	-1.000e+00	1.000e-02			-1.000e+00	1.000e+00	FIXED

Because we do not see a double peak as in figure 9.6, we have no need for the parameter asym. Setting this parameter to -1 means that we are left with a single peak. Moreover, the amplitude of the triple photoelectron peak is set to 0 as it was found to have no effect on the fit.

In contrast PMT 10 was reported to have the worst fit. For this PMT the result is shown in figure A.2. We find a gain of  $(2.165 \pm 0.124) \times 10^6$ , compared to  $(2.313 \pm 0.046) \times 10^6$ . When also taking into account bins with less than 10 counts, this changes to  $(2.402 \pm 0.041) \times 10^6$ , the fit is shown in figure A.3. This shows that requiring a minimum amount of counts in a single bin does affect the results of the fit.

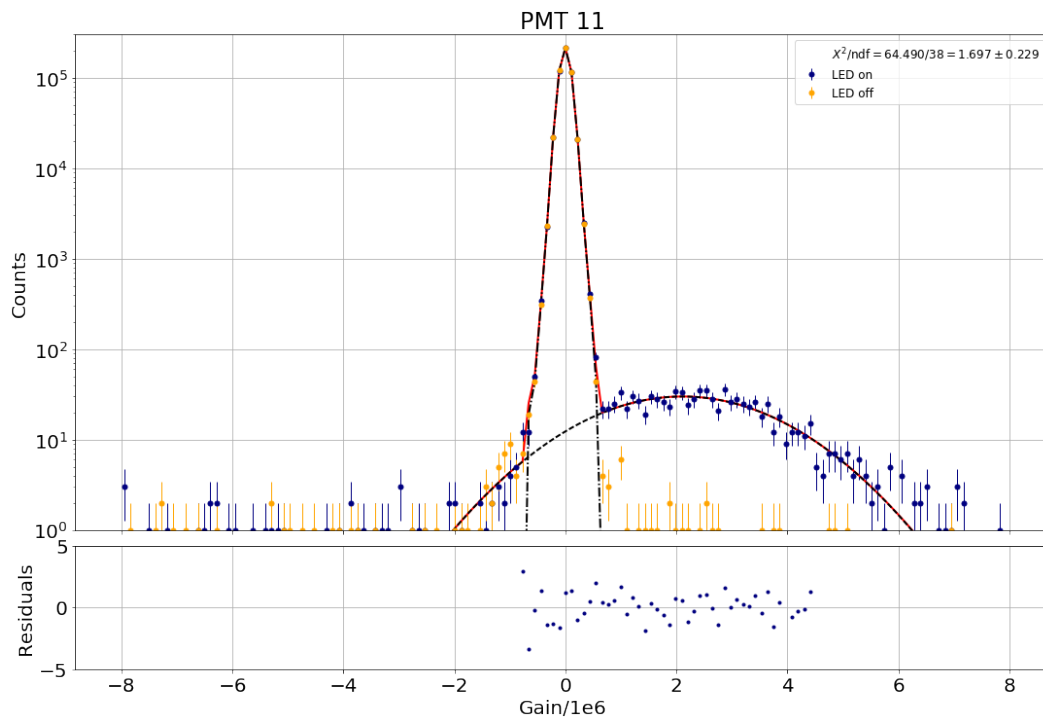


Figure A.1: Gain fit for PMT 11 of the Münster TPC at an LED voltage of 5.4 V.

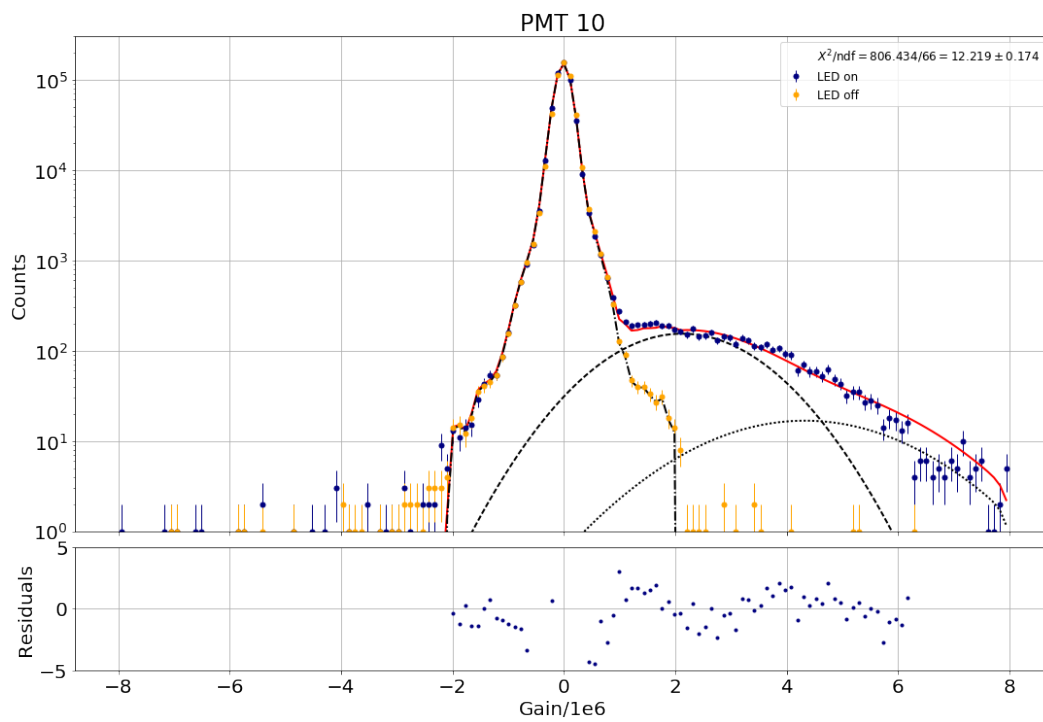


Figure A.2: Gain fit for PMT 10 of the Münster TPC at an LED voltage of 5.6 V.

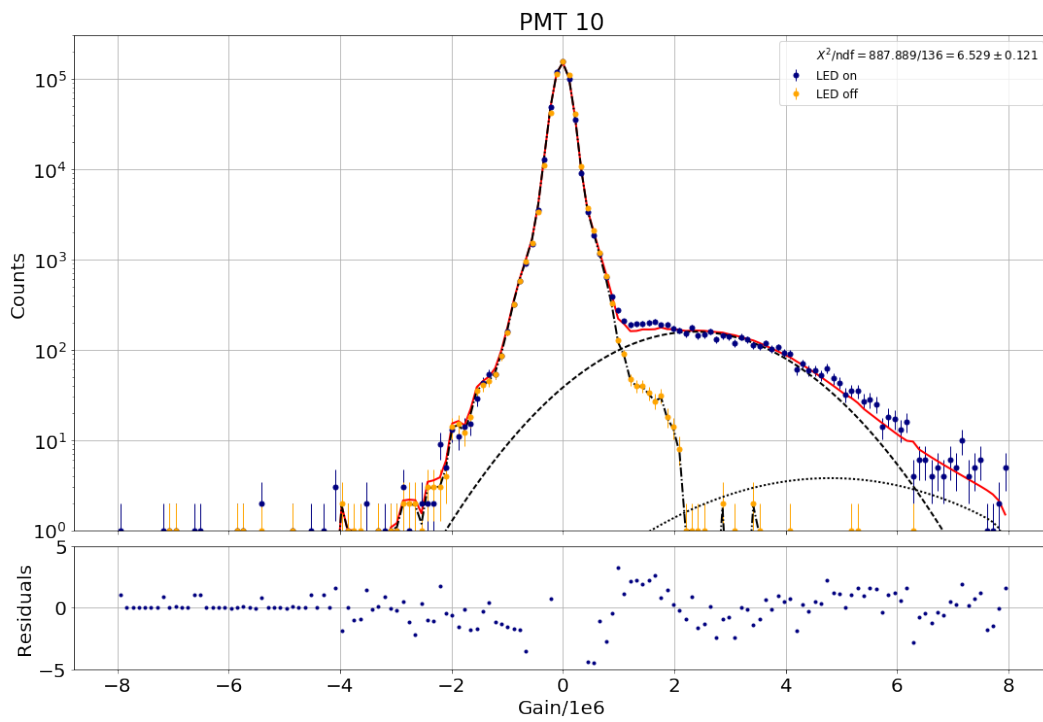


Figure A.3: Gain fit for PMT 10 of the Münster TPC at an LED voltage of 5.6 V, also taking into account bins with less than 10 counts.



## Bibliography

- [1] Georges Aad et al. “Observation of a new particle in the search for the Standard Model Higgs boson with the ATLAS detector at the LHC”. In: *Phys. Lett. B* 716 (2012), pp. 1–29. DOI: 10.1016/j.physletb.2012.08.020. arXiv: 1207.7214 [hep-ex].
- [2] Serguei Chatrchyan et al. “Observation of a New Boson at a Mass of 125 GeV with the CMS Experiment at the LHC”. In: *Phys. Lett. B* 716 (2012), pp. 30–61. DOI: 10.1016/j.physletb.2012.08.021. arXiv: 1207.7235 [hep-ex].
- [3] J. C. Kapteyn. “First Attempt at a Theory of the Arrangement and Motion of the Sidereal System”. In: *The Astrophysical Journal* 55 (May 1922), p. 302. DOI: 10.1086/142670. URL: <https://doi.org/10.1086/142670>.
- [4] J. H. Oort. “The force exerted by the stellar system in the direction perpendicular to the galactic plane and some related problems”. In: *Bulletin of the Astronomical Institutes of the Netherlands* 6 (1932), p. 249. URL: <https://hdl.handle.net/1887/6025>.
- [5] F. Zwicky. “Die Rotverschiebung von extragalaktischen Nebeln”. In: *Helv. Phys. Acta* 6 (1933), pp. 110–127. DOI: 10.1007/s10714-008-0707-4.
- [6] K. G. Begeman, A. H. Broeils, and R. H. Sanders. “Extended rotation curves of spiral galaxies: dark haloes and modified dynamics”. In: *Monthly Notices of the Royal Astronomical Society* 249.3 (Apr. 1991), pp. 523–537. DOI: 10.1093/mnras/249.3.523. URL: <https://doi.org/10.1093/mnras/249.3.523>.
- [7] V. C. Rubin, N. Thonnard, and Jr. Ford W. K. “Extended rotation curves of high-luminosity spiral galaxies. IV - Systematic dynamical properties, SA through SC”. In: *The Astrophysical Journal* 225 (Nov. 1978), p. L107. DOI: 10.1086/182804. URL: <https://doi.org/10.1086/182804>.
- [8] M. Milgrom. “A Modification of the Newtonian dynamics as a possible alternative to the hidden mass hypothesis”. In: *Astrophys. J.* 270 (1983), pp. 365–370. DOI: 10.1086/161130.
- [9] Myungkook James Jee et al. “Discovery of a Ringlike Dark Matter Structure in the Core of the Galaxy Cluster Cl 0024+17”. In: *Astrophys. J.* 661 (2007), pp. 728–749. DOI: 10.1086/517498. arXiv: 0705.2171 [astro-ph].
- [10] Douglas Clowe et al. “A direct empirical proof of the existence of dark matter”. In: *Astrophys. J. Lett.* 648 (2006), pp. L109–L113. DOI: 10.1086/508162. arXiv: astro-ph/0608407.

- [11] R. Adam et al. “Planck 2015 results. IX. Diffuse component separation: CMB maps”. In: *Astron. Astrophys.* 594 (2016), A9. DOI: 10.1051/0004-6361/201525936. arXiv: 1502.05956 [astro-ph.CO].
- [12] Arno A. Penzias and Robert Woodrow Wilson. “A Measurement of excess antenna temperature at 4080-Mc/s”. In: *Astrophys. J.* 142 (1965), pp. 419–421. DOI: 10.1086/148307.
- [13] D. J. Fixsen. “THE TEMPERATURE OF THE COSMIC MICROWAVE BACKGROUND”. In: *The Astrophysical Journal* 707.2 (Nov. 2009), pp. 916–920. DOI: 10.1088/0004-637x/707/2/916. URL: <https://doi.org/10.1088/0004-637x/707/2/916>.
- [14] Gianfranco Bertone, Dan Hooper, and Joseph Silk. “Particle dark matter: Evidence, candidates and constraints”. In: *Phys. Rept.* 405 (2005), pp. 279–390. DOI: 10.1016/j.physrep.2004.08.031. arXiv: hep-ph/0404175.
- [15] George F. Smoot et al. “Structure in the COBE differential microwave radiometer first year maps”. In: *Astrophys. J. Lett.* 396 (1992), pp. L1–L5. DOI: 10.1086/186504.
- [16] E. Komatsu et al. “Seven-Year Wilkinson Microwave Anisotropy Probe (WMAP) Observations: Cosmological Interpretation”. In: *Astrophys. J. Suppl.* 192 (2011), p. 18. DOI: 10.1088/0067-0049/192/2/18. arXiv: 1001.4538 [astro-ph.CO].
- [17] Y. Akrami et al. “Planck 2018 results. VII. Isotropy and Statistics of the CMB”. In: *Astron. Astrophys.* 641 (2020), A7. DOI: 10.1051/0004-6361/201935201. arXiv: 1906.02552 [astro-ph.CO].
- [18] N. Aghanim et al. “Planck 2018 results. V. CMB power spectra and likelihoods”. In: *Astron. Astrophys.* 641 (2020), A5. DOI: 10.1051/0004-6361/201936386. arXiv: 1907.12875 [astro-ph.CO].
- [19] Alan H. Guth. “The Inflationary Universe: A Possible Solution to the Horizon and Flatness Problems”. In: *Phys. Rev. D* 23 (1981). Ed. by Li-Zhi Fang and R. Ruffini, pp. 347–356. DOI: 10.1103/PhysRevD.23.347.
- [20] Andrei D. Linde. “A New Inflationary Universe Scenario: A Possible Solution of the Horizon, Flatness, Homogeneity, Isotropy and Primordial Monopole Problems”. In: *Phys. Lett. B* 108 (1982). Ed. by Li-Zhi Fang and R. Ruffini, pp. 389–393. DOI: 10.1016/0370-2693(82)91219-9.
- [21] Andrew R Liddle and Samuel M Leach. “How long before the end of inflation were observable perturbations produced?” In: *Phys. Rev. D* 68 (2003), p. 103503. DOI: 10.1103/PhysRevD.68.103503. arXiv: astro-ph/0305263.
- [22] Scott Dodelson and Lam Hui. “A Horizon ratio bound for inflationary fluctuations”. In: *Phys. Rev. Lett.* 91 (2003), p. 131301. DOI: 10.1103/PhysRevLett.91.131301. arXiv: astro-ph/0305113.
- [23] N. Aghanim et al. “Planck 2018 results. VI. Cosmological parameters”. In: *Astron. Astrophys.* 641 (2020), A6. DOI: 10.1051/0004-6361/201833910. arXiv: 1807.06209 [astro-ph.CO].



- [24] Edward W. Kolb and Michael S. Turner. *The Early Universe*. Vol. 69. 1990. ISBN: 978-0-201-62674-2.
- [25] Joseph Silk. “Cosmic black body radiation and galaxy formation”. In: *Astrophys. J.* 151 (1968), pp. 459–471. DOI: 10.1086/149449.
- [26] Michael R. Blanton et al. “Sloan Digital Sky Survey IV: Mapping the Milky Way, Nearby Galaxies and the Distant Universe”. In: *Astron. J.* 154.1 (2017), p. 28. DOI: 10.3847/1538-3881/aa7567. arXiv: 1703.00052 [astro-ph.GA].
- [27] Matthew Colless et al. “The 2dF Galaxy Redshift Survey: Spectra and redshifts”. In: *Mon. Not. Roy. Astron. Soc.* 328 (2001), p. 1039. DOI: 10.1046/j.1365-8711.2001.04902.x. arXiv: astro-ph/0106498.
- [28] J. Richard Bond, Lev Kofman, and Dmitri Pogosyan. “How filaments are woven into the cosmic web”. In: *Nature* 380 (1996), pp. 603–606. DOI: 10.1038/380603a0. arXiv: astro-ph/9512141.
- [29] Volker Springel et al. “Simulating the joint evolution of quasars, galaxies and their large-scale distribution”. In: *Nature* 435 (2005), pp. 629–636. DOI: 10.1038/nature03597. arXiv: astro-ph/0504097.
- [30] George R. Blumenthal et al. “Formation of Galaxies and Large Scale Structure with Cold Dark Matter”. In: *Nature* 311 (1984). Ed. by M. A. Srednicki, pp. 517–525. DOI: 10.1038/311517a0.
- [31] A. Jenkins et al. “Evolution of structure in cold dark matter universes”. In: *Astrophys. J.* 499 (1998), p. 20. DOI: 10.1086/305615. arXiv: astro-ph/9709010.
- [32] R. E. Smith et al. “Stable clustering, the halo model and nonlinear cosmological power spectra”. In: *Mon. Not. Roy. Astron. Soc.* 341 (2003), p. 1311. DOI: 10.1046/j.1365-8711.2003.06503.x. arXiv: astro-ph/0207664.
- [33] Anatoly A. Klypin et al. “Where are the missing Galactic satellites?” In: *Astrophys. J.* 522 (1999), pp. 82–92. DOI: 10.1086/307643. arXiv: astro-ph/9901240.
- [34] David H. Weinberg et al. “Cold dark matter: controversies on small scales”. In: *Proc. Nat. Acad. Sci.* 112 (2015), pp. 12249–12255. DOI: 10.1073/pnas.1308716112. arXiv: 1306.0913 [astro-ph.CO].
- [35] James S. Bullock et al. “Stealth Galaxies in the Halo of the Milky Way”. In: *Astrophys. J.* 717 (2010), pp. 1043–1053. DOI: 10.1088/0004-637X/717/2/1043. arXiv: 0912.1873 [astro-ph.CO].
- [36] James S. Bullock. “Notes on the Missing Satellites Problem”. In: (Sept. 2010). arXiv: 1009.4505 [astro-ph.CO].
- [37] Gilles Chabrier. “Galactic stellar and substellar initial mass function”. In: *Publ. Astron. Soc. Pac.* 115 (2003), pp. 763–796. DOI: 10.1086/376392. arXiv: astro-ph/0304382.
- [38] Edwin E. Salpeter. “The Luminosity Function and Stellar Evolution.” In: *The Astrophysical Journal* 121 (Jan. 1955), p. 161. DOI: 10.1086/145971. URL: <https://doi.org/10.1086/145971>.

- [39] C. Alcock et al. “The MACHO Project: Microlensing Results from 5.7 Years of Large Magellanic Cloud Observations”. In: *The Astrophysical Journal* 542.1 (Oct. 2000), pp. 281–307. DOI: 10.1086/309512. URL: <https://doi.org/10.1086/309512>.
- [40] P. Tisserand et al. “Limits on the Macho Content of the Galactic Halo from the EROS-2 Survey of the Magellanic Clouds”. In: *Astron. Astrophys.* 469 (2007), pp. 387–404. DOI: 10.1051/0004-6361:20066017. arXiv: astro-ph/0607207.
- [41] Paul Frederik Depta et al. “BBN constraints on the annihilation of MeV-scale dark matter”. In: *JCAP* 04 (2019), p. 029. DOI: 10.1088/1475-7516/2019/04/029. arXiv: 1901.06944 [hep-ph].
- [42] Gerard Jungman, Marc Kamionkowski, and Kim Griest. “Supersymmetric dark matter”. In: *Phys. Rept.* 267 (1996), pp. 195–373. DOI: 10.1016/0370-1573(95)00058-5. arXiv: hep-ph/9506380.
- [43] Gary Steigman, Basudeb Dasgupta, and John F. Beacom. “Precise Relic WIMP Abundance and its Impact on Searches for Dark Matter Annihilation”. In: *Phys. Rev. D* 86 (2012), p. 023506. DOI: 10.1103/PhysRevD.86.023506. arXiv: 1204.3622 [hep-ph].
- [44] Katherine Garrett and Gintaras Duda. “Dark Matter: A Primer”. In: *Adv. Astron.* 2011 (2011), p. 968283. DOI: 10.1155/2011/968283. arXiv: 1006.2483 [hep-ph].
- [45] Kim Griest and David Seckel. “Three exceptions in the calculation of relic abundances”. In: *Phys. Rev. D* 43 (1991), pp. 3191–3203. DOI: 10.1103/PhysRevD.43.3191.
- [46] Stefano Profumo and Alessio Provenza. “Increasing the neutralino relic abundance with slepton coannihilations: Consequences for indirect dark matter detection”. In: *JCAP* 12 (2006), p. 019. DOI: 10.1088/1475-7516/2006/12/019. arXiv: hep-ph/0609290.
- [47] P. A. Zyla et al. “Review of Particle Physics”. In: *PTEP* 2020.8 (2020), p. 083C01. DOI: 10.1093/ptep/ptaa104.
- [48] Leonard Susskind. “Dynamics of Spontaneous Symmetry Breaking in the Weinberg-Salam Theory”. In: *Phys. Rev. D* 20 (1979), pp. 2619–2625. DOI: 10.1103/PhysRevD.20.2619.
- [49] Stephen P. Martin. “A Supersymmetry primer”. In: *Adv. Ser. Direct. High Energy Phys.* 18 (1998). Ed. by Gordon L. Kane, pp. 1–98. DOI: 10.1142/9789812839657\_0001. arXiv: hep-ph/9709356.
- [50] Paul Langacker and Ming-xing Luo. “Implications of precision electroweak experiments for  $M_t$ ,  $\rho_0$ ,  $\sin^2 \theta_W$  and grand unification”. In: *Phys. Rev. D* 44 (1991), pp. 817–822. DOI: 10.1103/PhysRevD.44.817.
- [51] Ugo Amaldi, Wim de Boer, and Hermann Furstenau. “Comparison of grand unified theories with electroweak and strong coupling constants measured at LEP”. In: *Phys. Lett. B* 260 (1991), pp. 447–455. DOI: 10.1016/0370-2693(91)91641-8.
- [52] A. Djouadi et al. “The Minimal supersymmetric standard model: Group summary report”. In: *GDR (Groupement De Recherche) - Supersymetrie*. Dec. 1998. arXiv: hep-ph/9901246.

- [53] J. Harz et al. “Neutralino-stop coannihilation into electroweak gauge and Higgs bosons at one loop”. In: *Phys. Rev. D* 87.5 (2013), p. 054031. DOI: 10.1103/PhysRevD.87.054031. arXiv: 1212.5241 [hep-ph].
- [54] F. Gabbiani et al. “A Complete analysis of FCNC and CP constraints in general SUSY extensions of the standard model”. In: *Nucl. Phys. B* 477 (1996), pp. 321–352. DOI: 10.1016/0550-3213(96)00390-2. arXiv: hep-ph/9604387.
- [55] Bjorn Herrmann, Michael Klasen, and Karol Kovarik. “SUSY-QCD effects on neutralino dark matter annihilation beyond scalar or gaugino mass unification”. In: *Phys. Rev. D* 80 (2009), p. 085025. DOI: 10.1103/PhysRevD.80.085025. arXiv: 0907.0030 [hep-ph].
- [56] John R. Ellis, Toby Falk, and Keith A. Olive. “Neutralino - Stau coannihilation and the cosmological upper limit on the mass of the lightest supersymmetric particle”. In: *Phys. Lett. B* 444 (1998), pp. 367–372. DOI: 10.1016/S0370-2693(98)01392-6. arXiv: hep-ph/9810360.
- [57] J. Branahl et al. “SUSY-QCD corrected and Sommerfeld enhanced stau annihilation into heavy quarks with scheme and scale uncertainties”. In: *Phys. Rev. D* 100.11 (2019), p. 115003. DOI: 10.1103/PhysRevD.100.115003. arXiv: 1909.09527 [hep-ph].
- [58] Amin Aboubrahim, Michael Klasen, and Pran Nath. “What Fermilab  $(g - 2)_\mu$  experiment tells us about discovering SUSY at HL-LHC and HE-LHC”. In: (Apr. 2021). arXiv: 2104.03839 [hep-ph].
- [59] Mark D. Goodsell et al. “Constraining Electroweakinos in the Minimal Dirac Gaugino Model”. In: *SciPost Phys.* 9.4 (2020), p. 047. DOI: 10.21468/SciPostPhys.9.4.047. arXiv: 2007.08498 [hep-ph].
- [60] Michele Papucci, Joshua T. Ruderman, and Andreas Weiler. “Natural SUSY Endures”. In: *JHEP* 09 (2012), p. 035. DOI: 10.1007/JHEP09(2012)035. arXiv: 1110.6926 [hep-ph].
- [61] Albert M Sirunyan et al. “Search for additional neutral MSSM Higgs bosons in the  $\tau\tau$  final state in proton-proton collisions at  $\sqrt{s} = 13$  TeV”. In: *JHEP* 09 (2018), p. 007. DOI: 10.1007/JHEP09(2018)007. arXiv: 1803.06553 [hep-ex].
- [62] M. G. Aartsen et al. “Improved limits on dark matter annihilation in the Sun with the 79-string IceCube detector and implications for supersymmetry”. In: *JCAP* 04 (2016), p. 022. DOI: 10.1088/1475-7516/2016/04/022. arXiv: 1601.00653 [hep-ph].
- [63] S. Heinemeyer, O. Stal, and G. Weiglein. “Interpreting the LHC Higgs Search Results in the MSSM”. In: *Phys. Lett. B* 710 (2012), pp. 201–206. DOI: 10.1016/j.physletb.2012.02.084. arXiv: 1112.3026 [hep-ph].
- [64] Riccardo Barbieri, Lawrence J. Hall, and Vyacheslav S. Rychkov. “Improved naturalness with a heavy Higgs: An Alternative road to LHC physics”. In: *Phys. Rev. D* 74 (2006), p. 015007. DOI: 10.1103/PhysRevD.74.015007. arXiv: hep-ph/0603188.
- [65] Alejandra Melfo et al. “Inert Doublet Dark Matter and Mirror/Extra Families after Xenon100”. In: *Phys. Rev. D* 84 (2011), p. 034009. DOI: 10.1103/PhysRevD.84.034009. arXiv: 1105.4611 [hep-ph].

- [66] Genevieve Belanger et al. “Dilepton constraints in the Inert Doublet Model from Run 1 of the LHC”. In: *Phys. Rev. D* 91.11 (2015), p. 115011. DOI: 10.1103/PhysRevD.91.115011. arXiv: 1503.07367 [hep-ph].
- [67] Laura Lopez Honorez et al. “The Inert Doublet Model: An Archetype for Dark Matter”. In: *JCAP* 02 (2007), p. 028. DOI: 10.1088/1475-7516/2007/02/028. arXiv: hep-ph/0612275.
- [68] Yeong Gyun Kim, Kang Young Lee, and Seodong Shin. “Singlet fermionic dark matter”. In: *JHEP* 05 (2008), p. 100. DOI: 10.1088/1126-6708/2008/05/100. arXiv: 0803.2932 [hep-ph].
- [69] Michael A. Fedderke et al. “The Fermionic Dark Matter Higgs Portal: an effective field theory approach”. In: *JHEP* 08 (2014), p. 122. DOI: 10.1007/JHEP08(2014)122. arXiv: 1404.2283 [hep-ph].
- [70] Bastian Diaz Saez et al. “Fermion Singlet Dark Matter in a Pseudoscalar Dark Matter Portal”. In: (May 2021). arXiv: 2105.04255 [hep-ph].
- [71] Geneviève Bélanger et al. “Right Handed Neutrinos, TeV Scale BSM Neutral Higgs and FIMP Dark Matter in EFT Framework”. In: (Apr. 2021). arXiv: 2104.04373 [hep-ph].
- [72] Celine Boehm et al. “Is it possible to explain neutrino masses with scalar dark matter?” In: *Phys. Rev. D* 77 (2008), p. 043516. DOI: 10.1103/PhysRevD.77.043516. arXiv: hep-ph/0612228.
- [73] Alexandre Alves et al. “Dirac-fermionic dark matter in  $U(1)_X$  models”. In: *JHEP* 10 (2015), p. 076. DOI: 10.1007/JHEP10(2015)076. arXiv: 1506.06767 [hep-ph].
- [74] Ernest Ma. “Scotogenic  $U(1)_X$  Dirac neutrinos”. In: *Phys. Lett. B* 793 (2019), pp. 411–414. DOI: 10.1016/j.physletb.2019.05.006. arXiv: 1901.09091 [hep-ph].
- [75] Yasaman Farzan, Silvia Pascoli, and Michael A. Schmidt. “AMEND: A model explaining neutrino masses and dark matter testable at the LHC and MEG”. In: *JHEP* 10 (2010), p. 111. DOI: 10.1007/JHEP10(2010)111. arXiv: 1005.5323 [hep-ph].
- [76] Marco Cirelli and Alessandro Strumia. “Minimal Dark Matter: Model and results”. In: *New J. Phys.* 11 (2009), p. 105005. DOI: 10.1088/1367-2630/11/10/105005. arXiv: 0903.3381 [hep-ph].
- [77] Scott Dodelson and Lawrence M. Widrow. “Sterile-neutrinos as dark matter”. In: *Phys. Rev. Lett.* 72 (1994), pp. 17–20. DOI: 10.1103/PhysRevLett.72.17. arXiv: hep-ph/9303287.
- [78] Alexey Boyarsky, Oleg Ruchayskiy, and Mikhail Shaposhnikov. “The Role of sterile neutrinos in cosmology and astrophysics”. In: *Ann. Rev. Nucl. Part. Sci.* 59 (2009), pp. 191–214. DOI: 10.1146/annurev.nucl.010909.083654. arXiv: 0901.0011 [hep-ph].
- [79] Alexey Boyarsky et al. “Checking the Dark Matter Origin of a 3.53 keV Line with the Milky Way Center”. In: *Phys. Rev. Lett.* 115 (2015), p. 161301. DOI: 10.1103/PhysRevLett.115.161301. arXiv: 1408.2503 [astro-ph.CO].

- [80] Alexey Boyarsky et al. “Unidentified Line in X-Ray Spectra of the Andromeda Galaxy and Perseus Galaxy Cluster”. In: *Phys. Rev. Lett.* 113 (2014), p. 251301. DOI: 10.1103/PhysRevLett.113.251301. arXiv: 1402.4119 [astro-ph.CO].
- [81] Signe Riemer-Sørensen. “Constraints on the presence of a 3.5 keV dark matter emission line from Chandra observations of the Galactic centre”. In: *Astron. Astrophys.* 590 (2016), A71. DOI: 10.1051/0004-6361/201527278. arXiv: 1405.7943 [astro-ph.CO].
- [82] Michael E. Anderson, Eugene Churazov, and Joel N. Bregman. “Non-Detection of X-Ray Emission From Sterile Neutrinos in Stacked Galaxy Spectra”. In: *Mon. Not. Roy. Astron. Soc.* 452.4 (2015), pp. 3905–3923. DOI: 10.1093/mnras/stv1559. arXiv: 1408.4115 [astro-ph.HE].
- [83] A. Neronov, Denys Malyshev, and Dominique Eckert. “Decaying dark matter search with NuSTAR deep sky observations”. In: *Phys. Rev. D* 94.12 (2016), p. 123504. DOI: 10.1103/PhysRevD.94.123504. arXiv: 1607.07328 [astro-ph.HE].
- [84] F. A. Aharonian et al. “*Hitomi* constraints on the 3.5 keV line in the Perseus galaxy cluster”. In: *Astrophys. J. Lett.* 837.1 (2017), p. L15. DOI: 10.3847/2041-8213/aa61fa. arXiv: 1607.07420 [astro-ph.HE].
- [85] A. Boyarsky et al. “Sterile neutrino Dark Matter”. In: *Prog. Part. Nucl. Phys.* 104 (2019), pp. 1–45. DOI: 10.1016/j.pnpnp.2018.07.004. arXiv: 1807.07938 [hep-ph].
- [86] A. Neronov and D. Malyshev. “Toward a full test of the  $\nu$ MSM sterile neutrino dark matter model with Athena”. In: *Phys. Rev. D* 93.6 (2016), p. 063518. DOI: 10.1103/PhysRevD.93.063518. arXiv: 1509.02758 [astro-ph.HE].
- [87] Gerard 't Hooft. “Naturalness, chiral symmetry, and spontaneous chiral symmetry breaking”. In: *NATO Sci. Ser. B* 59 (1980). Ed. by Gerard 't Hooft et al., pp. 135–157. DOI: 10.1007/978-1-4684-7571-5\_9.
- [88] R. D. Peccei and Helen R. Quinn. “CP Conservation in the Presence of Pseudoparticles”. In: *Phys. Rev. Lett.* 38 (1977), pp. 1440–1443. DOI: 10.1103/PhysRevLett.38.1440.
- [89] Steven Weinberg. “A New Light Boson?” In: *Phys. Rev. Lett.* 40 (1978), pp. 223–226. DOI: 10.1103/PhysRevLett.40.223.
- [90] Peter W. Graham et al. “Experimental Searches for the Axion and Axion-Like Particles”. In: *Ann. Rev. Nucl. Part. Sci.* 65 (2015), pp. 485–514. DOI: 10.1146/annurev-nucl-102014-022120. arXiv: 1602.00039 [hep-ex].
- [91] Lars Bergström. “Nonbaryonic dark matter: Observational evidence and detection methods”. In: *Rept. Prog. Phys.* 63 (2000), p. 793. DOI: 10.1088/0034-4885/63/5/2r3. arXiv: hep-ph/0002126.
- [92] Björn Penning. “The pursuit of dark matter at colliders—an overview”. In: *J. Phys. G* 45.6 (2018), p. 063001. DOI: 10.1088/1361-6471/aabea7. arXiv: 1712.01391 [hep-ex].
- [93] R. Bernabei et al. “First model independent results from DAMA/LIBRA-phase2”. In: *Nucl. Phys. Atom. Energy* 19.4 (2018), pp. 307–325. DOI: 10.15407/jnpae2018.04.307. arXiv: 1805.10486 [hep-ex].

- [94] Y. J. Ko et al. “Comparison between DAMA/LIBRA and COSINE-100 in the light of Quenching Factors”. In: *JCAP* 11 (2019), p. 008. DOI: 10.1088/1475-7516/2019/11/008. arXiv: 1907.04963 [hep-ex].
- [95] E. Aprile et al. “Dark Matter Search Results from a One Ton-Year Exposure of XENON1T”. In: *Phys. Rev. Lett.* 121.11 (2018), p. 111302. DOI: 10.1103/PhysRevLett.121.111302. arXiv: 1805.12562 [astro-ph.CO].
- [96] Teresa Marrodán Undagoitia and Ludwig Rauch. “Dark matter direct-detection experiments”. In: *J. Phys. G* 43.1 (2016), p. 013001. DOI: 10.1088/0954-3899/43/1/013001. arXiv: 1509.08767 [physics.ins-det].
- [97] F. Alessandria et al. “The low energy spectrum of TeO<sub>2</sub> bolometers: results and dark matter perspectives for the CUORE-0 and CUORE experiments”. In: *JCAP* 01 (2013), p. 038. DOI: 10.1088/1475-7516/2013/01/038. arXiv: 1209.2519 [physics.ins-det].
- [98] C. P. Aguirre et al. “Dark Matter Search with CUORE-0 and CUORE”. In: *Phys. Procedia* 61 (2015). Ed. by Frank Avignone and Wick Haxton, pp. 13–20. DOI: 10.1016/j.phpro.2014.12.005.
- [99] C. Amole et al. “Dark Matter Search Results from the Complete Exposure of the PICO-60 C<sub>3</sub>F<sub>8</sub> Bubble Chamber”. In: *Phys. Rev. D* 100.2 (2019), p. 022001. DOI: 10.1103/PhysRevD.100.022001. arXiv: 1902.04031 [astro-ph.CO].
- [100] C. B. Krauss. “PICO-60 Results and PICO-40L Status”. In: *J. Phys. Conf. Ser.* 1468.1 (2020). Ed. by Masayuki Nakahata, p. 012043. DOI: 10.1088/1742-6596/1468/1/012043.
- [101] A. H. Abdelhameed et al. “First results from the CRESST-III low-mass dark matter program”. In: *Phys. Rev. D* 100.10 (2019), p. 102002. DOI: 10.1103/PhysRevD.100.102002. arXiv: 1904.00498 [astro-ph.CO].
- [102] L. Baudis et al. “First results from the Heidelberg Dark Matter Search Experiment”. In: *Phys. Rev. D* 63 (2001), p. 022001. DOI: 10.1103/PhysRevD.63.022001. arXiv: astro-ph/0008339.
- [103] C. E. Aalseth et al. “CoGeNT: A Search for Low-Mass Dark Matter using p-type Point Contact Germanium Detectors”. In: *Phys. Rev. D* 88 (2013), p. 012002. DOI: 10.1103/PhysRevD.88.012002. arXiv: 1208.5737 [astro-ph.CO].
- [104] D. W. Amaral et al. “Constraints on low-mass, relic dark matter candidates from a surface-operated SuperCDMS single-charge sensitive detector”. In: *Phys. Rev. D* 102.9 (2020), p. 091101. DOI: 10.1103/PhysRevD.102.091101. arXiv: 2005.14067 [hep-ex].
- [105] R. Agnese et al. “Silicon Detector Dark Matter Results from the Final Exposure of CDMS II”. In: *Phys. Rev. Lett.* 111.25 (2013), p. 251301. DOI: 10.1103/PhysRevLett.111.251301. arXiv: 1304.4279 [hep-ex].
- [106] R. Agnese et al. “Improved WIMP-search reach of the CDMS II germanium data”. In: *Phys. Rev. D* 92.7 (2015), p. 072003. DOI: 10.1103/PhysRevD.92.072003. arXiv: 1504.05871 [hep-ex].

- [107] L. Hehn et al. “Improved EDELWEISS-III sensitivity for low-mass WIMPs using a profile likelihood approach”. In: *Eur. Phys. J. C* 76.10 (2016), p. 548. DOI: 10.1140/epjc/s10052-016-4388-y. arXiv: 1607.03367 [astro-ph.CO].
- [108] C. Nones. “The bolometric way towards the direct dark matter detection: The EDELWEISS Experiment and the EURECA prospect”. In: *4th International Conference Current Problems in Nuclear Physics and Atomic Energy*. 2012.
- [109] G. Adhikari et al. “Strong constraints from COSINE-100 on the DAMA dark matter results using the same sodium iodide target”. In: (Apr. 2021). arXiv: 2104.03537 [hep-ex].
- [110] J. Amaré et al. “First Results on Dark Matter Annual Modulation from the ANAIS-112 Experiment”. In: *Phys. Rev. Lett.* 123.3 (2019), p. 031301. DOI: 10.1103/PhysRevLett.123.031301. arXiv: 1903.03973 [astro-ph.IM].
- [111] B. J. Park et al. “Development of ultra-pure NaI(Tl) detectors for the COSINE-200 experiment”. In: *Eur. Phys. J. C* 80.9 (2020), p. 814. DOI: 10.1140/epjc/s10052-020-8386-8. arXiv: 2004.06287 [physics.ins-det].
- [112] Marc Schumann. “Dark Matter Search with liquid Noble Gases”. In: (June 2012). arXiv: 1206.2169 [astro-ph.IM].
- [113] K. Rielage et al. “Update on the MiniCLEAN Dark Matter Experiment”. In: *Phys. Procedia* 61 (2015). Ed. by Frank Avignone and Wick Haxton, pp. 144–152. DOI: 10.1016/j.phpro.2014.12.024. arXiv: 1403.4842 [physics.ins-det].
- [114] K. Abe et al. “A direct dark matter search in XMASS-I”. In: *Phys. Lett. B* 789 (2019), pp. 45–53. DOI: 10.1016/j.physletb.2018.10.070. arXiv: 1804.02180 [astro-ph.CO].
- [115] P. A. Amaudruz et al. “First results from the DEAP-3600 dark matter search with argon at SNOLAB”. In: *Phys. Rev. Lett.* 121.7 (2018), p. 071801. DOI: 10.1103/PhysRevLett.121.071801. arXiv: 1707.08042 [astro-ph.CO].
- [116] D. S. Akerib et al. “Results from a search for dark matter in the complete LUX exposure”. In: *Phys. Rev. Lett.* 118.2 (2017), p. 021303. DOI: 10.1103/PhysRevLett.118.021303. arXiv: 1608.07648 [astro-ph.CO].
- [117] D. Yu. Akimov et al. “WIMP-nucleon cross-section results from the second science run of ZEPLIN-III”. In: *Phys. Lett. B* 709 (2012), pp. 14–20. DOI: 10.1016/j.physletb.2012.01.064. arXiv: 1110.4769 [astro-ph.CO].
- [118] D. S. Akerib et al. “Projected WIMP sensitivity of the LUX-ZEPLIN dark matter experiment”. In: *Phys. Rev. D* 101.5 (2020), p. 052002. DOI: 10.1103/PhysRevD.101.052002. arXiv: 1802.06039 [astro-ph.IM].
- [119] Qihong Wang et al. “Results of dark matter search using the full PandaX-II exposure”. In: *Chin. Phys. C* 44.12 (2020), p. 125001. DOI: 10.1088/1674-1137/abb658. arXiv: 2007.15469 [astro-ph.CO].
- [120] P. Agnes et al. “DarkSide-50 532-day Dark Matter Search with Low-Radioactivity Argon”. In: *Phys. Rev. D* 98.10 (2018), p. 102006. DOI: 10.1103/PhysRevD.98.102006. arXiv: 1802.07198 [astro-ph.CO].

- [121] J. Calvo et al. “Commissioning of the ArDM experiment at the Canfranc underground laboratory: first steps towards a tonne-scale liquid argon time projection chamber for Dark Matter searches”. In: *JCAP* 03 (2017), p. 003. DOI: 10.1088/1475-7516/2017/03/003. arXiv: 1612.06375 [physics.ins-det].
- [122] Hongguang Zhang et al. “Dark matter direct search sensitivity of the PandaX-4T experiment”. In: *Sci. China Phys. Mech. Astron.* 62.3 (2019), p. 31011. DOI: 10.1007/s11433-018-9259-0. arXiv: 1806.02229 [physics.ins-det].
- [123] E. Aprile et al. “Physics reach of the XENON1T dark matter experiment”. In: *JCAP* 04 (2016), p. 027. DOI: 10.1088/1475-7516/2016/04/027. arXiv: 1512.07501 [physics.ins-det].
- [124] C. E. Aalseth et al. “DarkSide-20k: A 20 tonne two-phase LAr TPC for direct dark matter detection at LNGS”. In: *Eur. Phys. J. Plus* 133 (2018), p. 131. DOI: 10.1140/epjp/i2018-11973-4. arXiv: 1707.08145 [physics.ins-det].
- [125] P. Agnes et al. “Sensitivity of future liquid argon dark matter search experiments to core-collapse supernova neutrinos”. In: *JCAP* 03 (2021), p. 043. DOI: 10.1088/1475-7516/2021/03/043. arXiv: 2011.07819 [astro-ph.HE].
- [126] E. Aprile et al. “Light Dark Matter Search with Ionization Signals in XENON1T”. In: *Phys. Rev. Lett.* 123.25 (2019), p. 251801. DOI: 10.1103/PhysRevLett.123.251801. arXiv: 1907.11485 [hep-ex].
- [127] Julien Billard et al. “Direct Detection of Dark Matter – APPEC Committee Report”. In: (Apr. 2021). arXiv: 2104.07634 [hep-ex].
- [128] E. Aprile et al. “Constraining the spin-dependent WIMP-nucleon cross sections with XENON1T”. In: *Phys. Rev. Lett.* 122.14 (2019), p. 141301. DOI: 10.1103/PhysRevLett.122.141301. arXiv: 1902.03234 [astro-ph.CO].
- [129] J. Billard, L. Strigari, and E. Figueroa-Feliciano. “Implication of neutrino backgrounds on the reach of next generation dark matter direct detection experiments”. In: *Phys. Rev. D* 89.2 (2014), p. 023524. DOI: 10.1103/PhysRevD.89.023524. arXiv: 1307.5458 [hep-ph].
- [130] Michael Klasen, Martin Pohl, and Günter Sigl. “Indirect and direct search for dark matter”. In: *Prog. Part. Nucl. Phys.* 85 (2015), pp. 1–32. DOI: 10.1016/j.ppnp.2015.07.001. arXiv: 1507.03800 [hep-ph].
- [131] Julio F. Navarro, Carlos S. Frenk, and Simon D. M. White. “The Structure of cold dark matter halos”. In: *Astrophys. J.* 462 (1996), pp. 563–575. DOI: 10.1086/177173. arXiv: astro-ph/9508025.
- [132] A. Burkert. “The Structure of dark matter halos in dwarf galaxies”. In: *Astrophys. J. Lett.* 447 (1995), p. L25. DOI: 10.1086/309560. arXiv: astro-ph/9504041.
- [133] A. Albert et al. “Searching for Dark Matter Annihilation in Recently Discovered Milky Way Satellites with Fermi-LAT”. In: *Astrophys. J.* 834.2 (2017), p. 110. DOI: 10.3847/1538-4357/834/2/110. arXiv: 1611.03184 [astro-ph.HE].



- [134] Frank G. Schröder. “Radio detection of Cosmic-Ray Air Showers and High-Energy Neutrinos”. In: *Prog. Part. Nucl. Phys.* 93 (2017), pp. 1–68. DOI: 10.1016/j.ppnp.2016.12.002. arXiv: 1607.08781 [astro-ph.IM].
- [135] H. Abdallah et al. “Search for dark matter annihilations towards the inner Galactic halo from 10 years of observations with H.E.S.S”. In: *Phys. Rev. Lett.* 117.11 (2016), p. 111301. DOI: 10.1103/PhysRevLett.117.111301. arXiv: 1607.08142 [astro-ph.HE].
- [136] H. Abdallah et al. “Search for dark matter signals towards a selection of recently detected DES dwarf galaxy satellites of the Milky Way with H.E.S.S.” In: *Phys. Rev. D* 102.6 (2020), p. 062001. DOI: 10.1103/PhysRevD.102.062001. arXiv: 2008.00688 [astro-ph.HE].
- [137] M. L. Ahnen et al. “Limits to Dark Matter Annihilation Cross-Section from a Combined Analysis of MAGIC and Fermi-LAT Observations of Dwarf Satellite Galaxies”. In: *JCAP* 02 (2016), p. 039. DOI: 10.1088/1475-7516/2016/02/039. arXiv: 1601.06590 [astro-ph.HE].
- [138] S. Archambault et al. “Dark Matter Constraints from a Joint Analysis of Dwarf Spheroidal Galaxy Observations with VERITAS”. In: *Phys. Rev. D* 95.8 (2017), p. 082001. DOI: 10.1103/PhysRevD.95.082001. arXiv: 1703.04937 [astro-ph.HE].
- [139] A. Acharyya et al. “Sensitivity of the Cherenkov Telescope Array to a dark matter signal from the Galactic centre”. In: *JCAP* 01 (2021), p. 057. DOI: 10.1088/1475-7516/2021/01/057. arXiv: 2007.16129 [astro-ph.HE].
- [140] A. Albert et al. “Dark Matter Limits From Dwarf Spheroidal Galaxies with The HAWC Gamma-Ray Observatory”. In: *Astrophys. J.* 853.2 (2018), p. 154. DOI: 10.3847/1538-4357/aaa6d8. arXiv: 1706.01277 [astro-ph.HE].
- [141] M. Ajello et al. “Fermi Large Area Telescope Performance After 10 Years Of Operation”. In: (June 2021). arXiv: 2106.12203 [astro-ph.IM].
- [142] M. N. Mazziotta et al. “Search for features in the cosmic-ray electron and positron spectrum measured by the Fermi Large Area Telescope”. In: *Phys. Rev. D* 98.2 (2018), p. 022006. DOI: 10.1103/PhysRevD.98.022006. arXiv: 1712.07005 [astro-ph.HE].
- [143] Oscar Adriani et al. “An anomalous positron abundance in cosmic rays with energies 1.5-100 GeV”. In: *Nature* 458 (2009), pp. 607–609. DOI: 10.1038/nature07942. arXiv: 0810.4995 [astro-ph].
- [144] Dan Hooper, Tim Linden, and Philipp Mertsch. “What Does The PAMELA Antiproton Spectrum Tell Us About Dark Matter?” In: *JCAP* 03 (2015), p. 021. DOI: 10.1088/1475-7516/2015/03/021. arXiv: 1410.1527 [astro-ph.HE].
- [145] Annika Reinert and Martin Wolfgang Winkler. “A Precision Search for WIMPs with Charged Cosmic Rays”. In: *JCAP* 01 (2018), p. 055. DOI: 10.1088/1475-7516/2018/01/055. arXiv: 1712.00002 [astro-ph.HE].
- [146] O. Adriani et al. “Ten years of PAMELA in space”. In: *Riv. Nuovo Cim.* 40.10 (2017), pp. 473–522. DOI: 10.1393/ncr/i2017-10140-x. arXiv: 1801.10310 [astro-ph.HE].

- [147] A. Albert et al. “Results from the search for dark matter in the Milky Way with 9 years of data of the ANTARES neutrino telescope”. In: *Phys. Lett. B* 769 (2017). [Erratum: *Phys.Lett.B* 796, 253–255 (2019)], pp. 249–254. DOI: 10.1016/j.physletb.2017.03.063. arXiv: 1612.04595 [astro-ph.HE].
- [148] A. Albert et al. “Search for dark matter towards the Galactic Centre with 11 years of ANTARES data”. In: *Phys. Lett. B* 805 (2020), p. 135439. DOI: 10.1016/j.physletb.2020.135439. arXiv: 1912.05296 [astro-ph.HE].
- [149] A. D. Avrorin et al. “A search for neutrino signal from dark matter annihilation in the center of the Milky Way with Baikal NT200”. In: *Astropart. Phys.* 81 (2016), pp. 12–20. DOI: 10.1016/j.astropartphys.2016.04.004. arXiv: 1512.01198 [astro-ph.HE].
- [150] A. D. Avrorin et al. “Search for neutrino emission from relic dark matter in the Sun with the Baikal NT200 detector”. In: *Astropart. Phys.* 62 (2015), pp. 12–20. DOI: 10.1016/j.astropartphys.2014.07.006. arXiv: 1405.3551 [astro-ph.HE].
- [151] K. Abe et al. “Indirect search for dark matter from the Galactic Center and halo with the Super-Kamiokande detector”. In: *Phys. Rev. D* 102.7 (2020), p. 072002. DOI: 10.1103/PhysRevD.102.072002. arXiv: 2005.05109 [hep-ex].
- [152] S. Adrian-Martinez et al. “Letter of intent for KM3NeT 2.0”. In: *J. Phys. G* 43.8 (2016), p. 084001. DOI: 10.1088/0954-3899/43/8/084001. arXiv: 1601.07459 [astro-ph.IM].
- [153] K. Abe et al. “Letter of Intent: The Hyper-Kamiokande Experiment — Detector Design and Physics Potential —”. In: (Sept. 2011). arXiv: 1109.3262 [hep-ex].
- [154] M. G. Aartsen et al. “The IceCube Neutrino Observatory - Contributions to ICRC 2017 Part IV: Searches for Beyond the Standard Model Physics”. In: (Oct. 2017). arXiv: 1710.01197 [astro-ph.HE].
- [155] M. G. Aartsen et al. “The IceCube Neutrino Observatory: Instrumentation and Online Systems”. In: *JINST* 12.03 (2017), P03012. DOI: 10.1088/1748-0221/12/03/P03012. arXiv: 1612.05093 [astro-ph.IM].
- [156] Riccardo Catena and Fredrik Hellström. “New constraints on inelastic dark matter from IceCube”. In: *JCAP* 10 (2018), p. 039. DOI: 10.1088/1475-7516/2018/10/039. arXiv: 1808.08082 [astro-ph.CO].
- [157] M.G. Aartsen et al. “Search for annihilating dark matter in the Sun with 3 years of IceCube data”. In: *Eur. Phys. J. C* 77.3 (2017). [Erratum: *Eur.Phys.J.C* 79, 214 (2019)], p. 146. DOI: 10.1140/epjc/s10052-017-4689-9. arXiv: 1612.05949 [astro-ph.HE].
- [158] M. G. Aartsen et al. “Search for Neutrinos from Dark Matter Self-Annihilations in the center of the Milky Way with 3 years of IceCube/DeepCore”. In: *Eur. Phys. J. C* 77.9 (2017), p. 627. DOI: 10.1140/epjc/s10052-017-5213-y. arXiv: 1705.08103 [hep-ex].
- [159] Nicole F. Bell, Matthew J. Dolan, and Sandra Robles. “Searching for Dark Matter in the Sun using Hyper-Kamiokande”. In: (July 2021). arXiv: 2107.04216 [hep-ph].

- [160] Antonio Boveia and Caterina Doglioni. “Dark Matter Searches at Colliders”. In: *Ann. Rev. Nucl. Part. Sci.* 68 (2018), pp. 429–459. DOI: 10.1146/annurev-nucl-101917-021008. arXiv: 1810.12238 [hep-ex].
- [161] G. Aad et al. “The ATLAS Experiment at the CERN Large Hadron Collider”. In: *JINST* 3 (2008), S08003. DOI: 10.1088/1748-0221/3/08/S08003.
- [162] S. Chatrchyan et al. “The CMS Experiment at the CERN LHC”. In: *JINST* 3 (2008), S08004. DOI: 10.1088/1748-0221/3/08/S08004.
- [163] Albert M Sirunyan et al. “Search for invisible decays of a Higgs boson produced through vector boson fusion in proton-proton collisions at  $\sqrt{s} = 13$  TeV”. In: *Phys. Lett. B* 793 (2019), pp. 520–551. DOI: 10.1016/j.physletb.2019.04.025. arXiv: 1809.05937 [hep-ex].
- [164] “LHC Machine”. In: *JINST* 3 (2008). Ed. by Lyndon Evans and Philip Bryant, S08001. DOI: 10.1088/1748-0221/3/08/S08001.
- [165] C. L. Cowan et al. “Detection of the free neutrino: A Confirmation”. In: *Science* 124 (1956), pp. 103–104. DOI: 10.1126/science.124.3212.103.
- [166] G. Bellini et al. “Final results of Borexino Phase-I on low energy solar neutrino spectroscopy”. In: *Phys. Rev. D* 89.11 (2014), p. 112007. DOI: 10.1103/PhysRevD.89.112007. arXiv: 1308.0443 [hep-ex].
- [167] John N. Bahcall and R. Davis. “Solar Neutrinos - a Scientific Puzzle”. In: *Science* 191 (1976), pp. 264–267. DOI: 10.1126/science.191.4224.264.
- [168] G. D. Orebi Gann et al. “The Future of Solar Neutrinos”. In: (July 2021). DOI: 10.1146/annurev-nucl-011921-061243. arXiv: 2107.08613 [hep-ph].
- [169] S. Fukuda et al. “Determination of solar neutrino oscillation parameters using 1496 days of Super-Kamiokande I data”. In: *Phys. Lett. B* 539 (2002), pp. 179–187. DOI: 10.1016/S0370-2693(02)02090-7. arXiv: hep-ex/0205075.
- [170] Q. R. Ahmad et al. “Direct evidence for neutrino flavor transformation from neutral current interactions in the Sudbury Neutrino Observatory”. In: *Phys. Rev. Lett.* 89 (2002), p. 011301. DOI: 10.1103/PhysRevLett.89.011301. arXiv: nucl-ex/0204008.
- [171] Y. Fukuda et al. “Evidence for oscillation of atmospheric neutrinos”. In: *Phys. Rev. Lett.* 81 (1998), pp. 1562–1567. DOI: 10.1103/PhysRevLett.81.1562. arXiv: hep-ex/9807003.
- [172] M. V. Diwan et al. “Long-Baseline Neutrino Experiments”. In: *Ann. Rev. Nucl. Part. Sci.* 66 (2016), pp. 47–71. DOI: 10.1146/annurev-nucl-102014-021939. arXiv: 1608.06237 [hep-ex].
- [173] C. Jarlskog. “Commutator of the Quark Mass Matrices in the Standard Electroweak Model and a Measure of Maximal CP Violation”. In: *Phys. Rev. Lett.* 55 (1985), p. 1039. DOI: 10.1103/PhysRevLett.55.1039.
- [174] S. P. Mikheev and A. Yu. Smirnov. “Resonant amplification of neutrino oscillations in matter and solar neutrino spectroscopy”. In: *Nuovo Cim. C* 9 (1986), pp. 17–26. DOI: 10.1007/BF02508049.

- [175] L. Wolfenstein. “Neutrino Oscillations in Matter”. In: *Phys. Rev. D* 17 (1978), pp. 2369–2374. DOI: 10.1103/PhysRevD.17.2369.
- [176] Ivan Esteban et al. “The fate of hints: updated global analysis of three-flavor neutrino oscillations”. In: *JHEP* 09 (2020), p. 178. DOI: 10.1007/JHEP09(2020)178. arXiv: 2007.14792 [hep-ph].
- [177] Y. Ashie et al. “A Measurement of atmospheric neutrino oscillation parameters by SUPER-KAMIOKANDE I”. In: *Phys. Rev. D* 71 (2005), p. 112005. DOI: 10.1103/PhysRevD.71.112005. arXiv: hep-ex/0501064.
- [178] Y. Ashie et al. “Evidence for an oscillatory signature in atmospheric neutrino oscillation”. In: *Phys. Rev. Lett.* 93 (2004), p. 101801. DOI: 10.1103/PhysRevLett.93.101801. arXiv: hep-ex/0404034.
- [179] M. G. Aartsen et al. “Determining neutrino oscillation parameters from atmospheric muon neutrino disappearance with three years of IceCube DeepCore data”. In: *Phys. Rev. D* 91.7 (2015), p. 072004. DOI: 10.1103/PhysRevD.91.072004. arXiv: 1410.7227 [hep-ex].
- [180] P. Adamson et al. “Measurement of the Neutrino Mass Splitting and Flavor Mixing by MINOS”. In: *Phys. Rev. Lett.* 106 (2011), p. 181801. DOI: 10.1103/PhysRevLett.106.181801. arXiv: 1103.0340 [hep-ex].
- [181] K. Abe et al. “Improved constraints on neutrino mixing from the T2K experiment with  $3.13 \times 10^{21}$  protons on target”. In: *Phys. Rev. D* 103.11 (2021), p. 112008. DOI: 10.1103/PhysRevD.103.112008. arXiv: 2101.03779 [hep-ex].
- [182] P. Adamson et al. “Measurement of the neutrino mixing angle  $\theta_{23}$  in NOvA”. In: *Phys. Rev. Lett.* 118.15 (2017), p. 151802. DOI: 10.1103/PhysRevLett.118.151802. arXiv: 1701.05891 [hep-ex].
- [183] A. Gando et al. “Constraints on  $\theta_{13}$  from A Three-Flavor Oscillation Analysis of Reactor Antineutrinos at KamLAND”. In: *Phys. Rev. D* 83 (2011), p. 052002. DOI: 10.1103/PhysRevD.83.052002. arXiv: 1009.4771 [hep-ex].
- [184] Y. Abe et al. “Improved measurements of the neutrino mixing angle  $\theta_{13}$  with the Double Chooz detector”. In: *JHEP* 10 (2014). [Erratum: *JHEP* 02, 074 (2015)], p. 086. DOI: 10.1007/JHEP02(2015)074. arXiv: 1406.7763 [hep-ex].
- [185] D. Adey et al. “Measurement of the Electron Antineutrino Oscillation with 1958 Days of Operation at Daya Bay”. In: *Phys. Rev. Lett.* 121.24 (2018), p. 241805. DOI: 10.1103/PhysRevLett.121.241805. arXiv: 1809.02261 [hep-ex].
- [186] C. D. Shin et al. “Observation of reactor antineutrino disappearance using delayed neutron capture on hydrogen at RENO”. In: *JHEP* 04 (2020), p. 029. DOI: 10.1007/JHEP04(2020)029. arXiv: 1911.04601 [hep-ex].
- [187] Babak Abi et al. “Deep Underground Neutrino Experiment (DUNE), Far Detector Technical Design Report, Volume II: DUNE Physics”. In: (Feb. 2020). arXiv: 2002.03005 [hep-ex].
- [188] Fengpeng An et al. “Neutrino Physics with JUNO”. In: *J. Phys. G* 43.3 (2016), p. 030401. DOI: 10.1088/0954-3899/43/3/030401. arXiv: 1507.05613 [physics.ins-det].

- [189] Thomas Hambye. “Leptogenesis: beyond the minimal type I seesaw scenario”. In: *New J. Phys.* 14 (2012), p. 125014. DOI: 10.1088/1367-2630/14/12/125014. arXiv: 1212.2888 [hep-ph].
- [190] Steven Weinberg. “Baryon and Lepton Nonconserving Processes”. In: *Phys. Rev. Lett.* 43 (1979), pp. 1566–1570. DOI: 10.1103/PhysRevLett.43.1566.
- [191] Frank T. Avignone III, Steven R. Elliott, and Jonathan Engel. “Double Beta Decay, Majorana Neutrinos, and Neutrino Mass”. In: *Rev. Mod. Phys.* 80 (2008), pp. 481–516. DOI: 10.1103/RevModPhys.80.481. arXiv: 0708.1033 [nucl-ex].
- [192] A. Gando et al. “Search for Majorana Neutrinos near the Inverted Mass Hierarchy Region with KamLAND-Zen”. In: *Phys. Rev. Lett.* 117.8 (2016). [Addendum: *Phys.Rev.Lett.* 117, 109903 (2016)], p. 082503. DOI: 10.1103/PhysRevLett.117.082503. arXiv: 1605.02889 [hep-ex].
- [193] M. Agostini et al. “Final Results of GERDA on the Search for Neutrinoless Double- $\beta$  Decay”. In: *Phys. Rev. Lett.* 125.25 (2020), p. 252502. DOI: 10.1103/PhysRevLett.125.252502. arXiv: 2009.06079 [nucl-ex].
- [194] D. Q. Adams et al. “Improved Limit on Neutrinoless Double-Beta Decay in  $^{130}\text{Te}$  with CUORE”. In: *Phys. Rev. Lett.* 124.12 (2020), p. 122501. DOI: 10.1103/PhysRevLett.124.122501. arXiv: 1912.10966 [nucl-ex].
- [195] R. Arnold et al. “Probing New Physics Models of Neutrinoless Double Beta Decay with SuperNEMO”. In: *Eur. Phys. J. C* 70 (2010), pp. 927–943. DOI: 10.1140/epjc/s10052-010-1481-5. arXiv: 1005.1241 [hep-ex].
- [196] Thomas J. Loredo and Don Q. Lamb. “Bayesian analysis of neutrinos observed from supernova SN-1987A”. In: *Phys. Rev. D* 65 (2002), p. 063002. DOI: 10.1103/PhysRevD.65.063002. arXiv: astro-ph/0107260.
- [197] J. Angrik et al. “KATRIN design report 2004”. In: (Feb. 2005).
- [198] E. W. Otten and C. Weinheimer. “Neutrino mass limit from tritium beta decay”. In: *Rept. Prog. Phys.* 71 (2008), p. 086201. DOI: 10.1088/0034-4885/71/8/086201. arXiv: 0909.2104 [hep-ex].
- [199] G. Drexlin et al. “Current direct neutrino mass experiments”. In: *Adv. High Energy Phys.* 2013 (2013), p. 293986. DOI: 10.1155/2013/293986. arXiv: 1307.0101 [physics.ins-det].
- [200] Ch. Kraus et al. “Final results from phase II of the Mainz neutrino mass search in tritium beta decay”. In: *Eur. Phys. J. C* 40 (2005), pp. 447–468. DOI: 10.1140/epjc/s2005-02139-7. arXiv: hep-ex/0412056.
- [201] V. N. Aseev et al. “An upper limit on electron antineutrino mass from Troitsk experiment”. In: *Phys. Rev. D* 84 (2011), p. 112003. DOI: 10.1103/PhysRevD.84.112003. arXiv: 1108.5034 [hep-ex].
- [202] M. Aker et al. “First direct neutrino-mass measurement with sub-eV sensitivity”. In: (May 2021). arXiv: 2105.08533 [hep-ex].

- [203] Florian Bonnet et al. “Systematic study of the  $d=5$  Weinberg operator at one-loop order”. In: *JHEP* 07 (2012), p. 153. DOI: 10.1007/JHEP07(2012)153. arXiv: 1204.5862 [hep-ph].
- [204] Diego Restrepo, Oscar Zapata, and Carlos E. Yaguna. “Models with radiative neutrino masses and viable dark matter candidates”. In: *JHEP* 11 (2013), p. 011. DOI: 10.1007/JHEP11(2013)011. arXiv: 1308.3655 [hep-ph].
- [205] Ernest Ma. “Verifiable radiative seesaw mechanism of neutrino mass and dark matter”. In: *Phys. Rev. D* 73 (2006), p. 077301. DOI: 10.1103/PhysRevD.73.077301. arXiv: hep-ph/0601225 [hep-ph].
- [206] Pablo Escribano, Mario Reig, and Avelino Vicente. “Generalizing the Scotogenic model”. In: *JHEP* 07 (2020), p. 097. DOI: 10.1007/JHEP07(2020)097. arXiv: 2004.05172 [hep-ph].
- [207] Samoil M. Bilenky, S. T. Petcov, and B. Pontecorvo. “Lepton Mixing,  $\mu \rightarrow e + \gamma$  Decay and Neutrino Oscillations”. In: *Phys. Lett. B* 67 (1977), p. 309. DOI: 10.1016/0370-2693(77)90379-3.
- [208] Igor P. Ivanov. “Building and testing models with extended Higgs sectors”. In: *Prog. Part. Nucl. Phys.* 95 (2017), pp. 160–208. DOI: 10.1016/j.ppnp.2017.03.001. arXiv: 1702.03776 [hep-ph].
- [209] M. Aker et al. “Improved Upper Limit on the Neutrino Mass from a Direct Kinematic Method by KATRIN”. In: *Phys. Rev. Lett.* 123.22 (2019), p. 221802. DOI: 10.1103/PhysRevLett.123.221802. arXiv: 1909.06048 [hep-ex].
- [210] T. de Boer et al. “Absolute neutrino mass as the missing link to the dark sector”. In: *Phys. Rev. D* 102.5 (2020), p. 051702. DOI: 10.1103/PhysRevD.102.051702. arXiv: 2007.05338 [hep-ph].
- [211] Georges Aad et al. “Combined Measurement of the Higgs Boson Mass in  $pp$  Collisions at  $\sqrt{s} = 7$  and 8 TeV with the ATLAS and CMS Experiments”. In: *Phys. Rev. Lett.* 114 (2015), p. 191803. DOI: 10.1103/PhysRevLett.114.191803. arXiv: 1503.07589 [hep-ex].
- [212] Manfred Lindner et al. “Fermionic WIMPs and vacuum stability in the scotogenic model”. In: *Phys. Rev. D* 94.11 (2016), p. 115027. DOI: 10.1103/PhysRevD.94.115027. arXiv: 1608.00577 [hep-ph].
- [213] Ivan Esteban et al. “Global analysis of three-flavour neutrino oscillations: synergies and tensions in the determination of  $\theta_{23}$ ,  $\delta_{CP}$ , and the mass ordering”. In: *JHEP* 01 (2019), p. 106. DOI: 10.1007/JHEP01(2019)106. arXiv: 1811.05487 [hep-ph].
- [214] J.A. Casas and A. Ibarra. “Oscillating neutrinos and  $\mu \rightarrow e, \gamma$ ”. In: *Nucl. Phys. B* 618 (2001), pp. 171–204. DOI: 10.1016/S0550-3213(01)00475-8. arXiv: hep-ph/0103065.
- [215] A.M. Baldini et al. “Search for the lepton flavour violating decay  $\mu^+ \rightarrow e^+ \gamma$  with the full dataset of the MEG experiment”. In: *Eur. Phys. J. C* 76.8 (2016), p. 434. DOI: 10.1140/epjc/s10052-016-4271-x. arXiv: 1605.05081 [hep-ex].

- [216] Francesco Renga. “The quest for  $\mu \rightarrow e\gamma$ : present and future”. In: *Hyperfine Interact.* 239.1 (2018), p. 58. DOI: 10.1007/s10751-018-1534-y. arXiv: 1811.05921 [hep-ex].
- [217] U. Bellgardt et al. “Search for the Decay  $\mu^+ \rightarrow e^+ e^+ e^-$ ”. In: *Nucl. Phys. B* 299 (1988), pp. 1–6. DOI: 10.1016/0550-3213(88)90462-2.
- [218] A. Blondel et al. “Research Proposal for an Experiment to Search for the Decay  $\mu \rightarrow eee$ ”. In: (Jan. 2013). arXiv: 1301.6113 [physics.ins-det].
- [219] C. Dohmen et al. “Test of lepton flavor conservation in  $\mu \rightarrow e$  conversion on titanium”. In: *Phys. Lett. B* 317 (1993), pp. 631–636. DOI: 10.1016/0370-2693(93)91383-X.
- [220] Yoshitaka Kuno. “PRISM/PRIME”. In: *Nuclear Physics B - Proceedings Supplements* 149 (2005). NuFact04, pp. 376–378. ISSN: 0920-5632. DOI: <https://doi.org/10.1016/j.nuclphysbps.2005.05.073>.
- [221] Simon May. “Minimal dark matter models with radiative neutrino masses: From Lagrangians to observables”. Master thesis. Mar. 2020. arXiv: 2003.04157 [hep-ph].
- [222] F. Staub. “SARAH”. In: (June 2008). arXiv: 0806.0538 [hep-ph].
- [223] Florian Staub. “SARAH 4 : A tool for (not only SUSY) model builders”. In: *Comput. Phys. Commun.* 185 (2014), pp. 1773–1790. DOI: 10.1016/j.cpc.2014.02.018. arXiv: 1309.7223 [hep-ph].
- [224] Simon May. “minimal-lagrangians: Generating and studying dark matter model Lagrangians with just the particle content”. In: *Comput. Phys. Commun.* 261 (2021), p. 107773. DOI: 10.1016/j.cpc.2020.107773. arXiv: 2003.08037 [hep-ph].
- [225] Werner Porod. “SPheno, a program for calculating supersymmetric spectra, SUSY particle decays and SUSY particle production at  $e^+e^-$  colliders”. In: *Comput. Phys. Commun.* 153 (2003), pp. 275–315. DOI: 10.1016/S0010-4655(03)00222-4. arXiv: hep-ph/0301101.
- [226] W. Porod and F. Staub. “SPheno 3.1: Extensions including flavour, CP-phases and models beyond the MSSM”. In: *Comput. Phys. Commun.* 183 (2012), pp. 2458–2469. DOI: 10.1016/j.cpc.2012.05.021. arXiv: 1104.1573 [hep-ph].
- [227] Geneviève Bélanger et al. “micrOMEGAs5.0 : Freeze-in”. In: *Comput. Phys. Commun.* 231 (2018), pp. 173–186. DOI: 10.1016/j.cpc.2018.04.027. arXiv: 1801.03509 [hep-ph].
- [228] G. Abbiendi et al. “Search for stable and longlived massive charged particles in  $e^+e^-$  collisions at  $\sqrt{s} = 130\text{--}209\text{ GeV}$ ”. In: *Phys. Lett. B* 572 (2003), pp. 8–20. DOI: 10.1016/S0370-2693(03)00639-7. arXiv: hep-ex/0305031.
- [229] Avelino Vicente and Carlos E. Yaguna. “Probing the scotogenic model with lepton flavor violating processes”. In: *JHEP* 02 (2015), p. 144. DOI: 10.1007/JHEP02(2015)144. arXiv: 1412.2545 [hep-ph].
- [230] Ernest Ma and Daijiro Suematsu. “Fermion Triplet Dark Matter and Radiative Neutrino Mass”. In: *Mod. Phys. Lett. A* 24 (2009), pp. 583–589. DOI: 10.1142/S021773230903059X. arXiv: 0809.0942 [hep-ph].

- [231] Yasaman Farzan. “A Minimal model linking two great mysteries: neutrino mass and dark matter”. In: *Phys. Rev. D* 80 (2009), p. 073009. DOI: 10.1103/PhysRevD.80.073009. arXiv: 0908.3729 [hep-ph].
- [232] C. El Aisati, C. Garcia-Cely, T. Hambye, L. Vanderheyden. “Prospects for discovering a neutrino line induced by dark matter annihilation”. In: *JCAP* 10 (2017), p. 021. DOI: 10.1088/1475-7516/2017/10/021. arXiv: 1706.06600 [hep-ph].
- [233] Manfred Lindner, Alexander Merle, and Viviana Niro. “Enhancing Dark Matter Annihilation into Neutrinos”. In: *Phys. Rev. D* 82 (2010), p. 123529. DOI: 10.1103/PhysRevD.82.123529. arXiv: 1005.3116 [hep-ph].
- [234] Chiara Arina, Suchita Kulkarni, and Joseph Silk. “Monochromatic neutrino lines from sneutrino dark matter”. In: *Phys. Rev. D* 92.8 (2015), p. 083519. DOI: 10.1103/PhysRevD.92.083519. arXiv: 1506.08202 [astro-ph.HE].
- [235] Yasaman Farzan. “Flavoring Monochromatic Neutrino Flux from Dark Matter Annihilation”. In: *JHEP* 02 (2012), p. 091. DOI: 10.1007/JHEP02(2012)091. arXiv: 1111.1063 [hep-ph].
- [236] Sarah Andreas, Michel H.G. Tytgat, and Quentin Swillens. “Neutrinos from Inert Doublet Dark Matter”. In: *JCAP* 04 (2009), p. 004. DOI: 10.1088/1475-7516/2009/04/004. arXiv: 0901.1750 [hep-ph].
- [237] A. Albert et al. “Search for Dark Matter Annihilation in the Earth using the ANTARES Neutrino Telescope”. In: *Phys. Dark Univ.* 16 (2017), pp. 41–48. DOI: 10.1016/j.dark.2017.04.005. arXiv: 1612.06792 [hep-ex].
- [238] S. Adrian-Martinez et al. “Search of Dark Matter Annihilation in the Galactic Centre using the ANTARES Neutrino Telescope”. In: *JCAP* 10 (2015), p. 068. DOI: 10.1088/1475-7516/2015/10/068. arXiv: 1505.04866 [astro-ph.HE].
- [239] A. Albert et al. “Combined search for neutrinos from dark matter self-annihilation in the Galactic Center with ANTARES and IceCube”. In: *Phys. Rev. D* 102.8 (2020), p. 082002. DOI: 10.1103/PhysRevD.102.082002. arXiv: 2003.06614 [astro-ph.HE].
- [240] T. de Boer et al. “Indirect detection constraints on the scotogenic dark matter model”. In: (May 2021). arXiv: 2105.04899 [hep-ph].
- [241] David Tucker-Smith and Neal Weiner. “Inelastic dark matter”. In: *Phys. Rev. D* 64 (2001), p. 043502. DOI: 10.1103/PhysRevD.64.043502. arXiv: hep-ph/0101138.
- [242] Prateek Agrawal et al. “A Classification of Dark Matter Candidates with Primarily Spin-Dependent Interactions with Matter”. In: (Mar. 2010). arXiv: 1003.1912 [hep-ph].
- [243] Marat Freytsis and Zoltan Ligeti. “On dark matter models with uniquely spin-dependent detection possibilities”. In: *Phys. Rev. D* 83 (2011), p. 115009. DOI: 10.1103/PhysRevD.83.115009. arXiv: 1012.5317 [hep-ph].
- [244] Mikhail A. Shifman, A. I. Vainshtein, and Valentin I. Zakharov. “Remarks on Higgs Boson Interactions with Nucleons”. In: *Phys. Lett. B* 78 (1978), pp. 443–446. DOI: 10.1016/0370-2693(78)90481-1.



- [245] Andrew Gould. “Resonant Enhancements in Weakly Interacting Massive Particle Capture by the Earth”. In: *ApJ* 321 (Oct. 1987), p. 571. DOI: 10.1086/165653.
- [246] Shmuel Nussinov, Lian-Tao Wang, and Itay Yavin. “Capture of Inelastic Dark Matter in the Sun”. In: *JCAP* 08 (2009), p. 037. DOI: 10.1088/1475-7516/2009/08/037. arXiv: 0905.1333 [hep-ph].
- [247] Arjun Menon et al. “Capture and Indirect Detection of Inelastic Dark Matter”. In: *Phys. Rev. D* 82 (2010), p. 015011. DOI: 10.1103/PhysRevD.82.015011. arXiv: 0905.1847 [hep-ph].
- [248] Jing Shu, Peng-fei Yin, and Shou-hua Zhu. “Neutrino Constraints on Inelastic Dark Matter after CDMS II”. In: *Phys. Rev. D* 81 (2010), p. 123519. DOI: 10.1103/PhysRevD.81.123519. arXiv: 1001.1076 [hep-ph].
- [249] Mattias Blennow, Stefan Clementz, and Juan Herrero-Garcia. “The distribution of inelastic dark matter in the Sun”. In: *Eur. Phys. J. C* 78.5 (2018). [Erratum: *Eur.Phys.J.C* 79, 407 (2019)], p. 386. DOI: 10.1140/epjc/s10052-018-5863-4. arXiv: 1802.06880 [hep-ph].
- [250] Alexander Belyaev, Neil D. Christensen, and Alexander Pukhov. “CalcHEP 3.4 for collider physics within and beyond the Standard Model”. In: *Comput. Phys. Commun.* 184 (2013), pp. 1729–1769. DOI: 10.1016/j.cpc.2013.01.014. arXiv: 1207.6082 [hep-ph].
- [251] Torsten Bringmann et al. “DarkSUSY 6 : An Advanced Tool to Compute Dark Matter Properties Numerically”. In: *JCAP* 07 (2018), p. 033. DOI: 10.1088/1475-7516/2018/07/033. arXiv: 1802.03399 [hep-ph].
- [252] G. Bélanger et al. “Limits on dark matter proton scattering from neutrino telescopes using micrOMEGAs”. In: *JCAP* 12 (2015), p. 036. DOI: 10.1088/1475-7516/2015/12/036. arXiv: 1507.07987 [hep-ph].
- [253] T. de Boer et al. “New constraints on radiative seesaw models from IceCube and other neutrino detectors”. In: *Phys. Rev. D* 103.12 (2021), p. 123006. DOI: 10.1103/PhysRevD.103.123006. arXiv: 2103.06881 [hep-ph].
- [254] Bugaev, Edgar and Montaruli, Teresa and Shlepin, Yuri and Sokalski, Igor A. “Propagation of tau neutrinos and tau leptons through the earth and their detection in underwater / ice neutrino telescopes”. In: *Astropart. Phys.* 21 (2004), pp. 491–509. DOI: 10.1016/j.astropartphys.2004.03.002. arXiv: hep-ph/0312295.
- [255] Marco Cirelli et al. “Spectra of neutrinos from dark matter annihilations”. In: *Nucl. Phys. B* 727 (2005). [Erratum: *Nucl.Phys.B* 790, 338–344 (2008)], pp. 99–138. DOI: 10.1016/j.nuclphysb.2007.10.001. arXiv: hep-ph/0506298.
- [256] Michael Klasen et al. “Scalar dark matter and fermion coannihilations in the radiative seesaw model”. In: *JCAP* 04 (2013), p. 044. DOI: 10.1088/1475-7516/2013/04/044. arXiv: 1302.5298 [hep-ph].
- [257] J. Harz et al. “Theoretical uncertainty of the supersymmetric dark matter relic density from scheme and scale variations”. In: *Phys. Rev. D* 93.11 (2016), p. 114023. DOI: 10.1103/PhysRevD.93.114023. arXiv: 1602.08103 [hep-ph].

- [258] Marcela Carena et al. “Invisible Z boson decays at  $e^+e^-$  colliders”. In: *Phys. Rev. D* 68 (2003), p. 113007. DOI: 10.1103/PhysRevD.68.113007. arXiv: hep-ph/0308053.
- [259] Qing-Hong Cao, Ernest Ma, and G. Rajasekaran. “Observing the Dark Scalar Doublet and its Impact on the Standard-Model Higgs Boson at Colliders”. In: *Phys. Rev. D* 76 (2007), p. 095011. DOI: 10.1103/PhysRevD.76.095011. arXiv: 0708.2939 [hep-ph].
- [260] Erik Lundstrom, Michael Gustafsson, and Joakim Edsjo. “The Inert Doublet Model and LEP II Limits”. In: *Phys. Rev. D* 79 (2009), p. 035013. DOI: 10.1103/PhysRevD.79.035013. arXiv: 0810.3924 [hep-ph].
- [261] “Combination of searches for invisible Higgs boson decays with the ATLAS experiment”. In: (Oct. 2020).
- [262] E. Aprile et al. “Implications on Inelastic Dark Matter from 100 Live Days of XENON100 Data”. In: *Phys. Rev. D* 84 (2011), p. 061101. DOI: 10.1103/PhysRevD.84.061101. arXiv: 1104.3121 [astro-ph.CO].
- [263] E. Aprile et al. “Effective field theory search for high-energy nuclear recoils using the XENON100 dark matter detector”. In: *Phys. Rev. D* 96.4 (2017), p. 042004. DOI: 10.1103/PhysRevD.96.042004. arXiv: 1705.02614 [astro-ph.CO].
- [264] Xun Chen et al. “Exploring the dark matter inelastic frontier with 79.6 days of PandaX-II data”. In: *Phys. Rev. D* 96.10 (2017), p. 102007. DOI: 10.1103/PhysRevD.96.102007. arXiv: 1708.05825 [hep-ex].
- [265] R. Bernabei et al. “Improved model-dependent corollary analyses after the first six annual cycles of DAMA/LIBRA-phase2”. In: *Nucl. Phys. Atom. Energy* 20.4 (2019), pp. 317–348. DOI: 10.15407/jnpae2019.04.317. arXiv: 1907.06405 [hep-ph].
- [266] E. Barbosa de Souza et al. “First search for a dark matter annual modulation signal with NaI(Tl) in the Southern Hemisphere by DM-Ice17”. In: *Phys. Rev. D* 95.3 (2017), p. 032006. DOI: 10.1103/PhysRevD.95.032006. arXiv: 1602.05939 [physics.ins-det].
- [267] G. Adhikari et al. “Search for a Dark Matter-Induced Annual Modulation Signal in NaI(Tl) with the COSINE-100 Experiment”. In: *Phys. Rev. Lett.* 123.3 (2019), p. 031302. DOI: 10.1103/PhysRevLett.123.031302. arXiv: 1903.10098 [astro-ph.IM].
- [268] J. Amare et al. “Annual Modulation Results from Three Years Exposure of ANAIS-112”. In: *Phys. Rev. D* 103.10 (2021), p. 102005. DOI: 10.1103/PhysRevD.103.102005. arXiv: 2103.01175 [astro-ph.IM].
- [269] S. Adrian-Martinez et al. “Limits on Dark Matter Annihilation in the Sun using the ANTARES Neutrino Telescope”. In: *Phys. Lett. B* 759 (2016), pp. 69–74. DOI: 10.1016/j.physletb.2016.05.019. arXiv: 1603.02228 [astro-ph.HE].
- [270] K. Choi et al. “Search for neutrinos from annihilation of captured low-mass dark matter particles in the Sun by Super-Kamiokande”. In: *Phys. Rev. Lett.* 114.14 (2015), p. 141301. DOI: 10.1103/PhysRevLett.114.141301. arXiv: 1503.04858 [hep-ex].
- [271] Sunghyun Kang, S. Scopel, and Gaurav Tomar. “Probing DAMA/LIBRA data in the full parameter space of WIMP effective models of inelastic scattering”. In: *Phys. Rev. D* 99.10 (2019), p. 103019. DOI: 10.1103/PhysRevD.99.103019. arXiv: 1902.09121 [hep-ph].

- [272] Felix Kahlhoefer et al. “Model-independent comparison of annual modulation and total rate with direct detection experiments”. In: *JCAP* 05 (2018), p. 074. DOI: 10.1088/1475-7516/2018/05/074. arXiv: 1802.10175 [hep-ph].
- [273] Sunghyun Kang et al. “DAMA/LIBRA-phase2 in WIMP effective models”. In: *JCAP* 07 (2018), p. 016. DOI: 10.1088/1475-7516/2018/07/016. arXiv: 1804.07528 [hep-ph].
- [274] Chiara Arina, Fu-Sin Ling, and Michel H. G. Tytgat. “IDM and iDM or The Inert Doublet Model and Inelastic Dark Matter”. In: *JCAP* 10 (2009), p. 018. DOI: 10.1088/1475-7516/2009/10/018. arXiv: 0907.0430 [hep-ph].
- [275] Tsuyoshi Hashimoto and Daijiro Suematsu. “Inflation and DM phenomenology in a scotogenic model extended with a real singlet scalar”. In: *Phys. Rev. D* 102.11 (2020), p. 115041. DOI: 10.1103/PhysRevD.102.115041. arXiv: 2009.13057 [hep-ph].
- [276] Carlos E. Yaguna. “Isospin-violating dark matter in the light of recent data”. In: *Phys. Rev. D* 95.5 (2017), p. 055015. DOI: 10.1103/PhysRevD.95.055015. arXiv: 1610.08683 [hep-ph].
- [277] Joseph Bramante et al. “Inelastic frontier: Discovering dark matter at high recoil energy”. In: *Phys. Rev. D* 94.11 (2016), p. 115026. DOI: 10.1103/PhysRevD.94.115026. arXiv: 1608.02662 [hep-ph].
- [278] Sebastian Baum, Katherine Freese, and Chris Kelso. “Dark Matter implications of DAMA/LIBRA-phase2 results”. In: *Phys. Lett. B* 789 (2019), pp. 262–269. DOI: 10.1016/j.physletb.2018.12.036. arXiv: 1804.01231 [astro-ph.CO].
- [279] G. Adhikari et al. “COSINE-100 and DAMA/LIBRA-phase2 in WIMP effective models”. In: *JCAP* 06 (2019), p. 048. DOI: 10.1088/1475-7516/2019/06/048. arXiv: 1904.00128 [hep-ph].
- [280] M. Antonello et al. “Characterization of SABRE crystal NaI-33 with direct underground counting”. In: *Eur. Phys. J. C* 81.4 (2021), p. 299. DOI: 10.1140/epjc/s10052-021-09098-5. arXiv: 2012.02610 [physics.ins-det].
- [281] Juri Fiaschi, Michael Klasen, and Simon May. “Singlet-doublet fermion and triplet scalar dark matter with radiative neutrino masses”. In: *JHEP* 05 (2019), p. 015. DOI: 10.1007/JHEP05(2019)015. arXiv: 1812.11133 [hep-ph].
- [282] Marco Cirelli, Nicolao Fornengo, and Alessandro Strumia. “Minimal dark matter”. In: *Nucl. Phys. B* 753 (2006), pp. 178–194. DOI: 10.1016/j.nuclphysb.2006.07.012. arXiv: hep-ph/0512090.
- [283] Kenny C. Y. Ng et al. “Solar Atmospheric Neutrinos: A New Neutrino Floor for Dark Matter Searches”. In: *Phys. Rev. D* 96.10 (2017), p. 103006. DOI: 10.1103/PhysRevD.96.103006. arXiv: 1703.10280 [astro-ph.HE].
- [284] Francesc Ferrer, Alejandro Ibarra, and Sebastian Wild. “A novel approach to derive halo-independent limits on dark matter properties”. In: *JCAP* 09 (2015), p. 052. DOI: 10.1088/1475-7516/2015/09/052. arXiv: 1506.03386 [hep-ph].

- [285] M. G. Aartsen et al. “Velocity Independent Constraints on Spin-Dependent DM-Nucleon Interactions from IceCube and PICO”. In: *Eur. Phys. J. C* 80.9 (2020), p. 819. DOI: 10.1140/epjc/s10052-020-8069-5. arXiv: 1907.12509 [astro-ph.HE].
- [286] Celine Boehm et al. “MeV dark matter: Has it been detected?”. In: *Phys. Rev. Lett.* 92 (2004), p. 101301. DOI: 10.1103/PhysRevLett.92.101301. arXiv: astro-ph/0309686.
- [287] M. Drewes et al. “A White Paper on keV Sterile Neutrino Dark Matter”. In: *JCAP* 01 (2017), p. 025. DOI: 10.1088/1475-7516/2017/01/025. arXiv: 1602.04816 [hep-ph].
- [288] Juri Fiaschi et al. “MeV neutrino dark matter: Relic density, lepton flavour violation and electron recoil”. In: *JHEP* 11 (2019), p. 129. DOI: 10.1007/JHEP11(2019)129. arXiv: 1908.09882 [hep-ph].
- [289] Jisuke Kubo, Ernest Ma, and Daijiro Suematsu. “Cold Dark Matter, Radiative Neutrino Mass,  $\mu \rightarrow e\gamma$ , and Neutrinoless Double Beta Decay”. In: *Phys. Lett. B* 642 (2006), pp. 18–23. DOI: 10.1016/j.physletb.2006.08.085. arXiv: hep-ph/0604114.
- [290] Joachim Kopp et al. “DAMA/LIBRA and leptonically interacting Dark Matter”. In: *Phys. Rev. D* 80 (2009), p. 083502. DOI: 10.1103/PhysRevD.80.083502. arXiv: 0907.3159 [hep-ph].
- [291] Rouven Essig, Jeremy Mardon, and Tomer Volansky. “Direct Detection of Sub-GeV Dark Matter”. In: *Phys. Rev. D* 85 (2012), p. 076007. DOI: 10.1103/PhysRevD.85.076007. arXiv: 1108.5383 [hep-ph].
- [292] Samuel K. Lee et al. “Modulation Effects in Dark Matter-Electron Scattering Experiments”. In: *Phys. Rev. D* 92.8 (2015), p. 083517. DOI: 10.1103/PhysRevD.92.083517. arXiv: 1508.07361 [hep-ph].
- [293] Abdesslam Arhrib et al. “Radiative Model of Neutrino Mass with Neutrino Interacting MeV Dark Matter”. In: *JCAP* 04 (2016), p. 049. DOI: 10.1088/1475-7516/2016/04/049. arXiv: 1512.08796 [hep-ph].
- [294] Morad Aaboud et al. “Combination of searches for invisible Higgs boson decays with the ATLAS experiment”. In: *Phys. Rev. Lett.* 122.23 (2019), p. 231801. DOI: 10.1103/PhysRevLett.122.231801. arXiv: 1904.05105 [hep-ex].
- [295] Albert M Sirunyan et al. “Combined measurements of Higgs boson couplings in proton–proton collisions at  $\sqrt{s} = 13$  TeV”. In: *Eur. Phys. J. C* 79.5 (2019), p. 421. DOI: 10.1140/epjc/s10052-019-6909-y. arXiv: 1809.10733 [hep-ex].
- [296] C. Boehm, Pierre Fayet, and R. Schaeffer. “Constraining dark matter candidates from structure formation”. In: *Phys. Lett. B* 518 (2001), pp. 8–14. DOI: 10.1016/S0370-2693(01)01060-7. arXiv: astro-ph/0012504.
- [297] Celine Boehm and Richard Schaeffer. “Constraints on dark matter interactions from structure formation: Damping lengths”. In: *Astron. Astrophys.* 438 (2005), pp. 419–442. DOI: 10.1051/0004-6361:20042238. arXiv: astro-ph/0410591.
- [298] D. Barducci et al. “Collider limits on new physics within micrOMEGAs 4.3”. In: *Comput. Phys. Commun.* 222 (2018), pp. 327–338. DOI: 10.1016/j.cpc.2017.08.028. arXiv: 1606.03834 [hep-ph].

- [299] Akira Sato. “Muon storage ring PRISM-FFAG to improve a sensitivity of mu-e conversion experiment below  $10^{*-17}$ ”. In: *PoS Nufact08* (2008). Ed. by Amos Breskin et al., p. 105. DOI: 10.22323/1.074.0105.
- [300] E. Aprile et al. “Low-mass dark matter search using ionization signals in XENON100”. In: *Phys. Rev. D* 94.9 (2016). [Erratum: *Phys.Rev.D* 95, 059901 (2017)], p. 092001. DOI: 10.1103/PhysRevD.94.092001. arXiv: 1605.06262 [astro-ph.CO].
- [301] J. I. Read. “The Local Dark Matter Density”. In: *J. Phys. G* 41 (2014), p. 063101. DOI: 10.1088/0954-3899/41/6/063101. arXiv: 1404.1938 [astro-ph.GA].
- [302] C. F. Bunge, J. A. Barrientos, and A. V. Bunge. “Roothaan-Hartree-Fock Ground-State Atomic Wave Functions: Slater-Type Orbital Expansions and Expectation Values for  $Z = 2-54$ ”. In: *Atom. Data Nucl. Data Tabl.* 53 (1993), pp. 113–162. DOI: 10.1006/adnd.1993.1003.
- [303] Martin C. Smith et al. “The RAVE Survey: Constraining the Local Galactic Escape Speed”. In: *Mon. Not. Roy. Astron. Soc.* 379 (2007), pp. 755–772. DOI: 10.1111/j.1365-2966.2007.11964.x. arXiv: astro-ph/0611671.
- [304] E. Aprile et al. “Exclusion of Leptophilic Dark Matter Models using XENON100 Electronic Recoil Data”. In: *Science* 349.6250 (2015), pp. 851–854. DOI: 10.1126/science.aab2069. arXiv: 1507.07747 [astro-ph.CO].
- [305] P. Agnes et al. “Constraints on Sub-GeV Dark-Matter–Electron Scattering from the DarkSide-50 Experiment”. In: *Phys. Rev. Lett.* 121.11 (2018), p. 111303. DOI: 10.1103/PhysRevLett.121.111303. arXiv: 1802.06998 [astro-ph.CO].
- [306] Marco Battaglieri et al. “US Cosmic Visions: New Ideas in Dark Matter 2017: Community Report”. In: *U.S. Cosmic Visions: New Ideas in Dark Matter*. July 2017. arXiv: 1707.04591 [hep-ph].
- [307] K. Ni. <http://www-kam2.icrr.u-tokyo.ac.jp/indico/event/3/session/45/contribution/390/material/slide1.pdf> talk given at TAUP. 2019.
- [308] Laura Baudis et al. “Response of liquid xenon to Compton electrons down to 1.5 keV”. In: *Phys. Rev. D* 87.11 (2013), p. 115015. DOI: 10.1103/PhysRevD.87.115015. arXiv: 1303.6891 [astro-ph.IM].
- [309] E. Aprile et al. “Removing krypton from xenon by cryogenic distillation to the ppq level”. In: *Eur. Phys. J. C* 77.5 (2017), p. 275. DOI: 10.1140/epjc/s10052-017-4757-1. arXiv: 1612.04284 [physics.ins-det].
- [310] E. Aprile et al. “First Axion Results from the XENON100 Experiment”. In: *Phys. Rev. D* 90.6 (2014). [Erratum: *Phys.Rev.D* 95, 029904 (2017)], p. 062009. DOI: 10.1103/PhysRevD.90.062009. arXiv: 1404.1455 [astro-ph.CO].
- [311] M. Szydagis et al. “NEST: A Comprehensive Model for Scintillation Yield in Liquid Xenon”. In: *JINST* 6 (2011), P10002. DOI: 10.1088/1748-0221/6/10/P10002. arXiv: 1106.1613 [physics.ins-det].
- [312] E. Aprile et al. “XENON1T dark matter data analysis: Signal and background models and statistical inference”. In: *Phys. Rev. D* 99.11 (2019), p. 112009. DOI: 10.1103/PhysRevD.99.112009. arXiv: 1902.11297 [physics.ins-det].

- [313] Gary J. Feldman and Robert D. Cousins. “A Unified approach to the classical statistical analysis of small signals”. In: *Phys. Rev. D* 57 (1998), pp. 3873–3889. DOI: 10.1103/PhysRevD.57.3873. arXiv: physics/9711021.
- [314] E. Aprile et al. “Observation and applications of single-electron charge signals in the XENON100 experiment”. In: *J. Phys. G* 41 (2014), p. 035201. DOI: 10.1088/0954-3899/41/3/035201. arXiv: 1311.1088 [physics.ins-det].
- [315] J. Angle et al. “A search for light dark matter in XENON10 data”. In: *Phys. Rev. Lett.* 107 (2011). [Erratum: *Phys.Rev.Lett.* 110, 249901 (2013)], p. 051301. DOI: 10.1103/PhysRevLett.107.051301. arXiv: 1104.3088 [astro-ph.CO].
- [316] Orr Abramoff et al. “SENSEI: Direct-Detection Constraints on Sub-GeV Dark Matter from a Shallow Underground Run Using a Prototype Skipper-CCD”. In: *Phys. Rev. Lett.* 122.16 (2019), p. 161801. DOI: 10.1103/PhysRevLett.122.161801. arXiv: 1901.10478 [hep-ex].
- [317] A. Aguilar-Arevalo et al. “First Direct-Detection Constraints on eV-Scale Hidden-Photon Dark Matter with DAMIC at SNOLAB”. In: *Phys. Rev. Lett.* 118.14 (2017), p. 141803. DOI: 10.1103/PhysRevLett.118.141803. arXiv: 1611.03066 [astro-ph.CO].
- [318] R. Agnese et al. “New Results from the Search for Low-Mass Weakly Interacting Massive Particles with the CDMS Low Ionization Threshold Experiment”. In: *Phys. Rev. Lett.* 116.7 (2016), p. 071301. DOI: 10.1103/PhysRevLett.116.071301. arXiv: 1509.02448 [astro-ph.CO].
- [319] Yonit Hochberg et al. “Detecting Superlight Dark Matter with Fermi-Degenerate Materials”. In: *JHEP* 08 (2016), p. 057. DOI: 10.1007/JHEP08(2016)057. arXiv: 1512.04533 [hep-ph].
- [320] Michael Klasen, Florian Lyonnet, and Farinaldo S. Queiroz. “NLO+NLL collider bounds, Dirac fermion and scalar dark matter in the B–L model”. In: *Eur. Phys. J. C* 77.5 (2017), p. 348. DOI: 10.1140/epjc/s10052-017-4904-8. arXiv: 1607.06468 [hep-ph].
- [321] E. Aprile et al. “ $^{222}\text{Rn}$  emanation measurements for the XENON1T experiment”. In: *Eur. Phys. J. C* 81.4 (2021), p. 337. DOI: 10.1140/epjc/s10052-020-08777-z. arXiv: 2009.13981 [physics.ins-det].
- [322] E. Aprile et al. “XENON1T dark matter data analysis: Signal and background models and statistical inference”. In: *Phys. Rev. D* 99.11 (2019), p. 112009. DOI: 10.1103/PhysRevD.99.112009. arXiv: 1902.11297 [physics.ins-det].
- [323] K. Abe et al. “Radon removal from gaseous xenon with activated charcoal”. In: *Nuclear Instruments and Methods in Physics Research Section A: Accelerators, Spectrometers, Detectors and Associated Equipment* 661.1 (2012), pp. 50–57. ISSN: 0168-9002. DOI: <https://doi.org/10.1016/j.nima.2011.09.051>. URL: <https://www.sciencedirect.com/science/article/pii/S0168900211018468>.
- [324] E. Aprile et al. “Online  $^{222}\text{Rn}$  removal by cryogenic distillation in the XENON100 experiment”. In: *Eur. Phys. J. C* 77.6 (2017), p. 358. DOI: 10.1140/epjc/s10052-017-4902-x. arXiv: 1702.06942 [physics.ins-det].

- [325] D. Schulte et al. “Ultra-clean radon-free four cylinder magnetically-coupled piston pump”. In: (July 2021). arXiv: 2107.00755 [physics.ins-det].
- [326] E. H. Bellamy et al. “Absolute calibration and monitoring of a spectrometric channel using a photomultiplier”. In: *Nucl. Instrum. Meth. A* 339 (1994), pp. 468–476. DOI: 10.1016/0168-9002(94)90183-X.
- [327] L.P. Ekström S.Y.F. Chu and R.B. Firestone. *The Lund/LBNL Nuclear Data Search*. 1999.
- [328] J.R. Bankwitz. *Investigation of  $^{220}\text{Rn}$  decays with the Münster xenon TPC and scintillation calibration detectors*, BSc thesis. 2018.
- [329] Ernest Ma. “Z(3) Dark Matter and Two-Loop Neutrino Mass”. In: *Phys. Lett. B* 662 (2008), pp. 49–52. DOI: 10.1016/j.physletb.2008.02.053. arXiv: 0708.3371 [hep-ph].
- [330] Genevieve Belanger et al. “Z<sub>3</sub> Scalar Singlet Dark Matter”. In: *JCAP* 01 (2013), p. 022. DOI: 10.1088/1475-7516/2013/01/022. arXiv: 1211.1014 [hep-ph].
- [331] Geneviève Bélanger et al. “Minimal semi-annihilating  $\mathbb{Z}_N$  scalar dark matter”. In: *JCAP* 06 (2014), p. 021. DOI: 10.1088/1475-7516/2014/06/021. arXiv: 1403.4960 [hep-ph].
- [332] Ernest Ma. “Dark Scalar Doublets and Neutrino Tribimaximal Mixing from A(4) Symmetry”. In: *Phys. Lett. B* 671 (2009), pp. 366–368. DOI: 10.1016/j.physletb.2008.12.038. arXiv: 0808.1729 [hep-ph].
- [333] Ernest Ma. “Radiative Mixing of the One Higgs Boson and Emergent Self-Interacting Dark Matter”. In: *Phys. Lett. B* 754 (2016), pp. 114–117. DOI: 10.1016/j.physletb.2016.01.033. arXiv: 1506.06658 [hep-ph].
- [334] Manfred Lindner, Daniel Schmidt, and Thomas Schwetz. “Dark Matter and neutrino masses from global U(1) B-L symmetry breaking”. In: *Phys. Lett. B* 705 (2011), pp. 324–330. DOI: 10.1016/j.physletb.2011.10.022. arXiv: 1105.4626 [hep-ph].
- [335] D. Aristizabal Sierra et al. “Dynamical flavor origin of  $\mathbb{Z}_N$  symmetries”. In: *Phys. Rev. D* 91.9 (2015), p. 096004. DOI: 10.1103/PhysRevD.91.096004. arXiv: 1412.5600 [hep-ph].
- [336] Ernest Ma, Ivica Picek, and Branimir Radovčić. “New Scotogenic Model of Neutrino Mass with  $U(1)_D$  Gauge Interaction”. In: *Phys. Lett. B* 726 (2013), pp. 744–746. DOI: 10.1016/j.physletb.2013.09.049. arXiv: 1308.5313 [hep-ph].
- [337] Ernest Ma. “Leptonic Source of Dark Matter and Radiative Majorana or Dirac Neutrino Mass”. In: *Phys. Lett. B* 809 (2020), p. 135736. DOI: 10.1016/j.physletb.2020.135736. arXiv: 1912.11950 [hep-ph].
- [338] Ernest Ma. “Gauged lepton number, Dirac neutrinos, dark matter, and muon g-2”. In: *Phys. Lett. B* 819 (2021), p. 136402. DOI: 10.1016/j.physletb.2021.136402. arXiv: 2104.10324 [hep-ph].
- [339] Shu-Yu Ho, Takashi Toma, and Koji Tsumura. “Systematic  $U(1)_{B-L}$  extensions of loop-induced neutrino mass models with dark matter”. In: *Phys. Rev. D* 94.3 (2016), p. 033007. DOI: 10.1103/PhysRevD.94.033007. arXiv: 1604.07894 [hep-ph].

- [340] Claudia Hagedorn et al. “Phenomenology of the Generalised Scotogenic Model with Fermionic Dark Matter”. In: *JHEP* 11 (2018), p. 103. DOI: 10.1007/JHEP11(2018)103. arXiv: 1804.04117 [hep-ph].
- [341] Vedran Brdar, Ivica Picek, and Branimir Radovic. “Radiative Neutrino Mass with Scotogenic Scalar Triplet”. In: *Phys. Lett. B* 728 (2014), pp. 198–201. DOI: 10.1016/j.physletb.2013.11.045. arXiv: 1310.3183 [hep-ph].
- [342] Nicolás Bernal, Julián Calle, and Diego Restrepo. “Anomaly-free Abelian gauge symmetries with Dirac scotogenic models”. In: *Phys. Rev. D* 103.9 (2021), p. 095032. DOI: 10.1103/PhysRevD.103.095032. arXiv: 2102.06211 [hep-ph].
- [343] Ernest Ma. “Linkage of Dirac Neutrinos to Dark U(1) Gauge Symmetry”. In: *Phys. Lett. B* 817 (2021), p. 136290. DOI: 10.1016/j.physletb.2021.136290. arXiv: 2101.12138 [hep-ph].
- [344] Cesar Bonilla et al. “Dark matter stability and Dirac neutrinos using only Standard Model symmetries”. In: *Phys. Rev. D* 101.3 (2020), p. 033011. DOI: 10.1103/PhysRevD.101.033011. arXiv: 1812.01599 [hep-ph].
- [345] Julian Calle et al. “Minimal radiative Dirac neutrino mass models”. In: *Phys. Rev. D* 99.7 (2019), p. 075008. DOI: 10.1103/PhysRevD.99.075008. arXiv: 1812.05523 [hep-ph].
- [346] Sudip Jana, P. K. Vishnu, and Shaikh Saad. “Minimal realizations of Dirac neutrino mass from generic one-loop and two-loop topologies at  $d = 5$ ”. In: *JCAP* 04 (2020), p. 018. DOI: 10.1088/1475-7516/2020/04/018. arXiv: 1910.09537 [hep-ph].
- [347] Matthew D. Schwartz. *Quantum Field Theory and the Standard Model*. Cambridge University Press, Mar. 2014. ISBN: 978-1-107-03473-0, 978-1-107-03473-0.
- [348] Edward Witten. “An SU(2) Anomaly”. In: *Phys. Lett. B* 117 (1982). Ed. by Mikhail A. Shifman, pp. 324–328. DOI: 10.1016/0370-2693(82)90728-6.
- [349] Ze-Peng Liu, Yue-Liang Wu, and Yu-Feng Zhou. “Sommerfeld enhancements with vector, scalar and pseudoscalar force-carriers”. In: *Phys. Rev. D* 88 (2013), p. 096008. DOI: 10.1103/PhysRevD.88.096008. arXiv: 1305.5438 [hep-ph].
- [350] Paul Langacker. “The Physics of Heavy  $Z'$  Gauge Bosons”. In: *Rev. Mod. Phys.* 81 (2009), pp. 1199–1228. DOI: 10.1103/RevModPhys.81.1199. arXiv: 0801.1345 [hep-ph].
- [351] Bob Holdom. “Two U(1)’s and Epsilon Charge Shifts”. In: *Phys. Lett. B* 166 (1986), pp. 196–198. DOI: 10.1016/0370-2693(86)91377-8.
- [352] Yann Mambrini. “The ZZ’ kinetic mixing in the light of the recent direct and indirect dark matter searches”. In: *JCAP* 1107 (2011), p. 009. DOI: 10.1088/1475-7516/2011/07/009. arXiv: 1104.4799 [hep-ph].
- [353] Juebin Lao et al. “Fermionic and scalar dark matter with hidden U(1) gauge interaction and kinetic mixing”. In: *Phys. Rev. D* 101.9 (2020), p. 095031. DOI: 10.1103/PhysRevD.101.095031. arXiv: 2003.02516 [hep-ph].



- [354] Jun-Xing Pan et al. “Scrutinizing a massless dark photon: basis independence”. In: *Nucl. Phys. B* 953 (2020), p. 114968. DOI: 10.1016/j.nuclphysb.2020.114968. arXiv: 1807.11363 [hep-ph].
- [355] B. Abi et al. “Measurement of the Positive Muon Anomalous Magnetic Moment to 0.46 ppm”. In: *Phys. Rev. Lett.* 126.14 (2021), p. 141801. DOI: 10.1103/PhysRevLett.126.141801. arXiv: 2104.03281 [hep-ex].
- [356] J. P. Lees et al. “Search for Invisible Decays of a Dark Photon Produced in  $e^+e^-$  Collisions at BaBar”. In: *Phys. Rev. Lett.* 119.13 (2017), p. 131804. DOI: 10.1103/PhysRevLett.119.131804. arXiv: 1702.03327 [hep-ex].
- [357] D. Banerjee et al. “Dark matter search in missing energy events with NA64”. In: *Phys. Rev. Lett.* 123.12 (2019), p. 121801. DOI: 10.1103/PhysRevLett.123.121801. arXiv: 1906.00176 [hep-ex].
- [358] Chuan-Hung Chen and Takaaki Nomura. “Influence of an inert charged Higgs boson on the muon  $g-2$  and radiative neutrino masses in a scotogenic model”. In: *Phys. Rev. D* 100.1 (2019), p. 015024. DOI: 10.1103/PhysRevD.100.015024. arXiv: 1903.03380 [hep-ph].
- [359] Fred Jegerlehner and Andreas Nyffeler. “The Muon  $g-2$ ”. In: *Phys. Rept.* 477 (2009), pp. 1–110. DOI: 10.1016/j.physrep.2009.04.003. arXiv: 0902.3360 [hep-ph].
- [360] Sean Tulin, Hai-Bo Yu, and Kathryn M. Zurek. “Beyond Collisionless Dark Matter: Particle Physics Dynamics for Dark Matter Halo Structure”. In: *Phys. Rev. D* 87.11 (2013), p. 115007. DOI: 10.1103/PhysRevD.87.115007. arXiv: 1302.3898 [hep-ph].
- [361] Manoj Kaplinghat, Sean Tulin, and Hai-Bo Yu. “Self-interacting Dark Matter Benchmarks”. In: (Aug. 2013). arXiv: 1308.0618 [hep-ph].
- [362] Lotty Ackerman et al. “Dark Matter and Dark Radiation”. In: *Phys. Rev. D* 79 (2009). Ed. by Hans Volker Klapdor-Kleingrothaus and Irina V. Krivosheina, p. 023519. DOI: 10.1103/PhysRevD.79.023519. arXiv: 0810.5126 [hep-ph].
- [363] Andrzej J. Buras et al. “Global analysis of leptophilic  $Z'$  bosons”. In: *JHEP* 06 (2021), p. 068. DOI: 10.1007/JHEP06(2021)068. arXiv: 2104.07680 [hep-ph].
- [364] Raul Costa et al. “Singlet Extensions of the Standard Model at LHC Run 2: Benchmarks and Comparison with the NMSSM”. In: *JHEP* 06 (2016), p. 034. DOI: 10.1007/JHEP06(2016)034. arXiv: 1512.05355 [hep-ph].
- [365] Georges Aad et al. “Constraints on new phenomena via Higgs boson couplings and invisible decays with the ATLAS detector”. In: *JHEP* 11 (2015), p. 206. DOI: 10.1007/JHEP11(2015)206. arXiv: 1509.00672 [hep-ex].
- [366] Kingman Cheung et al. “Bounds on Higgs-Portal models from the LHC Higgs data”. In: *JHEP* 10 (2015), p. 057. DOI: 10.1007/JHEP10(2015)057. arXiv: 1507.06158 [hep-ph].
- [367] D. López-Val and T. Robens. “ $\Delta r$  and the W-boson mass in the singlet extension of the standard model”. In: *Phys. Rev. D* 90 (2014), p. 114018. DOI: 10.1103/PhysRevD.90.114018. arXiv: 1406.1043 [hep-ph].

- [368] Dario Buttazzo, Filippo Sala, and Andrea Tesi. “Singlet-like Higgs bosons at present and future colliders”. In: *JHEP* 11 (2015), p. 158. DOI: 10.1007/JHEP11(2015)158. arXiv: 1505.05488 [hep-ph].
- [369] H. Georgi and S. L. Glashow. “Unity of All Elementary Particle Forces”. In: *Phys. Rev. Lett.* 32 (1974), pp. 438–441. DOI: 10.1103/PhysRevLett.32.438.
- [370] Harald Fritzsch and Peter Minkowski. “Unified Interactions of Leptons and Hadrons”. In: *Annals Phys.* 93 (1975), pp. 193–266. DOI: 10.1016/0003-4916(75)90211-0.
- [371] Riccardo Barbieri and Dimitri V. Nanopoulos. “An Exceptional Model for Grand Unification”. In: *Phys. Lett. B* 91 (1980), pp. 369–375. DOI: 10.1016/0370-2693(80)90998-3.
- [372] Jogesh C. Pati and Abdus Salam. “Lepton Number as the Fourth Color”. In: *Phys. Rev. D* 10 (1974). [Erratum: *Phys.Rev.D* 11, 703–703 (1975)], pp. 275–289. DOI: 10.1103/PhysRevD.10.275.
- [373] G. Senjanovic and Rabindra N. Mohapatra. “Exact Left-Right Symmetry and Spontaneous Violation of Parity”. In: *Phys. Rev. D* 12 (1975), p. 1502. DOI: 10.1103/PhysRevD.12.1502.
- [374] Paul Langacker. *The standard model and beyond*. 2010. ISBN: 978-1-4200-7906-7.
- [375] R. N. Mohapatra. *UNIFICATION AND SUPERSYMMETRY. THE FRONTIERS OF QUARK - LEPTON PHYSICS: The Frontiers of Quark-Lepton Physics*. Berlin: Springer, 1986. ISBN: 978-1-4757-1930-7, 978-1-4757-1928-4. DOI: 10.1007/978-1-4757-1928-4.
- [376] A. Takenaka et al. “Search for proton decay via  $p \rightarrow e^+ \pi^0$  and  $p \rightarrow \mu^+ \pi^0$  with an enlarged fiducial volume in Super-Kamiokande I-IV”. In: *Phys. Rev. D* 102.11 (2020), p. 112011. DOI: 10.1103/PhysRevD.102.112011. arXiv: 2010.16098 [hep-ex].
- [377] Daniël Boer, Ruud Peeters, and Sybrand Zeinstra. “Analysis of fine-tuning measures in models with extended Higgs sectors”. In: *Nucl. Phys. B* (2019), p. 114695. DOI: 10.1016/j.nuclphysb.2019.114695. arXiv: 1902.01258 [hep-ph].
- [378] Simone Biondini, Daniël Boer, and Ruud Peeters. “The hierarchy problem and fine-tuning in a decoupling approach to multi-scale effective potentials”. In: (Dec. 2020). arXiv: 2012.08441 [hep-ph].
- [379] Claudia Hagedorn et al. “Unification of Gauge Couplings in Radiative Neutrino Mass Models”. In: *JHEP* 09 (2016), p. 111. DOI: 10.1007/JHEP09(2016)111. arXiv: 1605.03986 [hep-ph].
- [380] Piotr H. Chankowski, Stefan Pokorski, and Jakub Wagner. “Z-prime and the Appelquist-Carrazzone decoupling”. In: *Eur. Phys. J. C* 47 (2006), pp. 187–205. DOI: 10.1140/epjc/s2006-02537-3. arXiv: hep-ph/0601097.
- [381] Robert Feger, Thomas W. Kephart, and Robert J. Saskowski. “LieART 2.0 – A Mathematica application for Lie Algebras and Representation Theory”. In: *Comput. Phys. Commun.* 257 (2020), p. 107490. DOI: 10.1016/j.cpc.2020.107490. arXiv: 1912.10969 [hep-th].

- [382] Tomas Jezo et al. “NLO+NLL limits on  $W'$  and  $Z'$  gauge boson masses in general extensions of the Standard Model”. In: *JHEP* 12 (2014), p. 092. DOI: 10.1007/JHEP12(2014)092. arXiv: 1410.4692 [hep-ph].
- [383] Daniel A. Camargo et al. “Collider bounds on 2-Higgs doublet models with  $U(1)_X$  gauge symmetries”. In: *Phys. Lett. B* 793 (2019), pp. 150–160. DOI: 10.1016/j.physletb.2019.04.048. arXiv: 1805.08231 [hep-ph].
- [384] Daniel A. Camargo et al. “A Two Higgs Doublet Model for Dark Matter and Neutrino Masses”. In: *Phys. Lett. B* 795 (2019), pp. 319–326. DOI: 10.1016/j.physletb.2019.06.020. arXiv: 1901.05476 [hep-ph].
- [385] G. Apollinari et al. “High Luminosity Large Hadron Collider HL-LHC”. In: *CERN Yellow Rep.* 5 (2015). Ed. by G Apollinari et al., pp. 1–19. DOI: 10.5170/CERN-2015-005.1. arXiv: 1705.08830 [physics.acc-ph].
- [386] Miguel D. Campos et al. “Neutrino Masses and Absence of Flavor Changing Interactions in the 2HDM from Gauge Principles”. In: *JHEP* 08 (2017), p. 092. DOI: 10.1007/JHEP08(2017)092. arXiv: 1705.05388 [hep-ph].
- [387] Kristjan Kannike. “Vacuum Stability Conditions From Copositivity Criteria”. In: *Eur. Phys. J. C* 72 (2012), p. 2093. DOI: 10.1140/epjc/s10052-012-2093-z. arXiv: 1205.3781 [hep-ph].
- [388] D. Jurčiukonis and L. Lavoura. “The three- and four-Higgs couplings in the general two-Higgs-doublet model”. In: *JHEP* 12 (2018), p. 004. DOI: 10.1007/JHEP12(2018)004. arXiv: 1807.04244 [hep-ph].
- [389] Anson Hook, Eder Izaguirre, and Jay G. Wacker. “Model Independent Bounds on Kinetic Mixing”. In: *Adv. High Energy Phys.* 2011 (2011), p. 859762. DOI: 10.1155/2011/859762. arXiv: 1006.0973 [hep-ph].
- [390] Daniel A. Camargo, Yann Mambrini, and Farinaldo S. Queiroz. “XENON1T takes a razor to a dark  $E_6$ -inspired model”. In: *Phys. Lett. B* 786 (2018), pp. 337–341. DOI: 10.1016/j.physletb.2018.09.057. arXiv: 1805.12162 [hep-ph].
- [391] Adam Alloul et al. “FeynRules 2.0 - A complete toolbox for tree-level phenomenology”. In: *Comput. Phys. Commun.* 185 (2014), pp. 2250–2300. DOI: 10.1016/j.cpc.2014.04.012. arXiv: 1310.1921 [hep-ph].
- [392] Johan Alwall et al. “MadGraph 5 : Going Beyond”. In: *JHEP* 06 (2011), p. 128. DOI: 10.1007/JHEP06(2011)128. arXiv: 1106.0522 [hep-ph].
- [393] Torbjorn Sjostrand, Stephen Mrenna, and Peter Z. Skands. “A Brief Introduction to PYTHIA 8.1”. In: *Comput. Phys. Commun.* 178 (2008), pp. 852–867. DOI: 10.1016/j.cpc.2008.01.036. arXiv: 0710.3820 [hep-ph].
- [394] J. de Favereau et al. “DELPHES 3, A modular framework for fast simulation of a generic collider experiment”. In: *JHEP* 02 (2014), p. 057. DOI: 10.1007/JHEP02(2014)057. arXiv: 1307.6346 [hep-ex].
- [395] Michelangelo L. Mangano et al. “Matching matrix elements and shower evolution for top-quark production in hadronic collisions”. In: *JHEP* 01 (2007), p. 013. DOI: 10.1088/1126-6708/2007/01/013. arXiv: hep-ph/0611129.

- [396] Tilman Plehn. “Lectures on LHC Physics”. In: *Lect. Notes Phys.* 844 (2012), pp. 1–193. DOI: 10.1007/978-3-642-24040-9. arXiv: 0910.4182 [hep-ph].
- [397] H. Schulze Eißing. *Investigations of the Münster dual phase xenon time projection chamber, BSc thesis*. 2017.

# Lebenslauf

PERSÖNLICHE DATEN	
Name	Sybrand Wessel Zeinstra
Geburtsdatum	06.12.1995
Geburtsort	Stadskanaal, NL
BERUFSERFAHRUNG	
seit 10.2018	Wissenschaftlicher Mitarbeiter Westfälische Wilhelms-Universität Münster
02.2015-04.2018	Studentischer Hilfskraft, Übungsgruppenleiter Rijksuniversiteit Groningen, NL
STUDIUM UND SCHULE	
seit 10.2018	Doktorarbeit: <i>Minimal models for dark matter and neutrino masses</i> Erster Gutachter: Prof. Dr. Michael Klasen Zweiter Gutachter: Priv.-Doz. Dr. Karol Kovařík
09.2016-08.2018	M.Sc. Physik an der Rijksuniversiteit Groningen Masterarbeit: <i>Studies of fine-tuning in extended Higgs models</i> Betreuer: Prof. Dr. Daniël Boer
09.2013-08.2016	B.Sc. Physik an der Rijksuniversiteit Groningen Bachelorarbeit: <i>Super-heavy dark matter as a source of ultra-high energy cosmic rays</i> Betreuer: Prof. Dr. Olaf Scholten
04.2014-06.2016	Honours College an der Rijksuniversiteit Groningen
2013	Hondsrug College Emmen (allgemeine Hochschulreife)